Contribution to the numerical modeling of Inertial Confinement Fusion

P.H. Maire

HABILITATION à DIRIGER des RECHERCHES

PRÉSENTÉE à

L'UNIVERSITÉ BORDEAUX I

ÉCOLE DOCTORALE DE MATHÉMATIQUES ET D'INFORMATIQUE

Par **Pierre-Henri Maire**

Contribution à la modélisation numérique de la Fusion par Confinement Inertiel.

Contribution to the numerical modeling of Inertial Confinement Fusion.

Soutenue le : 3 février 2011

Après avis des rapporteurs :

Matania Ben-Artzi ..	Professeur, Hebrew University of Jerusalem	
Thierry Colin	Professeur, Institut Polytechnique de Bordeaux	
Mikhail Shashkov	Senior Scientist, Los Alamos National Laboratory	

Devant la commission d'examen composée de :

Rémi Abgrall	Professeur, IPB	Examinateur
Matania Ben-Artzi ..	Professeur, Hebrew University of Jerusalem	Rapporteur
Thierry Colin	Professeur, IPB	Rapporteur
Bruno Després	Professeur, Université Paris VI	Examinateur
François Golse	Professeur, Ecole Polytechnique	Examinateur
Patrick Le Tallec ...	Professeur, Ecole Polytechnique	Examinateur
Charles Lion	Directeur du programme simulation, CEA	Examinateur
Olivier Pironneau ...	Professeur, Université Paris VI	Examinateur
Bernard Rebourcet .	Expert senior, CEA	Examinateur
Mikhail Shashkov	Senior Scientist, LANL	Rapporteur
Vladimir Tikhonchuk	Professeur, Université Bordeaux I	Examinateur

– 2011 –

To Hélène, my parents and my sisters

Acknowledgments

This work arose in part from years of research that has been performed during my six years stay at the CELIA laboratory of the University of Bordeaux. It has been a tremendous experience which could not have been achieved without the help and the support of many people.

First of all, I would like to express my gratitude to Guy Schurtz and Vladimir Tikhonchuk. Their constant support and their trust have greatly facilitated the development of the studies concerning new numerical methods at CELIA. Moreover, they are dynamic scientists who possess the gift of being able to make complex subjects, such as those related to plasma physics, understandable. I also wish to underline the major contribution of Guy Schurtz in the development of the CHIC code.

The long term work of Jérôme Breil and Stéphane Galera have made possible the implementation and the validation of these numerical methods in the CHIC code. It was a pleasure to exchange and work with them not only during their postdoctoral research but also after, and I hope that this will continue. I also really appreciated Ludovic Hallo enthusiasm, it was very stimulating to collaborate with him.

I would like to express my thanks and my gratitude to Rémi Sentis for having guided my first steps in applied mathematics during my PhD, seventeen years ago.

I met Rémi Abgrall for the first time in 2004 following the good advice of Professor Raviart. Rémi is not only a gifted applied mathematician but also an approachable and friendly person with whom I really appreciate to work. I am deeply grateful to him for having pushed and encouraged me to write this document. I hope that in the future we can pursue this fruitful collaboration.

I gratefully thank Matania Ben-Artzi, Thierry Colin and Mikhail Shashkov for having reviewed my work and for their constructive comments. I express my gratitude to Mikhail Shashkov for having invited me for long stays at Los Alamos National Laboratory. During these periods, I really appreciated his enthusiasm, he is a great scientist who knows how to motivate his co-workers to strive for excellence.

I would like also to thank François Golse, Charles Lion, Olivier Pironneau, Patrick Le Tallec for having accepted to be members of my committee in spite of their busy schedules. I am also indebted to Bernard Rebourcet, first for having made me discovered Lagrangian hydrodynamics fifteen years ago, second for his support and his advice during the writing of this document, particularly for his very careful reading of the manuscript.

The present work would not have been done without those initiated successively by Raphaël Loubère, Jean Ovadia, Constant Mazeran and Bruno Després concerning the development of cell-centered Lagrangian schemes. Here, I wish to acknowledge their major contributions to these new promising methods. I really enjoy to exchange and collaborate with them. Special thanks to Jean Ovadia with whom I spent almost a year to work daily on Lagrangian hydrodynamics. I want also to thank Boniface Nkonga, without whom the three-dimensional extension of the cell-centered scheme would not have been possible.

I want to warmly thank my Czech colleagues Richard Liska, Pavel Vachal and Milan

Kucharik with whom it was a pleasure to work with in Los Alamos as well as in Prague.

I would like to thank Didier Briand for his constant help not only as the network engineer of CELIA laboratory but also as a friend.

Finally, all my thoughts are with Helen, to thank her for her patience, support and encouragement that allowed me to conduct this work to completion.

Introduction

This document aims at presenting a part of the works that I undertook in the field of numerical modeling and simulation applied to the mechanics of highly-compressible fluids and high energy density plasmas, between 2003 and 2009 at Bordeaux University. At the start of 2003, I integrated the research unit CELIA (*CEntre des Lasers Intenses et Applications*), created and under joint supervision of the CEA (*Commissariat à l'Energie Atomique*), the University of Bordeaux, and the CNRS (*Centre National de la Recherche Scientifique*). More specifically, working in the Interaction-Inertial Confinement Fusion-Astrophysics group (*Interaction-Fusion par Confinement Inertiel-Astrophysique*) directed by Pr. Vladimir Tikhonchuk. The creation of this research unit, and the important participation of scientists of the CEA is a part of an academic research program engaged by the CEA in the context of the LMJ (*Laser Mega Joule*) program. The principle objective of this team concerns the numerical modeling and simulation of direct drive Inertial Confinement Fusion (ICF) applied to the production of energy by fusion. I took the responsibility for the conception and development of a multi-functional hydrodynamic code, named CHIC (*Code d'Hydrodynamique et d'Implosion du Celia*). Being coupled with various physical modules and diagnostic packages, this two-dimensional Lagrangian code allows the theoretical developments, conception and interpretation of various experiments in the domain of high energy density physics. After five years of collaborative work with Guy Schurtz and Jérôme Breil, the CHIC code has been developed, validated and became actually a backbone of the simulation capabilities of the plasma physics group of the CELIA. My research had as principle objective the conception and development of robust numerical schemes dedicated to the numerical simulation of experiments concerning the physics of hot dense plasma created by laser in the domain of ICF, laboratory astrophysics and laser processing. The physical processes at play in such systems are strongly coupled, complex and highly non-stationary. Let us emphasize that the hydrodynamic flow resulting from an ICF experiment is a source of very intense shock and rarefaction waves. This fluid flow undergoes unsteady phenomena with characteristic time scales ranging from 10^{-12} s to 10^{-8} s. These phenomena are characterized by very intense thermodynamic processes wherein the density of the material under consideration can be compressed up to several thousand times its nominal value, the pressure ranges from the atmospheric pressure (1 bar) to 100 Gbars and the temperatures may vary between 15 K and 500 MK. Furthermore, it is very difficult to realize them experimentally. This is a reason why numerical simulations are indispensable for both the conception and the interpretation of ICF experiments. Roughly speaking, the underlying two-dimensional mathematical model is a system of partial differential equations at the center of which we find the equations of compressible gas dynamics written under Lagrangian form, coupled to equations of electron and photon transport characterized by equations of non-linear diffusion. The main contribution of the present work consists of the development of two robust and accurate schemes devoted respectively to the numerical resolution of Lagrangian hydrodynamics and diffusion. The former numerical scheme is called EUCCLHYD (Explicit Unstructured Cell-Centered Lagrangian HYDrodynamics) whereas the latter is named CCLAD (Cell-Centered LAgrangian Diffusion).

The remainder of this document is organized as follows. In Chapter 1, we briefly describe the physical and numerical context related to ICF. Then, we present in Chapter 2 the Eulerian and Lagrangian forms of the conservation laws of fluid mechanics. The description of the EUCCLHYD scheme is performed in Chapter 3. We detail the construction of this unstructured high-order cell-centered Lagrangian scheme utilizing a general formalism based on a sub-cell force discretization. The two-dimensional Cartesian and axisymmetric versions of this scheme are thoroughly studied and several numerical results, which assess its robustness and its accuracy, are displayed. Chapter 4 is devoted to the presentation of the CCLAD scheme that solves accurately the anisotropic diffusion equation on distorted unstructured two-dimensional grids in both Cartesian and axisymmetric geometry. The robustness and the accuracy of this diffusion scheme is evaluated by means of various analytical test cases. Finally, concluding remarks and perspectives about future works are given in Chapter 5.

A list of selected publications corresponding to the aforementioned works is given hereafter in the ascending chronological order.

Selected publications

- P.-H. Maire, R. Abgrall, J. Breil, and J. Ovadia. A cell-centered Lagrangian scheme for two-dimensional compressible flow problems. *SIAM J. Sci. Comput.*, 29(4):1781–1824, 2007.
- J. Breil and P.-H. Maire. A cell-centered diffusion scheme on two-dimensional unstructured meshes. *J. Comp. Phys.*, 224(2):785–823, 2007.
- P.-H. Maire and J. Breil. A second-order cell-centered Lagrangian scheme for two-dimensional compressible flow problems. *Int. J. Numer. Meth. Fluids*, 56(8):1417–1423, 2008.
- P.-H. Maire and B. Nkonga. Multi-scale Godunov-type method for cell-centered discrete Lagrangian hydrodynamics. *J. Comp. Phys.*, 228(3):799–821, 2009.
- P.-H. Maire. A high-order cell-centered Lagrangian scheme for two-dimensional compressible fluid flows on unstructured meshes. *J. Comp. Phys.*, 228(7):2391–2425, 2009.
- P.-H. Maire. A high-order cell-centered Lagrangian scheme for compressible fluid flows in two-dimensional cylindrical geometry. *J. Comp. Phys.*, 228(18):6882–6915, 2009.
- P.-H. Maire. A unified sub-cell force-based discretization for cell-centered Lagrangian hydrodynamics on polygonal grids. *Int. J. Numer. Meth. Fluids*, 2010.
- P.-H. Maire. A high-order one-step sub-cell force-based discretization for cell-centered Lagrangian hydrodynamics on polygonal grids. *Computers and Fluids*, 2010.

Contents

Chapter 1

Physical and numerical context of ICF

It is known since the work performed by Hans Bethe and Carl Friedrich von Weizsäcker that thermonuclear fusion of hydrogen is at the origin of the energy that is radiated by stars. The thermodynamic conditions needed to produce these self-sustained fusion reactions can be obtained on earth in the 50's only by means of nuclear explosions. The project to domesticate this energy for civil use requires the confinement of fusible material brought to temperatures in the order of several hundred million degrees. Two methods of confinement are under development: the first consists of trapping particles forming the fusion plasma using an intense magnetic field, known as Magnetic Confinement Fusion (MCF). The international project ITER[1](International Thermonuclear Experimental Reactor) that is installed at the CEA center in Cadarache (France) is a result of 60 years of research in this domain. The second one, relied on a hydrodynamic confinement, that is obtained by the implosion at a very high velocity of a spherical shell of a fusible material. The Deuterium-Tritium (DT) fuel is thus confined only by the effect of its own inertia, and thus is termed **Inertial Confinement Fusion** (ICF). The pressures that allow such implosions are of the order of several hundred million times the atmospheric pressure. They are obtained by the ablation pressure created by intense laser beams that deliver to targets millimeters in size a power in the order 500 Terawatts (TW) over a few millionths of a second. The LMJ[2](Laser Mega Joule), currently under construction at the CEA-CESTA site and NIF[3] (National Ignition Facility) constructed in the Lawrence Livermore National Laboratory (LLNL) in the USA, will allow the thermonuclear fusion of hydrogen isotopes with a net energy gain of the order of ten. LLNL also develops an advanced energy project called LIFE[4](Laser Inertial Fusion Engine), which is based on physics and technology developed for the NIF. Let us also mention the HiPER[5] project, which proposes a construction of the European High Power laser Energy Research facility dedicated to demonstrating the feasibility of laser driven fusion as a future energy source. HiPER is being designed to enable a broad array of new science including extreme material studies, astrophysics in the laboratory, miniaturized particle accelerators and a wide range of fundamental physics research. The physical processes at play in such systems are numerous and complex: interaction of the laser light with a target and formation of a plasma, transport of the absorbed energy by electron heat conduction and by radiation, ablation of matter, formation of shock waves and acceleration of the target, implosion

[1]Refer to `http://www.iter.org/`.
[2]Refer to `http://www-lmj.cea.fr/`.
[3]Refer to `https://lasers.llnl.gov/`.
[4]Refer to `https://lasers.llnl.gov/about/missions/energy_for_the_future/life/`.
[5]Refer to `http://www.hiper-laser.org/`.

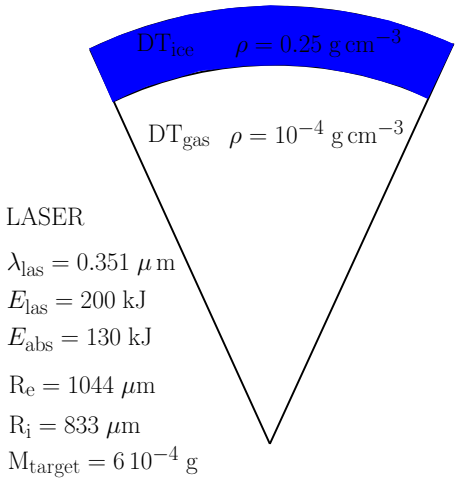

Figure 1.1: All DT target for HiPER.

of the fuel to extremely high densities, ignition of a chain fusion reaction and propagation of a divergent thermonuclear wave. These highly non-stationary processes are mutually coupled and it is very difficult to realize them experimentally. This a reason why numerical simulations are indispensable for both the conception and the interpretation of ICF experiments.

The remainder of this chapter is organized as follows. In Section 1.1 we present briefly the phenomenology of the Inertial Confinement Fusion. A detailed discussion of this vast and complex subject is beyond the scope of this document, thus interested readers should refer to the textbooks [90, 11, 43, 52]. In Section 1.2 we briefly describe the ICF code CHIC (Code d'Hydrodynamique et d'Implosion du Celia).

1.1 ICF phenomenology

1.1.1 ICF target

Inertial Confinement Fusion is a process where fusion reactions are triggered by compressing and heating a fuel target by means of a high energy beams of laser light. The best fuel from energy perspective is a one to one mix of deuterium (D) and tritium (T) which are both isotopes of hydrogen. This is due to the fact that the following fusion reaction has the highest cross section and for the lowest temperatures of the order of $100 - 300$ MK

$$D + T \longrightarrow^4 He + n + 17.6\,MeV. \tag{1.1}$$

This equation states that the fusion of DT produces an α particle (^{4}He) with an energy of 3.6 MeV plus a neutron (n) with an energy of 14 MeV. The fusion target is generally a spherical shell filled with a low-density gas of a mass density $\rho_{gas} \leq 10^{-3}\,g/cm^3$. The shell is composed of an outer region which forms the ablator and inner region of frozen deuterium-tritium (DT) which forms the main fuel. We have plotted in Figure 1.1 a schematic view of the all DT target that has been designed in the context of the HiPER project [57]. The outer radius of the target is $R_e = 1044\ \mu$m and the thickness of the shell is $\Delta R_s = 211\ \mu$m. Note that in this case, the shell is composed uniquely of frozen DT with density $\rho_{ice} = 0.25\ g/cm^3$ and filled with DT gas ($\rho_{gas} = 10^{-4}\ g/cm^3$). The total mass of the target is $M_{target} = 6.\ 10^{-4}\,g$. Let us point out that in reality, the frozen fuel is contained in the plastic shell of a thickness of a few microns.

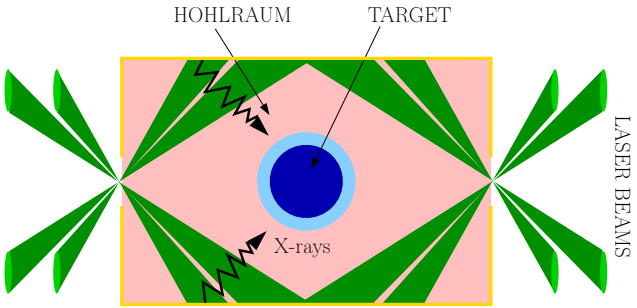

Figure 1.2: Indirect drive laser fusion.

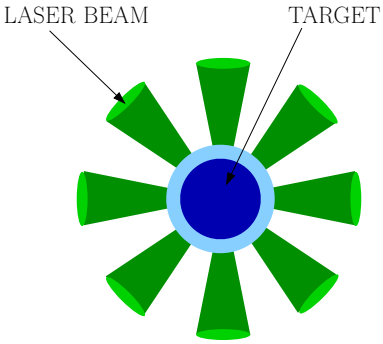

Figure 1.3: Direct drive laser fusion.

1.1.2 Indirect drive versus direct drive

In laser-driven ICF the energy is delivered to the spherical target by means of a high-power laser. There are typically two schemes to deliver energy. In the first scheme, termed as indirect drive, the target is held inside a cylindrical vessel with walls coated of a heavy material (gold) having good radiation properties, which is called the holhraum (German word for cavity), refer to Figure 1.2. The laser beams penetrate inside the holhraum and irradiate the wall. The absorbed laser energy is then partially re-radiated as X-rays, which drive the capsule implosion. Due to the smoothing induced by the re-emitted X-rays, this approach is less sensitive to the irradiation non-uniformity of the laser beams. The indirect drive scheme has been chosen for the current ICF projects NIF and LMJ. In the second scheme, termed as direct drive, the laser energy is directly delivered to the outer region of the target and transferred to electrons by means of inverse bremsstrahlung absorption process [43], refer to Figure 1.3. This latter scheme has a higher laser-target coupling efficiency than the former. This is the reason why the direct drive approach has been chosen to investigate the feasibility of energy production by means of inertial fusion. However, the direct drive scheme is more sensitive to the non-uniformity of the laser irradiation due the discrete distribution of laser beams. It requires a large number of very uniform beams to ensure a spherical implosion and to avoid the occurrence of hydrodynamic instabilities of Richtmyer-Meshkov or Rayleigh-Taylor type.

1.1.3 Ignition conditions

The fuel conditions that must be achieved for efficient burn and high yield relative to the driver energy can be obtained from an analysis of the burn of an inertially confined fuel mass according

to the fusion reaction (1.1). The number of fusion reactions n per second satisfies the differential equation

$$\frac{dn}{dt} = N_{\mathrm{D}}(t) N_{\mathrm{T}}(t) \langle \sigma v \rangle,$$

where $\langle \sigma v \rangle$ denotes the averaged reaction cross section which is a function of the temperature T. In addition, $N_{\mathrm{D}}(t)$ and $N_{\mathrm{T}}(t)$ are the number of D and T particles per unit volume at time t. For a one to one mix of DT, with an initial density $N_{\mathrm{D}}(0) = N_{\mathrm{T}}(0) = \frac{1}{2} N_0$, the number of remaining D and T particles at time t writes $N_{\mathrm{D}}(t) = N_{\mathrm{T}}(t) = \frac{1}{2} N_0 - n(t)$. Defining the burn fraction, ϕ, as $\phi = 2 \frac{n}{N_0}$ leads to

$$\frac{d\phi}{dt} = \frac{N_0}{2} (1 - \phi)^2 \langle \sigma v \rangle.$$

Assuming that the average reaction cross section is constant and integrating the above equation over the time interval $[0, \tau]$ yields

$$\frac{\phi}{1 - \phi} = \frac{N_0}{2} \langle \sigma v \rangle \tau. \tag{1.2}$$

Here, τ represents the confinement time of the fuel. Considering a sphere of DT fuel of radius R_f and mass density ρ_f, the confinement time is estimated as the duration of the hydrodynamic expansion of the sphere, that is, $\tau \sim \frac{R_f}{a_f}$, where $a_f = a_f(T)$ denotes the isentropic sound speed of the fuel. Knowing that the particle density is proportional to the mass density of the fuel, *i.e.*, $N_0 \sim \rho_f$, equation (1.2) transforms into

$$\frac{\phi}{1 - \phi} = \frac{\rho_f R_f}{H_b},$$

where $H_b = H_b(T)$ is uniquely a function of the temperature. For the range of temperatures $T \in [3.\ 10^8\mathrm{K}, 1.\ 10^9\mathrm{K}]$ corresponding to the thermonuclear combustion, this function is nearly constant and can be approximated by $H_b = 7$ g/cm^2, refer to [90, 11]. Finally, the burn fraction of the fuel, ϕ, within the above range of temperatures writes as

$$\phi = \frac{\rho_f R_f}{\rho_f R_f + H_b}, \tag{1.3}$$

This fundamental criteria is called the ρr requirement to achieve ignition. This is the counterpart of the Lawson confinement criteria employed in the context of MCF [90]. For instance, to burn 30 % of the fuel, we need to compress it to reach an areal mass density of $\rho_f R_f = 3$ g/cm^2. Bearing this in mind, the mass of the DT sphere is rewritten as

$$M_f = \frac{4}{3} \pi \frac{(\rho_f R_f)^3}{\rho_f^2}.$$

Hence, the mass of fuel required for a given ρr scales as the inverse of the squared density. From this it follows that for a ρr of 3 g/cm^2, at a normal liquid density of 0.21 g/cm^3, the mass of fuel required is equal to 2.5 kg. It represents an unrealistic quantity of DT which would lead to an amount of energy of the order of a nuclear explosion. The solution to obtain a mass of fuel compatible with the context of laboratory experiments consists in employing a fuel compressed to high density. Indeed, at a density of 250 g/cm^3, the sphere of DT would have $\rho_f R_f = 3$ g/cm^2 with a mass of 1.8 10^{-3} g which is a quite reasonable value. Let us point out that the above value for the density of the compressed fuel is 1000 times the density of the cryogenic DT at normal conditions. Therefore, ignition achievement necessitates a very strong compression which can be obtained by means of a high-power laser.

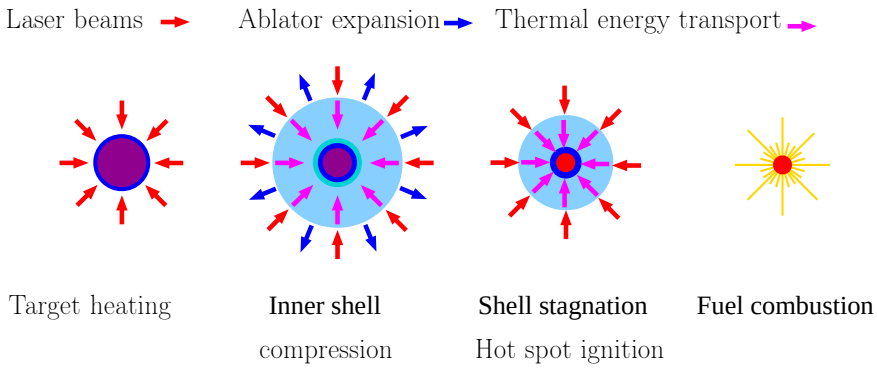

Figure 1.4: Main stages of laser-driven inertial fusion.

1.1.4 Main stages of laser-driven ICF

The four main stages of laser-driven ICF are displayed in Figure 1.4. The first stage corresponds to the laser irradiation of the target with a laser intensity approximately equal to $I_{\text{laser}} = 10^{15}$ W/cm^2. This sudden release of a huge amount of energy heats up the outer part of the shell (the ablator), creates the ablated plasma and compresses the remaining shell. Then starts the second stage which consists of the acceleration and isentropic implosion of the compressed shell. As the ablated plasma expands outward, momentum conservation involves an inward acceleration of the inner part of the shell which results in a compression of the fuel. The absorbed energy is transported inwardly by means of electron heat conduction and radiation. An ablation pressure of the order of 100 Mbars leads to an acceleration of the target to velocities about 300 km/s within a few nanoseconds. The time evolution of the laser intensity is designed to compress the fuel in an optimal fashion by following an almost isentropic path. This goal is accomplished by performing a laser pulse shaping which allows to launch a sequence of shock waves characterized by a precisely controlled timing. This amounts to approximate an isentropic compression by a succession of shock waves, refer to [168]. A typical laser pulse has been plotted in Figure 1.5. It has three characteristic parts: the pre-pulse that launches a shock through the solid shell, compresses and moves it inside, the raising part that accelerates the shell approximately isentropically to the velocity that will enable the fuel assembly; and the high intensity part that launches a shock through the shell and heats a small portion of the compressed fuel which is called the hot spot. The hot spot creation corresponds to the third stage. Due to the laser pulse shaping, it coincides with the stagnation of the shell which has been continuously decelerated by the bounces of the shock waves at the center of the target. It is worth to mention that the mass of the hot spot represents approximately less than one hundredth of the total fuel mass. This tiny mass of heated compressed fuel requires a ρr approximately equal to 0.2 g/cm^2 to ignite. Then it sparks the combustion in the remaining cold fuel. This results in the fourth stage wherein a thermonuclear burn front propagates radially outward in the main fuel producing high gain.

Here, we have briefly described the basic scheme of ICF knowing that nowadays more efficient alternative schemes for the inertial fusion energy production are under consideration. The interested reader may refer to [158].

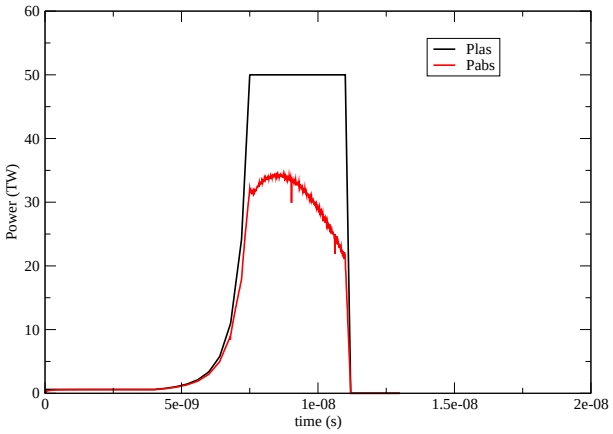

Figure 1.5: Typical shape of the laser pulse (black curve) consisting of a pre-pulse of a power of a few TW following by the raising part and the main pulse at the level of 50 TW. The red curve corresponds to the power absorbed by the plasma.

1.2 CHIC: a two-dimensional code for modeling high energy density physics

The CHIC code has been developed at CELIA laboratory (Bordeaux University). It has as main objective the numerical simulation of experiments concerning the physics of hot dense plasma created by laser in the domain of ICF, laboratory astrophysics and laser processing. This bi-dimensional code allows the theoretical developments, conception and interpretation of various experiments in the domain of high energy density physics. The detailed presentation of the underlying theoretical models is beyond the scope of the current work. The reader interested by this topic may report to the thoroughly review presented by Atzeni in [9]. This laser fusion code employs a single fluid, two-temperature (ions and electrons) description of the plasma flow. Roughly speaking this description consists of a system of integral-differential equations at the center of which we find the equations of compressible gas dynamics, coupled to equations of electron and photon transport characterized by equations of non-linear diffusion, the equations of laser energy transport and energy deposition, fusion reactions, etc.

As we have seen before, the hydrodynamic flow resulting from an implosion of an ICF target is a source of very intense shock and rarefaction waves. This fluid flow undergoes unsteady phenomena with characteristic time scales ranging from 10^{-12} s to 10^{-8} s. These phenomena are characterized by very intense thermodynamic processes wherein the density of the material under consideration can be compressed up to several thousand times its nominal value, the pressure ranges from the atmospheric pressure (1 bar) to 100 Gbars and the temperatures may vary between 15 K and 500 MK. During the target implosion, the size of the domain occupied by the fluid varies strongly over time. Moreover, the target being composed of several distinct materials, this flow generally contains several interfaces that need to be followed with accuracy during implosion. For all these reasons, we utilize the Lagrangian description of the gas dynamics equations which amounts to write it using the reference frame attached to the fluid motion. The Lagrangian formalism and its links with the classical Eulerian formalism are presented for the conservation laws of fluid mechanics in Chapter 2. The gas dynamics equations in the CHIC code are solved through the use of a cell-centered two-dimensional Lagrangian scheme which is called **EUCCLHYD** (Explicit Unstructured Cell-Centered Lagrangian HYDrodynamics). This finite volume scheme is based on a total energy formulation. It conserves the momentum and the total energy and satisfies an entropy inequality. It relies on a nodal solver that can be

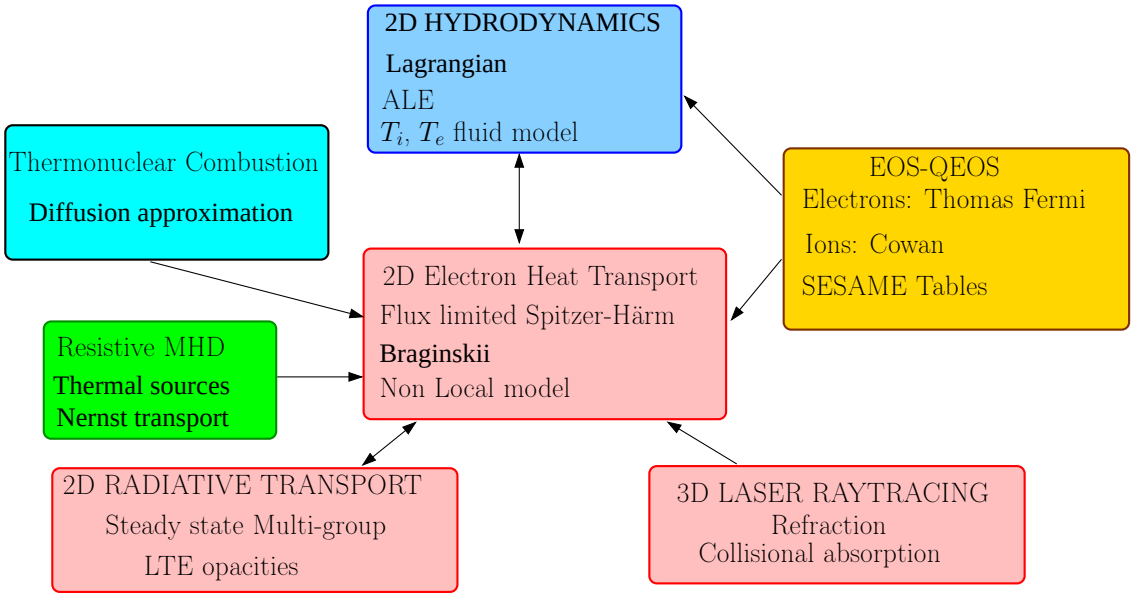

Figure 1.6: Schematic overview of the CHIC code.

interpreted as a two-dimensional extension of the Godunov acoustic solver. This scheme, that constitutes the numerical basis of the CHIC code, is thoroughly presented in Chapter 3.

Returning to the physical context of an imploding ICF target, let us recall that the laser energy is absorbed in low density plasma corona and the transport of the absorbed energy to dense plasma layers is assured by the electrons and photons. This energy transfer is described by a set of non-linear diffusion equations coupled to Lagrangian hydrodynamics. The radiation hydrodynamic simulations generally produce highly deformed meshes which makes the discretization of a diffusion equation a delicate procedure. Indeed, the classical finite volume schemes where the face conduction flux is discretized using a two-point finite difference approximation are not accurate enough and even inconsistent. Thus, on highly deformed meshes the isotherms produced by such schemes follow cell lines, a consequence of which is a degradation of the simulation precision. To address this issue, a robust and accurate finite volume cell-centered scheme, called **CCLAD** (Cell-Centered LAgrangian Diffusion), has been developed and implemented into the CHIC code. This scheme that also takes into account an anisotropic diffusion operator (Braginski conduction model for self-generated transverse magnetic field modeling) is detailed in Chaper 4. The coupling between Lagrangian hydrodynamics (EUCCLHYD) and diffusion (CCLAD) constitutes the numerical basis of the CHIC code.

This numerical basis is completed by various physical modules which are schematically displayed in Figure 1.6. These are: a library of tabular equations of state and opacities, a module calculating the propagation of the laser beams using a tri-dimensional ray tracing method, a module calculating energy transfer by radiation in the multigroup diffusion approximation, a Magneto Hydro Dynamic (MHD) module that describes the evolution of self-generated transverse magnetic fields, as well as a thermonuclear combustion module.

Let us point out that the accuracy and precision of the numerical simulations produced by this code is based not only on their intensive numerical validation using representative test cases, but also on the physical validation obtained from conclusive results of a number of experiments performed on high-power lasers, refer to [143, 138, 68, 10, 87, 88].

Chapter 2

Eulerian and Lagrangian formalisms for conservation laws in fluid mechanics

The main objective of this chapter is to recall classical notions of continuum mechanics that are required for the subsequent development of numerical methods. In continuum mechanics, there are two possible kinematic representations to describe the motion of a material. These are the Lagrangian description and the Eulerian description. The first one consists in describing the flow by following the pathlines of material parcels as they move through space and time. The second one consists in observing the flow at fixed locations in the space as time evolves. Here, we intend to present not only the Lagrangian and the Eulerian descriptions of the conservation laws of fluid mechanics using both integral and local forms but also the links between these two formulations. The writing of this chapter relies on the following references [148, 25, 141, 156, 63, 86, 44, 81, 41, 125, 146, 55, 115].

The remainder of this chapter is organized as follows. In Section 2.1, we start by introducing basic important concepts related to the kinematics of fluid motion such as the Lagrangian and Eulerian descriptions, the deformation gradient tensor and the material derivative. We recall the fundamental Reynolds transport formula that expresses the time rate of change of the volume integral of a fluid variable over a moving fluid domain. This formula, which is the basis to derive the integral form of the conservation laws, is also generalized to take into account the jump discontinuity of a fluid variable accross a moving discontinuity. In Section 2.2, we present the various Eulerian forms of the conservation laws of fluid mechanics. Basic concepts of thermodynamics are introduced. The constitutive laws modeling problem is addressed through the use of the Second Law of thermodynamics. Finally, the Rankine-Hugoniot relations, which express the conservation of the mass, the momentum and the total energy accross a moving discontinuity are derived by means of the generalized Reynolds transport formula. In Section 2.3, the Lagrangian integral and local forms of the conservation laws are derived by transforming the Eulerian conservation laws through the use of the Lagrange-Euler map. The Rankine-Hugoniot relations are written under the Lagrangian form. The study of the correspondence between the Eulerian and the Lagrangian Rankine-Hugoniot relations reveals the fundamental role of the Piola indentity. We conclude this chapter by introducing in Section 2.4, the Arbitrary Eulerian Lagrangian form of the conservation laws.

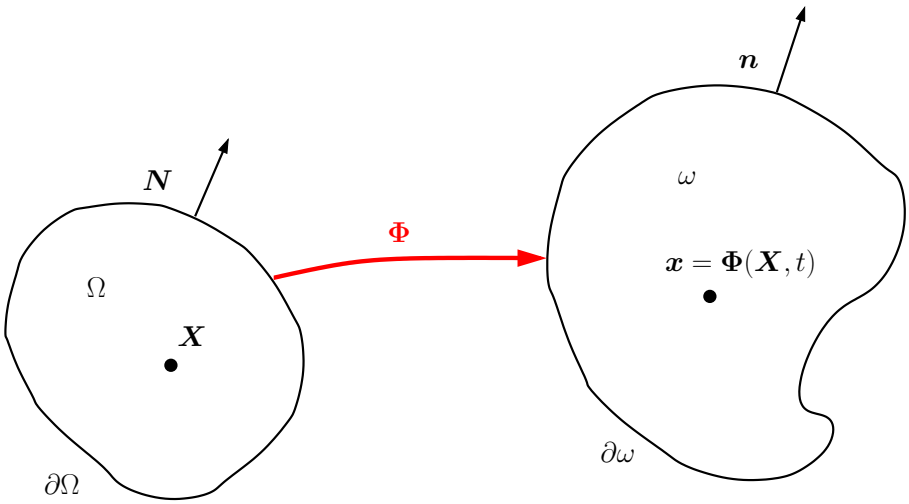

Figure 2.1: Notation for the flow map.

2.1 Kinematics of fluid motion

2.1.1 Lagrangian and Eulerian descriptions

Let us introduce the d-dimensional Euclidean space $\mathbb{R}^d$, where d is an integer ranging from 1 to 3. The space $\mathbb{R}^d$ is equipped with an orthonormal basis and an orthogonal coordinate system. For $d = 3$, the basis and the coordinate system are respectively denoted $(\boldsymbol{e}_x, \boldsymbol{e}_y, \boldsymbol{e}_z)$ and (x, y, z). Notation related to $d = 2$ and $d = 1$ are obviously deduced. The position vector of a point is denoted by $\boldsymbol{x} = (x, y, z)^t$. Let $\mathcal{D}$ be a region of $\mathbb{R}^d$ filled by a moving fluid. The fluid flow is described mathematically by the continuous transformation, $\boldsymbol{\Phi}$, of $\mathcal{D}$ into itself as

$$\boldsymbol{\Phi} : \boldsymbol{X} \longmapsto \boldsymbol{x} = \boldsymbol{\Phi}(\boldsymbol{X}, t). \tag{2.1}$$

Here, t, which is a non-negative real number, denotes the time and $\boldsymbol{X} = (X, Y, Z)$ is the position at time $t = 0$ of a particle moving with the fluid which occupies the position $\boldsymbol{x}$ at time $t > 0$. It turns out that $\boldsymbol{x}$ is determined as a function of $\boldsymbol{X}$ and t, and the fluid flow is represented by the transformation $\boldsymbol{x} = \boldsymbol{\Phi}(\boldsymbol{X}, t)$. By definition $\boldsymbol{\Phi}$ satisfies $\boldsymbol{\Phi}(\boldsymbol{X}, 0) = \boldsymbol{X}$. For a fixed time, transformation (2.1) determines the image of the region initially filled by the fluid. For a fixed $\boldsymbol{X}$, the time evolution of (2.1) describes the trajectory of a fluid particle initially located at $\boldsymbol{X}$. We assume that $\boldsymbol{\Phi}$ has continuous derivatives up to the second order in all variables, except possibly at certain singular surfaces, curves or points. We also assume that it has an inverse denoted $\boldsymbol{\Phi}^{-1}$ and defined by

$$\boldsymbol{\Phi}^{-1} : \boldsymbol{x} \longmapsto \boldsymbol{X} = \boldsymbol{\Phi}^{-1}(\boldsymbol{x}, t). \tag{2.2}$$

Let us consider $\omega = \omega(t)$ a moving sub-region of $\mathcal{D}$ at time t. ω corresponds to the image of a fixed sub-region Ω in the flow map, *i.e.*, $\omega = \{\boldsymbol{x} = \boldsymbol{\Phi}(\boldsymbol{X}, t) | \boldsymbol{X} \in \Omega\}$. The boundaries of ω and Ω are respectively denoted $\partial\omega$ and $\partial\Omega$, and their unit outward normals are $\boldsymbol{n}$ and $\boldsymbol{N}$, refer to Fig 2.1. At this point, we can introduce the two usual descriptions of the flows, namely the Lagrangian description and the Eulerian description. The Lagrangian description, otherwise called material description, consists in observing the fluid by following the motion of fluid particles from their initial location. The independent variables used for this description are $(\boldsymbol{X}, t)$. On the other hand the Eulerian description, otherwise called spatial description, consists in observing the fluid at fixed locations in the space. The independent variables used for that description are $(\boldsymbol{x}, t)$. We notice that through the use of transformation (2.1) any fluid

quantity f which is expressed in terms of the Eulerian variables $(\boldsymbol{x}, t)$ can also be expressed in terms of the Lagrangian variables $(\boldsymbol{X}, t)$ and conversely. To emphasize the used variables, we write either

$$f = f(\boldsymbol{x}, t) \quad \text{or} \quad f = f(\boldsymbol{X}, t).$$

For the sake of conciseness, same notation is used to denote the value of the physical quantity whatever the description employed. This amounts to write the following trivial equalities

$$f(\boldsymbol{X}, t) = f(\boldsymbol{x}, t) = f(\boldsymbol{\Phi}(\boldsymbol{X}, t), t). \tag{2.3}$$

To be more precise, $f(\boldsymbol{X}, t)$ is the value of the physical quantity experienced at time t by the fluid particle initially located at $\boldsymbol{X}$ whereas $f(\boldsymbol{x}, t)$ is the value of f experienced by the fluid particle which is located at position $\boldsymbol{x}$ at time t.

2.1.2 Material time derivative and velocity

Let f be a fluid variable with a sufficient smoothness to allow the computation of its first partial derivatives with respect to both Lagrangian and Eulerian variables. First, we introduce the material derivative of f which measures the rate of change of f following a fluid particle along its motion as

$$\frac{d}{dt} f \equiv \frac{\partial}{\partial t} f(\boldsymbol{X}, t). \tag{2.4}$$

Note that it corresponds to the partial time derivative in the Lagrangian description. The velocity of a fluid particle is denoted $\boldsymbol{U}$ and is defined as the material derivative of the position vector $\boldsymbol{x}$

$$\boldsymbol{U}(\boldsymbol{X}, t) = \frac{d}{dt}\boldsymbol{x} = \frac{\partial}{\partial t}\boldsymbol{\Phi}. \tag{2.5}$$

As defined, $\boldsymbol{U}$ is a function of the Lagrangian variables, however it is possible to also express it in terms of the Eulerian variables writing $\boldsymbol{U} = \boldsymbol{U}(\boldsymbol{x}, t)$. Knowing the velocity field expressed in terms of the Eulerian coordinates, it is thus possible to determine the fluid flow by solving the system of ordinary differential equations

$$\frac{d}{dt}\boldsymbol{x} = \boldsymbol{U}(\boldsymbol{x}, t), \quad \boldsymbol{x}(0) = \boldsymbol{X}, \tag{2.6}$$

which corresponds to the trajectory equations of the fluid flow. Considering the physical quantity f expressed in terms of the Eulerian variables, that is $f = f(\boldsymbol{x}, t)$, we compute its material derivative employing (2.3) and the chain rule of composite derivative to get

$$\frac{d}{dt} f = \frac{\partial}{\partial t} f + (\frac{\partial}{\partial t}\boldsymbol{\Phi}) \cdot \boldsymbol{\nabla}_x f, \tag{2.7}$$

where $\boldsymbol{\nabla}_x$ denotes the gradient operator with respect to Eulerian coordinates, which writes in the chosen coordinate system as $\boldsymbol{\nabla}_x f = (\frac{\partial}{\partial x} f, \frac{\partial}{\partial y} f, \frac{\partial}{\partial z} f)^t$. Substituting the velocity definition into (2.7) leads to

$$\frac{d}{dt} f = \frac{\partial}{\partial t} f + \boldsymbol{U} \cdot \boldsymbol{\nabla}_x f. \tag{2.8}$$

This last equation may be interpreted as expressing, for an arbitrary physical quantity $f = f(\boldsymbol{x}, t)$, the time rate of change of f apparent to a viewer located on the moving particle instantaneously at the position $\boldsymbol{x}$. Let $\boldsymbol{f}$ denotes a vector valued function, we compute its material derivative applying (2.8) componentwise to finally get

$$\frac{d}{dt}\boldsymbol{f} = \frac{\partial}{\partial t}\boldsymbol{f} + (\nabla_x \boldsymbol{f})\boldsymbol{U}, \tag{2.9}$$

where $\nabla_x \boldsymbol{f}$ represents the gradient tensor defined by (A.24).

2.1.3 Deformation gradient tensor

Let $\boldsymbol{X}_0$ be the initial position vector of a specific fluid particle and $\mathcal{D}_0$ a subset of the three-dimensional space that contains this particle. Its image in the fluid flow transformation writes $\boldsymbol{x}_0 = \boldsymbol{\Phi}(\boldsymbol{X}_0, t)$. Let $\boldsymbol{x} = \boldsymbol{\Phi}(\boldsymbol{X}, t)$ denotes the vector position of a fluid particle at time t which was initially located in the vicinity of $\boldsymbol{X}_0$, *i.e.*, $\boldsymbol{X} \in \mathcal{D}_0$. A first-order Taylor expansion of the transformation $\boldsymbol{\Phi}$ in the Lagrangian variable yields

$$\begin{aligned}\boldsymbol{x} =& \boldsymbol{\Phi}(\boldsymbol{X}_0 + \boldsymbol{X} - \boldsymbol{X}_0, t)\\ =& \boldsymbol{\Phi}(\boldsymbol{X}_0, t) + \nabla_X \boldsymbol{\Phi}(\boldsymbol{X}_0, t)(\boldsymbol{X} - \boldsymbol{X}_0) + O(\mid \boldsymbol{X} - \boldsymbol{X}_0 \mid^2).\end{aligned}$$

Here, $\nabla_X \boldsymbol{\Phi}$ denotes the gradient tensor of $\boldsymbol{\Phi}$ with respect to the Lagrangian coordinates, it represents the Jacobian matrix of the transformation characterizing the fluid flow. This Jacobian matrix is also named the deformation gradient tensor and is defined as

$$\mathsf{F} = \nabla_X \boldsymbol{x}, \tag{2.10}$$

since $\boldsymbol{x} = \boldsymbol{\Phi}(\boldsymbol{X}, t)$. This matrix, which is defined in terms of the Lagrangian variables, is invertible and its determinant, J, satisfies $J = \det \mathsf{F} > 0$ since $\mathsf{F}(\boldsymbol{X}, 0) = \mathsf{I}_d$ where I_d denotes the identity tensor. Before we proceed any further, let us recall a fundamental interpretation of the Jacobian determinant. Let $\mathsf{d}V$ denotes a Lagrangian volume element and $\mathsf{d}v$ its corresponding volume in the Eulerian space through the transformation of the flow, then these two volumes are related through the following formula

$$\mathsf{d}v = J\mathsf{d}V. \tag{2.11}$$

This formula shows that the Jacobian is a measure of the volume change produced by the fluid deformation.

Using definition (2.10), we rewrite the previous Taylor expansion as

$$\boldsymbol{x} - \boldsymbol{x}_0 = \mathsf{F}(\boldsymbol{X}_0, t)(\boldsymbol{X} - \boldsymbol{X}_0) + O(\mid \boldsymbol{X} - \boldsymbol{X}_0 \mid^2). \tag{2.12}$$

Passing to the limit $\boldsymbol{X} \to \boldsymbol{X}_0$ in the above equation leads to

$$\mathsf{d}\boldsymbol{x} = \mathsf{F}\mathsf{d}\boldsymbol{X}, \tag{2.13}$$

where $\mathsf{d}\boldsymbol{X}$ and $\mathsf{d}\boldsymbol{x}$ are infinitesimal displacement vectors respectively in the initial and final configurations of the flow. It turns out that the deformation gradient tensor quantifies the change in shape of infinitesimal displacement vectors through the fluid motion. To be more precise, let us introduce the right Cauchy-Green deformation tensor as

$$\mathsf{C} = \mathsf{F}^t\mathsf{F}. \tag{2.14}$$

It can be regarded as quantifying the squared length of infinitesimal fibers in the final configuration of the flow. Let $\mathsf{d}\boldsymbol{X} = L\boldsymbol{N}$ be an infinitesimal fluid fiber in the initial configuration, where $\boldsymbol{N}$ is its unit vector and L its length. Through the flow, this fiber transforms into $\mathsf{d}\boldsymbol{x} = l\boldsymbol{n}$. Here, l and $\boldsymbol{n}$ denote the length and the unit vector of the fiber in the final configuration. This length can be computed as

$$\begin{aligned}l^2 &= \mathsf{d}\boldsymbol{x} \cdot \mathsf{d}\boldsymbol{x}\\ &= \mathsf{F}\mathsf{d}\boldsymbol{X} \cdot \mathsf{F}\mathsf{d}\boldsymbol{X}\\ &= \mathsf{F}^t\mathsf{F}\mathsf{d}\boldsymbol{X} \cdot \mathsf{d}\boldsymbol{X}\\ &= L^2\mathsf{F}^t\mathsf{F}\boldsymbol{N} \cdot \boldsymbol{N}.\end{aligned}$$

We finally obtained that the ratio of the squared lengths between the initial and final configuration writes as

$$\frac{l^2}{L^2} = \mathsf{C}\boldsymbol{N}\cdot\boldsymbol{N}. \tag{2.15}$$

We note that C is a symmetric definite positive tensor.

2.1.4 Material derivative of the Jacobian matrix and its determinant

The material derivative of the Jacobian matrix, F, is computed as

$$\begin{aligned}\frac{d}{dt}\mathsf{F} =& \frac{d}{dt}\nabla_X \boldsymbol{x}\\ =& \nabla_X \boldsymbol{U} && \text{thanks to (2.5)}\\ =& (\nabla_x \boldsymbol{U})\,(\nabla_X \boldsymbol{x}).\end{aligned}$$

Here, we have introduced the velocity gradient tensor as $\nabla_x \boldsymbol{U}$. Using previous notation, material derivative of the Jacobian matrix reads

$$\frac{d}{dt}\mathsf{F} = (\nabla_x \boldsymbol{U})\mathsf{F}. \tag{2.16}$$

The velocity gradient tensor is the basic measure of deformation rate and quantifies the relative velocities of two material particles which Eulerian coordinates are $\boldsymbol{x}$ and $\boldsymbol{x}+\mathsf{d}\boldsymbol{x}$. Let us introduce the stretch rate tensor, D, and the spin tensor, W, which are respectively the symmetric and the skew-symmetric parts of the velocity gradients

$$\mathsf{D} = \frac{1}{2}(\nabla_x \boldsymbol{U} + \nabla_x \boldsymbol{U}^t), \quad \mathsf{W} = \frac{1}{2}(\nabla_x \boldsymbol{U} - \nabla_x \boldsymbol{U}^t). \tag{2.17}$$

By definition $\nabla_x \boldsymbol{U} = \mathsf{D} + \mathsf{W}$ and $\mathsf{D}^t = \mathsf{D}$, $\mathsf{W}^t = -\mathsf{W}$. Being given an infinitesimal fiber in the final configuration, $\mathsf{d}\boldsymbol{x} = l\boldsymbol{n}$, we compute its rate of stretching as

$$\frac{d}{dt}\mathsf{d}\boldsymbol{x} = \frac{dl}{dt}\boldsymbol{n} + l\frac{d\boldsymbol{n}}{dt}. \tag{2.18}$$

We can also compute it recalling that $\mathsf{d}\boldsymbol{x} = \mathsf{F}\mathsf{d}\boldsymbol{X}$

$$\begin{aligned}\frac{d}{dt}\mathsf{d}\boldsymbol{x} =& \frac{d}{dt}\mathsf{F}\mathsf{d}\boldsymbol{X}\\ =& l(\nabla_x \boldsymbol{U})\boldsymbol{n}. && \text{thanks to (2.16)}\end{aligned}$$

Dot-multiplying by $\boldsymbol{n}$ the right-hand side of the two last equations yields

$$\frac{dl}{dt} = l(\nabla_x \boldsymbol{U})\boldsymbol{n}\cdot\boldsymbol{n}. \tag{2.19}$$

Here, we have used the fact that $\boldsymbol{n}\cdot\frac{d\boldsymbol{n}}{dt} = 0$ since $\boldsymbol{n}^2 = 1$. Now, using the decomposition of the velocity gradient into its symmetric and skew-symmetric parts leads to

$$\frac{dl}{dt} = l\mathsf{D}\boldsymbol{n}\cdot\boldsymbol{n}, \tag{2.20}$$

since $\mathsf{W}^t = -\mathsf{W}$. Therefore, the stretch rate tensor quantifies the rate of stretching of an infinitesimal fiber following the fluid motion.

The end of this paragraph is devoted to the computation of the material derivative of the determinant of the Jacobian matrix. Knowing that $J = \det \mathsf{F}$, we make use of the chain rule of composed derivatives (A.26) in the following manner

$$\begin{aligned}\frac{dJ}{dt} =& \frac{\partial}{\partial \mathsf{F}}(\det \mathsf{F}) : \frac{d\mathsf{F}}{dt} \\ =& (\det \mathsf{F})\mathsf{F}^{-t} : \nabla_x \boldsymbol{U}\mathsf{F} && \text{thanks to (A.27) and (2.16)} \\ =& J\mathsf{F}^{-t}\mathsf{F}^{t} : \nabla_x \boldsymbol{U} && \text{thanks to (A.17a)} \\ =& J \operatorname{tr}(\nabla_x \boldsymbol{U}).\end{aligned}$$

Let us point out that if S and T are two arbitrary second-order tensors, their inner product is defined by $\mathsf{S} : \mathsf{T} = \operatorname{tr}(\mathsf{S}^t\mathsf{T})$, refer to Appendix A.1.3. Noticing that the right-hand side of the last line in the previous equation is proportional to the trace of the velocity gradient tensor which is nothing but the divergence of the velocity field (refer to (A.29)), material derivative of the determinant of the Jacobian matrix finally reads

$$\frac{dJ}{dt} = J\nabla_x \cdot \boldsymbol{U}. \tag{2.21}$$

Here $\nabla_x \cdot \boldsymbol{U}$ denotes the divergence of the velocity with respect to Eulerian coordinates, which writes in the chosen coordinate system $\nabla_x \cdot \boldsymbol{U} = \frac{\partial u}{\partial x} + \frac{\partial v}{\partial y} + \frac{\partial w}{\partial z}$, where (u, v, w) denote the components of the velocity field. Introducing the stretch rate tensor, equation (2.21) admits also the equivalent form

$$\frac{dJ}{dt} = J \operatorname{tr} \mathsf{D}. \tag{2.22}$$

It turns out that the trace of D is a measure of rate of change of volume.

2.1.5 Transport formula for volume integrals

Let $\omega = \omega(t)$ denotes an arbitrary moving volume and let $f(\boldsymbol{x}, t)$ be a scalar valued function representing some physical quantity. Transport formula consists in expressing the time rate of change of the integral of the physical quantity f over the moving volume ω, *i.e*,

$$\frac{d}{dt}\int_{\omega(t)} f(\boldsymbol{x}, t)\, \mathsf{d}v. \tag{2.23}$$

We shall write two versions of the transport formula, depending on whether the volume ω is moving with the fluid velocity or not. First, we derive the Reynolds transport formula which corresponds to a volume moving with the fluid velocity. Second, we derive the generalized Reynolds transport formula which applies to a volume moving with an arbitrary velocity. In writing these formulas, we make the assumption that function f is continuously differentiable over ω. Then, we conclude by investigating the case of a piecewise continuously differentiable function, which undergoes jump discontinuity across a discontinuity surface moving within the volume under consideration. Let us emphasize that these formulas are of fundamental importance to derive not only the balance equations of fluid mechanics but also the Rankine-Hugoniot jump relations. Reference books for this part are [63, 141, 55].

Reynolds transport formula

Here, we consider $f = f(\boldsymbol{x}, t)$ as a continuously differentiable function over the region ω moving with the fluid velocity $\boldsymbol{U}$. Since ω is time-dependent, we cannot compute the time derivative (2.23) directly. To do so, we shall use the following change of variables

$$\int_{\omega} f(\boldsymbol{x}, t)\, \mathsf{d}v = \int_{\Omega} f(\boldsymbol{X}, t) J\, \mathsf{d}V. \tag{2.24}$$

In writing this equality, we have introduced the fixed Lagrangian coordinate, $\boldsymbol{X}$, as new variable of integration and used the fact that for this change of variable the change of volume element is ruled by (2.11). The initial volume occupied by the fluid, Ω is mapped into ω at time t through the flow transformation, *i.e.*, $\omega = \boldsymbol{\Phi}(\Omega, t)$. Thanks to the above change of variables, we can compute the time derivative (2.23) as follows

$$\begin{aligned}
\frac{d}{dt}\int_\omega f(\boldsymbol{x},t)\,\mathsf{d}v &= \int_\Omega J(\frac{df}{dt} + f\frac{dJ}{dt})\,\mathsf{d}V \\
&= \int_\Omega J[\frac{df}{dt} + f\nabla_x\cdot\boldsymbol{U}]\,\mathsf{d}V \qquad \text{thanks to (2.21)} \\
&= \int_\omega (\frac{df}{dt} + f\nabla_x\cdot\boldsymbol{U})\,\mathsf{d}v. \qquad \text{thanks to (2.11)}
\end{aligned}$$

Substituting the definition of the material derivative (2.8) in the right-hand side of the last line leads to the transport theorem otherwise named the Reynolds transport formula

$$\frac{d}{dt}\int_\omega f(\boldsymbol{x},t)\,\mathsf{d}v = \int_\omega [\frac{\partial f}{\partial t} + \nabla_x\cdot(f\boldsymbol{U})]\,\mathsf{d}v. \tag{2.25}$$

Through the use of the divergence theorem (A.33b), Reynolds transport formula can also be written under the following form

$$\frac{d}{dt}\int_\omega f(\boldsymbol{x},t)\,\mathsf{d}v = \int_\omega \frac{\partial f}{\partial t}\,\mathsf{d}v + \int_{\partial\omega} f\boldsymbol{U}\cdot\boldsymbol{n}\,\mathsf{d}s, \tag{2.26}$$

where $\boldsymbol{n}$ denotes the outward unit normal to the boundary $\partial\omega$. This equation states that the rate of increase of the total amount of f attached to the moving volume ω is balanced by the rate of increase of the total amount of f inside ω plus the net rate of outward flux of f transferred by the fluid through the boundary $\partial\omega$.

To extend the Reynolds transport formula to the vector valued function $\boldsymbol{f}$, we proceed with the computation of the time derivative of its volume integral as before

$$\begin{aligned}
\frac{d}{dt}\int_\omega \boldsymbol{f}(\boldsymbol{x},t)\,\mathsf{d}v &= \int_\Omega J[\frac{d\boldsymbol{f}}{dt} + \boldsymbol{f}\nabla_x\cdot\boldsymbol{U}]\,\mathsf{d}V \\
&= \int_\omega (\frac{d\boldsymbol{f}}{dt} + \boldsymbol{f}\nabla_x\cdot\boldsymbol{U})\,\mathsf{d}v \\
&= \int_\omega [\frac{\partial \boldsymbol{f}}{\partial t} + (\nabla_x\boldsymbol{f})\boldsymbol{U} + \boldsymbol{f}\nabla_x\cdot\boldsymbol{U}]\,\mathsf{d}v. \qquad \text{thanks to (2.9)}
\end{aligned}$$

The use of tensor identity (A.31b) in the right-hand side of the last line yields the vector form of the transport formula

$$\frac{d}{dt}\int_\omega \boldsymbol{f}(\boldsymbol{x},t)\,\mathsf{d}v = \int_\omega [\frac{\partial \boldsymbol{f}}{\partial t} + \nabla_x\cdot(\boldsymbol{f}\otimes\boldsymbol{U})]\,\mathsf{d}v, \tag{2.27}$$

where symbol $\otimes$ denotes the tensor product of two vectors defined by (A.1) and (A.2). Proceeding with the divergence theorem (A.33a) as before yields

$$\frac{d}{dt}\int_\omega \boldsymbol{f}(\boldsymbol{x},t)\,\mathsf{d}v = \int_\omega \frac{\partial \boldsymbol{f}}{\partial t}\,\mathsf{d}v + \int_{\partial\omega} \boldsymbol{f}(\boldsymbol{U}\cdot\boldsymbol{n})\,\mathsf{d}s. \tag{2.28}$$

A straightforward application of the Reynolds transport formula consists in deriving the continuity equation from the principle of mass conservation. This fundamental principle corresponds to the postulate that the mass of fluid in a material volume ω does not change as ω

moves with the fluid. Let $\rho = \rho(\boldsymbol{x}, t)$ denotes the mass density of the fluid, *i.e.*, the mass per unit volume. Mass conservation writes as

$$\frac{d}{dt}\int_{\omega} \rho(\boldsymbol{x}, t)\, \mathsf{d}v = 0. \tag{2.29}$$

Expressing the integrand in terms of the Lagrangian coordinate and integrating between initial and final time yields

$$\begin{aligned}\int_{\omega} \rho(\boldsymbol{x}, t)\, \mathsf{d}v &= \int_{\Omega} \rho(\boldsymbol{X}, t) J\, \mathsf{d}V \\ &= \int_{\Omega} \rho^0(\boldsymbol{X})\, \mathsf{d}V,\end{aligned}$$

where ρ^0 is the initial density field. From this equation, it follows easily that

$$\frac{d}{dt}(\rho J) = 0, \tag{2.30a}$$

$$\rho J = \rho^0. \tag{2.30b}$$

Here, we have derived two forms of the Lagrangian equation of continuity. Combining (2.25) for $f = \rho$ and (2.29), we derive the Eulerian equation of continuity in its integral form

$$\int_{\omega} [\frac{\partial \rho}{\partial t} + \nabla_x \cdot (\rho \boldsymbol{U})]\, \mathsf{d}v = 0.$$

Since ω is an arbitrary volume, this last equation implies

$$\frac{\partial \rho}{\partial t} + \nabla_x \cdot (\rho \boldsymbol{U}) = 0, \tag{2.31}$$

which is the local form of the Eulerian equation of continuity. It is a necessary and sufficient condition for a motion to conserve the mass of each moving fluid volume. A by-product of the transport theorem and mass conservation is obtained by computing the time rate of change of the integral over a moving volume of the density times an arbitrary function

$$\begin{aligned}\frac{d}{dt}\int_{\omega} \rho f\, \mathsf{d}v =& \frac{d}{dt}\int_{\Omega} \rho J f\, \mathsf{d}V \\ =& \int_{\Omega} \rho J \frac{df}{dt}\, \mathsf{d}V. \qquad\qquad \text{thanks to (2.30a)}\end{aligned}$$

Coming back to the Eulerian coordinates in the right-hand side of the last line, we finally get

$$\frac{d}{dt}\int_{\omega} \rho f\, \mathsf{d}v = \int_{\omega} \rho \frac{df}{dt}\, \mathsf{d}v. \tag{2.32}$$

This formula, which is also valid for vector valued function, will be of great interest when we will perform the spatial discretization of the gas dynamics equations.

Generalized Reynolds transport formula

In this paragraph, we aim at deriving the counterpart of the Reynolds transport formula in the case of an arbitrary motion which is different to the fluid motion. This arbitrary motion is characterized by the one-to-one continuously differentiable abstract map, $\boldsymbol{\Psi}$, defined as

$$\begin{aligned}\boldsymbol{\Psi}\ &: \Omega_{\xi} \longrightarrow \omega, \\ &\boldsymbol{\xi} \longmapsto \boldsymbol{x} = \boldsymbol{\Psi}(\boldsymbol{\xi}, t).\end{aligned}$$

Here, ω denotes a sub-region of the Eulerian configuration and Ω_ξ its pre-image under the abstract map $\boldsymbol{\Psi}$. Let us note that map $\boldsymbol{\Psi}$ is parameterized by the time $t \geq 0$. We also assume that $\boldsymbol{\Psi}(\boldsymbol{\xi}, 0) = \boldsymbol{\xi}$. The velocity field, $\boldsymbol{V} = \boldsymbol{V}(\boldsymbol{\xi}, t)$, associated to this map is defined as

$$\boldsymbol{V} = \frac{\partial}{\partial t}\boldsymbol{\Psi}(\boldsymbol{\xi}, t). \tag{2.33}$$

Let f be a smooth scalar valued function which represents a fluid property, we can express f either in terms of Eulerian coordinates $\boldsymbol{x}$ or in terms of the initial configuration coordinates $\boldsymbol{\xi}$, since $f = f(\boldsymbol{x}, t) = f(\boldsymbol{\Psi}(\boldsymbol{\xi}, t), t)$. Using the chain rule, we define the time derivative of $f = f(\boldsymbol{x}(\boldsymbol{\xi}, t), t)$ following the particle initially located at $\boldsymbol{\xi}$

$$\frac{df}{dt}\Big|_\xi = \frac{\partial f}{\partial t} + \boldsymbol{V} \cdot \boldsymbol{\nabla}_x f. \tag{2.34}$$

The subscript $\boldsymbol{\xi}$ in the above equation emphasizes the fact that the time derivative is performed $\boldsymbol{\xi}$ being held fixed. Let us point out that this time derivative is the counterpart of the material time derivative (2.8) associated to the Lagrangian-to-Eulerian map. We readily obtain that these times derivatives are linked by

$$\frac{df}{dt}\Big|_\xi = \frac{df}{dt} + (\boldsymbol{V} - \boldsymbol{U}) \cdot \boldsymbol{\nabla}_x f,$$

where $\boldsymbol{U}$ is the fluid velocity. Proceeding with map Ψ as we did with the Lagrangian-to-Eulerian map, we introduce the determinant of its Jacobian matrix as

$$J_\xi(\boldsymbol{\xi}, t) = \det(\nabla_\xi \boldsymbol{\Psi}). \tag{2.35}$$

Here, $\nabla_\xi \boldsymbol{\Psi}$ denotes the Jacobian matrix of map $\boldsymbol{\Psi}$. Since $\boldsymbol{\Psi}$ is always one-to-one, it follows that $\det(\nabla_\xi \boldsymbol{\Psi})$ never vanishes and therefore, by continuity, $J_\xi(\boldsymbol{\xi}, t) > 0$. If $\mathsf{d}v$ and $\mathsf{d}V_\xi$ denote respectively volume elements in the Eulerian and initial configurations, then they are related by the Jacobian as $\mathsf{d}v = J_\xi \mathsf{d}V_\xi$. Proceeding as we did in Section 2.1.4, one can show that the abstract time derivative of the Jacobian J_ξ is given by

$$\frac{d}{dt}\Big|_\xi J_\xi = J_\xi \nabla_x \cdot \boldsymbol{V}. \tag{2.36}$$

Combining this equation and (2.34), one deduces

$$\frac{d}{dt}\Big|_\xi (f J_\xi) = J_\xi [\frac{\partial f}{\partial t} + \nabla_x \cdot (f\boldsymbol{V})]. \tag{2.37}$$

Bearing this in mind, we compute the time derivative of the volume integral $\int_{\omega=\boldsymbol{\Psi}(\Omega_\xi,t)} f(\boldsymbol{x}, t)\, \mathsf{d}v$ as

$$\begin{aligned}
\frac{d}{dt}\int_{\omega=\boldsymbol{\Psi}(\Omega_\xi,t)} f(\boldsymbol{x}, t)\, \mathsf{d}v &= \int_{\Omega_\xi} \frac{d}{dt}|_\xi [f(\boldsymbol{x}(\xi, t), t) J_\xi]\, \mathsf{d}V_\xi \\
&= \int_{\Omega_\xi} J_\xi [\frac{\partial f}{\partial t} + \nabla_x \cdot (f\boldsymbol{V})]\, \mathsf{d}V_\xi. \qquad \text{thanks to (2.37)}
\end{aligned}$$

Then, pulling back to the Eulerian configuration in the integral of the righ-hand side yields

$$\frac{d}{dt}\int_{\omega=\boldsymbol{\Psi}(\Omega_\xi,t)} f(\boldsymbol{x}, t)\, \mathsf{d}v = \int_\omega [\frac{\partial f}{\partial t} + \nabla_x \cdot (f\boldsymbol{V})]\, \mathsf{d}v.$$

Finally, applying the divergence formula yields the transport formula with respect to the arbitrary motion $\boldsymbol{\Psi}$

$$\frac{d}{dt}\int_{\omega=\boldsymbol{\Psi}(\Omega_\xi,t)} f(\boldsymbol{x},t)\,\mathsf{d}v = \int_\omega \frac{\partial f}{\partial t}\,\mathsf{d}v + \int_{\partial\omega} f\boldsymbol{V}\cdot\boldsymbol{n}\,\mathsf{d}s. \tag{2.38}$$

Comparing the above transport formula to the transport formula (2.26) corresponding to the fluid motion leads to the very important result

$$\frac{d}{dt}\int_{\omega=\boldsymbol{\Psi}(\Omega_\xi,t)} f(\boldsymbol{x},t)\,\mathsf{d}v = \frac{d}{dt}\int_{\omega=\boldsymbol{\Phi}(\Omega,t)} f(\boldsymbol{x},t)\,\mathsf{d}v - \int_{\partial\omega} f(\boldsymbol{U}-\boldsymbol{V})\cdot\boldsymbol{n}\,\mathsf{d}s. \tag{2.39}$$

Let us recall that $\boldsymbol{\Phi}$ and $\boldsymbol{U}$ denote respectively the fluid map and the fluid velocity. Here, $\boldsymbol{U}-\boldsymbol{V}$ is the relative velocity of the fluid with respect to the arbitrary motion. The above equation states that the time derivative of the volume integral of f following the arbitrary motion is equal to the time derivative of the volume integral of f following the fluid motion decreased by the flux of f transferred through the boundary $\partial\omega$ with the relative fluid velocity $\boldsymbol{U}-\boldsymbol{V}$. We remark that if the arbitrary motion coincides with the fluid motion, *i.e.*, $\boldsymbol{V}=\boldsymbol{U}$, then transport formula (2.38) collapses to the classical transport formula (2.26). Transport formula (2.39) will be of great importance to derive the Arbitrary Lagrangian Eulerian integral form of the conservation laws of fluid mechanics, refer to Section 2.4.

Transport formula and discontinuity surfaces

In this section, we aim at deriving the counterpart of formulas (2.26) and (2.28) for **piecewise** continuously differentiable functions. Let $\boldsymbol{f}=\boldsymbol{f}(\boldsymbol{x},t)$ be a vector valued function defined over the Eulerian volume ω at time t. We assume that this function undergone a jump discontinuity across a surface, σ, located within the volume, ω, and we also let the fluid velocity, $\boldsymbol{U}$, be discontinuous at σ. Namely, ω is divided into two non-overlapping volumes ω_1 and ω_2 over which $\boldsymbol{f}$ is continuously differentiable, σ being the intersection surface of ω_1 and ω_2, *i.e.*, $\sigma=\omega_1\cap\omega_2$, refer to Fig. 2.2. At any point, $\boldsymbol{x}_\sigma$, located on the discontinuity surface we define its unit normal, $\boldsymbol{n}_\sigma$, pointing in the direction of ω_2. We also define its displacement velocity, $\boldsymbol{w}=\boldsymbol{w}(\boldsymbol{x}_\sigma,t)$, which can differ from the fluid velocity $\boldsymbol{U}$. The jumps of the function $\boldsymbol{f}$ across the discontinuity surface σ is defined as

$$[\![\boldsymbol{f}]\!] = \boldsymbol{f}_2-\boldsymbol{f}_1,$$

where for an arbitrary $\boldsymbol{x}_\sigma\in\sigma$, the one-sided limits of $\boldsymbol{f}$ on both sides of the discontinuity surface are defined as

$$\boldsymbol{f}_1=\lim_{h\to0^+}\boldsymbol{f}(\boldsymbol{x}_\sigma-h\boldsymbol{n}_\sigma),\quad \boldsymbol{f}_2=\lim_{h\to0^+}\boldsymbol{f}(\boldsymbol{x}_\sigma+h\boldsymbol{n}_\sigma).$$

Let us define over each sub-region, ω_i, $i=1,2$, the following piecewise continuous velocity field

$$\boldsymbol{V}(\boldsymbol{x},t)=\begin{cases}\boldsymbol{U}(\boldsymbol{x},t) & \text{if } \boldsymbol{x}\in\omega_i\cup(\partial\omega_i\setminus\sigma),\\ \boldsymbol{w}(\boldsymbol{x},t) & \text{if } \boldsymbol{x}\in\sigma.\end{cases}$$

This velocity field follows from an arbitrary motion $\boldsymbol{\Psi}$ which is assumed to be a one-to-one continuous map. Let $\Omega_{\xi,i}$ be the pre-image of ω_i by the map $\boldsymbol{\Psi}$, *i.e.*, $\omega_i=\boldsymbol{\Psi}(\Omega_{\xi,i},t)$. Knowing that $\boldsymbol{f}$ is continuously differentiable over each sub-region ω_i, we apply the generalized Reynolds transport formula (2.38) to obtain

$$\frac{d}{dt}\int_{\omega_1=\boldsymbol{\Psi}(\Omega_{1,\xi},t)} f(\boldsymbol{x},t)\,\mathsf{d}v = \int_{\omega_1}\frac{\partial\boldsymbol{f}}{\partial t}\,\mathsf{d}v + \int_{\partial\omega_1\setminus\sigma}\boldsymbol{f}(\boldsymbol{U}\cdot\boldsymbol{n})\,\mathsf{d}s + \int_\sigma \boldsymbol{f}_1(\boldsymbol{w}\cdot\boldsymbol{n}_\sigma)\,\mathsf{d}s,$$
$$\frac{d}{dt}\int_{\omega_2=\boldsymbol{\Psi}(\Omega_{2,\xi},t)} f(\boldsymbol{x},t)\,\mathsf{d}v = \int_{\omega_2}\frac{\partial\boldsymbol{f}}{\partial t}\,\mathsf{d}v + \int_{\partial\omega_2\setminus\sigma}\boldsymbol{f}(\boldsymbol{U}\cdot\boldsymbol{n})\,\mathsf{d}s - \int_\sigma \boldsymbol{f}_2(\boldsymbol{w}\cdot\boldsymbol{n}_\sigma)\,\mathsf{d}s.$$

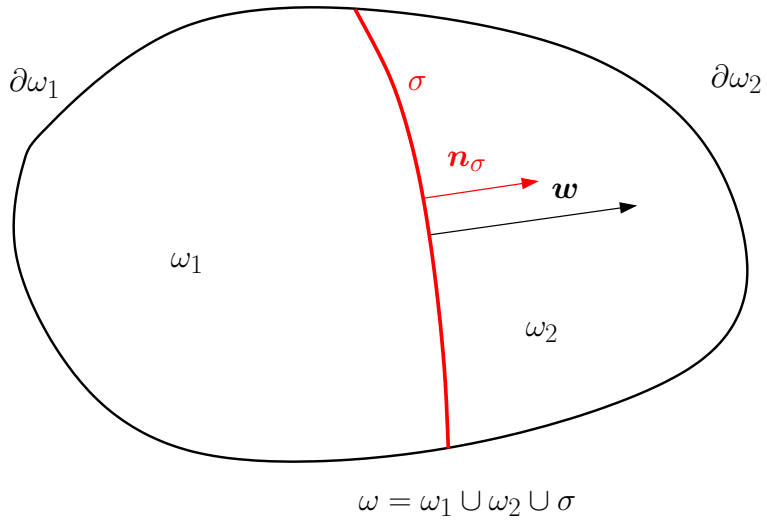

Figure 2.2: Notation for a moving discontinuity σ in the Eulerian frame.

Summing the two previous equations yields

$$\frac{d}{dt}\int_{\omega_1=\boldsymbol{\Psi}(\Omega_{1,\xi},t)} f(\boldsymbol{x},t)\,\mathrm{d}v + \frac{d}{dt}\int_{\omega_2=\boldsymbol{\Psi}(\Omega_{2,\xi},t)} f(\boldsymbol{x},t)\,\mathrm{d}v = \int_{\omega_1\cup\omega_2}\frac{\partial \boldsymbol{f}}{\partial t}\,\mathrm{d}v + \int_{\partial\omega}\boldsymbol{f}(\boldsymbol{U}\cdot\boldsymbol{n})\,\mathrm{d}s - \int_\sigma [\![\boldsymbol{f}]\!](\boldsymbol{w}\cdot\boldsymbol{n}_\sigma)\,\mathrm{d}s.$$

The velocity field, $\boldsymbol{V}$, of the arbitrary motion, $\boldsymbol{\Psi}$, coincides with the fluid velocity, $\boldsymbol{U}$, everywhere except on the discontinuity surface, σ. Therefore:

$$\frac{d}{dt}\int_{\omega_1=\boldsymbol{\Psi}(\Omega_{1,\xi},t)} f(\boldsymbol{x},t)\,\mathrm{d}v + \frac{d}{dt}\int_{\omega_2=\boldsymbol{\Psi}(\Omega_{2,\xi},t)} f(\boldsymbol{x},t)\,\mathrm{d}v = \frac{d}{dt}\int_{\omega=\boldsymbol{\Phi}(\Omega,t)} \boldsymbol{f}(\boldsymbol{x},t)\,\mathrm{d}v.$$

Combining the two previous equations, we get

$$\frac{d}{dt}\int_\omega \boldsymbol{f}(\boldsymbol{x},t)\,\mathrm{d}v = \int_{\omega_1\cup\omega_2}\frac{\partial \boldsymbol{f}}{\partial t}\,\mathrm{d}v + \int_{\partial\omega}\boldsymbol{f}(\boldsymbol{U}\cdot\boldsymbol{n})\,\mathrm{d}s - \int_\sigma [\![\boldsymbol{f}]\!](\boldsymbol{w}\cdot\boldsymbol{n}_\sigma)\,\mathrm{d}s. \tag{2.40}$$

The third term in the right-hand side corresponds to the flux through σ resulting from the jump across this surface. We notice that this term cancels when $[\![\boldsymbol{f}]\!] \to 0$ and we recover the classical transport formula (2.28). Substituting tensor identity (A.1) in the surface integrals of the right-hand side, Equation (2.40) rewrites

$$\frac{d}{dt}\int_\omega \boldsymbol{f}(\boldsymbol{x},t)\,\mathrm{d}v = \int_{\omega_1\cup\omega_2}\frac{\partial \boldsymbol{f}}{\partial t}\,\mathrm{d}v + \int_{\partial\omega}(\boldsymbol{f}\otimes\boldsymbol{U})\boldsymbol{n}\,\mathrm{d}s - \int_\sigma [\![\boldsymbol{f}\otimes\boldsymbol{w}]\!]\boldsymbol{n}_\sigma\,\mathrm{d}s. \tag{2.41}$$

Finally, replacing the second term in the right-hand side by means of the divergence formula (A.36), we obtain

$$\frac{d}{dt}\int_\omega \boldsymbol{f}(\boldsymbol{x},t)\,\mathrm{d}v = \int_{\omega_1\cup\omega_2}[\frac{\partial \boldsymbol{f}}{\partial t} + \nabla_x\cdot(\boldsymbol{f}\otimes\boldsymbol{U})]\,\mathrm{d}v + \int_\sigma [\![\boldsymbol{f}\otimes(\boldsymbol{U}-\boldsymbol{w})]\!]\boldsymbol{n}_\sigma\,\mathrm{d}s. \tag{2.42}$$

Proceeding with the scalar valued function, f, as before yields successively

$$\frac{d}{dt}\int_\omega f(\boldsymbol{x},t)\,\mathrm{d}v = \int_{\omega_1\cup\omega_2}\frac{\partial f}{\partial t}\,\mathrm{d}v + \int_{\partial\omega} f(\boldsymbol{U}\cdot\boldsymbol{n})\,\mathrm{d}s - \int_\sigma [\![f]\!](\boldsymbol{w}\cdot\boldsymbol{n}_\sigma)\,\mathrm{d}s. \tag{2.43}$$

$$\frac{d}{dt}\int_{\omega} f(\boldsymbol{x},t)\,\mathsf{d}v = \int_{\omega_1\cup\omega_2}[\frac{\partial f}{\partial t}+\nabla_x\cdot(f\boldsymbol{U})]\,\mathsf{d}v + \int_{\sigma}[\![f(\boldsymbol{U}-\boldsymbol{w})]\!]\cdot\boldsymbol{n}_\sigma\,\mathsf{d}s. \tag{2.44}$$

Last equation results from application of divergence formula (A.35) for piecewise continuously differential scalar valued functions.

Comment 1 *It is important to notice that the above transport formulas can be applied in the particular case of a fixed region ω crossed by a moving discontinuity σ. With this assumption, keeping the same notation as before, transport formula for scalar valued and vector valued function write*

$$\frac{d}{dt}\int_{\omega} f(\boldsymbol{x},t)\,\mathsf{d}v = \int_{\omega_1\cup\omega_2}\frac{\partial f}{\partial t}\,\mathsf{d}v - \int_{\sigma}[\![f]\!](\boldsymbol{w}\cdot\boldsymbol{n}_\sigma)\,\mathsf{d}s, \tag{2.45a}$$

$$\frac{d}{dt}\int_{\omega} \boldsymbol{f}(\boldsymbol{x},t)\,\mathsf{d}v = \int_{\omega_1\cup\omega_2}\frac{\partial \boldsymbol{f}}{\partial t}\,\mathsf{d}v - \int_{\sigma}[\![\boldsymbol{f}\otimes\boldsymbol{w}]\!]\boldsymbol{n}_\sigma\,\mathsf{d}s. \tag{2.45b}$$

These formulas are obtained using once more the generalized Reynolds transport formulas over each sub-regions ω_i considering the arbitrary motion, $\boldsymbol{\Psi}$, determined by the following piecewise continuous velocity field

$$\boldsymbol{V}(\boldsymbol{x},t) = \begin{cases}\boldsymbol{0} & \text{if } \boldsymbol{x}\in\omega_i\cup(\partial\omega_i\setminus\sigma),\\ \boldsymbol{w}(\boldsymbol{x},t) & \text{if } \boldsymbol{x}\in\sigma.\end{cases}$$

We shall use transport formulas (2.45) *when deriving the jump relations associated to conservation laws written under Lagrangian formalism.*

Comment 2 *Let us remark that a straightforward application of transport formula* (2.44) *to the mass density, i.e., $f=\rho$, yields mass conservation equation through the discontinuity surface σ. The principle of mass conservation* (2.29) *leads to*

$$\int_{\omega_1\cup\omega_2}[\frac{\partial\rho}{\partial t}+\nabla_x\cdot(\rho\boldsymbol{U})]\,\mathsf{d}v + \int_{\sigma}[\![\rho(\boldsymbol{U}-\boldsymbol{w})]\!]\cdot\boldsymbol{n}_\sigma\,\mathsf{d}s = 0.$$

Since ρ and $\boldsymbol{U}$ are continuously differentiable over ω_1 and ω_2, by virtue of the continuity equation (2.31)*, volume integrals in the left-hand side cancel and mass conservation equation reduces to*

$$\int_{\sigma}[\![\rho(\boldsymbol{U}-\boldsymbol{w})]\!]\cdot\boldsymbol{n}_\sigma\,\mathsf{d}s = 0.$$

Since this equation holds for any arbitrary surface, we deduce

$$[\![\rho(\boldsymbol{U}-\boldsymbol{w})]\!]\cdot\boldsymbol{n}_\sigma = 0, \quad \forall\boldsymbol{x}_\sigma\in\sigma. \tag{2.46}$$

This amounts to write

$$\rho_1(\boldsymbol{U}_1-\boldsymbol{w})\cdot\boldsymbol{n}_\sigma = \rho_2(\boldsymbol{U}_2-\boldsymbol{w})\cdot\boldsymbol{n}_\sigma.$$

Therefore, jump relation (2.46) *simply states the continuity of mass flux through the discontinuity surface. This is one of the Rankine-Hugoniot relations which will be derived later for conservation laws of fluid mechanics.*

2.1.6 Transport formula for surface integrals

Let us consider $f=f(\boldsymbol{x},t)$ a scalar valued function representing some physical quantity. We propose to compute the time rate of change of the integral of f over the surface $s=s(t)$ which is moving with fluid. This computation will be done expressing the integrand by means of the Lagrangian coordinates after performing the classical change of variables $\boldsymbol{x}\mapsto\boldsymbol{X}$. To this end, we need to know how the surface element transforms between Eulerian and Lagrangian configurations.

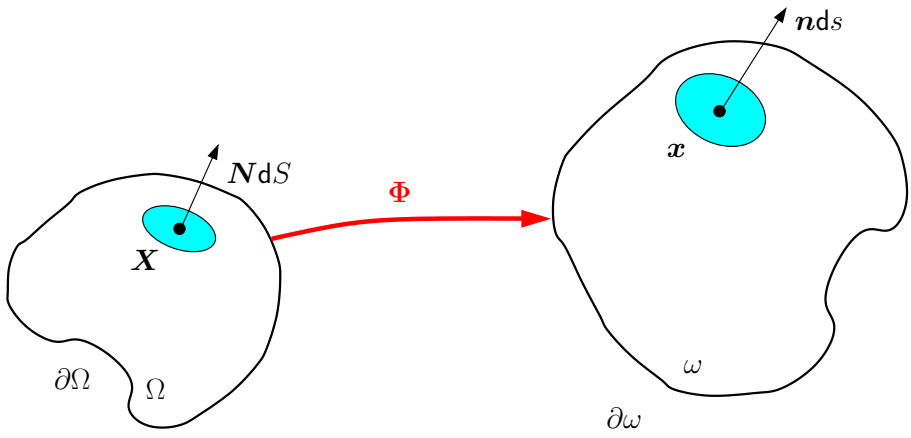

Figure 2.3: Area elements transformation.

Nanson formula

Knowing that the Eulerian and Lagrangian volume elements are related by $\mathsf{d}v = J\mathsf{d}V$, the aim of this paragraph is to determine an analogous formula to relate Eulerian and Lagrangian area elements. Let us consider a material fluid volume Ω and $\boldsymbol{X}$ a fluid particle located on its boundary $\partial\Omega$. Let $\mathsf{d}S$ be the area element in the vicinity of this fluid particle, characterized by its unit outward normal $\boldsymbol{N}$. Through the flow transformation, at time t, the material fluid volume and the material position vector are mapped into $\omega = \boldsymbol{\Phi}(\Omega, t)$, $\boldsymbol{x} = \boldsymbol{\Phi}(\boldsymbol{X}, t)$. Let $\mathsf{d}s$ and $\boldsymbol{n}$ denote the area element centered at the position vector $\boldsymbol{x}$ and its outward unit normal in the Eulerian space, refer to Fig. 2.3. The element volume $\mathsf{d}V$ is computed as the infinitesimal volume corresponding to the cylinder characterized by the base $\mathsf{d}S$ and displacement vector $\mathsf{d}\boldsymbol{X}$

$$\mathsf{d}V = \mathsf{d}\boldsymbol{X} \cdot \boldsymbol{N}\mathsf{d}S. \tag{2.47}$$

Using the same reasoning, the corresponding element volume in the Eulerian space writes as

$$\mathsf{d}v = \mathsf{d}\boldsymbol{x} \cdot \boldsymbol{n}\mathsf{d}s. \tag{2.48}$$

Substituting $\mathsf{d}v = J\mathsf{d}V$ and $\mathsf{d}\boldsymbol{x} = \mathsf{F}\mathsf{d}\boldsymbol{X}$ in equations (2.47) and (2.48), we obtain

$$\begin{aligned} J\boldsymbol{N}\mathsf{d}S \cdot \mathsf{d}\boldsymbol{X} =& \mathsf{F}\mathsf{d}\boldsymbol{X} \cdot \boldsymbol{n}\mathsf{d}s \\ =& \mathsf{F}^t\boldsymbol{n}\mathsf{d}s \cdot \mathsf{d}\boldsymbol{X}. \end{aligned}$$

Since this equality holds for an arbitrary displacement vector $\mathsf{d}\boldsymbol{X}$, we deduce

$$\boldsymbol{n}\mathsf{d}s = J\mathsf{F}^{-t}\boldsymbol{N}\mathsf{d}S, \tag{2.49}$$

where the superscript, $-t$, applied to tensor F denotes the transpose of its inverse. This formula expresses the transport of an orientated area element through the flow deformation. It is known as the Nanson formula. This formula will be one of the main ingredient to derive the Lagrangian forms of the conservation laws of fluid mechanics.

Time rate of change of a surface integral

Having in mind the Nanson formula, we can compute the time rate of change of a surface integral. First, let us notice that

$$\int_{s(t)} f(\boldsymbol{x}, t)\boldsymbol{n}\,\mathsf{d}s = \int_{S(t)} f(\boldsymbol{X}, t)J\mathsf{F}^{-t}\boldsymbol{N}\,\mathsf{d}S.$$

Here $s = s(t)$ denotes the moving surface in the Eulerian configuration, S is its pre-image in the Lagrangian configuration, *i.e.*, $s(t) = \mathbf{\Phi}(S, t)$ where $\mathbf{\Phi}$ is the flow map. Second, let us recall that the material derivative of an arbitrary matrix G is given by

$$\frac{d}{dt}\mathsf{G}^{-1} = -\mathsf{G}^{-1}\frac{d}{dt}(\mathsf{G})\mathsf{G}^{-1}. \tag{2.50}$$

This intermediate result is obtained by time differentiating $\mathsf{G}^{-1}\mathsf{G} = \mathsf{I}_d$. Applying this to the tensor deformation gradient and using (2.16) yields

$$\frac{d}{dt}\mathsf{F}^{-1} = -\mathsf{F}^{-1}\nabla_x \boldsymbol{U}. \tag{2.51}$$

Combining the above results, we compute the material derivative of the surface integral as

$$\begin{aligned}
\frac{d}{dt}\int_{s(t)} f(\boldsymbol{x},t)\boldsymbol{n}\,\mathsf{d}s &= \int_{S(t)} \frac{d}{dt}[f(\boldsymbol{X},t)J\mathsf{F}^{-t}]\boldsymbol{N}\,\mathsf{d}S \\
&= \int_{S(t)} \{[\frac{df}{dt} + f\nabla_x\cdot\boldsymbol{U}]\mathsf{I}_d - f(\nabla_x\boldsymbol{U})^t\}J\mathsf{F}^{-t}\boldsymbol{N}\,\mathsf{d}S \quad \text{thanks to (2.21) and (2.51)} \\
&= \int_{s(t)} \{[\frac{df}{dt} + f\nabla_x\cdot\boldsymbol{U}]\mathsf{I}_d - f(\nabla_x\boldsymbol{U})^t\}\boldsymbol{n}\,\mathsf{d}s. \quad \text{thanks to (2.49)}
\end{aligned}$$

Using the definition of the material derivative in the Eulerian configuration (2.7) leads to the final formula

$$\frac{d}{dt}\int_{s(t)} f(\boldsymbol{x},t)\boldsymbol{n}\,\mathsf{d}s = \int_{s(t)} [\frac{\partial f}{dt} + \nabla_x\cdot(f\boldsymbol{U})]\boldsymbol{n}\,\mathsf{d}s - \int_{s(t)} f(\nabla_x\boldsymbol{U})^t\boldsymbol{n}\,\mathsf{d}s. \tag{2.52}$$

2.2 Eulerian forms of fluid mechanics conservation laws

We recall the classical conservation laws of fluid mechanics with thermal conduction, which express respectively mass, momentum and total energy conservation. Their detailed derivation can be found in many textbooks of fluid mechanics [63, 141, 148]. These conservation laws are expressed using an integral form since this is how they are derived physically. Moreover, the integral form allows to hold general fluid flows such as those containing discontinuities.

2.2.1 Eulerian integral form of fluid mechanics conservation laws

Conservation Laws of fluid mechanics

Let ω be a moving fluid region and $\partial\omega$ its boundary surface. The first conservation law results from the principle of mass conservation, which states that the mass contained in the moving fluid volume is conserved. It has been already written, refer to (2.29), however we recall it for sake of completeness

$$\frac{d}{dt}\int_{\omega} \rho(\boldsymbol{x},t)\,\mathsf{d}v = 0,$$

where ρ denotes the mass density of the fluid.

The second conservation law corresponds to the principle of balance of momentum, which states that the rate of increase of momentum of ω is balanced by the momentum supplied by applied forces. This is nothing but the second Newton's law applied to moving fluid region ω as

$$\frac{d}{dt}\int_{\omega} \rho\boldsymbol{U}\,\mathsf{d}v = \int_{\partial\omega} \boldsymbol{\tau}\,\mathsf{d}s + \int_{\omega} \rho\boldsymbol{g}\,\mathsf{d}v. \tag{2.53}$$

Here, $\boldsymbol{g}$ denotes a volume force defined per unit mass of fluid such as gravity, $\boldsymbol{\tau}$ represents a force defined per unit area acting on the boundary surface $\partial\omega$. Let $\boldsymbol{n}$ be the unit outward normal located at $\boldsymbol{x} \in \partial\omega$, the force $\boldsymbol{\tau} = \boldsymbol{\tau}(\boldsymbol{x}, t, \boldsymbol{n})$, acting on the plane passing through point $\boldsymbol{x}$ and characterized by the unit normal $\boldsymbol{n}$, is completely defined by

$$\tau(\boldsymbol{x}, t, \boldsymbol{n}) = \mathsf{T}\boldsymbol{n},$$

where T is a second-order tensor named the Cauchy stress tensor. The interesting reader can refer to [63] for the proof of this fundamental result. Satisfaction of the principle of balance of angular momentum requires that this stress tensor must be symmetric, *i.e.*, $\mathsf{T}^t = \mathsf{T}$, refer to [148].

The third conservation law expresses the principle of balance of total energy. Namely, the rate of increase of total energy of ω is balanced by the energy supplied by the power of applied forces, heat conducted through the surface $\partial\omega$ and heat volume source

$$\frac{d}{dt}\int_\omega \rho E \,\mathsf{d}v = \int_{\partial\omega} \boldsymbol{\tau}\cdot\boldsymbol{U}\,\mathsf{d}s - \int_{\partial\omega} \boldsymbol{q}\cdot\boldsymbol{n}\,\mathsf{d}s + \int_\omega \rho(\boldsymbol{g}\cdot\boldsymbol{U} + r)\,\mathsf{d}v. \tag{2.54}$$

In this equation E is the specific total energy, *i.e.*, total energy per unit mass, which writes as the sum of the specific kinetic energy plus the specific internal energy, $E = \frac{1}{2} \mid \boldsymbol{U} \mid^2 + \varepsilon$. In addition, $\boldsymbol{q} = \boldsymbol{q}(\boldsymbol{x}, t)$ is the heat flux vector. It represents the rate at which energy is transferred out of the volume through a unit area of the surface. $r = r(\boldsymbol{x}, t)$ is the heat supply per unit mass and unit time absorbed by the fluid and furnished from the external world. Equation (2.54) is nothing but the first law of thermodynamics [45] which states that the rate of change of the total energy of a material volume is equal to the rate at which work is being done on the volume plus the rate at which heat is conducted into the volume. Gathering the previous results, we write the integral form of the conservation laws as

$$\begin{aligned}
&\frac{d}{dt}\int_\omega \rho\mathsf{d}v = 0,\\
&\frac{d}{dt}\int_\omega \rho\boldsymbol{U}\,\mathsf{d}v - \int_{\partial\omega} \mathsf{T}\boldsymbol{n}\,\mathsf{d}s = \int_\omega \rho\boldsymbol{g}\,\mathsf{d}v,\\
&\frac{d}{dt}\int_\omega \rho E\,\mathsf{d}v - \int_{\partial\omega} \mathsf{T}\boldsymbol{U}\cdot\boldsymbol{n}\,\mathsf{d}s + \int_{\partial\omega} \boldsymbol{q}\cdot\boldsymbol{n}\,\mathsf{d}s = \int_\omega \rho(\boldsymbol{g}\cdot\boldsymbol{U} + r)\,\mathsf{d}v.
\end{aligned}$$

We complete the above system by adding the Geometric Conservation Law (GCL) which expresses the time rate of change of the moving fluid volume, *i.e.*, $\int_\omega \mathsf{d}v$. This equation is obtained by computing the material derivative of the moving fluid volume as follows

$$\begin{aligned}
\frac{d}{dt}\int_\omega \mathsf{d}v &= \frac{d}{dt}\int_\Omega J\,\mathsf{d}V,\\
&= \int_\Omega J\nabla\cdot\boldsymbol{U}\,\mathsf{d}V, \quad \text{thanks to (2.21)},\\
&= \int_\omega \nabla\cdot\boldsymbol{U}\,\mathsf{d}v.
\end{aligned}$$

Application of the divergence theorem to the right-hand side of the last equation yields

$$\frac{d}{dt}\int_\omega \mathsf{d}v - \int_{\partial\omega} \boldsymbol{U}\cdot\boldsymbol{n}\,\mathsf{d}s = 0.$$

This last equation is strongly linked to the trajectory equation which describes the motion of an arbitrary point, $\boldsymbol{x}$, located on the moving boundary, $\partial\omega$, as

$$\frac{d\boldsymbol{x}}{dt} = \boldsymbol{U}(\boldsymbol{x}, t), \quad \boldsymbol{x}(0) = \boldsymbol{X}.$$

Summary of the Eulerian integral conservation laws

Here, we summarize the conservation laws which govern the time evolution of mass, volume, momentum and total energy of a moving fluid domain ω.

$$\frac{d}{dt}\int_{\omega}\rho \mathsf{d}v = 0, \tag{2.55a}$$

$$\frac{d}{dt}\int_{\omega}\mathsf{d}v - \int_{\partial\omega}\boldsymbol{U}\cdot\boldsymbol{n}\,\mathsf{d}s = 0, \tag{2.55b}$$

$$\frac{d}{dt}\int_{\omega}\rho\boldsymbol{U}\,\mathsf{d}v - \int_{\partial\omega}\mathsf{T}\boldsymbol{n}\,\mathsf{d}s = \int_{\omega}\rho\boldsymbol{g}\,\mathsf{d}v, \tag{2.55c}$$

$$\frac{d}{dt}\int_{\omega}\rho E\,\mathsf{d}v - \int_{\partial\omega}\mathsf{T}\boldsymbol{U}\cdot\boldsymbol{n}\,\mathsf{d}s + \int_{\partial\omega}\boldsymbol{q}\cdot\boldsymbol{n}\,\mathsf{d}s = \int_{\omega}\rho(\boldsymbol{g}\cdot\boldsymbol{U}+r)\,\mathsf{d}v. \tag{2.55d}$$

Let us point out that the above system is not closed since the expressions of the Cauchy stress tensor, T, and the heat flux, $\boldsymbol{q}$, in terms of the other fluid variables, are still missing. In addition, some thermodynamic relations among the fluid variables are also missing. These particular points will be investigated later in Section 2.2.3 determining not only the constitutive laws for T and $\boldsymbol{q}$ but also the equation of state by means of thermodynamic arguments. **We also remark that this integral form of the conservation laws over a moving fluid domain is particularly well adapted to describe the time evolution of fluid flow contained in regions undergoing large shape changes, due to sudden strong compression or expansion**. This formulation, known as the control volume formulation of the conservation laws, is widely used to derive numerical methods within the framework of finite volume discretizations over moving grids. Although this formulation makes use of a control volume attached to the Eulerian configuration, it is often referred to as the **updated Lagrangian formulation** of the conservation laws. This comes from the fact that in the discretized version of this approach, the control volume moving with the fluid flow needs to be updated by means of the trajectory equation.

Initial and boundary conditions for the Eulerian integral form

Let us suppose that the heat supply, r, the volume force, $\boldsymbol{g}$, the constitutive laws for the Cauchy stress, T, and the heat flux, $\boldsymbol{q}$ are given. Usually the above unsteady conservation laws are solved in a finite moving domain $\mathcal{D} = \mathcal{D}(t)$, which is an open set of the d-dimensional space $\mathbb{R}^d$. Therefore, a proper modelling of the fluid flow governed by the system of conservation laws (2.55) requires not only to prescribe initial conditions but also boundary conditions at the boundary, $\partial\mathcal{D}$, of the domain $\mathcal{D}$. Knowing that the fluid flow transformation, Φ, maps the inital domain occupied by the fluid, $\mathcal{D}^0$, into $\mathcal{D}(t)$, initial conditions are prescribed for all $\boldsymbol{x}\in\mathcal{D}^0$ as

$$\rho(\boldsymbol{x},0) = \rho^0(\boldsymbol{x}), \tag{2.56a}$$

$$\boldsymbol{U}(\boldsymbol{x},0) = \boldsymbol{U}^0(\boldsymbol{x}), \tag{2.56b}$$

$$E(\boldsymbol{x},0) = E^0(\boldsymbol{x}). \tag{2.56c}$$

Here, ρ^0, $\boldsymbol{U}^0$ and E^0 denote respectively the initial density, velocity and specific total energy. Let us note that it also possible to define an initial condition for specific internal energy instead of using (2.56c), since $E = \frac{1}{2}\mid\boldsymbol{U}\mid^2 + \varepsilon$.

Concerning the boundary conditions, depending on whether the heat flux is neglected or not, we distinguish the two following cases.

- $\boldsymbol{q} = \boldsymbol{0}$: Depending on the problem we want to solve, we can prescribe either kinematic or dynamic boundary conditions along the boundary of the domain. To set up these boundary conditions, we subdivide the boundary as $\partial\mathcal{D} = \partial\mathcal{D}_k \cup \partial\mathcal{D}_d$, where $\partial\mathcal{D}_k$ and $\partial\mathcal{D}_d$ are the subsets of the boundary corresponding respectively to the kinematic and the dynamic boundary conditions. With this notation, boundary conditions are implemented for all time $t > 0$ as follows

$$\boldsymbol{U}(\boldsymbol{x}, t) = \boldsymbol{U}^\star(\boldsymbol{x}, t), \quad \forall \boldsymbol{x} \in \partial\mathcal{D}_k, \tag{2.57a}$$

$$\mathsf{T}(\boldsymbol{x}, t)\boldsymbol{n} = \boldsymbol{\tau}^\star(\boldsymbol{x}, t), \quad \forall \boldsymbol{x} \in \partial\mathcal{D}_d, \tag{2.57b}$$

  Here, $\boldsymbol{U}^\star$ and $\boldsymbol{\tau}^\star$ denote the prescribed boundary velocity and force, $\boldsymbol{n}$ is the unit outward normal to $\partial\mathcal{D}_d$. Let us emphasize that the dynamic boundary condition (2.57b) is a natural boundary condition in the sense that it is automatically included in the integral form of the conservation law (2.55c). It is important to note that (2.57a) corresponds to a solid-wall boundary condition for a wall moving at speed $\boldsymbol{U}^\star$. At free surfaces, such as those encountered for fluid expanding in vacuum, the dynamic boundary condition (2.57b) collapses to a stress-free boundary condition, *i.e.*, $\mathsf{T}\boldsymbol{n} = \boldsymbol{0}$.

- $\boldsymbol{q} \neq \boldsymbol{0}$: There is heat propagation throughout the fluid by means of conduction. In this case, a boundary condition attached to this physical phenomenon has to be imposed. The natural corresponding boundary condition, in the sense that it is automatically included in the integral form of the conservation law (2.55d), consists in prescribing the heat flux at the boundary as follows

$$\boldsymbol{q}(\boldsymbol{x}, t) \cdot \boldsymbol{n} = q^\star(\boldsymbol{x}, t), \quad \forall \boldsymbol{x} \in \partial\mathcal{D}, \tag{2.58}$$

  where $q^\star$ denotes the prescribed normal heat flux. Anticipating the study made in Section 2.2.3 concerning heat flux constitutive law, we point out that it is also possible to prescribe other types of boundary condition for heat conduction as we shall see in Comment 4.

2.2.2 Eulerian local form of fluid mechanics conservation laws

Under conditions of sufficient smoothness, the local form of the conservation laws are deduced from the integral form (2.55) employing the transport formula (2.25) for $f = (\rho, \rho E)$ and the transport formula (2.27) for $\boldsymbol{f} = \rho\boldsymbol{U}$. This substitution leads to

$$\begin{aligned}
&\int_\omega \frac{\partial \rho}{\partial t} + \nabla \cdot (\rho \boldsymbol{U})\, \mathrm{d}v = 0,\\
&\int_\omega \frac{\partial}{\partial t}(\rho \boldsymbol{U}) + \nabla \cdot (\rho \boldsymbol{U} \otimes \boldsymbol{U})\, \mathrm{d}v - \int_{\partial\omega} \mathsf{T}\boldsymbol{n}\, \mathrm{d}s = \int_\omega \rho \boldsymbol{g}\, \mathrm{d}v,\\
&\int_\omega \frac{\partial}{\partial t}(\rho E) + \nabla \cdot (\rho E \boldsymbol{U})\, \mathrm{d}v - \int_{\partial\omega} \mathsf{T}\boldsymbol{U} \cdot \boldsymbol{n}\, \mathrm{d}s + \int_{\partial\omega} \boldsymbol{q} \cdot \boldsymbol{n}\, \mathrm{d}s = \int_\omega \rho(\boldsymbol{g} \cdot \boldsymbol{U} + r)\, \mathrm{d}v.
\end{aligned}$$

Transformation of the surface integrals, present in the left-hand side of the two last equations, into volume integrals by means of the divergence formulas (A.33a) and (A.33b) leads to

$$\begin{aligned}
&\int_\omega \frac{\partial \rho}{\partial t} + \nabla \cdot (\rho \boldsymbol{U})\, \mathrm{d}v = 0,\\
&\int_\omega \frac{\partial}{\partial t}(\rho \boldsymbol{U}) + \nabla \cdot (\rho \boldsymbol{U} \otimes \boldsymbol{U})\, \mathrm{d}v - \int_\omega \nabla \cdot \mathsf{T}\, \mathrm{d}v = \int_\omega \rho \boldsymbol{g}\, \mathrm{d}v,\\
&\int_\omega \frac{\partial}{\partial t}(\rho E) + \nabla \cdot (\rho E \boldsymbol{U})\, \mathrm{d}v - \int_\omega \nabla \cdot (\mathsf{T}\boldsymbol{U})\, \mathrm{d}v + \int_\omega \nabla \cdot \boldsymbol{q}\, \mathrm{d}v = \int_\omega \rho(\boldsymbol{g} \cdot \boldsymbol{U} + r)\, \mathrm{d}v.
\end{aligned}$$

Knowing that the previous equations hold for any arbitrary moving fluid volume, we deduce that the local form of the conservation laws with respect to the spatial (Eulerian) configuration writes

$$\frac{\partial \rho}{\partial t} + \nabla_x \cdot (\rho \boldsymbol{U}) = 0, \tag{2.59a}$$

$$\frac{\partial}{\partial t}(\rho \boldsymbol{U}) + \nabla_x \cdot (\rho \boldsymbol{U} \otimes \boldsymbol{U}) - \nabla_x \cdot \mathsf{T} = \rho \boldsymbol{g}, \tag{2.59b}$$

$$\frac{\partial}{\partial t}(\rho E) + \nabla_x \cdot (\rho E \boldsymbol{U}) - \nabla_x \cdot (\mathsf{T}\boldsymbol{U}) + \nabla_x \cdot \boldsymbol{q} = \rho(\boldsymbol{g} \cdot \boldsymbol{U} + r). \tag{2.59c}$$

Assuming that the variables describing the flow are sufficiently smooth, introduction of the material derivative in system (2.59) leads to the following non-conservative local form of the gas dynamics equations

$$\rho \frac{d}{dt}(\frac{1}{\rho}) - \nabla \cdot \boldsymbol{U} = 0, \tag{2.60a}$$

$$\rho \frac{d}{dt}\boldsymbol{U} - \nabla_x \cdot \mathsf{T} = \rho \boldsymbol{g}, \tag{2.60b}$$

$$\rho \frac{d}{dt}E - \nabla_x \cdot (\mathsf{T}\boldsymbol{U}) + \nabla_x \cdot \boldsymbol{q} = \rho(\boldsymbol{g} \cdot \boldsymbol{U} + r). \tag{2.60c}$$

Note that the momentum equation has been derived by means of the identity (A.31b) and using mass conservation (2.59a). Dot multiplying momentum equation by the velocity vector, we obtain the balance equation of kinetic energy

$$\rho \frac{d}{dt}(\frac{1}{2} \mid \boldsymbol{U} \mid^2) - (\nabla_x \cdot \mathsf{T}) \cdot \boldsymbol{U} = \rho \boldsymbol{g} \cdot \boldsymbol{U}. \tag{2.61}$$

Subtracting kinetic energy equation from total energy equation yields internal energy equation

$$\rho \frac{d}{dt}\varepsilon - \nabla_x \cdot (\mathsf{T}\boldsymbol{U}) + (\nabla_x \cdot \mathsf{T}) \cdot \boldsymbol{U} + \nabla_x \cdot \boldsymbol{q} = \rho r.$$

Expanding the second term in the left-hand side using tensor identity (A.31a) and combining it with the third term, we finally get

$$\rho \frac{d}{dt}\varepsilon + [\nabla_x \cdot (\mathsf{T} - \mathsf{T}^t)] \cdot \boldsymbol{U} - \mathsf{T}^t : \nabla_x \boldsymbol{U} + \boldsymbol{\nabla}_x \cdot \boldsymbol{q} = \rho r.$$

Let us emphasize that symmetry of the stress tensor is not only required to ensure angular momentum conservation but also to ensure Galilean invariance[1] of internal energy equation. To this end, the second term in the left-hand side must cancel for any arbitrary velocity field. This involves the symmetry of the stress tensor, *i.e.*, $\mathsf{T} = \mathsf{T}^t$. Having this in mind, internal energy equation writes

$$\rho \frac{d}{dt}\varepsilon - \mathsf{T} : \nabla_x \boldsymbol{U} + \boldsymbol{\nabla}_x \cdot \boldsymbol{q} = \rho r. \tag{2.62}$$

Introducing the symmetric part of the velocity gradient, by means of identity (A.18), internal energy equation is rewritten

$$\rho \frac{d}{dt}\varepsilon - \mathsf{T} : \mathsf{D} + \boldsymbol{\nabla}_x \cdot \boldsymbol{q} = \rho r, \tag{2.63}$$

[1]Galilean invariance is a principle of relativity which states that the fundamental laws of physics are the same in all inertial frames. This means that the corresponding partial differential equations remain invariant under linear uniform motions, *i.e.*, under transformations of the form $\boldsymbol{x}^\star = \boldsymbol{x} + \boldsymbol{A}t$, where $\boldsymbol{A}$ is a uniform velocity.

where D is the stretch rate tensor defined by (2.17).

Employing the symmetry of T and tensor identity (A.18), we show that the integral form of kinetic energy balance writes as

$$\frac{d}{dt}\int_\omega \frac{1}{2}\rho \mid \boldsymbol{U} \mid^2 \, \mathsf{d}v = \int_\omega \rho \boldsymbol{g}\cdot\boldsymbol{U}\,\mathsf{d}v + \int_{\partial\omega} \mathsf{T}\boldsymbol{U}\cdot\boldsymbol{n}\,\mathsf{d}s - \int_\omega \mathsf{T}:\mathsf{D}\,\mathsf{d}v. \tag{2.64}$$

This equation states that the time rate of change of kinetic energy of an arbitrary moving volume is equal to the rate at which work is being done by volume and surface forces, diminished by a dissipation term. This term renders the interaction of stress and strain, it corresponds to the rate at which work is being done in changing shape of fluid volume. The counterpart of this dissipation term is recovered in the integral form of the specific internal energy balance, which is obtained by integrating (2.62) over the arbitrary moving volume ω

$$\frac{d}{dt}\int_\omega \rho\varepsilon\,\mathsf{d}v = \int_\omega \mathsf{T}:\mathsf{D}\,\mathsf{d}v - \int_{\partial\omega}\boldsymbol{q}\cdot\boldsymbol{n}\,\mathsf{d}s + \int_\omega \rho r\,\mathsf{d}v. \tag{2.65}$$

2.2.3 Basic concepts of thermodynamics

We intend to recall basic notions of thermodynamics which are required to the describe the thermodynamic closure of the conservation laws system (2.59). For a complete description of this subtle subject, the reader might refer to [45].

Notation

In what follows, the fluid under consideration consists of a single homogeneous medium, that is a one-phase system. Its description is characterized by the following state variables: the specific volume $\tau = \frac{1}{\rho}$, the specific entropy η, the specific internal energy ε, the pressure P and the temperature T. Its is assumed that P and T are strictly positive variables. The thermodynamics structure of the fluid system is given by the fundamental equation of state

$$\varepsilon = \varepsilon(\eta, \tau). \tag{2.66}$$

Pressure and temperature are defined by

$$P = -(\frac{\partial\varepsilon}{\partial\tau})_\eta, \quad T = (\frac{\partial\varepsilon}{\partial\eta})_\tau. \tag{2.67}$$

These definitions involve the fundamental differential relation

$$T\mathsf{d}\eta = \mathsf{d}\varepsilon + P\mathsf{d}\tau, \tag{2.68}$$

which is known as the Gibbs relation [45]. We complete the set of state variables by introducing the specific enthalpy as

$$h = \varepsilon + P\tau. \tag{2.69}$$

Differentiating specific enthalpy definition and substituting it into Gibbs relation yields

$$T\mathsf{d}\eta = \mathsf{d}h - \tau\mathsf{d}P. \tag{2.70}$$

Before concluding this paragraph, let us point out that the equation of state is an intrinsic property of the material studied. It can be specified under various forms depending on the number of states variables which are employed. For practical applications involving thermal processes it is usual to define the equation of state by expressing the specific internal energy

and the pressure in terms of the density and the temperature, *i.e.*, $P = P(\rho, T)$ and $\varepsilon = \varepsilon(\rho, T)$. For applications wherein temperature is not required, an equation of state written under the form $P = P(\rho, \varepsilon)$ is sufficient. This is precisely the case for ideal gas which is characterized by an equation of state written as

$$P = (\gamma - 1)\rho\varepsilon, \tag{2.71}$$

where γ stands for the polytropic index, which is an intrinsic characteristic of the gas.

The First Law of thermodynamics

The one-phase system under consideration is said to undergo a reversible or quasi static process if it is in equilibrium with its surroundings at each instant. Let us consider a one-phase system initially at rest which undergoes a reversible process. First Law of thermodynamics states that the infinitesimal change in internal energy per unit mass, $\mathsf{d}\varepsilon$, is equal to the sum of the heat per unit mass supplied to the system, δQ, and the work per unit mass done by the system $\mathsf{d}W$ during the quasi static process, *i.e.*, $\mathsf{d}\varepsilon = \mathsf{d}Q + \delta W$. In our case, the work per unit mass done by the system reduces to the mechanical work per unit mass done by the pressure, that is $\delta W = -P\mathsf{d}\tau$. The minus sign in the previous formula ensures that a positive work corresponds to a work supplied to the system. With the previous notation, the differential form of the First Law writes as

$$\mathsf{d}\varepsilon = \delta Q - P\mathsf{d}\tau. \tag{2.72}$$

It is important to note that the First Law of thermodynamics corresponds to a conservation principle. In addition, employing the Gibbs relation (2.68), we deduce that the infinitesimal entropy change per unit mass, $\mathsf{d}\eta$ of a one-phase system undergoing a infinitesimal reversible process is given by

$$\mathsf{d}\eta = \frac{\delta Q}{T}, \tag{2.73}$$

where δQ is the infinitesimal heat per unit mass supplied to the system during the reversible process and T is the temperature. Using the definition of the specific enthalpy, First Law rewrites as

$$\mathsf{d}h = \delta Q + \tau\mathsf{d}P. \tag{2.74}$$

Being given an infinitesimal heat supply δQ, it is interesting to quantify the corresponding change in temperature for the one-phase system under consideration. This is done by defining the specific heat capacity as

$$C = \frac{\delta Q}{\mathsf{d}T}.$$

More precisely, making use of the two previous statements of the First Law, we define specific heat capacities for constant volume, C_v, and constant pressure, C_p, respectively as

$$C_v = (\frac{\partial \varepsilon}{\partial T})_\tau, \quad C_p = (\frac{\partial h}{\partial T})_P. \tag{2.75}$$

Let us point out that the specific heats are intrinsic characteristics of the material under consideration. For an ideal gas, the specific internal energy and specific enthalpy depends uniquely on the temperature, thus $\mathsf{d}\varepsilon = C_v\mathsf{d}T$ and $\mathsf{d}h = C_p\mathsf{d}T$. In addition, if we assume constant specific heats, specific internal energy and specific enthalpy are expressed as $\varepsilon = C_vT, \quad h = C_pT$. In this case, the specific heat coefficients satisfy the Meyer relation, that is $C_p - C_v = \frac{\mathcal{R}}{\mathcal{M}}$, where $\mathcal{R}$ is the universal gas constant and $\mathcal{M}$ the molar mass of the fluid under consideration. In

addition, the ratio of specific heats is given by $\frac{C_p}{C_v} = \gamma$, where γ is the polytropic coefficient of the gas. Combining the previous results allows to write the equation of state under the form

$$\varepsilon = C_v T, \quad P = \rho \frac{\mathcal{R}}{\mathcal{M}} T, \tag{2.76}$$

where the specific heat at constant volume is given by $C_v = \frac{\mathcal{R}}{\mathcal{M}(\gamma-1)}$. Eliminating the temperature in the above equation of states allows to recover the classical form $P = (\gamma - 1)\rho\varepsilon$.

The Second Law of thermodynamics

Knowing that for a reversible infinitesimal transformation the change of entropy per unit mass reads $\mathsf{d}\eta = \frac{\delta Q}{T}$, the Second Law of thermodynamics states that for an arbitrary infinitesimal transformation the change of entropy per unit mass writes under the form

$$\mathsf{d}\eta = \frac{\delta Q}{T} + \mathsf{d}\eta_{\text{irr}}, \quad \text{with } \mathsf{d}\eta_{\text{irr}} \geq 0. \tag{2.77}$$

The first term in the right-hand side corresponds to entropy exchange with surroundings due to heat transfer. This is the reversible part of entropy change. The second term, which is always non-negative, characterizes the irreversible part of entropy change due to non-equilibrium process. At this point, let us introduce some vocabulary. We define an adiabatic process as a thermodynamic process in which no heat is transferred to or from the system under consideration, *i.e.*, $\delta Q = 0$. A reversible adiabatic process is said to be isentropic. In this case, we have $\delta Q = 0$, $\mathsf{d}\eta_{\text{irr}} = 0$ and thus $\mathsf{d}\eta = 0$.

Bearing this in mind, let us give the Second Law statement for a moving fluid domain ω. To this end, we define the entropy of the moving fluid domain as being

$$\int_\omega \rho\eta \, \mathsf{d}v.$$

Following the approach of [45, 63, 148, 40], the Second Law of thermodynamics statement for the moving fluid domain ω is introduced by means of the fundamental inequality

$$\frac{d}{dt}\int_\omega \rho\eta \, \mathsf{d}v \geq \int_\omega \rho \frac{r}{T} \, \mathsf{d}v - \int_{\partial\omega} \frac{\boldsymbol{q}\cdot\boldsymbol{n}}{T} \, \mathsf{d}s. \tag{2.78}$$

Noticing that $\int_\omega \rho r \, \mathsf{d}v - \int_{\partial\omega} \boldsymbol{q}\cdot\boldsymbol{n} \, \mathsf{d}s$ is the rate at which heat is supplied to the fluid within ω, refer to (2.65), it turns out that the right member of this inequality is the macroscopic counterpart of the $\frac{\delta Q}{T}$ term present in (2.77). The left member of this inequality is the rate at which entropy increases in the arbitrary fluid volume ω. The first term in the right member is the supply of entropy due to the heat supply r. The second term of the right member represents the rate at which entropy is introduced into the fluid by conduction of heat through the boundary of the fluid volume. This inequality expresses that the rate of increase of entropy is no less than that increase due to heat conduction into the fluid plus heat supply. Let us point out that the equal sign will hold in the above fundamental inequality (2.78) uniquely for a reversible process. We remark that the Second Law has been written under integral form. Applying transport formula and divergence formula to (2.78) yields the local form of the Second Law

$$\rho\frac{d\eta}{dt} \geq \rho\frac{r}{T} - \nabla_x \cdot (\frac{\boldsymbol{q}}{T}). \tag{2.79}$$

Note that this local form has been obtained under condition of sufficient smoothness for the fluid variables.

2.2.4 Constitutive laws modeling

Now, we present the consequences of the fundamental inequality (2.78) regarding the modeling of the fluid constitutive laws. Namely, we express the thermodynamic constraints that must satisfy the stress tensor and the heat flux. To this end, we express the rate of change of entropy in terms of the stress tensor and the heat flux by means of the Gibbs formula (2.68) as

$$\begin{aligned}\rho T\frac{d\eta}{dt} =& \frac{d\varepsilon}{dt} + \rho P\frac{d}{dt}(\frac{1}{\rho}) \\ =& \frac{d\varepsilon}{dt} + P\nabla_x \cdot \boldsymbol{U} && \text{thanks to (2.60a)} \\ =& \mathsf{T} : \mathsf{D} + P\,\mathrm{tr}\,\mathsf{D} - \nabla_x \cdot \boldsymbol{q} + \rho r. && \text{thanks to (2.63)}\end{aligned}$$

For classical fluids, it is usual to introduce the following decomposition for the stress tensor

$$\mathsf{T} = -P\,\mathsf{I}_d + \mathsf{V}. \tag{2.80}$$

Here, P denotes the thermodynamic pressure introduced previously. Second-order tensor V stands for the viscous stress tensor. A fluid for which $\mathsf{V} = 0$ is called a perfect fluid. In this particular case, the stress tensor reduces to the spherical tensor $\mathsf{T} = -P\,\mathsf{I}_d$. This corresponds to a fluid wherein tangential stresses are negligible. Using decomposition (2.80), time rate of change of entropy becomes

$$\rho T\frac{d\eta}{dt} = \mathsf{V} : \mathsf{D} - \nabla_x \cdot \boldsymbol{q} + \rho r. \tag{2.81}$$

Here, we have utilized identity $\mathsf{I}_d : \mathsf{D} = \mathrm{tr}(\mathsf{D})$. Equation (2.81) represents the rate of change of entropy following a fluid particle. The first term in the right-hand side is the rate per unit volume at which heat is generated by the deformation of fluid elements. Since this term involves a dissipation of kinetic energy into internal energy, it is called the dissipation function. The second term in the right-hand side corresponds to the conduction of heat from neighboring fluid elements. The last term is due to the heat supply. Dividing equation (2.81) by temperature and integrating it over the moving region ω, we finally obtain the following integral balance

$$\frac{d}{dt}\int_\omega \rho\eta\,\mathsf{d}v = \int_\omega \frac{1}{T}(\mathsf{V} : \mathsf{D} - \boldsymbol{q}\cdot\frac{\boldsymbol{\nabla}_x T}{T})\,\mathsf{d}v + \int_\omega \rho\frac{r}{T}\,\mathsf{d}v - \int_{\partial\omega}\frac{\boldsymbol{q}\cdot\boldsymbol{n}}{T}\,\mathsf{d}s. \tag{2.82}$$

Comparison of this equation to the fundamental inequality (2.78) shows that the first term in the right-hand side corresponds to the irreversible part of entropy production. Consistency with the Second Law of thermodynamics (2.78) implies that this term must be necessarily non-negative. Since the temperature is positive, this involves the following inequality

$$\mathsf{V} : \mathsf{D} - \boldsymbol{q}\cdot\frac{\boldsymbol{\nabla}_x T}{T} \geq 0. \tag{2.83}$$

This condition is satisfied provided that the viscous stress tensor and the heat flux vector satisfy the following inequalities

$$\mathsf{V} : \mathsf{D} \geq 0, \quad \boldsymbol{q}\cdot\boldsymbol{\nabla}_x T \leq 0. \tag{2.84}$$

These are the constraints imposed by thermodynamics on the modeling of the constitutive laws that characterize the fluid. The first constraint simply expresses that viscous deformation converts mechanical energy into heat while the second states that heat flux direction is opposite to temperature gradient. For classical fluids, *i.e.*, linearly viscous fluids, one can show that V

is a linear function of the stretch rate tensor D and $\boldsymbol{q}$ is a linear function of $\boldsymbol{\nabla}_x T$, refer to [41]. More precisely V and $\boldsymbol{q}$ are expressed as

$$\mathsf{V} = \lambda \operatorname{tr}(\mathsf{D})\mathsf{I}_d + 2\mu\mathsf{D}, \tag{2.85a}$$

$$\boldsymbol{q} = -\mathsf{K}\boldsymbol{\nabla}_x T. \tag{2.85b}$$

Here, the scalars, λ, μ, are the viscosity coefficients, and the second-order tensor, K, is the conductivity tensor. Let us mention that fluids for which the viscous stress is governed by (2.85a) are called Newtonian fluids. The second constitutive law corresponds to the Fourier Law. Thermodynamic constraints (2.83) and (2.84) imposes that viscosity coefficients satisfy $\mu \geq$, $\lambda + \frac{2}{3}\mu \geq 0$ and tensor conductivity is a symmetric positive definite tensor. Let us note that these results can also be obtained using the framework of irreversible thermodynamics which postulates that a thermodynamical system tends to equilibrium at a rate linearly dependent on its displacement from equilibrium. The reader might refer to [45] for having more details about this subject.

Comment 3 *Let us notice that a proper modeling of constitutive laws requires not only to satisfy thermodynamics constraints deduced from the Second Law of thermodynamics but also to be consistent with the principle of material objectivity or material frame indifference. This latter principle, states that constitutive laws must be invariant under a change of spatial frame. More precisely, if a constitutive equation is satisfied for a motion $\boldsymbol{x} = \boldsymbol{x}(\boldsymbol{X}, t)$ it must be also satisfied for the motion $\boldsymbol{x}^\star = \boldsymbol{x}^\star(\boldsymbol{X}, t)$ related to the first motion by*

$$\boldsymbol{x}^\star = \mathsf{Q}(t)\boldsymbol{x} + \boldsymbol{c}(t),$$

where Q is a second-order tensor characterizing an orthogonal transformation, i.e., $\mathsf{Q}\mathsf{Q}^t = \mathsf{I}_d$ and $\boldsymbol{c}$ a vector. For a detailed presentation of this topic, interested reader can refer to [25, 44, 41, 125]. For instance, the linear constitutive law (2.85a) *for the viscous stress is derived in [41] by means of the principle of material objectivity.*

Comment 4 *Introducing the heat flux constitutive law* (2.85b)*, i.e., $\boldsymbol{q} = -\mathsf{K}\boldsymbol{\nabla}_x T$, into the internal energy equation* (2.63) *leads to*

$$\rho \frac{d}{dt}\varepsilon - \boldsymbol{\nabla}_x \cdot (\mathsf{K}\boldsymbol{\nabla}_x T) = \rho r + \mathsf{T} : \mathsf{D}. \tag{2.86}$$

Let us recall that K is the conductivity tensor of the fluid, $\mathsf{T} : \mathsf{D}$ is the stress power and r is the heat supply per unit mass. In addition, $\frac{d}{dt}$ denotes the material derivative, i.e., $\frac{d}{dt}() = \frac{\partial}{\partial t}() + \boldsymbol{U} \cdot \boldsymbol{\nabla}_x()$. Knowing that specific internal energy can be expressed in terms of density and temperature by means of the equation of state $\varepsilon = \varepsilon(\rho, T)$, it turns out that the above equation is a non-linear convection-diffusion equation governing temperature evolution. In addition, if the fluid under consideration is an ideal fluid, internal energy equation can be recast as

$$\rho C_v \frac{dT}{dt} - \boldsymbol{\nabla}_x \cdot (\mathsf{K}\boldsymbol{\nabla}_x T) = \rho r + \mathsf{T} : \mathsf{D}, \tag{2.87}$$

where $C_v = C_v(T)$ is the specific heat capacity at constant volume. Suppose that the fluid variables except the temperature are known, to solve the above equation on the moving computational domain $\mathcal{D}$, we must supplement it by initial and boundary conditions. The initial condition writes as

$$T(\boldsymbol{x}, 0) = T^0(\boldsymbol{x}), \quad \forall\, \boldsymbol{x} \in \mathcal{D}^0, \tag{2.88}$$

where $\mathcal{D}^0$ denotes the initial computational domain. Concerning the boundary conditions, there are three possible types. The first type, named Dirichlet boundary condition, consists in specifying the temperature on the boundary of the domain. The second type, named Neumann boundary condition, amounts to prescribe the heat flux, $\boldsymbol{q}$, on the boundary. Note that we have already introduced it in the study devoted to the general boundary conditions of the conservation laws, refer to the last paragraph of Section 2.2.1. The third type, named Robin boundary condition, corresponds to a weighted combination of Dirichlet and Neumann boundary conditions. Let $\partial\mathcal{D} = \partial\mathcal{D}_D \cup \partial\mathcal{D}_N \cup \partial\mathcal{D}_R$ be a partition of the boundary domain corresponding to the three previous types. The boundary conditions associated to the internal energy equations write under the general form

$$T(\boldsymbol{x},t) = T^\star(\boldsymbol{x},t), \quad \forall \boldsymbol{x} \in \partial\mathcal{D}_D, \tag{2.89a}$$

$$\boldsymbol{q}(\boldsymbol{x},t)\cdot\boldsymbol{n} = q_N^\star(\boldsymbol{x},t), \quad \forall \boldsymbol{x} \in \partial\mathcal{D}_N, \tag{2.89b}$$

$$\alpha T(\boldsymbol{x},t) + \beta\boldsymbol{q}(\boldsymbol{x},t)\cdot\boldsymbol{n} = q_R^\star(\boldsymbol{x},t), \quad \forall \boldsymbol{x} \in \partial\mathcal{D}_R. \tag{2.89c}$$

Here, $T^\star$, $q_N^\star$ and $q_R^\star$ denote respectively prescribed temperature and fluxes. In addition, $\alpha = \alpha(\boldsymbol{x},t)$ and $\beta = \beta(\boldsymbol{x},t)$ are specified real valued functions. Note that β is an adimensional variable, whereas α has the dimension of an inverse length.

2.2.5 Jump equations describing moving discontinuity

Motivations

In this section, we assume that the fluid variables, *i.e.*, $\rho, \boldsymbol{U}, E, \mathsf{T}, \boldsymbol{q}$ are only piecewise continuously differentiable whereas the source terms, *i.e.*, $\boldsymbol{g}, r$ are continuous. Let σ be the propagating surface at which the fluid variables are discontinuous. The motion of this discontinuity surface at point $\boldsymbol{x}_\sigma \in \sigma$ is governed by the velocity $\boldsymbol{w} = \boldsymbol{w}(\boldsymbol{x}_\sigma, t)$. At σ, the partial differential equations corresponding to the local form of conservation laws developed in Section 2.2.2 do not exist in the classical sense due to the occurrence of Dirac measures. To circumvent this difficulty, we shall use the integral form of the conservation laws (2.55) since it is defined almost everywhere. The application of the transport formulas for piecewise continuously differentiable functions, which have been presented in Section 2.1.5, allows to derive jump conditions at σ for the fluid variables.

Rankine-Hugoniot relations for conservation laws

The jump conditions, otherwise named Rankine-Hugoniot conditions, express the conservation of mass, momentum and total energy across the discontinuity surface. We recall briefly their derivation following the approach described in [63]. Note that we use the notation that has been introduced in Section 2.1.5. Knowing that the jump condition associated to the mass conservation has been already derived in Section 2.1.5, we just recall its final form

$$[\![\rho(\boldsymbol{U}-\boldsymbol{w})]\!]\cdot\boldsymbol{n}_\sigma = 0, \quad \forall \boldsymbol{x}_\sigma \in \sigma.$$

Here, the symbol $[\![]\!]$ denotes the jump through the discontinuity surface. Knowing that σ divides the fluid region into the subregions ω_1 and ω_2, $\boldsymbol{n}_\sigma$ is the unit outward normal to σ with respect to ω_1, refer to Fig. 2.2. If f is a fluid variable, $[\![f]\!] = f_2 - f_1$ where f_1 and f_2 are the one-sided limits of f from the negative and the positive direction with respect to $\boldsymbol{n}_\sigma$. To derive the jump relation associated to momentum, we first apply transport formula (2.42) to $\rho\boldsymbol{U}$ to obtain the material derivative of momentum written under the form

$$\frac{d}{dt}\int_\omega \rho\boldsymbol{U}(\boldsymbol{x},t)\,\mathsf{d}v = \int_{\omega_1\cup\omega_2}[\frac{\partial}{\partial t}(\rho\boldsymbol{U}) + \nabla\cdot(\rho\boldsymbol{U}\otimes\boldsymbol{U})]\,\mathsf{d}v + \int_\sigma [\![\rho\boldsymbol{U}\otimes(\boldsymbol{U}-\boldsymbol{w})]\!]\boldsymbol{n}_\sigma\,\mathsf{d}s.$$

Secondly, we apply divergence formula (A.36) to express the contribution of the surface integral of the stress force as

$$\int_{\partial\omega} \mathsf{T}\boldsymbol{n}\,\mathrm{d}s = \int_{\omega_1\cup\omega_2} \nabla\cdot\mathsf{T}\,\mathrm{d}v + \int_{\sigma} [\![\mathsf{T}]\!]\boldsymbol{n}_\sigma\,\mathrm{d}s.$$

Combining the previous equations according to the integral conservation law of momentum (2.55c), we finally obtain

$$\int_{\omega_1\cup\omega_2} [\frac{\partial}{\partial t}(\rho\boldsymbol{U}) + \nabla\cdot(\rho\boldsymbol{U}\otimes\boldsymbol{U}) - \nabla\cdot\mathsf{T}]\,\mathrm{d}v + \int_{\sigma} \{[\![\rho\boldsymbol{U}\otimes(\boldsymbol{U}-\boldsymbol{w})]\!] - [\![\mathsf{T}]\!]\}\,\boldsymbol{n}_\sigma\,\mathrm{d}s = \int_{\omega} \rho\boldsymbol{g}\,\mathrm{d}v.$$

Knowing that the fluid variables are continuously differentiable over ω_1 and ω_2, the local form of the momentum equation (2.59b) is satisfied over each sub-domains which involves the cancellation of the volume integrals. Hence, momentum conservation reduces to

$$\int_{\sigma} \{[\![\rho\boldsymbol{U}\otimes(\boldsymbol{U}-\boldsymbol{w})]\!] - [\![\mathsf{T}]\!]\}\,\boldsymbol{n}_\sigma\,\mathrm{d}s = \boldsymbol{0}.$$

Since this equation holds for any arbitrary surface, jump relation for momentum writes as

$$[\![\rho\boldsymbol{U}\otimes(\boldsymbol{U}-\boldsymbol{w})]\!]\boldsymbol{n}_\sigma - [\![\mathsf{T}]\!]\boldsymbol{n}_\sigma = \boldsymbol{0}, \quad \forall\boldsymbol{x}_\sigma\in\sigma.$$

Proceeding with total energy conservation law as before yields the last jump relation

$$[\![\rho E(\boldsymbol{U}-\boldsymbol{w})]\!]\cdot\boldsymbol{n}_\sigma + [\![\boldsymbol{q}-\mathsf{T}\boldsymbol{U}]\!]\cdot\boldsymbol{n}_\sigma = 0, \quad \forall\boldsymbol{x}_\sigma\in\sigma.$$

Combining the previous results, we can write a system of three jump relations expressing respectively the conservation of mass, momentum and total energy across a discontinuity surface propagation with speed $\boldsymbol{w}$

$$[\![\rho(\boldsymbol{U}-\boldsymbol{w})]\!]\cdot\boldsymbol{n}_\sigma = 0, \tag{2.90a}$$
$$[\![\rho\boldsymbol{U}\otimes(\boldsymbol{U}-\boldsymbol{w})]\!]\boldsymbol{n}_\sigma - [\![\mathsf{T}]\!]\boldsymbol{n}_\sigma = \boldsymbol{0}, \tag{2.90b}$$
$$[\![\rho E(\boldsymbol{U}-\boldsymbol{w})]\!]\cdot\boldsymbol{n}_\sigma + [\![\boldsymbol{q}-\mathsf{T}\boldsymbol{U}]\!]\cdot\boldsymbol{n}_\sigma = 0. \tag{2.90c}$$

Let us remark that these jump relations are expressed in terms of the normal velocity of the discontinuity $\boldsymbol{w}\cdot\boldsymbol{n}_\sigma$. Moreover, they do not depend on the choice made for the direction of the unit vector $\boldsymbol{n}_\sigma$. We assume that the Cauchy stress tensor and the heat flux are expressed in terms of the fluid variables by some constitutive laws. Suppose we fix the fluid variables denoted by subscript 1, *i.e.*, $(\rho_1,\boldsymbol{U}_1,E_1)$, and attempt to determine the set of fluid variables $(\rho_2,\boldsymbol{U}_2,E_2)$ which can be connected to $(\rho_1,\boldsymbol{U}_1,E_1)$ by a discontinuity satisfying (2.90) for some $\boldsymbol{w}\cdot\boldsymbol{n}_\sigma$. This gives a system of $d+2$ equations in $d+3$ unknowns in $\mathbb{R}^d$. Therefore, we will obtain a family of solutions depending on one parameter.

We conclude this paragraph by studying the system of jump relations. First, let us note that jump equation (2.90a) is equivalent to

$$\rho_1(\boldsymbol{U}_1-\boldsymbol{w})\cdot\boldsymbol{n}_\sigma = \rho_2(\boldsymbol{U}_2-\boldsymbol{w})\cdot\boldsymbol{n}_\sigma.$$

This relation states that the mass flux crossing the discontinuity surface is continuous. This amounts to set

$$m = \rho_i(\boldsymbol{U}_i-\boldsymbol{w})\cdot\boldsymbol{n}_\sigma,\ i=1,2 \tag{2.91}$$

where m denotes the mass flux. Knowing that $\boldsymbol{U}-\boldsymbol{w}$ is the relative velocity of the fluid with respect to the discontinuity velocity, we point out that $m>0$ corresponds to the case where the fluid is crossing the discontinuity surface in the direction given by the unit normal $\boldsymbol{n}_\sigma$. Using

the above equation, it is straightforward to show that the discontinuity normal velocity writes as

$$\boldsymbol{w}\cdot\boldsymbol{n}_\sigma = \frac{[\![\rho\boldsymbol{U}]\!]\cdot\boldsymbol{n}_\sigma}{[\![\rho]\!]}. \tag{2.92}$$

Knowing that $\frac{m}{\rho_i} = (\boldsymbol{U}_i - \boldsymbol{w})\cdot\boldsymbol{n}_\sigma$, Equation (2.90a) is rewritten as

$$m[\![\frac{1}{\rho}]\!] = [\![\boldsymbol{U}]\!]\cdot\boldsymbol{n}_\sigma. \tag{2.93}$$

Using the definition of the dyadic product (A.1), we transform (2.90b) into

$$[\![\rho\boldsymbol{U}(\boldsymbol{U}-\boldsymbol{w})\cdot\boldsymbol{n}_\sigma]\!] - [\![\mathsf{T}]\!]\boldsymbol{n}_\sigma = \boldsymbol{0}.$$

Then, substituting mass flux m in the first term of the previous equation, we obtain

$$m[\![\boldsymbol{U}]\!] - [\![\mathsf{T}]\!]\boldsymbol{n}_\sigma = \boldsymbol{0}. \tag{2.94}$$

In writing the momentum jump under this form, we clearly observe that it corresponds to momentum conservation through the discontinuity surface. Proceeding with total energy jump (2.90c) as before yields

$$m[\![E]\!] + [\![\boldsymbol{q}]\!]\cdot\boldsymbol{n}_\sigma - [\![\mathsf{T}\boldsymbol{U}]\!]\cdot\boldsymbol{n}_\sigma = 0. \tag{2.95}$$

It remains to determine the jump relation associated to internal energy $\varepsilon = E - \frac{1}{2}\mid\boldsymbol{U}\mid^2$. To this end, we start deriving the jump relation of kinetic energy dot-multiplying momentum jump relation (2.94) by $\overline{\boldsymbol{U}} = \frac{1}{2}(\boldsymbol{U}_2+\boldsymbol{U}_1)$

$$m[\![\frac{1}{2}\mid\boldsymbol{U}\mid^2]\!] - [\![\mathsf{T}]\!]\boldsymbol{n}_\sigma\cdot\overline{\boldsymbol{U}} = 0.$$

For an arbitrary tensor T, through the use of the transpose definition (A.6), last equation rewrites as

$$m[\![\frac{1}{2}\mid\boldsymbol{U}\mid^2]\!] - [\![\mathsf{T}^{\mathrm{t}}]\!]\overline{\boldsymbol{U}}\cdot\boldsymbol{n}_\sigma = 0. \tag{2.96}$$

Subtracting (2.96) to total energy jump equation (2.95) and noticing that $[\![\mathsf{T}\boldsymbol{U}]\!] = [\![\mathsf{T}]\!]\overline{\boldsymbol{U}} + \overline{\mathsf{T}}[\![\boldsymbol{U}]\!]$, yields the internal energy jump equation

$$m[\![\varepsilon]\!] + [\![\boldsymbol{q}]\!]\cdot\boldsymbol{n}_\sigma - \overline{\mathsf{T}}[\![\boldsymbol{U}]\!]\cdot\boldsymbol{n}_\sigma - [\![\mathsf{T}-\mathsf{T}^t]\!]\overline{\boldsymbol{U}}\cdot\boldsymbol{n} = 0.$$

In deriving this equation, we have considered the Cauchy stress tensor as an arbitrary tensor forgetting that it is symmetric. This explains the occurrence of the last term in the left-hand side of the above equation. To ensure the Galilean invariance of the internal energy jump equation, this term must cancel, *i.e.*, $\mathsf{T}-\mathsf{T}^t = \mathsf{O}$. Let us emphasize that symmetry of the Cauchy stress tensor is required not only to ensure conservation of angular momentum but also to ensure Galilean invariance of the internal energy jump relation. Knowing that Cauchy stress tensor is symmetric leads to the final form of the internal energy jump relation

$$m[\![\varepsilon]\!] + [\![\boldsymbol{q}]\!]\cdot\boldsymbol{n}_\sigma - \overline{\mathsf{T}}[\![\boldsymbol{U}]\!]\cdot\boldsymbol{n}_\sigma = 0. \tag{2.97}$$

Gathering the previous results, jump relations at the discontinuity surface write as

$$\begin{aligned}
&m[\![\frac{1}{\rho}]\!] - [\![\boldsymbol{U}]\!]\cdot\boldsymbol{n}_\sigma = 0,\\
&m[\![\boldsymbol{U}]\!] - [\![\mathsf{T}]\!]\boldsymbol{n}_\sigma = \boldsymbol{0},\\
&m[\![\varepsilon]\!] + [\![\boldsymbol{q}]\!]\cdot\boldsymbol{n}_\sigma - \overline{\mathsf{T}}[\![\boldsymbol{U}]\!]\cdot\boldsymbol{n}_\sigma = 0,
\end{aligned}$$

where a bar over a variable denote the average, *i.e.*, $\overline{\mathsf{T}} = \frac{1}{2}(\mathsf{T}_2+\mathsf{T}_1)$. Let us remark that these relations depend only on the difference between the one-sided fluid velocity, *i.e.*, $(\boldsymbol{U}_2-\boldsymbol{U}_1)$. Therefore, these jump relations satisfy the principle of Galilean invariance.

Entropy inequality

We proceed as before to derive the jump relation associated to entropy inequality (2.78). First, applying transport formula (2.44) for piecewise continuously differentiable function $\rho\eta$ leads to

$$\frac{d}{dt}\int_{\omega}\rho\eta(\boldsymbol{x},t)\,\mathrm{d}v=\int_{\omega_1\cup\omega_2}[\frac{\partial}{\partial t}(\rho\eta)+\nabla\cdot(\rho\eta\boldsymbol{U})]\,\mathrm{d}v+\int_{\sigma}[\![\rho\eta(\boldsymbol{U}-\boldsymbol{w})]\!]\cdot\boldsymbol{n}_{\sigma}\,\mathrm{d}s.$$

Substituting this in the entropy inequality yields the following inequality

$$\int_{\omega_1\cup\omega_2}[\frac{\partial}{\partial t}(\rho\eta)+\nabla\cdot(\rho\eta\boldsymbol{U})]\,\mathrm{d}v+\int_{\sigma}[\![\rho\eta(\boldsymbol{U}-\boldsymbol{w})]\!]\cdot\boldsymbol{n}_{\sigma}\,\mathrm{d}s\geq\int_{\omega}\rho\frac{r}{T}\,\mathrm{d}v-\int_{\partial\omega}\frac{\boldsymbol{q}\cdot\boldsymbol{n}}{T}\,\mathrm{d}s.$$

Secondly, expressing the surface integral, in the left-hand side of the above inequality, through the use of the divergence formula for piecewise smooth function (A.35) yields

$$\int_{\omega_1\cup\omega_2}\{\rho\frac{d\eta}{dt}+\nabla_x\cdot(\frac{\boldsymbol{q}}{T})-\rho\frac{r}{T}\}\,\mathrm{d}v+\int_{\sigma}[\![\rho\eta(\boldsymbol{U}-\boldsymbol{w})+\frac{\boldsymbol{q}}{T}]\!]\cdot\boldsymbol{n}_{\sigma}\,\mathrm{d}s\geq 0.$$

Here, note that we have made use of the following equality: $\rho\frac{d\eta}{dt}=\frac{\partial}{\partial t}(\rho\eta)+\nabla\cdot(\rho\eta\boldsymbol{U})$, which holds since the fluid variables are smooth over each sub-regions ω_1 and ω_2. Knowing that the local form (2.79) of the entropy inequality holds over ω_1 and ω_2, the above inequality is satisfied provided that the integrand of the second integral is non-negative. This amounts to write the following jump inequality

$$[\![\rho\eta(\boldsymbol{U}-\boldsymbol{w})+\frac{\boldsymbol{q}}{T}]\!]\cdot\boldsymbol{n}_{\sigma}\geq 0. \tag{2.98}$$

Introducing the mass flux in the above equation leads to

$$m[\![\eta]\!]+[\![\frac{\boldsymbol{q}}{T}]\!]\cdot\boldsymbol{n}_{\sigma}\geq 0. \tag{2.99}$$

Let us point out that the above inequality depends on the choice made for the direction of the unit normal $\boldsymbol{n}_{\sigma}$.

Contact discontinuity and shock wave

Depending on the value of m , we can distinguish the two following cases of discontinuity surface.

Contact discontinuity This corresponds to a discontinuity surface across which there is no mass flux, *i.e.*, $m=0$. Therefore, jump relations reduce to

$$\begin{aligned}
&[\![\boldsymbol{U}]\!]\cdot\boldsymbol{n}_{\sigma}=0,\\
&[\![\mathsf{T}]\!]\boldsymbol{n}_{\sigma}=\boldsymbol{0},\\
&[\![\boldsymbol{q}]\!]\cdot\boldsymbol{n}_{\sigma}-\overline{\mathsf{T}}[\![\boldsymbol{U}]\!]\cdot\boldsymbol{n}_{\sigma}=0,\\
&[\![\frac{\boldsymbol{q}}{T}]\!]\cdot\boldsymbol{n}_{\sigma}\geq 0.
\end{aligned}$$

Let us emphasize that normal component of the velocity and normal stress are continuous at contact discontinuity. Moreover, the normal velocity of the contact discontinuity is equal to the normal velocity of the fluid, *i.e.*, $\boldsymbol{w}\cdot\boldsymbol{n}_{\sigma}=\boldsymbol{U}_i\cdot\boldsymbol{n}_{\sigma}$, $i=1,2$. Let $\boldsymbol{U}_{t,1},\boldsymbol{U}_{t,2}$ denotes the tangential one-sided velocities, *i.e.*, $\boldsymbol{U}_i=(\boldsymbol{U}_i\cdot\boldsymbol{n}_{\sigma})\boldsymbol{n}_{\sigma}+\boldsymbol{U}_{t,i}$, $i=1,2$. Knowing that the normal velocities are continuous at σ, velocity jump reduces to a tangential velocity jump, *i.e.*, $[\![\boldsymbol{U}]\!]=[\![\boldsymbol{U}_t]\!]$, and the last equation in the above system becomes

$$[\![\boldsymbol{q}]\!]\cdot\boldsymbol{n}_{\sigma}-\overline{\mathsf{T}}[\![\boldsymbol{U}_t]\!]\cdot\boldsymbol{n}_{\sigma}=0.$$

We finally remark that if $[\![\boldsymbol{U}_t]\!] \neq 0$, there is a sliding motion in the vicinity of σ which induces a discontinuity of the normal heat flux. Moreover, for of a perfect fluid, *i.e.*, $\mathsf{T} = -P\,\mathsf{I}_d$, the last but one jump relation involves the continuity of the normal heat flux, *i.e.*, $\boldsymbol{q}_1 \cdot \boldsymbol{n}_\sigma = \boldsymbol{q}_2 \cdot \boldsymbol{n}_\sigma = \overline{\boldsymbol{q}} \cdot \boldsymbol{n}_\sigma$. In this case, last inequality reduces to $\overline{\boldsymbol{q}} \cdot \boldsymbol{n}_\sigma [\![\frac{1}{T}]\!] \geq 0$, which simply means that heat flows from hot region to cold region.

Shock wave This corresponds to a discontinuity surface across which there is a mass flux, *i.e.*, $m \neq 0$. A shock wave is characterized by the discontinuity of all the fluid variables. We shall see later that the jump relations corresponding to a shock wave can be further investigated in the case of a perfect fluid.

2.2.6 Eulerian forms of the gas dynamics equations

Gas dynamics equations, otherwise named Euler equations, are deduced from the conservation laws of fluid mechanics by setting $\mathsf{T} = -P\,\mathsf{I}_d$ and $\boldsymbol{q} = \boldsymbol{0}$. Namely, gas dynamics equations characterize fluids in which viscous stress and heat conduction are negligible. We also make the assumption that the supply heat is equal to zero, *i.e.*, $r = 0$.

Eulerian integral form of the gas dynamics equations

Applying the assumption of a non-viscous and non-conductive fluid to the system of conservation laws (2.55) yields the integral Eulerian form of gas dynamics equations

$$\frac{d}{dt}\int_\omega \rho \,\mathrm{d}v = 0, \tag{2.100a}$$

$$\frac{d}{dt}\int_\omega \mathrm{d}v - \int_{\partial\omega} \boldsymbol{U}\cdot\boldsymbol{n}\,\mathrm{d}s = 0, \tag{2.100b}$$

$$\frac{d}{dt}\int_\omega \rho\boldsymbol{U}\,\mathrm{d}v + \int_{\partial\omega} P\boldsymbol{n}\,\mathrm{d}s = \int_\omega \rho\boldsymbol{g}\,\mathrm{d}v, \tag{2.100c}$$

$$\frac{d}{dt}\int_\omega \rho E\,\mathrm{d}v + \int_{\partial\omega} P\boldsymbol{U}\cdot\boldsymbol{n}\,\mathrm{d}s = \int_\omega \rho\boldsymbol{g}\cdot\boldsymbol{U}\,\mathrm{d}v. \tag{2.100d}$$

Knowing that the heat flux has been neglected, thermodynamic constraint imposed by the Second Law of thermodynamics (2.101) collapses to

$$\frac{d}{dt}\int_\omega \rho\eta\,\mathrm{d}v \geq 0. \tag{2.101}$$

To solve the above system on a computational domain, it has to be completed by initial and boundary conditions as it has been already mentioned at the end of Section 2.2.1. Knowing that the stress tensor reduces to the spherical tensor $\mathsf{T} = -P\,\mathsf{I}_d$, kinematic and dynamic boundary conditions (2.57) transform to

$$\boldsymbol{U}(\boldsymbol{x},t)\cdot\boldsymbol{n} = U_n^\star(\boldsymbol{x},t), \quad \forall \boldsymbol{x} \in \partial\mathcal{D}_k, \tag{2.102a}$$

$$P(\boldsymbol{x},t) = P^\star(\boldsymbol{x},t), \quad \forall \boldsymbol{x} \in \partial\mathcal{D}_d, \tag{2.102b}$$

where $U_n^\star$ and $P^\star$ are the prescribed normal velocity and pressure. Solid-wall boundary condition (2.102a) states that the normal component of the velocity is prescribed. This due to the fact that inviscid fluids are free to slip along the wall.

We conclude this paragraph by pointing out that this Eulerian integral form of the gas dynamics conservation laws is also referred as to the integral updated Lagrangian formulation.

Eulerian local forms of the gas dynamics equations

Proceeding with the local Eulerian form of the conservation laws as before yields the local Eulerian form of the gas dynamics equations

$$\frac{\partial \rho}{\partial t} + \nabla_x \cdot (\rho \boldsymbol{U}) = 0, \tag{2.103a}$$

$$\frac{\partial}{\partial t}(\rho \boldsymbol{U}) + \nabla_x \cdot (\rho \boldsymbol{U} \otimes \boldsymbol{U}) + \boldsymbol{\nabla} P = \rho \boldsymbol{g}, \tag{2.103b}$$

$$\frac{\partial}{\partial t}(\rho E) + \nabla_x \cdot (\rho E \boldsymbol{U}) + \nabla \cdot (P \boldsymbol{U}) = \rho \boldsymbol{g} \cdot \boldsymbol{U}. \tag{2.103c}$$

Thermodynamic closure of the previous system is ensured by the equation of state which relates pressure, density and internal energy as follows $P = P(\rho, \varepsilon)$. For smooth fluid variables, gas dynamics equations can also be written under the non-conservative form

$$\rho \frac{d}{dt}(\frac{1}{\rho}) - \nabla_x \cdot \boldsymbol{U} = 0, \tag{2.104a}$$

$$\rho \frac{d}{dt} \boldsymbol{U} + \boldsymbol{\nabla}_x P = \rho \boldsymbol{g}, \tag{2.104b}$$

$$\rho \frac{d}{dt} E + \nabla_x \cdot (P \boldsymbol{U}) = \rho \boldsymbol{g} \cdot \boldsymbol{U}. \tag{2.104c}$$

In addition the local form of the fundamental inequality writes

$$\rho \frac{d\eta}{dt} \geq 0. \tag{2.105}$$

Let us notice that the rate of change of entropy following a fluid particle, given by Equation (2.81), now reduces to the trivial equation

$$\rho T \frac{d\eta}{dt} = 0, \tag{2.106}$$

since $\boldsymbol{q} = \boldsymbol{0}$ and $\mathsf{V} = \mathsf{O}$. This equation states that for smooth flows, entropy is conserved along the trajectory of fluid particles. Such a flow is named isentropic flow. At first glance, the latter equation might seem to be paradoxical with respect to the fundamental inequality (2.105) since it means that entropy is conserved along fluid particle trajectory. To solve this paradox, it is important to note that Equation (2.81) has been derived under conditions of sufficient smoothness for the fluid variables. Hence, Equation (2.106) is only valid for sufficiently smooth fluid flows. For non-smooth fluid flows, such as those generated by shock waves, we have shown that entropy undergoes a jump at discontinuity surfaces present in the flow, refer to (2.98), and hence Equation (2.106) is not valid anymore. In this case, the relevant form of the gas dynamics equations is the integral form (2.100), which must be completed by the fundamental inequality (2.101) to ensure the consistency with the Second Law of thermodynamics. This very important requirement, which ensures the dissipation of kinetic energy into internal energy through shock waves, will be one of the cornerstones to achieve a relevant numerical discretization of the gas dynamics equations.

Rankine-Hugoniot relations for gas dynamics equations

Substituting $\mathsf{T} = -P\,\mathsf{I}_d$ and $\boldsymbol{q} = \mathbf{0}$ in the jump equations (2.93), (2.94), (2.95) and (2.98) yields the gas dynamics Rankine-Hugoniot relations

$$m[\![\frac{1}{\rho}]\!] - [\![\boldsymbol{U}]\!] \cdot \boldsymbol{n}_\sigma = 0, \tag{2.107a}$$

$$m[\![\boldsymbol{U}]\!] + [\![P]\!]\boldsymbol{n}_\sigma = \mathbf{0}, \tag{2.107b}$$

$$m[\![E]\!] + [\![P\boldsymbol{U}]\!] \cdot \boldsymbol{n}_\sigma = 0, \tag{2.107c}$$

$$m[\![\eta]\!] \geq 0. \tag{2.107d}$$

These jump relations state the conservation of mass, momentum and total energy across the moving discontinuity surface σ. Here, m denotes the mass flux across σ. Let us recall that the normal velocity of σ is given by (2.92). Equation (2.107c) can be replaced by the internal energy jump relation which is deduced from (2.97)

$$m[\![\varepsilon]\!] + \overline{P}[\![\boldsymbol{U}]\!] \cdot \boldsymbol{n}_\sigma = 0, \tag{2.108}$$

where the bar denotes the average, *i.e.*, $\overline{P} = \frac{1}{2}(P_1 + P_2)$. Depending on whether or not the mass flux cancels, the discontinuity surface can be either a contact discontinuity ($m = 0$) or a shock wave ($m \neq 0$). Proceeding as in Section 2.2.5, we distinguish the two following cases.

Contact discontinuity In this case, there is no mass flux crossing σ. Pressure and normal component of the velocity are continuous at the contact discontinuity, *i.e.*, $[\![P]\!] = 0$ and $[\![\boldsymbol{U}]\!] \cdot \boldsymbol{n}_\sigma = 0$. The normal component of the shock velocity is equal to the normal component of the fluid velocity, *i.e.*, $\boldsymbol{w} \cdot \boldsymbol{n}_\sigma = \boldsymbol{U}_1 \cdot \boldsymbol{n}_\sigma = \boldsymbol{U}_2 \cdot \boldsymbol{n}_\sigma$. However, density, internal energy and tangential component of the velocity may be discontinuous at σ.

Shock wave In this case, there is a mass flux crossing σ. Since, $m \neq 0$ mass flux is eliminated in (2.107d) through the use of (2.107a). Moreover, projecting vector equation (2.107b) onto the unit normal $\boldsymbol{n}_\sigma$ and the tangent plane to shock wave, we obtain the final form of the Rankine-Hugoniot relations governing shock wave propagation

$$m[\![\frac{1}{\rho}]\!] - [\![\boldsymbol{U}]\!] \cdot \boldsymbol{n}_\sigma = 0, \tag{2.109a}$$

$$m[\![\boldsymbol{U}]\!] \cdot \boldsymbol{n}_\sigma + [\![P]\!] = 0, \tag{2.109b}$$

$$[\![\boldsymbol{U}_t]\!] \cdot \boldsymbol{n}_\sigma = \mathbf{0}, \tag{2.109c}$$

$$[\![\varepsilon]\!] + \overline{P}[\![\frac{1}{\rho}]\!] = 0, \tag{2.109d}$$

$$m[\![\eta]\!] \geq 0. \tag{2.109e}$$

We notice that all the fluid variables are discontinuous at σ except the tangential component of the velocity. Equation (2.109d) determines all the possible thermodynamical states $(\frac{1}{\rho}_2, P_2)$ which may be reached across a shock wave from an initial state $(\frac{1}{\rho}_1, P_1)$. This equation, otherwise named Hugoniot relation, writes explicitly as

$$\varepsilon_2 - \varepsilon_1 + \frac{1}{2}(P_1 + P_2)(\frac{1}{\rho_2} - \frac{1}{\rho_1}) = 0. \tag{2.110}$$

Being given an equation of state written under the form $P = P(\frac{1}{\rho}, \varepsilon)$, (2.110) determines a curve in the thermodynamical plane $(\frac{1}{\rho}, P)$ known as the Hugoniot curve. Last equation of system

(2.109) ensure thermodynamic consistency with the Second Law. This equation states that the specific entropy of a fluid particle crossing the shock wave is always increasing in the direction of the mass flux. It allows to determine the physical relevant solution of system (2.109), that is a compressive shock. In other words, across shock wave which satisfies entropy inequality (2.109e), density and pressure increase in the direction of the mass flux. For an ideal gas equation of state, *i.e.*, $P = (\gamma - 1)\rho\varepsilon$, it is possible to solve analytically the Rankine-Hugoniot equations, refer to [134, 81, 168] and also Appendix B.

One-dimensional Eulerian gas dynamics

Making the assumption of one-dimensional flow with slab symmetry, gas dynamics equations write under local form as

$$\frac{\partial}{\partial t}\rho + \frac{\partial}{\partial x}(\rho u) = 0, \tag{2.111a}$$

$$\frac{\partial}{\partial t}(\rho u) + \frac{\partial}{\partial x}(\rho u^2) + \frac{\partial}{\partial x}P = \rho g, \tag{2.111b}$$

$$\frac{\partial}{\partial t}(\rho E) + \frac{\partial}{\partial x}(\rho E u) + \frac{\partial}{\partial x}(P u) = \rho g u. \tag{2.111c}$$

Let us recall that thermodynamics closure is ensure by an equation of state which takes the form $P = P(\rho, \varepsilon)$, where $\varepsilon = E - \frac{1}{2}u^2$. The above system consists of a set of partial differential equations which are valid provided that fluid variables are continuously differentiable. The occurrence of discontinuity waves in the flow is taken into account by means of the Rankine-Hugoniot jump relations that follow from (2.107)

$$m[\![\frac{1}{\rho}]\!] - [\![u]\!] = 0, \tag{2.112a}$$

$$m[\![u]\!] + [\![P]\!] = 0, \tag{2.112b}$$

$$m[\![E]\!] + [\![Pu]\!] = 0. \tag{2.112c}$$

In writing this equation we have defined the unit normal at the discontinuity by $\boldsymbol{n}_\sigma = \boldsymbol{e}_x$ where $\boldsymbol{e}_x$ is the unit normal in the direction of positive x coordinate. Here, m denotes the mass flux of fluid particles crossing the discontinuity. It is defined by $m = \rho_1(u_1 - w) = \rho_2(u_2 - w)$ where w denotes the speed of the discontinuity wave. Second Law of thermodynamics is enforced by the entropy jump relation

$$m[\![\eta]\!] \geq 0.$$

This inequality states that the specific entropy of a fluid particle crossing the discontinuity is always increasing in the direction of the flow.

2.3 Lagrangian form of the fluid mechanics conservation laws

After having studied the conservation laws of fluid mechanics written under Eulerian formalism, we aim at deriving their Lagrangian form.

2.3.1 Lagrangian integral form of the conservation laws

We start the derivation by writing the integral Lagrangian form. To this end, we transform the Eulerian integral form (2.55) by means of the change of variables which relates Lagrangian, $\boldsymbol{X}$, and Eulerian, $\boldsymbol{x}$, coordinates, *i.e.*, the mapping $\boldsymbol{x} = \boldsymbol{\Phi}(\boldsymbol{X}, t)$.

Notation

Let us recall notation that has been introduced in Section 2.1. If Ω denotes a region of the initial (Lagrangian) configuration, then its image by the fluid flow map in the actual (Eulerian) configuration is $\omega = \omega(t)$ defined by $\omega(t) = \{\boldsymbol{x} = \boldsymbol{\Phi}(\boldsymbol{X}, t) \mid \boldsymbol{X} \in \Omega\}$. The volume element in the Eulerian configuration, $\mathsf{d}v$, is expressed in terms of the volume element in the Lagrangian configuration, $\mathsf{d}V$, by means of the relation $\mathsf{d}v = J\,\mathsf{d}V$, where J denotes the Jacobian of the fluid flow map. Let $\partial\omega$ and $\partial\Omega$ denote the boundary of the Eulerian and Lagrangian regions, and $\boldsymbol{n}\,\mathsf{d}s$, $\boldsymbol{N}\,\mathsf{d}S$ their respective orientated surface elements. These orientated surface elements are related by means of the Nanson formula (2.49), *i.e.*, $\boldsymbol{n}\mathsf{d}s = J\mathsf{F}^{-t}\boldsymbol{N}\mathsf{d}S$ where F^{-t} is the transpose of the inverse of the Jacobian matrix of the fluid flow map.

Integral Lagrangian form derivation

Having this in mind, this enables the Eulerian integral form of the conservation laws (2.55) to be transformed into the Lagrangian integral form as follows

$$\frac{d}{dt}\int_\Omega \rho J\,\mathsf{d}V = 0, \tag{2.113a}$$

$$\frac{d}{dt}\int_\Omega J\,\mathsf{d}V - \int_{\partial\Omega} J\boldsymbol{U}\cdot\mathsf{F}^{-t}\boldsymbol{N}\,\mathsf{d}S = 0, \tag{2.113b}$$

$$\frac{d}{dt}\int_\Omega \rho J\boldsymbol{U}\,\mathsf{d}V - \int_{\partial\Omega} J\mathsf{T}\mathsf{F}^{-t}\boldsymbol{N}\,\mathsf{d}S = \int_\Omega \rho J\boldsymbol{g}\,\mathsf{d}V, \tag{2.113c}$$

$$\frac{d}{dt}\int_\Omega \rho JE\,\mathsf{d}V - \int_{\partial\Omega} J\mathsf{T}\boldsymbol{U}\cdot\mathsf{F}^{-t}\boldsymbol{N}\,\mathsf{d}S + \int_{\partial\Omega} J\boldsymbol{q}\cdot\mathsf{F}^{-t}\boldsymbol{N}\,\mathsf{d}S = \int_\Omega \rho J(\boldsymbol{g}\cdot\boldsymbol{U} + r)\,\mathsf{d}V. \tag{2.113d}$$

Equation (2.113b) states the time rate of change of the volume. It has been derived by transforming the Geometric Conservation Law (2.55b). The remaining equations correspond to mass, momentum and total energy balance written in the Lagrangian configuration. Knowing that T is the Cauchy stress tensor, then $J\mathsf{T}\mathsf{F}^{-t}$ represents the first Piola-Kirchhoff stress tensor, otherwise called Piola-Lagrange stress tensor [141, 63]. It naturally appears when writing the balance of momentum with respect to the Lagrangian configuration, refer to [117, 86]. Indeed, the force element acting on the Eulerian surface element $\boldsymbol{n}\mathsf{d}s$, writes as $\mathsf{T}\boldsymbol{n}\mathsf{d}s$. By means of (2.49), we express this force element with respect to the Lagrangian configuration as $J\mathsf{T}\mathsf{F}^{-t}\,\boldsymbol{N}\mathsf{d}S$. Using similar arguments, it is clear that vector $J\mathsf{F}^{-1}\boldsymbol{q}$ corresponds to the Lagrangian heat flux. Indeed, knowing that $\boldsymbol{q}\cdot\boldsymbol{n}\,\mathsf{d}s$ represents the rate at which energy is crossing the boundary in the Eulerian frame, its counterpart in the Lagrangian frame is obtained through the use of the Nanson's formula, that is

$$\begin{aligned}\boldsymbol{q}\cdot\boldsymbol{n}\,\mathsf{d}s =& \boldsymbol{q}\cdot J\mathsf{F}^{-t}\,\mathsf{d}S\\ =& J\mathsf{F}^{-1}\boldsymbol{q}\cdot\boldsymbol{N}\,\mathsf{d}S.\end{aligned}$$

Second Law of thermodynamics is expressed by transforming the fundamental inequality (2.78) into

$$\frac{d}{dt}\int_\Omega \rho J\eta\,\mathsf{d}V \geq \int_\Omega \rho J\frac{r}{T}\,\mathsf{d}V - \int_{\partial\Omega}\frac{1}{T}\boldsymbol{q}\cdot J\mathsf{F}^{-t}\boldsymbol{N}\,\mathsf{d}S. \tag{2.114}$$

Geometric conservation law for the deformation gradient

System (2.113) has to be completed by adding the conservation law associated to the deformation gradient F. The time derivative of the relation that defines the deformation gradient tensor,

i.e., $\mathsf{F} = \nabla_X \boldsymbol{\Phi} = \nabla_X \boldsymbol{x}$, provides its evolution equation written under local form

$$\frac{d}{dt}\mathsf{F} - \nabla_X \boldsymbol{U} = \mathsf{O}. \tag{2.115}$$

Integrating this equation over the Lagrangian volume Ω and applying divergence formula (A.34a) to the right-hand side yields the integral form of the deformation gradient conservation law

$$\frac{d}{dt}\int_\Omega \mathsf{F}\,\mathrm{d}V - \int_{\partial\Omega} \boldsymbol{U} \otimes \boldsymbol{N}\,\mathrm{d}S = \mathsf{O}. \tag{2.116}$$

Comment 5 *Knowing the fluid velocity and the initial condition* $\mathsf{F} = \mathsf{I}_d$*, equation* (2.115) *allows us to compute the deformation gradient tensor at any time. However, to recover the fluid flow map* $\boldsymbol{\Phi}$ *from the deformation gradient* F *requires the compatibility conditions*

$$\boldsymbol{\nabla}_X \times \boldsymbol{\mathcal{F}}_i = \boldsymbol{0},\ i = X, Y, Z. \tag{2.117}$$

Here, $\boldsymbol{\mathcal{F}}_i$ *is the vector whose* j*th component is* F_{ij} *and* $\boldsymbol{\nabla}_X \times$ *denotes the curl operator. Being given an arbitrary vector* $\boldsymbol{U} = \boldsymbol{U}(\boldsymbol{X})$ *its curl is defined as*

$$\boldsymbol{\nabla}_X \times \boldsymbol{U} = \left(\frac{\partial w}{\partial Y} - \frac{\partial v}{\partial Z}, \frac{\partial u}{\partial Z} - \frac{\partial w}{\partial X}, \frac{\partial v}{\partial X} - \frac{\partial u}{\partial Y}\right)^t.$$

Compatibility condition (2.117) *states that vector* $\boldsymbol{\mathcal{F}_i}$ *is curl-free, hence it is a conservative vector which derives from a scalar potential. Namely,* $\boldsymbol{\mathcal{F}_i}$ *takes the form*

$$\boldsymbol{\mathcal{F}_i} = \boldsymbol{\nabla}_X \Phi_i,$$

where Φ_i *denotes the corresponding scalar potential which allows to define the fluid flow map. Let us remark that if the compatibility conditions* (2.117) *are satisfied at initial time then the compatibility conditions will be satisfied for all time.*

Initial and boundary conditions for the Lagrangian integral form

We want to solve system (2.113) on the fixed computation domain $\mathcal{D}^0$. Proceeding as we did for the Eulerian form, refer to last paragraph of Section 2.2.1, yields the following initial conditions prescribed for all $\boldsymbol{X} \in \mathcal{D}^0$

$$\rho(\boldsymbol{X}, 0) = \rho^0(\boldsymbol{X}), \tag{2.118a}$$
$$\boldsymbol{U}(\boldsymbol{x}, 0) = \boldsymbol{U}^0(\boldsymbol{X}), \tag{2.118b}$$
$$E(\boldsymbol{X}, 0) = E^0(\boldsymbol{X}), \tag{2.118c}$$
$$\mathsf{F}(\boldsymbol{X}, 0) = \mathsf{I}_d. \tag{2.118d}$$

Compared to the Eulerian initial conditions (2.56), note that we have added (2.118d) specifying the initial condition for the deformation gradient F. Concerning the boundary conditions, depending on whether the heat flux is neglected or not, we distinguish the two following cases.

- $\boldsymbol{q} = \boldsymbol{0}$: Depending on the problem we want to solve, we can prescribe either kinematic or dynamic boundary conditions along the boundary of the fixed domain $\mathcal{D}^0$. Let $\partial\mathcal{D}^0 = \partial\mathcal{D}^0_k \cup \partial\mathcal{D}^0_d$ be a partition corresponding respectively to the kinematic and the dynamic boundary conditions. With this notation, boundary conditions are implemented for all time $t > 0$ as follows

$$\boldsymbol{U}(\boldsymbol{X}, t) = \boldsymbol{U}^\star(\boldsymbol{X}, t), \quad \forall \boldsymbol{X} \in \partial\mathcal{D}^0_k, \tag{2.119a}$$
$$J\mathsf{T}\mathsf{F}^{-t}(\boldsymbol{X}, t)\boldsymbol{N} = \boldsymbol{\mathcal{T}}^\star(\boldsymbol{X}, t), \quad \forall \boldsymbol{X} \in \partial\mathcal{D}^0_d, \tag{2.119b}$$

Here, $\boldsymbol{U}^\star$ and $\boldsymbol{\mathcal{T}}^\star$ denote the prescribed boundary velocity and force per unit surface, $\boldsymbol{N}$ is the unit outward normal to $\partial\mathcal{D}_d^0$. Let us note that the dynamic boundary condition has been applied to Lagrangian normal $\boldsymbol{N}$ using the first Piola-Kirchhoff stress tensor $J\mathsf{T}\mathsf{F}^{-t}$. This boundary condition is equivalent to its Eulerian counterpart (2.119b) provided that the Lagrangian and Eulerian prescribed forces per unit mass are related by $\boldsymbol{\mathcal{T}}^\star\,\mathsf{d}S = \boldsymbol{\tau}^\star\,\mathsf{d}s$.

- $\boldsymbol{q} \neq \boldsymbol{0}$: The natural corresponding boundary condition, in the sense that it is automatically included in the integral form of the conservation law (2.113d), consists in prescribing the heat flux at the boundary as follows

$$J\mathsf{F}^{-1}\boldsymbol{q}(\boldsymbol{X},t)\cdot\boldsymbol{N} = Q^\star(\boldsymbol{X},t), \quad \forall \boldsymbol{X}\in\partial\mathcal{D}^0, \tag{2.120}$$

where $Q^\star$ denotes the prescribed normal heat flux. Let us point out that this boundary condition has been imposed using the Lagrangian heat flux $J\mathsf{F}^{-1}\boldsymbol{q}$. It is equivalent to its Eulerian counterpart provided that the prescribed Eulerian and Lagrangian heat fluxes are related by $Q^\star\,\mathsf{d}S = q^\star\,\mathsf{d}s$. We conclude by remarking that it is also possible to impose others boundary conditions such as Dirichlet or Robin boundary conditions, refer to Comment 4.

2.3.2 Lagrangian local form of the conservation laws

To obtain the local Lagrangian form of the conservation laws, we simply transform the integral form obtained previously by applying the divergence formula after having made an assumption of sufficient smoothness for the fluid variables. Before we proceed any further, let us focus more precisely on the transformation of the divergence and gradient operators between the Lagrangian and the Eulerian configuration.

Transformation of the divergence and gradient operators between Eulerian and Lagrangian configurations

Let us consider a vector $\boldsymbol{U} = \boldsymbol{U}(\boldsymbol{x},t)$ and a scalar function $P = P(\boldsymbol{x},t)$ which are expressed in terms of the spatial coordinates. Let us recall the definition of the divergence and gradients operators in terms with respect to Eulerian coordinates

$$\nabla_x\cdot\boldsymbol{U} = \frac{\partial u}{\partial x}+\frac{\partial v}{\partial y}+\frac{\partial w}{\partial z}, \quad \boldsymbol{\nabla}_x P = (\frac{\partial P}{\partial x},\frac{\partial P}{\partial y},\frac{\partial P}{\partial z})^t.$$

where (u,v,w) denotes the components of the velocity field in the orthogonal coordinate system (x,y,z). Here, subscript x emphasizes the fact that the divergence and gradient operators are expressed with respect to Eulerian coordinates. Now, if we consider $\boldsymbol{U}$ and P as functions expressed in terms of Lagrangian coordinates, then we define the divergence and gradient operators with respect to Lagrangian coordinates as follows

$$\nabla_X\cdot\boldsymbol{U} = \frac{\partial u}{\partial X}+\frac{\partial v}{\partial Y}+\frac{\partial w}{\partial Z}, \quad \boldsymbol{\nabla}_X P = (\frac{\partial P}{\partial X},\frac{\partial P}{\partial Y},\frac{\partial P}{\partial Z})^t.$$

Divergence operator transformation We investigate how the divergence operator transforms when pulling back to the Lagrangian configuration. To this end, we apply the divergence

theorem twice as follows

$$\begin{aligned}\int_\omega \nabla_x \cdot \boldsymbol{U}\,\mathrm{d}v &= \int_{\partial\omega} \boldsymbol{U}\cdot\boldsymbol{n}\,\mathrm{d}s\\ &= \int_{\partial\Omega} \boldsymbol{U}\cdot J\mathsf{F}^{-t}\boldsymbol{N}\,\mathrm{d}S \quad \text{thanks to (2.49)}\\ &= \int_{\partial\Omega} J\mathsf{F}^{-1}\boldsymbol{U}\cdot\boldsymbol{N}\,\mathrm{d}S\\ &= \int_\Omega \nabla_X\cdot(J\mathsf{F}^{-1}\boldsymbol{U})\,\mathrm{d}V.\end{aligned}$$

Coming back to the Lagrangian coordinates in the left-hand side of the previous equation, one gets

$$\int_\omega \nabla_x\cdot\boldsymbol{U}\,\mathrm{d}v = \int_\Omega J\nabla_x\cdot\boldsymbol{U}\,\mathrm{d}V.$$

The combination of the previous results leads to

$$\int_\Omega J\nabla_x\cdot\boldsymbol{U}\,\mathrm{d}V = \int_\Omega \nabla_X\cdot(J\mathsf{F}^{-1}\boldsymbol{U})\,\mathrm{d}V.$$

Since this formula is valid for any arbitrary volume Ω, we deduce the final formula which expresses the transformation of the divergence operator into the Lagrangian configuration

$$\nabla_x\cdot\boldsymbol{U} = \frac{1}{J}\nabla_X\cdot(J\mathsf{F}^{-1}\boldsymbol{U}). \tag{2.121}$$

Now, developing the right-hand side of (2.121) through the use of identity (A.31a) yields

$$\nabla_x\cdot\boldsymbol{U} = \frac{1}{J}\nabla_X\cdot(J\mathsf{F}^{-t})\cdot\boldsymbol{U} + \mathsf{F}^{-1}:\nabla_X\boldsymbol{U}.$$

If $\boldsymbol{U}$ is an arbitrary constant vector, the previous identity yields

$$\nabla_X\cdot(J\mathsf{F}^{-t}) = \mathsf{O}. \tag{2.122}$$

This is the Piola identity which is well known in continuum mechanics [117, 146]. This result can be recovered by integrating the left-hand side of (2.122) over a Lagrangian fluid volume Ω and applying the divergence formula as

$$\begin{aligned}\int_\Omega \nabla_X\cdot(J\mathsf{F}^{-t})\,\mathrm{d}V &= \int_{\partial\Omega} J\mathsf{F}^{-t}\boldsymbol{N}\,\mathrm{d}S\\ &= \int_{\partial\omega}\boldsymbol{n}\,\mathrm{d}s, \quad \text{thanks to (2.49)}\\ &= \int_\omega \nabla_x\cdot\mathsf{I}_d\,\mathrm{d}v, \quad \text{thanks to (A.33a)}\\ &= \mathbf{0}.\end{aligned}$$

Here, I_d is the unit tensor. Using the second line of the above equation yields the following geometric identity

$$\int_{\partial\Omega} J\mathsf{F}^{-t}\boldsymbol{N}\,\mathrm{d}S = \int_{\partial\omega}\boldsymbol{n}\,\mathrm{d}s = \mathbf{0}. \tag{2.123}$$

We recover the well known geometric interpretation that the integral of the unit outward normal over a closed surface is equal to zero.

We notice that formula (2.121) which applies for vector can be easily extended to the case of second-order tensor. Being given T an arbitrary second-order tensor, divergence formula reads

$$\begin{aligned}\int_\omega \nabla_x \cdot \mathsf{T}\,\mathsf{d}v &= \int_{\partial\omega} \mathsf{T}\boldsymbol{n}\,\mathsf{d}s \\ &= \int_{\partial\Omega} \mathsf{T}J\mathsf{F}^{-t}\boldsymbol{N}\,\mathsf{d}S \quad \text{thanks to (2.49)} \\ &= \int_\Omega \nabla_X \cdot (\mathsf{T}J\mathsf{F}^{-t})\,\mathsf{d}V.\end{aligned}$$

Recalling that $\mathsf{d}v = J\mathsf{d}V$, we finally obtain

$$\nabla_x \cdot \mathsf{T} = \frac{1}{J}\nabla_X \cdot (J\mathsf{T}\mathsf{F}^{-t}). \tag{2.124}$$

Comment 6 *Let us remark that in the case of a two-dimensional fluid flow the compatibility conditions* (2.117) *are equivalent to the Piola identity* (2.122)*. This result is obtained by computing the components of the divergence of* $J\mathsf{F}^{-t}$

$$J\mathsf{F}^{-t} = \begin{pmatrix} F_{YY} & -F_{YX} \\ -F_{XY} & F_{XX} \end{pmatrix}, \quad \nabla_X \cdot (J\mathsf{F}^{-t}) = \begin{pmatrix} \frac{\partial}{\partial X}F_{YY} - \frac{\partial}{\partial Y}F_{YX} \\ -\frac{\partial}{\partial X}F_{XY} + \frac{\partial}{\partial Y}F_{XX} \end{pmatrix}.$$

Now, using the notation introduced in Comment 5, we note that the right-hand side of the last equation corresponds to the non-zero components of $\boldsymbol{\nabla}_X \times \boldsymbol{\mathcal{F}}_X$ *and* $\boldsymbol{\nabla}_X \times \boldsymbol{\mathcal{F}}_Y$*, which ends the proof.*

Gradient operator transformation We express the relation between the gradient operator expressed in terms of the Eulerian coordinates and its counterpart expressed in terms of the Lagrangian coordinates. To this end, we apply (2.124) using a scalar tensor defined by $\mathsf{T} = P\,\mathsf{I}_d$ where $P = P(\boldsymbol{X}, t) = P(\boldsymbol{x}, t)$ is a scalar function. On the one hand $\nabla_x \cdot (P\mathsf{I}_d) = \boldsymbol{\nabla}_x P$, on the other hand (2.124) is rewritten

$$\boldsymbol{\nabla}_x P = \frac{1}{J}\nabla_X \cdot (J\mathsf{F}^{-t}P). \tag{2.125}$$

Developing the right-hand side, employing tensor identity (A.31d) and the Piola identity (2.122), we finally obtain the following variant of (2.125) which relates the gradient operator in both configuration as

$$\boldsymbol{\nabla}_x P = \mathsf{F}^{-t}\nabla_X P. \tag{2.126}$$

Note that this last result could have been obtained employing the chain rule of composed derivatives.

Diffusion operator transformation Combining the previous results, we propose to derive the formula expressing the transformation of the divergence diffusion operator, *i.e.*, $\nabla_x \cdot (\boldsymbol{\nabla}_x)$. To this end, let us consider the vector valued function $\boldsymbol{q}$, defined by $\boldsymbol{q} = -\mathsf{K}\boldsymbol{\nabla}_x T$, where K is a positive definite second-order tensor and T a scalar valued function. Here, $\boldsymbol{q}$ corresponds to the heat flux vector, T is the temperature and K the conductivity tensor. Let us recall that the expression of $\boldsymbol{q}$ in terms of $\boldsymbol{\nabla}_x T$ is nothing but the Fourier law that governs heat propagation [81]. Using Fourier law, the diffusion operator is defined by

$$\nabla_x \cdot \boldsymbol{q} = -\nabla_x \cdot (\mathsf{K}\boldsymbol{\nabla}_x T). \tag{2.127}$$

Here, the diffusion operator is written with respect to Eulerian coordinates. To transform it into Lagrangian frame, we first transform the divergence of the flux using (2.121)

$$\nabla_x \cdot \boldsymbol{q} = \frac{1}{J} \nabla_X \cdot (J\mathsf{F}^{-1}\boldsymbol{q}).$$

Second, we transform the gradient operator present in the Fourier law according to (2.125), *i.e.*, $\boldsymbol{q} = -\mathsf{K}\mathsf{F}^{-t}\nabla_X T$. Finally, the diffusion operator expresses as

$$\nabla_x \cdot \boldsymbol{q} = -\frac{1}{J} \nabla_X \cdot (J\mathsf{F}^{-1}\mathsf{K}\mathsf{F}^{-t}\nabla_X T), \tag{2.128}$$

where in the right-hand side T is expressed in terms of Lagrangian coordinates. This allows to define an effective Lagrangian conductivity tensor which depends on the gradient deformation tensor as

$$\mathsf{K}_L = J\mathsf{F}^{-1}\mathsf{K}\mathsf{F}^{-t}$$

We note that this tensor is also positive definite. If $\boldsymbol{A}$ denotes an arbitrary vector, then $\mathsf{K}_L\boldsymbol{A} \cdot \boldsymbol{A} = \mathsf{K}\mathsf{F}^{-t}\boldsymbol{A} \cdot \mathsf{F}^{-t}\boldsymbol{A}$, thus $\mathsf{K}_L\boldsymbol{A} \cdot \boldsymbol{A} > 0$, since K is positive definite. Let us consider the case of an isotropic material, *i.e.*, $\mathsf{K} = \kappa \mathsf{I}_d$, where $\kappa > 0$ denotes the heat conductivity. Then, (2.127) reduces to

$$\nabla_x \cdot \boldsymbol{q} = -\frac{1}{J} \nabla_X \cdot (J\kappa\mathsf{F}^{-1}\mathsf{F}^{-t}\nabla_X T). \tag{2.129}$$

Let us point out that the isotropic Eulerian diffusion operator has been transformed into an anisotropic Lagrangian diffusion operator. In this case, the anisotropic Lagrangian conductivity tensor is symmetric positive definite and corresponds to the inverse of the right Cauchy-Green tensor, *i.e.*, $\mathsf{C} = \mathsf{F}^t\mathsf{F}$, refer to Paragraph 2.1.3.

Transformation of the integral conservation laws into their local form Under condition of sufficient smoothness for the fluid variables, transforming the surface integrals present in the system (2.113) into volume integrals by means of the divergence formula yields

$$\begin{aligned}
&\frac{d}{dt}\int_\Omega \rho J \,\mathrm{d}V = 0,\\
&\frac{d}{dt}\int_\Omega J \,\mathrm{d}V - \int_\Omega \nabla_X \cdot (J\mathsf{F}^{-1}\boldsymbol{U}) \,\mathrm{d}V = 0,\\
&\frac{d}{dt}\int_\Omega \rho J\boldsymbol{U} \,\mathrm{d}V - \int_\Omega \nabla_X \cdot (J\mathsf{T}\mathsf{F}^{-t}) \,\mathrm{d}V = \int_\Omega \rho J\boldsymbol{g} \,\mathrm{d}V,\\
&\frac{d}{dt}\int_\Omega \rho JE \,\mathrm{d}V - \int_\Omega \nabla_X \cdot (J\mathsf{F}^{-1}\mathsf{T}\boldsymbol{U}) \,\mathrm{d}V + \int_\Omega \nabla_X \cdot (J\mathsf{F}^{-1}\boldsymbol{q}) \,\mathrm{d}V = \int_\Omega \rho J(\boldsymbol{g}\cdot\boldsymbol{U} + r) \,\mathrm{d}V.
\end{aligned}$$

The requirement that these equations hold for arbitrary Lagrangian region Ω necessitates that the integrands vanish. This allows to write the Lagrangian local form of the conservation laws

$$\frac{d}{dt}(\rho J) = 0, \tag{2.130a}$$

$$\frac{d}{dt}J - \nabla_X \cdot (J\mathsf{F}^{-1}\boldsymbol{U}) = 0, \tag{2.130b}$$

$$\frac{d}{dt}(\rho J\boldsymbol{U}) - \nabla_X \cdot (J\mathsf{T}\mathsf{F}^{-t}) = \rho J\boldsymbol{g}, \tag{2.130c}$$

$$\frac{d}{dt}(\rho JE) - \nabla_X \cdot (J\mathsf{F}^{-1}\mathsf{T}\boldsymbol{U}) + \nabla_X \cdot (J\mathsf{F}^{-1}\boldsymbol{q}) = \rho J(\boldsymbol{g}\cdot\boldsymbol{U} + r). \tag{2.130d}$$

Let us recall that F is the deformation gradient tensor, which is also the Jacobian matrix of the flow map, and J the determinant of this transformation, *i.e.*, $J = \det \mathsf{F}$. This system has to be completed by adding the local conservation law of the deformation gradient (2.115). Proceeding with the entropy inequality (2.114) as before yields its local form

$$\frac{d}{dt}(\rho J \eta) \geq \rho J \frac{r}{T} - \nabla_X \cdot (J\mathsf{F}^{-1}\frac{\boldsymbol{q}}{T}). \tag{2.131}$$

We notice that the mass conservation equation reduces to a simple differential equation which after integration reads $\rho J = \rho^0$, where $\rho^0 = \rho^0(\boldsymbol{X})$ denotes the initial density. Substituting mass conservation in the system (2.130) yields

$$\rho^0 \frac{d}{dt}(\frac{1}{\rho}) - \nabla_X \cdot (J\mathsf{F}^{-1}\boldsymbol{U}) = 0, \tag{2.132a}$$

$$\rho^0 \frac{d}{dt}(\rho \boldsymbol{U}) - \nabla_X \cdot (J\mathsf{T}\mathsf{F}^{-t}) = \rho^0 \boldsymbol{g}, \tag{2.132b}$$

$$\rho^0 \frac{d}{dt}(\rho E) - \nabla_X \cdot (J\mathsf{F}^{-1}\mathsf{T}\boldsymbol{U}) + \nabla_X \cdot (J\mathsf{F}^{-1}\boldsymbol{q}) = \rho^0(\boldsymbol{g}\cdot\boldsymbol{U} + r). \tag{2.132c}$$

Comment 7 *Let us remark that it is possible to derive the local Lagrangian form of the conservation laws* (2.130) *by directly transforming the local Eulerian form of the conservation laws* (2.59)*. This is done employing the following identities*

$$\frac{d}{dt}(fJ) = J[\frac{\partial f}{\partial t} + \nabla \cdot (f\boldsymbol{U})], \tag{2.133a}$$

$$\frac{d}{dt}(\boldsymbol{f}J) = J[\frac{\partial \boldsymbol{f}}{\partial t} + \nabla \cdot (\boldsymbol{f} \otimes \boldsymbol{U})], \tag{2.133b}$$

where f and $\boldsymbol{f}$ denote arbitrary scalar valued and vector valued functions. These formulas are easily obtained by combining the definition of the material derivative (2.8) *and* (2.21)*. To transform the local Eulerian conservation laws* (2.59) *into Lagrangian form, we first make use of formulas* (2.133a) *and* (2.133b) *respectively for $f = \rho, \rho E$ and $\boldsymbol{f} = \rho\boldsymbol{U}$. We finally get*

$$\frac{d}{dt}(\rho J) = 0,$$
$$\frac{d}{dt}(\rho J\boldsymbol{U}) - J\nabla_x \cdot \mathsf{T} = \rho J\boldsymbol{g},$$
$$\frac{d}{dt}(\rho JE) - J\nabla_x \cdot (\mathsf{T}\boldsymbol{U}) + J\nabla_x \cdot \boldsymbol{q} = \rho J(\boldsymbol{g}\cdot\boldsymbol{U} + r).$$

This system is completed by the time rate of change of the Jacobian (2.21) *and finally writes*

$$\frac{d}{dt}(\rho J) = 0, \tag{2.134a}$$

$$\frac{d}{dt}J - J\nabla_x \cdot \boldsymbol{U} = 0, \tag{2.134b}$$

$$\frac{d}{dt}(\rho J\boldsymbol{U}) - J\nabla_x \cdot \mathsf{T} = \rho J\boldsymbol{g} \tag{2.134c}$$

$$\frac{d}{dt}(\rho JE) - J\nabla_x \cdot (\mathsf{T}\boldsymbol{U}) + J\nabla_x \cdot \boldsymbol{q} = \rho J(\boldsymbol{g}\cdot\boldsymbol{U} + r). \tag{2.134d}$$

Let us emphasize that system (2.134) *is not completely written in Lagrangian form since the divergence and gradient operators are still expressed in terms of the Eulerian coordinates. To achieve the transformation we have to use the formulas* (2.121) *and* (2.125) *which transform the divergence and gradient operators into the Lagrangian frame. Substituting these formulas into* (2.134) *allows to recover the local Lagrangian formulation* (2.130)*.*

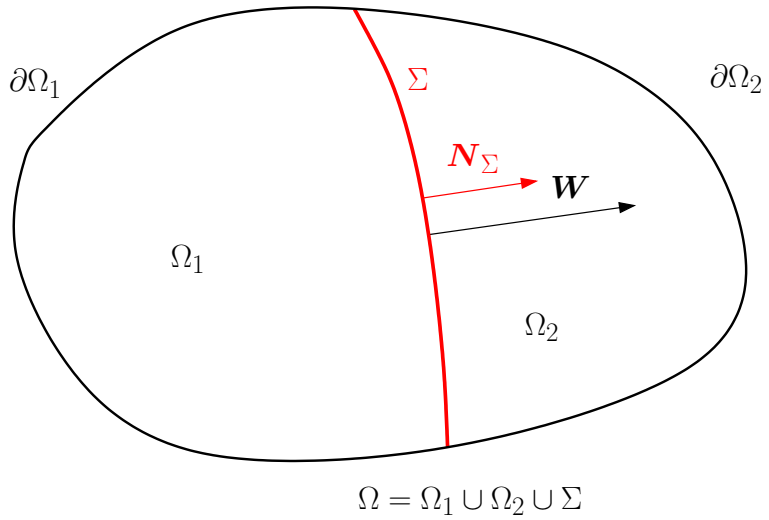

Figure 2.4: Notation for a moving discontinuity Σ in the Lagrangian frame.

2.3.3 Jump equations at moving discontinuity in Lagrangian representation

In deriving the local Lagrangian form of the conservation laws, we have made the assumption of a sufficient smoothness for fluid variables. In this paragraph, we aim at deriving the jump equations corresponding to the Lagrangian conservation laws when the fluid variables experience a jump at a moving discontinuity surface. In order to do so, we need to write the transport formula associated to piecewise differentiable functions in Lagrangian configuration.

Transport formulas for piecewise continuously differentiable functions in Lagrangian framework

For this purpose, let us consider a Lagrangian fluid region Ω, which is split into the two sub-regions Ω_1 and Ω_2 by a moving discontinuity surface Σ, *i.e.*, $\Omega = \Omega_1 \cup \Omega_2 \Sigma$, refer to Fig. 2.4. Let us assume that Σ is sufficiently smooth to define at each point $\boldsymbol{X}_\Sigma \in \Sigma$ a unit outward normal $\boldsymbol{N}_\Sigma$ with respect to Ω_1. Let $\boldsymbol{W} = \boldsymbol{W}(\boldsymbol{X}_\Sigma, t)$ be the velocity of the discontinuity surface. Knowing that Ω is a fixed region, the time derivative of the volume integral over Ω of a piecewise continuously differentiable scalar (resp. vector) valued function $f = f(\boldsymbol{X}, t)$ (resp. $\boldsymbol{f} = \boldsymbol{f}(\boldsymbol{X}, t)$) is given by

$$\frac{d}{dt}\int_\Omega f(\boldsymbol{X},t)\,\mathrm{d}V = \int_{\Omega_1\cup\Omega_2} \frac{df}{dt}\,\mathrm{d}V - \int_\Sigma [\![f]\!](\boldsymbol{W}\cdot\boldsymbol{N}_\Sigma)\,\mathrm{d}S, \tag{2.135a}$$

$$\frac{d}{dt}\int_\omega \boldsymbol{f}(\boldsymbol{X},t)\,\mathrm{d}X = \int_{\Omega_1\cup\Omega_2} \frac{d\boldsymbol{f}}{dt}\,\mathrm{d}V - \int_\Sigma [\![\boldsymbol{f}\otimes\boldsymbol{W}]\!]\boldsymbol{N}_\Sigma\,\mathrm{d}S. \tag{2.135b}$$

These equations are the transport formulas in the Lagrangian configuration, refer to Comment 1 for their derivation. Let us recall that $[\![f]\!] = f_2 - f_1$ where f_i, $i = 1, 2$ are the one-sided values of f on both sides of Σ.

Lagrangian jump relations for physical conservations laws

Applying (2.135) to the Lagrangian conservation laws (2.113) and using the divergence formulas for piecewise continuously differentiable functions yields the following Lagrangian jump relations

$$[\![\rho J]\!](\boldsymbol{W}\cdot\boldsymbol{N}_\Sigma)=0, \tag{2.136a}$$
$$[\![J]\!](\boldsymbol{W}\cdot\boldsymbol{N}_\Sigma)+[\![J\mathsf{F}^{-1}\boldsymbol{U}]\!]\cdot\boldsymbol{N}_\Sigma=0, \tag{2.136b}$$
$$[\![\rho J\boldsymbol{U}]\!](\boldsymbol{W}\cdot\boldsymbol{N}_\Sigma)+[\![J\mathsf{T}\mathsf{F}^{-t}]\!]\boldsymbol{N}_\Sigma=\boldsymbol{0}, \tag{2.136c}$$
$$[\![\rho JE]\!](\boldsymbol{W}\cdot\boldsymbol{N}_\Sigma)+[\![J\mathsf{F}^{-1}(\mathsf{T}\boldsymbol{U}-\boldsymbol{q})]\!]\cdot\boldsymbol{N}_\Sigma=0. \tag{2.136d}$$

These jump relations express respectively mass, volume, momentum and total energy conservation across the discontinuity surface Σ moving with speed $\boldsymbol{W}$. Equation (2.136a) shows that we can set

$$M=\rho_1 J_1(\boldsymbol{W}\cdot\boldsymbol{N}_\Sigma)=\rho_2 J_2(\boldsymbol{W}\cdot\boldsymbol{N}_\Sigma). \tag{2.137}$$

M is nothing but the mass flux swept by the moving discontinuity. With this notation, system (2.136) rewrites

$$M[\![\frac{1}{\rho}]\!]+[\![J\mathsf{F}^{-1}\boldsymbol{U}]\!]\cdot\boldsymbol{N}_\Sigma=0, \tag{2.138a}$$
$$M[\![\boldsymbol{U}]\!]+[\![J\mathsf{T}\mathsf{F}^{-t}]\!]\boldsymbol{N}_\Sigma=0, \tag{2.138b}$$
$$M[\![E]\!]+[\![J\mathsf{F}^{-1}(\mathsf{T}\boldsymbol{U}-\boldsymbol{q})]\!]\cdot\boldsymbol{N}_\Sigma=0. \tag{2.138c}$$

Following the naming used in the Eulerian framework, the case $M=0$ corresponds to a contact discontinuity, whereas the case $M\neq 0$ corresponds to a shock wave.

Kinematical jump condition

The above system is completed by the jump relation corresponding to the conservation law (2.116) of the deformation gradient F

$$[\![\mathsf{F}]\!](\boldsymbol{W}\cdot\boldsymbol{N}_\Sigma)+[\![\boldsymbol{U}]\!]\otimes\boldsymbol{N}_\Sigma=\mathsf{O}. \tag{2.139}$$

In deriving this equation, we have assumed that the deformation gradient tensor is a piecewise continuously differentiable tensor valued function. Let us emphasize that this smoothness assumption on F corresponds to the continuity of the fluid flow map, $\boldsymbol{\Phi}$, since $\mathsf{F}=\nabla_X\boldsymbol{\Phi}$. The above jump equation for the deformation gradient is also known as Hadamard kinematic compatibility condition [141]. Let us investigate further the consequences of this kinematical jump condition. First, let us point out that if $(\boldsymbol{W}\cdot\boldsymbol{N}_\Sigma)=0$, (2.139) reduces to $[\![\boldsymbol{U}]\!]\otimes\boldsymbol{N}_\Sigma=\mathsf{O}$ which yields $[\![\boldsymbol{U}]\!]=\boldsymbol{0}$. Thus, if the discontinuity is a contact, then the velocity field is continuous. Second, if $(\boldsymbol{W}\cdot\boldsymbol{N}_\Sigma)\neq 0$, then the kinematical jump condition rewrites

$$[\![\mathsf{F}]\!]=-\frac{1}{(\boldsymbol{W}\cdot\boldsymbol{N}_\Sigma)}[\![\boldsymbol{U}]\!]\otimes\boldsymbol{N}_\Sigma.$$

Therefore, if the velocity field is continuous, then the deformation gradient is also continuous. If $\boldsymbol{A}$ denotes an arbitrary vector valued smooth function, then the second-order tensor $[\![\mathsf{F}]\!]$ is characterized by

$$[\![\mathsf{F}]\!]\boldsymbol{A}=-\frac{(\boldsymbol{A}\cdot\boldsymbol{N}_\Sigma)}{(\boldsymbol{W}\cdot\boldsymbol{N}_\Sigma)}[\![\boldsymbol{U}]\!].$$

It turns out that $[\![\mathsf{F}]\!]$ is proportional to the projection along $\boldsymbol{N}_\Sigma$ onto $[\![\boldsymbol{U}]\!]$. Thus, setting $\boldsymbol{A}=\boldsymbol{N}_\Sigma$ and $\boldsymbol{A}=\boldsymbol{T}_\Sigma$, where $\boldsymbol{T}_\Sigma$ is a unit vector of the tangent plane to Σ, second-order tensor $[\![\mathsf{F}]\!]$ is fully determined by its projections onto $\boldsymbol{N}_\Sigma$ and $\boldsymbol{T}_\Sigma$ as follows

$$[\![\mathsf{F}]\!]\boldsymbol{N}_\Sigma=-\frac{1}{(\boldsymbol{W}\cdot\boldsymbol{N}_\Sigma)}[\![\boldsymbol{U}]\!],\quad [\![\mathsf{F}]\!]\boldsymbol{T}_\Sigma=\boldsymbol{0}. \tag{2.140}$$

This means that the tangential component of the deformation gradient is continuous, whereas its normal component experiences a jump which is proportional to the velocity jump.

Comment 8 *In Lagrangian frame, under the assumption of a continuous fluid flow map, deformation gradient jump relation involves the continuity of the fluid velocity at contact discontinuity surface. This result seems paradoxical in comparison to what happens for contact discontinuity in the Eulerian frame. Let us recall that in this case, the tangential component of the fluid velocity can suffer a jump at the discontinuity surface. The occurrence of such a situation in Lagrangian frame would imply sliding and shear on both sides of the discontinuity surface, and thus the loss of continuity for the flow map at the contact surface. The discontinuity of Φ at the contact would also involve the appearance of a Dirac measure for the deformation gradient which would necessitate specific mathematical treatment. This shows one fundamental difference between Lagrangian and Eulerian representation in their respective ability to cope with shear flow. This also explains why sliding surfaces require specific treatment in the context of numerical algorithms devoted to Lagrangian hydrodynamics.*

Correspondence between Lagrangian and Eulerian jump relations

Let us pursue this paragraph by showing that the Lagrangian jump relations imply the Eulerian jump relations that have been derived in Section 2.2.5. Let us point out that the Eulerian discontinuity surface σ is related to the Lagrangian discontinuity Σ by means of the fluid flow map $\mathbf{\Phi}$. Therefore, we have the following correspondence between oriented element surfaces along the discontinuity surfaces in each configuration

$$\boldsymbol{n}_\sigma \,\mathrm{d}s = J_1 \mathsf{F}_1^{-t} \boldsymbol{N}_\Sigma \,\mathrm{d}S = J_2 \mathsf{F}_2^{-t} \boldsymbol{N}_\Sigma \,\mathrm{d}S, \tag{2.141}$$

where $\boldsymbol{n}_\sigma$ denotes the unit outward normal to σ with respect to ω_1, refer to Section 2.2.5. Equation (2.141) has been obtained my means of Nanson formula (2.49). It simply states the continuity of the Eulerian normal $\boldsymbol{n}_\sigma$. We notice, that (2.141) is also a consequence of the jump relation associated to the Piola identity (2.122). This jump relation is readily derived applying divergence formula for piecewise continuously differentiable function as follows

$$\int_{\Omega_1 \cup \Omega_2} \nabla_X \cdot (J\mathsf{F}^{-t}) \,\mathrm{d}V + \int_\Sigma [\![J\mathsf{F}^{-t}]\!] \boldsymbol{N}_\Sigma \,\mathrm{d}S = \int_{\partial\Omega} J\mathsf{F}^{-t} \boldsymbol{N} \,\mathrm{d}S.$$

By virtue of the local form and the integral form of Piola identity, respectively (2.122) and (2.123), the above equation reduces to

$$[\![J\mathsf{F}^{-t}]\!] \boldsymbol{N}_\Sigma = \boldsymbol{0}, \tag{2.142}$$

which is nothing but Equation (2.141). Bearing this in mind, we cast Lagrangian jump relations (2.138) into the following form

$$M[\![\frac{1}{\rho}]\!] + [\![\boldsymbol{U}]\!] \cdot \overline{J\mathsf{F}^{-t}} \boldsymbol{N}_\Sigma = 0, \tag{2.143a}$$

$$M[\![\boldsymbol{U}]\!] + [\![\mathsf{T}]\!] \overline{J\mathsf{F}^{-t}} \boldsymbol{N}_\Sigma = 0, \tag{2.143b}$$

$$M[\![E]\!] + [\![\mathsf{T}\boldsymbol{U} - \boldsymbol{q}]\!] \cdot \overline{J\mathsf{F}^{-t}} \boldsymbol{N}_\Sigma = 0, \tag{2.143c}$$

where the bar notation over a quantity denotes its average, *i.e.*, $\overline{f} = \frac{1}{2}(f_1 + f_2)$. In writing (2.143), we have made use of the following identities

$$[\![\boldsymbol{A} \cdot \boldsymbol{B}]\!] = [\![\boldsymbol{A}]\!] \cdot \overline{\boldsymbol{B}} + \overline{\boldsymbol{A}} \cdot [\![\boldsymbol{B}]\!],$$
$$[\![\mathsf{S}\boldsymbol{A}]\!] = [\![\mathsf{S}]\!] \overline{\boldsymbol{A}} + \overline{\mathsf{S}} [\![\boldsymbol{A}]\!],$$

where $\boldsymbol{A}$, $\boldsymbol{B}$ and S denote respectively two arbitrary vectors and an arbitrary second-order tensor. Now, comparing the above Lagrangian jump relations to the Eulerian jump relations (2.93), (2.94) and (2.95), and recalling $\overline{J\mathsf{F}^{-t}}\boldsymbol{N}_\Sigma\,\mathsf{d}S = \boldsymbol{n}_\sigma\,\mathsf{d}s$, it turns out that Eulerian form results from the Lagrangian form provided that we ensure the correspondence relation

$$-m\,\mathsf{d}s = M\,\mathsf{d}S, \tag{2.144}$$

where m denotes the Eulerian mass flux given by $m = \rho_i(\boldsymbol{U}_i - \boldsymbol{w})\cdot\boldsymbol{n}_\sigma,\ i = 1,2$. This relation states that the mass crossing the discontinuity surface is identical regardless the configuration employed. The minus sign in the above equation is due to the fact that m stands for the mass flux crossing the discontinuity in the Eulerian frame whereas M stands for the mass flux swept by the moving discontinuity in the Lagrangian frame. Let us investigate further the physical consequences of this relation by expressing both the Lagrangian and Eulerian mass flux. According to the definition of Lagrangian and Eulerian mass fluxes, (2.144) transforms into

$$\begin{aligned}
&\rho_i(\boldsymbol{w} - \boldsymbol{U}_i)\cdot\boldsymbol{n}_\sigma\,\mathsf{d}s = \rho_i J_i\boldsymbol{W}\cdot\boldsymbol{N}_\Sigma\,\mathsf{d}S,\ i = 1,2\\
&\rho_i(\boldsymbol{w} - \boldsymbol{U}_i)\cdot(J_i\mathsf{F}_i^{-t})\boldsymbol{N}_\Sigma\,\mathsf{d}S = \rho_i J_i\boldsymbol{W}\cdot\boldsymbol{N}_\Sigma\,\mathsf{d}S,\ i = 1,2
\end{aligned}$$

thanks to (2.49). After simplification, we finally obtain

$$\mathsf{F}_i^{-1}(\boldsymbol{w} - \boldsymbol{U}_i)\cdot\boldsymbol{N}_\Sigma = \boldsymbol{W}\cdot\boldsymbol{N}_\Sigma. \tag{2.145}$$

This explains how the discontinuity speed transforms between Lagrangian and Eulerian configurations. Let us give a physical interpretation of this relation. Let $\boldsymbol{X}_\Sigma = \boldsymbol{X}_\Sigma(t)$ be the vector position of a point attached to the discontinuity surface Σ during its motion in the Lagrangian frame. Let $\boldsymbol{x}_\sigma$ be the image of $\boldsymbol{X}_\Sigma$ in the continuous flow map $\boldsymbol{\Phi}$, *i.e.*, $\boldsymbol{x}_\sigma = \boldsymbol{\Phi}(\boldsymbol{X}_\Sigma(t), t)$. Knowing that the Eulerian discontinuity, $\boldsymbol{\sigma}$, is itself the image of the Lagrangian discontinuity, Σ, in the flow map yields $\boldsymbol{x}_\sigma \in \sigma$. Bearing this in mind, the respective speeds of the Lagrangian and Eulerian discontinuities read as

$$\boldsymbol{W} = \frac{d}{dt}\boldsymbol{X}_\Sigma, \quad \boldsymbol{w} = \frac{d}{dt}\boldsymbol{x}_\sigma,\ i = 1,2. \tag{2.146}$$

Now, recalling that $\boldsymbol{x}_\sigma = \boldsymbol{\Phi}(\boldsymbol{X}_\Sigma(t), t)$ and employing the chain rule leads to

$$\frac{d}{dt}\boldsymbol{x}_\sigma = (\nabla_X\boldsymbol{\Phi})_i\frac{d}{dt}\boldsymbol{X}_\Sigma + (\frac{\partial}{\partial t}\boldsymbol{\Phi})_i.$$

Here, we have made use of subscript i to denote the one-sided values of the Jacobian matrix and the time derivative of the fluid map on both sides of the discontinuity. Substituting the discontinuity speeds expressions by means of (2.146) into the above equation leads to

$$\boldsymbol{w} = \mathsf{F}_i\boldsymbol{W} + \boldsymbol{U}_i,\ i = 1,2. \tag{2.147}$$

It turns out that Equation (2.145) simply states the continuity of the normal component of the Lagrangian discontinuity speed. Note also that (2.147) rewrites as the following jump relation

$$[\![\mathsf{F}]\!]\boldsymbol{W} + [\![\boldsymbol{U}]\!] = \boldsymbol{0}. \tag{2.148}$$

We point out that this jump relation is not a new one since it follows from the kinematical jump equation (2.139). First, if $(\boldsymbol{W}\cdot\boldsymbol{N}_\Sigma) = 0$, then (2.139) implies that $[\![\boldsymbol{U}]\!] = \boldsymbol{0}$, thus (2.148) is trivially satisfied. Second, if $(\boldsymbol{W}\cdot\boldsymbol{N}_\Sigma) \neq 0$, multiplying (2.139) by the vector $\boldsymbol{W}$ and recalling that from definition of the dyadic product (A.1), $([\![\boldsymbol{U}]\!]\otimes\boldsymbol{N}_\Sigma)\boldsymbol{W} = [\![\boldsymbol{U}]\!](\boldsymbol{W}\cdot\boldsymbol{N}_\Sigma)$, leads to (2.148).

We conclude by noticing that a rigorous demonstration of the equivalence between Lagrangian and Eulerian Rankine-Hugoniot equations, in the context of elastic flow, can be found in [128].

Jump relation for entropy inequality

We conclude this section by deriving the Lagrangian jump relations corresponding to the fundamental entropy inequality (2.114). Employing the transport formula (2.135a) and the divergence formula for piecewise continuously differentiable functions as before yields the entropy jump relation

$$-[\![\rho J\eta]\!] + [\![J\mathsf{F}^{-1}\frac{\boldsymbol{q}}{T}]\!]\cdot\boldsymbol{N}_\Sigma \geq 0.$$

Introducing the Lagrangian mass flux M in the above equation leads to

$$-M[\![\eta]\!] + [\![J\mathsf{F}^{-1}\frac{\boldsymbol{q}}{T}]\!]\cdot\boldsymbol{N}_\Sigma \geq 0. \tag{2.149}$$

Using Piola identity, *i.e.*, $\overline{J\mathsf{F}^{-t}}\boldsymbol{N}_\Sigma\,\mathrm{d}S = \boldsymbol{n}_\sigma\,\mathrm{d}s$ and the correspondence $M\,\mathrm{d}S = -m\,\mathrm{d}s$, we are able to show that the Eulerian entropy inequality (2.99) results from the Lagrangian entropy inequality.

2.3.4 Lagrangian forms of the gas dynamics equations

Here, we make the assumption that the fluid under consideration is a perfect fluid, that is the viscous stress and the heat conduction are negligible. Moreover, there is no heat supply, . *i.e.*, $r = 0$.

Lagrangian integral form of the gas dynamics equations

Setting $\mathsf{T} = -P\,\mathsf{I}_d$, $\boldsymbol{q} = \boldsymbol{0}$ and $r = 0$ in the Lagrangian integral conservation laws (2.113) yields the gas dynamics equations written under integral Lagrangian form

$$\frac{d}{dt}\int_\Omega \rho J\,\mathrm{d}V = 0, \tag{2.150a}$$

$$\frac{d}{dt}\int_\Omega J\,\mathrm{d}V - \int_{\partial\Omega} J\boldsymbol{U}\cdot\mathsf{F}^{-t}\boldsymbol{N}\,\mathrm{d}S = 0, \tag{2.150b}$$

$$\frac{d}{dt}\int_\Omega \rho\boldsymbol{U}J\,\mathrm{d}V + \int_{\partial\Omega} JP\mathsf{F}^{-t}\boldsymbol{N}\,\mathrm{d}S = \int_\Omega \rho\boldsymbol{g}J\,\mathrm{d}V, \tag{2.150c}$$

$$\frac{d}{dt}\int_\Omega \rho EJ\,\mathrm{d}V + \int_{\partial\Omega} JP\boldsymbol{U}\cdot\mathsf{F}^{-t}\boldsymbol{N}\,\mathrm{d}S = \int_\Omega \rho\boldsymbol{g}\cdot\boldsymbol{U}J\,\mathrm{d}V. \tag{2.150d}$$

The thermodynamical closure of this system is ensured by an equation of state written under the form $P = P(\rho,\varepsilon)$ where ε is the specific internal energy. Let us recall that the evolution of the deformation gradient F is governed by the integral conservation law (2.116). The consistency of the above system with the Second Law of thermodynamics is ensured by the following entropy inequality

$$\frac{d}{dt}\int_\Omega \rho J\eta\,\mathrm{d}V \geq 0. \tag{2.151}$$

Let us point out that this inequality reduces to an equality in case of smooth flow.

System (2.150) is completed by initial and boundary conditions. The initial conditions are given by (2.118). Regarding boundary conditions, since the fluid under consideration is a perfect fluid (2.119) collapses to

$$\boldsymbol{U}(\boldsymbol{X},t)\cdot\boldsymbol{N} = U_n^\star(\boldsymbol{X},t), \quad \forall\boldsymbol{X}\in\partial\mathcal{D}_k^0, \tag{2.152a}$$

$$P(\boldsymbol{X},t) = P^\star(\boldsymbol{X},t), \quad \forall\boldsymbol{X}\in\partial\mathcal{D}_d^0, \tag{2.152b}$$

where $U_n^\star$ and $P^\star$ are the prescribed normal velocity and pressure which are identical to their Eulerian counterparts.

Lagrangian local form of the gas dynamics equations

Proceeding with the Lagrangian local form of the conservation laws as before, we deduce the Lagrangian local form of the gas dynamics equations. Let us emphasize that this local form, which consists in writing the conservation laws as partial differential equations, is valid for continuously differentiable fluid variables. Bearing this in mind, local form of the gas dynamics equations writes

$$\begin{aligned}
&\frac{d}{dt}(\rho J) = 0,\\
&\frac{d}{dt}J - \nabla_X \cdot (J\mathsf{F}^{-1}\boldsymbol{U}) = 0,\\
&\frac{d}{dt}(\rho J\boldsymbol{U}) + \nabla_X \cdot (JP\mathsf{F}^{-t}) = \rho J\boldsymbol{g},\\
&\frac{d}{dt}(\rho JE) + \nabla_X \cdot (J\mathsf{F}^{-1}P\boldsymbol{U}) = \rho J\boldsymbol{g}\cdot\boldsymbol{U}.
\end{aligned}$$

By means of mass conservation equation, *i.e.*, $\rho J = \rho^0$, previous system takes the form

$$\rho^0 \frac{d}{dt}(\frac{1}{\rho}) - \nabla_X \cdot (J\mathsf{F}^{-1}\boldsymbol{U}) = 0, \tag{2.153a}$$

$$\rho^0 \frac{d}{dt}\boldsymbol{U} + \nabla_X \cdot (JP\mathsf{F}^{-t}) = \rho^0\boldsymbol{g}, \tag{2.153b}$$

$$\rho^0 \frac{d}{dt}E + \nabla_X \cdot (J\mathsf{F}^{-1}P\boldsymbol{U}) = \rho^0\boldsymbol{g}\cdot\boldsymbol{U}. \tag{2.153c}$$

Rankine-Hugoniot equations for Lagrangian gas dynamics

When the fluid variables are not smooth the integral form of the gas dynamics equations remain valid, but their formulations as partial differential equations hold only in the weak sense. If the fluid variables experience a jump discontinuity across a moving surface, the solution satisfies the Rankine-Hugoniot jump relations, which are deduced from the transport formula for discontinuous solutions. For Lagrangian gas dynamics, Rankine-Hugoniot equations follow from (2.138) by setting $\mathsf{T} = -P\,\mathsf{I}_d$ and $\boldsymbol{q} = \boldsymbol{0}$

$$M[\![\frac{1}{\rho}]\!] + [\![J\mathsf{F}^{-1}\boldsymbol{U}]\!]\cdot\boldsymbol{N}_\Sigma = 0, \tag{2.154a}$$

$$M[\![\boldsymbol{U}]\!] - [\![PJ\mathsf{F}^{-t}]\!]\boldsymbol{N}_\Sigma = 0, \tag{2.154b}$$

$$M[\![E]\!] - [\![J\mathsf{F}^{-1}(P\boldsymbol{U})]\!]\cdot\boldsymbol{N}_\Sigma = 0. \tag{2.154c}$$

Let us recall that M is the mass flux swept by the discontinuity. These jump relations are associated to the physical conservation laws of mass, momentum and total energy. They must be completed by adding the jump equation associated to the deformation gradient tensor (2.139). Moreover, consistency with the Second Law of thermodynamics is ensured by the following entropy inequality which follows from (2.149)

$$-M[\![\eta]\!] \geq 0. \tag{2.155}$$

The correspondence $M\,\mathsf{d}S = -m\,\mathsf{d}s$ allows to recover the Eulerian entropy inequality (2.109e) from its Lagrangian counterpart. Namely, the specific entropy of a fluid particle that crosses discontinuity in the direction of the unit normal is always increasing.

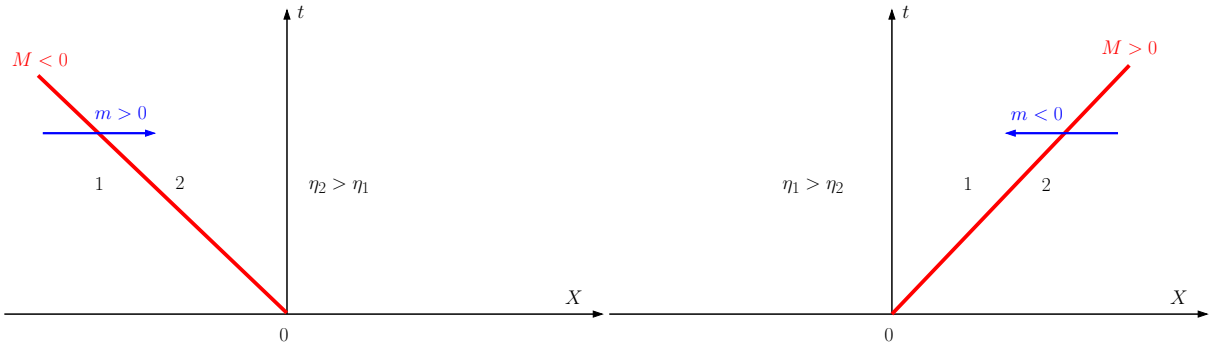

Figure 2.5: Leftward (left) and rightward (right) shock waves displayed in a (X,t) diagram of the Lagrangian frame. Shock waves have been colored red.

One-dimensional Lagrangian local form of the gas dynamics equations

For a one-dimensional flow with slab symmetry, several simplification occur. For instance, F and J reduce to the partial derivative $\frac{\partial x}{\partial X}$. Having this in mind Lagrangian gas dynamics equations readily write

$$\rho^0 \frac{d}{dt}(\frac{1}{\rho}) - \frac{\partial}{\partial X} u = 0, \tag{2.156a}$$

$$\rho^0 \frac{d}{dt} u + \frac{\partial}{\partial X} P = \rho^0 g, \tag{2.156b}$$

$$\rho^0 \frac{d}{dt} E + \frac{\partial}{\partial X}(Pu) = \rho^0 g u, \tag{2.156c}$$

where u and g denote the X-components of the velocity and the body force.

The one-dimensional Lagrangian Rankine-Hugoniot equations follow from (2.154) by setting $J = \mathsf{F} = \frac{\partial x}{\partial X}$

$$M[\![\frac{1}{\rho}]\!] + [\![u]\!] = 0, \tag{2.157a}$$

$$M[\![u]\!] - [\![P]\!] = 0, \tag{2.157b}$$

$$M[\![E]\!] - [\![Pu]\!] = 0. \tag{2.157c}$$

In writing these equations, we have set $\boldsymbol{N}_\Sigma = \boldsymbol{e}_X$ where $\boldsymbol{e}_X$ is the unit rightward vector. With this choice, the state labelled by subscript 1 (resp. 2) corresponds to the left (resp. right) state. To ensure consistency with the Second Law of thermodynamics, the above equations are completed by the jump inequality related to specific entropy

$$-M[\![\eta]\!] \geq 0.$$

Here, $M = \rho_1 J_1 W = \rho_2 J_2 W$ is the mass flux swept by the discontinuity wave and W is the Lagrangian speed of the wave. If $W > 0$ (resp. $W < 0$), the discontinuity wave is a rightward (resp. leftward) shock wave. For one-dimensional flow, the correspondence between Eulerian and Lagrangian mass flux writes $M = -m$, where $m = \rho_1(u_1 - w) = \rho_2(u_2 - w)$ denotes the mass flux crossing the discontinuity wave and w is the Eulerian wave speed. Depending on whether M is positive or not, we distinguish the two following cases.

- $M > 0$: The discontinuity is a rightward shock wave which is crossed by leftward fluid particles since $m < 0$, refer to Fig. 2.5 (right). According to entropy inequality, specific entropy increase is ruled by $\eta_1 > \eta_2$.

- $M < 0$: The discontinuity is a leftward shock wave which is crossed by rightward fluid particles since $m > 0$, refer to Fig. 2.5 (left). According to entropy inequality, specific entropy increase is ruled by $\eta_2 > \eta_1$.

2.4 Arbitrary Lagrangian Eulerian integral form of the conservation laws of fluid mechanics

Numerical schemes in compressible fluid dynamics make use of two classical kinematic descriptions: the Lagrangian description and the Eulerian description. Lagrangian algorithms are characterized by computational cells that move with fluid velocity. They allow an easy and natural tracking of free surfaces and interfaces between different materials. However, they suffer from a lack of robustness when they are facing large flow distortions. On the other hand, Eulerian algorithms are characterized by a fixed computational grid through which fluid moves. They can handle large distortions without any difficulties. However, the numerical diffusion inherent in advection terms discretization leads to an inaccurate interface definition and a loss in the resolution of flow details. The Arbitrary Lagrangian-Eulerian (ALE) description has been initially introduced in the seminal paper [71] to solve to a certain extent the shortcomings of purely Lagrangian and purely Eulerian descriptions by combining the best features of both aforementioned approaches. The main feature of the ALE methodology is to move the computational grid with a prescribed velocity field to improve the accuracy and the robustness of the simulation. In this section we aim at recalling the derivation of ALE integral and local forms of the conservation laws of fluid mechanics. The interest of the ALE form lies in the fact that it encompasses both Lagrangian and Eulerian forms.

To derive the ALE integral form of the conservation laws, we shall make use of the transport formula (2.39) corresponding to an arbitrary motion which differs the fluid motion. For a scalar valued function f, this formula writes as

$$\frac{d}{dt}\int_{\omega=\boldsymbol{\Psi}(\Omega_\xi,t)} f(\boldsymbol{x},t)\,\mathsf{d}v = \frac{d}{dt}\int_{\omega=\boldsymbol{\Phi}(\Omega,t)} f(\boldsymbol{x},t)\,\mathsf{d}v - \int_{\partial\omega} f(\boldsymbol{U}-\boldsymbol{V})\cdot\boldsymbol{n}\,\mathsf{d}s.$$

Here, $\boldsymbol{\Phi}$ and Ψ are respectively the arbitrary motion map and the fluid map, whereas vectors $\boldsymbol{V}$ and $\boldsymbol{U}$ stands for the arbitrary velocity and the fluid velocity. In addition, ω denotes a subset of the Eulerian configuration whose pre-images in arbitrary motion and fluid motion are respectively Ω_ξ and Ω. Left-hand side of the above transport formula represents the time derivative of integral of f over the volume ω following the arbitrary motion. The first term in the right-hand side corresponds to the time derivative of integral of f over ω following the fluid motion. Applying the above transport formula to $f = (\rho, 1_\omega, \rho\boldsymbol{U}, \rho E)$ yields the intermediate system

$$\begin{aligned}
&\frac{d}{dt}\int_{\omega=\boldsymbol{\Psi}(\Omega_\xi,t)} \rho\,\mathsf{d}v = \frac{d}{dt}\int_{\omega=\boldsymbol{\Phi}(\Omega,t)} \rho\,\mathsf{d}v - \int_{\partial\omega} \rho(\boldsymbol{U}-\boldsymbol{V})\cdot\boldsymbol{n}\,\mathsf{d}s,\\
&\frac{d}{dt}\int_{\omega=\boldsymbol{\Psi}(\Omega_\xi,t)} 1_\omega\,\mathsf{d}v = \frac{d}{dt}\int_{\omega=\boldsymbol{\Phi}(\Omega,t)} 1_\omega\,\mathsf{d}v - \int_{\partial\omega} 1_\omega(\boldsymbol{U}-\boldsymbol{V})\cdot\boldsymbol{n}\,\mathsf{d}s,\\
&\frac{d}{dt}\int_{\omega=\boldsymbol{\Psi}(\Omega_\xi,t)} \rho\boldsymbol{U}\,\mathsf{d}v = \frac{d}{dt}\int_{\omega=\boldsymbol{\Phi}(\Omega,t)} \rho\boldsymbol{U}\,\mathsf{d}v - \int_{\partial\omega} \rho\boldsymbol{U}(\boldsymbol{U}-\boldsymbol{V})\cdot\boldsymbol{n}\,\mathsf{d}s,\\
&\frac{d}{dt}\int_{\omega=\boldsymbol{\Psi}(\Omega_\xi,t)} \rho E\,\mathsf{d}v = \frac{d}{dt}\int_{\omega=\boldsymbol{\Phi}(\Omega,t)} \rho E\,\mathsf{d}v - \int_{\partial\omega} \rho E(\boldsymbol{U}-\boldsymbol{V})\cdot\boldsymbol{n}\,\mathsf{d}s.
\end{aligned}$$

Here, 1_ω denotes the indicator function of the set ω, *i.e.*,

$$1_\omega(\boldsymbol{x}) = \begin{cases} 1 \text{ if } \boldsymbol{x} \in \omega, \\ 0 \text{ if } \boldsymbol{x} \notin \omega. \end{cases}$$

It remains to replace in each equation of the above system, the time derivative of the volume integral following the fluid motion using the integral form of the conservation laws which has been derived in Section 2.2.1. More precisely, making use of the balance equations (2.55a)-(2.55d), yields the final form of the ALE integral conservation laws

$$\frac{d}{dt}\int_{\omega=\boldsymbol{\Psi}(\Omega_\xi,t)} \rho \,\mathsf{d}v + \int_{\partial\omega} \rho(\boldsymbol{U}-\boldsymbol{V})\cdot\boldsymbol{n}\,\mathsf{d}s = 0, \tag{2.158a}$$

$$\frac{d}{dt}\int_{\omega=\boldsymbol{\Psi}(\Omega_\xi,t)} \mathsf{d}v - \int_{\partial\omega} \boldsymbol{V}\cdot\boldsymbol{n}\,\mathsf{d}s = 0, \tag{2.158b}$$

$$\frac{d}{dt}\int_{\omega=\boldsymbol{\Psi}(\Omega_\xi,t)} \rho\boldsymbol{U} \,\mathsf{d}v - \int_{\partial\omega} \mathsf{T}\boldsymbol{n}\,\mathsf{d}s + \int_{\partial\omega} \rho\boldsymbol{U}(\boldsymbol{U}-\boldsymbol{V})\cdot\boldsymbol{n}\,\mathsf{d}s = \int_\omega \rho\boldsymbol{g}\,\mathsf{d}v, \tag{2.158c}$$

$$\frac{d}{dt}\int_{\omega=\boldsymbol{\Psi}(\Omega_\xi,t)} \rho E \,\mathsf{d}v - \int_{\partial\omega} (\mathsf{T}\boldsymbol{U}-\boldsymbol{q})\cdot\boldsymbol{n}\,\mathsf{d}s + \int_{\partial\omega} \rho E(\boldsymbol{U}-\boldsymbol{V})\cdot\boldsymbol{n}\,\mathsf{d}s = \int_\omega \rho(\boldsymbol{g}\cdot\boldsymbol{U}+r)\,\mathsf{d}v. \tag{2.158d}$$

These equations state respectively the balance of mass, volume, momentum and total energy over the volume ω, which is moving following the arbitrary motion characterized by the prescribed velocity field $\boldsymbol{V}$. Let us remark that (2.158b) expresses the time rate of change of the fluid volume contained in ω in its motion with the arbitrary velocity $\boldsymbol{V}$. This equation, also named Geometric Conservation Law (GCL), is strongly linked to the trajectory of the fluid particles given by

$$\frac{d}{dt}\boldsymbol{x} = \boldsymbol{V}(\boldsymbol{x},t), \quad \boldsymbol{x}(0) = \boldsymbol{\xi}, \tag{2.159}$$

where $\boldsymbol{\xi}$ denotes the initial location of a fluid particle located at $\boldsymbol{x}$ at time t in the arbitrary motion. To set up completely the ALE formulation, it remains to determine the velocity, $\boldsymbol{V}$, which characterizes the arbitrary motion. Usually, this arbitrary velocity field is defined at the vertices of the computational grid attached to the numerical discretization of the conservation laws. It is prescribed in order to improve the accuracy and the robustness of the numerical simulations and thus strongly depends on the practical study under consideration. There is a huge literature devoted to this topic, interested reader might consult [51] and the references herein for more informations about this subject.

We conclude by giving the ALE integral form of the fundamental inequality which ensures consistency with the Second Law of thermodynamics. The ALE version of the fundamental inequality follows from (2.78) by applying once more the transport formula relative to the arbitrary motion as

$$\frac{d}{dt}\int_{\omega=\boldsymbol{\Psi}(\Omega_\xi,t)} \rho\eta \,\mathsf{d}v + \int_{\partial\omega} \rho\eta(\boldsymbol{U}-\boldsymbol{V})\cdot\boldsymbol{n}\,\mathsf{d}s \geq \int_\omega \rho\frac{r}{T}\,\mathsf{d}v - \int_{\partial\omega} \frac{\boldsymbol{q}\cdot\boldsymbol{n}}{T}\,\mathsf{d}s. \tag{2.160}$$

Comment 9 *ALE formulation has the interesting feature to encompass various Eulerian integral forms of the conservation laws. This versatility is due to the fact that the velocity* $\boldsymbol{V}$ *can be arbitrarily chosen. For instance, by setting* $\boldsymbol{V} = \boldsymbol{0}$*, the arbitrary motion* $\boldsymbol{\Psi}$ *collapses to identity and thus ALE integral form of the conservation law reduces* (2.158) *to the classical Eulerian integral form of the conservation laws over the fixed domain* $\omega = \Omega_\xi$*. This latter form is extensively used to construct finite volume discretizations of the conservation laws applied to*

aerodynamics [65]. Now, enforcing the arbitrary motion to coincide with the fluid motion, i.e., $\boldsymbol{V} = \boldsymbol{U}$*, allows to recover the Eulerian integral form of the conservation laws over a domain* ω *which moves with the fluid velocity* (2.55)*. This form, otherwise called updated Lagrangian, will be of great interest to construct finite volume discretizations of the conservation laws, devoted to the numerical simulation of multi-material fluid flows which suffer large expansions or compressions. That is, flows for which the domain occupied by the fluid encounters large changes in its shape as time evolves. This updated Lagrangian form is the cornerstone to develop computational methods devoted to the numerical simulation of Lagrangian hydrodynamics.*

Chapter 3

Cell-centered schemes for Lagrangian hydrodynamics

Fluid dynamics relies on two kinematic descriptions: the Eulerian description and the Lagrangian description. In the former, the conservation laws are written using a fixed reference frame whereas in the latter they are written through the use of a moving reference frame that follows the fluid motion. Lagrangian representation is particularly well adapted to describe the time evolution of fluid flows contained in regions undergoing large shape changes due to strong compressions or expansions. Moreover, in this representation, there is no mass flux across the boundary surface of a control volume moving with the fluid velocity. Therefore, Lagrangian formalism provides a natural framework to track accurately material interfaces present in multi-material compressible fluid flows. All these reasons incite the use of the Lagrangian description to model the compressible flows encountered in the context of Inertial Confinement Fusion, refer to Chapter 1. Indeed, the hydrodynamic flow resulting from the implosion of an ICF target is a source of very intense shock and rarefaction waves. The size of the domain occupied by the fluid varies strongly over time. Furthermore, the target being composed of several distinct materials, this type of flow generally contains several interfaces that need to be followed with accuracy during implosion.

Bearing this context in mind, our main motivation consists in deriving a robust and accurate numerical method that solves the compressible gas dynamics equations written under Lagrangian form. Before we proceed any further in the description of this method, we start by presenting a brief historical overview about Lagrangian numerical methods. For a thoroughly presentation of the classical computational methods in Lagrangian and Eulerian hydrocodes, the interested reader may refer to the review paper of Benson [23].

In contrast to Eulerian methods, Lagrangian methods are characterized by a moving computational grid. Thus, in the Lagrangian framework, one has to discretize not only the physical conservation laws but also the vertex velocity to define the mesh motion. Moreover, the numerical fluxes of the physical conservation laws must be determined in a compatible manner with the vertex velocity. More precisely, the zone volume that is computed directly from its coordinates must be equal to the zone volume that is deduced from solving the discrete volume equation, otherwise called the Geometric Conservation Law (GCL). This critical requirement related to the GCL is the cornerstone on which any proper multi-dimensional Lagrangian scheme should rely.

The most natural method to fulfill this requirement consists in employing a staggered discretization wherein the velocity is located at the nodes whereas the thermodynamic variables (density, pressure and specific internal energy) are defined at the cell center. This choice leads to solve a partial differential equation for the specific internal energy. Although it is written under

a non-conservative form, the adding of an artificial viscosity term renders this equation compatible with the Second Law of thermodynamics. This term, that mimics the physical viscosity, ensures a proper transformation of kinetic energy into internal energy through shock waves. The first staggered scheme has been introduced for one-dimensional flows by Von Neumann and Richtmyer during the 40's in Los Alamos and published later in their seminal paper [164]. The bi-dimensional extension to elastic-plastic flows has been derived by Wilkins in [166]. In its initial version, this scheme did not conserve the total energy, in addition it was sensitive to numerical spurious modes. Since two decades, many improvements have been done in order to solve theses flaws. In their paper [36], Caramana and Shashkov show that with an appropriate discretization of the subzonal forces resulting from subzonal pressures, hourglass motion and spurious vorticity can be eliminated. The introduction of a compatible discretization of the divergence and gradient operators leads to a compatible staggered scheme which conserves the total energy [31, 35]. Regarding the artificial viscosity, its discretization has also been considerably improved. First, by introducing formulations for multidimensional shock wave computations in [34] and then by using a discretization based on mimetic finite difference method in [32, 92]. With all these improvements, staggered Lagrangian schemes are accurate and robust numerical methods, which can produce impressive results, even on unstructured polygonal grids [33]. We want also to mention the recent papers [30, 110] wherein two-dimensional staggered discretizations are developed by constructing artificial viscosities which relies on the use of an approximate Riemann solver.

Up to our knowledge, the interpretation of the staggered schemes of Wilkins and Goad [166, 64] by means of the finite element method has been initially introduced by Lascaux at the beginning of the 70's in [82, 83]. This finite element interpretation has been further developed producing various interesting staggered schemes. In [14], Barlow presents a compatible finite element Lagrangian hydrodynamics algorithm used in a multi-material Arbitrary Lagrangian Eulerian (ALE) strategy. We also note the development of a variational multi-scale stabilized approach in finite element computation of Lagrangian hydrodynamics, where a piecewise linear approximation was adopted for the variables [145, 144]. The case of Q1/P0 finite element is studied in [147], where the kinematic variables are represented using a piecewise linear continuous approximation, while the thermodynamic variables utilize a piecewise constant representation. More recently, a high-order extension of the staggered discretization based on a curvilinear finite element method has been derived in [50], the corresponding artificial viscosity being described in [78].

The staggered grid schemes employed in most hydro-codes have been remarkably successful over the past decades in solving complex multi-dimensional compressible fluid flows. However, they clearly have some theoretical and practical deficiencies. Mesh imprinting and symmetry breaking are important examples. The need to use artificial viscosities, hourglass filters and sub-zonal pressure schemes is also undesirable. A staggered scheme is also inelegant as all variables are not conserved over the same space. High resolution cell-centered Lagrangian Godunov schemes can overcome some of these problems. In contrast to staggered approach, these conservative schemes are based on a cell-centered placement of all the fluid variables and solve the total energy equation. The numerical face fluxes are determined by means of one-dimensional approximate Riemann solvers in the direction normal to the cell interface. The main difficulty lies in the definition of consistent Lagrangian nodal velocities with which to move the computational mesh. This probably explains why progress has been slow in extending these ideas to Lagrangian schemes, while Eulerian Godunov methods have been well established for a long time.

A first attempt has been done by Dukowicz and his co-workers while developing CAVEAT code in Los Alamos during the 80's. In [8, 7] they proposed to use a weighted least squares

algorithm to compute the vertex velocity by requiring that the vertex velocity projected in the direction of a face normal should equal the normal velocity resulting from the approximate Riemann solver. It turns out that this algorithm is capable of generating additional spurious components in the vertex velocity field. Thus, it leads to an artificial grid motion which requires a very expensive treatment [54]. This flaw follows from the fact that the volume flux is not compatible with the node motion in the sense that the GCL is not satisfied.

A solution to circumvent this problem consists in deriving cell-centered discretizations based on a total Lagrangian formulation of the gas dynamics equations. That it is, a formulation wherein the divergence and gradient operators are expressed in terms of the Lagrangian coordinates. In this framework, the computational grid is fixed, however one has to follow the time evolution of the Jacobian matrix associated to the Lagrange-Euler flow map. In addition, a new difficulty arises due to the fact that the gas dynamics system written under total Lagrangian form is only weakly hyperbolic [72, 98, 116, 49, 47]. This loss of strict hyperbolicity is related to the supplementary conservation law that results from the time evolution of the deformation gradient tensor. Following this approach, a Lagrangian Discontinuous Galerkin-type method has been successfully developed in [6]. However, the use of this method is limited to a representation in the initial configuration since it cannot be rigorously interpreted as a moving mesh method. This issue has been addressed by Després and Mazeran in [49] where they propose a first-order cell-centered discretization of the gas dynamics equations that can be written in both total and updated Lagrangian forms thus leading to a moving mesh finite volume scheme which satisfies exactly the GCL. The numerical fluxes are defined at the node in the following manner: there is a unique nodal velocity and one nodal pressure per each cell surrounding the node. These fluxes are computed through the use of a node-centered approximate Riemann solver. This scheme conserves the momentum and the total energy and also satisfies an entropy inequality. It has been called GLACE in [38] where a high-order multi-dimensional extension is provided, the acronym GLACE being shorthand for Godunov-type LAgrangian scheme Conservative for total Energy. A thorough study of the properties of the GLACE node-centered solver reveals a strong sensitivity to the cell aspect ratio which can leads to severe numerical instabilities [136]. This problem is critical for ICF Lagrangian simulations characterized by computational grids that frequently contain very high aspect ratio cells. To overcome this difficulty, we have proposed an alternative scheme [108] that successfully solves the cell aspect ratio problem and keeps the compatibility between fluxes discretization and vertices velocity computation. This first-order scheme is also characterized by node-based fluxes, it conserves the momentum and the total energy, and fulfills a local entropy inequality. Its main feature lies in the discretization of the pressure gradient, which is designed using two pressures at each node of a cell, each nodal pressure being associated with the direction of the unit outward normals related to the edges originating from the node. These nodal pressures are linked to the nodal velocity thanks to approximate Riemann invariants. This scheme, which is called EUCCLHYD (Explicit Unstructured Cell-Centered Lagrangian HYDrodynamics), has been extended to higher order using first a classical MUSCL-type approach [109], and then a prolongation of works initiated by Ben-Artzi and Falcovitz [21] concerning the Generalized Riemann Problem [105]. The application of this scheme to the tri-dimensional geometry is presented in [111]. The extension to the bi-dimensional axisymmetric geometry is described in [104]; this latter version being absolutely necessary for simulations of the implosion of an ICF target of a spherical symmetry. More recently, we have contributed to the implementation of a general formulation of cell-centered schemes for Lagrangian hydrodynamics that is based on the use of the concept of sub-cell forces which has been initially introduced in the context of staggered discretization [35]. This formulation covers different centered schemes proposed previously and is described in [107, 106]. This framework, adapted here to cell-centered discretization, should provide deeper

understanding of relations between cell-centered and staggered Lagrangian schemes. Note that this formulation has quite a lot in common with the approach taken very recently in [12]. In this work, the author also draws an analogy between forces and the momentum fluxes in the momentum equation and uses this to produce a total energy conservation equation expressed in work form as it is has been done in [107], which allows the total energy to be evolved for forces which include terms that appear as a pressure average and a linear vector artificial viscosity. Last, it is worth pointing out the recent work presented in [126] which consists in a high-order curvilinear finite volume method that solves the Lagrangian gas dynamics. This original GCL satisfying approach relies on a weak formulation to compute the nodal velocity using an acoustic Riemann solver approximation. Let us emphasize that in its first-order version this method naturally recovers the first-order EUCCLHYD scheme.

We conclude this review by saying that cell-centered finite volume schemes [38, 105] that fulfill the GCL compatibility requirement seem to be a promising alternative to the usual staggered finite difference discretizations [35] for compressible Lagrangian hydrodynamics. These cell-centered Godunov-type discretizations exhibit the good property of being naturally conservative. This point is of great importance since convergent conservative schemes are known to converge to weak solutions in the presence of shocks by the Lax-Wendroff theorem [85]. Furthermore, they do not require the use of an artificial viscosity since the numerical dissipation built in the approximate Riemann solver automatically converts kinetic energy into internal energy through shock waves. Last, these cell-centered schemes allow a straightforward implementation of conservative remapping methods when they are used in the context of the Arbitrary Lagrangian Eulerian (ALE) strategy.

The aim of the present work is to develop a general formalism to derive cell-centered schemes for two-dimensional Lagrangian hydrodynamics on unstructured grids that meet the compatibility GCL requirement. For a general polygonal grid, the discrete equations that govern the time rate of change of volume, momentum and total energy are obtained by means of a control volume formulation of the gas dynamics equations written using a cell-centered placement of the physical variables. The motion of the vertices of the grid is deduced from the trajectory equations, once the vertex velocity is defined. The general formalism that we present relies on a sub-cell force-based discretization wherein the sub-cell force form is determined in such a manner that the resulting scheme satisfies an entropy inequality. Invoking the fundamental conservation principles of the momentum and the total energy leads to the construction of a node-centered solver that determines the nodal velocity. The high-order extension of this general cell-centered scheme is derived through the use of a non-trivial two-dimensional extension of the Generalized Riemann Problem (GRP) methodology [21] in its acoustic version. This general framework is developed for both two-dimensional Cartesian and cylindrical geometries.

The remainder of this chapter is organized as follows. In Section 3.1, we recall briefly the high-order cell-centered discretization of the one-dimensional Lagrangian hydrodynamics. The high-order sub-cell force-based discretization in two-dimensional Cartesian geometry is thoroughly described in Section 3.2. The robustness and the accuracy of this formulation are demonstrated in Section 3.3 by means of various numerical tests. Finally, the extension to axisymmetric geometry is described in Section 3.4, which is followed by the presentation of the corresponding numerical results in Section 3.5.

3.1 High-order discretization for one-dimensional Lagrangian hydrodynamics

The aim of this section is to recall the one-dimensional cell-centered Lagrangian discretization wherein the numerical fluxes are computed using approximated Riemann solvers. This topic is

quite well known and has been investigated by several authors, refer for instance to [159, 21, 122, 60, 65, 47, 139, 46, 61].

3.1.1 Governing equations

For the sake of completeness, we recall hereafter the local Lagrangian form of the one-dimensional gas dynamics equation with slab symmetry (refer to (2.156) page 53)

$$\begin{aligned}
&\rho^0 \frac{d}{dt}(\frac{1}{\rho}) - \frac{\partial}{\partial X} u = 0,\\
&\rho^0 \frac{d}{dt} u + \frac{\partial}{\partial X} P = 0,\\
&\rho^0 \frac{d}{dt} E + \frac{\partial}{\partial X}(Pu) = 0.
\end{aligned}$$

Note that the body force has been suppressed. Let us recall, that X denotes the Lagrangian coordinate and $\rho^0 = \rho^0(X) > 0$ is the initial density. In the above system, all the fluid variables are expressed in terms of X and t. In many textbooks [65, 21, 47], the above system is rewritten through the use of the mass coordinate. This other Lagrangian coordinate is defined as $\mathrm{d}m = \rho^0(X)\mathrm{d}X$. Introducing this change of coordinates in the above system yields

$$\begin{aligned}
&\frac{d}{dt}(\frac{1}{\rho}) - \frac{\partial}{\partial m} u = 0,\\
&\frac{d}{dt} u + \frac{\partial}{\partial m} P = 0,\\
&\frac{d}{dt} E + \frac{\partial}{\partial m}(Pu) = 0.
\end{aligned}$$

A thoroughly study of this system from both mathematical and numerical point of view has been performed in [122]. However, one must have in mind that the use of the mass coordinate is restricted to one-dimensional system since it is not possible to extend it to multi-dimensional framework. For this reason, we shall not use anymore this representation.

In what follows, we aim at deriving a moving mesh discretization of the one-dimensional gas dynamics equation. To this end, we introduce the updated Lagrangian form of the gas dynamics equation through the use of the trajectory equation. Namely, considering a fluid particle initially located at X, we denote by $x(X,t)$ its position at time t. If $u = u(x,t)$ denotes the x-component of the fluid velocity, then the fluid paths are solution of the trajectory equation

$$\frac{dx}{dt} = u, \quad x(X,0) = X. \tag{3.1}$$

Here, x stands for the Eulerian coordinate. Expressing the fluid variables in terms of the Eulerian coordinate and noticing that mass conservation amounts to write $\mathrm{d}m = \rho^0(X)\mathrm{d}X = \rho(x(X,t),t)\mathrm{d}x$, the above system rewrites as

$$\rho \frac{d}{dt}(\frac{1}{\rho}) - \frac{\partial u}{\partial x} = 0, \tag{3.2a}$$

$$\rho \frac{d}{dt} u + \frac{\partial P}{\partial x} = 0, \tag{3.2b}$$

$$\rho \frac{d}{dt} E + \frac{\partial}{\partial x}(Pu) = 0, \tag{3.2c}$$

where this time $\frac{d}{dt} = \frac{\partial}{\partial t} + u\frac{\partial}{\partial x}$ denotes the material derivative. The specific internal energy ε is defined by $\varepsilon = E - \frac{1}{2}u^2$. The thermodynamic closure is given by the equation of state

$P = P(\rho, \varepsilon)$. To ensure the thermodynamic consistency of the above system with the Second Law of thermodynamics, it must be completed by the following entropy inequality

$$\rho \frac{d\eta}{dt} \geq 0, \tag{3.3}$$

where η denotes the specific entropy. The specific entropy is related to the other thermodynamic variables by means of the fundamental Gibbs relation

$$T\mathrm{d}\eta = \mathrm{d}\varepsilon + P\mathrm{d}(\frac{1}{\rho}), \tag{3.4}$$

where T denotes the temperature.

3.1.2 Mathematical properties of the one-dimensional system of the gas dynamics equations

Before we proceed any further with the numerical discretization of system (3.2), we recall some important properties related to its mathematical structures. These notions, which are presented hereafter for the sake of completeness, can be found in [122, 65, 47, 21, 134]. Assuming that the fluid variables are continuously differentiable, we are going to transform (3.2) in a more convenient form using as primary variables (P, u, η). To this end, we start by deriving the equation relative to specific entropy which follows directly from the Gibbs relation (3.4)

$$\rho T \frac{d\eta}{dt} = \rho \frac{d\varepsilon}{dt} + \rho P \frac{d}{dt}(\frac{1}{\rho}). \tag{3.5}$$

From the specific internal energy definition, it follows that $\frac{d\varepsilon}{dt} = \frac{dE}{dt} - u\frac{du}{dt}$. Thus, multiplying (3.2b) by u and subtracting the resulting equation from (3.2c) leads to

$$\rho \frac{d\varepsilon}{dt} + P\frac{\partial u}{\partial x} = 0. \tag{3.6}$$

Finally, replacing (3.6) and (3.2a) in (3.5) provides the final form of the entropy equation

$$\rho T \frac{d\eta}{dt} = 0. \tag{3.7}$$

This equation states that for smooth flows, entropy is conserved along fluid particle paths. This corresponds to an **isentropic** flow, where the entropy level of each fluid particle does not change with time, but may vary from particle to particle. In addition, if the initial specific entropy is uniform, *i.e.*, $\eta(x, 0) = \eta^0$, then it remains uniform at later time, *i.e.*, $\eta(x, t) = \eta^0$. This particular situation, wherein the flow has uniform and constant entropy, corresponds to a **homoentropic** flow.

Now, considering the equation of state written under the form $P = P(\rho, \eta)$ and differentiating it with respect to ρ and η yields

$$\mathrm{d}P = (\frac{\partial P}{\partial \rho})_\eta \mathrm{d}\rho + (\frac{\partial P}{\partial \eta})_\rho \mathrm{d}\eta.$$

This leads to define the isentropic sound speed, a, as

$$a^2 = \left(\frac{\partial P}{\partial \rho}\right)_\eta. \tag{3.8}$$

In writing this definition, we have made the fundamental assumption that the equation of state is such that $(\frac{\partial P}{\partial \rho})_\eta > 0$. Using the above definition and the fact that the flow under consideration is isentropic leads to

$$\frac{dP}{dt} = a^2 \frac{d\rho}{dt}. \tag{3.9}$$

Using this latter equation and the equation satisfied by entropy, we express the system of gas dynamics equations in terms of the variables (P, u, η) as

$$\frac{dP}{dt} + \rho a^2 \frac{\partial u}{\partial x} = 0, \tag{3.10a}$$

$$\frac{du}{dt} + \frac{1}{\rho}\frac{\partial P}{\partial x} = 0, \tag{3.10b}$$

$$\frac{d\eta}{dt} = 0. \tag{3.10c}$$

Recalling that the material derivative is given by $\frac{d}{dt} = \frac{\partial}{\partial t} + u\frac{\partial}{\partial x}$, the above system also writes under the equivalent form

$$\frac{\partial P}{\partial t} + u\frac{\partial P}{\partial x} + \rho a^2 \frac{\partial u}{\partial x} = 0, \tag{3.11a}$$

$$\frac{\partial u}{\partial t} + u\frac{\partial u}{\partial x} + \frac{1}{\rho}\frac{\partial P}{\partial x} = 0, \tag{3.11b}$$

$$\frac{\partial \eta}{\partial t} + u\frac{\partial \eta}{\partial x} = 0. \tag{3.11c}$$

This latter system is put under the compact form

$$\frac{\partial}{\partial t}\begin{pmatrix} P \\ u \\ \eta \end{pmatrix} + \mathsf{A}\frac{\partial}{\partial x}\begin{pmatrix} P \\ u \\ \eta \end{pmatrix} = \mathbf{0},$$

where the matrix A is defined by

$$\mathsf{A} = \begin{pmatrix} u & \rho a^2 & 0 \\ \frac{1}{\rho} & u & 0 \\ 0 & 0 & u \end{pmatrix} \tag{3.12}$$

This matrix admits three distinct real eigenvalues which write

$$\lambda^- = u - a, \quad \lambda^0 = u \ \text{ and } \ \lambda^+ = u + a. \tag{3.13}$$

Therefore, system (3.11) is **strictly hyperbolic**. Each eigenvalue defines a family of characteristic curves, these curves are denoted $(\mathcal{C}^-)$, $(\mathcal{C}^0)$ and $(\mathcal{C}^+)$, and they are defined as the integral curves of the following equations

$$(\mathcal{C}^-)\ \frac{dx}{dt} = u - a, \quad (\mathcal{C}^0)\ \frac{dx}{dt} = u, \quad (\mathcal{C}^+)\ \frac{dx}{dt} = u + a. \tag{3.14}$$

We observe that the specific entropy is conserved along $(\mathcal{C}^0)$, which coincides with the trajectory equation. Moreover, along the characteristic curves $\mathcal{C}^\pm$, one can easily show that the following equations hold

$$\mathrm{d}P \pm \rho a \mathrm{d}u = 0. \tag{3.15}$$

For a homoentropic flow, the density and the sound speed can be expressed uniquely in terms of the pressure and the above differential forms can be integrated in the form

$$u \pm \int \frac{\mathrm{d}P}{\rho(P)a(P)} = \text{cst}. \tag{3.16}$$

The quantities in the left-hand side are called **Riemann invariants**.

3.1.3 First-order space discretization

Let $\Omega = [X_{\rm b}, X_{\rm e}]$ be the domain initially filled by the fluid. This domain is partitioned into I cells $\Omega_i = [X_{i-\frac{1}{2}}, X_{i+\frac{1}{2}}]$. The vertex motion is given by the discretized trajectory equation

$$\frac{d}{dt}x_{i+\frac{1}{2}} = u_{i+\frac{1}{2}}, \quad x_{i+\frac{1}{2}}(0) = X_{i+\frac{1}{2}}, \tag{3.17}$$

where $u_{i+\frac{1}{2}}$ denotes the vertex velocity. Let $\omega_i(t) = [x_{i-\frac{1}{2}}(t), x_{i+\frac{1}{2}}(t)]$ denotes the Eulerian moving cell corresponding to the Lagrangian cell Ω_i in the flow map. Let $(\frac{1}{\rho_i}, u_i, E_i)$ be the mass averaged values of $(\frac{1}{\rho}, u, E)$ over the cell $\omega_i(t)$. We recall that in the Lagrangian framework the mass m_i of the cell $\omega_i(t)$ is constant

$$m_i = \rho_i(t)\Delta x_i(t), \quad \forall t > 0, \tag{3.18}$$

where $\Delta x_i = x_{i+\frac{1}{2}} - x_{i-\frac{1}{2}}$ denotes the volume of the cell. Using the transport formula (2.32) page 16, the integration of (3.2) over ω_i leads to the following set of evolution equations for the discrete variables $(\frac{1}{\rho_i}, u_i, E_i)$

$$m_i \frac{d}{dt}(\frac{1}{\rho_i}) - (u_{i+\frac{1}{2}} - u_{i-\frac{1}{2}}) = 0, \tag{3.19a}$$

$$m_i \frac{d}{dt}u_i + P_{i+\frac{1}{2}} - P_{i-\frac{1}{2}} = 0, \tag{3.19b}$$

$$m_i \frac{d}{dt}E_i + (Pu)_{i+\frac{1}{2}} - (Pu)_{i-\frac{1}{2}} = 0, \tag{3.19c}$$

where $u_{i+\frac{1}{2}}$, $P_{i+\frac{1}{2}}$ and $(Pu)_{i+\frac{1}{2}}$ denotes the numerical fluxes at node $x_{i+\frac{1}{2}}$. Here, we make the fundamental assumption that

$$(Pu)_{i+\frac{1}{2}} = P_{i+\frac{1}{2}}u_{i+\frac{1}{2}}.$$

We notice that (3.18) is consistent with (3.19a) since the time differentiation of (3.18) using (3.17) leads to (3.19a).

The fluxes $u_{i+\frac{1}{2}}$ and $P_{i+\frac{1}{2}}$ are obtained by exactly or approximately solving the Riemann problem at the cell interface $x_{i+\frac{1}{2}}$ for the left state $\mathbf{\Phi}_l = (\frac{1}{\rho}_{i-1}, u_{i-1}, E_{i-1})^t$ and the right state $\mathbf{\Phi}_r = (\frac{1}{\rho}_i, u_i, E_i)^t$.

3.1.4 The Riemann problem

The purpose of this section is to recall basic notions related to the resolution of the Riemann problem for gas dynamics equations. Using the exact solution, we show how to construct approximate solutions which will be useful to derive numerical fluxes at cells interface.

Exact solution

The Riemann problem and its solution in terms of $p-u$ curves is discussed in many references [65, 21, 139]. Here, we recall briefly the main steps leading to its resolution in the case of perfect gas equation of state, following the approach presented in [53]. The Riemann problem is illustrated in Figure 3.1 by means of an $x-t$ diagram. The data of the initial discontinuity are specified by $(\frac{1}{\rho}_l, u_l, P_l)^t$ on the left side and $(\frac{1}{\rho}_r, u_r, P_r)^t$ on the right side. At later time, the initial discontinuity is solved by a system of waves which consists of a contact discontinuity, a leftward wave and a rightward wave. Those waves may be either a shock or a rarefaction wave. The pressure $P^\star$ and the velocity $u^\star$ are unique except in the case of cavitation. Moreover, these quantities are continuous across the contact discontinuity while the specific volume is discontinuous and is denoted $\frac{1}{\rho_l^\star}$ on the left side of the interface and $\frac{1}{\rho_r^\star}$ on the right side.

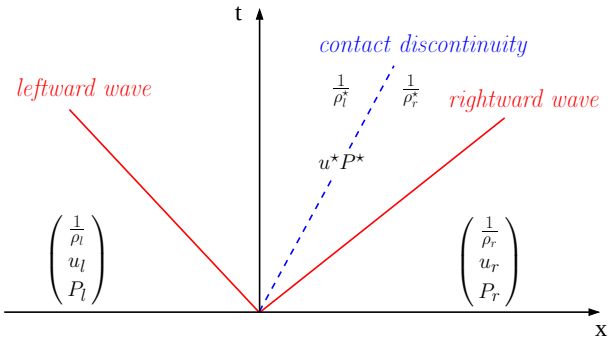

Figure 3.1: $x-t$ diagram for the Riemann problem.

The case of shock waves In this situation, the left, intermediate and right states are linked by the Rankine-Hugoniot relations, refer to (2.157), which write for the leftward wave

$$M_l(\frac{1}{\rho_l^\star}-\frac{1}{\rho_l}) = u^\star - u_l, \tag{3.20a}$$

$$-M_l\,(u^\star - u_l) = P^\star - P_l, \tag{3.20b}$$

$$\varepsilon_l^\star - \varepsilon_l + \frac{P^\star + P_l}{2}(\frac{1}{\rho_l^\star}-\frac{1}{\rho_l}) = 0, \tag{3.20c}$$

$$\eta_l^\star - \eta_l \geq 0. \tag{3.20d}$$

The counterpart for the rightward wave writes

$$M_r(\frac{1}{\rho_r^\star}-\frac{1}{\rho_r}) = -(u^\star - u_r,) \tag{3.21a}$$

$$M_r\,(u^\star - u_r) = P^\star - P_r, \tag{3.21b}$$

$$\varepsilon_r^\star - \varepsilon_r + \frac{P^\star + P_r}{2}(\frac{1}{\rho_r^\star}-\frac{1}{\rho_r}) = 0, \tag{3.21c}$$

$$\eta_r^\star - \eta_r \geq 0. \tag{3.21d}$$

Here, $M_s > 0$ is the fluid mass swept over by the shock wave in unit time per unit area and the subscript s represents l or r for leftward or rightward wave. Let us note that M_s is defined implicitly by

$$M_s^2 = -\frac{P^\star - P_s}{\frac{1}{\rho_s^\star}-\frac{1}{\rho_s}},$$
$$\varepsilon_s^\star - \varepsilon_s + \frac{1}{2}\,(P^\star + P_s)\left(\frac{1}{\rho_s^\star}-\frac{1}{\rho_s}\right) = 0, \quad \text{and} \quad \varepsilon = \varepsilon(\rho, P).$$

By virtue of (3.20d) and (3.21d), one can show that $P^\star \geq P_s$, refer to Appendix B page 221. Namely, to be coherent with the Second Law of thermodynamics a shock wave must be a compressive wave.[1]Using Appendix B, for a gamma gas law, *i.e.*, $P_s = (\gamma_s - 1)\,\rho_s\varepsilon_s$, the mass swept by the shock expresses as

$$M_s = \sqrt{\frac{\rho_s}{2}[(\gamma_s+1)P^\star + (\gamma_s-1)P_s]}. \tag{3.22}$$

[1]This statement is valid provided that the equation of state is such that its Hugoniot curve is convex with respect to the specific volume.

The case of rarefaction waves Through the rarefaction waves, the left, intermediate and right states are linked by means of the Riemann invariants and the isentropy of the flow. This leads to write for the leftward wave

$$-(u^\star - u_l) = \int_{P_l}^{P^\star} \frac{\mathrm{d}P}{\rho(P)a(P)}, \tag{3.23a}$$

$$\varepsilon_l^\star - \varepsilon_l + \int_{\rho_l}^{\rho_l^\star} P\mathrm{d}(\frac{1}{\rho}) = 0, \tag{3.23b}$$

The analogous relations for the rightward wave write

$$u^\star - u_r = \int_{P_r}^{P^\star} \frac{\mathrm{d}P}{\rho(P)a(P)}, \tag{3.24a}$$

$$\varepsilon_r^\star - \varepsilon_r + \int_{\rho_r}^{\rho_r^\star} P\mathrm{d}(\frac{1}{\rho}) = 0. \tag{3.24b}$$

Let us remark that equations (3.23b) and (3.24b) are nothing but the integrals of the isentropy relation, *i.e.*, $\mathrm{d}\eta = 0$. We also note that (3.23a) and (3.24a) can be put under a form similar to (3.20b) and (3.21b). To this end, we define M_s for rarefaction wave as follows

$$M_s = \frac{P_s - P^\star}{\displaystyle\int_{P^\star}^{P_s} \frac{\mathrm{d}P}{\rho(P)a(P)}},$$

knowing that $P^\star \leq P_s$ since the wave under consideration is a rarefaction wave. For a gamma gas law, one obtains

$$M_s = \frac{\gamma_s - 1}{2a_s} \frac{P_s - P^\star}{1 - \left(\frac{P^\star}{P_s}\right)^{\frac{\gamma_s - 1}{2\gamma_s}}}, \tag{3.25}$$

where $a_s = \sqrt{\gamma_s \frac{P_s}{\rho_s}}$ is the sound speed.

The interface pressure $P^\star$ and velocity $u^\star$ are then obtained by solving the non-linear system

$$-M_l\,(u^\star - u_l) = P^\star - P_l, \tag{3.26a}$$

$$M_r\,(u^\star - u_r) = P^\star - P_r, \tag{3.26b}$$

where the swept mass flux $M_s = M_s(P_s, P^\star)$ is defined by

$$M_s = \begin{cases} \dfrac{P_s - P^\star}{\displaystyle\int_{P^\star}^{P_s} \frac{\mathrm{d}P}{\rho(P)a(P)}} & \text{if } P^\star \leq P_s, \\[2ex] \sqrt{-\dfrac{P^\star - P_s}{\frac{1}{\rho_s^\star} - \frac{1}{\rho_s}}} & \text{if } P^\star > P_s. \end{cases} \tag{3.27}$$

This non-linear system can be solved using an iterative method such as the Newton algorithm [21]. Its numerical solution produce an exact Riemann solver [139, 66]. For practical applications, this type of solver is scarcely employed due to its rather expensive cost. In what follows, we recall the construction of two approximate Riemann solvers which will be useful for developing efficient numerical schemes.

Approximate solutions

The first approximate Riemann solver is derived by noticing that in the limit of weak waves, $P^\star - P_s \to 0$, the swept mass flux, M_s tends to the limit $M_s \to \rho_s a_s$ for both shock and rarefaction waves. Replacing the swept mass flux M_s by the acoustic impedance, $z_s = \rho_s a_s$, into (3.26), leads to a linear system satisfied by $(u^\star, P^\star)$. Its solution readily writes

$$u^\star = \frac{z_l u_l + z_r u_r}{z_l + z_r} - \frac{P_r - P_l}{z_l + z_r}, \tag{3.28a}$$

$$P^\star = \frac{z_l P_r + z_r P_l}{z_l + z_r} - \frac{z_l z_r}{z_l + z_r}\left(u_r - u_l\right). \tag{3.28b}$$

These formulas correspond to the well known **acoustic approximate Riemann solver** otherwise called Godunov acoustic solver [66]. This solver is cheap and quite versatile. Since, its use only requires the knowledge of the isentropic sound speed, it can handle tabulated equations of state. However, this solver can produce non physical intermediate densities, $(\rho_l^\star, \rho_r^\star)$, in the case of very strong shock waves. To illustrate this flaw, let us consider a rightward shock waves, using (3.21a) and $M_r = \rho_r a_r$ one obtains

$$\frac{1}{\rho_r^\star} = \frac{1}{\rho_r}\left[\frac{a_r - (u^\star - a_r)}{a_r}\right].$$

We note that for a shock wave such that $u^\star - u_r > a_r$, one has $\frac{1}{\rho_r^\star} < 0$, which is clearly not acceptable. For Eulerian schemes, this drawback is fatal since the intermediate densities are required to compute the mass flux. This non-physical behavior is not so serious in the case of Lagrangian schemes since the intermediate densities are not needed to compute the fluxes.

To correct this non-physical behavior, we construct an approximate solver by using the following approximation for the swept mass flux

$$M_s = \rho_s(a_s + \Gamma_s \mid u^\star - u_s \mid), \tag{3.29}$$

where Γ_s is a material dependent parameter to be defined. This approximation has been initially proposed by Dukowicz [53] for shock wave. We note that in case of a rightward shock wave, $u^\star - a_r > 0$ thus using the previous approximation the intermediate density writes

$$\frac{1}{\rho_r^\star} = \frac{1}{\rho_r}\left[\frac{a_r + (\Gamma_r - 1)(u^\star - a_r)}{a_r + \Gamma_r(u^\star - a_r)}\right].$$

This intermediate density is always positive, regardless the strength of the shock wave, provided that $\Gamma_r > 1$. In the limit of infinite strength shock waves one gets

$$\frac{\rho_r}{\rho_r^\star} \to \frac{\Gamma_r - 1}{\Gamma_r}.$$

This limit allows to define the value of the parameter Γ for a gamma gas law, recalling that in this case $\frac{\rho_r}{\rho_r^\star} \to \frac{\gamma_r - 1}{\gamma_r + 1}$, hence $\Gamma_r = \frac{\gamma_r + 1}{2}$. We note that with this definition of the Γ parameter the approximation (3.29) allows us to approach the asymptotic behavior of the swept mass flux not only for the weak shock wave but also for the infinite strength shock wave.

3.1.5 Semi-discrete entropy inequality

We compute the rate of entropy production corresponding to the semi-discretized system (3.19). From Gibbs formula (3.4) it follows that the rate of entropy production within cell ω_i writes

$$m_i T_i \frac{d}{dt}\eta_i = m_i[\frac{d}{dt}\varepsilon_i + P_i \frac{d}{dt}(\frac{1}{\rho_i})].$$

Knowing that $\frac{d\varepsilon_i}{dt} = \frac{dE_i}{dt} - u_i\frac{du_i}{dt}$ and subtracting u_i(3.19b) from (3.19c) leads to

$$m_i\frac{d}{dt}\varepsilon_i + P_{i+\frac{1}{2}}(u_{i+\frac{1}{2}} - u_i) - P_{i-\frac{1}{2}}(u_{i-\frac{1}{2}} - u_i) = 0. \tag{3.30}$$

From (3.19a) we obtain the pressure work

$$m_i P_i\frac{d}{dt}(\frac{1}{\rho_i}) - [P_i(u_{i+\frac{1}{2}} - u_i) - P_i(u_{i-\frac{1}{2}} - u_i)] = 0. \tag{3.31}$$

Finally, adding (3.30) and (3.31) we get

$$m_i[\frac{d}{dt}\varepsilon_i + P_i\frac{d}{dt}(\frac{1}{\rho_i})] = (P_i - P_{i+\frac{1}{2}})(u_{i+\frac{1}{2}} - u_i) - (P_i - P_{i-\frac{1}{2}})(u_{i-\frac{1}{2}} - u_i). \tag{3.32}$$

This last formula shows that the entropy production depends on the jump between the averaged quantities u_i, P_i and the solution of the Riemann problem $u_{i+\frac{1}{2}}$, $P_{i+\frac{1}{2}}$ at each cell interface. By applying the relations (3.26b) and (3.26a) at cell interfaces $X_{i-\frac{1}{2}}$ and $X_{i+\frac{1}{2}}$ we obtain

$$M_{i,i-\frac{1}{2}}(u_{i-\frac{1}{2}} - u_i) = P_{i-\frac{1}{2}} - P_i, \quad \text{for the rightward wave at } x_{i-\frac{1}{2}}, \tag{3.33a}$$

$$-M_{i,i+\frac{1}{2}}(u_{i+\frac{1}{2}} - u_i) = P_{i+\frac{1}{2}} - P_i, \quad \text{for the leftward wave at } x_{i+\frac{1}{2}}. \tag{3.33b}$$

In these formulas $M_{i,i-\frac{1}{2}}$ ($M_{i,i+\frac{1}{2}}$) denotes the mass swept over by the rightward (leftward) wave emanating from $x_{i-\frac{1}{2}}$ ($x_{i+\frac{1}{2}}$). Substituting (3.33a) and (3.33b) into (3.32) yields

$$m_i[\frac{d}{dt}\varepsilon_i + P_i\frac{d}{dt}(\frac{1}{\rho_i})] = M_{i,i+\frac{1}{2}}(u_{i+\frac{1}{2}} - u_i)^2 + M_{i,i-\frac{1}{2}}(u_{i-\frac{1}{2}} - u_i)^2 \geq 0. \tag{3.34}$$

Since $M_{i,i-\frac{1}{2}}$ and $M_{i,i+\frac{1}{2}}$ are always positive, the right-hand side of (3.34) is always positive. Thus, the semi-discrete scheme satisfies a local entropy inequality. In the case of the acoustic approximate Riemann solver we have $M_{i,i-\frac{1}{2}} = M_{i,i+\frac{1}{2}} = z_i$ and the entropy production in cell ω_i is written

$$m_i[\frac{d}{dt}\varepsilon_i + P_i\frac{d}{dt}(\frac{1}{\rho_i})] = z_i[(u_{i+\frac{1}{2}} - u_i)^2 + (u_{i-\frac{1}{2}} - u_i)^2] \geq 0. \tag{3.35}$$

The right-hand side of (3.34) and (3.35) corresponds to the dissipation associated to the numerical viscosity of the scheme. In this sense, the right-hand side of (3.34) is closely related to the entropy production associated to the von Neumann Richtmyer staggered scheme [139]. In the framework of vNR staggered scheme the velocity is vertex centered and the cell pressure is augmented by an artificial shock viscosity contribution denoted by q which is used in the momentum and the internal energy equations. The original form of q is proportional to the square of the jump velocity [164], refer also to Equation (B.12) in Appendix B. Typically q is set to zero when the flow is expanding and consequently the entropy production is set to zero. Thus, vNR scheme is able to preserve isentropic flows. On the other hand, entropy inequality (3.34) shows that first-order Godunov scheme is unable to preserve isentropic flows except for the uniform ones. We observe in the right-hand side of (3.35) that the entropy production term is proportional to the square of the jump between the nodal and the cell-centered velocity. This term can be dramatically reduced by employing a high-order extension based on piecewise linear reconstruction of the pressure and the velocity. In this case the flux computation will be performed by replacing the left and right cell-centered states by the left and right extrapolated states resulting from the piecewise linear reconstruction. Thus the jump between the nodal and the cell-centered velocity turns into the jump between the nodal velocity and the extrapolated velocity at the node. This results in a decreasing entropy production.

3.1.6 First-order time discretization

We assume that at time $t = t^n$ all the fluid variables are known and cell-centered, we will denote them with the superscript n. Let $\Delta t = t^{n+1} - t^n$ denote the time increment. We discretize the system (3.19) using a standard forward Euler scheme

$$m_i(\frac{1}{\rho_i^{n+1}} - \frac{1}{\rho_i^n}) - \Delta t(u^n_{i+\frac{1}{2}} - u^n_{i-\frac{1}{2}}) = 0, \tag{3.36a}$$

$$m_i(u_i^{n+1} - u_i^n) + \Delta t(P^n_{i+\frac{1}{2}} - P^n_{i-\frac{1}{2}}) = 0, \tag{3.36b}$$

$$m_i(E_i^{n+1} - E_i^n) + \Delta t(P^n_{i+\frac{1}{2}} u^n_{i+\frac{1}{2}} - P^n_{i-\frac{1}{2}} u^n_{i-\frac{1}{2}}) = 0, \tag{3.36c}$$

where $u^n_{i+\frac{1}{2}}$ and $P^n_{i+\frac{1}{2}}$ are the fluxes at node $x_{i+\frac{1}{2}}$ obtained by solving the Riemann problem for the left state $\mathbf{\Phi}_l = (\frac{1}{\rho^n_{i-1}}, u^n_{i-1}, E^n_{i-1})^t$ and the right state $\mathbf{\Phi}_r = (\frac{1}{\rho^n_i}, u^n_i, E^n_i)^t$. In the case of the approximate acoustic Riemann solver we have the explicit formulas

$$u^\star_{i+\frac{1}{2}} = \frac{z^n_i u^n_i + z^n_{i+1} u^n_{i+1}}{z^n_i + z^n_{i+1}} - \frac{P^n_{i+1} - P^n_i}{z^n_i + z^n_{i+1}}, \tag{3.37a}$$

$$P^\star_{i+\frac{1}{2}} = \frac{z^n_{i+1} P^n_i + z^n_i P^n_{i+1}}{z^n_i + z^n_{i+1}} - \frac{z^n_i z^n_{i+1}}{z^n_i + z^n_{i+1}}(u^n_{i+1} - u^n_i), \tag{3.37b}$$

where $z^n_i = \rho^n_i a^n_i$ is the acoustic impedance and a^n_i is the isentropic sound speed. Boundary conditions are implemented knowing that in the Lagrangian framework either the pressure or the velocity is prescribed at the boundary

- At $x = x_{\mathrm{b}}$

imposed pressure $P^\star_{\mathrm{b}}$	imposed velocity $u^\star_{\mathrm{b}}$
$P_{\frac{1}{2}} = P^\star_{\mathrm{b}},$	$P_{\frac{1}{2}} = P^n_1 + z^n_1(u_{\frac{1}{2}} - u^n_1),$
$u_{\frac{1}{2}} = u^n_1 - \dfrac{P^n_1 - P_{\frac{1}{2}}}{z^n_1}.$	$u_{\frac{1}{2}} = u^\star_{\mathrm{b}}.$

- At $x = x_{\mathrm{e}}$

imposed pressure $P^\star_{\mathrm{e}}$	imposed velocity $u^\star_{\mathrm{e}}$
$P_{I+\frac{1}{2}} = P^\star_{\mathrm{e}},$	$P_{I+\frac{1}{2}} = P^n_I - z^n_I(u_{I+\frac{1}{2}} - u^n_I),$
$u_{I+\frac{1}{2}} = u^n_I + \dfrac{P^n_I - P_{I+\frac{1}{2}}}{z^n_I}.$	$u_{I+\frac{1}{2}} = u^\star_{\mathrm{e}}.$

We note that the previous set of discrete equations (3.36) leads to a first order accurate scheme both in space and time. In addition, the vertex motion is given by

$$x^{n+1}_{i+\frac{1}{2}} = x^n_{i+\frac{1}{2}} + \Delta t\ u^n_{i+\frac{1}{2}}. \tag{3.38}$$

with $x^0_{i+\frac{1}{2}} = X_{i+\frac{1}{2}}$. This last equation corresponds to the discretization of (3.17). To complete the Lagrangian phase, we evaluate the new specific internal energy $\varepsilon^{n+1}_i = E^{n+1}_i - \frac{1}{2}(u^{n+1}_i)^2$. Finally, we compute the pressure $P^{n+1}_i = P(\rho^{n+1}_i, \varepsilon^{n+1}_i)$, the sound speed a^{n+1}_i and the acoustic impedance z^{n+1}_i.

The time step is evaluated following the well known Courant Friedrich Levy (CFL) stability condition [139]. At time t^n we compute

$$\Delta t_e = C_e \min_{i=1,\cdots,I} \frac{\Delta x_i^n}{a_i^n},$$

where C_e is a strictly positive coefficient and a_i is the sound speed in the cell Ω_i. Knowing Δt^n, the current time step, the evaluation of the next time step Δt^{n+1} is performed as follows

$$\Delta t^{n+1} = \min(\Delta t_e, C_m \Delta t^n), \tag{3.39}$$

where C_m is a multiplicative coefficient, which allows the time step to increase. For numerical applications, we use $C_e = 0.25$ and $C_m = 1.01$.

3.1.7 Discrete entropy inequality

We are going to show in this subsection that the first-order scheme corresponding to the approximate acoustic solver satisfies a discrete entropy inequality provided that the time step is small enough. The first-order time discretization of the Gibbs formula writes

$$m_i T_i^n(\eta_i^{n+1} - \eta_i^n) = m_i[\varepsilon_i^{n+1} - \varepsilon_i^n + P_i^n(\frac{1}{\rho_i^{n+1}} - \frac{1}{\rho_i^n})].$$

First, we compute the time increment of internal energy as

$$m_i(\varepsilon_i^{n+1} - \varepsilon_i^n) = m_i[E_i^{n+1} - E_i^n - \frac{1}{2}(u_i^{n+1} - u_i^n)(u_i^{n+1} + u_i^n)],$$

replacing the time increments of total energy and momentum by means of (3.36c) and (3.36b) in the right-hand side of the above equation leads to

$$m_i(\varepsilon_i^{n+1} - \varepsilon_i^n) = \Delta t[-P_{i+\frac{1}{2}}^n(u_{i+\frac{1}{2}}^n - u_i^n) + P_{i-\frac{1}{2}}^n(u_{i-\frac{1}{2}}^n - u_i^n) - \frac{\Delta t}{2m_i}(P_{i+\frac{1}{2}}^n - P_{i-\frac{1}{2}}^n)^2]. \tag{3.40}$$

Using (3.36a), the pressure work writes

$$m_i P_i^n(\frac{1}{\rho_i^{n+1}} - \frac{1}{\rho_i^n}) = \Delta t P_i^n[(u_{i+\frac{1}{2}}^n - u_i^n) - (u_{i-\frac{1}{2}}^n - u_i^n)]. \tag{3.41}$$

Finally, combining (3.40) and (3.41) yields

$$m_i T_i^n(\eta_i^{n+1} - \eta_i^n) = \Delta t[(P_i^n - P_{i+\frac{1}{2}}^n)(u_{i+\frac{1}{2}}^n - u_i^n) - (P_i^n - P_{i-\frac{1}{2}}^n)(u_{i-\frac{1}{2}}^n - u_i^n) - \frac{\Delta t}{2m_i}(P_{i+\frac{1}{2}}^n - P_{i-\frac{1}{2}}^n)^2].$$

This equation corresponds to the rate of entropy production within cell ω_i. From the approximate acoustic solver it follows

$$\begin{aligned} P_i^n - P_{i+\frac{1}{2}}^n &= z_i^n(u_{i+\frac{1}{2}}^n - u_i^n), \\ P_i^n - P_{i-\frac{1}{2}}^n &= -z_i^n(u_{i-\frac{1}{2}}^n - u_i^n), \end{aligned}$$

where $z_i^n = \rho_i^n a_i^n$ is the acoustic impedance. Using the above expressions, the entropy production rate can be recast as

$$m_i T_i^n(\eta_i^{n+1} - \eta_i^n) = z_i^n \Delta t Q(u_{i-\frac{1}{2}}^n - u_i^n, u_{i+\frac{1}{2}}^n - u_i^n), \tag{3.42}$$

In writing this equation, we have introduced the quadratic form, Q_i, defined by $Q_i(v,w) = (1-\alpha_i)v^2 - 2\alpha_i vw + (1-\alpha_i)w^2$ for all $(v,w) \in \mathbb{R}^2$ and $\alpha_i = \frac{z_i^n \Delta t}{2m_i}$. The 2×2 matrix associated to this quadratic form writes

$$\mathsf{A}_{Q_i} = \begin{pmatrix} 1-\alpha_i & -\alpha_i \\ -\alpha_i & 1-\alpha_i \end{pmatrix},$$

and we have $Q_i(v,w) = \mathsf{A}_{Q_i}\begin{pmatrix} v \\ w \end{pmatrix} \cdot \begin{pmatrix} v \\ w \end{pmatrix}$. Noticing that $\det \mathsf{A}_{Q_i} = 1 - 2\alpha_i$, we claim that A_{Q_i} is positive definite provided $\alpha_i \leq \frac{1}{2}$. Thus, the entropy inequality is satisfied under the following condition

$$\Delta t \leq \frac{m_i}{z_i^n} = \frac{\Delta x_i^n}{a_i^n}. \tag{3.43}$$

We notice that we recover the well known CFL condition related to the von Neumann stability analysis [139]. Thus, the condition (3.43) ensures not only the stability but also the thermodynamic consistency of the discretized scheme. However, it is important to notice that the right-hand side of (3.42) is equal to zero only for uniform flows. For non uniform flows, under the condition (3.43), we will always have $m_i T_i^n(\eta_i^{n+1} - \eta_i^n) > 0$. Therefore, the numerical scheme does not preserve isentropic flows. This fact can lead to bad numerical results, especially concerning the specific internal energy for flows wherein strong expansions occur. However, this flaw can be corrected using high-order scheme.

3.1.8 The high-order extension using the Generalized Riemann problem

Here, we derive a high-order extension of the previous scheme using the Generalized Riemann Problem methodology, which was introduced by [19, 21] following the pioneering works of van Leer [159] and Kolgan [160, 79]. Let us assume a piecewise linear representation of the pressure and the velocity at time t^n, that is, for all $x \in [x^n_{i-\frac{1}{2}}, x^n_{i+\frac{1}{2}}]$

$$\begin{aligned} \widetilde{u}(x) &= u_i^n + \delta u_i^n (x - x_i^n), \\ \widetilde{P}(x) &= P_i^n + \delta P_i^n (x - x_i^n), \end{aligned}$$

where $x_i^n = \frac{1}{2}(x^n_{i-\frac{1}{2}} + x^n_{i+\frac{1}{2}})$ is the midpoint of $[x^n_{i-\frac{1}{2}}, x^n_{i+\frac{1}{2}}]$. In these equations δu_i^n and δP_i^n denote the slopes of the velocity and the pressure which can be determined using for instance a least squares method.

The generic high-order Godunov-type scheme can be written under the following form

$$m_i\left(\frac{1}{\rho_i^{n+1}} - \frac{1}{\rho_i^n}\right) - \Delta t\left(u^{n+\frac{1}{2}}_{i+\frac{1}{2}} - u^{n+\frac{1}{2}}_{i-\frac{1}{2}}\right) = 0, \tag{3.44a}$$

$$m_i(u_i^{n+1} - u_i^n) + \Delta t\left(P^{n+\frac{1}{2}}_{i+\frac{1}{2}} - P^{n+\frac{1}{2}}_{i-\frac{1}{2}}\right) = 0, \tag{3.44b}$$

$$m_i(E_i^{n+1} - E_i^n) + \Delta t\left[(Pu)^{n+\frac{1}{2}}_{i+\frac{1}{2}} - (Pu)^{n+\frac{1}{2}}_{i-\frac{1}{2}}\right] = 0. \tag{3.44c}$$

The grid motion is governed by the discrete trajectory equation

$$x^{n+1}_{i+\frac{1}{2}} = x^n_{i+\frac{1}{2}} + \Delta t u^{n+\frac{1}{2}}_{i+\frac{1}{2}}.$$

Here, $u^{n+\frac{1}{2}}_{i+\frac{1}{2}}$, $P^{n+\frac{1}{2}}_{i+\frac{1}{2}}$ and $(Pu)^{n+\frac{1}{2}}_{i+\frac{1}{2}}$ are the time-averaged numerical fluxes at node $x_{i+\frac{1}{2}}$ over the time interval $[t^n, t^{n+1}]$. The main feature of GRP methodology consists in deriving these midpoint fluxes analytically by solving the generalized Riemann problem at each point $(x^n_{i+\frac{1}{2}}, t^n)$.

In what follows, we describe the main steps to compute these fluxes. First, we define the second-order approximation of the above numerical fluxes by means of the following Taylor expansion

$$u_{i+\frac{1}{2}}^{n+\frac{1}{2}} = u_{i+\frac{1}{2}}^{n} + \frac{\Delta t}{2}(\frac{d}{dt}u)_{i+\frac{1}{2}}^{n},$$
$$P_{i+\frac{1}{2}}^{n+\frac{1}{2}} = P_{i+\frac{1}{2}}^{n} + \frac{\Delta t}{2}(\frac{d}{dt}P)_{i+\frac{1}{2}}^{n}.$$

Regarding the total energy flux, $(Pu)_{i+\frac{1}{2}}^{n+\frac{1}{2}}$, it is deduced from the previous formulas by setting

$$(Pu)_{i+\frac{1}{2}}^{n+\frac{1}{2}} = P_{i+\frac{1}{2}}^{n} u_{i+\frac{1}{2}}^{n} + \frac{\Delta t}{2}[P_{i+\frac{1}{2}}^{n}(\frac{d}{dt}u)_{i+\frac{1}{2}}^{n} + u_{i+\frac{1}{2}}^{n}(\frac{d}{dt}P)_{i+\frac{1}{2}}^{n}].$$

In the above formulas, $u_{i+\frac{1}{2}}^{n}$ and $P_{i+\frac{1}{2}}^{n}$ are obtained by solving a classical Riemann problem at the interface $x_{i+\frac{1}{2}}^{n}$ using the extrapolated values of the pressure and the velocity computed from their piecewise linear reconstruction on each side of the interface.

We observe that once a Riemann solver has been chosen, the GRP scheme amounts to compute the time derivatives $(\frac{d}{dt}u)_{i+\frac{1}{2}}^{n}$, $(\frac{d}{dt}P)_{i+\frac{1}{2}}^{n}$. To determine these time derivatives one has to solve the generalized Riemann problem for system (3.2) subject to the piecewise linear initial data

$$\boldsymbol{\Phi}(x,0) = \begin{cases} \boldsymbol{\Phi}_l + \boldsymbol{\delta\Phi}_l x & \text{if } x < 0, \\ \boldsymbol{\Phi}_r + \boldsymbol{\delta\Phi}_r x & \text{if } x > 0, \end{cases} \tag{3.45}$$

where $\boldsymbol{\Phi} = (\frac{1}{\rho}, u, E)^t$ and $\boldsymbol{\delta\Phi}$ denotes the corresponding slopes vector. The associated Riemann problem is the initial value problem for (3.2) with the piecewise constant values $\boldsymbol{\Phi}_l$ and $\boldsymbol{\Phi}_r$ (zero slopes in (3.45)). Following [21], the associated Riemann solution is denoted $\boldsymbol{R}^A(x/t, \boldsymbol{\Phi}_l, \boldsymbol{\Phi}_r)$. It can be obtained approximately or exactly. The initial structure of the solution $\boldsymbol{\Phi}(x,t)$ to (3.2) and (3.45) is determined by the associated Riemann solution and is described asymptotically as

$$\lim_{t\to 0} \boldsymbol{\Phi}(\lambda t, t) = \boldsymbol{R}^A(\lambda, \boldsymbol{\Phi}_l, \boldsymbol{\Phi}_r), \quad \lambda = x/t. \tag{3.46}$$

The solution $\boldsymbol{\Phi}(x,t)$ to the generalized Riemann problem can be represented by an asymptotic expansion in terms of x and t whose zero-order term is given by equation (3.46). To compute the time derivatives, it is sufficient to evaluate the first-order perturbation built into $\boldsymbol{\Phi}(x,t)$, that is, to evaluate

$$(\frac{d}{dt}P)^\star = \lim_{t\to 0}\frac{d}{dt}P(0,t), \quad (\frac{d}{dt}u)^\star = \lim_{t\to 0}\frac{d}{dt}u(0,t).$$

This problem, which corresponds to the linear GRP, is completely solved in the monograph [21].

For our application, instead of dealing with the general problem, we specialize to the acoustic case which is by far more simple. This particular case is exposed in [21, 89], we recall it not only for sake of completeness but also because we will also use it to construct a two-dimensional high-order extension. Let us assume that the initial flow variables are all continuous at $x = 0$ so that $\boldsymbol{\Phi}_l = \boldsymbol{\Phi}_r$, but we allow jumps in their slopes $\boldsymbol{\delta\Phi}_l \neq \boldsymbol{\delta\Phi}_r$. Hence, the GRP solution is continuous at $x = t = 0$. The waves emanating from the origin are just the characteristics curves which are displayed in Figure 3.2. Following [89], we rewrite the first two equations of (3.2) as

$$\frac{d}{dt}P + \rho a^2 \frac{\partial u}{\partial x} = 0, \tag{3.47a}$$
$$\frac{d}{dt}u + \frac{1}{\rho}\frac{\partial P}{\partial x} = 0. \tag{3.47b}$$

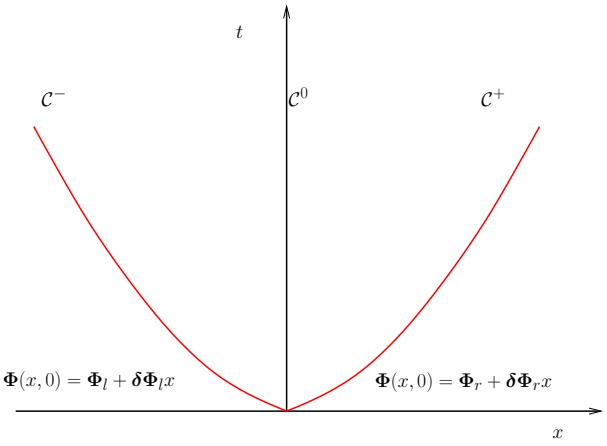

Figure 3.2: Characteristic curves in the acoustic case corresponding to the piecewise linear initial data $\mathbf{\Phi}_l = \mathbf{\Phi}_r$, $\boldsymbol{\delta\Phi}_l \neq \boldsymbol{\delta\Phi}_r$. Note that the characteristic curves have been plotted in the frame attached to the fluid motion.

Linearizing the above system around the state $\mathbf{\Phi}^\star = \mathbf{\Phi}_l = \mathbf{\Phi}_r$ yields

$$\begin{aligned}\frac{d}{dt}P + \rho^\star (a^\star)^2 \frac{\partial u}{\partial x} &= 0,\\ \frac{d}{dt}u + \frac{1}{\rho^\star}\frac{\partial P}{\partial x} &= 0.\end{aligned}$$

This system can be recast in the more compact form

$$\frac{d}{dt}\begin{pmatrix} P \\ u \end{pmatrix} + \mathsf{M}^\star \frac{\partial}{\partial x}\begin{pmatrix} P \\ u \end{pmatrix} = \mathbf{0},$$

where the matrix $\mathsf{M}^\star$ is given by

$$\mathsf{M}^\star = \begin{pmatrix} 0 & \rho^\star (a^\star)^2 \\ \frac{1}{\rho^\star} & 0 \end{pmatrix}.$$

Noticing that $\mathsf{M}^\star$ admits the two eigenvalues $-a^\star$ and $a^\star$, we diagonalize the above system to finally obtain

$$\begin{aligned}\frac{d}{dt}(P - z^\star u) - a^\star \frac{\partial}{\partial x}(P - z^\star u) &= 0,\\ \frac{d}{dt}(P + z^\star u) + a^\star \frac{\partial}{\partial x}(P + z^\star u) &= 0.\end{aligned}$$

Here, $z^\star$ denotes the acoustic impedence defined by $z^\star = \rho^\star a^\star$ and $P \pm z^\star u$ are the two linearized Riemann invariants respectively associated to the characteristics curves $\mathcal{C}^\pm$. To achieve the determination of the time derivatives it remains to express the partial derivatives with respect to x in terms of the pressure and velocity slopes as follows

$$\begin{aligned}(\frac{d}{dt}P)^\star - z^\star (\frac{d}{dt}u)^\star &= a^\star(\delta P_r - z^\star \delta u_r),\\ (\frac{d}{dt}P)^\star + z^\star (\frac{d}{dt}u)^\star &= -a^\star(\delta P_l + z^\star \delta u_l).\end{aligned}$$

In writing these equations, we have proceeded with the substitution of the partial derivatives in an upwind manner, that it is, by replacing the partial derivatives in the first (second) equation

with slopes variables associated to the right (left) state. Now, to take into account a possible initial weak discontinuity ($\mathbf{\Phi}_l \neq \mathbf{\Phi}_r$ with $\|\mathbf{\Phi}_l - \mathbf{\Phi}_r\| \ll 1$) we rewrite the previous system as

$$(\frac{d}{dt}P)^\star - z_r(\frac{d}{dt}u)^\star = a_r(\delta P_r - z_r\delta u_r), \tag{3.48a}$$

$$(\frac{d}{dt}P)^\star + z_l(\frac{d}{dt}u)^\star = -a_l(\delta P_l + z_l\delta u_l). \tag{3.48b}$$

Finally, it turns out that the time derivatives for pressure and velocity at the contact discontinuity satisfy a 2×2 linear system characterized by a positive determinant. Thus, it always admits a unique solution which writes

$$(\frac{d}{dt}P)^\star = \frac{a_r(\delta P_r - z_r\delta u_r)z_l - a_l(\delta P_l + z_l\delta u_l)z_r}{z_l + z_r}, \tag{3.49a}$$

$$(\frac{d}{dt}u)^\star = -\frac{a_l(\delta P_l + z_l\delta u_l) + a_r(\delta P_r - z_r\delta u_r)}{z_l + z_r}, \tag{3.49b}$$

Let us note that no supplementary information concerning the equation of state is needed for the time derivatives computation, therefore this methodology can also apply to fluids characterized by tabulated equation of state supplying the sound speed. Now, we are in position to give a summary of the acoustic GRP method applied to the one-dimensional Lagrangian hydrodynamics.

3.1.9 Summary of the one-dimensional GRP acoustic methodology

The algorithm to construct a high-order discretization of the one-dimensional gas dynamics equations using the GRP methodology in its acoustic version proceeds through the following steps

Step 0. Construct a piecewise linear representation of the velocity field and the pressure at time t^n over the cell Ω_i^n

$$u_i^n(x) = u_i^n + \delta u_i^n(x - x_i^n), \quad P_i^n(x) = P_i^n + \delta P_i^n(x - x_i^n).$$

This piecewise linear reconstruction can be computed using a least squares procedure [103]. The advantage of such a procedure is that linear fields are preserved, even for irregular mesh. Note that a classical limitation procedure has to be applied to the slopes in order to achieve a monotonic piecewise linear reconstruction, for instance refer to [21].

Step 1. Given the piecewise linear pressure and velocity at time t^n over the cell ω_i^n, we solve the Riemann problem for (3.2) at each grid point $x_{i+\frac{1}{2}}^n$ to define the Riemann solution

$$u_{i+\frac{1}{2}}^n = \frac{z_i^n u_i^n(x_{i+\frac{1}{2}}^n) + z_{i+1}^n u_{i+1}^n(x_{i+\frac{1}{2}}^n)}{z_i^n + z_{i+1}^n} - \frac{P_{i+1}^n(x_{i+\frac{1}{2}}^n) - P_i^n(x_{i+\frac{1}{2}}^n)}{z_i^n + z_{i+1}^n},$$

$$P_{i+\frac{1}{2}}^n = \frac{z_i^n P_{i+1}^n(x_{i+\frac{1}{2}}^n) + z_{i+1}^n P_i^n(x_{i+\frac{1}{2}}^n)}{z_i^n + z_{i+1}^n} - \frac{z_i^n z_{i+1}^n}{z_i^n + z_{i+1}^n}[u_{i+1}^n(x_{i+\frac{1}{2}}^n) - u_i^n(x_{i+\frac{1}{2}}^n)].$$

Here, we have written the solution corresponding to the approximate acoustic Riemann solver.

Step 2. Determine the time derivatives $(\frac{du}{dt})^n_{i+\frac{1}{2}}$ and $(\frac{dP}{dt})^n_{i+\frac{1}{2}}$ using (3.49) where the left (resp. right) state corresponds to the cell ω_i^n (resp. ω_{i+1}^n). The midpoint numerical fluxes are computed according to the Taylor expansion

$$u^{n+\frac{1}{2}}_{i+\frac{1}{2}} = u^n_{i+\frac{1}{2}} + \frac{\Delta t}{2}(\frac{d}{dt}u)^n_{i+\frac{1}{2}},$$
$$P^{n+\frac{1}{2}}_{i+\frac{1}{2}} = P^n_{i+\frac{1}{2}} + \frac{\Delta t}{2}(\frac{d}{dt}P)^n_{i+\frac{1}{2}}.$$

Step 3. Evaluate the new cell averages $(\frac{1}{\rho_i^{n+1}}, u_i^{n+1}, E_i^{n+1})$ using the updating formulas

$$m_i(\frac{1}{\rho_i^{n+1}} - \frac{1}{\rho_i^n}) - \Delta t(u^{n+\frac{1}{2}}_{i+\frac{1}{2}} - u^{n+\frac{1}{2}}_{i-\frac{1}{2}}) = 0,$$
$$m_i(u_i^{n+1} - u_i^n) + \Delta t(P^{n+\frac{1}{2}}_{i+\frac{1}{2}} - P^{n+\frac{1}{2}}_{i-\frac{1}{2}}) = 0,$$
$$m_i(E_i^{n+1} - E_i^n) + \Delta t[(Pu)^{n+\frac{1}{2}}_{i+\frac{1}{2}} - (Pu)^{n+\frac{1}{2}}_{i-\frac{1}{2}}] = 0,$$

and advance the grid by means of the discrete trajectory equation

$$x^{n+1}_{i+\frac{1}{2}} = x^n_{i+\frac{1}{2}} + \Delta t u^{n+\frac{1}{2}}_{i+\frac{1}{2}}.$$

We note that the above algorithm is slightly different from the one proposed in [21] in the sense that we are computing the slopes using a least squares procedure (Step 0), whereas in the original approach the slopes are updated using the time derivatives $(\frac{du}{dt})^n_{i+\frac{1}{2}}$ and $(\frac{dP}{dt})^n_{i+\frac{1}{2}}$. This modification does not matter since high-order accuracy is still achieved. It has been done here in the perspective of the two-dimensional extension.

3.2 High-order discretization for two-dimensional Lagrangian hydrodynamics in Cartesian geometry

The goal of this section is to derive a general formalism that relies on the use of a sub-cell force-based discretization. We aim at constructing a family of conservative cell-centered schemes for two-dimensional Lagrangian hydrodynamics on general unstructured grids that satisfies the GCL and an entropy inequality. This formalism is based on the following crucial arguments.

- **GCL compatibility requirement:** the volume flux is expressed as a function of the vertex velocity by computing the time rate of change of the volume of a polygonal cell.

- **Sub-cell force discretization:** in each cell, momentum flux is written as the summation of the sub-cell forces that are acting at each vertex of the cell. We note that the sub-cell force concept has been firstly introduced in staggered discretization [35] to derive compatible conservative staggered schemes. In the present work, the sub-cell force corresponds to the integral of the pressure gradient over a sub-cell, knowing that a sub-cell is the quadrilateral obtained by joining the cell center, a particular vertex and the midpoints of the two edges impinging at this vertex. The total energy flux is simply deduced from the momentum flux by dot-multiplying sub-cell force by its corresponding vertex velocity.

- **Thermodynamic consistency:** to achieve the discretization, it remains to construct an approximation of the sub-cell force and to compute the vertex velocity. The former task is completed by deriving an expression of the sub-cell force that is consistent with thermodynamics. Namely, after computing the time rate of change of entropy within a cell using the semi-discrete gas dynamics equations, we deduce a general way of writing the sub-cell force so that a cell entropy inequality is satisfied. In this manner, the sub-cell force writes as a pressure contribution plus a tensorial viscous contribution, which is proportional to the difference between the cell-centered and the vertex velocities. To satisfy the second law of thermodynamics, the local 2×2 sub-cell tensor involved in the viscous part of the sub-cell force must be positive semi-definite. This tensor is the cornerstone of the scheme. Some particular expressions of this tensor are given, they allow to recover known schemes such as those described in [49] and [108], and to make the link with a node-centered approximate Riemann solver.

- **Conservation principle:** the vertex velocity is computed by invoking the global conservation of the total energy. This last statement amounts to write that the summation of the sub-cell forces over the sub-cells surrounding a vertex is equal to zero. This balance equation also ensures the momentum conservation and leads to a node-centered solver that uniquely determines the nodal velocity.

The high-order extension of this family of cell-centered schemes is achieved using a one-step time discretization, wherein the fluxes are computed by means of a Taylor expansion. The time derivatives of the fluxes are obtained through the use of a node-centered solver [105, 106] which can be viewed as a two-dimensional extension of the Generalized Riemann Problem (GRP) methodology introduced by Ben-Artzi and Falcovitz [21].

3.2.1 Governing equations

Let $\mathcal{D}$ be an open set of $\mathbb{R}^2$, filled with an inviscid fluid and equipped with the orthonormal frame $(0, x, y)$ and the orthonormal basis $(\boldsymbol{e}_x, \boldsymbol{e}_y)$ which is naturally completed by the unit vector $\boldsymbol{e}_z = \boldsymbol{e}_x \times \boldsymbol{e}_y$. We are interested in discretizing the integral updated Lagrangian formulation of the gas dynamics equations, refer to (2.100) page 36. This formulation, which consists in following a control volume moving with fluid velocity, writes as

$$\frac{d}{dt}\int_{\omega(t)} \rho \,\mathrm{d}v = 0, \tag{3.50a}$$

$$\frac{d}{dt}\int_{\omega(t)} \mathrm{d}v - \int_{\partial\omega(t)} \boldsymbol{U}\cdot\boldsymbol{n}\,\mathrm{d}s = 0, \tag{3.50b}$$

$$\frac{d}{dt}\int_{\omega(t)} \rho\boldsymbol{U}\,\mathrm{d}v + \int_{\partial\omega(t)} P\boldsymbol{n}\,\mathrm{d}s = \boldsymbol{0}, \tag{3.50c}$$

$$\frac{d}{dt}\int_{\omega(t)} \rho E\,\mathrm{d}v + \int_{\partial\omega(t)} P\boldsymbol{U}\cdot\boldsymbol{n}\,\mathrm{d}s = 0. \tag{3.50d}$$

Here, $\omega(t)$ denotes the moving control volume and $\boldsymbol{n}$ is the unit outward normal to the boundary surface $\partial\omega(t)$. The variables ρ, $\boldsymbol{U}$, P and E denote respectively the density, velocity, pressure and specific total energy of the fluid. Let us recall that equations (3.50a)-(3.50d) express the conservation of mass, volume, momentum and total energy. The second equation expresses the time rate of change of the volume of the fluid and is often named Geometric Conservation Law (GCL). It is strongly linked to the trajectory equation

$$\frac{d}{dt}\boldsymbol{x} = \boldsymbol{U}(\boldsymbol{x}(t), t), \quad \boldsymbol{x}(0) = \boldsymbol{X}, \tag{3.51}$$

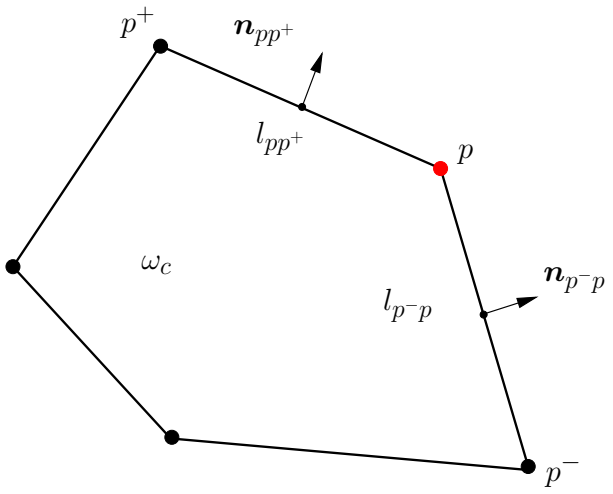

Figure 3.3: Notation for a polygonal cell.

where $\boldsymbol{x} = \boldsymbol{x}(t)$ is the position vector of a material point at time $t > 0$, which was initially located at $\boldsymbol{X}$.

The thermodynamic closure of the set of the above system is obtained by means of the equation of state (EOS) $P = P(\rho, \varepsilon)$, where $\varepsilon = E - \frac{1}{2} \mid \boldsymbol{U} \mid^2$ denotes the specific internal energy.

3.2.2 Compatible cell-centered discretization

We discretize the previous set of equations over a partition of the domain $\mathcal{D}$ into polygonal cells. Let us introduce the notation and the assumptions that are necessary to develop our cell-centered discretization.

Notation and assumptions

Each polygonal cell is assigned a unique index c and is denoted by $\omega_c(t)$. A generic point (vertex) is labelled by the index p, its corresponding position vector is $\boldsymbol{x}_p$. For a cell c, we introduce the set $\mathcal{P}(c)$ which is the counterclockwise ordered list of points of cell c. Conversely, for a given point p, we introduce the set $\mathcal{C}(p)$ containing the cells that surround point p. Being given $p \in \mathcal{P}(c)$, p^- and p^+ are the previous and next points with respect to p in the counterclockwise ordered list of vertices of cell c. The length and the unit outward normal related to the edge $[p, p^+]$ are l_{pp^+} and $\boldsymbol{n}_{pp^+}$, refer to Figure 3.3. The control volume formulation (3.50) applied to the polygonal cell $\omega_c(t)$ leads to

$$m_c \frac{d}{dt}(\frac{1}{\rho_c}) - \int_{\partial\omega_c(t)} \boldsymbol{U} \cdot \boldsymbol{n} \, \mathrm{d}s = 0, \tag{3.52a}$$

$$m_c \frac{d}{dt}\boldsymbol{U}_c + \int_{\partial\omega_c(t)} P\boldsymbol{n} \, \mathrm{d}s = \boldsymbol{0}, \tag{3.52b}$$

$$m_c \frac{d}{dt}E_c + \int_{\partial\omega_c(t)} P\boldsymbol{U} \cdot \boldsymbol{n} \, \mathrm{d}s = 0. \tag{3.52c}$$

Here, $\partial\omega_c(t)$ is the boundary of the cell $\omega_c(t)$ and m_c denotes the mass of the polygonal cell, which is constant according to (3.50a). For a flow variable ϕ, we define its mass averaged value

over the cell $\omega_c(t)$ as

$$\phi_c = \frac{1}{m_c}\int_{\omega_c(t)} \rho\phi \, \mathrm{d}v.$$

We notice that the first equation corresponds to the GCL since $m_c = \rho_c v_c$ where v_c is the volume of cell c. We have obtained a set of semi-discrete evolution equations for the primary variables $(\frac{1}{\rho_c}, \boldsymbol{U}_c, E_c)$. The thermodynamic closure is given by the EOS, $P_c = P(\rho_c, \varepsilon_c)$ where $\epsilon_c = E_c - \frac{1}{2} \mid \boldsymbol{U}_c \mid^2$. The motion of the grid is ruled by the semi-discrete trajectory equation written at each point

$$\frac{d}{dt}\boldsymbol{x}_p = \boldsymbol{U}_p(\boldsymbol{x}_p(t), t), \quad \boldsymbol{x}_p(0) = \boldsymbol{X}_p. \tag{3.53}$$

To proceed with the space discretization, it remains not only to compute the numerical fluxes related to volume, momentum and total energy but also to determine the nodal velocity to compute the grid motion.

Geometric Conservation Law compatibility

Here, the expression GCL compatibility means that we are deriving a discrete divergence operator for the volume equation (3.50b) by requiring consistency of the divergence of the velocity field with the time rate of change of volume of a cell [112]. Noticing that $m_c = \rho_c v_c$, Eq. (3.52a) rewrites

$$\frac{d}{dt}v_c = \int_{\partial\omega_c(t)} \boldsymbol{U}\cdot\boldsymbol{n} \, \mathrm{d}s. \tag{3.54}$$

This equations states that the time rate of change of the cell volume v_c must be equal to the volume swept by the element boundary during its displacement with the fluid velocity. Assuming that the volume $v_c(t)$ in the left-hand side can be computed exactly, this amounts to require the exact computation of the volume flux in the right-hand side also. In this manner, we obtain a compatible discretization of the volume flux. Using the triangulation displayed in Figure 3.4, the polygonal cell volume writes

$$v_c(t) = \frac{1}{2}\sum_{p\in\mathcal{P}(c)} \left[\boldsymbol{x}_p(t) \times \boldsymbol{x}_{p^+}(t)\right]\cdot\boldsymbol{e}_z. \tag{3.55}$$

We remark that the volume is expressed as a function of the position vectors of the vertices. Using the chain rule derivative, time differentiation of Eq. (3.55) yields

$$\frac{d}{dt}v_c = \sum_{p\in\mathcal{P}(c)} \boldsymbol{\nabla}_{\boldsymbol{x}_p} v_c \cdot \frac{d}{dt}\boldsymbol{x}_p,$$

where $\boldsymbol{\nabla}_{\boldsymbol{x}_p} v_c$ is the gradient of the cell volume, v_c with respect to the position vector $\boldsymbol{x}_p$. This gradient is computed directly through the use of (3.55)

$$\begin{aligned}\boldsymbol{\nabla}_{\boldsymbol{x}_p} v_c =& \frac{1}{2}\boldsymbol{\nabla}_{\boldsymbol{x}_p}\left[(\boldsymbol{x}_{p^+} - \boldsymbol{x}_{p^-}) \times \boldsymbol{e}_z \cdot \boldsymbol{x}_p\right] \\ =& \frac{1}{2}(\boldsymbol{x}_{p^+} - \boldsymbol{x}_{p^-}) \times \boldsymbol{e}_z.\end{aligned}$$

We define the normal vector at corner pc by setting

$$l_{pc}\boldsymbol{n}_{pc} = \boldsymbol{\nabla}_{\boldsymbol{x}_p} v_c = \frac{1}{2}(\boldsymbol{x}_{p^+} - \boldsymbol{x}_{p^-}) \times \boldsymbol{e}_z, \tag{3.56}$$

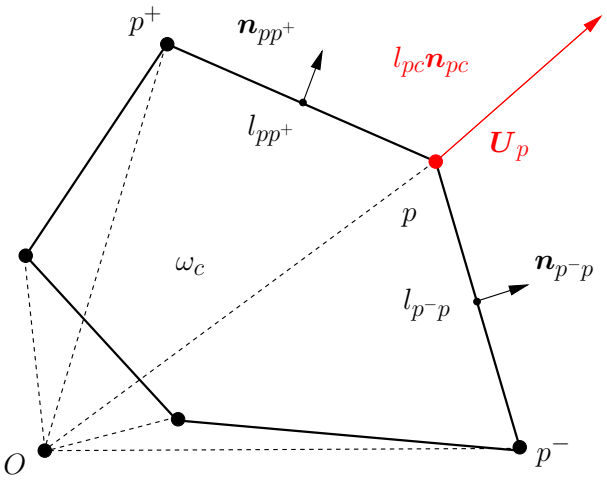

Figure 3.4: Triangulation of the polygonal cell ω_c.

where the length, l_{pc}, is determined knowing that $\boldsymbol{n}_{pc}^2 = 1$. We notice that this corner vector can be expressed in terms of the two outward normals impinging at node p as

$$l_{pc}\boldsymbol{n}_{pc} = \frac{1}{2}(l_{p^-p}\boldsymbol{n}_{p^-p} + l_{pp^+}\boldsymbol{n}_{pp^+}). \tag{3.57}$$

It turns out that the corner vector $l_{pc}\boldsymbol{n}_{pc}$ is the fundamental geometric object that allows to define uniquely the time rate of change of cell volume as

$$\frac{d}{dt}v_c = \sum_{p\in\mathcal{P}(c)} l_{pc}\boldsymbol{n}_{pc}\cdot\boldsymbol{U}_p. \tag{3.58}$$

Here, we have used the trajectory equation (3.53), *i.e.*, $\frac{d}{dt}\boldsymbol{x}_p = \boldsymbol{U}_p$. Let us point out that the corner vector $l_{pc}\boldsymbol{n}_{pc}$ satisfies the fundamental geometrical identity

$$\sum_{p\in\mathcal{P}(c)} l_{pc}\boldsymbol{n}_{pc} = \boldsymbol{0}. \tag{3.59}$$

This equation states that the summation of the outward normals to a closed polygonal contour is equal to zero. This result is nothing but the discrete form of the Piola identity, refer to (2.123) page 43. This also implies that the volume of a polygonal cell moving in a uniform flow does not change. We claim that with this purely geometric derivation we have completely defined the volume flux. Moreover, this definition is by construction compatible with mesh motion. We also remark that this result can be used to derive the discrete divergence operator, $(\nabla\cdot\boldsymbol{U})_c$ over cell c. Knowing that by definition

$$(\nabla\cdot\boldsymbol{U})_c = \frac{1}{v_c}\int_{\partial\omega_c(t)} \boldsymbol{U}\cdot\boldsymbol{n}\,\mathrm{d}s,$$

combining (3.54) and (3.58) we get

$$(\nabla\cdot\boldsymbol{U})_c = \frac{1}{v_c}\frac{d}{dt}v_c = \frac{1}{v_c}\sum_{p\in\mathcal{P}(c)} l_{pc}\boldsymbol{n}_{pc}\cdot\boldsymbol{U}_p.$$

Let us remark that property (3.59) shows that the null space of the discrete divergence operator is spanned by the set of constant vectors. We recover the compatible discretization of

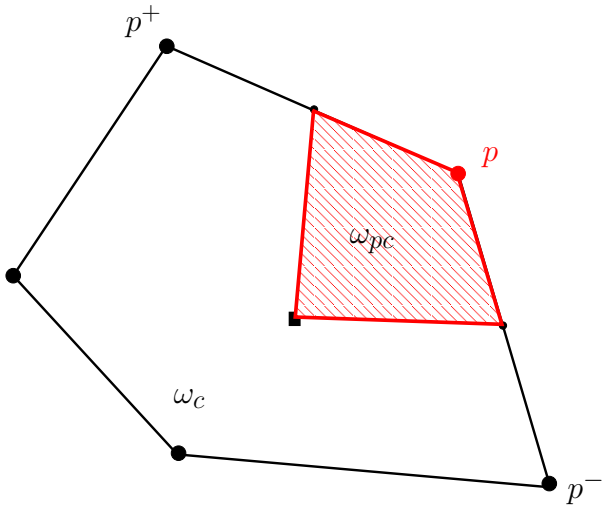

Figure 3.5: Sub-cell ω_{pc} related to polygonal cell ω_c and point p.

the divergence operator currently used in the derivation of the compatible Lagrangian hydrodynamics scheme [31, 165, 35]. This kind of formalism was used in staggered and cell-centered (Free-Lagrange) discretizations long time ago [112, 149]. We also note that the fundamental role played by the corner vector has been recently rediscovered in [38].

Sub-cell force-based discretization

It remains to discretize momentum and total energy equations. To this end, we adapt to cell-centered discretization the fundamental concept of sub-cell force initially introduced in [35] in the context of staggered discretization. Before we proceed any further, let us introduce some supplementary notation. Being given a polygonal cell, ω_c, for each vertex $p \in \mathcal{P}(c)$, we define the sub-cell ω_{pc} by connecting the centroid of ω_c to the midpoints of edges $[p^-, p]$ and $[p, p^+]$ impinging at node p, refer to Figure 3.5. In two dimensions the sub-cell, as just defined, is always a quadrilateral regardless of the type of cells that compose the underlying grid. Let us point out that the set of the sub-cells of a given cell consists of a partition of this cell, *i.e.*, $\omega_c = \cup_{p\in\mathcal{P}(c)}\omega_{pc}$. Using the sub-cell definition, cell ω_c and its boundary $\partial\omega_c$ can be decomposed as

$$\omega_c = \bigcup_{p\in\mathcal{P}(c)} \omega_{pc}, \quad \partial\omega_c = \bigcup_{p\in\mathcal{P}(c)} \partial\omega_{pc} \cap \partial\omega_c. \tag{3.60}$$

This decomposition allows to rewrite the momentum flux as a summation of contributions coming from each sub-cell boundary

$$\int_{\partial\omega_c} P\boldsymbol{n}\,\mathrm{d}s = \sum_{p\in\mathcal{P}(c)} \int_{\partial\omega_{pc}\cap\partial\omega_c} P\boldsymbol{n}\,\mathrm{d}s.$$

Thus, we define the sub-cell force related to cell c and point p as

$$\boldsymbol{F}_{pc} = \int_{\partial\omega_{pc}\cap\partial\omega_c} P\boldsymbol{n}\,\mathrm{d}s. \tag{3.61}$$

This definition enables us to rewrite momentum equation (3.52b) as

$$m_c\frac{d}{dt}\boldsymbol{U}_c + \sum_{p\in\mathcal{P}(c)} \boldsymbol{F}_{pc} = \boldsymbol{0},$$

which is the Newton law applied to a particle of mass m_c moving with velocity $\boldsymbol{U}_c$. We also use the sub-cell-based decomposition to write the total energy flux

$$\int_{\partial\omega_c} P\boldsymbol{U}\cdot\boldsymbol{n}\,\mathrm{d}s = \sum_{p\in\mathcal{P}(c)}\int_{\partial\omega_{pc}\cap\partial\omega_c} P\boldsymbol{U}\cdot\boldsymbol{n}\,\mathrm{d}s.$$

ω_{pc} contribution to the total energy flux is expressed in terms of sub-cell force $\boldsymbol{F}_{cp}$ using the approximation

$$\begin{aligned}\int_{\partial\omega_{pc}\cap\partial\omega_c} P\boldsymbol{U}\cdot\boldsymbol{n}\,\mathrm{d}s &= \left(\int_{\partial\omega_{pc}\cap\partial\omega_c} P\boldsymbol{n}\,\mathrm{d}s\right)\cdot\boldsymbol{U}_p\\ &= \boldsymbol{F}_{pc}\cdot\boldsymbol{U}_p.\end{aligned}$$

Using the above notation, total energy equation (3.52c) rewrites

$$m_c\frac{d}{dt}E_c + \sum_{p\in\mathcal{P}(c)}\boldsymbol{F}_{pc}\cdot\boldsymbol{U}_p = 0.$$

This leads to the mechanical interpretation that the time variation of total energy results from the summation over the sub-cell of the rate of work done by sub-cell force $\boldsymbol{F}_{pc}$. Gathering the previous results, system (3.52) transforms into

$$m_c\frac{d}{dt}(\frac{1}{\rho_c}) - \sum_{p\in\mathcal{P}(c)} l_{pc}\boldsymbol{n}_{pc}\cdot\boldsymbol{U}_p = 0, \tag{3.62a}$$

$$m_c\frac{d}{dt}\boldsymbol{U}_c + \sum_{p\in\mathcal{P}(c)}\boldsymbol{F}_{pc} = \boldsymbol{0}, \tag{3.62b}$$

$$m_c\frac{d}{dt}E_c + \sum_{p\in\mathcal{P}(c)}\boldsymbol{F}_{pc}\cdot\boldsymbol{U}_p = 0. \tag{3.62c}$$

The cell-centered discrete unknowns $(\frac{1}{\rho_c}, \boldsymbol{U}_c, E_c)$ satisfy a system of semi-discrete evolution equations wherein the numerical fluxes are expressed as functions of the nodal velocity, $\boldsymbol{U}_p$, and the sub-cell force $\boldsymbol{F}_{pc}$. Let us recall that thermodynamic closure is given by the EOS, $P_c = P(\rho_c, \varepsilon_c)$ where $\epsilon_c = E_c - \frac{1}{2} \mid \boldsymbol{U}_c \mid^2$ and grid motion is governed by the semi-discrete trajectory equation (3.53). To complete the discretization, it remains to compute the nodal velocity and construct an approximation of the sub-cell force. These tasks will be achieved by investigating the properties of the scheme regarding its thermodynamic consistency and its conservation for momentum and total energy.

Thermodynamic consistency

We derive a general form of the sub-cell force requiring that the semi-discrete scheme (3.62) satisfies a semi-discrete entropy inequality within cell ω_c. This semi-discrete entropy inequality by mimicing its continuous counterpart, will ensure that kinetic energy will be dissipated into internal energy through shock waves. Thanks to Gibbs formula, the time rate of change of entropy within cell c writes

$$\begin{aligned}m_cT_c\frac{d}{dt}\eta_c =& m_c\left[\frac{d}{dt}\varepsilon_c + P_c\frac{d}{dt}\left(\frac{1}{\rho_c}\right)\right]\\ =& m_c\left[\frac{d}{dt}E_c - \boldsymbol{U}_c\cdot\frac{d}{dt}\boldsymbol{U}_c + P_c\frac{d}{dt}\left(\frac{1}{\rho_c}\right)\right].\end{aligned}$$

where η_c is the specific entropy and T_c the temperature in cell c. By substituting (3.62a) and dot-multiplying (3.62b) by $\boldsymbol{U}_c$ we get

$$m_c T_c \frac{d}{dt}\eta_c = -\sum_{p\in\mathcal{P}(c)} \left[\boldsymbol{F}_{pc}\cdot(\boldsymbol{U}_p-\boldsymbol{U}_c) - l_{pc}P_c\boldsymbol{n}_{pc}\cdot\boldsymbol{U}_p\right].$$

Recalling that the corner vector $l_{pc}\boldsymbol{n}_{pc}$ satisfies the geometrical identity (3.59), the time rate of change of entropy has the final form

$$m_c T_c \frac{d}{dt}\eta_c = -\sum_{p\in\mathcal{P}(c)} \left[(\boldsymbol{F}_{pc} - l_{pc}P_c\boldsymbol{n}_{pc})\cdot(\boldsymbol{U}_p-\boldsymbol{U}_c)\right]. \tag{3.63}$$

Assuming that $T_c > 0$, to satisfy the second law of thermodynamics the right-hand side of Eq. (3.63) must be non-negative. A sufficient condition to obtain this consists in defining the sub-cell force as

$$\boldsymbol{F}_{pc} = l_{pc}P_c\boldsymbol{n}_{pc} - \mathsf{M}_{pc}(\boldsymbol{U}_p-\boldsymbol{U}_c), \tag{3.64}$$

where M_{pc} is a 2×2 **positive semi-definite** matrix, *i.e.*, $\mathsf{M}_{pc}\boldsymbol{U}\cdot\boldsymbol{U}\geq 0, \quad \forall\boldsymbol{U}\in\mathbb{R}^2$. The sub-cell-based matrix, M_{pc}, has the dimension of a length times a density times a velocity, *i.e.*, $[\mathsf{M}_{pc}] = L\,\rho\,U$. Moreover, its definition must be compatible with the principle of material frame-indifference [24], namely it should not depend on the frame of reference used to describe it. In a nutshell, M_{pc} must be invariant by uniform translation and must transform as $\mathsf{M}^{\diamond}_{pc} = \mathcal{R}\mathsf{M}_{pc}\mathcal{R}^t$ for any rigid rotation $\mathcal{R}$. **From now on, we suppose that the latter assumptions hold**. Substituting (3.64) into (3.63) leads to the entropy inequality

$$m_c T_c \frac{d}{dt}\eta_c = \sum_{p\in\mathcal{P}(c)} \mathsf{M}_{pc}\,(\boldsymbol{U}_p-\boldsymbol{U}_c)\cdot(\boldsymbol{U}_p-\boldsymbol{U}_c)\geq 0, \tag{3.65}$$

Let us remark that entropy production within cell c is directly governed by the sub-cell matrix M_{pc} and the velocity jump between the nodal and the cell-centered velocity, $\Delta\boldsymbol{U}_{pc} = \boldsymbol{U}_p - \boldsymbol{U}_c$.

Conservation principles

We achieve the determination of the sub-cell force by invoking the conservation principles of total energy and momentum. Knowing that the total energy over the whole grid is defined as $\mathcal{E}(t) = \sum_c m_c E_c(t)$, the conservation principle of total energy amounts to write

$$\frac{d}{dt}\mathcal{E} = -\int_{\partial\mathcal{D}} P\boldsymbol{U}\cdot\boldsymbol{n}\,\mathrm{d}s,$$

where the right-hand side expresses the rate of pressure work on the boundary, $\partial\mathcal{D}$, of the domain, $\mathcal{D}$, occupied by the fluid. By definition of total energy, this last equation rewrites

$$\sum_c m_c\frac{d}{dt}E_c = -\int_{\partial\mathcal{D}} P\boldsymbol{U}\cdot\boldsymbol{n}\,\mathrm{d}s. \tag{3.66}$$

Before we proceed any further, let us discretize the right-hand side. To this end, let us introduce some specific notation, assuming that the boundary is a closed contour. Let p be a node located on the boundary $\partial\mathcal{D}$, we denote by p^- and p^+ the previous and next points on the boundary with respect to p in the counterclockwise ordered list of points located on $\partial\mathcal{D}$. The curvilinear boundary $\partial\mathcal{D}$ is discretized using the decomposition $\partial\mathcal{D} = \cup_p\partial\mathcal{D}_p$. Here, $\partial\mathcal{D}_p = [i^-,p]\cup[p,i^+]$,

where $i^{\pm}$ is the midpoint of the segment $[p^{\pm}, p]$. Using this decomposition, the boundary term contribution is discretized as

$$\begin{aligned}\int_{\partial\mathcal{D}} P\boldsymbol{U}\cdot\boldsymbol{n}\,\mathrm{d}s &= \sum_{p\in\partial\mathcal{D}}\int_{\partial\mathcal{D}_p} P\boldsymbol{U}\cdot\boldsymbol{n}\,\mathrm{d}s \\ &= \sum_{p\in\partial\mathcal{D}}\left(\int_{\partial\mathcal{D}_p} P\boldsymbol{n}\,\mathrm{d}s\right)\cdot\boldsymbol{U}_p.\end{aligned}$$

The term between parentheses in the right-hand side of the second line represents a corner force that acts from the exterior boundary onto boundary points. Then, it is natural to set

$$\boldsymbol{F}_p^{\star} = \int_{\partial\mathcal{D}_p} P\boldsymbol{n}\,\mathrm{d}s, \tag{3.67}$$

where $\boldsymbol{F}_p^{\star}$ is the boundary corner force acting onto point p. Using the previous and substituting the specific total energy equation (3.62c) into (3.66) yields

$$\sum_c \sum_{p\in\mathcal{P}(c)} \boldsymbol{F}_{pc}\cdot\boldsymbol{U}_p = \sum_{p\in\partial\mathcal{D}} \boldsymbol{F}_p^{\star}\cdot\boldsymbol{U}_p.$$

This equation represents the balance of total energy over the entire domain. Now, interchanging order of double sum in the left-hand side leads to

$$\sum_p \left(\sum_{c\in\mathcal{C}(p)} \boldsymbol{F}_{pc}\right)\cdot\boldsymbol{U}_p = \sum_{p\in\partial\mathcal{D}} \boldsymbol{F}_p^{\star}\cdot\boldsymbol{U}_p,$$

where $\mathcal{C}(p)$ is the set of cells surrounding point p. Finally, left-hand side of the above equation is divided into two parts depending on the points location

$$\sum_{p\in\mathcal{D}^o}\left(\sum_{c\in\mathcal{C}(p)} \boldsymbol{F}_{pc}\right)\cdot\boldsymbol{U}_p + \sum_{p\in\partial\mathcal{D}}\left(\sum_{c\in\mathcal{C}(p)} \boldsymbol{F}_{pc}\right)\cdot\boldsymbol{U}_p = \sum_{p\in\partial\mathcal{D}} \boldsymbol{F}_p^{\star}\cdot\boldsymbol{U}_p, \tag{3.68}$$

where $\mathcal{D}^o$ is the interior of the domain $\mathcal{D}$. **Knowing that the total energy balance** (3.68) **must hold regardless the value of the nodal velocity, total energy conservation is ensured if and only if**

$$\forall\, p\in\mathcal{D}^o, \quad \sum_{c\in\mathcal{C}(p)} \boldsymbol{F}_{pc} = \boldsymbol{0}, \tag{3.69a}$$

$$\forall\, p\in\partial\mathcal{D}, \quad \sum_{c\in\mathcal{C}(p)} \boldsymbol{F}_{pc} = \boldsymbol{F}_p^{\star}. \tag{3.69b}$$

It remains to check that these conditions also lead to momentum conservation. Let $\mathcal{Q}$ denotes the total momentum over the entire domain, *i.e.*, $\mathcal{Q} = \sum_c m_c\boldsymbol{U}_c$. We compute its time rate of

change as follows

$$\begin{aligned}
\frac{d}{dt}\mathcal{Q} &= \sum_c m_c \frac{d}{dt}\boldsymbol{U}_c \\
&= -\sum_c \sum_{p\in\mathcal{P}(c)} \boldsymbol{F}_{pc}, \quad \text{thanks to (3.62b)} \\
&= -\sum_{p\in\mathcal{D}^o} \sum_{c\in\mathcal{C}(p)} \boldsymbol{F}_{pc} - \sum_{p\in\partial\mathcal{D}} \sum_{c\in\mathcal{C}(p)} \boldsymbol{F}_{pc}, \quad \text{by interchanging the double sum} \\
&= -\sum_{p\in\partial\mathcal{D}} \boldsymbol{F}_p^\star, \quad \text{thanks to (3.69)} \\
&= -\sum_{p\in\partial\mathcal{D}} \int_{\partial\mathcal{D}_p} P\boldsymbol{n}\,\mathrm{d}s, \quad \text{thanks to (3.67)}.
\end{aligned}$$

We conclude that up to the boundary terms contribution, momentum is conserved over the entire domain. Hence, conditions (3.69a) and (3.69b) turn out to ensure not only total energy but also momentum conservation. Moreover, as we shall show it in next section, they also provide a vectorial equation that enables us to determine the nodal velocity.

Comment 10 *The fundamental equation* (3.68) *can be interpreted as discrete variational formulation wherein the point velocity* $\boldsymbol{U}_p$ *is a test function. It can also be viewed as a principal of virtual work.*

3.2.3 Node-centered solver for the grid velocity

Remembering that the general sub-cell force form reads $\boldsymbol{F}_{pc} = l_{pc}P_c\boldsymbol{n}_{pc} - \mathsf{M}_{pc}(\boldsymbol{U}_p - \boldsymbol{U}_c)$, where M_{pc} is a 2×2 positive semi-definite matrix, and using the conservation condition (3.69), we are now in position to write the 2×2 system that determines the nodal velocity $\boldsymbol{U}_p$.

Abstract formulation

In the general case this system writes

$$\forall\, p\in\mathcal{D}^o, \quad \mathsf{M}_p\boldsymbol{U}_p = \sum_{c\in\mathcal{C}(p)} \left(l_{pc}P_c\boldsymbol{n}_{pc} + \mathsf{M}_{pc}\boldsymbol{U}_c\right), \tag{3.70a}$$

$$\forall\, p\in\partial\mathcal{D}, \quad \mathsf{M}_p\boldsymbol{U}_p = \sum_{c\in\mathcal{C}(p)} \left(l_{pc}P_c\boldsymbol{n}_{pc} + \mathsf{M}_{pc}\boldsymbol{U}_c\right) - \boldsymbol{F}_p^\star, \tag{3.70b}$$

where M_p denotes the 2×2 node-centered matrix defined as

$$\mathsf{M}_p = \sum_{c\in\mathcal{C}(p)} \mathsf{M}_{pc}. \tag{3.71}$$

We emphasize that we have divided the nodal velocity determination into two cases depending on the node location. As M_{pc} is positive semi-definite, M_p also shares the same property. To enforce the solvability of Eq. (3.70a) and Eq. (3.70b), we assume that the matrix M_{pc} is positive **definite**. This ensures that M_p matrix is invertible. Therefore, provided that the M_{pc} matrix is defined, the nodal velocity, $\boldsymbol{U}_p$ is uniquely determined by inverting equations (3.70a) and (3.70b). We recall that M_{pc} has the physical dimension of a length times a density times a velocity. If M_{pc} does not depend on the nodal velocity, hence (3.70a) and (3.70b) are linear equations and their resolutions can be easily obtained. Conversely, if M_{pc} depends explicitly on

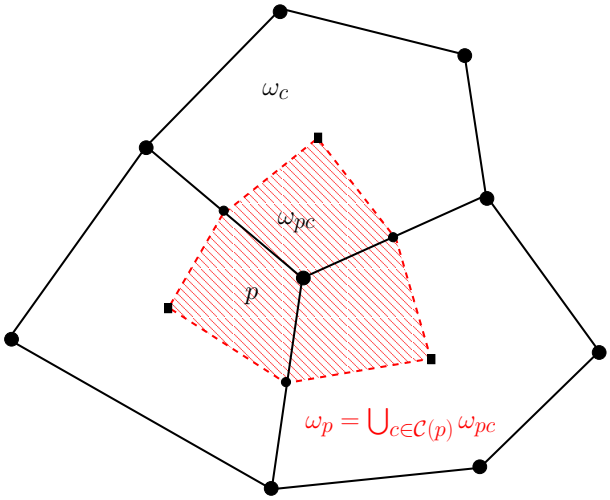

Figure 3.6: Fragment of a polygonal grid in the vicinity of an interior point p. The boundary, $\partial\omega_p$, of the dual cell, ω_p, is displayed using red dashed line.

the nodal velocity, one has to solve non-linear equations by using an iterative method such as fixed point algorithm. In this latter case, the invariance by translation requirement necessitates that M_{pc} is expressed as instance as a function of the difference between the cell and the nodal velocity, *i.e.*, $\mathsf{M}_{pc} \equiv \mathsf{M}_{pc}(\boldsymbol{U}_p - \boldsymbol{U}_c)$. We shall see in the next paragraphs two expressions for M_{pc} that are based on the use of approximate Riemann problems. Before discussing, boundary conditions implementation, let us a give an interpretation of the two terms that determine the nodal velocity. For a given interior node, assuming that M_{pc} does not depend on the nodal velocity, from (3.70a) it follows that the nodal velocity writes

$$\boldsymbol{U}_p = \mathsf{M}_p^{-1}\left[\sum_{c\in\mathcal{C}(p)} l_{pc}P_c\boldsymbol{n}_{pc} + \sum_{c\in\mathcal{C}(p)} \mathsf{M}_{pc}\boldsymbol{U}_c\right].$$

The second term between brackets in the right-hand side is simply a weighted interpolation of cell velocities at point p, whereas the first corresponds to a discretization of the pressure gradient at point p. This interpretation is easy to obtain by computing the pressure gradient integral over the union of sub-cells that share point p. To this end, we define the dual cell ω_p and its boundary $\partial\omega_p$ as

$$\omega_p = \bigcup_{c\in\mathcal{C}(p)} \omega_{pc}, \quad \partial\omega_p = \bigcup_{c\in\mathcal{C}(p)} \partial\omega_{pc} \cap \omega_c^o, \tag{3.72}$$

where ω_c^o denotes the interior of cell c, refer to Figure 3.6. Accordingly, the mean pressure gradient at point p is defined by

$$(\boldsymbol{\nabla}P)_p = \frac{1}{v_p}\int_{\partial\omega_p} P\boldsymbol{n}\,\mathrm{d}s, \tag{3.73}$$

where v_p is the volume of the dual cell ω_p. Using the sub-cell decomposition, (3.73) rewrites

$$\begin{aligned}(\boldsymbol{\nabla}P)_p =& \frac{1}{v_p}\sum_{c\in\mathcal{C}(p)}\int_{\partial\omega_{pc}\cap\omega_c^o} P\boldsymbol{n}\,\mathrm{d}s\\ =& -\frac{1}{v_p}\sum_{c\in\mathcal{C}(p)} l_{pc}P_c\boldsymbol{n}_{pc}.\end{aligned}$$

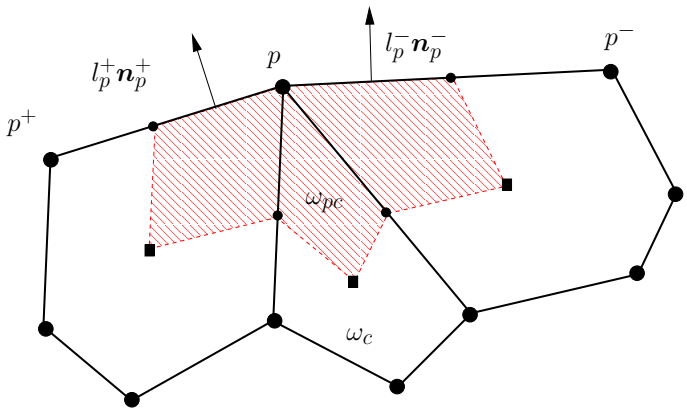

Figure 3.7: Fragment of a polygonal grid in the vicinity of point p located on the boundary $\partial\mathcal{D}$.

Here, we have used the fact that the boundary of the sub-cell ω_{pc} is a closed polygonal contour, thus the outward unit normals to $\partial\omega_{pc} \cap \omega_c^o$ sum to $-l_{pc}\boldsymbol{n}_{pc}$. Using the mean pressure gradient at node p, the nodal velocity rewrites as

$$\boldsymbol{U}_p = \sum_{c\in\mathcal{C}(p)} \mathsf{M}_p^{-1}\mathsf{M}_{pc}\boldsymbol{U}_c - v_p\mathsf{M}_p^{-1}\left(\boldsymbol{\nabla}P\right)_p .$$

This formula can be viewed as a two-dimensional generalization of the point velocity obtained using an acoustic Riemann solver, refer to Eq. (3.28a) page 67.

Boundary conditions implementation

We conclude this section by describing the boundary conditions implementation. In Lagrangian formalism, this task is quite simple as we have to consider only two types of boundary conditions, refer to (2.102) page 36. Namely, on the boundary of the domain, $\partial\mathcal{D}$, either the pressure or the normal component of the velocity is prescribed. We present a boundary conditions implementation which is fully compatible with the node-centered solver previously developed. To this end, let us consider a generic point p located on the boundary, we denote p^- and p^+ its previous and next neighbor with respect to p in the counterclockwise ordered list of boundary points. Without loss of generality we make the assumption that $\partial\mathcal{D}$ is a closed contour. The two outward normals to the edges located on the boundary impinging on point p are $l_p^-\boldsymbol{n}_p^-$ and $l_p^+\boldsymbol{n}_p^+$, where $l_p^\pm$ is equal to the half of the length of the segment $[p, p^\pm]$, refer to Figure 3.7. These outward normals are linked to the corner vectors $l_{pc}\boldsymbol{n}_{pc}$ as follows

$$\sum_{c\in\mathcal{C}(p)} l_{pc}\boldsymbol{n}_{pc} = l_p^-\boldsymbol{n}_p^- + l_p^+\boldsymbol{n}_p^+. \tag{3.74}$$

Once more, this follows from the fact that the dual cell contour is closed (red dashed line in Figure 3.7). Now, let us distinguish between the two following cases.

- **Prescribed pressure:** the boundary corner force acting onto point p defining by (3.67) writes

  $$\boldsymbol{F}_p^\star = l_p^-\Pi_p^{-,\star}\boldsymbol{n}_p^- + l_p^+\Pi_p^{+,\star}\boldsymbol{n}_p^+,$$

  where $\Pi_p^{\pm,\star}$ are the prescribed pressures on both sides of point p. Substituting this expression of the boundary corner force into (3.70b) leads to

  $$\mathsf{M}_p\boldsymbol{U}_p = \sum_{c\in\mathcal{C}(p)} \left(l_{pc}P_c\boldsymbol{n}_{pc} + \mathsf{M}_{pc}\boldsymbol{U}_c\right) - \left(l_p^-\Pi_p^{-,\star}\boldsymbol{n}_p^- + l_p^+\Pi_p^{+,\star}\boldsymbol{n}_p^+\right). \tag{3.75}$$

Due to (3.74), we note that this formula preserves uniform fluid flows. Namely, if $(P_c, \boldsymbol{U}_c) = (P^0, \boldsymbol{U}^0), \quad \forall\, c$, then $\boldsymbol{U}_p = \boldsymbol{U}^0$.

- **Prescribed normal velocity:** let $\mathcal{V}_p^{\pm,*}$ denotes the prescribed normal velocity on both sides of point p. If the two outward normals $\boldsymbol{n}_p^-$ and $\boldsymbol{n}_p^+$ are not colinear, then $\boldsymbol{U}_p$ is defined as the unique solution of the 2×2 linear system

$$\begin{aligned} \boldsymbol{U}_p \cdot \boldsymbol{n}_p^- &= \mathcal{V}_p^{-,*} \\ \boldsymbol{U}_p \cdot \boldsymbol{n}_p^+ &= \mathcal{V}_p^{+,*}. \end{aligned}$$

  On the other hand, $\boldsymbol{U}_p$ satisfies (3.70b) written as

$$\mathsf{M}_p \boldsymbol{U}_p = \sum_{c \in \mathcal{C}(p)} (l_{pc} P_c \boldsymbol{n}_{pc} + \mathsf{M}_{pc} \boldsymbol{U}_c) - \Big(\sum_{c \in \mathcal{C}(p)} l_{pc} \boldsymbol{n}_{pc} \Big) \Pi_p^\star,$$

  where $\Pi_p^\star$ stands for an averaged pressure acting onto point p. This pressure is an auxiliary unknown, for which we can write the supplementary equation

$$\big(l_p^- \boldsymbol{n}_p^- + l_p^+ \boldsymbol{n}_p^+ \big) \cdot \boldsymbol{U}_p = l_p^- \mathcal{V}_p^{-,*} + l_p^+ \mathcal{V}_p^{+,*}.$$

  Note that this equation follows from the prescribed velocity boundary condition. Combining the above results, we write the 3×3 system satisfied by the nodal velocity, $\boldsymbol{U}_p$, and the auxiliary unknown, $\Pi_p^\star$

$$\mathsf{M}_p \boldsymbol{U}_p + \Big(\sum_{c \in \mathcal{C}(p)} l_{pc} \boldsymbol{n}_{pc} \Big) \Pi_p^\star = \sum_{c \in \mathcal{C}(p)} (l_{pc} P_c \boldsymbol{n}_{pc} + \mathsf{M}_{pc} \boldsymbol{U}_c)\,, \tag{3.76a}$$

$$\Big(\sum_{c \in \mathcal{C}(p)} l_{pc} \boldsymbol{n}_{pc} \Big) \cdot \boldsymbol{U}_p = l_p^- \mathcal{V}_p^{-,*} + l_p^+ \mathcal{V}_p^{+,*}. \tag{3.76b}$$

  The 3×3 matrix associated to the above system writes under block forms as

$$\mathsf{A}_p = \begin{pmatrix} \mathsf{M}_p & \displaystyle\sum_{c \in \mathcal{C}(p)} l_{pc} \boldsymbol{n}_{pc} \\ \displaystyle\sum_{c \in \mathcal{C}(p)} l_{pc} \boldsymbol{n}_{pc} & 0 \end{pmatrix}.$$

  Recalling that M_p is positive definite, we deduce that A_p is also positive definite. Thus, system (3.76) always admits a unique solution.

At this point, we can conclude that the sub-cell force formalism provides a general framework allowing to construct compatible cell-centered schemes satisfying an entropy inequality and the mechanical conservation principles. The numerical fluxes and the nodal velocity are computed in a compatible manner by means of a node-centered solver which permits to consistently derive boundary conditions. The key point in designing these schemes lies in the definition of the corner matrix M_{pc}. We shall investigate this latter point in the two next paragraphs, by presenting two examples of such a construction and making the link with approximate Riemann solvers.

First example: GLACE scheme

This first example consists of a cell-centered scheme, introduced by Després and Mazeran in [49] and named GLACE in [38]. The acronym GLACE is shorthand for Godunov-type LAgrangian scheme Conservative for total Energy. This scheme can be rewritten by means of the sub-cell

force-based approach by introducing one nodal pressure, Π_{pc}, at each corner pc. This amounts to introduce the sub-cell force

$$\boldsymbol{F}_{pc}^{\text{GLACE}} = l_{pc}\Pi_{pc}\boldsymbol{n}_{pc}. \tag{3.77}$$

The corner pressure Π_{pc} is expressed in terms of the cell pressure and the velocity jump between cell and node velocity, through the use of the following Riemann invariant written along the corner normal direction $\boldsymbol{n}_{pc}$

$$\Pi_{pc} - P_c = z_c(\boldsymbol{U}_p - \boldsymbol{U}_c)\cdot\boldsymbol{n}_{pc}, \tag{3.78}$$

where $z_c = \rho_c a_c$ is the acoustic impedance. Combining (3.77) and (3.78), we obtain the expression of the sub-cell force associated to GLACE scheme

$$\boldsymbol{F}_{pc}^{\text{GLACE}} = l_{pc}P_c\boldsymbol{n}_{pc} - z_c l_{pc}(\boldsymbol{n}_{pc}\otimes\boldsymbol{n}_{pc})(\boldsymbol{U}_p - \boldsymbol{U}_c). \tag{3.79}$$

Comparing the above expression and the generic form of the sub-cell force (3.64), we deduce that the corner matrix corresponding to GLACE scheme is given by

$$\mathsf{M}_{pc}^{\text{GLACE}} = z_c l_{pc}(\boldsymbol{n}_{pc}\otimes\boldsymbol{n}_{pc}). \tag{3.80}$$

We note that $\mathsf{M}_{pc}^{\text{GLACE}}$ is proportional to the orthogonal projection onto direction $\boldsymbol{n}_{pc}$. It is easy to check that this 2×2 matrix is symmetric positive but only semi-definite as its kernel is spanned by $\boldsymbol{n}_{pc}^{\perp}$, where $\boldsymbol{n}_{pc}^{\perp}$ denotes the unit vector directly orthogonal to $\boldsymbol{n}_{pc}$. From (3.65) it follows that the entropy production associated to this scheme writes

$$m_c T_c \frac{d}{dt}\eta_c^{\text{GLACE}} = \sum_{p\in\mathcal{P}(c)} \mathsf{M}_{pc}^{\text{GLACE}}\,(\boldsymbol{U}_p - \boldsymbol{U}_c)\cdot(\boldsymbol{U}_p - \boldsymbol{U}_c).$$

We point out that sub-cell entropy production can go to zero for flows wherein $(\boldsymbol{U}_p - \boldsymbol{U}_c)\perp\boldsymbol{n}_{pc}$. This fact probably explains why GLACE scheme exhibits, for certain flows, severe numerical instabilities such as hourglass modes, refer to [38, 136]. Moreover, the fact that $\mathsf{M}_{pc}^{\text{GLACE}}$ is only semi-definite can lead to singularities in the boundary conditions implementation, which are solved by an ad hoc treatment [38].

Finally, we assess the ability of GLACE scheme to recover the one-dimensional acoustic solver in the case of a one-dimensional flow aligned for instance with the x direction of a Cartesian grid. Let Δx and Δy denote the mesh spacing along x and y directions. Without loss of generality, we compute the nodal velocity of the point located at the origin, assuming that the initial flow is characterized by the state (ρ_l, u_l, P_l) on the left side of the interface defined by the y axis, and the state (ρ_r, u_r, P_r) on its right side, where u_l and u_r denote the x components of the velocity flow on both sides, refer to Figure 3.8. The four quadrangular cells surrouding the origin are labelled from 1 to 4. The four corner unit normals related to the origin are denoted $\boldsymbol{n}_i,\ i = 1\ldots 4$ and given by

$$\boldsymbol{n}_1 = \frac{1}{\sqrt{\Delta x^2+\Delta y^2}}\begin{pmatrix}\Delta y\\ \Delta x\end{pmatrix},\quad \boldsymbol{n}_2 = \frac{1}{\sqrt{\Delta x^2+\Delta y^2}}\begin{pmatrix}-\Delta y\\ \Delta x\end{pmatrix},$$
$$\boldsymbol{n}_3 = \frac{1}{\sqrt{\Delta x^2+\Delta y^2}}\begin{pmatrix}-\Delta y\\ -\Delta x\end{pmatrix},\quad \boldsymbol{n}_4 = \frac{1}{\sqrt{\Delta x^2+\Delta y^2}}\begin{pmatrix}\Delta y\\ -\Delta x\end{pmatrix}.$$

Their corresponding lengths are $l_i = \sqrt{\Delta x^2+\Delta y^2},\ i = 1\ldots 4$. Remembering that the corner matrices are given by $\mathsf{M}_i^{\text{GLACE}} = z_i l_i(\boldsymbol{n}_i\otimes\boldsymbol{n}_i),\ i = 1\ldots 4$, where $z_1 = z_4 = z_l$ and $z_2 = z_3 = z_r$, we compute the velocity of the origin, $\boldsymbol{U}_O^{\text{GLACE}}$, as the solution of the linear system

$$\mathsf{M}_O^{\text{GLACE}}\boldsymbol{U}_O = \sum_{i=1}^{4} l_i P_i\boldsymbol{n}_i + \mathsf{M}_i^{\text{GLACE}}\boldsymbol{U}_i,$$

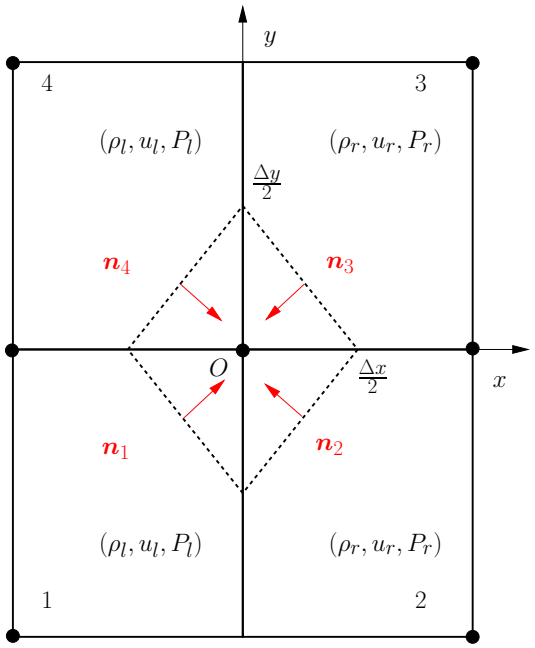

Figure 3.8: Notation for the nodal solver associated to the GLACE scheme on a quadrangular grid. The unit normals $\boldsymbol{n}_1$ to $\boldsymbol{n}_4$ correspond to the four corner normals related to the origin.

where $\mathsf{M}_O^{\text{GLACE}} = \sum_{i=1}^4 \mathsf{M}_i^{\text{GLACE}}$, $P_1 = P_4 = P_l$, $P_2 = P_3 = P_r$, $\boldsymbol{U}_1 = \boldsymbol{U}_4 = u_l \boldsymbol{e}_x$ and $\boldsymbol{U}_2 = \boldsymbol{U}_3 = u_r \boldsymbol{e}_x$. With these data, a straightforward computation shows that the nodal velocity of the origin is aligned with the x axis and its x component is given by

$$\boldsymbol{U}_O^{\text{GLACE}} = \left(\frac{z_l u_l + z_r u_r}{z_l + z_r} - \frac{\sqrt{\Delta x^2 + \Delta y^2}}{\Delta y} \frac{P_r - P_l}{z_l + z_r} \right) \boldsymbol{e}_x.$$

Let us emphasize that we do not recover exactly the one-dimensional acoustic solver. The discrepancy with the usual formula lies in the geometric factor $\frac{\sqrt{\Delta x^2+\Delta y^2}}{\Delta y}$. This factor, which has no physical dimension, can become singular in the case of a mesh characterized by a high-aspect ratio, *i.e.*, when $\Delta y \ll \Delta x$. Let us point out that this situation occurs frequently for Lagrangian hydrodynamics numerical simulations wherein high aspect ratio grids are used. This is typically the case for computations devoted to the numerical simulation of Inertial Confinement Fusion.

Second example: EUCCLHYD scheme

The second example consists of a cell-centered Lagrangian scheme, which has been initially presented in [108] and revisited in [105, 111]. This scheme is called EUCCLHYD which stands for Explicit Unstructured Cell-Centered Lagrangian HYDrodynamics. It aims at correcting the flaws associated to GLACE scheme, particularly the one related to the high aspect ratio dependency. The EUCCLHYD scheme differs from the GLACE scheme in the sense that two nodal pressures denoted by Π_{pc}^- and Π_{pc}^+ are introduced per corner pc. For each corner, we also define the half-edge outward normals $l_{pc}^- \boldsymbol{n}_{pc}^-$ and $l_{pc}^+ \boldsymbol{n}_{pc}^+$, where $\boldsymbol{n}_{pc}^-$ and $\boldsymbol{n}_{pc}^+$ are unit outward normals to edges $[p^-, p]$, $[p, p^+]$ and $l_{pc}^\pm$ is equal to the half of the length of the corresponding edges, refer to Figure 3.9. A simple geometric argument shows that

$$l_{pc} \boldsymbol{n}_{pc} = l_{pc}^- \boldsymbol{n}_{pc}^- + l_{pc}^+ \boldsymbol{n}_{pc}^+.$$

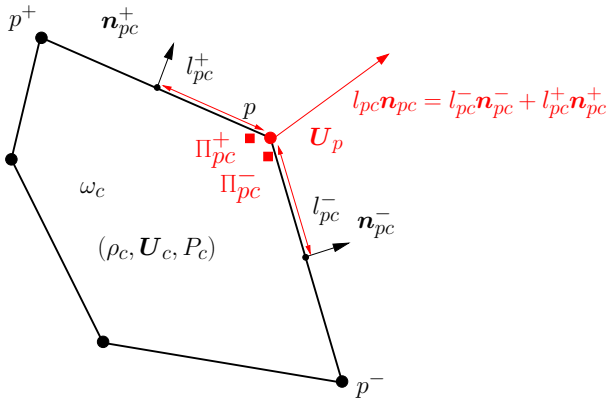

Figure 3.9: Notation related to EUCCLHYD scheme at corner pc for a polygonal cell.

With these notations, sub-cell force writes

$$\boldsymbol{F}_{pc}^{\text{EUCCL}} = l_{pc}^-\Pi_{pc}^-\boldsymbol{n}_{pc}^- + l_{pc}^+\Pi_{pc}^+\boldsymbol{n}_{pc}^+. \tag{3.81}$$

The two nodal pressures are expressed as functions of the cell pressure and the jump between cell and point velocity, by means of the two following Riemann invariants written along each half-edge normal direction

$$\Pi_{pc}^- - P_c = z_c(\boldsymbol{U}_p - \boldsymbol{U}_c)\cdot\boldsymbol{n}_{pc}^-, \tag{3.82a}$$

$$\Pi_{pc}^+ - P_c = z_c(\boldsymbol{U}_p - \boldsymbol{U}_c)\cdot\boldsymbol{n}_{pc}^+. \tag{3.82b}$$

Combining (3.81) and (3.82), we obtain the expression of the sub-cell force associated to EUCCLHYD scheme

$$\boldsymbol{F}_{pc}^{\text{EUCCL}} = l_{pc}P_c\boldsymbol{n}_{pc} - z_c\left[l_{pc}^-(\boldsymbol{n}_{pc}^-\otimes\boldsymbol{n}_{pc}^-) + l_{pc}^+(\boldsymbol{n}_{pc}^+\otimes\boldsymbol{n}_{pc}^+)\right](\boldsymbol{U}_p - \boldsymbol{U}_c). \tag{3.83}$$

From the comparison between this last expression and the generic form of the sub-cell force (3.64), we deduce that the corner matrix corresponding to EUCCLHYD scheme writes

$$\mathsf{M}_{pc}^{\text{EUCCL}} = z_c\left[l_{pc}^-(\boldsymbol{n}_{pc}^-\otimes\boldsymbol{n}_{pc}^-) + l_{pc}^+(\boldsymbol{n}_{pc}^+\otimes\boldsymbol{n}_{pc}^+)\right]. \tag{3.84}$$

We observe that $\mathsf{M}_{pc}^{\text{EUCCL}}$ is always symmetric positive definite provided that $\boldsymbol{n}_{pc}^-$ and $\boldsymbol{n}_{pc}^+$ are not colinear. This situation can exceptionally occur at some corners for degenerate polygonal cells containing hanging nodes. However, one can show that the $\mathsf{M}_{p}^{\text{EUCCL}}$ matrix which follows from the sum of the $\mathsf{M}_{pc}^{\text{EUCCL}}$ is always symmetric positive definite and thus invertible. Moreover, $\mathsf{M}_{pc}^{\text{EUCCL}}$ being positive definite, entropy production is always positive and can go to zero only for uniform flows. Up to our knowledge, this scheme does not exhibit hourglass instabilities and thus does not necessitate any hourglass filter.

Now, let us assess the ability of this scheme to recover the one-dimensional acoustic solver in the case of a one-dimensional flow aligned for instance with the x direction of a Cartesian grid. To this end, we use exactly the same set up as previously. Some elementary algebra shows that the velocity of point O is written

$$\boldsymbol{U}_O^{\text{EUCCL}} = \left(\frac{z_l u_l + z_r u_r}{z_l + z_r} - \frac{P_r - P_l}{z_l + z_r}\right)\boldsymbol{e}_x.$$

Contrary to GLACE scheme, EUCCLHYD scheme recovers exactly the one-dimensional acoustic solver without any dependency to the grid aspect ratio.

We pursue this paragraph devoted to EUCCLHYD scheme by presenting a least squares interpretation[2] of the nodal solver. Let us recall that the nodal velocity, for an interior point,

[2]We thank Burton Wendroff for having suggested this interpretation.

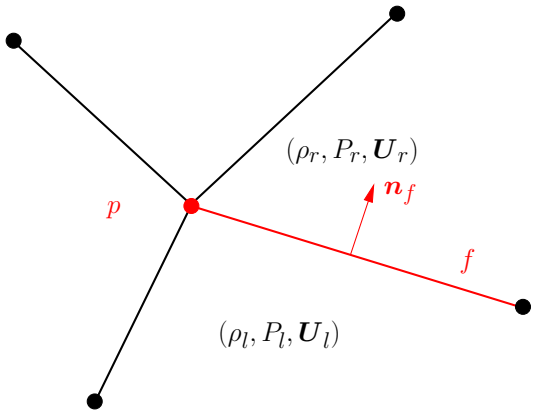

Figure 3.10: Fragment of grid: notation related to point p and face f.

is obtained by solving the linear system $\displaystyle\sum_{c\in\mathcal{C}(p)} \boldsymbol{F}_{cp}^{\mathrm{EUCCL}} = \boldsymbol{0}$, where the sub-cell force writes

$$\boldsymbol{F}_{pc}^{\mathrm{EUCCL}} = (l_{pc}^{-}\boldsymbol{n}_{pc}^{-} + l_{pc}^{+}\boldsymbol{n}_{pc}^{+})P_c + z_c\left[l_{pc}^{-}(\boldsymbol{n}_{pc}^{-}\otimes\boldsymbol{n}_{pc}^{-}) + l_{pc}^{+}(\boldsymbol{n}_{pc}^{+}\otimes\boldsymbol{n}_{pc}^{+})\right](\boldsymbol{U}_p - \boldsymbol{U}_c).$$

Here, we have adopted a point of view which is corner-based, *i.e.*, in the equation that determines the nodal velocity the sum is made over the sub-cells (corners) surrounding point p. Let us change our viewpoint by summing over the edges that impinge on point p. To this end, we denote by $\mathcal{F}(p)$ the set of faces that are connected to point p, and we use the label f to denote such a generic face. As the number of cells surrounding point p is equal to the number of faces connected to it, the above equation transforms into

$$\begin{aligned}\sum_{c\in\mathcal{C}(p)} \boldsymbol{F}_{pc}^{\mathrm{EUCCL}} &= \sum_{f\in\mathcal{F}(p)} l_f(P_r - P_l)\boldsymbol{n}_f - l_f[(z_l + z_r)(\boldsymbol{U}_p\cdot\boldsymbol{n}_f) - z_l(\boldsymbol{U}_l\cdot\boldsymbol{n}_f) + z_r(\boldsymbol{U}_r\cdot\boldsymbol{n}_f)]\boldsymbol{n}_f \\ &= -\sum_{f\in\mathcal{F}(p)} l_f(z_l + z_r)\left[(\boldsymbol{U}_p\cdot\boldsymbol{n}_f) - \frac{z_l(\boldsymbol{U}_l\cdot\boldsymbol{n}_f) + z_r(\boldsymbol{U}_r\cdot\boldsymbol{n}_f) - (P_r - P_l)}{z_l + z_r}\right]\boldsymbol{n}_f.\end{aligned}$$

Here, we have changed the notations using the subscripts r (resp. l) to denote the physical variables located on the right side (resp. left side) of face f, with respect to the direction of the unit normal $\boldsymbol{n}_f$, refer to Figure 3.10. By setting

$$\mathcal{V}_f^{\star} = \frac{z_l(\boldsymbol{U}_l\cdot\boldsymbol{n}_f) + z_r(\boldsymbol{U}_r\cdot\boldsymbol{n}_f) - (P_r - P_l)}{z_l + z_r},$$

we recover the normal velocity corresponding to the solution of the one-dimensional acoustic Riemann problem in the direction of the unit normal $\boldsymbol{n}_f$. Using the above notation, the nodal velocity is the solution of the linear system

$$\sum_{f\in\mathcal{F}(p)} l_f(z_l + z_r)\left[(\boldsymbol{U}_p\cdot\boldsymbol{n}_f) - \mathcal{V}_f^{\star}\right]\boldsymbol{n}_f = \boldsymbol{0}. \tag{3.85}$$

A straightforward calculation shows that the left-hand side of this equation is nothing but the gradient of the quadratic functional defined by

$$I(\boldsymbol{U}) = \frac{1}{2}\sum_{f\in\mathcal{F}(p)} l_f(z_l + z_r)\left[(\boldsymbol{U}\cdot\boldsymbol{n}_f) - \mathcal{V}_f^{\star}\right]^2.$$

Therefore, the solution of (3.85) corresponds to the minimum of the functional I, *i.e.*, $\boldsymbol{U}_p = \text{argmin}_{\boldsymbol{U}\in\mathbb{R}^2} I(\boldsymbol{U})$. It turns out that the nodal velocity is obtained from a weighted least squares procedure. This approach results from the over-determined system obtained by equating the projection of nodal velocity onto the edge normal with the normal velocity coming from the 1D acoustic Riemann solver. Here, the face-based weight is given by $l_f(z_l + z_r)$. This least squares interpretation shows that our nodal solver is quite close to the nodal solver developed in CAVEAT [8, 7], except that the face-based weights differ. In CAVEAT scheme [7], the face-based weight is designed in a heuristic manner, namely it is equal to the sum of the material densities on either side of each face. This choice results in a grid velocity which is not compatible with the Geometric Conservation Law. Finally, we want to mention that it is also possible to improve the robustness of this nodal solver giving up the acoustic approximation by introducing the generalized non-linear corner impedances

$$z_{pc}^{\pm} = \rho_c \left[a_c + \Gamma_c \mid (\boldsymbol{U}_p - \boldsymbol{U}_c) \cdot \boldsymbol{n}_{pc}^{\pm} \mid \right], \tag{3.86}$$

recalling that a_c is the isentropic sound speed and Γ_c is a material dependent parameter, which is given by $\frac{\gamma+1}{2}$ in case of a gamma gas law. Note that this formula is the two-dimensional extension of the swept mass flux proposed by Dukowicz [53] to approximate one-dimensional Riemann problem, refer to Eq. (3.29) page 67. We also mention that we recover the acoustic approximation simply by setting $\Gamma_c = 0$ in the above formula. Using this new approximation, Riemann invariants rewrite

$$\Pi_{pc}^{\pm} - P_c = z_{pc}^{\pm}(\boldsymbol{U}_p - \boldsymbol{U}_c) \cdot \boldsymbol{n}_{pc}^{\pm}.$$

Hence, the corner matrix is modified as

$$\mathsf{M}_{pc}^{\text{EUCCL}} = z_{pc}^{-} l_{pc}^{-} (\boldsymbol{n}_{pc}^{-} \otimes \boldsymbol{n}_{pc}^{-}) + z_{pc}^{+} l_{pc}^{+} (\boldsymbol{n}_{pc}^{+} \otimes \boldsymbol{n}_{pc}^{+}). \tag{3.87}$$

The equation that solves the nodal velocity becomes non-linear due to the dependency of the corner matrix to the nodal velocity. This non-linearity is solved by means of an iterative algorithm such as fixed point method. In practice, it takes few iterations to converge.

Other possible schemes

In this paragraph, we propose a methodology to define other possible schemes. Here, we assume that the corner matrix, M_{pc}, is symmetric positive definite, hence it admits two distinct positive eigenvalues, λ_{pc}^{-} and λ_{pc}^{+}. Their corresponding eigenvectors are the unit vectors $\boldsymbol{\nu}_{pc}^{-}$ and $\boldsymbol{\nu}_{pc}^{+}$, which form an orthonormal basis. Bearing this in mind, the corner matrix could be defined as follows

$$\mathsf{M}_{pc} = \zeta_{pc}^{-} \lambda_{pc}^{-} (\boldsymbol{\nu}_{pc}^{-} \otimes \boldsymbol{\nu}_{pc}^{-}) + \zeta_{pc}^{+} \lambda_{pc}^{+} (\boldsymbol{\nu}_{pc}^{+} \otimes \boldsymbol{\nu}_{pc}^{+}). \tag{3.88}$$

In writing these equations, we suppose that $\lambda_{pc}^{\pm}$ is homogeneous to a length whereas $\zeta_{pc}^{\pm}$ is a generalized impedance which could be defined as

$$\zeta_{pc} = \rho_c \left[a_c + \mid (\boldsymbol{U}_p - \boldsymbol{U}_c) \cdot \boldsymbol{\nu}_{pc}^{\pm} \mid \right].$$

Finally, it turns out that the determination of a symmetric positive definite corner matrix amounts to define per corner, two lengths and two orthonormal vectors in a relevant manner. Here, relevant means that these lengths and orthonormal vectors should be defined as local functions of the fluid flow.

3.2.4 High-order extension based on the acoustic GRP method

We aim at deriving the high-order extension of the compatible cell-centered discretization presented in the previous section. To construct a high-order extension, many methods are available. The most obvious one, consists in defining a monotonic piecewise linear reconstruction of the pressure and the velocity by means of a slope limiter. The nodal velocity is computed through the use of the node-centered solver wherein the input data are defined as the nodal extrapolated values of the pressure and the velocity. The time discretization is simply based on a two-steps Runge-Kutta procedure. Such a methodology has been successfully developed in [109, 111]. However, this approach is rather expensive since it needs a two-step integration in time. This point becomes particularly crucial when coupling the hydrodynamic scheme with more complex physics. For this reason, we prefer to use a one-step time integrator based on the GRP (Generalized Riemann problem) method of Ben-Artzi and Falcovitz [19, 20, 18, 21, 22, 89]. This method consists in solving the higher-order Riemann problem with piecewise linear polynomials, whereby the approximate solution is given as a time power series expansion right at the interface, thus providing a numerical flux for a high-order Godunov-type method. Here, we are using the acoustic version of the GRP method. This approximation provides a framework in which the solution of the GRP is simple to compute and easy to handle. In the case of one-dimensional Lagrangian hydrodynamics, this method has been completely derived in the monograph [21]. Note that we have also recalled it for sake of completeness in Sec. 3.1.8 page 71. In what follows, we present the non-trivial extension of the acoustic GRP methodology to our two-dimensional Lagrangian scheme.

Second-order time discretization

Let us introduce the time discretization of the semi-discrete system (3.62) page 81. All the physical and geometric variables are assumed to be known at the beginning of time step t^n and we denote them using the superscript n. Their updated values at time $t^{n+1} = t^n + \Delta t$, where Δt is the current time step, are obtained by means of the following system

$$m_c \left(\frac{1}{\rho_c^{n+1}} - \frac{1}{\rho_c^n} \right) - \sum_{p \in \mathcal{P}(c)} \int_{t^n}^{t^{n+1}} (l_{pc} \boldsymbol{n}_{pc})(t) \cdot \boldsymbol{U}_p(t) \, \mathrm{d}t = 0, \tag{3.89a}$$

$$m_c \left(\boldsymbol{U}_c^{n+1} - \boldsymbol{U}_c^n \right) + \sum_{p \in \mathcal{P}(c)} \int_{t^n}^{t^{n+1}} \boldsymbol{F}_{pc}(t) \, \mathrm{d}t = \boldsymbol{0}, \tag{3.89b}$$

$$m_c \left(E_c^{n+1} - E_c^n \right) + \sum_{p \in \mathcal{P}(c)} \int_{t^n}^{t^{n+1}} \boldsymbol{F}_{pc}(t) \cdot \boldsymbol{U}_p(t) \, \mathrm{d}t = 0. \tag{3.89c}$$

Here, the sub-cell force $\boldsymbol{F}_{pc}$ is a time-dependent function which writes

$$\boldsymbol{F}_{pc}(t) = (l_{pc} \boldsymbol{n}_{pc})(t) P_c(t) - \mathsf{M}_{pc} [\boldsymbol{U}_p(t) - \boldsymbol{U}_c(t)],$$

where the corner matrix, M_{pc} is assumed to be positive definite. As this matrix is generally expressed in terms of geometric variables such as lengths and unit normal vectors, it also time-dependent. The motion of the grid is governed by the discrete trajectory equation

$$\boldsymbol{x}_p^{n+1} = \boldsymbol{x}_p^n + \int_{t^n}^{t^{n+1}} \boldsymbol{U}_p(t) \, \mathrm{d}t, \quad \boldsymbol{x}_p^0 = \boldsymbol{X}_p. \tag{3.90}$$

We want to perform a one-step time integration of the numerical fluxes, which is at least second-order accurate. To this end, we make use of the following Taylor expansions of the nodal velocity

and the sub-cell force

$$\forall t \in [t^n, t^{n+1}], \quad \begin{cases} \boldsymbol{U}_p(t) = \boldsymbol{U}_p(t^n) + (t-t^n)\dfrac{d}{dt}\boldsymbol{U}_p(t^n) + O((t-t^n)^2), \\ \boldsymbol{F}_{pc}(t) = \boldsymbol{F}_{pc}(t^n) + (t-t^n)\dfrac{d}{dt}\boldsymbol{F}_{pc}(t^n) + O((t-t^n)^2). \end{cases}$$

Employing these Taylor expansions, integrals over the time interval $[t^n, t^{n+1}]$ of the nodal velocity and the sub-cell force are approximated by

$$\int_{t^n}^{t^{n+1}} \boldsymbol{U}_p(t)\,\mathrm{d}t = \Delta t \left[\boldsymbol{U}_p^n + \frac{\Delta t}{2}\frac{d}{dt}\boldsymbol{U}_p^n\right],$$
$$\int_{t^n}^{t^{n+1}} \boldsymbol{F}_{pc}(t)\,\mathrm{d}t = \Delta t \left[\boldsymbol{F}_{pc}^n + \frac{\Delta t}{2}\frac{d}{dt}\boldsymbol{F}_{pc}^n\right],$$

where $\frac{d}{dt}\boldsymbol{U}_p^n$ and $\frac{d}{dt}\boldsymbol{F}_{pc}^n$ denote the time derivative of the nodal velocity and the sub-cell force evaluated at time t^n. Let us introduce the time centered values

$$\boldsymbol{U}_p^{n+\frac{1}{2}} = \boldsymbol{U}_p^n + \frac{\Delta t}{2}\frac{d}{dt}\boldsymbol{U}_p^n,$$
$$\boldsymbol{F}_{pc}^{n+\frac{1}{2}} = \boldsymbol{F}_{pc}^n + \frac{\Delta t}{2}\frac{d}{dt}\boldsymbol{F}_{pc}^n.$$

From the first above equation, it follows that the second-order time discretization of the trajectory equation writes

$$\boldsymbol{x}_p^{n+1} = \boldsymbol{x}_p^n + \Delta t \boldsymbol{U}_p^{n+\frac{1}{2}}, \quad \boldsymbol{x}_p^0 = \boldsymbol{X}_p.$$

Now, observe that the position vector of point p can be parameterized as

$$\boldsymbol{x}_p(t) = \boldsymbol{x}_p^n + (t-t^n)\boldsymbol{U}_p^{n+\frac{1}{2}}, \quad \forall t \in [t^n, t^{n+1}].$$

This shows that the corner vector, $l_{pc}\boldsymbol{n}_{pc}(t)$, has a linear dependency with respect to time. Thus, the Taylor expansion of the corner vector is computed exactly by

$$l_{pc}\boldsymbol{n}_{pc}(t) = l_{pc}^n\boldsymbol{n}_{pc}^n + (t-t^n)\frac{d}{dt}[l_{pc}\boldsymbol{n}_{pc}(t^n)].$$

Finally, setting $l_{pc}^{n+\frac{1}{2}}\boldsymbol{n}_{pc}^{n+\frac{1}{2}} = l_{pc}^n\boldsymbol{n}_{pc}^n + \frac{\Delta t}{2}\frac{d}{dt}(l_{pc}\boldsymbol{n}_{pc})^n$, the volume flux is computed as

$$\int_{t^n}^{t^{n+1}} (l_{pc}\boldsymbol{n}_{pc})(t)\cdot\boldsymbol{U}_p(t)\,\mathrm{d}t = \Delta t l_{pc}^{n+\frac{1}{2}}\boldsymbol{n}_{pc}^{n+\frac{1}{2}}\cdot\boldsymbol{U}_p^{n+\frac{1}{2}}.$$

Gathering the previous results yields the following formal second-order time discretization of system (3.89)

$$m_c\left(\frac{1}{\rho_c^{n+1}} - \frac{1}{\rho_c^n}\right) - \Delta t \sum_{p\in\mathcal{P}(c)} l_{pc}^{n+\frac{1}{2}}\boldsymbol{n}_{pc}^{n+\frac{1}{2}}\cdot\boldsymbol{U}_p^{n+\frac{1}{2}} = 0, \tag{3.91a}$$

$$m_c\left(\boldsymbol{U}_c^{n+1} - \boldsymbol{U}_c^n\right) + \Delta t \sum_{p\in\mathcal{P}(c)} \boldsymbol{F}_{pc}^{n+\frac{1}{2}} = \boldsymbol{0}, \tag{3.91b}$$

$$m_c\left(E_c^{n+1} - E_c^n\right) + \Delta t \sum_{p\in\mathcal{P}(c)} \boldsymbol{F}_{pc}^{n+\frac{1}{2}}\cdot\boldsymbol{U}_p^{n+\frac{1}{2}} = 0. \tag{3.91c}$$

The grid displacement is computed using the discrete trajectory equation

$$\boldsymbol{x}_p^{n+1} = \boldsymbol{x}_p^n + \Delta t \boldsymbol{U}_p^{n+\frac{1}{2}}, \quad \boldsymbol{x}_p^0 = \boldsymbol{X}_p. \tag{3.92}$$

Here, the time-centered variables are defined by

$$l_{pc}^{n+\frac{1}{2}} \boldsymbol{n}_{pc}^{n+\frac{1}{2}} = l_{pc}^n \boldsymbol{n}_{pc}^n + \frac{\Delta t}{2} \frac{d}{dt} (l_{pc} \boldsymbol{n}_{pc})^n, \tag{3.93a}$$

$$\boldsymbol{U}_p^{n+\frac{1}{2}} = \boldsymbol{U}_p^n + \frac{\Delta t}{2} \frac{d}{dt} \boldsymbol{U}_p^n, \tag{3.93b}$$

$$\boldsymbol{F}_{pc}^{n+\frac{1}{2}} = \boldsymbol{F}_{pc}^n + \frac{\Delta t}{2} \frac{d}{dt} \boldsymbol{F}_{pc}^n. \tag{3.93c}$$

To achieve the above second-order time discretization it remains to compute the time derivatives of both nodal velocity and sub-cell force. This will be the main task of a next paragraph invoking the conservation principle of total energy. Regarding the time derivative of the corner normal, it will be computed using its geometric definition.

Discrete geometric conservation law

We show that the previous time discretization fulfills the discrete geometric conservation law (DGCL) [123, 51]. This means that the zone volume that is computed directly from its coordinates is equal to the zone volume that is deduced from solving the discrete volume equation (3.91a). This result is of first importance and shows the consistency of our cell-centered discretization. To demonstrate this, the change in coordinate zone volume $(\Delta v_c)^{\text{crd}}$ during the time step $\Delta t = t^{n+1} - t^n$, where the position vectors are incremented by an amount $\Delta \boldsymbol{x}_p = \boldsymbol{x}_p^{n+1} - \boldsymbol{x}_p^n$, $\forall\, p \in \mathcal{P}(c)$, is defined as

$$(\Delta v_c)^{\text{crd}} = v_c^{n+1} - v_c^n. \tag{3.94}$$

We compute the right-hand side of this equation using formula (3.55) page 78

$$(\Delta v_c)^{\text{crd}} = \frac{1}{2} \sum_{p \in \mathcal{P}(c)} \left[\boldsymbol{x}_p^{n+1} \times \boldsymbol{x}_{p^+}^{n+1} - \boldsymbol{x}_p^n \times \boldsymbol{x}_{p^+}^n \right] \cdot \boldsymbol{e}_z.$$

Replacing the expressions of the position vectors at time t^{n+1} and using the fact the sum is cyclic yields

$$(\Delta v_c)^{\text{crd}} = \sum_{p \in \mathcal{P}(c)} \left\{ \frac{1}{2} \left[\boldsymbol{x}_{p^+}^n - \boldsymbol{x}_{p^-}^n + \frac{1}{2} \left(\Delta \boldsymbol{x}_{p^+} - \Delta \boldsymbol{x}_{p^-} \right) \right] \times \boldsymbol{e}_z \right\} \cdot \Delta \boldsymbol{x}_p. \tag{3.95}$$

On the other hand, the change in volume deduced from the discrete volume equation (3.91a) writes

$$(\Delta v_c)^{\text{gcl}} = \sum_{p \in \mathcal{P}(c)} l_{pc}^{n+\frac{1}{2}} \boldsymbol{n}_{pc}^{n+\frac{1}{2}} \cdot \Delta \boldsymbol{x}_p, \tag{3.96}$$

since by the discrete trajectory equation (3.92), $\Delta \boldsymbol{x}_p = \Delta t \boldsymbol{U}_p^{n+\frac{1}{2}}$. The definition of the corner vector (3.57) page 79, and the definition of its time-centered discretization (3.93a) shows that

$$\left\{ \frac{1}{2} \left[\boldsymbol{x}_{p^+}^n - \boldsymbol{x}_{p^-}^n + \frac{1}{2} \left(\Delta \boldsymbol{x}_{p^+} - \Delta \boldsymbol{x}_{p^-} \right) \right] \times \boldsymbol{e}_z \right\} = l_{pc}^{n+\frac{1}{2}} \boldsymbol{n}_{pc}^{n+\frac{1}{2}}.$$

Hence, the zone volume computed from its coordinates and the zone volume that results from the discrete volume equation are rigorously equal.

Comment 11 *We have shown that the above second-order time discretization fulfills the discrete geometric conservation law (DGCL) [51]. This means that the zone volume that is computed directly from its coordinates is equal to the zone volume that is deduced from solving the discrete volume equation* (3.91a)*. This result is of first importance and shows the consistency of our cell-centered discretization. We point out that this property is not straightforward for usual two-dimensional staggered discretization [17] unless a special discretization is employed [100].*

Conservation principles

Let us investigate total energy conservation over the entire domain at the discrete level. To this end, we transpose at the discrete time level, the reasoning developed in Section 3.2.2 page 82. Recalling that total energy over the whole grid at time t^n is defined by $\mathcal{E}^n = \sum_c m_c E_c^n$, its conservation over the time interval $[t^n, t^{n+1}]$ writes as

$$\mathcal{E}^{n+1} - \mathcal{E}^n = -\int_{t^n}^{t^{n+1}} \int_{\partial\mathcal{D}} P\boldsymbol{U}\cdot\boldsymbol{n}\,\mathrm{d}s\,\mathrm{d}t,$$

where the right-hand side expresses the time rate of pressure work on the boundary, $\partial\mathcal{D}$, of the domain, $\mathcal{D}$, occupied by the fluid. By definition of total energy, this last equation rewrites

$$\sum_c m_c(E_c^{n+1} - E^n) = -\int_{t^n}^{t^{n+1}} \int_{\partial\mathcal{D}} P\boldsymbol{U}\cdot\boldsymbol{n}\,\mathrm{d}s\,\mathrm{d}t. \tag{3.97}$$

Introducing as before the boundary corner force acting onto point p yields

$$\boldsymbol{F}_p^\star(t) = \int_{\partial\mathcal{D}_p} P\boldsymbol{n}\,\mathrm{d}s.$$

Substituting the specific total energy equation (3.91c) into (3.97) leads to

$$\sum_c \sum_{p\in\mathcal{P}(c)} \boldsymbol{F}_{pc}^{n+\frac{1}{2}}\cdot\boldsymbol{U}_p^{n+\frac{1}{2}} = \sum_{p\in\partial\mathcal{D}} \boldsymbol{F}_p^{\star,n+\frac{1}{2}}\cdot\boldsymbol{U}_p^{n+\frac{1}{2}}. \tag{3.98}$$

where $\boldsymbol{F}_p^{\star,n+\frac{1}{2}}$ is a time-centered evaluation of the prescribed boundary force acting onto point p. This boundary force is expressed as

$$\boldsymbol{F}_p^{\star,n+\frac{1}{2}} = \boldsymbol{F}_p^{n,\star} + \frac{\Delta t}{2}\frac{d}{dt}\boldsymbol{F}_p^{n,\star}. \tag{3.99}$$

Here, $\boldsymbol{F}_p^{n,\star}$ denotes the value of the prescribed boundary force at time t^n whereas $\frac{\Delta t}{2}\frac{d}{dt}\boldsymbol{F}_p^{n,\star}$ represents its time derivative at time t^n. Interchanging the order of summation in the left-hand side of (3.98) yields

$$\sum_p \Big(\sum_{c\in\mathcal{C}(p)} \boldsymbol{F}_{pc}^{n+\frac{1}{2}}\Big)\cdot\boldsymbol{U}_p^{n+\frac{1}{2}} = \sum_{p\in\partial\mathcal{D}} \boldsymbol{F}_p^{\star,n+\frac{1}{2}}\cdot\boldsymbol{U}_p^{n+\frac{1}{2}},$$

where $\mathcal{C}(p)$ is the set of cells surrounding point p. Splitting the left-hand side of the above equation into two parts depending on the points location leads to

$$\sum_{p\in\mathcal{D}^o} \Big(\sum_{c\in\mathcal{C}(p)} \boldsymbol{F}_{pc}^{n+\frac{1}{2}}\Big)\cdot\boldsymbol{U}_p^{n+\frac{1}{2}} + \sum_{p\in\partial\mathcal{D}} \Big(\sum_{c\in\mathcal{C}(p)} \boldsymbol{F}_{pc}^{n+\frac{1}{2}}\Big)\cdot\boldsymbol{U}_p^{n+\frac{1}{2}} = \sum_{p\in\partial\mathcal{D}} \boldsymbol{F}_p^{\star,n+\frac{1}{2}}\cdot\boldsymbol{U}_p^{n+\frac{1}{2}}, \tag{3.100}$$

where $\mathcal{D}^o$ is the interior of the domain $\mathcal{D}$. The total energy conservation principle requires that the above equation must hold regardless the value of the nodal velocity. This amounts to state the following necessary and sufficient condition to have total energy conservation

$$\forall\, p \in \mathcal{D}^o, \quad \sum_{c\in\mathcal{C}(p)} \boldsymbol{F}_{pc}^{n+\frac{1}{2}} = \boldsymbol{0}, \tag{3.101a}$$

$$\forall\, p \in \partial\mathcal{D}, \quad \sum_{c\in\mathcal{C}(p)} \boldsymbol{F}_{pc}^{n+\frac{1}{2}} = \boldsymbol{F}_{p}^{\star,n+\frac{1}{2}}. \tag{3.101b}$$

Substituting the expression of the time-centered sub-cell force, $\boldsymbol{F}_{pc}^{n+\frac{1}{2}} = \boldsymbol{F}_{pc}^{n} + \frac{\Delta t}{2}\frac{d}{dt}\boldsymbol{F}_{pc}^{n}$ and invoking the fact that (3.101a) and (3.101b) must be satisfied regardless of the time step value leads to the following necessary and sufficient conditions that respectively determine the sub-cell force and its time derivative at time t^n

$$\forall\, p \in \mathcal{D}^o, \quad \sum_{c\in\mathcal{C}(p)} \boldsymbol{F}_{pc}^{n} = \boldsymbol{0}, \tag{3.102a}$$

$$\forall\, p \in \partial\mathcal{D}, \quad \sum_{c\in\mathcal{C}(p)} \boldsymbol{F}_{pc}^{n} = \boldsymbol{F}_{p}^{\star,n}. \tag{3.102b}$$

$$\forall\, p \in \mathcal{D}^o, \quad \sum_{c\in\mathcal{C}(p)} \frac{d}{dt}\boldsymbol{F}_{pc}^{n} = \boldsymbol{0}, \tag{3.103a}$$

$$\forall\, p \in \partial\mathcal{D}, \quad \sum_{c\in\mathcal{C}(p)} \frac{d}{dt}\boldsymbol{F}_{pc}^{n} = \frac{d}{dt}\boldsymbol{F}_{p}^{\star,n}. \tag{3.103b}$$

Condition (3.102) corresponds to the sub-cell forces balance at point p, whereas condition (3.103) represents the balance of the time derivative of the sub-cell forces acting onto point p. We claim that these conditions also provide momentum conservation over the entire domain, the proof is left to the reader.

Node-centered solver for the grid velocity at time t^n

For the high-order extension, the grid velocity at time t^n is obtained employing the following nodal extrapolation of the sub-cell force

$$\boldsymbol{F}_{pc}^{n} = l_{pc}^{n}\widetilde{P}_c(\boldsymbol{x}_p^n)\boldsymbol{n}_{pc}^{n} - \mathsf{M}_{pc}^{n}\left[\boldsymbol{U}_p^n - \widetilde{\boldsymbol{U}}_c(\boldsymbol{x}_p^n)\right], \tag{3.104}$$

where $\widetilde{P}_c = \widetilde{P}_c(\boldsymbol{x})$ and $\widetilde{\boldsymbol{U}}_c = \widetilde{\boldsymbol{U}}_c(\boldsymbol{x})$ denote some piecewise linear representations of the pressure and the velocity over the cell ω_c, which will be determined later. Knowing that M_{pc}^n is a 2×2 positive definite matrix, and using the conservation condition (3.102) leads to the 2×2 system that solves the nodal velocity $\boldsymbol{U}_p^n$

$$\forall\, p \in \mathcal{D}^o, \quad \mathsf{M}_p^n\boldsymbol{U}_p^n = \sum_{c\in\mathcal{C}(p)} \left[l_{pc}^{n}\widetilde{P}_c(\boldsymbol{x}_p^n)\boldsymbol{n}_{pc}^{n} + \mathsf{M}_{pc}^{n}\widetilde{\boldsymbol{U}}_c(\boldsymbol{x}_p^n)\right], \tag{3.105a}$$

$$\forall\, p \in \partial\mathcal{D}, \quad \mathsf{M}_p^n\boldsymbol{U}_p^n = \sum_{c\in\mathcal{C}(p)} \left[l_{pc}^{n}\widetilde{P}_c(\boldsymbol{x}_p^n)\boldsymbol{n}_{pc}^{n} + \mathsf{M}_{pc}^{n}\widetilde{\boldsymbol{U}}_c(\boldsymbol{x}_p^n)\right] - \boldsymbol{F}_{p}^{\star,n}, \tag{3.105b}$$

where M_p^n denotes the 2×2 node-centered matrix defined as

$$\mathsf{M}_p^n = \sum_{c \in \mathcal{C}(p)} \mathsf{M}_{pc}^n. \tag{3.106}$$

The nodal velocity determination has been divided into two cases depending on the node location. Noticing that M_p^n is positive definite, $\boldsymbol{U}_p^n$ is uniquely defined by solving systems (3.105a) and (3.105b). For the details concerning boundary conditions implementation and also the two examples of definition of the corner matrix, refer to Section 3.2.3 page 84.

Node-centered solver for the time derivative of the grid velocity at time t^n

In this paragraph we aim at describing the node-centered solver which allows to compute the time derivative of the grid velocity at time t^n. To this end, we shall use the conservation condition (3.103) that has been derived in the last paragraph. Knowing that the sub-cell force reads $\boldsymbol{F}_{pc} = l_{pc} P_c \boldsymbol{n}_{pc} - \mathsf{M}_{pc}(\boldsymbol{U}_p - \boldsymbol{U}_c)$, we time differentiate it using the chain rule

$$\frac{d}{dt}\boldsymbol{F}_{pc} = l_{pc}\boldsymbol{n}_{pc}\frac{d}{dt}P_c - \mathsf{M}_{pc}(\frac{d}{dt}\boldsymbol{U}_p - \frac{d}{dt}\boldsymbol{U}_c) + \frac{d}{dt}(l_{pc}\boldsymbol{n}_{pc})P_c - \frac{d}{dt}(\mathsf{M}_{pc})(\boldsymbol{U}_p - \boldsymbol{U}_c).$$

Here, we have assumed that all the variables that are involved in the sub-cell force expression are time-dependent. Regarding the corner matrix, this assumption is quite reasonable as the corner matrix, in the two examples given in Section 3.105 page 97, is expressed in terms of geometric quantities.

First, we compute the time derivative of the physical variables by writing the gas dynamics equations in non-conservative form using the variables $(P, \boldsymbol{U}, \eta)$

$$\frac{d}{dt}P + \rho a^2 \nabla \cdot \boldsymbol{U} = 0, \tag{3.107a}$$

$$\frac{d}{dt}\boldsymbol{U} + \frac{1}{\rho}\boldsymbol{\nabla} P = 0, \tag{3.107b}$$

$$\frac{d}{dt}\eta = 0, \tag{3.107c}$$

where a denotes the isentropic sound speed and η the specific entropy. We recall that for a sufficiently smooth flow these equations are equivalent to the conservative form of the gas dynamics equations, refer to [65]. By means of (3.107a) and (3.107b) we express the time derivative of pressure and velocity within cell c in terms of velocity divergence and pressure gradient

$$\frac{d}{dt}P_c = -\,\rho_c a_c^2 \left(\nabla \cdot \boldsymbol{U}\right)_c, \tag{3.108}$$

$$\frac{d}{dt}\boldsymbol{U}_c = -\,\frac{1}{\rho_c}\left(\boldsymbol{\nabla} P\right)_c. \tag{3.109}$$

We point out that $(\nabla \cdot \boldsymbol{U})_c$ and $(\boldsymbol{\nabla} P)_c$ stand for the averaged values over cell c of the velocity divergence and the pressure gradient, which will be computed in the next paragraph using a piecewise linear reconstruction based on a least squares approach.

Now, to achieve the computation of the time derivative of the sub-cell force it remains to express the time derivatives of the corner normal and the corner matrix. We recall that the corner normal and the corner matrix are expressed as functions of the normal vectors to the

two edges of cell c impinging at node p as follows

$$
\begin{aligned}
&l_{pc}\boldsymbol{n}_{cp} = l_{pc}^{-}\boldsymbol{n}_{pc}^{-} + l_{pc}^{+}\boldsymbol{n}_{pc}^{+},\\
&\mathsf{M}_{pc}^{\mathrm{GLACE}} = z_c l_{pc}\left(\boldsymbol{n}_{pc}\otimes\boldsymbol{n}_{pc}\right), \quad \text{GLACE scheme}\\
&\mathsf{M}_{pc}^{\mathrm{EUCCL}} = z_c\left[l_{pc}^{-}\left(\boldsymbol{n}_{pc}^{-}\otimes\boldsymbol{n}_{pc}^{-}\right) + l_{pc}^{+}\left(\boldsymbol{n}_{pc}^{+}\otimes\boldsymbol{n}_{pc}^{+}\right)\right], \quad \text{EUCCLHYD scheme}
\end{aligned}
$$

Here, $z_c = \rho_c a_c$ denotes the acoustic impedance. We recall that the normal vectors $l_{pc}^{-}\boldsymbol{n}_{pc}^{-}$, $l_{pc}^{+}\boldsymbol{n}_{pc}^{+}$ and $l_{pc}\boldsymbol{n}_{pc}$ are defined in terms of the position vectors as follows

$$
\begin{aligned}
l_{pc}^{-}\boldsymbol{n}_{pc}^{-} &= \frac{1}{2}\left(\boldsymbol{x}_p - \boldsymbol{x}_{p^-}\right)\times\boldsymbol{e}_z,\\
l_{pc}^{+}\boldsymbol{n}_{pc}^{+} &= \frac{1}{2}\left(\boldsymbol{x}_{p^+} - \boldsymbol{x}_p\right)\times\boldsymbol{e}_z,\\
l_{pc}\boldsymbol{n}_{pc} &= \frac{1}{2}\left(\boldsymbol{x}_{p^+} - \boldsymbol{x}_{p^-}\right)\times\boldsymbol{e}_z,
\end{aligned}
$$

where $\boldsymbol{e}_z = \boldsymbol{e}_x \times \boldsymbol{e}_y$. Thus, their corresponding time derivatives are given by

$$
\begin{aligned}
\frac{d}{dt}\left(l_{pc}^{-}\boldsymbol{n}_{pc}^{-}\right) &= \frac{1}{2}\left(\boldsymbol{U}_p - \boldsymbol{U}_{p^-}\right)\times\boldsymbol{e}_z,\\
\frac{d}{dt}\left(l_{pc}^{+}\boldsymbol{n}_{pc}^{+}\right) &= \frac{1}{2}\left(\boldsymbol{U}_{p^+} - \boldsymbol{U}_p\right)\times\boldsymbol{e}_z,\\
\frac{d}{dt}\left(l_{pc}\boldsymbol{n}_{pc}\right) &= \frac{1}{2}\left(\boldsymbol{U}_{p^+} - \boldsymbol{U}_{p^-}\right)\times\boldsymbol{e}_z.
\end{aligned}
$$

Regarding the two above expressions of the corner matrix, their time derivatives are computed following the chain rule

$$
\frac{d}{dt}\mathsf{M}_{pc}^{\mathrm{GLACE}} = z_c\left[\frac{d}{dt}\left(l_{pc}\boldsymbol{n}_{pc}\right)\otimes\boldsymbol{n}_{pc} + \left(l_{pc}\boldsymbol{n}_{pc}\right)\otimes\frac{d}{dt}\boldsymbol{n}_{pc}\right], \quad \text{GLACE scheme} \tag{3.110}
$$

$$
\frac{d}{dt}\mathsf{M}_{pc}^{\mathrm{EUCCL}} = z_c\sum_{\pm}\left[\frac{d}{dt}\left(l_{pc}^{\pm}\boldsymbol{n}_{pc}^{\pm}\right)\otimes\boldsymbol{n}_{pc}^{\pm} + \left(l_{pc}^{\pm}\boldsymbol{n}_{pc}^{\pm}\right)\otimes\frac{d}{dt}\boldsymbol{n}_{pc}^{\pm}\right]. \quad \text{EUCCLHYD scheme} \tag{3.111}
$$

We point out that the computation of the time derivative of the unit normals $\boldsymbol{n}_{pc}^{\pm}$ and $\boldsymbol{n}_{pc}$ is also required. It can be deduced quite easily using the previous formulas and the chain rule derivative as follows

$$
\frac{d}{dt}\boldsymbol{n}_{pc}^{\pm} = \frac{d}{dt}\left(\frac{l_{pc}^{\pm}\boldsymbol{n}_{pc}^{\pm}}{l_{pc}^{\pm}}\right).
$$

We remark that for both formulations we have not taken into account the time derivative of the acoustic impedance. This is due to the fact that acoustic impedance is just a multiplicative coefficient to get the correct physical dimension in the definition of the corner matrix. Combining the previous results, we write the time derivative of the sub-cell force at time t^n as

$$
\frac{d}{dt}\boldsymbol{F}_{pc}^{n} = -\rho_c^n (a_c^n)^2\left(\nabla\cdot\boldsymbol{U}\right)_c^n l_{pc}^n\boldsymbol{n}_{pc}^n - \mathsf{M}_{pc}^n\left[\frac{d}{dt}\boldsymbol{U}_p^n + \frac{1}{\rho_c^n}\left(\boldsymbol{\nabla}P\right)_c^n\right] + P_c^n\frac{d}{dt}(l_{pc}^n\boldsymbol{n}_{pc}^n) - \frac{d}{dt}(\mathsf{M}_{pc}^n)(\boldsymbol{U}_p^n - \boldsymbol{U}_c^n).
$$

Finally, substituting this last expression in the conservation condition (3.103a) we obtain the system satisfied by the time derivative of the nodal velocity for an interior node

$$
\begin{aligned}
\forall\, p\in\mathcal{D}^o, \quad \mathsf{M}_p^n\frac{d}{dt}\boldsymbol{U}_p^n = &-\sum_{c\in\mathcal{C}(p)}\frac{1}{\rho_c}\left[\mathsf{M}_{pc}^n\left(\boldsymbol{\nabla}P\right)_c^n + (z_c^n)^2 l_{pc}^n\boldsymbol{n}_{pc}^n\left(\nabla\cdot\boldsymbol{U}\right)_c^n\right]\\
&+\sum_{c\in\mathcal{C}(p)}\left[P_c^n\frac{d}{dt}(l_{pc}^n\boldsymbol{n}_{pc}^n) - \frac{d}{dt}(\mathsf{M}_{pc}^n)(\boldsymbol{U}_p^n - \boldsymbol{U}_c^n)\right].
\end{aligned} \tag{3.112}
$$

For a node located on the boundary, using (3.103b), we immediately get

$$\forall\, p \in \partial\mathcal{D}, \quad \mathsf{M}_p^n \frac{d}{dt}\boldsymbol{U}_p^n = -\sum_{c\in\mathcal{C}(p)} \frac{1}{\rho_c}\left[\mathsf{M}_{pc}^n\,(\boldsymbol{\nabla}P)_c^n + (z_c^n)^2 l_{pc}^n \boldsymbol{n}_{pc}^n\,(\nabla\cdot\boldsymbol{U})_c^n\right] + \sum_{c\in\mathcal{C}(p)}\left[P_c^n \frac{d}{dt}(l_{pc}^n\boldsymbol{n}_{pc}^n) - \frac{d}{dt}(\mathsf{M}_{pc}^n)(\boldsymbol{U}_p^n - \boldsymbol{U}_c^n)\right] - \frac{d}{dt}\boldsymbol{F}_p^{\star,n}. \tag{3.113}$$

As the matrix M_p^n is positive definite, the previous systems are invertible and thus provide always a unique time derivative for the nodal velocity. Concerning boundary conditions implementation for the time derivative of the grid velocity, we follow the methodology exposed previously computing the time derivative of the prescribed boundary force. To achieve the computation of the numerical fluxes, it remains to compute the averaged pressure gradient and velocity divergence within cell c using a piecewise monotonic linear reconstruction.

Comment 12 *Here, we have constructed a node-centered solver to compute the time derivatives of both grid velocity and sub-cell force. We point out that this solver has been derived using the sub-cell force framework. It is nothing but a two-dimensional extension of the acoustic GRP solver [21, 39].*

Piecewise monotonic linear reconstruction

To perform the piecewise linear monotone reconstruction of the pressure and velocity, we used a classical least squares procedure [16, 15], followed by a slope limitation procedure. Let $W \equiv W(\boldsymbol{x})$ denotes a fluid variable (pressure or velocity components), which has a piecewise linear representation in cell c defined by

$$\widetilde{W}_c(\boldsymbol{x}) = W_c + (\boldsymbol{\nabla}W)_c \cdot (\boldsymbol{x} - \boldsymbol{x}_c)\,, \tag{3.114}$$

where W_c is the mean value of W in cell c and $(\boldsymbol{\nabla}W)_c$ is the gradient of W that we are looking for. We note that $\boldsymbol{x}_c = \frac{1}{v_c}\int_{\omega_c}\boldsymbol{x}\,\mathrm{d}v$ is the cell centroid so that the reconstruction is conservative. The gradient in (3.114) is computed by imposing that

$$\widetilde{W}_c(\boldsymbol{x}_d) = W_d \quad \text{for } d \in \mathcal{C}(c),$$

where $\mathcal{C}(c)$ is the set of the neighboring cells of cell c. This problem is generally over-determined and thus this gradient is obtain by using a least squares procedure. Thus, it is the solution of the following minimization problem

$$(\boldsymbol{\nabla}W)_c = \mathrm{argmin}_{\boldsymbol{G}\in\mathbb{R}^2} \sum_{d\in\mathcal{C}(c)} \left[W_d - W_c - \boldsymbol{G}\cdot(\boldsymbol{x}_d - \boldsymbol{x}_c)\right]^2.$$

A straightforward computation shows that this solution is written

$$(\boldsymbol{\nabla}W)_c = \mathsf{M}_c^{-1} \sum_{d\in\mathcal{C}(c)} (W_d - W_c)\,(\boldsymbol{x}_d - \boldsymbol{x}_c)\,, \tag{3.115}$$

where M_c is the 2×2 matrix which reads

$$\mathsf{M}_c = \sum_{d\in\mathcal{C}(c)} (\boldsymbol{x}_d - \boldsymbol{x}_c)\otimes(\boldsymbol{x}_d - \boldsymbol{x}_c)\,.$$

We notice that M_c is symmetric positive definite and thus always invertible. **The main feature of this least squares procedure is that it is valid for any type of unstructured mesh**

and moreover it preserves the linear fields. This last point is particularly important in view of computing isentropic compression properly.

To preserve monotonicity, we limit the value that the gradient is allowed to take. For each cell, we introduce the slope limiter $\phi_c \in [0,1]$ and the limited reconstructed field as

$$\widetilde{W}_c^{\lim}(\boldsymbol{x}) = W_c + \phi_c(\boldsymbol{\nabla} W)_c \cdot (\boldsymbol{x} - \boldsymbol{x}_c)\,, \tag{3.116}$$

where $(\boldsymbol{\nabla} W)_c$ denotes the approximate gradient given by (3.115). The coefficient ϕ_c is determined by enforcing the following local monotonicity criterion

$$W_c^{\min} \leq \widetilde{W}_c^{\lim}(\boldsymbol{x}) \leq W_c^{\max}, \quad \forall \boldsymbol{x} \in c, \tag{3.117}$$

where we have set

$$W_c^{\min} = \min\left[\min_{d\in\mathcal{C}(c)}\{W_d\}, W_c\right] \quad \text{and} \quad W_c^{\max} = \max\left[\max_{d\in\mathcal{C}(c)}\{W_d\}, W_c\right].$$

Since the reconstructed field is linear we note that it is sufficient to enforce the following conditions at any point $p \in \mathcal{P}(c)$

$$W_c^{\min} \leq \widetilde{W}_c^{\lim}(\boldsymbol{x}_p) \leq W_c^{\max}, \tag{3.118}$$

so that the quantity W in the cell c does not lie outside the range of the average quantities in the neighboring cells. Thanks to this formula, we can define the slope limiter as

$$\phi_c = \min_{p\in\mathcal{P}(c)} \phi_{c,p}$$

knowing that

$$\phi_{c,p} = \begin{cases} \mu(\frac{W_c^{\max}-W_c}{\widetilde{W}_c(\boldsymbol{x}_p)-W_c}) & \text{if } \widetilde{W}_c(\boldsymbol{x}_p) - W_c > 0, \\ \mu(\frac{W_c^{\min}-W_c}{\widetilde{W}_c(\boldsymbol{x}_p)-W_c}) & \text{if } \widetilde{W}_c(\boldsymbol{x}_p) - W_c < 0, \\ 1 & \text{if } \widetilde{W}_c(\boldsymbol{x}_p) - W_c = 0. \end{cases}$$

Here, μ denotes a real valued function characterizing the limiter. By setting $\mu(x) = \min(1,x)$ we recover the Barth-Jespersen limiter which consists of the multi-dimensional extension [16] of the van Leer's classical method. We can also define a smoother -in the sense that it is more differentiable- limiter by setting $\mu(x) = \frac{x^2+2x}{x^2+x+2}$. This limiter has been introduced by Venkatakrishnan [162] in order to improve the convergence towards steady solutions for the Euler equations.

Comment 13 *These limiters are known to preserve two-dimensional linear fields provided that the neighboring cells whose cell-means are actually involved in the limiting are chosen in a good neighborhood. The characterization of such a neighborhood has been derived by Swartz in [155]. The definition is as follows: one has chosen a good neighborhood for a given central cell if and only if the convex hull of the centroids of its associated neighbors contains that central cell. We make such a choice in performing our limitation.*

We conclude this section by investigating the limitation procedure applied to the velocity field. We point out that the previous limiting algorithm has been developed for scalar variables. For vectors, limiting is usually applied separately to each component. However, such a procedure is frame dependent and thus leads to rotational symmetry distortion. Namely, component limiters do not preserve symmetry since a rotation of the coordinate axis produces different results. This drawback is crucial in the framework of Lagrangian hydrodynamics since we are dealing with

moving mesh discretizations which are particularly sensitive about symmetry loss. To correct this flaw, we have to construct a limiting procedure which is frame invariant for vectors. One possible choice is to use the Vector Image Polygon (VIP) methodology derived in [101, 102]. This method consists in constructing the VIP as the convex hull of the vector-space points corresponding to the neighbor vectors. If a slope-extrapolated vector lies inside the VIP, the slope is monotonicity preserving, otherwise, slope limiting is required. On the other hand, the slope is set to zero by analogy with the scalar case. Here, we describe an alternative procedure to perform a limitation of vector field which preserves rotational symmetry. First, let us introduce a piecewise linear representation of the velocity field

$$\widetilde{\boldsymbol{U}}_c(\boldsymbol{x}) = \boldsymbol{U}_c + (\boldsymbol{\nabla U})_c\,(\boldsymbol{x} - \boldsymbol{x}_c)\,, \tag{3.119}$$

where $(\boldsymbol{\nabla U})_c$ denotes the constant gradient tensor of the velocity field in cell c. This tensor has been obtained using the least squares procedure applied to each component. At this point, we define in each cell c the local orthonormal basis $(\boldsymbol{\xi}_c, \boldsymbol{\eta}_c)$ where $\boldsymbol{\xi}_c \times \boldsymbol{\eta}_c = \boldsymbol{e}_z$. This local basis must be frame invariant. Among the possible choices, we define it by using the eigenvectors of the right Cauchy-Green tensor related to the deformation that maps the two flow configurations between time t^n and time t^{n+1}, refer to (2.14) page 12 for the definition of this tensor. To define a limiter for the velocity slopes within cell c, we locally transform the Cartesian coordinates into coordinates given by the orthonormal basis $(\boldsymbol{\xi}_c, \boldsymbol{\eta}_c)$. The decomposition of the vector $\boldsymbol{V}$ in this basis reads $\boldsymbol{V} = V_\xi \boldsymbol{\xi}_c + V_\eta \boldsymbol{\eta}_c$, where $V_\xi = (\boldsymbol{V} \cdot \boldsymbol{\xi}_c)$ and $V_\eta = (\boldsymbol{V} \cdot \boldsymbol{\eta}_c)$. This can be rewritten under the more concise form

$$\begin{pmatrix} V_\xi \\ V_\eta \end{pmatrix} = \mathsf{A}_c \boldsymbol{V}, \quad \text{where} \quad \mathsf{A}_c = \begin{pmatrix} \xi_{c,x} & \xi_{c,y} \\ \eta_{c,x} & \eta_{c,y} \end{pmatrix}.$$

A straightforward computation shows that $\mathsf{A}_c \mathsf{A}_c^t = \mathsf{I}$, thus its inverse reads $\mathsf{A}_c^{-1} = \mathsf{A}_c^t$. Transforming $\boldsymbol{U}_c$ and (3.119) with respect to the local basis $(\boldsymbol{\xi}, \boldsymbol{\eta})$, and applying the scalar limitation procedure to the ξ and η components of the velocity field leads to define one slope limiter for each direction

$$\phi_{\xi,c} = \min_{p \in \mathcal{P}(c)} \phi_{\xi,c,p} \quad \text{and} \quad \phi_{\eta,c} = \min_{p \in \mathcal{P}(c)} \phi_{\eta,c,p}.$$

These slope limiters are given by

$$\phi_{\xi,c,p} = \begin{cases} \mu(\frac{U_{\xi,c}^{\max} - U_{\xi,c}}{U_{\xi,c,p} - U_{\xi,c}}) & \text{if } U_{\xi,c,p} - U_{\xi,c} > 0, \\ \mu(\frac{U_{\xi,c}^{\min} - U_{\xi,c}}{U_{\xi,c,p} - U_{\xi,c}}) & \text{if } U_{\xi,c,p} - U_{\xi,c} < 0, \\ 1 & \text{if } U_{\xi,c,p} - U_{\xi,c} = 0, \end{cases} \quad \phi_{\eta,c,p} = \begin{cases} \mu(\frac{U_{\eta,c}^{\max} - U_{\eta,c}}{U_{\eta,c,p} - U_{\eta,c}}) & \text{if } U_{\eta,c,p} - U_{\eta,c} > 0, \\ \mu(\frac{U_{\eta,c}^{\min} - U_{\eta,c}}{U_{\eta,c,p} - U_{\eta,c}}) & \text{if } U_{\eta,c,p} - U_{\eta,c} < 0, \\ 1 & \text{if } U_{\eta,c,p} - U_{\eta,c} = 0. \end{cases}$$

Here, $U_{\xi,c}^{\min\,/\,\max}$ and $U_{\eta,c}^{\min\,/\,\max}$ are the minimum and maximum value resulting from projections of the neighboring cells velocities onto the local directions. We have also set $\binom{U_{\xi,c}}{U_{\eta,c}} = \mathsf{A}_c \boldsymbol{U}_c$ and $\binom{U_{\xi,c,p}}{U_{\eta,c,p}} = \mathsf{A}_c \widetilde{\boldsymbol{U}}_c(\boldsymbol{x}_p)$. Finally, we transform this pair of limiters back into the Cartesian coordinates and conclude that the limited gradient tensor is

$$(\boldsymbol{\nabla U})_c^{\lim} = \Phi_c (\boldsymbol{\nabla U})_c, \tag{3.120}$$

where Φ_c is the 2×2 matrix which reads

$$\Phi_c = \mathsf{A}_c^t \begin{pmatrix} \phi_{\xi,c} & 0 \\ 0 & \phi_{\eta,c} \end{pmatrix} \mathsf{A}_c = \begin{pmatrix} \xi_{c,x}^2 \phi_{\xi,c} + \eta_{c,x}^2 \phi_{\eta,c} & \xi_{c,x}\xi_{c,y}\phi_{\xi,c} + \eta_{c,x}\eta_{c,y}\phi_{\eta,c} \\ \xi_{c,x}\xi_{c,y}\phi_{\xi,c} + \eta_{c,x}\eta_{c,y}\phi_{\eta,c} & \xi_{c,y}^2 \phi_{\xi,c} + \eta_{c,y}^2 \phi_{\eta,c} \end{pmatrix}.$$

Thus, the limited velocity field reconstruction within cell c writes as

$$\widetilde{\boldsymbol{U}}_c^{\lim}(\boldsymbol{x}) = \boldsymbol{U}_c + \Phi_c(\boldsymbol{\nabla}\boldsymbol{U})_c\,(\boldsymbol{x}-\boldsymbol{x}_c)\,. \tag{3.121}$$

We claim that we have defined a tensorial limitation procedure for the velocity vector which is frame invariant and thus preserves rotational symmetry.

An heuristic justification for the nodal extrapolation

In deriving the node-centered solver, we have employed the node-extrapolated values of the piecewise reconstructed pressure and velocity to define the sub-cell force, refer to (3.104) page 97. This nodal extrapolation is quite unusual in the context of high-order finite volume methods. In what follows, we give an heuristic justification to illustrate the relevancy of such an extrapolation. First, we recall that the sub-cell force at time t^n reads

$$\boldsymbol{F}_{pc}^n = l_{pc}^n \widetilde{P}_c(\boldsymbol{x}_p^n)\boldsymbol{n}_{pc}^n - \mathsf{M}_{pc}^n\left[\boldsymbol{U}_p^n - \widetilde{\boldsymbol{U}}_c(\boldsymbol{x}_p^n)\right],$$

where $\widetilde{P}_c(\boldsymbol{x}_p^n)$ and $\widetilde{\boldsymbol{U}}_c(\boldsymbol{x}_p^n)$ are the node-extrapolated values of the pressure and velocity. Let us introduce $\boldsymbol{F}_{pc}^{n,\mathrm{pres}} = l_{pc}^n \widetilde{P}_c(\boldsymbol{x}_p^n)\boldsymbol{n}_{pc}^n$, which corresponds to the pressure contribution to the sub-cell force. Recalling that the piecewise linear representation of the pressure writes as

$$\widetilde{P}_c(\boldsymbol{x}) = P_c^n + (\boldsymbol{\nabla}P)_c^n \cdot (\boldsymbol{x}-\boldsymbol{x}_c^n),$$

let us compute the sum of the pressure contribution to the sub-cell force

$$\sum_{p\in\mathcal{P}(c)} \boldsymbol{F}_{pc}^{n,\mathrm{pres}} = \sum_{p\in\mathcal{P}(c)} l_{pc}^n P_c^n \boldsymbol{n}_{pc}^n + \sum_{p\in\mathcal{P}(c)} l_{pc}^n (\boldsymbol{\nabla}P)_c^n \cdot (\boldsymbol{x}_p^n - \boldsymbol{x}_c^n)\boldsymbol{n}_{pc}^n.$$

Note that the first term in the right-hand side cancels owing to the geometric identity (3.59) page 79. Using the definition of the dyadic product, refer to (A.1) page 213, The second term can be recast as

$$\sum_{p\in\mathcal{P}(c)} \boldsymbol{F}_{pc}^{n,\mathrm{pres}} = (\sum_{p\in\mathcal{P}(c)} l_{pc}\boldsymbol{n}_{pc}\otimes\boldsymbol{x}_p)(\boldsymbol{\nabla}P)_c.$$

In writing this last equation, we have dropped the superscript n for the sake of simplicity. The contribution of the centroid position vector cancels owing to geometric identity (3.59) page 79. It remains to compute the tensor between parentheses. To this end, we recall that

$$l_{pc}\boldsymbol{n}_{pc}\otimes\boldsymbol{x}_p = \frac{1}{2}\begin{pmatrix}(y_p-y_{p^-})x_p & (y_p-y_{p^-})y_p\\ -(x_p-x_{p^-})x_p & -(x_p-x_{p^-})y_p\end{pmatrix} + \frac{1}{2}\begin{pmatrix}(y_{p^+}-y_p)x_p & (y_{p^+}-y_p)y_p\\ -(x_{p^+}-x_p)x_p & -(x_{p^+}-x_p)y_p\end{pmatrix}.$$

Shifting the indices $p\to p^+$ and $p^-\to p$ in the first term of the summation leads to

$$\sum_{p\in\mathcal{P}(c)} l_{pc}\boldsymbol{n}_{pc}\otimes\boldsymbol{x}_p = \begin{pmatrix}\frac{1}{2}\displaystyle\sum_{p\in\mathcal{P}(c)}(y_{p^+}-y_p)(x_p+x_{p^+}) & 0\\ 0 & -\frac{1}{2}\displaystyle\sum_{p\in\mathcal{P}(c)}(x_{p^+}-x_p)(y_p+y_{p^+})\end{pmatrix}.$$

We achieve the computation by noticing that

$$v_c = \frac{1}{2}\sum_{p\in\mathcal{P}(c)}(y_{p^+}-y_p)(x_p+x_{p^+}) = -\frac{1}{2}\sum_{p\in\mathcal{P}(c)}(x_{p^+}-x_p)(y_p+y_{p^+}),$$

where v_c denotes the volume of the cell. It turns out that we have demonstrated the following tensorial identity

$$\sum_{p\in\mathcal{P}(c)} l_{pc}\boldsymbol{n}_{pc}\otimes\boldsymbol{x}_p = v_c\mathsf{I}_d, \tag{3.122}$$

which is valid for any polygonal cell. Here, I_d is the unit tensor of $\mathbb{R}^2$. Finally, we obtain

$$\sum_{p\in\mathcal{P}(c)} \boldsymbol{F}_{pc}^{n,\text{pres}} = v_c(\boldsymbol{\nabla}P)_c, \tag{3.123}$$

which shows the consistency of the pressure contribution to the sub-cell force with the pressure gradient. This consistency results from the tensorial identity (3.122) and from the choice of having utilized a nodal extrapolation. Note that the above tensorial identity has been also derived in a more general framework in [48], it is one of the main ingredients to show the weak consistency of the GLACE scheme.

GRP algorithm for the two-dimensional Lagrangian scheme

Here, we summarize the GRP algorithm corresponding to the high-order discretization of our two-dimensional cell-centered Lagrangian scheme in its abstract formulation. The physical variables and the geometry are given at time t^n.

Step 0. Construct a piecewise monotonic linear representation of the velocity field and the pressure over the cell ω_c^n at time t^n

$$\begin{aligned}\widetilde{\boldsymbol{U}}_c^{\lim}(\boldsymbol{x}) &= \boldsymbol{U}_c^n + \Phi_c(\nabla\boldsymbol{U})_c^n\cdot(\boldsymbol{x}-\boldsymbol{x}_c^n),\\ \widetilde{P}_c^{\lim}(\boldsymbol{x}) &= P_c^n + \Phi_c(\boldsymbol{\nabla}P)_c^n\cdot(\boldsymbol{x}-\boldsymbol{x}_c^n),\end{aligned}$$

where $\boldsymbol{x}_c^n$ denotes the centroid of ω_c^n, $(\nabla\boldsymbol{U})_c^n$ and $(\boldsymbol{\nabla}P)_c^n$ are respectively the velocity and the pressure gradient in ω_c^n whereas Φ_c and Φ_c denote their respective slope limiters.

Step 1. Compute the nodal velocity $\boldsymbol{U}_p^n$ and the sub-cell force $\boldsymbol{F}_{cp}^n$ by means of the node-centered solver

$$\begin{aligned}\boldsymbol{U}_p^n &= (\mathsf{M}_p^n)^{-1}\sum_{c\in\mathcal{C}(p)}\left[l_{pc}^n\widetilde{P}_c^{\lim}(\boldsymbol{x}_p^n)\boldsymbol{n}_{pc}^n + \mathsf{M}_{pc}^n\widetilde{\boldsymbol{U}}_c^{\lim}(\boldsymbol{x}_p^n)\right],\\ \boldsymbol{F}_{pc}^n &= l_{pc}^n\widetilde{P}_c^{\lim}(\boldsymbol{x}_p^n)\boldsymbol{n}_{pc}^n - \mathsf{M}_{pc}^n\left[\boldsymbol{U}_p^n - \widetilde{\boldsymbol{U}}_c^{\lim}(\boldsymbol{x}_p^n)\right].\end{aligned}$$

Here, the superscript n is used for geometric quantities such as lengths and unit normals to emphasize that they are evaluated at time t^n. We note that the input data for the nodal solver are the extrapolated pressure and velocity at node p. In addition, we recall that $\mathsf{M}_p^n = \sum_{c\in\mathcal{C}(p)}\mathsf{M}_{pc}^n$.

Step 2. Compute the time derivatives of nodal velocity and sub-cell force, $\frac{d}{dt}\boldsymbol{U}_p^n$, $\frac{d}{dt}\boldsymbol{F}_{pc}^n$, by

means of the node-centered solver for the time derivatives

$$\frac{d}{dt}\boldsymbol{U}_p^n = -(\mathsf{M}_p^n)^{-1}\sum_{c\in\mathcal{C}(p)}\frac{1}{\rho_c}\left[\mathsf{M}_{pc}^n\left(\boldsymbol{\nabla}P\right)_c^n + (z_c^n)^2 l_{pc}^n \boldsymbol{n}_{pc}^n\left(\nabla\cdot\boldsymbol{U}\right)_c^n\right]$$
$$+ (\mathsf{M}_p^n)^{-1}\sum_{c\in\mathcal{C}(p)}\left[P_c^n\frac{d}{dt}(l_{pc}^n\boldsymbol{n}_{pc}^n) - \frac{d}{dt}\mathsf{M}_{pc}^n(\boldsymbol{U}_p^n - \boldsymbol{U}_c^n)\right],$$

$$\frac{d}{dt}\boldsymbol{F}_{pc}^n = -\rho_c^n(a_c^n)^2\left(\nabla\cdot\boldsymbol{U}\right)_c^n l_{pc}^n\boldsymbol{n}_{pc}^n - \mathsf{M}_{pc}^n\left[\frac{d}{dt}\boldsymbol{U}_p^n + \frac{1}{\rho_c^n}\left(\boldsymbol{\nabla}P\right)_c^n\right]$$
$$+ P_c^n\frac{d}{dt}(l_{pc}^n\boldsymbol{n}_{pc}^n) - \frac{d}{dt}(\mathsf{M}_{pc}^n)(\boldsymbol{U}_p^n - \boldsymbol{U}_c^n).$$

Deduce from this the computation of the time-centered values

$$\boldsymbol{U}_p^{n+\frac{1}{2}} = \boldsymbol{U}_p^n + \frac{\Delta t}{2}\frac{d}{dt}\boldsymbol{U}_p^n,$$
$$\boldsymbol{F}_{pc}^{n+\frac{1}{2}} = \boldsymbol{F}_{pc}^n + \frac{\Delta t}{2}\frac{d}{dt}\boldsymbol{F}_{pc}^n.$$

Step 3. Compute the motion of the mesh thanks to the discrete kinematic equation

$$\boldsymbol{x}_p^{n+1} - \boldsymbol{x}_p^n = \Delta t\boldsymbol{U}_p^{n+\frac{1}{2}},$$

and update the geometrical quantities. Then, evaluate the new cell averages $(\frac{1}{\rho_c^{n+1}}, \boldsymbol{U}_c^{n+1}, E_c^{n+1})$ using the updating formulas

$$m_c\left(\frac{1}{\rho_c^{n+1}} - \frac{1}{\rho_c^n}\right) - \Delta t\sum_{p\in\mathcal{P}(c)} l_{pc}^{n+\frac{1}{2}}\boldsymbol{n}_{pc}^{n+\frac{1}{2}}\cdot\boldsymbol{U}_p^{n+\frac{1}{2}} = 0,$$
$$m_c\left(\boldsymbol{U}_c^{n+1} - \boldsymbol{U}_c^n\right) + \Delta t\sum_{p\in\mathcal{P}(c)}\boldsymbol{F}_{pc}^{n+\frac{1}{2}} = \boldsymbol{0},$$
$$m_c\left(E_c^{n+1} - E_c^n\right) + \Delta t\sum_{p\in\mathcal{P}(c)}\boldsymbol{F}_{pc}^{n+\frac{1}{2}}\cdot\boldsymbol{U}_p^{n+\frac{1}{2}} = 0.$$

Finally, compute the new thermodynamic state as $P_c^{n+1} = P(\rho_c^{n+1}, \varepsilon_c^{n+1})$, where $\varepsilon_c^{n+1} = E_c^{n+1} - \frac{1}{2}\mid\boldsymbol{U}_c^{n+1}\mid^2$.

3.2.5 Practical issues

Treatment of exceptional points

Exceptional points are grid points at the termination of lines internal to the computational domain, and where boundary conditions are therefore not applied, refer to Figure 3.11. These points occur naturally in most applications in order to improve spatial grid anisotropy, and the consequent time step reduction, that will otherwise arise for grids with highly tapered regions or at a center of convergence. In the framework of compatible staggered Lagrangian hydrodynamics, a specific treatment has been successfully introduced in [99] to deal with exceptional points. Here, we present the methodology that we have developed for our cell-centered compatible discretization. Before we proceed any further, we investigate the capability of the EUCCLHYD node-centered solver to handle such exceptional point without any special treatment. To this

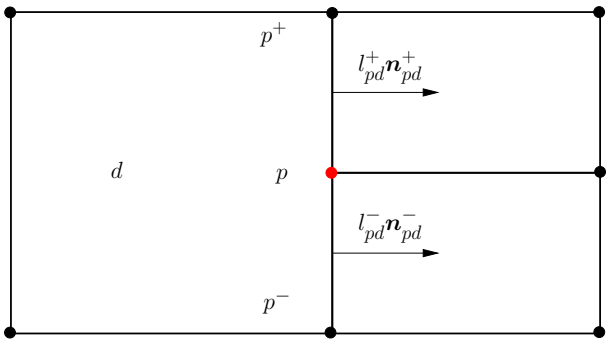

Figure 3.11: Fragment of a grid that containing an exceptional point displayed using red color.

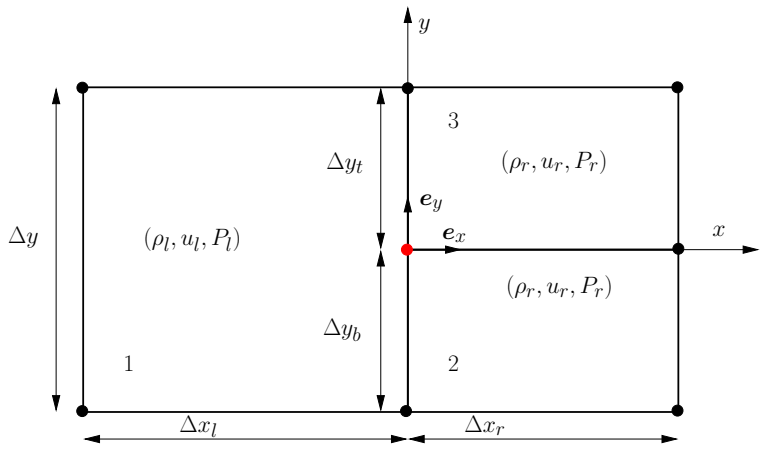

Figure 3.12: Exceptional point located at the origin and surrounded by three cells.

end, let us consider the case of an exceptional point located at the origin and surrounded by three cells as displayed in Figure 3.12. The left-side cell is a degenerate pentagon characterized by a flat angle at the vertex which corresponds to the exceptional point. The right-side cells are two rectangles. We assume that the initial fluid flow around the origin is defined by the state (ρ_l, u_l, P_l) on the left side of the interface $y = 0$ and the state (ρ_r, u_r, P_r) on its right side. u_l and u_r denote the x components of the one-dimensional velocity field. The three cells around the origin are labelled from 1 to 3 in the counterclockwise order. With these notations the half-edge outward normals write

$$
\begin{aligned}
l_1^- \boldsymbol{n}_1^- &= \frac{\Delta y_b}{2}\begin{pmatrix}1\\0\end{pmatrix}, \quad l_1^+ \boldsymbol{n}_1^+ = \frac{\Delta y_t}{2}\begin{pmatrix}1\\0\end{pmatrix},\\
l_2^- \boldsymbol{n}_2^- &= \frac{\Delta x_r}{2}\begin{pmatrix}0\\1\end{pmatrix}, \quad l_2^+ \boldsymbol{n}_2^+ = \frac{\Delta y_b}{2}\begin{pmatrix}-1\\0\end{pmatrix},\\
l_3^- \boldsymbol{n}_3^- &= \frac{\Delta y_t}{2}\begin{pmatrix}-1\\0\end{pmatrix}, \quad l_3^+ \boldsymbol{n}_3^+ = \frac{\Delta x_r}{4}\begin{pmatrix}0\\-1\end{pmatrix}.
\end{aligned}
$$

Recalling that the corner matrices are defined by $\mathsf{M}_i = z_i[l_i^-(\boldsymbol{n}_i^- \otimes \boldsymbol{n}_i^-) + l_i^+(\boldsymbol{n}_i^+ \otimes \boldsymbol{n}_i^+)]$, $i = 1 \ldots 3$, where $z_1 = z_l$ and $z_2 = z_3 = z_r$, we compute the velocity of the exceptional point by solving the linear system

$$
\mathsf{M}_O \boldsymbol{U}_O = \sum_{i=1}^{3} l_i \boldsymbol{n}_i P_i + \mathsf{M}_i \boldsymbol{U}_i,
$$

where $\mathsf{M}_O = \sum_{i=1}^{3} \mathsf{M}_i$, $l_i \boldsymbol{n}_i = l_i^- \boldsymbol{n}_i^- + l_i^+ \boldsymbol{n}_i^+$, $P_1 = P_r$, $P_2 = P_3 = P_r$, $\boldsymbol{U}_1 = u_l \boldsymbol{e}_x$ and $\boldsymbol{U}_2 = \boldsymbol{U}_3 = u_r \boldsymbol{e}_x$. With this set up, after some elementary algebra one gets

$$\boldsymbol{U}_O = \left(\frac{z_l u_l + z_r u_r}{z_l + z_r} - \frac{P_r - P_l}{z_l + z_r} \right) \boldsymbol{e}_x.$$

This is exactly the interface velocity that one would obtain using the one-dimensional acoustic solver. This shows the ability of the EUCCLHYD solver to deal with exceptional point in case of one-dimensional flows without any special treatment. However, in case of two-dimensional flows, one has to implement a special treatment to these exceptional points to prevent the occurrence of distorted polygonal cells. Generally, this special treatment consists in enslaving their velocity to that of their neighboring points in order to prevent large excursions of the numerical solution about them. We describe hereafter the special procedure applied within the node-centered solver to take into account exceptional point. Let us consider an exceptional point surrounded by three cells as displayed in Figure 3.11. Let p denotes the exceptional point and d the corresponding pentagonal cell. The two neighboring points to p are p^- and p^+ in the counterclockwise order with respect to cell d. We introduce the vectors $l_{pd}^- \boldsymbol{n}_{pd}^-$ and $l_{pd}^+ \boldsymbol{n}_{pd}^+$, which are half-edge outward normals to the edges impinging at point p. The sum of these two vectors is the corner normal associated to point p and cell d, which reads $l_{pd} \boldsymbol{n}_{pd}$. The fact that the sum of the corner normals surrounding point p is equal to zero yields

$$\sum_{c \in \mathcal{C}(p) \setminus d} l_{pc} \boldsymbol{n}_{pc} + l_{pd} \boldsymbol{n}_{pd} = \boldsymbol{0}, \tag{3.124}$$

where $\mathcal{C}(p)$ is the set of cells surrounding point p. We assume that the velocity of the regular points has been already computed using the standard node-centered solver. In particular, velocities of the two neighboring points to p are known and we denote them $\boldsymbol{U}_{p^-}$ and $\boldsymbol{U}_{p^+}$. Point p differs from regular points in the sense that it is not a dynamical point. Namely, its motion is enslaved to the motion of its neighboring points. Thus, the normal velocity of the exceptional point is obtained by means of a linear interpolation of the normal velocity of its neighbors, as follows

$$l_{pd} \boldsymbol{n}_{pd} \cdot \boldsymbol{U}_p = l_{pd}^- \boldsymbol{n}_{pd}^- \cdot \boldsymbol{U}_{p^-} + l_{pd}^+ \boldsymbol{n}_{pd}^+ \cdot \boldsymbol{U}_{p^+}. \tag{3.125}$$

This means that point p can only slide along segment $[p^-, p^+]$. We remark that this scalar equation is not sufficient to determine the velocity of point p. To this end, we have to write the necessary and sufficient condition that provides total energy and momentum conservation. This condition writes as follows

$$\sum_{c \in \mathcal{C}(p) \setminus d} \boldsymbol{F}_{pc} = \boldsymbol{F}_p^\star, \tag{3.126}$$

where $\boldsymbol{F}_{pc} = l_{pc} P_c \boldsymbol{n}_{pc} - \mathsf{M}_{pc}(\boldsymbol{U}_p - \boldsymbol{U}_c)$ is the standard sub-cell force acting from cell $c \in \mathcal{C}(p) \setminus d$ onto point p and $\boldsymbol{F}_p^\star$ is an exceptional force acting from cell d to point p which enforces the enslavement of point p to the edge $[p^-, p^+]$. This latter force is expressed in terms of the exceptional nodal pressure $\Pi_p^\star$ as follows

$$\boldsymbol{F}_p^\star = -l_{pd} \boldsymbol{n}_{pd} \Pi_p^\star. \tag{3.127}$$

This unknown extra pressure can be viewed as an average pressure which enslaves point p. The combination of the previous equations leads to the 3×3 system satisfied by the nodal velocity and pressure

$$\mathsf{M}_p \boldsymbol{U}_p + \Big(\sum_{c \in \mathcal{C}(p) \setminus d} l_{pc} \boldsymbol{n}_{pc} \Big) \Pi_p^\star = \sum_{c \in \mathcal{C}(p) \setminus d} (l_{pc} \boldsymbol{n}_{pc} P_c + \mathsf{M}_{pc} \boldsymbol{U}_c), \tag{3.128a}$$

$$\Big(\sum_{c \in \mathcal{C}(p) \setminus d} l_{pc} \boldsymbol{n}_{pc} \Big) \cdot \boldsymbol{U}_p = -l_{pd}^- \boldsymbol{n}_{pd}^- \cdot \boldsymbol{U}_{p^-} - l_{pd}^+ \boldsymbol{n}_{pd}^+ \cdot \boldsymbol{U}_{p^+}, \tag{3.128b}$$

where $\mathsf{M}_p = \sum_{c\in\mathcal{C}(p)\setminus d} \mathsf{M}_{pc}$ is symmetric positive definite. This system has always a unique solution as its matrix written below in block form

$$\begin{pmatrix} \mathsf{M}_p & \displaystyle\sum_{c\in\mathcal{C}(p)\setminus d} l_{pc}\boldsymbol{n}_{pc} \\ \displaystyle\sum_{c\in\mathcal{C}(p)\setminus d} l_{pc}\boldsymbol{n}_{pc} & 0 \end{pmatrix}$$

is a 3×3 symmetric positive definite matrix. We note that this system is quite similar to the system (3.76) derived for the boundary condition corresponding to a prescribed normal velocity. This is not a surprise since the method we have employed to deal with the exceptional point amounts to prescribe an internal boundary condition.

Time step control

For numerical applications, the time step is evaluated following two criteria. The first one is a standard CFL criterion. The second one is more intuitive, but reveals very useful in practice: we limit the variation of the volume of cells over one time step.

CFL criterion We propose a CFL like criterion in order to ensure a positive entropy production in cell c during the time step. At time t_n, for each cell c we denote by λ_c^n the minimal value of the distance between two points of the cell. We define

$$\Delta t_e = C_e \min_c \frac{\lambda_c^n}{a_c^n},$$

where C_e is a strictly positive coefficient and a_c is the sound speed in the cell. The coefficient C_e is computed heuristically and we provide no rigorous analysis which allows such formula. However, extensive numerical experiments show that $C_e = 0.25$ is a value which provides stable numerical results. The rigorous derivation of this criterion can be obtained by computing the time step which ensures a positive entropy production in cell c during the time interval $[t^n, t^{n+1}]$. This task can be achieved employing a two-dimensional generalization of the one-dimensional analysis which has been performed in Section 3.1.7 page 70.

Criterion on the volume variation We estimate the volume of cell c at $t = t^{n+1}$ using the Taylor expansion

$$v_c^{n+1} = v_c^n + \frac{d}{dt} v_c(t^n)\Delta t.$$

Here, the time derivative $\frac{d}{dt}v_c$ is computed by using (3.58) page 79. Let C_v be a positive coefficient, $C_v \in]0,1[$. We look for Δt such that

$$\frac{|v_c^{n+1} - v_c^n|}{v_c^n} \leq C_v.$$

To this end, let us define

$$\Delta t_v = C_v \min_c \left\{ \frac{v_c^n}{|\frac{d}{dt} v_c(t^n)|} \right\}.$$

For numerical applications, we choose $C_v = 0.1$. Last, the estimation of the next time step Δt^{n+1} is given by

$$\Delta t^{n+1} = \min\left(\Delta t_e, \Delta t_v, C_m \Delta t^n\right), \tag{3.129}$$

where Δt^n is the current time step and C_m is a multiplicative coefficient which allows the time step to increase. We generally set $C_m = 1.01$.

3.3 Numerical tests in two-dimensional Cartesian geometry

In this section, we perform several numerical tests to assess the robustness and the accuracy of the schemes presented previously. Almost all the simulations are run using a perfect gas EOS written under the form $P = (\gamma - 1)\rho\varepsilon$, where γ denotes the polytropic index. First, we present a comparison between first-order GLACE and EUCCLHYD discretizations to highlight their respective strength and weakness on demanding test cases representative of strongly compressible fluid flows. Then, we run the high-order discretization of EUCCLHYD scheme to evaluate its performance on several well known test cases such as Sod, Sedov, Saltzman and Noh problems.

3.3.1 Comparison between first-order GLACE and EUCCLHYD discretizations

In this section, all problems are running with the first-order GLACE and EUCCLHYD discretizations using a purely acoustic node-centered solver.

Checkerboard problem

This test case, which is taken from [136], aims at assessing the sensitivity of both formulations to hourglass instability. The initial domain $[0,1] \times [0,1]$ is paved with 10×10 square cells. The initial thermodynamic conditions are characterized by $(\rho^0, P^0) = (1, 1)$ and a polytropic index $\gamma = \frac{5}{3}$. Let (i, j) denote the logical coordinates of a generic cell of the mesh, the indices i and j are ranging from 1 to 10. The initial velocity field corresponding to the cell labelled (i, j) is set to $\boldsymbol{U}^0_{i,j} = [(-1)^{i+j}, 0]$. The stopping time is $t_{\text{final}} = 1$ and we use a constant time step $\Delta t = 10^{-2}$. The map of the x-component of the initial velocity field is displayed in Figure 3.13 (left). We have also displayed the x-component of the velocity field and the grid obtained after 5 time steps for GLACE scheme. We remark that for this scheme the initial x-velocity perturbation has triggered an hourglass pattern in y direction which cannot be damped. On the other hand, we observe on Figure 3.14 (left) that EUCCLHYD scheme has damped this initial x-velocity perturbation. After 100 time steps, refer to Figure 3.14 (right), the x-velocity has almost vanished due to the dissipation of kinetic energy into internal energy. This simple test case, shows the great sensitivity of the GLACE scheme to hourglass instability. It also demonstrates the ability of EUCCLHYD scheme to damp consistently such instabilities. The discrepancy between these two schemes is strongly related to their entropy production.

Sedov problem on a Cartesian grid

We consider the Sedov problem for a point-blast in a uniform medium with cylindrical symmetry. An exact solution based on self-similarity arguments is available, see for instance [74]. The initial conditions are characterized by $(\rho^0, P^0, \boldsymbol{U}^0) = (1, 10^{-6}, \boldsymbol{0})$ and the polytropic index is set equal to $\frac{7}{5}$. We set an initial delta-function energy source at the origin prescribing the pressure in the cell containing the origin as follows

$$P_{\text{or}} = (\gamma - 1)\rho_{\text{or}} \frac{\mathcal{E}^0}{v_{\text{or}}},$$

where v_{or} denotes the volume of the cell that contains the origin and $\mathcal{E}^0$ is the total amount of released energy. By choosing $\mathcal{E}^0 = 0.244816$, as it is suggested in [74], the solution consists of a diverging shock whose front is located at radius $R = 1$ at time $t = 1$. Knowing that for an infinite strength shock wave the density ratio tends to $\frac{\gamma+1}{\gamma-1}$, refer to Appendix B page 221, we deduce that the peak density reaches the value 6. The initial domain, $[0, 1.2] \times [0, 1.2]$,

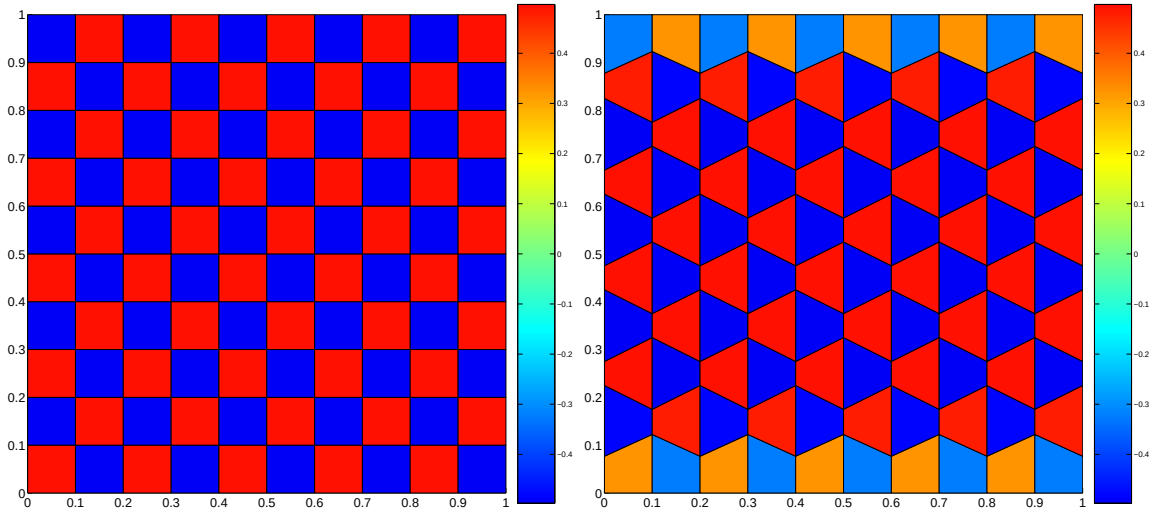

Figure 3.13: Checkerboard problem. Grid and map of the x-component of the velocity field at initial time (left) and after 5 time steps for GLACE scheme (right).

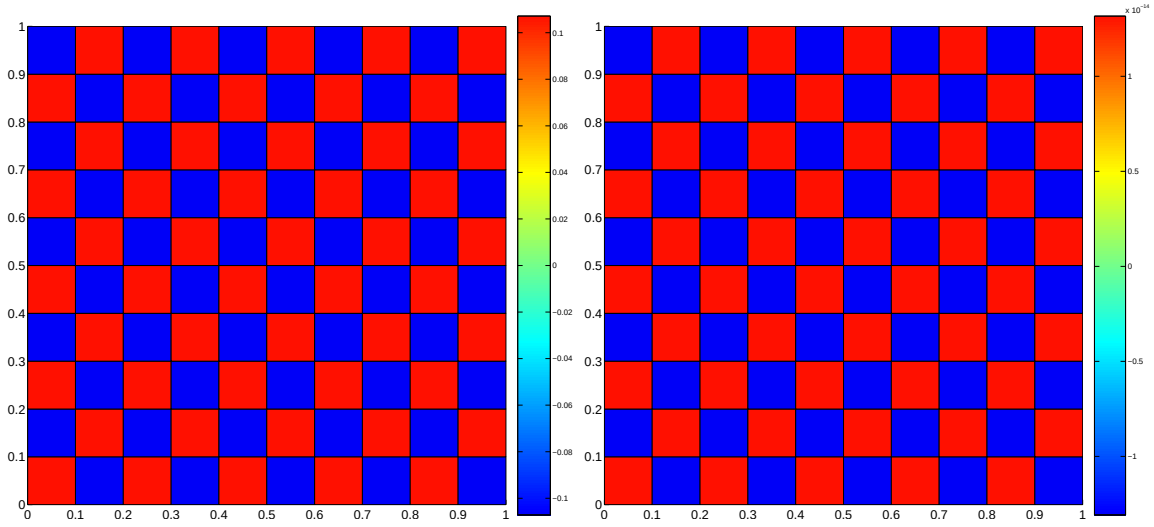

Figure 3.14: Checkerboard problem. Grid and map of the x-component of the velocity field for EUCCLHYD scheme after 5 time steps (left) and after 100 time steps (right).

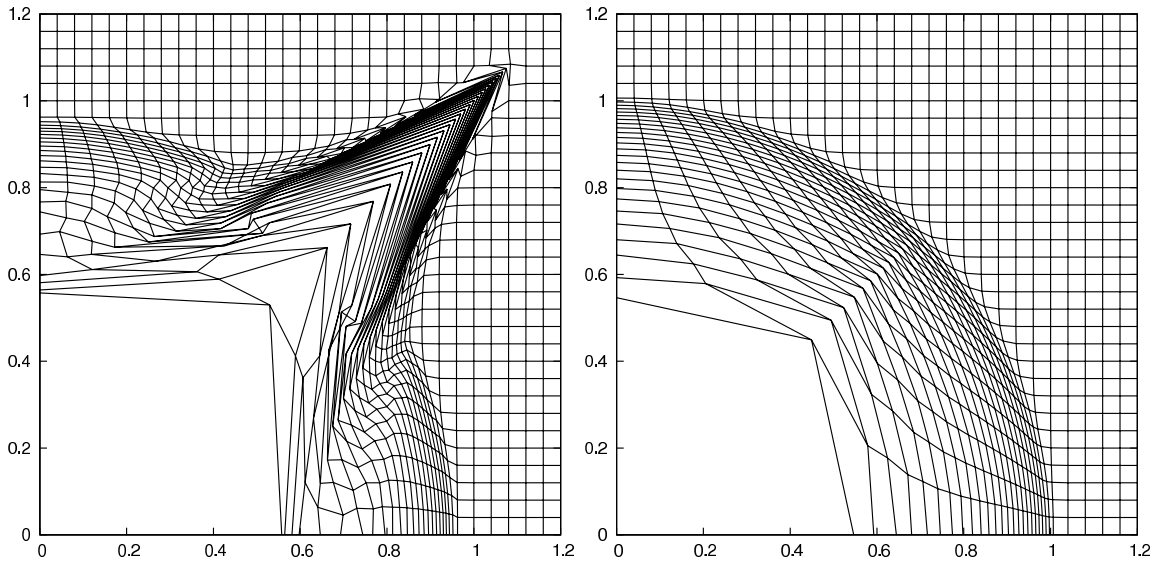

Figure 3.15: Sedov problem on Cartesian grid. Grids at final time for first-order GLACE scheme (left) and EUCCLHYD scheme (right).

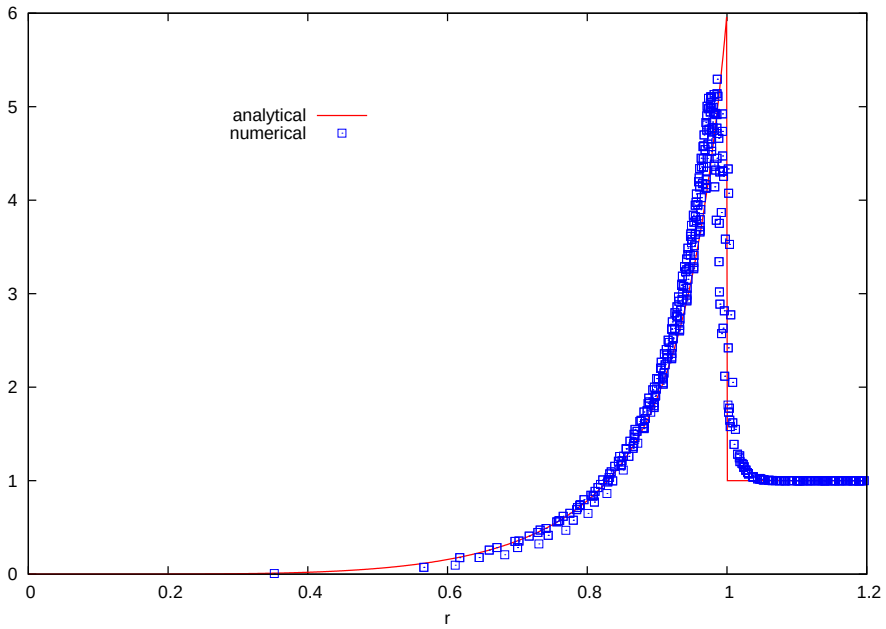

Figure 3.16: Sedov problem on Cartesian grid. Density in all the cells as functions of the cell-center radius at final time for first-order EUCCLHYD scheme.

is paved using 30×30 equally space zones. We have displayed in Figure 3.15 the grids at final time obtained with both schemes. We can observe a quite good agreement regarding the shock location on the grid obtained with EUCCLHYD scheme. This agreement is confirmed by the observation of Figure 3.16, where we have plotted the density in all cells as functions of the radius of the cell-center versus the analytical solution. GLACE scheme fails to solve correctly this problem as the final grid is completely folded. We note the formation of a strong jet aligned with the first bissectrix of the domain. This jet formation is probably a consequence of an inadequate entropy production of the scheme.

Collapse of a ring

In this test case, we study the ability of both schemes to compute the collapse of a ring on itself. This test case is taken from [98, 116]. The internal and the external radii of the ring are set to $r_{\text{int}} = 9.5$ and $r_{\text{ext}} = 10$. The computational domain is defined in polar coordinates by $(r, \theta) \in [r_{\text{int}}, r_{\text{ext}}] \times [0, \frac{\pi}{2}]$ where $r = \sqrt{x^2 + y^2}$ and $\theta = \arctan(\frac{y}{x})$. The initial conditions are $(\rho^0, \boldsymbol{U}^0, P^0) = (7.82, -2\,10^5 \frac{r_{\text{ext}}}{r}\boldsymbol{e}_r, 10^{-6})$, where $\boldsymbol{e}_r$ denotes the unit radial vector. We note that the initial velocity field is divergence free. The ring is initially filled with a material characterized by a stiffened gas EOS, which is written under the form $P = (\gamma - 1)\rho\varepsilon + \Pi_\infty$, where $\gamma = 3.5$ and $\Pi_\infty = 350\,10^9$. The simulations are performed on a 20×9 polar grid paved using equally spaced zones in the radial and the angular directions. Pressure boundary conditions, $P^\star = 10^{-6}$, are prescribed at the inner and outer radii while symmetry boundary conditions are imposed on x and y axis. The final time is set to $t_{\text{final}} = 37\,10^{-6}$. The density maps and the grids obtained for both schemes are plotted in Figure 3.17. We remark that the compression is better rendered at final time by GLACE scheme than by EUCCLHYD scheme. This fact is confirmed by inspecting Figure 3.18 where we have displayed the density as functions of the cell-center radius against the density that results from a one-dimensional reference computation obtained using 2000 zones. Note that this reference solution has been computed using a high-order cell-centered scheme which solves the one-dimensional Lagrangian gas dynamics equations in cylindrical geometry. In this figure, the density plot associated with GLACE formulation almost coincides with the reference density whereas the density corresponding to EUCCLHYD scheme is very far from it. This discrepancy is due to an overestimate of entropy production in EUCCLHYD formulation that prevents the ring from compressing. We shall see in next section that this flaw is corrected using the high-order extension of this latter scheme.

3.3.2 High-order EUCCLHYD results

From now on, we will only consider numerical results obtained with the high-order GRP extension of the EUCCLHYD scheme. In this case the monotonicity of the piecewise linear reconstruction is ensured by means of a slope limiter. Here, we utilize the Barth-Jespersen and the Venkatakrishnan limiters that have been defined page 101. Let us point out that the comparison between this two limiters has been perfomed in [105]. It shows that the Venkatakrishnan limiter is more diffusive than the Barth-Jespersen one. In the aforementioned reference, we have performed the convergence analysis of the present high-order scheme employing a test problem characterized by a smooth analytical solution. This study shows that the high-order EUCCLHYD scheme exhibits an almost second-order rate of convergence.

Sod problem

We consider a two-material variant of the very well known Sod problem which has been initially defined in [153]. It consists of a shock tube of unity length. The interface is located at $x = 0.5$.

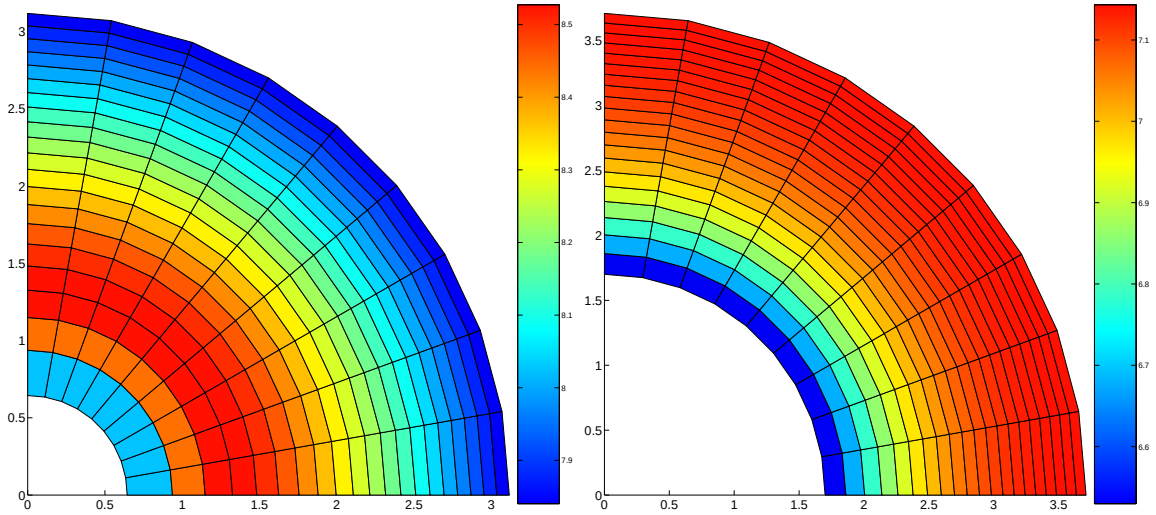

Figure 3.17: Collapse of a ring. Grids and density maps at final time: GLACE scheme (left) and EUCCLHYD scheme (right).

At the initial time, the states on the left and the right sides of $x = 0.5$ are constant. The left state is a high pressure fluid characterized by $(\rho_l, P_l, u_l) = (1, 1, 0)$, the right state is a low pressure fluid defined by $(\rho_r, P_r, u_r) = (0.125, 0.1, 0)$. The left material is characterized by $\gamma_l = \frac{7}{5}$ and the right material by $\gamma_r = \frac{5}{3}$. The computational domain is defined by $(x, y) \in [0, 1] \times [0, 0.1]$. The initial mesh is a Cartesian grid with 100×2 equally spaced cells. The boundary conditions are wall boundary conditions, that is, the normal velocity is set to zero at each boundary. The numerical results obtained with the high-order acoustic EUCCLHYD scheme are presented in Figure 3.19 and 3.20 as spatial distributions of density, pressure, internal energy and velocity with the numerical solutions plotted as discrete points, and the corresponding exact solution shown as solid lines. Monotonicity is ensured by the Barth-Jespersen limiter. The numerical results show the classical improvement of the high-order solution relative to the first-order one. We also note that our results are very similar to those obtained by Ben-Artzi and Falcovitz in [21].

Sedov problem on various grids

We compute the Sedov problem with the same set up than previously using high-order EUCCLHYD scheme in its non-linear version. That is, the node-centered solver is defined by means of the generalized non-linear corner impedances (3.86) page 92. Monotonicity is ensured through the use of the Venkatakrishnan limiter. First, we run Sedov problem with a 30×30 Cartesian grid on the domain $(x, y) \in [0, 1.2] \times [0, 1.2]$. Then, keeping the same conditions, we make use of an unstructured grid produced by a Voronoi tessellation. This grid, which contains 775 polygonal cells, is displayed in Figure 3.21 (left). The third and last grid has been plotted in Figure 3.21. It is made of three structured zones paved with quadrangular cells. The central square zone is meshed with 15×15 cells and the two remaining curvilinear zones are meshes with 45×15 cells. The junction of these three zones is a triple point, that is a vertex surrounding by three cells.

We observe that high-order EUCCLHYD formulation preserves very well the one-dimensional cylindrical symmetry of the solution regardless the grid that has been employed to compute it, refer to Figures 3.22, 3.23 and 3.24. Moreover, the shock location and its level are accurately resolved without any spurious oscillations. We point out that the quality of the mesh in the

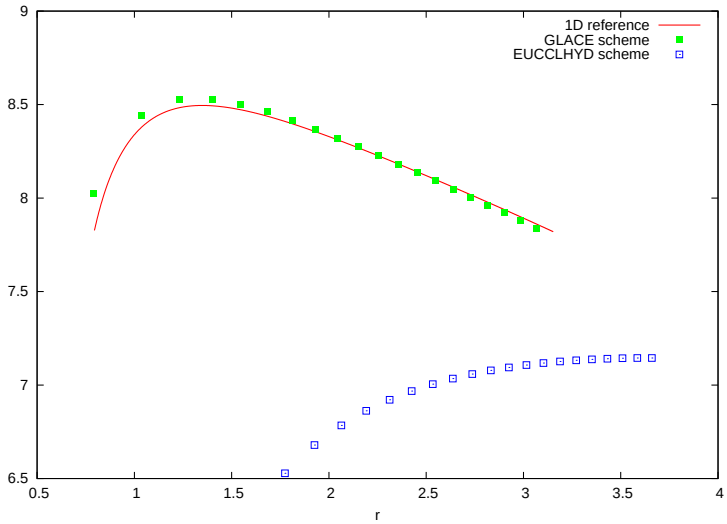

Figure 3.18: Collapse of a ring. Density as functions of cell-center radius for first-order GLACE and EUCCLHYD schemes versus the one-dimensional reference solution at stopping time $t_{\text{final}=37\,10^{-6}}$.

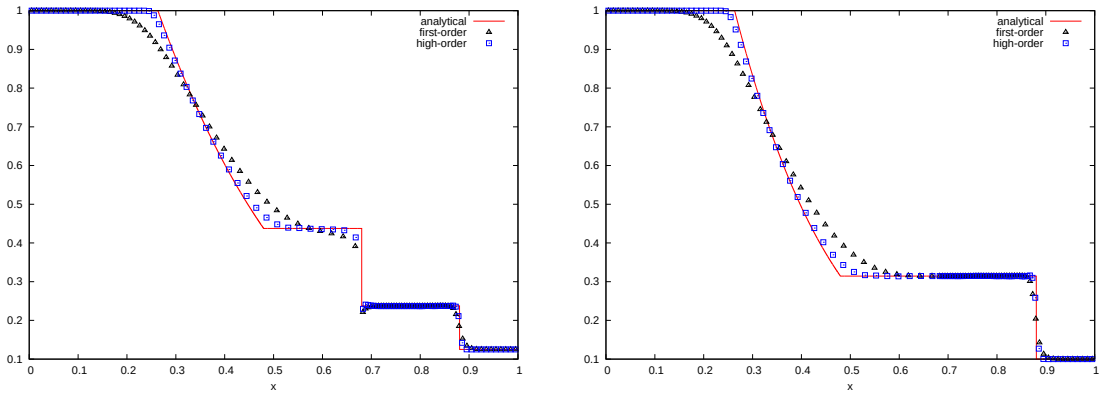

Figure 3.19: Two-material Sod problem. Numerical versus analytical solution for the density (left) and the pressure (right).

vicinity of the triple point is particularly good as it can be seen in Figure 3.25.

Saltzman problem

This test case taken from [54] is a well known difficult problem that allows to evaluate the robustness of Lagrangian schemes. It consists of a strong piston-driven shock wave calculated using an initially nonuniform mesh. The computational domain is defined by $(x, y) \in [0, 1] \times [0, 0.1]$. The skewed initial mesh, displayed in Figure 3.26, is obtained transforming a uniform 100×10 Cartesian grid with the mapping

$$\begin{cases} x_{\text{sk}} = x + (0.1 - y)\sin(\pi x), \\ y_{\text{sk}} = y. \end{cases}$$

The initial conditions are $(\rho_0, \varepsilon_0, \boldsymbol{U}_0) = 1, 10^{-6}, \mathbf{0})$ and the polytropic index is $\gamma = \frac{5}{3}$. At $x = 0$, a unit inward normal velocity is prescribed, the other boundaries are reflective wall. The

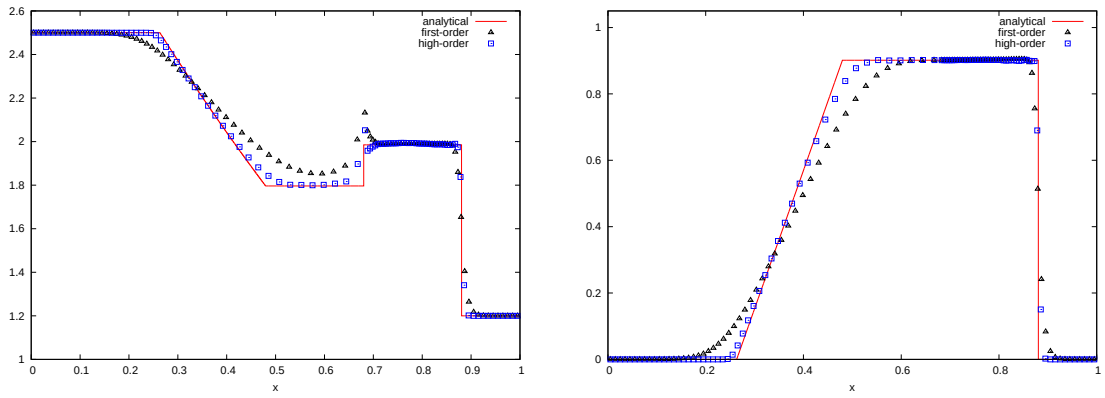

Figure 3.20: Two-material Sod problem. Numerical versus analytical solution for the internal energy (left) and the velocity (right).

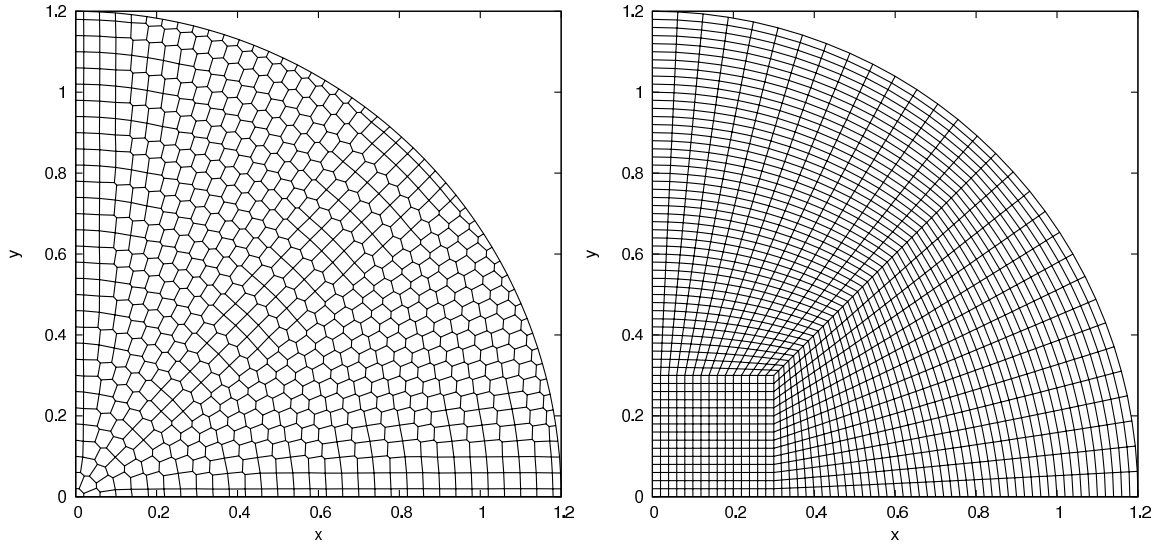

Figure 3.21: Initial unstructured grids for Sedov problem: polygonal grid resulting from a Voronoi tessellation (left), unstructured quadrangular grid (right).

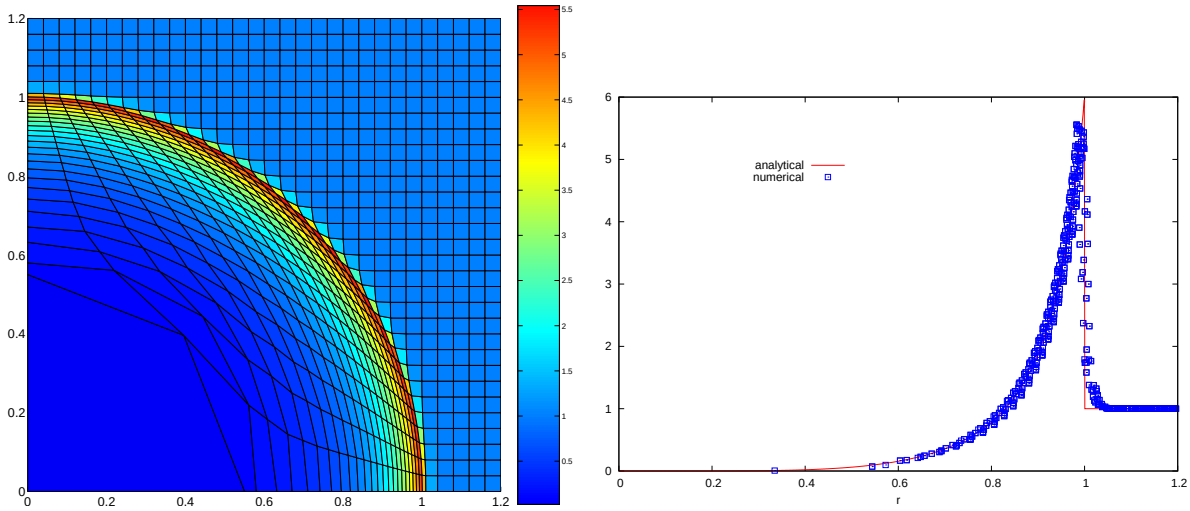

Figure 3.22: Sedov problem on Cartesian grid at stopping time $t = 1$. Density map (left) and density in all the cells as function of cell center radii versus analytical solution (right).

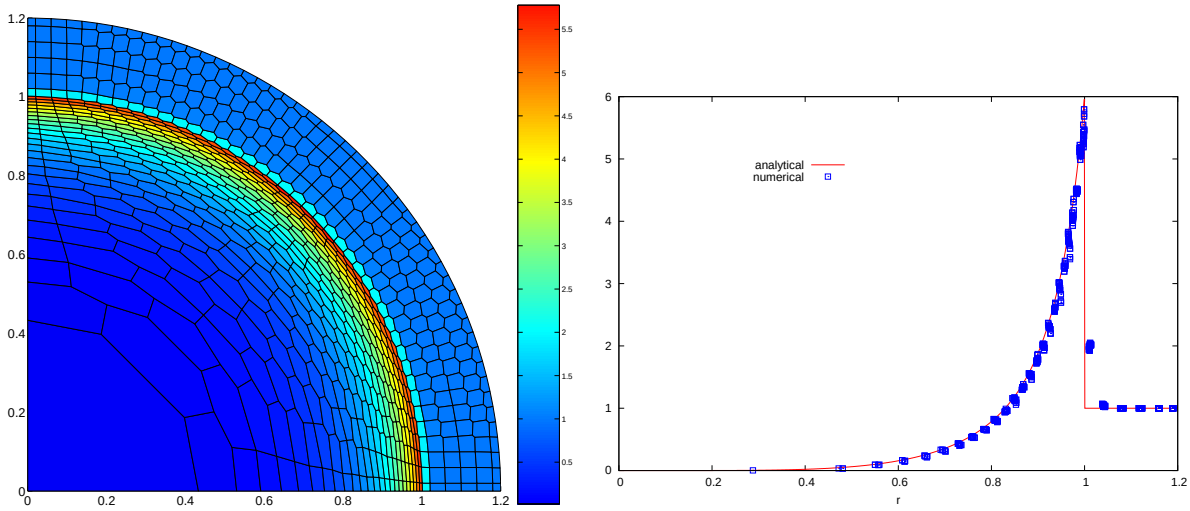

Figure 3.23: Sedov problem on polygonal grid at stopping time $t = 1$. Density map (left) and density in all the cells as function of cell center radii versus analytical solution (right).

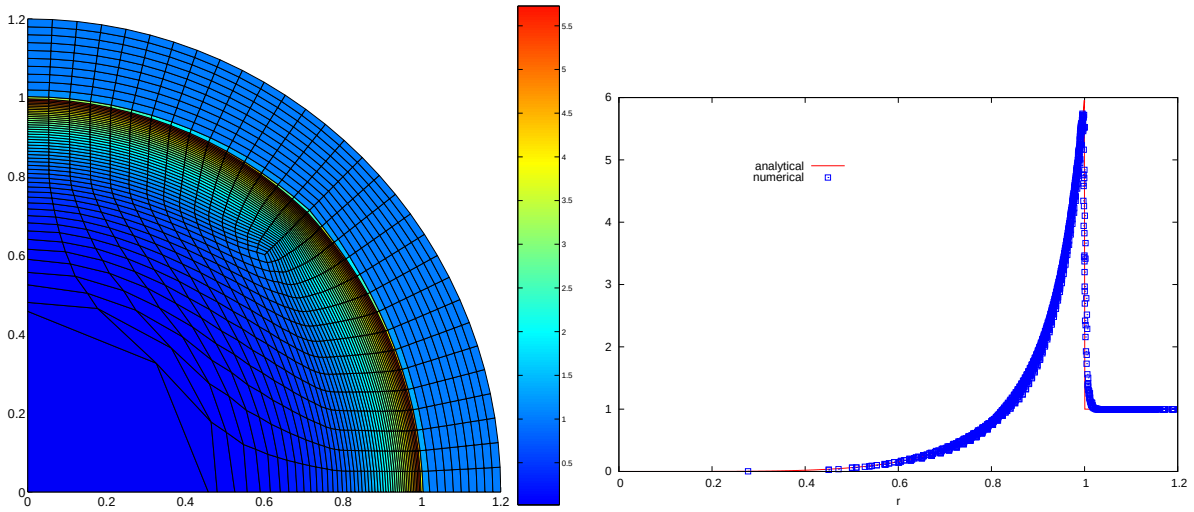

Figure 3.24: Sedov problem on unstructured grid at stopping time $t = 1$. Density map (left) and density in all the cells as function of cell center radii versus analytical solution (right).

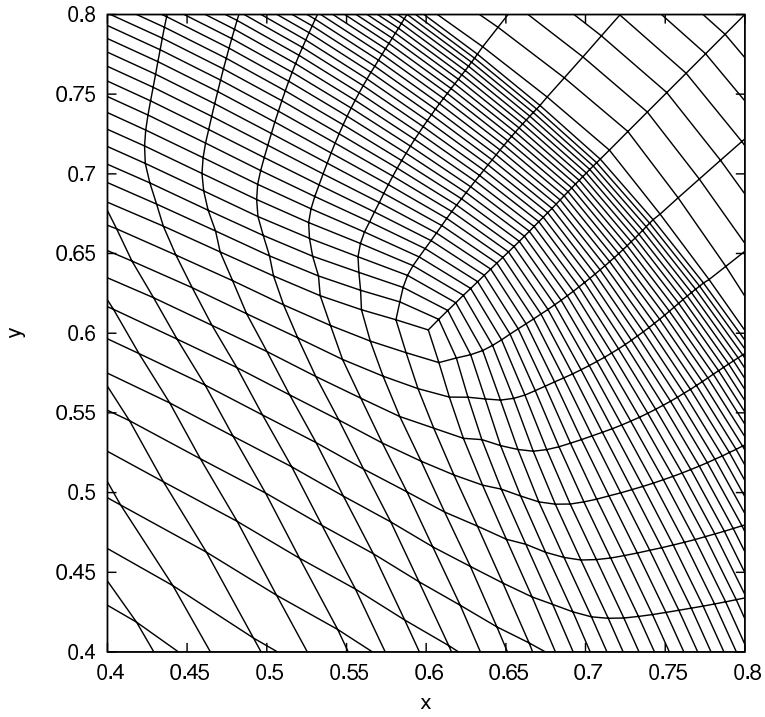

Figure 3.25: Sedov problem on unstructured grid at stopping time $t = 1$. Zoom in the vicinity of the triple point.

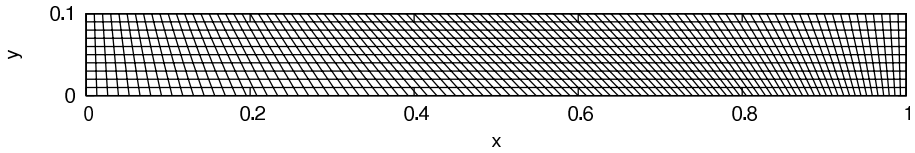

Figure 3.26: Saltzman problem. Initial skewed grid.

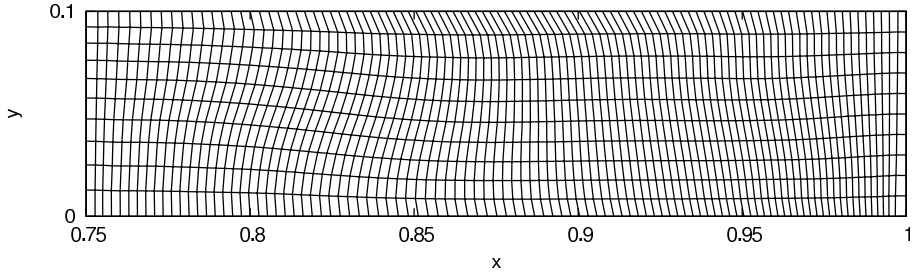

Figure 3.27: Saltzman problem grid at time $t = 0.75$.

analytical solution is a one-dimensional infinite strength shock wave that moves at speed $D = \frac{4}{3}$ in the right direction. Thus, the shock wave hits the face $x = 1$ at time $t = 0.75$. Behind the shock, the density is equal to 4. We run this test using the Venkatakrishnan limiter. We have displayed in Figure 3.27 the grid at time $t = 0.75$ which corresponds to the first bounce of the shock wave. We remark that the one-dimensional solution is very well preserved. Moreover, the location of the shock wave and the shock plateau are in good agreement with the analytical solution, refer to Figure 3.28. In Figure 3.29, we have plotted the grid and the density map at time $t = 0.95$. Although the mesh is more wavy than before, it still exhibits a good quality. **The computation is run until time** $t = 0.99$ **without any robustness problem**. The corresponding grid is displayed in Figure 3.30. These results, in which no spurious modes appear, show the robustness of the high-order EUCCLHYD scheme.

Collapse of a ring revisited

Here, we rerun the problem corresponding to the collapse of a ring which has been presented in previous section. This time, we are using high-order EUCCLHYD scheme in its acoustic version and the monotonicity is ensured by the Barth-Jespersen limiter. We have plotted in Figure 3.31, the density as function of cell-center radius for first and high-order EUCCLHYD scheme versus the reference one-dimensional converged solution. We remark, that the high-order extension brings a dramatic improvement of the numerical solution compared to the first-order solution. This is essentially due to a lower rate of entropy production.

Noh problem on various grids

The Noh problem [124] is a well known test problem that has been used extensively to validate Lagrangian scheme in the regime of infinite strength shock waves. In this test case, a cold gas with unit density is given an initial inward radial velocity of magnitude 1. The initial pressure is given by $P^0 = 10^{-6}$. A diverging cylindrical shock wave is generated which propagates at speed $D = \frac{1}{3}$. The density plateau behind the shock wave reaches the value 16. In order to demonstrate the robustness and the accuracy of high-order EUCCLHYD scheme, we run this test with various options using various types of grids. The monotonicity is provided through the use of the Barth-Jespersen limiter and we use the non-linear node-centered solver defined by means of the generalized non-linear corner impedances (3.86) page 92.

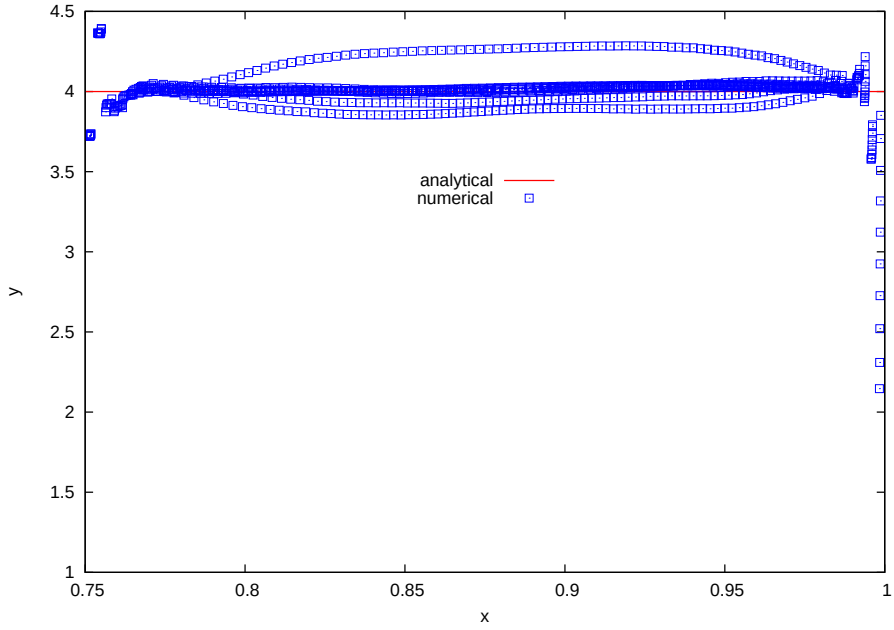

Figure 3.28: Saltzman problem. Density in all the cells as function of the cell center x-coordinate versus analytical solution at time $t = 0.75$.

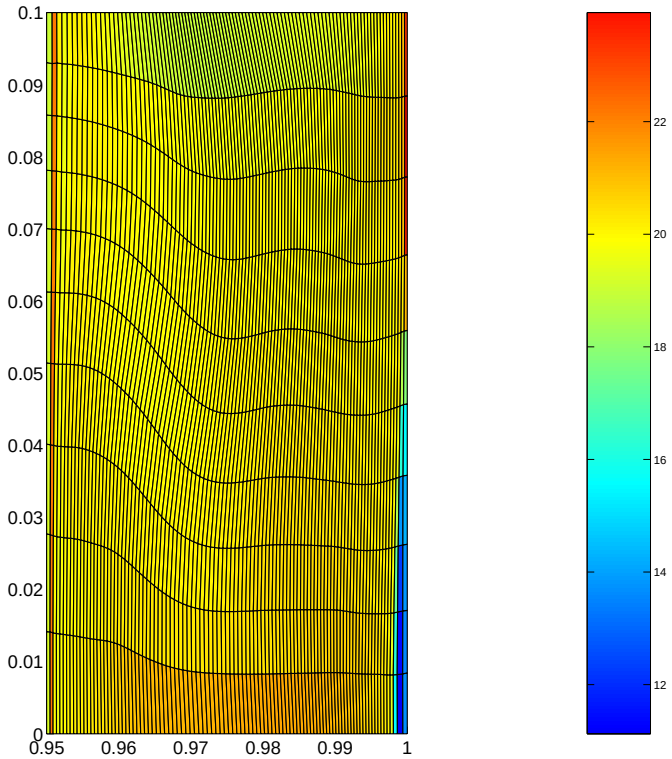

Figure 3.29: Saltzman problem. Grid and density map at time $t = 0.95$.

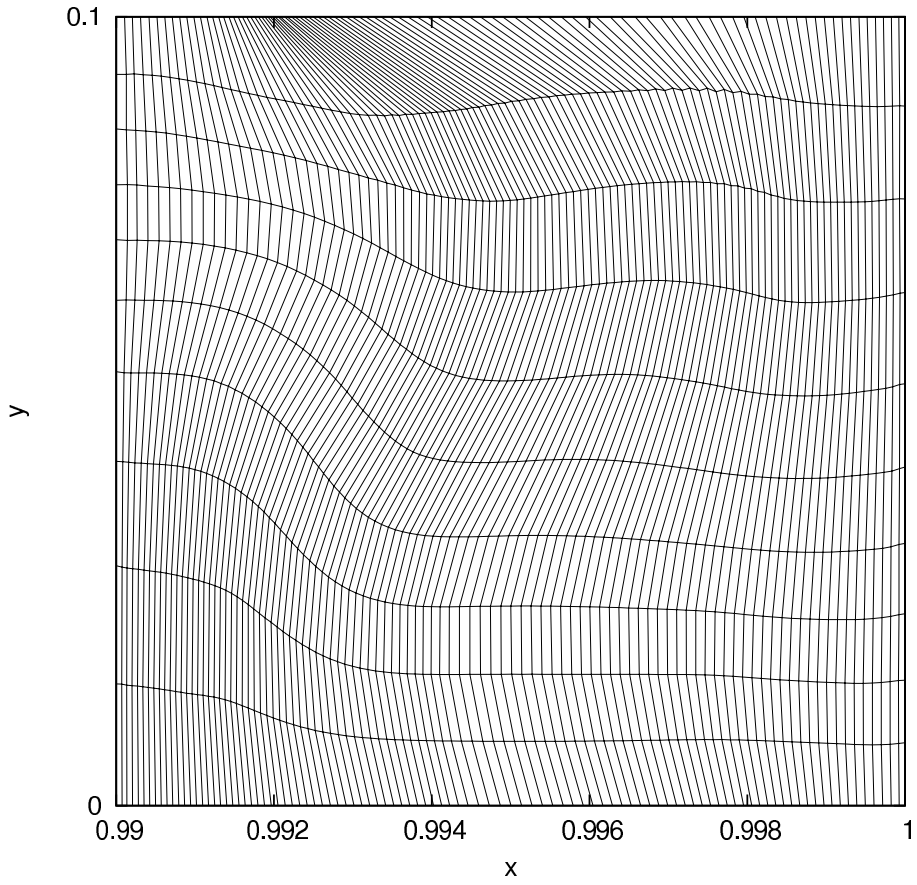

Figure 3.30: Saltzman problem. Grid at time $t = 0.99$.

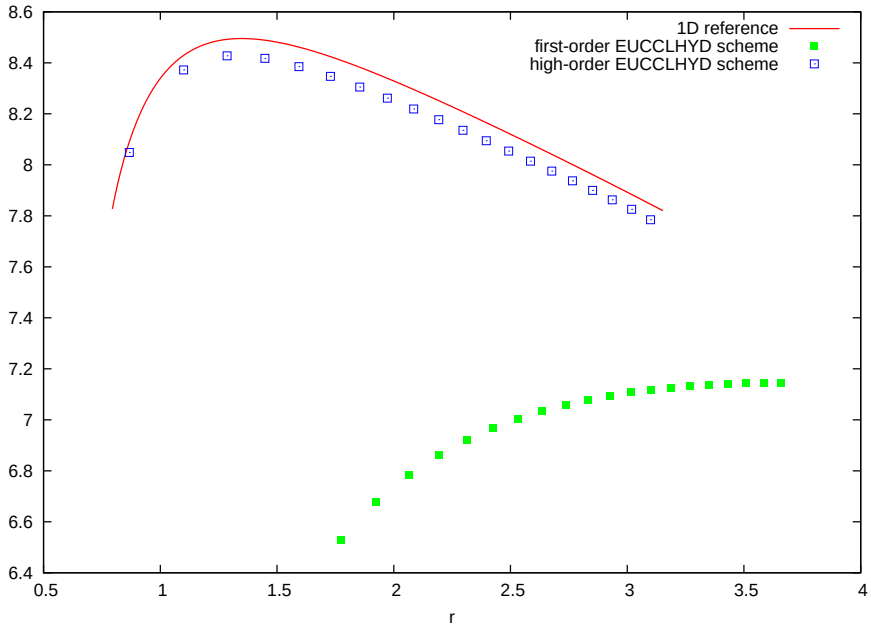

Figure 3.31: Collapse of a ring. Density as function of cell center radius for first and high-order EUCCLHYD scheme versus a one-dimensional reference solution at stopping time $t_{\text{final}} = 37\,10^{-6}$.

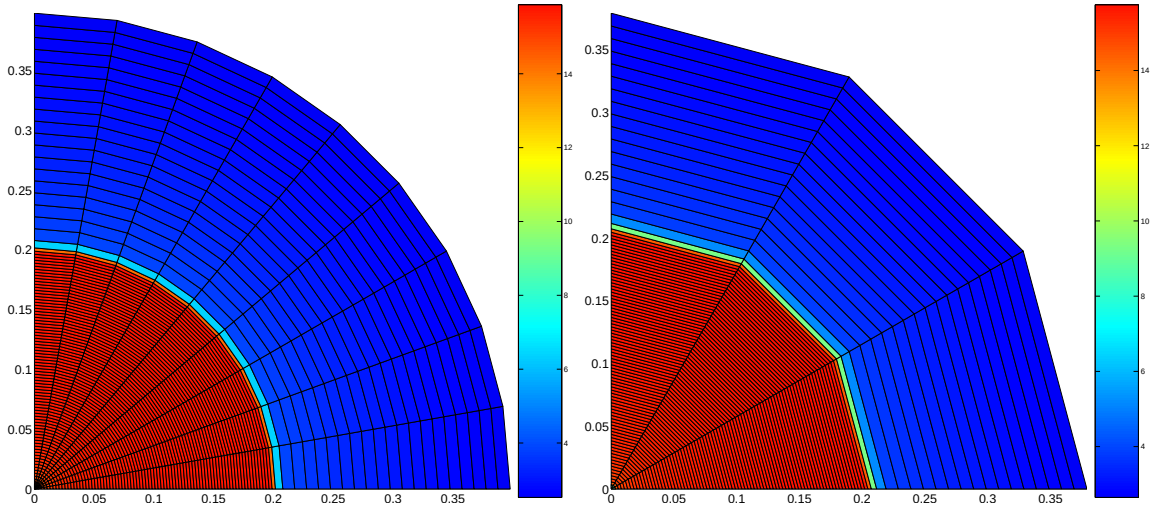

Figure 3.32: Noh problem on polar grids. Grids and density maps at stopping time $t_{\text{final}} = 0.6$. Computations are performed with 100 equal radial zones. The left side result corresponds to a polar mesh made of 9 equal angular zones whereas the right side result corresponds to a polar mesh made of 3 equal angular zones.

One-dimensional Noh problem on polar grids In this paragraph, we run Noh problem using polar grids with equi-angular zoning. The initial computational domain is defined in polar coordinates by $(r, \theta) \in [0, 1] \times [0, \frac{\pi}{2}]$. First, we address the problem of wave front invariance. This requirement which has been introduced in [34] in the framework of staggered schemes, points out that the artificial viscosity should have no effect along a wave front of constant phase. In the case of our cell-centered scheme, there is no artificial viscosity, however we have to check that the numerical viscosity inherent to our scheme satisfies this wave front invariance requirement. To examine this, we run the Noh problem with two polar grids characterized by the same zoning in the radial direction and two different angular zonings, respectively 3 and 9 angular zones. The boundary conditions on the x and y axis are wall boundary conditions whereas a pressure given by $P^\star = P^0$ is prescribed at the outer radius $r = 1$. The density maps at the stopping time $t_{\text{final}} = 0.6$ are displayed in Figure 3.32. We note that the symmetry is perfectly preserved. The shock location and the shock plateau agree with the analytical solution. In Figure 3.33, we have plotted the density as function of radius for these two different angular zonings. The small difference between the two curves shows that the wave front invariance requirement is pretty well satisfied. Second, we compare the pure acoustic version of high-order EUCCLHYD scheme to the non-linear version running the Noh problem on a 100×3 uniform polar grid. The corresponding numerical densities are plotted in Figure 3.34 as function of radius at the stopping time. The shock plateau and the shock location are almost the same, however in the acoustic case, we note the appearance of density peaks located near the origin and the shock front. These peak occurrences are probably due to the fact that the acoustic formulation does not produce enough dissipation in this case.

Two-dimensional Noh problem on a 50×50 Cartesian grid To assess the robustness of our scheme, we run the Noh problem on a 50×50 Cartesian grid. This configuration leads to a more severe test case since the mesh is not aligned with the flow. Monotonicity is ensured by Venkatakrishnan limiter. We have displayed the grid and the density map in Figure 3.35. We note that the cylindrical symmetry is quite well preserved and that the shock is located at a circle whose radius is approximately 0.2. The results for this test case are almost as good

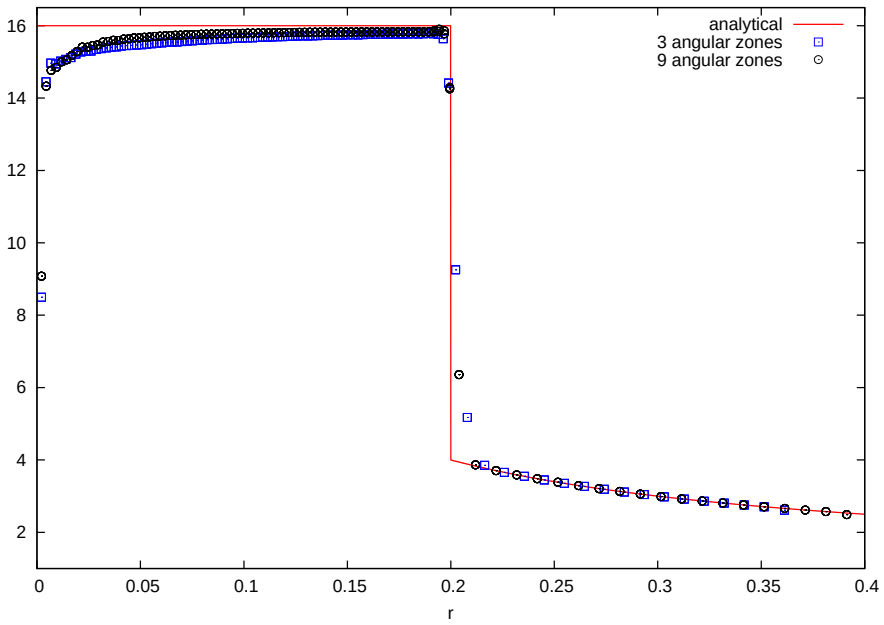

Figure 3.33: Noh problem on polar grids. Density as function of cell-center radius at stopping time $t_{\text{final}} = 0.6$ versus analytical solution.

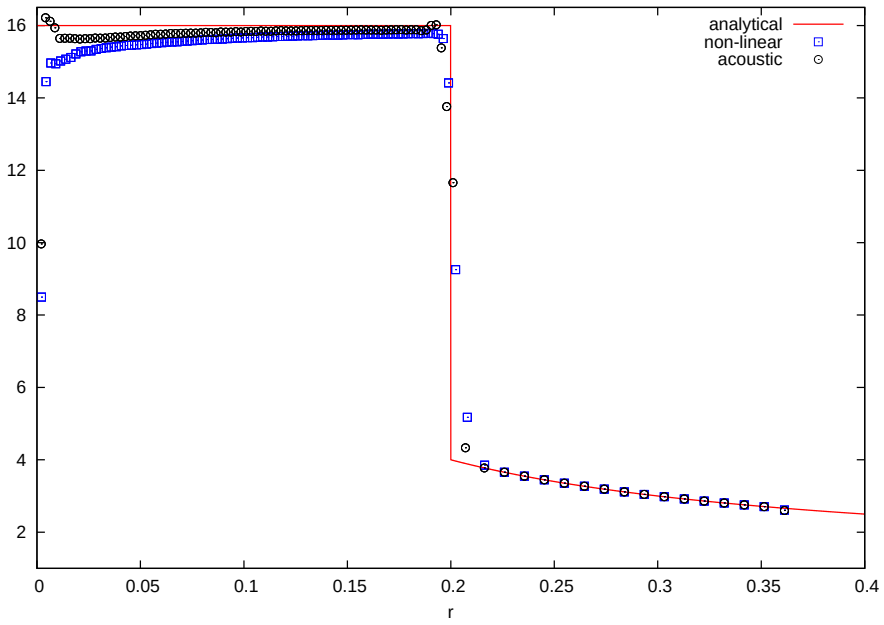

Figure 3.34: Noh problem on a 100×3 polar grid. Density as a function of radius for the Noh problem at stopping time $t_{\text{final}} = 0.6$. Pure acoustic and non-linear node-centered solver versus analytical solution.

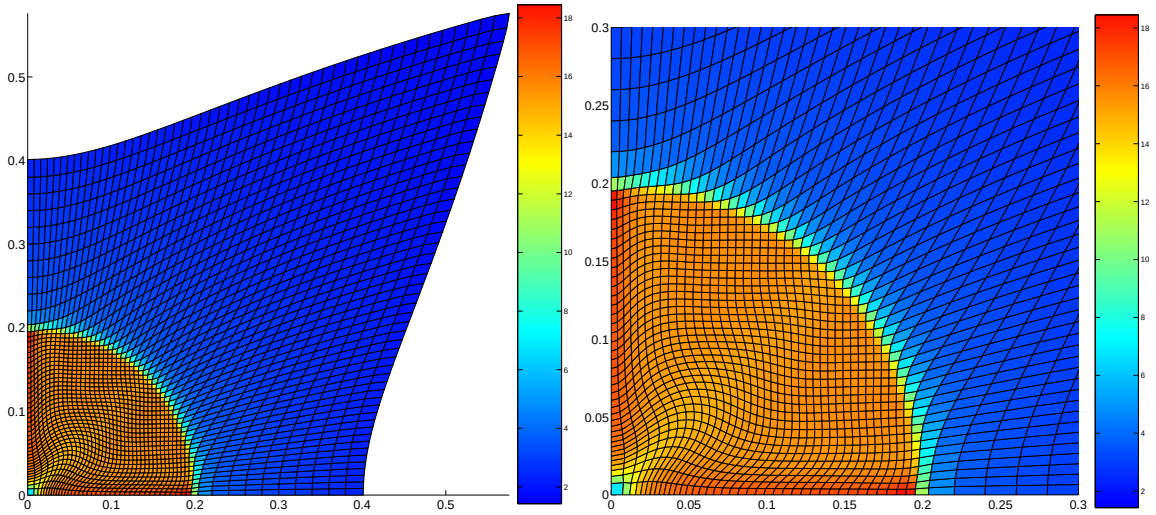

Figure 3.35: Grid and density map for the Noh problem at time $t_{\text{final}} = 0.6$ on a 50 Cartesian grid. Whole grid (left) and zoom on the shocked region (right).

as those obtained by Campbell and Shashkov [32] using their staggered scheme with a mimetic tensorial artificial viscosity.

Two-dimensional Noh problem on a non-conformal grid We finish this section with the computation of the Noh problem on a non-conformal grid to illustrate the ability of high-order EUCCLHYD scheme to handle non-conformal grids. This grid is constructed using a polar grid and adding to it one level of refinement, refer to Figure 3.36 (left). Thus, we get a grid made of triangles, quadrangles and pentagons. We put the stress on the fact that no special treatment is required in the node-centered solver to handle such a grid. We have displayed the grid at the stopping time $t_{\text{final}} = 0.6$ in Figure 3.36 (right). We point out that the symmetry is well preserved and the shock location agrees with the analytical solution. The density in all the

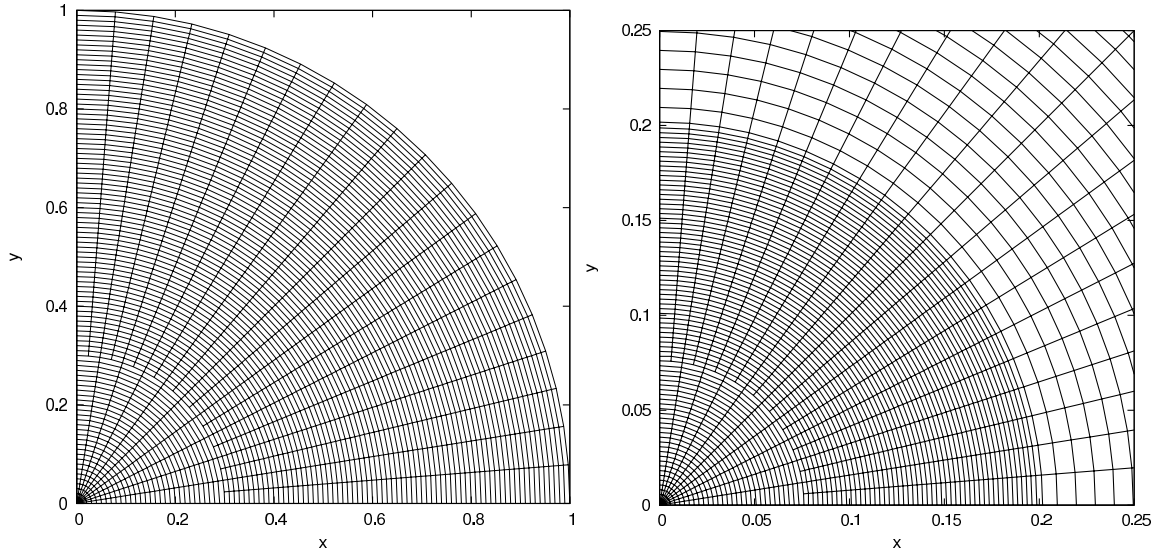

Figure 3.36: Noh problem on a non-conformal grid. Initial grid (left) and zoom on the final grid at $t_{\text{final}} = 0.6$ (left).

cells as function of radius of the cell centroid is plotted in Figure 3.37. The shock location and the shock plateau are in good agreement with the analytical solution. We notice some small overshoots in the density plateau corresponding to the location of the non-conformal cells. These overshoots are probably a consequence of the loss of convexity of the pentagonal cells located at the interface where the refinement occurs.

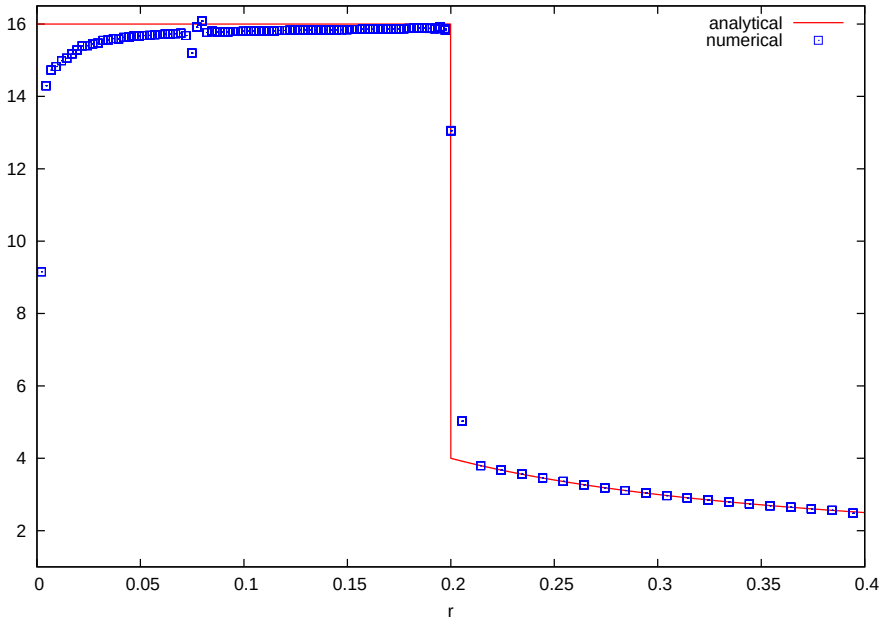

Figure 3.37: Noh problem on a non-conformal grid. Density versus cell centroid radius at $t = 0.6$.

Study of the linear phase of the Richtmyer-Meshkov instability

Here, we reproduce a test case that has been initially presented in [105]. This test case is devoted to the study of the linear phase of the Richtmyer-Meshkov instability [140] for a piston-driven flow. This hydrodynamic instability occurs when a shock wave hits a perturbed interface separating two materials with distinct densities. This situation is frequently encountered during the implosion of an Inertial Confinement Fusion target. For sufficiently small perturbations, analytical solutions can be derived using linear perturbation theory [167]. In this context, the linear theory shows that the amplitude of the perturbation grows linearly as function of time. We first study the unperturbed fluid configuration, which consists of the collision of a shock wave with a flat contact discontinuity. Such a collision produces a transmitted shock wave and a reflected wave that can be either a shock or a rarefaction depending on the density ratio between the two materials present on both side of the interface. This shock-contact interaction defines a one-dimensional Riemann problem, which can be solved analytically.

We are going to study the configuration displayed in Figure 3.38. The interface is located at $x = 0$ and the computational domain corresponding to the shock tube is defined by $(x, y) \in [-5, 4.2] \times [0, 0.5]$, since the $y = 0$ line is a symmetry axis for this problem. For the initial and boundary conditions described in Figure 3.38, the incident piston-driven shock hits the interface at time $t = 3.015$. This interaction leads to transmitted and reflected shock waves, which also later interact with the piston and the right boundary wall. The time history of the shock-contact interaction is displayed in Figure 3.39 using a classical $(t - x)$ diagram which shows the Eulerian x coordinate of selected points versus time. We can observe in this figure the

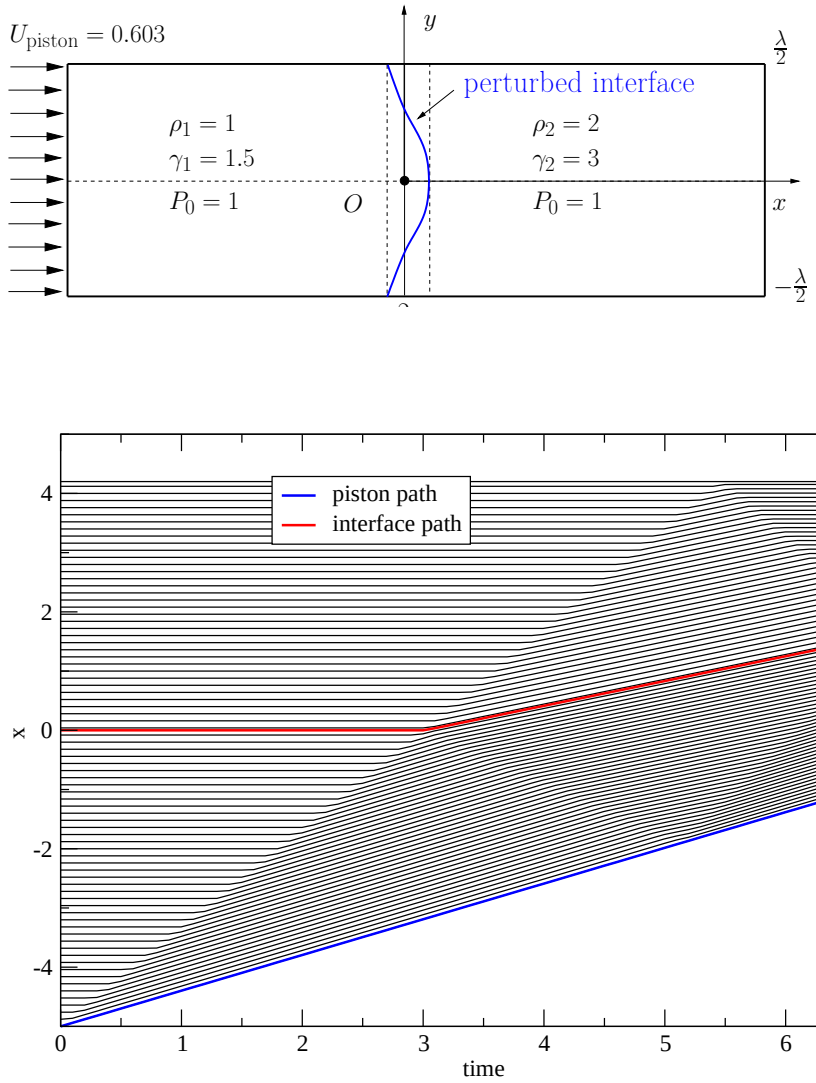

Figure 3.39: $t - x$ diagram for the shock-contact interaction problem. The piston path is displayed using blue color whereas the interface path is plotted using red color.

incident, transmitted and reflected shock waves. We run a computation for the unperturbed configuration with the high-order EUCCLHYD scheme (BJ limiter) using 460 equally-spaced cells in the x direction and one cell in the y direction. The density as function of x coordinate is plotted in Figure 3.40 versus analytical solution at time $t = 5$. We point out the very good agreement between numerical and analytical solutions. Moreover, we note that transmitted and reflected shocks are sharply resolved. The perturbed configuration is investigated by initializing the perturbed interface as

$$x(y) = \alpha_0 \cos(\frac{2\pi}{\lambda} y), \quad \text{for} \quad y \in [-\frac{\lambda}{2}, \frac{\lambda}{2}], \tag{3.130}$$

where α_0 denotes the initial amplitude and λ is the wavelength of the perturbation. The shape of the perturbed interface is displayed in Figure 3.38. For a small enough initial amplitude, linear theory predicts that the perturbation amplitude, $\alpha(t)$, grows linearly as function of time, after the shock has interacted with the interface. Using a direct two-dimensional simulation of the perturbed configuration, we shall recover this important result and compare the numerical perturbation amplitude with the one obtained through the use of the linear theory.

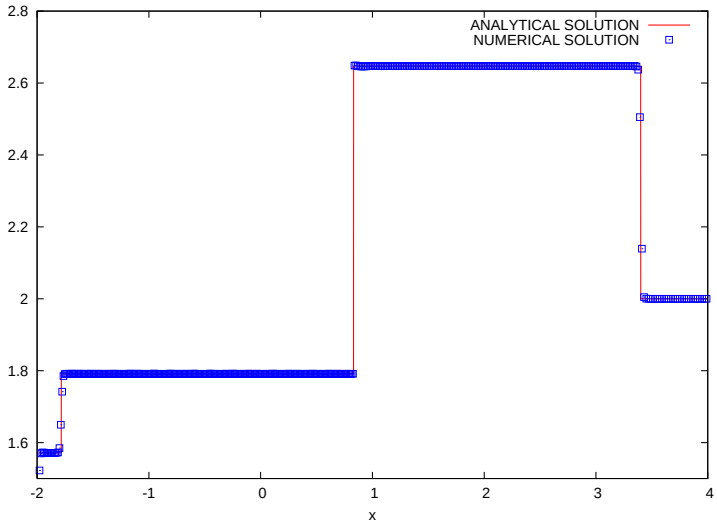

Figure 3.40: Interaction of a shock wave with a contact discontinuity. Density as function of x coordinate versus analytical solution at time $t = 5$.

The corresponding numerical simulations are performed as follows. The computational domain, $(x, y) \in [-5, 4.2] \times [0, 0.5]$, is paved with 460×25 equally spaced cells. Note that we have set $\lambda = 1$ and meshed only a half wavelength due to the symmetry of the problem about x axis. We run three computations utilizing respectively the first-order EUCCLHYD scheme and its high-order extension with Venkatakrishan and Barth-Jespersen limiters. The perturbed interface is defined by setting $\alpha_0 = 10^{-4}$ and moving the vertices initially located on the line $x = 0$ onto the curve defined by equation (3.130). The numerical computation of the perturbed amplitude, $\alpha(t)$, is obtained as follows

$$\alpha(t) = \frac{1}{\alpha_0}[x_{\text{pert}}(t) - x_{\text{unpert}}(t)]. \tag{3.131}$$

Here, $x_{\text{pert}}(t)$ (resp. $x_{\text{unpert}}(t)$) is the abscissa of a point located on the perturbed (resp. unperturbed) interface. Using this formula for the three previous computations, we compute the corresponding perturbation amplitudes and compare them to the reference one resulting from the linear theory [167]. We have plotted in Figure 3.41 (left) the numerical perturbation amplitudes as function of time versus the reference amplitude resulting from the linear theory. We remark that the high-order computations recover quite well the linear theory whereas the first-order calculation exhibits a highly damped evolution of the perturbation. This damping is the consequence of the numerical dissipation inherent to the first-order scheme. Concerning the high-order results, we note that the perturbation amplitude obtained using the Barth-Jespersen limiter is closer to the linear theory curve than the perturbation amplitude obtained using the Venkatakrishnan limiter. This follows from the fact that the Venkatakrishnan limiter is more diffusive than the Barth-Jespersen one. We have also performed a computation using a finer grid with 920×50 cells with the Barth-Jespersen limiter. We observe in Figure 3.41 (right) that the resulting amplitude perturbation follows the linear theory, i.e the slopes are identical. These results demonstrate the ability of the high-order EUCCLHYD scheme to simulate very accurately complex phenomena such as hydrodynamic instabilities.

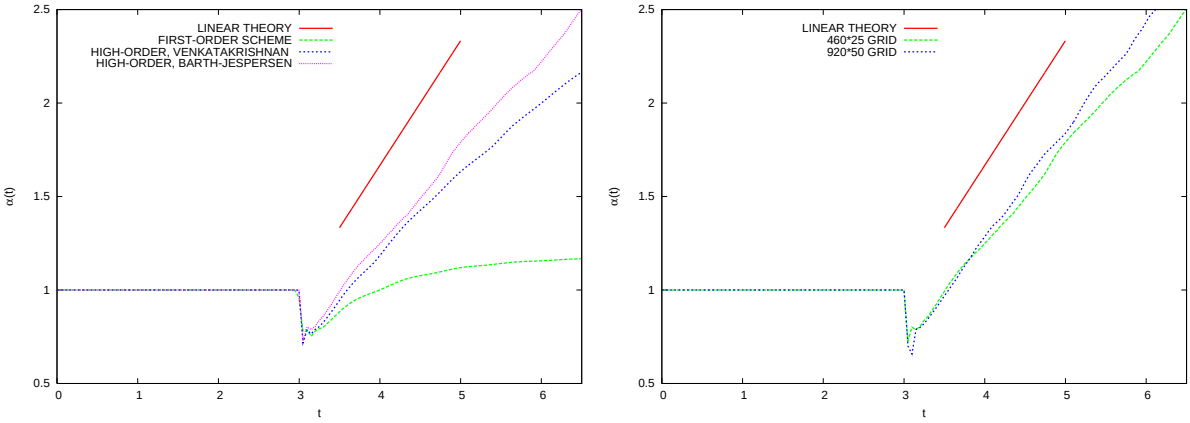

Figure 3.41: Shock-contact interaction problem. Numerical perturbation amplitudes as function of time versus linear theory. Comparison between first-order, high-order Barth-Jespersen and Venkatakrishnan for the 460×24 grid (left). Convergence analysis for the high-order Barth-Jespersen computations (right).

3.4 High-order discretization for two-dimensional Lagrangian hydrodynamics in cylindrical geometry

This section deals with high-order cell-centered discretizations of the Lagrangian hydrodynamics equations written in cylindrical geometry. The present discretizations are extensions, in two-dimensional axisymmetric geometry, of the cell-centered Lagrangian schemes described in Section 3.2. They can also be viewed as a generalization of the work developed in [104] by means of sub-cell force. This axisymmetric extension is motivated since in many application problems, such as inertial confinement problems, physical domains have axisymmetric features. In this framework, the importance of preserving spherical symmetry is well recognized, particularly for the numerical simulations of implosions. Concerning the critical issue related to spherical symmetry preservation many works have been done in the framework of staggered-grid hydrodynamics. The most widely used method that preserves symmetry exactly on polar grids with equiangular zoning is the area-weighted method. In this approach one uses a Cartesian form of the momentum equation in cylindrical coordinates system, hence integration is not performed with respect to the true volume in cylindrical coordinates, but rather with respect to area. However, due to the loss of compatibility between gradient and divergence operators, this formulation, in its usual form, does not allow the conservation of total energy as it has been explained by Whalen [165]. This flaw has been corrected in [35] by constructing a compatible area-weighted scheme which preserves total energy. In [113, 114], Shashkov and Margolin use a curvilinear grid to construct conservative symmetry preserving discretizations. Their strategy use high-order curves to connect the nodes, so that planar, cylindrical and spherical symmetry are exactly maintained while differential operators are discretized in a compatible way. It is worth to mention that this method preserves symmetry even on polar mesh with non-equal angles. In [37], Caramana and Whalen show how to achieve the problem of exactly preserving a one-dimensional symmetry, in a two-dimensional coordinate system distinct from that symmetry. This result is attained through a modification of the pressure gradient operator used to compute the force in a staggered-grid hydrodynamics algorithm. Regarding the control volume discretization, a general methodology is described in [112], where a discrete divergence operator is derived by requiring consistency of the divergence of the velocity field with the time rate of change of volume of a cell. The discrete gradient operator is deduced from the discrete diver-

gence using conservation of total energy which implies the adjointness of the discrete gradient and divergence operators. We want also to mention the recent paper [13] wherein a new staggered discretization for 2D Lagrangian hydrodynamics is presented. This area-weighted scheme is total energy conserving and symmetry preserving on polar equiangular grids.

Here, we propose an alternative discretization wherein all conserved quantities, including momentum, and hence cell velocity are cell-centered. The main feature of this discretization lies in the fact that the interface fluxes and the node velocity are computed coherently thanks to an approximate Riemann solver located at the nodes. Indeed, the rate of change of any Lagrangian volume is computed coherently with the nodes displacement. Regarding the axisymmetric extension of these Godunov-type schemes, we observe that recent developments have been described in [116, 152]. However, we note that these extensions are only first-order discretizations and therefore not sufficiently accurate for real-life applications. It is also worth to mention that a special cell-centered method, which preserves symmetry, has been developed in [154]. In what follows, two schemes, which are compatible with the GCL, are obtained through the use of a sub-cell force-based discretization. These two schemes differ in the way the momentum equation is discretized. The first one, which uses a gradient operator compatible with the divergence operator, corresponds to the control volume scheme, while the second one corresponds to the area-weighted scheme. Both formulations share the same discretization for the total energy equation. We note that in both schemes numerical fluxes are computed using the same node-centered solver which can be viewed as two-dimensional extension of an approximate Riemann solver. The control volume scheme conserves momentum, total energy and satisfies a local entropy inequality in its first-order semi-discrete form. However, it does not preserves spherical symmetry. On the other hand, the area-weighted formulation conserves total energy and preserves spherical symmetry for one-dimensional spherical flow computed on equiangular polar grid. The genuinely two-dimensional high-order extension of both schemes is constructed utilizing the GRP methodology in its acoustic approximation.

3.4.1 Lagrangian hydrodynamics in pseudo-Cartesian geometry

In this section, we aim at writing the gas dynamics equations using a set of generalized orthogonal coordinates which encompasses both Cartesian and cylindrically symmetric coordinates. According to [8], this unified representation is termed pseudo-Cartesian geometry. Utilizing this generalized coordinates, we derive the expressions of the divergence and gradient operators which shall be useful for the subsequent space discretizations.

Governing equations

Let us recall briefly that in the Lagrangian formalism the rates of change of mass, volume, momentum and total energy are computed assuming that the computational volumes follow the material motion. This representation leads to the following set of equations for an arbitrary moving control volume $\omega(t)$

$$\frac{d}{dt}\int_{\omega(t)} \rho \,\mathrm{d}v = 0, \tag{3.132a}$$

$$\frac{d}{dt}\int_{\omega(t)} \mathrm{d}v - \int_{\omega(t)} \nabla\cdot\boldsymbol{U} \,\mathrm{d}v = 0, \tag{3.132b}$$

$$\frac{d}{dt}\int_{\omega(t)} \rho\boldsymbol{U} \,\mathrm{d}v + \int_{\omega(t)} \boldsymbol{\nabla} P \,\mathrm{d}v = \mathbf{0}, \tag{3.132c}$$

$$\frac{d}{dt}\int_{\omega(t)} \rho E \,\mathrm{d}v + \int_{\omega(t)} \nabla\cdot(P\boldsymbol{U}) \,\mathrm{d}v = 0. \tag{3.132d}$$

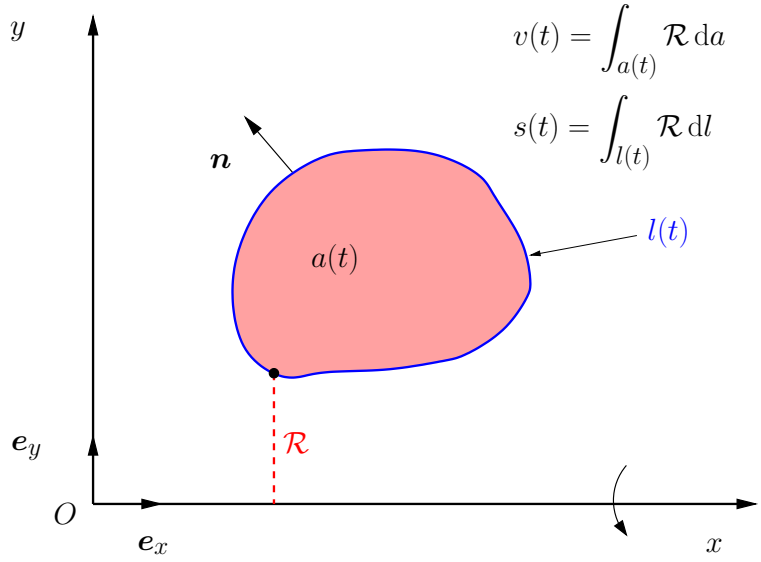

Figure 3.42: Notation related to the pseudo Cartesian geometry.

where $\frac{d}{dt}$ denotes the material, or Lagrangian, time derivative. Here, as usual, ρ, $\boldsymbol{U}$, P, E denote the mass density, velocity, pressure and specific total energy of the fluid. Equations (3.132a), (3.132c) and (3.132d) express the conservation of mass, momentum and total energy. The thermodynamic closure of the set of equations (3.132) is obtained by using an equation of state written under the form $P = P(\rho, \varepsilon)$, where the specific internal energy, ε, is related to the specific total energy by $\varepsilon = E - \frac{1}{2} \mid \boldsymbol{U} \mid^2$.

Note that the above equations are not written under the usual form, that is, we have not yet applied the divergence theorem to replace the volume integrals by surface integrals. This task will be performed later after having defined the divergence and gradient operators through the use of the generalized pseudo-Cartesian coordinates. Before, we proceed any further, let us first introduce the pseudo-Cartesian representation. We note that the case of Cartesian or cylindrical geometry can be combined by introducing the pseudo-Cartesian frame (O, x, y), equipped with the orthonormal basis $(\boldsymbol{e}_x, \boldsymbol{e}_y)$, through the use of the pseudo radius

$$\mathcal{R}(y) = 1 - \alpha + \alpha y,$$

where $\alpha = 1$ for cylindrical geometry and $\alpha = 0$ for Cartesian geometry. We remark that y corresponds to the radial coordinate in the cylindrical case. This means that we assume rotational symmetry about x axis, refer to Figure 3.42. We note that if we refer to standard cylindrical coordinates, (z, r), then x corresponds to z and y to r. In this framework, the volume $v(t) = \int_{a(t)} \mathcal{R}\,\mathrm{d}a$ is obtained by rotating the area $a(t)$ about the x axis. Thus, the volume element, $\mathrm{d}v$, writes $\mathrm{d}v = \mathcal{R}\,\mathrm{d}a$, where $\mathrm{d}a = \mathrm{d}x\mathrm{d}y$ is the area element in the pseudo-Cartesian coordinates. Note that we have omitted the factor 2π due to the integration in the azimuthal direction, namely we consider all integrated quantities to be defined per unit radian. The surface $s(t) = \int_{l(t)} \mathcal{R}\,\mathrm{d}l$, which bounds the volume $v(t)$, is obtained by rotating, $l(t)$, the boundary of the area a, about the x axis. Thus, the surface element, $\mathrm{d}s$, writes $\mathrm{d}s = \mathcal{R}\,\mathrm{d}l$, where $\mathrm{d}l$ is the line element along the perimeter of $a(t)$.

Divergence and gradient operators in pseudo-Cartesian geometry

To construct a finite volume discretization of system (3.132), we are going to express the volume integrals of the divergence and gradient operators in terms of surface integrals. Using the

pseudo-radius, $\mathcal{R}$, the divergence operator expressed in pseudo-Cartesian coordinates writes as

$$\nabla \cdot \boldsymbol{U} = \frac{\partial u}{\partial x} + \frac{1}{\mathcal{R}} \frac{\partial}{\partial y}(\mathcal{R} w),$$

where (u, w) are the components of the vector $\boldsymbol{U}$. Regarding the gradient operator, it writes as usual

$$\boldsymbol{\nabla} P = \frac{\partial P}{\partial x} \boldsymbol{e}_x + \frac{\partial P}{\partial y} \boldsymbol{e}_y.$$

The divergence theorem states the

$$\int_v \nabla \cdot \boldsymbol{U} \, \mathrm{d}v = \int_s \boldsymbol{U} \cdot \boldsymbol{n} \, \mathrm{d}s,$$

where $\boldsymbol{n}$ is the unit outward normal to the boundary surface s. Now, using the fact that the surface element $\mathrm{d}s$ expresses as $\mathrm{d}s = \mathcal{R}\mathrm{d}l$, the divergence formula rewrites as

$$\int_v \nabla \cdot \boldsymbol{U} \, \mathrm{d}v = \int_l \boldsymbol{U} \cdot \boldsymbol{n} \mathcal{R} \, \mathrm{d}l. \tag{3.133}$$

The volume integral of the gradient operator follows from the vector identity

$$\boldsymbol{U} \cdot \boldsymbol{\nabla} P = \nabla \cdot (P \boldsymbol{U}) - P \nabla \cdot \boldsymbol{U}.$$

Integrating by part this identity over the volume v and using the divergence formula leads to

$$\int_v \boldsymbol{U} \cdot \boldsymbol{\nabla} P \, \mathrm{d}v = \int_l P \boldsymbol{U} \cdot \boldsymbol{n} \mathcal{R} \, \mathrm{d}l - \int_a P \nabla \cdot \boldsymbol{U} \mathcal{R} \, \mathrm{d}a.$$

Assuming that $\boldsymbol{U}$ is a constant vector yields

$$\int_v \boldsymbol{\nabla} P \, \mathrm{d}v = \int_l P \boldsymbol{n} \mathcal{R} \, \mathrm{d}l - \alpha \boldsymbol{e}_y \int_a P \, \mathrm{d}a. \tag{3.134}$$

This result is obtained by noticing that the divergence of a constant vector in pseudo-Cartesian geometry is given by $\nabla \cdot \boldsymbol{U} = \frac{\alpha}{\mathcal{R}} \boldsymbol{U} \cdot \boldsymbol{e}_y$. In deriving this equation, we have used the above vector identity which ensures the compatibility between the volume integral of the gradient operator with that of the divergence operator. Note that for $\alpha = 0$, we recover the classical Cartesian expression of the volume integral of the gradient operator. In the context of a finite volume discretization, the use of (3.134) leads to the **control volume** (CV) formulation.

An alternative approach to express the volume integral of the gradient operator consists in making the following approximation

$$\begin{aligned} \int_v \boldsymbol{\nabla} P \, \mathrm{d}v &= \int_a \boldsymbol{\nabla} P \mathcal{R} \, \mathrm{d}a \\ &= \bar{\mathcal{R}} \int_a \boldsymbol{\nabla} P \, \mathrm{d}a. \end{aligned} \tag{3.135}$$

Here, we have used the mean value theorem, namely $\bar{\mathcal{R}}$ is defined as the averaged pseudo-radius

$$\bar{\mathcal{R}} = \frac{1}{\mid a \mid} \int_a \mathcal{R} \, \mathrm{d}a, \tag{3.136}$$

where $\mid a \mid = \int_a \mathrm{d}a$ is the surface of the area a. We remark that in the case of Cartesian geometry $\bar{\mathcal{R}} = 1$ since $\alpha = 0$. Finally, applying the divergence formula to the surface integral in the right-hand side of (3.135) yields

$$\int_v \boldsymbol{\nabla} P \, \mathrm{d}v = \bar{\mathcal{R}} \int_l P \boldsymbol{n} \, \mathrm{d}l. \tag{3.137}$$

This results in the Cartesian expression of the gradient operator weighted by the averaged pseudo-radius. This alternative approach leads to the so-called **area-weighted** (AW) formulation. We point out that, in this case, the compatibility between the volume integrals of the divergence and gradient operators has been lost. Let us note that formulas (3.137) and (3.134) coincide in the case of the Cartesian geometry since $\alpha = 0$ and $\bar{\mathcal{R}} = 1$.

In what follows, we shall derive and thoroughly analyze the discrete schemes deduced from the control volume and the area-weighted formulations.

Comment 14 *We remark that if the scalar P is constant over the volume v, then equation* (3.134) *yields the following geometric identity*

$$\int_l \boldsymbol{n}\mathcal{R}\,\mathrm{d}l = \alpha \mid a \mid \boldsymbol{e}_y. \tag{3.138}$$

This formula can also be written component-wise

$$\int_l n_x\mathcal{R}\,\mathrm{d}l = 0,$$
$$\int_l n_y\mathcal{R}\,\mathrm{d}l = \alpha \mid a \mid,$$

where (n_x, n_y) are the components of the unit outward vector $\boldsymbol{n}$. For $\alpha = 0$, we recover the well known result, that for a closed contour, the integral of the normal over this contour is equal to zero. Note that this result does not hold anymore in the case of cylindrical geometry.

3.4.2 Compatible control volume cell-centered discretization

In this section, we develop a compatible cell-centered discretization of the gas dynamics equations written in pseudo-Cartesian geometry. This finite volume discretization constructed by means of the expressions of the divergence and gradient operators (3.133) and (3.134) is called control volume discretization. It is obtained by extending to pseudo-Cartesian geometry the concept of sub-cell force that has been introduced previously, refer to Section 3.2.2 page 80. The present sub-cell force-based discretization is performed over a domain $\mathcal{D}$ which is paved using a collection of polygonal cells without gap or overlaps.

Notation and assumptions

Using the divergence formula (3.133) and the gradient operator definition given by (3.134), we rewrite the set of equations (3.132) as

$$m_c\frac{d}{dt}\left(\frac{1}{\rho_c}\right) - \int_{\partial\omega_c(t)} \boldsymbol{U}\cdot\boldsymbol{n}\mathcal{R}\,\mathrm{d}l = 0, \tag{3.139a}$$
$$m_c\frac{d}{dt}\boldsymbol{U}_c + \int_{\partial\omega_c(t)} P\boldsymbol{n}\mathcal{R}\,\mathrm{d}l = \alpha a_c P_c \boldsymbol{e}_y, \tag{3.139b}$$
$$m_c\frac{d}{dt}E_c + \int_{\partial\omega_c(t)} P\boldsymbol{U}\cdot\boldsymbol{n}\mathcal{R}\,\mathrm{d}l = 0. \tag{3.139c}$$

Here, a_c is the area of the cell $\omega_c(t)$ and m_c its mass, which is constant according to equation (3.132a). For any fluid variable ϕ, ϕ_c denotes its mass density average, *i.e.*,

$$\phi_c = \frac{1}{m_c}\int_{\omega_c(t)} \rho\phi\,\mathrm{d}v.$$

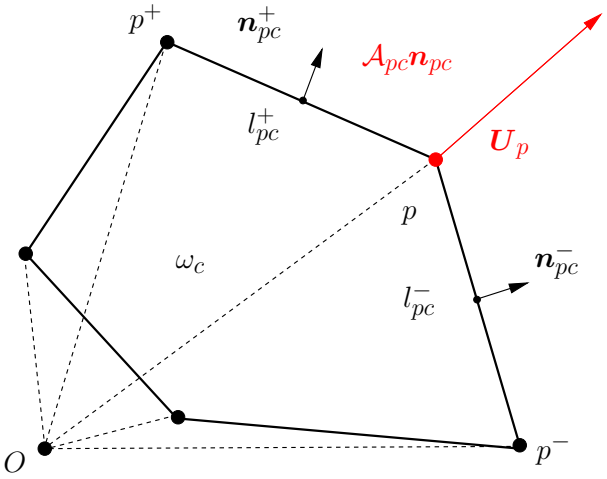

Figure 3.43: Triangulation of the polygonal cell ω_c in cylindrical geometry.

We have written a set of semi-discrete evolution equations for the cell-centered variables $(\frac{1}{\rho_c}, \boldsymbol{U}_c, E_c)$ for which the thermodynamic closure is given by the equation of state, $P_c = P(\rho_c, \varepsilon_c)$ where the cell specific internal energy is computed as $\varepsilon_c = E_c - \frac{1}{2} \mid \boldsymbol{U}_c \mid^2$. The motion of the grid is ruled by the trajectory equation written at each point

$$\frac{d}{dt}\boldsymbol{x}_p = \boldsymbol{U}_p(\boldsymbol{x}_p(t), t), \ \boldsymbol{x}_p(0) = \boldsymbol{X}_p,$$

where $\boldsymbol{x}_p$ denotes the position vector of point p and $\boldsymbol{U}_p$ its velocity. Let us note that by setting $\alpha = 0$ in the previous set of equations we recover system (3.52) which has been introduced in Cartesian geometry, refer to page 77. To achieve the discretization, it remains to determine not only the numerical fluxes, namely the surface integrals in the above system, but also the nodal velocity to move the grid.

Geometric conservation law in cylindrical geometry

Let $v_c = \int_{\omega_c(t)} \mathcal{R}\, \mathrm{d}a$ be the measure of the volume obtained by rotating the polygonal cell ω_c about x axis. Equation (3.139a) rewrites as the geometric conservation law

$$\frac{d}{dt}v_c - \int_{\partial\omega_c(t)} \boldsymbol{U}\cdot\boldsymbol{n}\mathcal{R}\ \mathrm{d}L = 0. \tag{3.140}$$

Proceeding with the volume equation as in the case of Cartesian geometry, we use the fact that v_c is a function of the position vector $\boldsymbol{x}_p$ of point p for all $p \in \mathcal{P}(c)$. To this end, let us compute this volume performing the triangular decomposition displayed in Figure 3.43. That is, using the Guldin theorem, we compute it summing the elementary volumes obtained by rotating each triangle O, p, p^+ about x axis, and we finally get

$$v_c(t) = \frac{1}{2}\sum_{p\in\mathcal{P}(c)} \frac{1}{3}\left[\mathcal{R}_O + \mathcal{R}_p(t) + \mathcal{R}_{p^+}(t)\right]\left[\boldsymbol{x}_p(t)\times\boldsymbol{x}_{p^+}(t)\right]\cdot\boldsymbol{e}_z, \tag{3.141}$$

where $\boldsymbol{e}_z = \boldsymbol{e}_x \times \boldsymbol{e}_y$. Let us remark that $\mathcal{R}_O$ denotes the pseudo radius corresponding to the origin, which is defined by $\mathcal{R}_O = 1$ for Cartesian geometry and $\mathcal{R}_O = 0$ for cylindrical geometry. As in Cartesian geometry, we note that the zone volume is expressed as a function of the position

vectors and the pseudo radii of its vertices. Applying the chain rule, time differentiation of the cell volume yields

$$\frac{d}{dt}v_c = \sum_{p\in\mathcal{P}(c)} \boldsymbol{\nabla}_{\boldsymbol{x}_p} v_c \cdot \frac{d}{dt}\boldsymbol{x}_p,$$

where $\boldsymbol{\nabla}_{\boldsymbol{x}_p} v_c$ is the gradient of the cell volume with respect to the position vector $\boldsymbol{x}_p$. This gradient is computed directly through the use of (3.141) and after some algebra one obtains

$$\boldsymbol{\nabla}_{\boldsymbol{x}_p} v_c = \frac{1}{2}\left[\frac{1}{3}(\mathcal{R}_{p^-}+2\mathcal{R}_p)(\boldsymbol{x}_p-\boldsymbol{x}_{p^-})\times\boldsymbol{e}_z + \frac{1}{3}(\mathcal{R}_{p^+}+2\mathcal{R}_p)(\boldsymbol{x}_{p^+}-\boldsymbol{x}_{p^-})\times\boldsymbol{e}_z\right].$$

This last formula allows to define the corner area vector as

$$\mathcal{A}_{pc}\boldsymbol{n}_{pc} = \frac{1}{2}\left[\frac{1}{3}(\mathcal{R}_{p^-}+2\mathcal{R}_p)(\boldsymbol{x}_p-\boldsymbol{x}_{p^-})\times\boldsymbol{e}_z + \frac{1}{3}(\mathcal{R}_{p^+}+2\mathcal{R}_p)(\boldsymbol{x}_{p^+}-\boldsymbol{x}_{p^-})\times\boldsymbol{e}_z\right], \tag{3.142}$$

where $\mathcal{A}_{pc}$ is the corner area that can be computed knowing that $\boldsymbol{n}_{pc}^2 = 1$. Noticing that the half-edge outward normals are given by $l_{pc}^-\boldsymbol{n}_{pc}^- = \frac{1}{2}(\boldsymbol{x}_p-\boldsymbol{x}_{p^-})\times\boldsymbol{e}_z$ and $l_{pc}^+\boldsymbol{n}_{pc}^+ = \frac{1}{2}(\boldsymbol{x}_{p^+}-\boldsymbol{x}_p)\times\boldsymbol{e}_z$, we rewrite (3.142) as

$$\mathcal{A}_{pc}\boldsymbol{n}_{pc} = \frac{1}{3}(\mathcal{R}_{p^-}+2\mathcal{R}_p)l_{pc}^-\boldsymbol{n}_{pc}^- + \frac{1}{3}(\mathcal{R}_{p^+}+2\mathcal{R}_p)l_{pc}^+\boldsymbol{n}_{pc}^+. \tag{3.143}$$

As noticed by Whalen in [165], the corner area vector turns out to be the fundamental geometric object that allows to define uniquely the time rate of change of the cell volume as

$$\frac{d}{dt}v_c = \sum_{p\in\mathcal{P}(c)} \mathcal{A}_{pc}\boldsymbol{n}_{pc}\cdot\boldsymbol{U}_p. \tag{3.144}$$

We point out that (3.144) is the extension of (3.58) page 79 to cylindrical geometry. This last result allows to define the discrete divergence operator over cell ω_c as follows

$$(\nabla\cdot\boldsymbol{U})_c = \frac{1}{v_c}\frac{d}{dt}v_c = \frac{1}{v_c}\sum_{p\in\mathcal{P}(c)} \mathcal{A}_{pc}\boldsymbol{n}_{pc}\cdot\boldsymbol{U}_p. \tag{3.145}$$

We also note that applying (3.145) to a constant vector, we can recover the discrete analogous of the geometric identity (3.138)

$$\sum_{p\in\mathcal{P}(c)} \mathcal{A}_{pc}\boldsymbol{n}_{pc} = \alpha a_c \boldsymbol{e}_y. \tag{3.146}$$

It is also interesting to observe that this identity can be directly recovered proceeding as follows

$$\begin{aligned}
\sum_{p\in\mathcal{P}(c)} \mathcal{A}_{pc}\boldsymbol{n}_{pc} &= \sum_{p\in\mathcal{P}(c)} \frac{1}{3}(\mathcal{R}_{p^-}+2\mathcal{R}_p)l_{pc}^-\boldsymbol{n}_{pc}^- + \frac{1}{3}(\mathcal{R}_{p^+}+2\mathcal{R}_p)l_{pc}^+\boldsymbol{n}_{pc}^+ \\
&= \sum_{p\in\mathcal{P}(c)} (\mathcal{R}_p+\mathcal{R}_{p^+})l_{pc}^+\boldsymbol{n}_{pc}^+, \quad \text{shifting indices } p^-\to p \text{ and } p\to p^+ \\
&= \sum_{p\in\mathcal{P}(c)} \alpha(y_p+y_{p^+})l_{pc}^+\boldsymbol{n}_{pc}^+, \quad \text{using the definition of } \mathcal{R}_p \\
&= \frac{1}{2}\sum_{p\in\mathcal{P}(c)} \alpha(y_p+y_{p^+})\begin{pmatrix} y_{p^+}-y_p \\ -(x_{p^+}-x_p)\end{pmatrix}.
\end{aligned}$$

We conclude by noticing that first $\sum_{p\in\mathcal{P}(c)} yp^{+2} - y_p^2 = 0$, as the summation is cyclic, and second $-\frac{1}{2}\sum_{p\in\mathcal{P}(c)}(y_p+y_{p^+})(x_{p^+}-x_p) = a_c$ which ends the proof.

We claim that we have completely defined the volume flux in terms of the corner area vector and the nodal velocity. Moreover, this derivation is compatible with the mesh motion.

Sub-cell force-based discretization

Proceeding with the discretization as in the Cartesian case, we discretize momentum and total energy equations by means of sub-cell force. Introducing, the partition of each polygonal cell ω_c into sub-cells ω_{pc} for $p \in \mathcal{P}(c)$, the sub-cell force that acts from sub-cell ω_{pc} onto point p is defined as

$$\boldsymbol{F}_{pc} = \int_{\partial\omega_{pc}\cap\partial\omega_c} P\boldsymbol{n}\mathcal{R}\,\mathrm{d}l. \tag{3.147}$$

We also use the sub-cell-based partition to write the total energy flux

$$\int_{\partial\omega_c} P\boldsymbol{U}\cdot\boldsymbol{n}\mathcal{R}\,\mathrm{d}l = \sum_{p\in\mathcal{P}(c)}\int_{\partial\omega_{pc}\cap\partial\omega_c} P\boldsymbol{U}\cdot\boldsymbol{n}\mathcal{R}\,\mathrm{d}l.$$

As previously the sub-cell contribution to the total energy flux is expressed in terms of sub-cell force $\boldsymbol{F}_{cp}$ using the approximation

$$\begin{aligned}\int_{\partial\omega_{pc}\cap\partial\omega_c} P\boldsymbol{U}\cdot\boldsymbol{n}\mathcal{R}\,\mathrm{d}l &= \left(\int_{\partial\omega_{pc}\cap\partial\omega_c} P\boldsymbol{n}\mathcal{R}\,\mathrm{d}l\right)\cdot\boldsymbol{U}_p\\ &= \boldsymbol{F}_{pc}\cdot\boldsymbol{U}_p.\end{aligned}$$

Substituting the previous results into system (3.139) yields

$$m_c\frac{d}{dt}(\frac{1}{\rho_c}) - \sum_{p\in\mathcal{P}(c)}\mathcal{A}_{pc}\boldsymbol{n}_{pc}\cdot\boldsymbol{U}_p = 0, \tag{3.148a}$$

$$m_c\frac{d}{dt}\boldsymbol{U}_c + \sum_{p\in\mathcal{P}(c)}\boldsymbol{F}_{pc} = \alpha P_c a_c\boldsymbol{e}_y, \tag{3.148b}$$

$$m_c\frac{d}{dt}E_c + \sum_{p\in\mathcal{P}(c)}\boldsymbol{F}_{pc}\cdot\boldsymbol{U}_p = 0. \tag{3.148c}$$

We have expressed the numerical fluxes in terms of the corner area vector, the sub-cell force and the nodal velocity. To complete the discretization it remains to determine the sub-cell force and the nodal velocity. This task will be achieved by invoking the thermodynamic consistency and the conservation principle of total energy.

Thermodynamic consistency

We derive a general form of the sub-cell force requiring that the semi-discrete scheme (3.148) satisfies a semi-discrete entropy inequality. Thanks to Gibbs formula, the time rate of change of entropy within cell c writes

$$m_c T_c\frac{d}{dt}\eta_c = m_c\left[\frac{d}{dt}\varepsilon_c + P_c\frac{d}{dt}\left(\frac{1}{\rho_c}\right)\right],$$

where η_c is the specific entropy and T_c the temperature in cell c. We first compute the time rate of change of specific internal energy by dot-multiplying (3.148b) by $\boldsymbol{U}_c$ and subtracting it from (3.148c) to obtain

$$m_c\frac{d}{dt}\varepsilon_c = -\sum_{p\in\mathcal{P}(c)}\boldsymbol{F}_{pc}\cdot(\boldsymbol{U}_p-\boldsymbol{U}_c) - \alpha P_c a_c\boldsymbol{e}_y.$$

We rearrange the second term in the right hand-side through the use of the geometric identity (3.146) and rewrite the above equation as

$$m_c \frac{d}{dt}\varepsilon_c = -\sum_{p\in\mathcal{P}(c)} [\boldsymbol{F}_{pc}\cdot(\boldsymbol{U}_p-\boldsymbol{U}_c) + \mathcal{A}_{pc}P_c\boldsymbol{n}_{pc}\cdot\boldsymbol{U}_c]. \tag{3.149}$$

We compute the time rate of change of pressure work by multiplying (3.148a) by P_c

$$m_c P_c \frac{d}{dt}\left(\frac{1}{\rho_c}\right) = \sum_{p\in\mathcal{P}(c)} \mathcal{A}_{pc}P_c\boldsymbol{n}_{pc}\cdot\boldsymbol{U}_p.$$

Adding the above equation and (3.149) leads to the following final form of the time rate of change of specific entropy within cell c

$$m_c T_c \frac{d}{dt}\eta_c = -\sum_{p\in\mathcal{P}(c)} \left[(\boldsymbol{F}_{pc}-\mathcal{A}_{pc}P_c\boldsymbol{n}_{pc})\cdot(\boldsymbol{U}_p-\boldsymbol{U}_c)\right]. \tag{3.150}$$

The sub-cell force-based discretization satisfies a local entropy inequality provided that the right-hand side of (3.150) is non-negative. A sufficient condition to ensure this consists in postulating the following form for the sub-cell force

$$\boldsymbol{F}_{pc} = \mathcal{A}_{pc}P_c\boldsymbol{n}_{pc} - \mathsf{M}_{pc}(\boldsymbol{U}_p-\boldsymbol{U}_c), \tag{3.151}$$

where M_{pc} is a 2×2 **positive semi-definite** matrix, *i.e.*, $\mathsf{M}_{pc}\boldsymbol{U}\cdot\boldsymbol{U}\geq 0, \quad \forall \boldsymbol{U}\in\mathbb{R}^2$. Note that the above expression of the sub-cell force is the natural extension to pseudo-Cartesian geometry of the expression initially derived in Cartesian geometry, refer to (3.64) page 82. The physical dimension of M_{pc} corresponds to an area times a density times a velocity. As in the Cartesian case, the matrix expression must satisfies the principle of Galilean invariance. From now on, we assume that M_{pc} is positive semi-definite. Substituting (3.151) into (3.150) yields the entropy inequality

$$m_c T_c \frac{d}{dt}\eta_c = \sum_{p\in\mathcal{P}(c)} \mathsf{M}_{pc}\,(\boldsymbol{U}_p-\boldsymbol{U}_c)\cdot(\boldsymbol{U}_p-\boldsymbol{U}_c)\geq 0, \tag{3.152}$$

as the right-hand side is a positive semi-definite quadratic form. We remark that entropy production within cell c is directly governed by the sub-cell matrix M_{pc} and the velocity jump between the nodal and the cell-centered velocity, $\Delta\boldsymbol{U}_{pc} = \boldsymbol{U}_p - \boldsymbol{U}_c$.

Conservation principles

As in the Cartesian case, we invoke the conservation of total energy to determine a balance equation satisfied by the sub-cell forces surrounding a given node.

Recall that total energy over the entire domain is defined as $\mathcal{E}(t) = \sum_c m_c E_c(t)$, its conservation amounts to write

$$\frac{d}{dt}\mathcal{E} = -\int_{\partial\mathcal{D}} P\boldsymbol{U}\cdot\boldsymbol{n}\mathcal{R}\,\mathrm{d}l,$$

where the right-hand side expresses the time rate of pressure work on the boundary, $\partial\mathcal{D}$, of the domain, $\mathcal{D}$, occupied by the fluid. By definition of total energy, this last equation rewrites

$$\sum_c m_c \frac{d}{dt}E_c = -\int_{\partial\mathcal{D}} P\boldsymbol{U}\cdot\boldsymbol{n}\mathcal{R}\,\mathrm{d}l. \tag{3.153}$$

Substituting the specific total energy equation (3.148c) into (3.153) yields the balance of total energy over the entire domain

$$\sum_c \sum_{p\in\mathcal{P}(c)} \boldsymbol{F}_{pc}\cdot\boldsymbol{U}_p = \sum_{p\in\partial\mathcal{D}} \boldsymbol{F}_p^\star\cdot\boldsymbol{U}_p, \tag{3.154}$$

where $\boldsymbol{F}_p^\star$ is the boundary corner force acting from the exterior boundary onto point p that results from the discretization of the right-hand side of (3.153). More precisely, $\boldsymbol{F}_p^\star$ is the analogous of (3.67) page 83 in pseudo-Cartesian geometry

$$\boldsymbol{F}_p^\star = \int_{\partial\mathcal{D}_p} P\boldsymbol{n}\mathcal{R}\,\mathrm{d}l, \tag{3.155}$$

where $\partial\mathcal{D}_p$ is a subdivision of the curvilinear boundary attached to point p, which is defined page 83. Now, interchanging order of double sum in the left-hand side of (3.154) yields

$$\sum_p (\sum_{c\in\mathcal{C}(p)} \boldsymbol{F}_{pc})\cdot\boldsymbol{U}_p = \sum_{p\in\partial\mathcal{D}} \boldsymbol{F}_p^\star\cdot\boldsymbol{U}_p,$$

where $\mathcal{C}(p)$ is the set of cells surrounding point p. Finally, the left-hand side of the above equation is divided into two parts depending on the points location

$$\sum_{p\in\mathcal{D}^o} (\sum_{c\in\mathcal{C}(p)} \boldsymbol{F}_{pc})\cdot\boldsymbol{U}_p + \sum_{p\in\partial\mathcal{D}} (\sum_{c\in\mathcal{C}(p)} \boldsymbol{F}_{pc})\cdot\boldsymbol{U}_p = \sum_{p\in\partial\mathcal{D}} \boldsymbol{F}_p^\star\cdot\boldsymbol{U}_p, \tag{3.156}$$

where $\mathcal{D}^o$ is the interior of the domain $\mathcal{D}$. **Knowing that the total energy balance** (3.68) **must hold regardless the value of the nodal velocity, total energy conservation is ensured if and only if**

$$\forall\, p\in\mathcal{D}^o,\quad \sum_{c\in\mathcal{C}(p)} \boldsymbol{F}_{pc} = \boldsymbol{0}, \tag{3.157a}$$

$$\forall\, p\in\partial\mathcal{D},\quad \sum_{c\in\mathcal{C}(p)} \boldsymbol{F}_{pc} = \boldsymbol{F}_p^\star. \tag{3.157b}$$

We note that we recover exactly the same conservation condition than the one obtained in Cartesian geometry, refer to (3.68) page 83. This result is remarkable in the sense that it is written under the same form regardless the geometry employed. It demonstrates the generality of the sub-cell force formalism. Now, it remains to investigate in what extent the previous condition leads to momentum conservation. If $\mathcal{Q}$ denotes the total momentum over the entire domain, *i.e.*, $\mathcal{Q} = \sum_c m_c\boldsymbol{U}_c$, its time rate of change is given by

$$\begin{aligned}
\frac{d}{dt}\mathcal{Q} &= \sum_c m_c\frac{d}{dt}\boldsymbol{U}_c \\
&= -\sum_c \sum_{p\in\mathcal{P}(c)} \boldsymbol{F}_{pc} + \alpha(\sum_c P_c a_c)\boldsymbol{e}_y, \quad \text{thanks to (3.148b)} \\
&= -\sum_{p\in\mathcal{D}^o} \sum_{c\in\mathcal{C}(p)} \boldsymbol{F}_{pc} - \sum_{p\in\partial\mathcal{D}} \sum_{c\in\mathcal{C}(p)} \boldsymbol{F}_{pc} + \alpha(\sum_c P_c a_c)\boldsymbol{e}_y, \quad \text{interchanging order of double sum} \\
&= -\sum_{p\in\partial\mathcal{D}} \boldsymbol{F}_p^\star + \alpha(\sum_c P_c a_c)\boldsymbol{e}_y, \quad \text{thanks to (3.157)} \\
&= -\int_{\partial\mathcal{D}} P\boldsymbol{n}\mathcal{R}\,\mathrm{d}l + \alpha(\sum_c P_c a_c)\boldsymbol{e}_y, \quad \text{thanks to (3.155).}
\end{aligned}$$

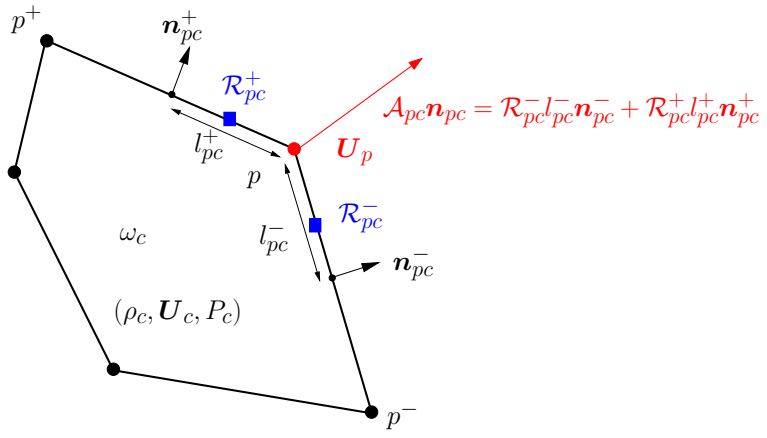

Figure 3.44: Notation related to EUCCLHYD scheme at corner pc for a polygonal cell in pseudo-Cartesian geometry.

We conclude that up to the boundary terms and the radial source term contributions, momentum is conserved over the entire domain. Hence, conditions (3.157a) and (3.157b) turn out to ensure not only total energy but also momentum conservation.

Node-centered solver

The node-centered solver that solves the grid velocity is obtained as the consequence of total energy conservation. Substituting the expression of the sub-cell force (3.151) into condition (3.157) yields

$$\forall\, p \in \mathcal{D}^o, \quad \mathsf{M}_p \boldsymbol{U}_p = \sum_{c \in \mathcal{C}(p)} \left(\mathcal{A}_{pc} P_c \boldsymbol{n}_{pc} + \mathsf{M}_{pc} \boldsymbol{U}_c \right), \tag{3.158a}$$

$$\forall\, p \in \partial\mathcal{D}, \quad \mathsf{M}_p \boldsymbol{U}_p = \sum_{c \in \mathcal{C}(p)} \left(\mathcal{A}_{pc} P_c \boldsymbol{n}_{pc} + \mathsf{M}_{pc} \boldsymbol{U}_c \right) - \boldsymbol{F}_p^\star. \tag{3.158b}$$

As in Cartesian geometry, M_p is the sum of the corner matrices around node p, which is defined as $\mathsf{M}_p = \sum_{c \in \mathcal{C}(p)} \mathsf{M}_{pc}$. We construct the natural extension of EUCCLHYD scheme to cylindrical geometry by defining the corner matrix as

$$\mathsf{M}_{pc} = z_{pc}^- \mathcal{R}_{pc}^- l_{pc}^- (\boldsymbol{n}_{pc}^- \otimes \boldsymbol{n}_{pc}^-) + z_{pc}^- \mathcal{R}_{pc}^+ l_{pc}^+ (\boldsymbol{n}_{pc}^+ \otimes \boldsymbol{n}_{pc}^+), \tag{3.159}$$

where the radii $\mathcal{R}_{pc}^\pm$ are defined as

$$\mathcal{R}_{pc}^\pm = \frac{1}{3}(\mathcal{R}_{p^\pm} + 2\mathcal{R}_p). \tag{3.160}$$

Using the above notation and according to (3.143) page 133 the corner vector expresses as

$$\mathcal{A}_{pc}\boldsymbol{n}_{pc} = \mathcal{R}_{pc}^- l_{pc}^- \boldsymbol{n}_{pc}^- + \mathcal{R}_{pc}^+ l_{pc}^+ \boldsymbol{n}_{pc}^+. \tag{3.161}$$

We recall that $l_{pc}^\pm \boldsymbol{n}_{pc}^\pm$ are the half-edge outward normals, refer to Figure 3.44, and $z_{pc}^\pm$ are the non-linear impedances, refer to (3.86) page 92. One can easily check that this definition leads to symmetric positive definite corner matrix. Therefore, M_p is also symmetric positive definite and thus always invertible, which allows to define uniquely the nodal velocity $\boldsymbol{U}_p$ by solving equations (3.158a) and (3.158b).

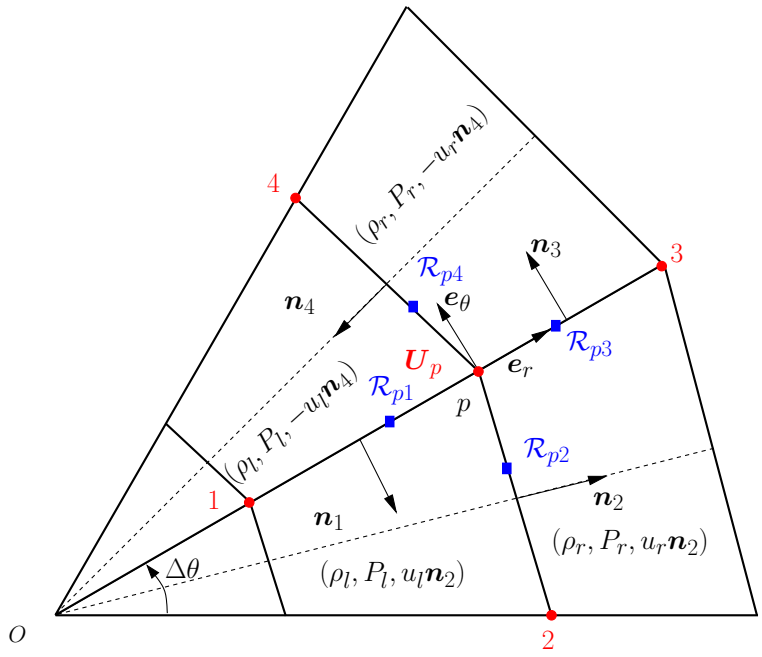

Figure 3.45: Fragment of an equal angle polar grid and notation for a one-dimensional spherical flow.

Spherical symmetry preservation of the node-centered solver

Here, we show that the nodal solver based on the above definition of the M_{pc} matrix, preserves the spherical symmetry in the case of a one-dimensional spherical flow computed on an equal angle polar grid. To this end, let us consider the point p surrounded by four quadrangular cells as displayed in Figure 3.45. To simplify the computation, we use the orthonormal basis $(\boldsymbol{e}_r, \boldsymbol{e}_\theta)$ located at point p. Due to the spherical symmetry of the flow, the thermodynamical quantities and the magnitude of the radial cell-centered velocities are equal in cells having the same centroid radius, refer to Figure 3.45. The four points that are directly connected to point p are labelled from 1 to 4 in the counterclockwise order. The unit normals and the length of the edges impinging at point p are denoted $\boldsymbol{n}_i$ and l_i with $i = 1 \dots 4$. In the local basis $(\boldsymbol{e}_r, \boldsymbol{e}_\theta)$, these unit normals write

$$\boldsymbol{n}_1 = \begin{pmatrix} 0 \\ -1 \end{pmatrix}, \quad \boldsymbol{n}_2 = \begin{pmatrix} \cos\frac{\Delta\theta}{2} \\ -\sin\frac{\Delta\theta}{2} \end{pmatrix}, \quad \boldsymbol{n}_3 = \begin{pmatrix} 0 \\ 1 \end{pmatrix}, \quad \boldsymbol{n}_4 = \begin{pmatrix} -\cos\frac{\Delta\theta}{2} \\ -\sin\frac{\Delta\theta}{2} \end{pmatrix}.$$

We also introduce the radius attached to the edge connecting point p by setting

$$\mathcal{R}_{pi} = \frac{1}{3}(2\mathcal{R}_p + \mathcal{R}_i), \quad \text{for } i = 1 \dots 4.$$

Now, using the acoustic approximation, we evaluate the M_p matrix and the $\boldsymbol{RH}$ vector which corresponds to the right-hand side of (3.158a). The nodal velocity is the solution of the linear system $\mathsf{M}_p \boldsymbol{U}_p = \boldsymbol{RH}$. Some elementary calculations provide the entries of the matrix M_p

$$\begin{aligned}
M_{p,rr} &= (z_l + z_r) l_2 (\mathcal{R}_{p2} + \mathcal{R}_{p4}) \cos^2 \frac{\Delta\theta}{2}, \\
M_{p,r\theta} &= M_{p,\theta r} = (z_l + z_r) l_2 (\mathcal{R}_{p4} - \mathcal{R}_{p2}) \cos\frac{\Delta\theta}{2} \sin\frac{\Delta\theta}{2}, \\
M_{p,\theta\theta} &= (z_l + z_r) l_2 (\mathcal{R}_{p2} + \mathcal{R}_{p4}) \sin^2 \frac{\Delta\theta}{2} + 2(z_l l_1 \mathcal{R}_{p1} + z_r l_3 \mathcal{R}_{p3}).
\end{aligned}$$

The components of the right-hand side write

$$RH_r = [z_l u_l + z_r u_r - (P_r - P_l)]\, l_2(\mathcal{R}_{p2} + \mathcal{R}_{p4}) \cos\frac{\Delta\theta}{2},$$
$$RH_\theta = [z_l u_l + z_r u_r - (P_r - P_l)]\, l_2(\mathcal{R}_{p4} - \mathcal{R}_{p2}) \sin\frac{\Delta\theta}{2}.$$

In writing the above equations, we have used the fact that $l_2 = l_4$ due to the symmetry of the grid. Solving the linear system $\mathsf{M}_p \boldsymbol{U}_p = \boldsymbol{RH}$ yields the nodal velocity expressed in the local basis $(\boldsymbol{e}_r, \boldsymbol{e}_\theta)$ as

$$\boldsymbol{U}_p = \frac{z_l u_l + z_r u_r - (P_r - P_l)}{z_l + z_r} \frac{1}{\cos\frac{\Delta\theta}{2}} \boldsymbol{e}_r.$$

The nodal velocity is radial, thus the nodal solver preserves the spherical symmetry on equal angle polar grid. Moreover, We have recovered the classical one-dimensional acoustic Godunov solver modified by a geometrical factor which corresponds to the projection of the cell velocity direction onto the radial vector $\boldsymbol{e}_r$. This geometrical factor has no consequence since $\cos\frac{\Delta\theta}{2} \to 1$ when $\Delta\theta \to 0$. We point out that the symmetry preservation is due to the fact that the mesh is equally spaced in the angular direction. If the mesh does not satisfy this assumption, then $l_2 \neq l_4$ and thus the nodal velocity is not radial anymore.

High-order extension based on the acoustic GRP method

To develop the high-order extension of our control volume discretization in cylindrical geometry, we proceed as in the case of Cartesian geometry by using the Generalized Riemann Problem methodology in the acoustic approximation. The second-order time discretization of the semi-discrete scheme (3.148) writes

$$m_c \left(\frac{1}{\rho_c^{n+1}} - \frac{1}{\rho_c^n}\right) - \Delta t \sum_{p\in\mathcal{P}(c)} \langle \mathcal{A}_{pc}\boldsymbol{n}_{pc}\rangle^{n+\frac{1}{2}} \cdot \boldsymbol{U}_p^{n+\frac{1}{2}} = 0, \tag{3.162a}$$

$$m_c \left(\boldsymbol{U}_c^{n+1} - \boldsymbol{U}_c^n\right) + \Delta t \sum_{p\in\mathcal{P}(c)} \boldsymbol{F}_{pc}^{n+\frac{1}{2}} = \alpha (P_c a_c)^{n+\frac{1}{2}} \boldsymbol{e}_y, \tag{3.162b}$$

$$m_c \left(E_c^{n+1} - E_c^n\right) + \Delta t \sum_{p\in\mathcal{P}(c)} \boldsymbol{F}_{pc}^{n+\frac{1}{2}} \cdot \boldsymbol{U}_p^{n+\frac{1}{2}} = 0, \tag{3.162c}$$

where $\langle \mathcal{A}_{pc}\boldsymbol{n}_{pc}\rangle^{n+\frac{1}{2}}$ stands for the mean value of the corner area vector over the time interval $[t^n, t^{n+1}]$. The grid motion is defined through the use of the discrete trajectory equation which reads as usual

$$\boldsymbol{x}_p^{n+\frac{1}{2}} = \boldsymbol{x}_p^n + \Delta t \boldsymbol{U}_p^{n+\frac{1}{2}},\ \boldsymbol{x}_p(0) = \boldsymbol{X}_p.$$

As in Cartesian geometry, time-centered nodal velocity and sub-cell force are expressed using the following Taylor expansions

$$\boldsymbol{U}_p^{n+\frac{1}{2}} = \boldsymbol{U}_p^n + \frac{\Delta t}{2}\frac{d}{dt}\boldsymbol{U}_p^n,$$
$$\boldsymbol{F}_{pc}^{n+\frac{1}{2}} = \boldsymbol{F}_{pc}^n + \frac{\Delta t}{2}\frac{d}{dt}\boldsymbol{F}_{pc}^n,$$

where the time derivatives of the nodal velocity and the sub-cell force will be determined using total energy conservation. The source term in momentum equation (3.162b) is discretized as

$$(P_c a_c)^{n+\frac{1}{2}} = P_c^n a_c^n + \frac{\Delta t}{2}\left(a_c^n \frac{d}{dt}P_c^n + P_c^n \frac{d}{dt}a_c^n\right). \tag{3.163}$$

Here, the cell-centered time derivative of pressure is computed using the gas dynamics equation written in non-conservative form, refer to (3.107) page 98.

$$\frac{d}{dt}P = -\rho a^2 \nabla \cdot \boldsymbol{U}.$$

The time derivative of the area a_c is evaluated by time differentiating the geometric identity (3.146) page 133

$$\frac{d}{dt}a_c = \sum_{p\in\mathcal{P}(c)} \frac{d}{dt}(\mathcal{A}_{pc}\boldsymbol{n}_{pc}) \cdot \boldsymbol{e}_y. \tag{3.164}$$

Finally, the intermediate value of the corner area vector, $\langle \mathcal{A}_{pc}\boldsymbol{n}_{pc}\rangle^{n+\frac{1}{2}}$ is discretized so that the GCL is rigorously satisfied at the discrete level. Knowing that by definition

$$\langle \mathcal{A}_{pc}\boldsymbol{n}_{pc}\rangle^{n+\frac{1}{2}} = \frac{1}{\Delta t}\int_{t^n}^{t^{n+1}} (\mathcal{A}_{pc}\boldsymbol{n}_{pc})(t)\,\mathrm{d}t,$$

the previous requirement involves that the integral in the right-hand side of the above equation must be computed exactly. As the integrand is a quadratic function of time, exact integration is obtained if one employs Simpson quadrature rule, which yields

$$\langle \mathcal{A}_{pc}\boldsymbol{n}_{pc}\rangle^{n+\frac{1}{2}} = \frac{1}{6}\left[(\mathcal{A}_{pc}\boldsymbol{n}_{pc})(t^n) + 4(\mathcal{A}_{pc}\boldsymbol{n}_{pc})(t^{n+\frac{1}{2}}) + (\mathcal{A}_{pc}\boldsymbol{n}_{pc})(t^{n+1})\right], \tag{3.165}$$

where $t^{n+\frac{1}{2}} = t^n + \frac{\Delta t}{2}$. Using this discretization of the corner area vector we conclude that the zone volume computed from its coordinates and the zone volume that results from solving the discrete volume equation (3.162a) are rigorously equal.

Conservation principle for the discrete scheme We show that the requirement of total energy conservation for the discrete scheme (3.162) allows to derive a node-centered solver which solves not only the nodal velocity but also its time derivative. As the demonstration coincides with the one that has been done in Cartesian geometry, refer to page 96, we only recall the main result which consists in the following necessary and sufficient condition to have total energy conservation at the discrete level

$$\forall\, p \in \mathcal{D}^o, \quad \sum_{c\in\mathcal{C}(p)} \boldsymbol{F}_{pc}^{n+\frac{1}{2}} = \boldsymbol{0}, \tag{3.166a}$$

$$\forall\, p \in \partial\mathcal{D}, \quad \sum_{c\in\mathcal{C}(p)} \boldsymbol{F}_{pc}^{n+\frac{1}{2}} = \boldsymbol{F}_p^{\star,n+\frac{1}{2}}. \tag{3.166b}$$

Here, we have subdivided this condition in two cases depending on whether the points are located inside the domain or on its boundary. Substituting the expression of the time-centered sub-cell force, $\boldsymbol{F}_{pc}^{n+\frac{1}{2}} = \boldsymbol{F}_{pc}^n + \frac{\Delta t}{2}\frac{d}{dt}\boldsymbol{F}_{pc}^n$ and invoking the fact that (3.166a) and (3.166b) must be satisfied regardless of the time step Δt leads to the following necessary and sufficient conditions that concern, firstly the sub-cell force at time t^n

$$\forall\, p \in \mathcal{D}^o, \quad \sum_{c\in\mathcal{C}(p)} \boldsymbol{F}_{pc}^{n} = \boldsymbol{0}, \tag{3.167a}$$

$$\forall\, p \in \partial\mathcal{D}, \quad \sum_{c\in\mathcal{C}(p)} \boldsymbol{F}_{pc}^{n} = \boldsymbol{F}_p^{\star,n}, \tag{3.167b}$$

and secondly its time derivative at time t^n

$$\forall\, p \in \mathcal{D}^o, \quad \sum_{c\in\mathcal{C}(p)} \frac{d}{dt}\boldsymbol{F}_{pc}^n = \boldsymbol{0}, \tag{3.168a}$$

$$\forall\, p \in \partial\mathcal{D}, \quad \sum_{c\in\mathcal{C}(p)} \frac{d}{dt}\boldsymbol{F}_{pc}^n = \frac{d}{dt}\boldsymbol{F}_{p}^{\star,n}, \tag{3.168b}$$

where $\boldsymbol{F}_p^{\star,n+\frac{1}{2}}$ is a time-centered evaluation of the prescribed boundary force acting onto point p, which reads

$$\boldsymbol{F}_p^{\star,n+\frac{1}{2}} = \boldsymbol{F}_p^{n,\star} + \frac{\Delta t}{2}\frac{d}{dt}\boldsymbol{F}_p^{n,\star}. \tag{3.169}$$

where $\boldsymbol{F}_p^{n,\star}$ denotes the value of the prescribed boundary force at time t^n and $\frac{\Delta t}{2}\frac{d}{dt}\boldsymbol{F}_p^{n,\star}$ its time derivative at time t^n. These two values are supposed to be known.

Let us emphasize that the above conditions exactly coincide with the ones that have been derived in Cartesian geometry. This underlines, once more, the general feature of the sub-cell force formalism. Condition (3.167) corresponds to the sub-cell forces balance at point p, whereas condition (3.168) represents the balance of the time derivative of the sub-cell forces acting onto point p. We claim that these conditions also provide momentum conservation over the entire domain, the proof is left to the reader.

Node-centered solver for the grid velocity The nodal velocity is obtained by solving the system which results from the conservation condition (3.167) wherein the sub-cell force $\boldsymbol{F}_{pc}^n$ is expressed as follows

$$\boldsymbol{F}_{pc}^n = \mathcal{A}_{pc}^n \widetilde{P}_c(\boldsymbol{x}_p^n)\boldsymbol{n}_{pc}^n - \mathsf{M}_{pc}^n\left[\boldsymbol{U}_p^n - \widetilde{\boldsymbol{U}}_c(\boldsymbol{x}_p^n)\right]. \tag{3.170}$$

In this equation, $\widetilde{P}_c = \widetilde{P}_c(\boldsymbol{x})$ and $\widetilde{\boldsymbol{U}}_c = \widetilde{\boldsymbol{U}}_c(\boldsymbol{x})$ denote the piecewise linear representations of the pressure and the velocity over the cell ω_c. Substituting the above expression in (3.167) leads to the system satisfied by the nodal velocity

$$\forall\, p \in \mathcal{D}^o, \quad \mathsf{M}_p^n\boldsymbol{U}_p^n = \sum_{c\in\mathcal{C}(p)}\left[\mathcal{A}_{pc}^n\widetilde{P}_c(\boldsymbol{x}_p^n)\boldsymbol{n}_{pc}^n + \mathsf{M}_{pc}^n\widetilde{\boldsymbol{U}}_c(\boldsymbol{x}_p^n)\right], \tag{3.171a}$$

$$\forall\, p \in \partial\mathcal{D}, \quad \mathsf{M}_p^n\boldsymbol{U}_p^n = \sum_{c\in\mathcal{C}(p)}\left[\mathcal{A}_{pc}^n\widetilde{P}_c(\boldsymbol{x}_p^n)\boldsymbol{n}_{pc}^n + \mathsf{M}_{pc}^n\widetilde{\boldsymbol{U}}_c(\boldsymbol{x}_p^n)\right] - \boldsymbol{F}_p^{\star,n}, \tag{3.171b}$$

where M_p^n denotes the 2×2 positive semi-definite node-centered matrix defined as $\mathsf{M}_p^n = \sum_{c\in\mathcal{C}(p)}\mathsf{M}_{pc}^n$. Note that the second system allows to define the boundary conditions, refer to page 84 for more details.

Node-centered solver for the time derivative of the grid velocity Using the chain rule, time differentiation of the sub-cell force in pseudo-Cartesian geometry yields

$$\frac{d}{dt}\boldsymbol{F}_{pc} = \mathcal{A}_{pc}\boldsymbol{n}_{pc}\frac{d}{dt}P_c - \mathsf{M}_{pc}(\frac{d}{dt}\boldsymbol{U}_p - \frac{d}{dt}\boldsymbol{U}_c) + \frac{d}{dt}(\mathcal{A}_{pc}\boldsymbol{n}_{pc})P_c - \frac{d}{dt}(\mathsf{M}_{pc})(\boldsymbol{U}_p - \boldsymbol{U}_c).$$

Here, we have assumed that all the variables that are involved in the sub-cell force expression depend on time. Regarding the corner matrix, this assumption makes sense as the corner matrix derived page 137 writes

$$\mathsf{M}_{pc} = z_{pc}^-\mathcal{R}_{pc}^- l_{pc}^-(\boldsymbol{n}_{pc}^-\otimes\boldsymbol{n}_{pc}^-) + z_{pc}^-\mathcal{R}_{pc}^+ l_{pc}^+(\boldsymbol{n}_{pc}^+\otimes\boldsymbol{n}_{pc}^+).$$

Using the gas dynamics equations written in non-conservative form, refer to (3.107), we recall that the time derivative of pressure and velocity within cell c read

$$\frac{d}{dt}P_c = -\,\rho_c a_c^2\,(\nabla\cdot\boldsymbol{U})_c\,,$$
$$\frac{d}{dt}\boldsymbol{U}_c = -\,\frac{1}{\rho_c}\,(\boldsymbol{\nabla}P)_c\,,$$

where the cell-averaged velocity divergence and pressure gradient result from a piecewise linear reconstruction based on a least squares approach, refer to page 100.

To achieve the computation of the time derivative of the sub-cell force it remains to express the time derivatives of the area corner vector and the corner matrix. We recall that the area corner vector and the corner matrix are expressed as functions of the normal vectors related to the half-edges impinging on point p as follows

$$\mathcal{A}_{pc}\boldsymbol{n}_{cp} = \mathcal{R}^-_{pc}l^-_{pc}\boldsymbol{n}^-_{pc} + \mathcal{R}^+_{pc}l^+_{pc}\boldsymbol{n}^+_{pc},$$
$$\mathsf{M}_{pc} = z^-_{pc}\mathcal{R}^-_{pc}l^-_{pc}\left(\boldsymbol{n}^-_{pc}\otimes\boldsymbol{n}^-_{pc}\right) + z^+_{pc}\mathcal{R}^+_{pc}l^+_{pc}\left(\boldsymbol{n}^+_{pc}\otimes\boldsymbol{n}^+_{pc}\right),$$

where $\mathcal{R}^\pm_{pc} = \frac{1}{3}(2\mathcal{R}_p + \mathcal{R}^\pm_p)$. Recalling that the normal vectors $l^-_{pc}\boldsymbol{n}^-_{pc}$, $l^+_{pc}\boldsymbol{n}^+_{pc}$ are defined in terms of the position vectors, their time derivatives are easily computed. Using chain rule derivative, one obtains the time derivative of the area corner vector. Concerning the corner matrix, its time derivative writes

$$\frac{d}{dt}\mathsf{M}_{pc} = \sum_{\pm} z^\pm_{pc}\left[\frac{d}{dt}\left(\mathcal{R}^\pm_{pc}l^\pm_{pc}\boldsymbol{n}^\pm_{pc}\right)\otimes\boldsymbol{n}^\pm_{pc} + \left(\mathcal{R}^\pm_{pc}l^\pm_{pc}\boldsymbol{n}^\pm_{pc}\right)\otimes\frac{d}{dt}\boldsymbol{n}^\pm_{pc}\right].$$

Combining the previous results, we write the time derivative of the sub-cell force at time t^n as

$$\frac{d}{dt}\boldsymbol{F}^n_{pc} = -\rho^n_c(a^n_c)^2\,(\nabla\cdot\boldsymbol{U})^n_c\,\mathcal{A}^n_{pc}\boldsymbol{n}^n_{pc} - \mathsf{M}^n_{pc}\left[\frac{d}{dt}\boldsymbol{U}^n_p + \frac{1}{\rho^n_c}\,(\boldsymbol{\nabla}P)^n_c\right] + P^n_c\frac{d}{dt}(\mathcal{A}^n_{pc}\boldsymbol{n}^n_{pc}) - \frac{d}{dt}(\mathsf{M}^n_{pc})(\boldsymbol{U}^n_p - \boldsymbol{U}^n_c).$$

Finally, substituting this last expression in the conservation condition (3.103a), we obtain the system satisfied by the time derivative of the nodal velocity for an interior node

$$\begin{aligned}\forall\, p\in\mathcal{D}^o,\quad \mathsf{M}^n_p\frac{d}{dt}\boldsymbol{U}^n_p = &-\sum_{c\in\mathcal{C}(p)}\frac{1}{\rho_c}\left[\mathsf{M}^n_{pc}\,(\boldsymbol{\nabla}P)^n_c + (z^n_c)^2\mathcal{A}^n_{pc}\boldsymbol{n}^n_{pc}\,(\nabla\cdot\boldsymbol{U})^n_c\right]\\ &+\sum_{c\in\mathcal{C}(p)}\left[P^n_c\frac{d}{dt}(\mathcal{A}^n_{pc}\boldsymbol{n}^n_{pc}) - \frac{d}{dt}(\mathsf{M}^n_{pc})(\boldsymbol{U}^n_p - \boldsymbol{U}^n_c)\right].\end{aligned}\tag{3.172}$$

For a node located on the boundary, using (3.103b), we readily get

$$\begin{aligned}\forall\, p\in\partial\mathcal{D},\quad \mathsf{M}^n_p\frac{d}{dt}\boldsymbol{U}^n_p = &-\sum_{c\in\mathcal{C}(p)}\frac{1}{\rho_c}\left[\mathsf{M}^n_{pc}\,(\boldsymbol{\nabla}P)^n_c + (z^n_c)^2\mathcal{A}^n_{pc}\boldsymbol{n}^n_{pc}\,(\nabla\cdot\boldsymbol{U})^n_c\right]\\ &+\sum_{c\in\mathcal{C}(p)}\left[P^n_c\frac{d}{dt}(\mathcal{A}^n_{pc}\boldsymbol{n}^n_{pc}) - \frac{d}{dt}(\mathsf{M}^n_{pc})(\boldsymbol{U}^n_p - \boldsymbol{U}^n_c)\right] - \frac{d}{dt}\boldsymbol{F}^{\star,n}_p.\end{aligned}\tag{3.173}$$

GRP algorithm for the two-dimensional Lagrangian scheme in pseudo-Cartesian geometry We summarize the high-order discretization of the two-dimensional Lagrangian hydrodynamics equations written in pseudo-Cartesian geometry using the control volume formulation. We assume that all the physical and geometric variables are known at time t^n.

Step 0. Construct a piecewise monotonic linear representation of the velocity field and the pressure over the cell ω_c^n at time t^n

$$\widetilde{\boldsymbol{U}}_c^{\lim}(\boldsymbol{x}) = \boldsymbol{U}_c^n + \Phi_c(\nabla \boldsymbol{U})_c^n \cdot (\boldsymbol{x} - \boldsymbol{x}_c^n),$$
$$\widetilde{P}_c^{\lim}(\boldsymbol{x}) = P_c^n + \Phi_c(\boldsymbol{\nabla} P)_c^n \cdot (\boldsymbol{x} - \boldsymbol{x}_c^n),$$

where $\boldsymbol{x}_c^n$ denotes the centroid of ω_c^n, $(\nabla \boldsymbol{U})_c^n$ and $(\boldsymbol{\nabla} P)_c^n$ are the velocity and the pressure gradient in ω_c^n. In addition, Φ_c and Φ_c denote their respective slope limiters.

Step 1. Compute the nodal velocity $\boldsymbol{U}_p^n$ and the sub-cell force $\boldsymbol{F}_{cp}^n$ by means of the node-centered solver

$$\boldsymbol{U}_p^n = (\mathsf{M}_p^n)^{-1} \sum_{c \in \mathcal{C}(p)} \left[\mathcal{A}_{pc}^n \widetilde{P}_c^{\lim}(\boldsymbol{x}_p^n) \boldsymbol{n}_{pc}^n + \mathsf{M}_{pc}^n \widetilde{\boldsymbol{U}}_c^{\lim}(\boldsymbol{x}_p^n) \right],$$
$$\boldsymbol{F}_{pc}^n = \mathcal{A}_{pc}^n \widetilde{P}_c^{\lim}(\boldsymbol{x}_p^n) \boldsymbol{n}_{pc}^n - \mathsf{M}_{pc}^n \left[\boldsymbol{U}_p^n - \widetilde{\boldsymbol{U}}_c^{\lim}(\boldsymbol{x}_p^n) \right].$$

Here, the superscript n is used for geometrical quantities such as lengths and normals to emphasize the fact that they are evaluated at time t^n. We note that the input data for the nodal solver are the extrapolated pressure and velocity at node p. The corner matrix, M_{pc}^n, is the cornerstone of the scheme, we recall that $\mathsf{M}_p^n = \sum_{c \in \mathcal{C}(p)} \mathsf{M}_{pc}^n$.

Step 2. Compute the time derivatives of nodal velocity and sub-cell force, $\frac{d}{dt}\boldsymbol{U}_p^n$, $\frac{d}{dt}\boldsymbol{F}_{pc}^n$, by means of the node-centered solver for the time derivatives

$$\frac{d}{dt}\boldsymbol{U}_p^n = -(\mathsf{M}_p^n)^{-1} \sum_{c \in \mathcal{C}(p)} \frac{1}{\rho_c} \left[\mathsf{M}_{pc}^n \left(\boldsymbol{\nabla} P\right)_c^n + (z_c^n)^2 \mathcal{A}_{pc}^n \boldsymbol{n}_{pc}^n \left(\nabla \cdot \boldsymbol{U}\right)_c^n \right]$$
$$+ (\mathsf{M}_p^n)^{-1} \sum_{c \in \mathcal{C}(p)} \left[P_c^n \frac{d}{dt}(\mathcal{A}_{pc}^n \boldsymbol{n}_{pc}^n) - \frac{d}{dt}(\mathsf{M}_{pc}^n)(\boldsymbol{U}_p^n - \boldsymbol{U}_c^n) \right],$$

$$\frac{d}{dt}\boldsymbol{F}_{pc}^n = -\rho_c^n (a_c^n)^2 \left(\nabla \cdot \boldsymbol{U}\right)_c^n \mathcal{A}_{pc}^n \boldsymbol{n}_{pc}^n - \mathsf{M}_{pc}^n \left[\frac{d}{dt}\boldsymbol{U}_p^n + \frac{1}{\rho_c^n} \left(\boldsymbol{\nabla} P\right)_c^n \right]$$
$$+ P_c^n \frac{d}{dt}(\mathcal{A}_{pc}^n \boldsymbol{n}_{pc}^n) - \frac{d}{dt}(\mathsf{M}_{pc}^n)(\boldsymbol{U}_p^n - \boldsymbol{U}_c^n).$$

Deduce from this the computation of the time-centered values

$$\boldsymbol{U}_p^{n+\frac{1}{2}} = \boldsymbol{U}_p^n + \frac{\Delta t}{2} \frac{d}{dt}\boldsymbol{U}_p^n,$$
$$\boldsymbol{F}_{pc}^{n+\frac{1}{2}} = \boldsymbol{F}_{pc}^n + \frac{\Delta t}{2} \frac{d}{dt}\boldsymbol{F}_{pc}^n.$$

Step 3. Compute the motion of the mesh thanks to the discrete kinematic equation

$$\boldsymbol{x}_p^{n+1} - \boldsymbol{x}_p^n = \Delta t \boldsymbol{U}_p^{n+\frac{1}{2}},$$

and update the geometrical quantities. Then, evaluate the new cell averages $(\frac{1}{\rho_c^{n+1}}, \boldsymbol{U}_c^{n+1}, E_c^{n+1})$

using the updating formulas

$$m_c\left(\frac{1}{\rho_c^{n+1}}-\frac{1}{\rho_c^n}\right)-\Delta t\sum_{p\in\mathcal{P}(c)}\langle\mathcal{A}_{pc}\boldsymbol{n}_{pc}\rangle^{n+\frac{1}{2}}\cdot\boldsymbol{U}_p^{n+\frac{1}{2}}=0,$$

$$m_c\left(\boldsymbol{U}_c^{n+1}-\boldsymbol{U}_c^n\right)+\Delta t\sum_{p\in\mathcal{P}(c)}\boldsymbol{F}_{pc}^{n+\frac{1}{2}}=\alpha(P_ca_c)^{n+\frac{1}{2}}\boldsymbol{e}_y,$$

$$m_c\left(E_c^{n+1}-E_c^n\right)+\Delta t\sum_{p\in\mathcal{P}(c)}\boldsymbol{F}_{pc}^{n+\frac{1}{2}}\cdot\boldsymbol{U}_p^{n+\frac{1}{2}}=0.$$

Finally, compute the new thermodynamic state as $P_c^{n+1}=P(\rho_c^{n+1},\varepsilon_c^{n+1})$, where $\varepsilon_c^{n+1}=E_c^{n+1}-\frac{1}{2}\mid\boldsymbol{U}_c^{n+1}\mid^2$.

3.4.3 Compatible area-weighted cell-centered discretization

Here, we derive a compatible area-weighted cell-centered discretization to solve the crucial problem of symmetry preservation. It is well known that spherical symmetry in cylindrical geometry is not preserved with the control volume scheme because the areas along the angular direction are not equal even when the angles between the radial lines are equal, refer to [35, 37, 104]. Thus for pressures that are radially symmetric the force is not in the radial direction, leading to a symmetry violation. However, for an equal angle zoned grid cylindrical symmetry is preserved in Cartesian geometry. This is because the lengths along the angular direction are then equal. This is precisely this fact that is used here to construct area-weighted schemes in cylindrical geometry that preserve spherical symmetry on equal angle zoned polar grid

Area-weighted discretization of the momentum equation

The area-weighted formulation is derived by modifying the expression of the sub-cell force in the momentum equation corresponding the control volume formulation. This modification is performed to ensure the symmetry preservation for the momentum equation. It is obtained by considering the alternative expression of the discrete gradient operator (3.137) that has been derived page 130

$$\int_v\boldsymbol{\nabla}P\,\mathrm{d}v=\bar{\mathcal{R}}\int_l P\boldsymbol{n}\,\mathrm{d}l,$$

where $\bar{\mathcal{R}}$ denotes the mean pseudo-radius defined by

$$\bar{\mathcal{R}}=\frac{1}{\mid a\mid}\int_a\mathcal{R}\,\mathrm{d}a.$$

The definition of the area-weighted sub-cell force follows from the above equation by setting

$$\boldsymbol{F}_{pc}^{aw}=\bar{\mathcal{R}}_c\int_{\partial\omega_{pc}\cap\partial\omega_{pc}}P\boldsymbol{n}\,\mathrm{d}l. \tag{3.174}$$

Here, $\partial\omega_{pc}$ denotes the boundary of the sub-cell ω_{pc} related to point p and cell c. The mean pseudo-radius over the cell ω_c, $\bar{\mathcal{R}}_c$, is defined according to the above expression by setting

$$\bar{\mathcal{R}}_c=\frac{v_c}{a_c}, \tag{3.175}$$

where a_c is the area of the cell ω_c and v_c its volume obtained by rotating it about x axis. The difference between the area-weighted and the control volume expression of the sub-cell forces writes

$$\boldsymbol{F}_{pc}^{cv}-\boldsymbol{F}_{pc}^{aw}=\int_{\partial\omega_{pc}\cap\partial\omega_c}P(\mathcal{R}-\bar{\mathcal{R}}_c)\boldsymbol{n}\,\mathrm{d}l. \tag{3.176}$$

In writing this equation, we have used the definition of the control volume sub-cell force (3.147) page 134. It is interesting to note that these expressions are consistent in the sense that their difference tends to zero when the volume of the sub-cell tends to zero. We also remark that the area-weighted sub-cell force can be rewritten under the form

$$\boldsymbol{F}_{pc}^{aw} = \bar{\mathcal{R}}_c \boldsymbol{F}_{pc}^{ca}, \tag{3.177}$$

where $\boldsymbol{F}_{pc}^{ca} = \int_{\partial\omega_{pc}\cap\partial\omega_c} P\boldsymbol{n}\,\mathrm{d}l$ denotes the sub-cell force that has been defined in Cartesian geometry.

Using the above definitions, the discretization of the momentum equation that results from the use of the area-weighted sub-cell force writes as

$$m_c \frac{d\boldsymbol{U}_c}{dt} + \bar{\mathcal{R}}_c \sum_{p\in\mathcal{P}(c)} \boldsymbol{F}_{pc}^{ca} = \boldsymbol{0}. \tag{3.178}$$

Substituting $m_c = \rho_c v_c$ and the definition of the cell-averaged pseudo-radius (3.175) into the above equation leads to the equivalent form of the momentum equation

$$\mu_c \frac{d\boldsymbol{U}_c}{dt} + \sum_{p\in\mathcal{P}(c)} \boldsymbol{F}_{pc}^{ca} = \boldsymbol{0}, \tag{3.179}$$

where $\mu_c = \rho_c a_c$ corresponds to the mass defined in Cartesian geometry. Note that this mass is not a Lagrangian quantity in the sense that it is not constant anymore. This latter equation, shows that the area-weighted discretization of the momentum equation corresponds to the discretization that has been used in Cartesian geometry. This is the reason why this discretization preserves spherical symmetry on equal angle zoned polar grids.

Area-weighted discretization of the gas dynamics equations

Finally, the area-weighted discretization of the Lagrangian gas dynamics equations follows from the control-volume discretization (3.148) page 134 replacing the control volume discretization of the momentum equation (3.148b) by its area-weighted discretization derived in the latter paragraph

$$m_c \frac{d}{dt}\left(\frac{1}{\rho_c}\right) - \sum_{p\in\mathcal{P}(c)} \mathcal{A}_{pc}\boldsymbol{n}_{pc}\cdot\boldsymbol{U}_p = 0, \tag{3.180a}$$

$$m_c \frac{d}{dt}\boldsymbol{U}_c + \sum_{p\in\mathcal{P}(c)} \boldsymbol{F}_{pc}^{aw} = \boldsymbol{0}, \tag{3.180b}$$

$$m_c \frac{d}{dt}E_c + \sum_{p\in\mathcal{P}(c)} \boldsymbol{F}_{pc}^{cv}\cdot\boldsymbol{U}_p = 0. \tag{3.180c}$$

To complete the definition of the area-weighted scheme, we give hereafter the expressions of the area-weighted and control volume sub-cell forces $\boldsymbol{F}_{pc}^{aw}$ and $\boldsymbol{F}_{pc}^{cv}$. Noticing that the area-weighted sub-cell force is equal to the cell-averaged pseudo-radius times the sub-cell force that has been derived in Cartesian geometry, leads to

$$\boldsymbol{F}_{pc}^{aw} = \bar{\mathcal{R}}_c[l_{pc}P_c\boldsymbol{n}_{pc} - \mathsf{M}_{pc}^{ca}(\boldsymbol{U}_p - \boldsymbol{U}_c)]. \tag{3.181}$$

Here, M_{pc}^{ca} denotes a positive definite corner matrix defined in Cartesian geometry. For instance, this matrix can be chosen as

$$\mathsf{M}_{pc}^{ca} = z_{pc}^{-}l_{pc}^{-}(\boldsymbol{n}_{pc}^{-}\otimes\boldsymbol{n}_{pc}^{-}) + z_{pc}^{+}l_{pc}^{+}(\boldsymbol{n}_{pc}^{+}\otimes\boldsymbol{n}_{pc}^{+})].$$

Note that this expression corresponds to the general non-linear version of the EUCCLHYD scheme in Cartesian geometry that has been introduced page 92. Let us recall that the coefficient $z_{pc}^{\pm}$ given by (3.86), is the generalized non-linear corner impendance that follows from the use of the Dukowicz approximate Riemann solver. Concerning the control volume sub-cell force, $\boldsymbol{F}_{pc}^{cv}$, it is defined according to (3.151) page 135 as

$$\boldsymbol{F}_{pc}^{cv} = \mathcal{A}_{pc} P_c \boldsymbol{n}_{pc} - \mathsf{M}_{pc}(\boldsymbol{U}_p - \boldsymbol{U}_c).$$

The corner matrix, M_{pc}, in the above equation reads

$$\mathsf{M}_{pc} = z_{pc}^{-}\mathcal{R}_{pc}^{-}l_{pc}^{-}(\boldsymbol{n}_{pc}^{-} \otimes \boldsymbol{n}_{pc}^{-}) + z_{pc}^{-}\mathcal{R}_{pc}^{+}l_{pc}^{+}(\boldsymbol{n}_{pc}^{+} \otimes \boldsymbol{n}_{pc}^{+}),$$

where the pseudo-radius $\mathcal{R}_{pc}^{\pm}$ is given by

$$\mathcal{R}_{pc}^{\pm} = \frac{1}{3}(\mathcal{R}_{p^{\pm}} + 2\mathcal{R}_p).$$

Using this notation, we recall that the corner area vector $\mathcal{A}_{pc}$ expresses as

$$\mathcal{A}_{pc} = \mathcal{R}_{pc}^{-}l_{pc}^{-}\boldsymbol{n}_{pc}^{-} + \mathcal{R}_{pc}^{+}l_{pc}^{+}\boldsymbol{n}_{pc}^{+}.$$

Let us point out that using the above definitions, the present area-weighted discretization coincides with the one that has been derived in [104]. This area-weighted discretization is compatible with the Geometric Conservation Law since the volume equation (3.180a) coincides with the one derived in the control volume preservation. We also observe that the total energy equation (3.180c) remains unchanged. Therefore, the principle conservation of the total energy still holds under the condition (3.157) page 136. This implies that the node-centered solver corresponding to the area-weighted discretization coincides with the node-centered solver (3.158) derived for the control volume formulation, refer to page 137. From this, it follows that the high-order extension of the area-weighted discretization is constructed in a similar manner to that was employed for the control volume discretization, refer to Section 3.4.2 page 139. However, the area-weighted discretization does not satisfy an entropy inequality. This is due to the fact that the are-weighted sub-cell force has been derived using a definition of the discrete gradient operator that is not compatible with the definition of the discrete divergence operator. Namely, the discrete area-weighted gradient operator does not follows from an integration by part of the vector identity $\boldsymbol{U}\cdot\boldsymbol{\nabla}P = \nabla\cdot(P\boldsymbol{U}) - P\nabla\cdot\boldsymbol{U}$. Using Gibbs formula and (3.180), the computation of the rate of entropy production within cell ω_c is readily obtained and writes

$$m_c\frac{d\varepsilon}{dt} + m_c P_c \frac{d}{dt}(\frac{1}{\rho_c}) = -\sum_{p\in\mathcal{P}(c)}(\boldsymbol{F}_{pc}^{cv} - \mathcal{A}_{pc}P_c\boldsymbol{n}_{pc})\cdot(\boldsymbol{U}_p - \boldsymbol{U}_c) + \sum_{p\in\mathcal{P}(c)}(\boldsymbol{F}_{pc}^{cv} - \boldsymbol{F}_{pc}^{aw})\cdot\boldsymbol{U}_c.$$

Now, replacing the control volume sub-cell force by its above expression in the first sum of the right-hand side yields

$$m_c\frac{d\varepsilon}{dt} + m_c P_c \frac{d}{dt}(\frac{1}{\rho_c}) = \sum_{p\in\mathcal{P}(c)}\mathsf{M}_{pc}(\boldsymbol{U}_p - \boldsymbol{U}_c)\cdot(\boldsymbol{U}_p - \boldsymbol{U}_c) + \sum_{p\in\mathcal{P}(c)}(\boldsymbol{F}_{pc}^{cv} - \boldsymbol{F}_{pc}^{aw})\cdot\boldsymbol{U}_c. \quad (3.182)$$

The first sum is non-negative as M_{pc} is positive semi-definite, it also corresponds to the rate of entropy production associated to the control volume scheme, refer to (3.152) page 135. Regarding the second term in the right-hand side, it has no definite sign, thus it is not possible to obtain an entropy inequality for the area-weighted scheme.

3.5 Numerical tests in two-dimensional cylindrical geometry

In this section, we present classical test cases to assess the robustness and the accuracy of the high-order control volume and area-weighted schemes. For each problem, we use a perfect gas equation of state which is taken to be of the form $P = (\gamma - 1)\rho\varepsilon$, where γ is the polytropic index. The computations have been made using the Dukowicz approximation for the nodal solver [53], namely the coefficient Γ_c in the mass swept flux is set equal to $\frac{\gamma+1}{2}$.

3.5.1 Spherical Sod problem

Here, we consider the extension of the classical Sod shock tube [153] to the case of spherical geometry. The present problem consists of a spherical shock tube of unity radius. The interface is located at $r = 0.5$. At the initial time, the states on the left and on the right sides of the interface are constant. The left state is a high pressure fluid characterized by $(\rho_l, P_l, u_l) = (1, 1, 0)$, the right state is a low pressure fluid defined by $(\rho_r, P_r, u_r) = (0.125, 0.1, 0)$. The gamma gas law is defined by $\gamma = \frac{7}{5}$. The computational domain is defined in polar coordinates by $(r, \theta) \in [0, 1] \times [0, \frac{\Pi}{2}]$ where $r = \sqrt{(x^2 + y^2)}$ and $\theta = \arctan(\frac{y}{x})$. The initial grid is a polar grid with 100×9 equally spaced zones both in the radial and angular direction. The boundary conditions are wall boundary conditions, that is, the normal velocity is set to zero at each boundary.

The aim of this test case is to assess the symmetry preservation ability for the area-weighted and control volume schemes. In what follows, we define a numerical indicator that measures the loss of symmetry preservation. The polar grid is described using logical $j-$lines radially outward and logical $i-$lines in the angular direction. For the logical $i-$line, let us introduce the averaged radius

$$\bar{r}_i = \frac{1}{J+1} \sum_{j=1}^{J+1} r_{i,j},$$

where $J + 1$ denotes the number of logical $j-$lines and $r_{i,j}$ is the radius of the node located at the intersection of the logical $i-$lines and the logical $j-$line. Then, we define the difference between the averaged radius and the generic radius along the logical $i-$line

$$\Delta r_i = \max_{j=1,\ldots,J+1} \mid r_{i,j} - \bar{r}_i \mid .$$

Finally, we introduce the global indicator which characterizes the symmetry preservation by setting

$$\Delta r = \max_{i=1,\ldots,I+1} \Delta r_i,$$

where $I + 1$ denotes the number of logical $i-$lines.

We run the spherical Sod problem using the high-order area-weighted scheme and the first and high-order control volume scheme. The corresponding Δr indicators are displayed in Figure 3.46 as function of time, using a logarithmic scale. We remark that symmetry preservation is ensured to numerical roundoff for the area-weighted scheme. As expected, the control volume scheme does not ensure symmetry preservation. However, it is interesting to note that the high-order extension performs better than the first-order version, as it can be seen in Figure 3.47.

We have also displayed in Figure 3.48 the numerical density computed with the high-order area-weighted scheme as function of the cell center radius versus a reference solution. This reference solution has been computed using a one-dimensional second-order spherical Lagrangian code with 10,000 cells. We note the good agreement between the numerical and the reference

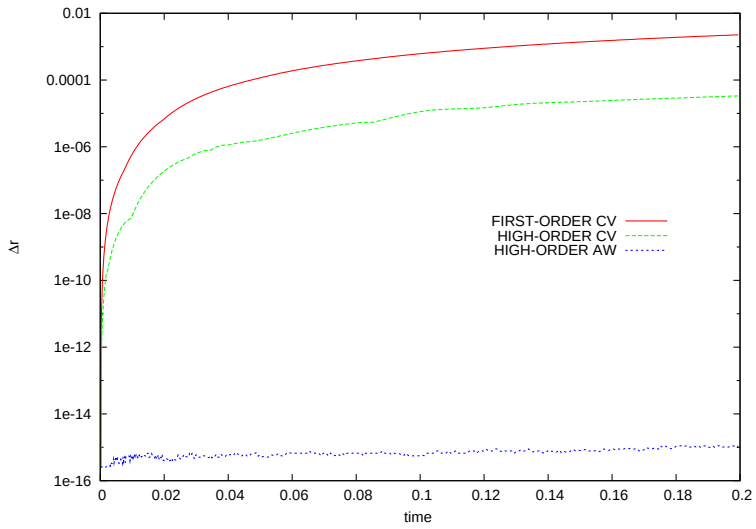

Figure 3.46: Symmetry preservation indicator as function of time for the spherical Sod problem.

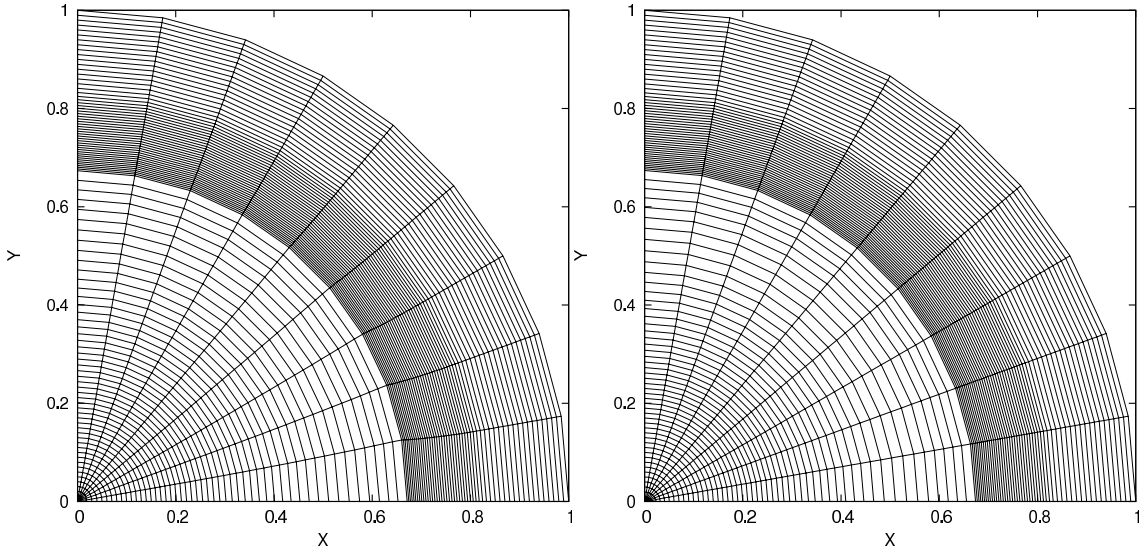

Figure 3.47: Spherical Sod problem computed with the control volume scheme. Grids at the stopping time for the first-order scheme (left) and the high-order scheme (right).

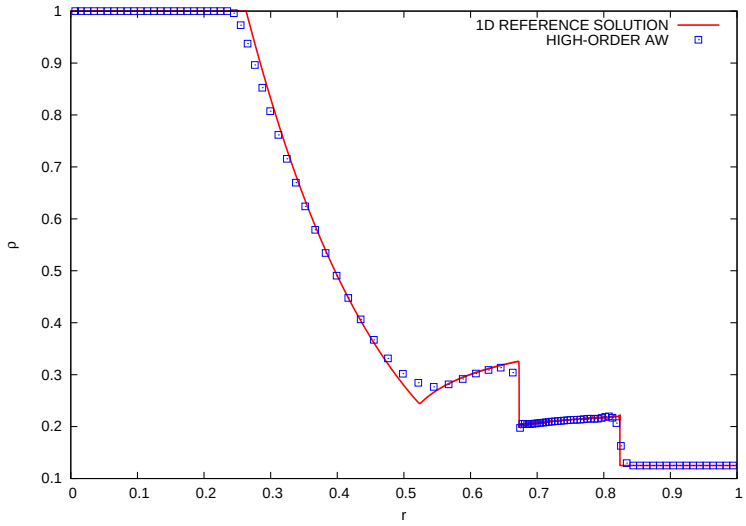

Figure 3.48: Spherical Sod problem. Density as function of the cell center radius versus reference solution at time $t = 0.2$.

solution. One can clearly see the non-oscillatory behavior of the proposed high-order scheme. We emphasize that in particular the beginning and the end of the rarefaction fan are difficult to capture and that especially here, our high-order scheme performs quite well.

3.5.2 Kidder's isentropic compression

In [76], Kidder has constructed an analytical solution of the self-similar isentropic compression of a shell filled with perfect gas. This analytical solution is useful in order to assess the ability of a Lagrangian scheme to properly compute a spherical isentropic compression. This last point is a fundamental requirement in the domain of the numerical simulation of Inertial Confinement Fusion, refer to Chapter 1. Here, we want to check that the high-order area-weighted scheme does not produce spurious entropy during the isentropic compression.

Following [27], we recall the main features of this solution in order to define the set up of the test case. Initially, the shell has the internal (resp. external) radius R_{b} (resp. R_{e}). Let P_{b}, P_{e}, ρ_{b}, and ρ_{e} be the pressures and densities located at R_{b} and R_{e}. Since the compression is isentropic, we define $s = \frac{P_{\mathrm{e}}}{\rho_{\mathrm{e}}^{\gamma}}$, and we have $\rho_{\mathrm{b}} = \rho_{\mathrm{e}} \left(\frac{P_{\mathrm{b}}}{P_{\mathrm{e}}}\right)^{\frac{1}{\gamma}}$. Let $r(R,t)$ be the radius at time $t > 0$ of a fluid particle initially located at radius R. Looking for a solution of the gas dynamics equation under the form $r(R,t) = h(t)R$, using the isentropic feature of the flow and setting $\gamma = 1 + \frac{2}{\nu}$, where $\nu = 1, 2, 3$ indicates planar, cylindrical or spherical symmetry, we finally get the self-similar analytical solution for $t \in [0, \tau[$

$$\rho(r(R,t),t) = h(t)^{-\frac{2}{\gamma-1}} \rho_0 \left[\frac{r(R,t)}{h(t)}\right],$$
$$u(r(R,t),t) = \frac{d}{dt}h(t)\frac{r(R,t)}{h(t)},$$
$$P(r(R,t),t) = h(t)^{-\frac{2\gamma}{\gamma-1}} P_0 \left[\frac{r(R,t)}{h(t)}\right].$$

Here, τ denotes the focusing time of the shell which is written

$$\tau = \sqrt{\frac{\gamma-1}{2}\frac{R_{\mathrm{e}}^2 - R_{\mathrm{b}}^2}{a_{\mathrm{e}}^2 - a_{\mathrm{b}}^2}},$$

where $a^2 = s\gamma\rho^{\gamma-1}$ is the square of the isentropic sound speed. The particular form of the polytropic index enables us to get the analytical expression $h(t) = \sqrt{1-\left(\frac{t}{\tau}\right)^2}$, which is valid for any $t \in [0, \tau[$. Note that $h(t)$ goes to zero when t goes to τ, hence τ corresponds to the collapse of the shell on itself. For $R \in [R_\mathrm{b}, R_\mathrm{e}]$, the initial density and pressure, ρ_0, P_0, are defined by

$$\rho^0(R) = \left(\frac{R_\mathrm{e}^2 - R^2}{R_\mathrm{e}^2 - R_\mathrm{b}^2}\rho_\mathrm{b}^{\gamma-1} + \frac{R^2 - R_\mathrm{b}^2}{R_\mathrm{e}^2 - R_\mathrm{b}^2}\rho_\mathrm{e}^{\gamma-1}\right)^{\frac{1}{\gamma-1}},$$
$$P^0(R) = s\left(\rho^0(R)\right)^\gamma.$$

Note that the initial velocity is equal to zero since the shell is assumed to be initially at rest. The isentropic compression is obtained imposing the following pressure laws at the internal and external faces of the shell:

$$P(r(R_\mathrm{b}, t), t) = P_\mathrm{b} h(t)^{-\frac{2\gamma}{\gamma-1}},$$
$$P(r(R_\mathrm{e}, t), t) = P_\mathrm{e} h(t)^{-\frac{2\gamma}{\gamma-1}}.$$

We point out that the velocity field is a linear function of the radius r which is a typical property of self-similar isentropic compression.

For numerical applications, we consider the spherical shell characterized by $R_\mathrm{b} = 0.9$ and $R_\mathrm{e} = 1$. We set $P_\mathrm{b} = 0.1$, $P_\mathrm{e} = 10$, and $\rho_\mathrm{e} = 10^{-2}$. Due to spherical symmetry we have $\nu = 3$, hence $\gamma = \frac{5}{3}$. The previous values lead to $\rho_\mathrm{b} = 6.31\ 10^{-4}$, $s = 2.15\ 10^4$ and, $\tau = 6.72\ 10^{-3}$.

The initial computational domain is defined in polar coordinates by $(r, \theta) \in [0.9, 1] \times [0, \frac{\pi}{6}]$, where $r = \sqrt{(x^2 + y^2)}$ and $\theta = \arctan(\frac{y}{x})$. The computational domain is paved using equally spaced zones in the radial and the angular directions. Kidder's problem is run with the three following polar grids: 25×15, 50×30 and 100×60. The stopping time is chosen to be very close to the focusing time setting $t_\mathrm{s} = 0.99\tau$. The computations are performed with the high-order scheme using the Barth-Jespersen limiter. To precisely estimate the entropy production of the numerical scheme we define the entropy parameter as

$$\alpha_s = \frac{P}{s\rho^\gamma},$$

where P is the pressure resulting from the numerical scheme. It is worth noting that for a perfect isentropic compression α_s should be equal to one.

We have plotted in Figure 3.49 the radial component of the velocity versus the analytical solution at the stopping time. We note that the linear feature of the velocity is very well preserved. We can also see the convergence of the numerical solutions toward the analytical one. In order to evaluate the entropy production, we have displayed in Figure 3.50 the entropy parameter for the high-order GRP scheme. It turns out that the high-order GRP extension dramatically decreases the value of the entropy parameter and reaches the analytical value. Therefore, we can conclude that our GRP high-order area-weighted scheme is able to compute properly isentropic compressions.

3.5.3 Sedov problem

We consider the Sedov problem for a point-blast in a uniform medium with spherical symmetry. An exact solution based on self-similarity arguments is available, see for instance [74]. The initial conditions are characterized by $(\rho_0, P_0, \boldsymbol{U}_0) = (1, 10^{-6}, \mathbf{0})$ and the polytropic index is set

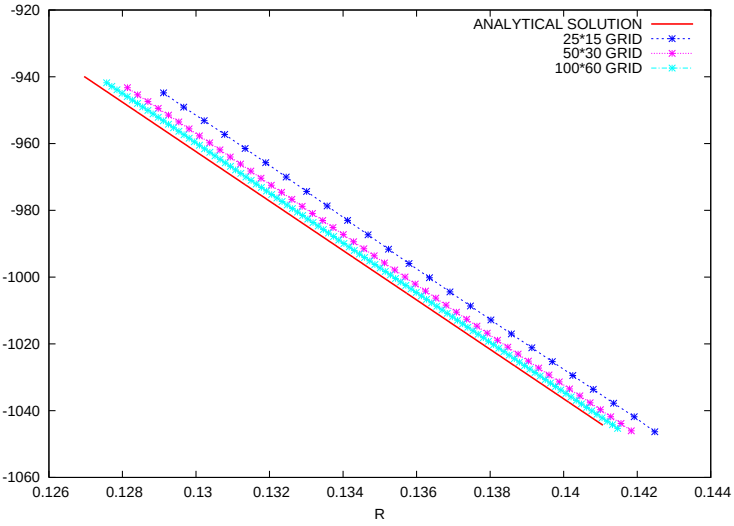

Figure 3.49: Kidder's isentropic compression. Radial component of the velocity as function of radius versus analytical solution at stopping time $t_{\rm s} = 0.99\tau$.

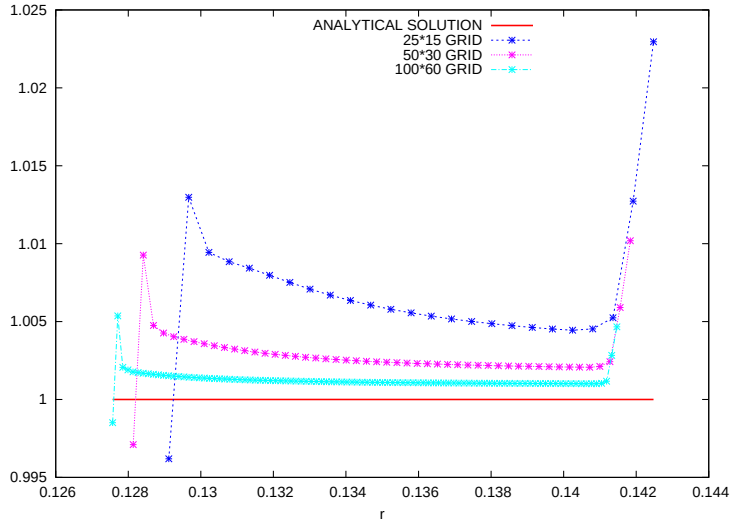

Figure 3.50: Kidder's isentropic compression. Entropy parameter, α_s, as a function of radius versus analytical solution at stopping time $t_{\rm s} = 0.99\tau$.

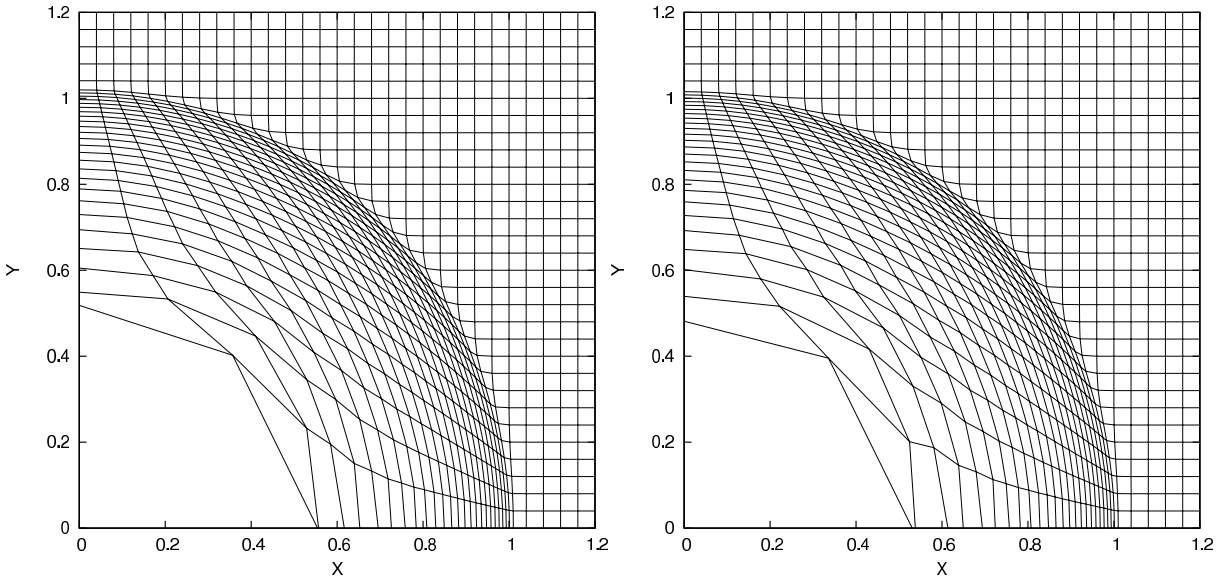

Figure 3.51: Grid at the stopping time for the Sedov problem run with the Cartesian grid. area-weighted scheme (left) and control volume scheme (right).

equal to $\frac{7}{5}$. We set an initial delta-function energy source at the origin prescribing the pressure in the cell containing the origin as follows

$$P_{\text{or}} = (\gamma - 1)\rho_{\text{or}} \frac{\mathcal{E}_0}{v_{\text{or}}},$$

where v_{or} denotes the volume of the cell and $\mathcal{E}_0$ is the total amount of released energy. Choosing $\mathcal{E}_0 = 0.425536$, as it is suggested in [74], the solution consists of a diverging shock whose front is located at radius $r = 1$ at time $t = 1$. The peak density reaches the value 6.

First, we run a computation using a square grid with an edge of length 1.2 divided into 30×30 square zones. Then, keeping the same conditions, we run the Sedov problem on a polygonal grid produced by a Voronoi tessellation. For each grid we use successively the control volume scheme and the area-weighted scheme with their high-order extension.

The final mesh for both schemes corresponding to the Cartesian grid are displayed in Figure 3.51. The results are quite similar for both formulation. We note that the spherical shape of the shock wave is quite well preserved. As it can be seen in Figure 3.52 the shock location is very well resolved without any spurious oscillations. The peak density reached by the numerical solution is in good agreement with the theoretical value. Similar results corresponding to the polygonal grid are presented in Figures 3.53 and 3.54. Once more, we note the spherical shape of the shock wave and the good agreement with the analytical solution. These last results reveal the ability of our high-order Lagrangian scheme to handle unstructured grids.

3.5.4 Noh problem

The Noh problem [124] is a well known test problem that has been used extensively to validate Lagrangian scheme in the regime of strong shock waves. In this test case, a cold gas with unit density is given an initial inward radial velocity of magnitude 1. Then, a diverging spherical shock wave is generated which propagates at speed $D = \frac{1}{3}$. The density plateau behind the shock wave reaches the value 64. In order to demonstrate the robustness and the accuracy of our GRP area-weighted scheme, we shall run this test using polar grids with equi-angular zoning. The initial computational domain is defined in polar coordinates by $(r, \theta) \in [0, 1] \times [0, \frac{\pi}{2}]$.

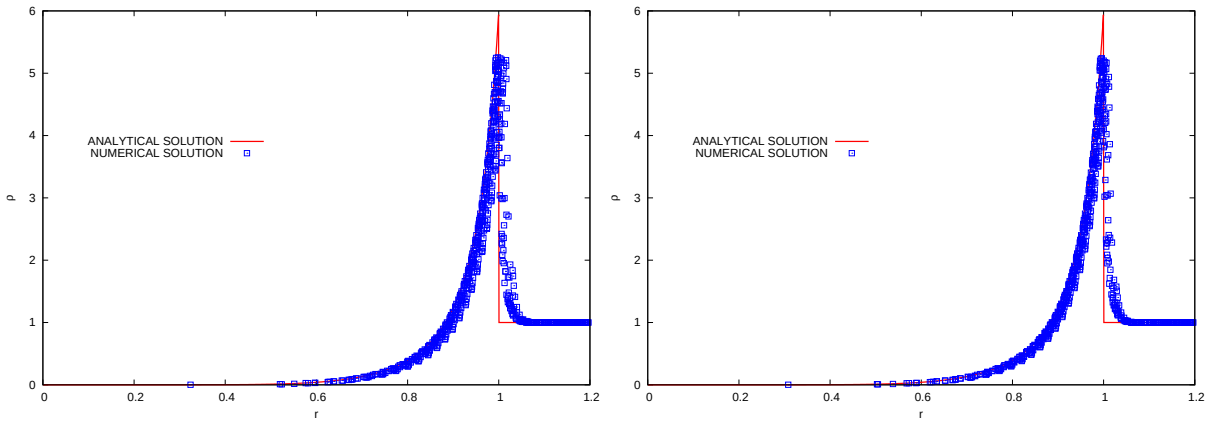

Figure 3.52: Density in all the cells as a function of cell center radii for the Sedov problem on the Cartesian grid at time $t = 1$. area-weighted scheme (left) and control volume scheme (right).

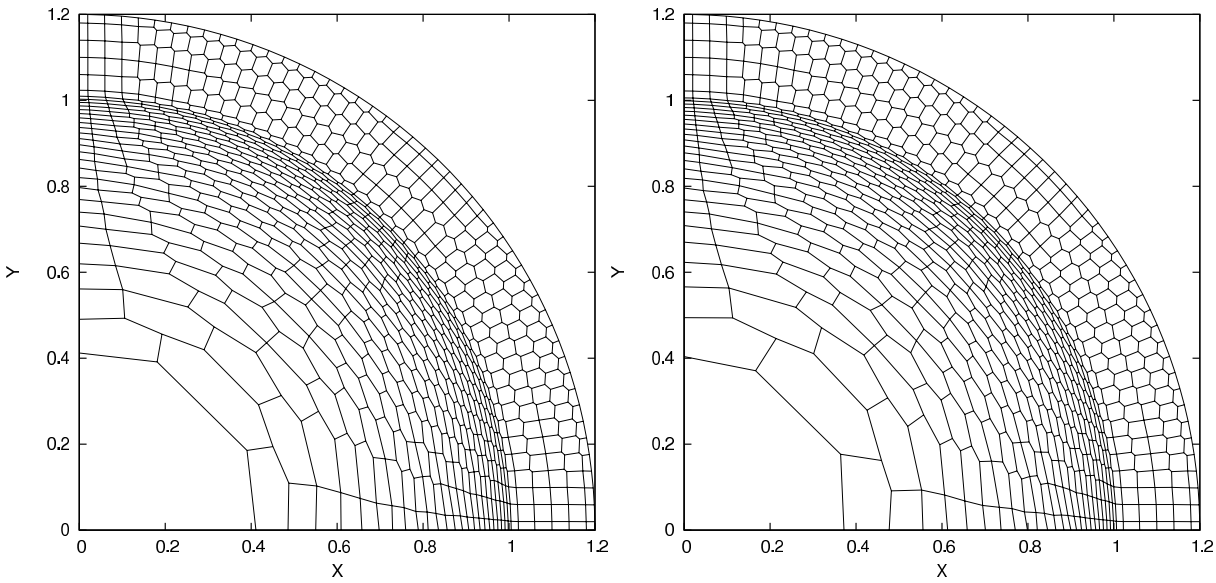

Figure 3.53: Grid at the stopping time for the Sedov problem run with the polygonal grid. Area-weighted scheme (left) and control volume scheme (right).

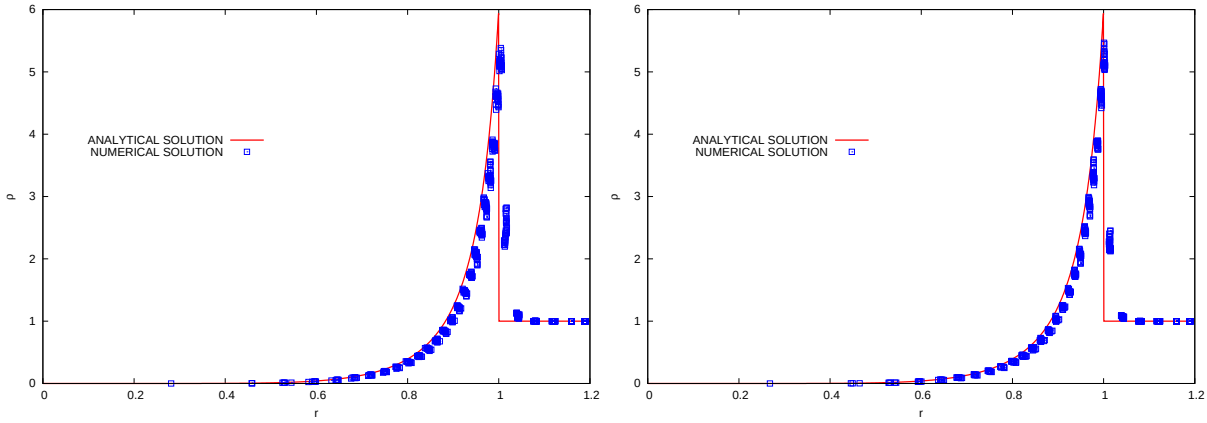

Figure 3.54: Density in all the cells as a function of cell center radii for the Sedov problem on the polygonal grid at time $t = 1$. Area-weighted scheme (left) and control volume scheme (right).

First, we address the problem of wave front invariance. This requirement which has been introduced in [34] in the framework of staggered schemes, points out that the artificial viscosity should have no effect along a wave front of constant phase. In the case of our cell-centered scheme, there is no artificial viscosity, however we have to check that the numerical viscosity inherent to our scheme satisfies this wave front invariance requirement. To examine this, we run the Noh problem with two polar grids characterized by the same zoning in the radial direction and two different angular zonings. The density maps at the stopping time $t = 0.6$ are displayed in Figure 3.55. We note that the symmetry is perfectly preserved. The shock location and the shock plateau agree quite well with the analytical solution. In Figure 3.56, we have plotted the density as a function of radius for these two different angular zonings. The small difference between the two curves shows that the wave front invariance requirement is quite well satisfied.

Finally, we assess the convergence of our scheme computing the Noh problem with the three following polar grids: 100×9, 200×9 and 400×9. We can observe in Figure 3.57 the convergence of the numerical solutions toward the analytical one.

To assess the robustness and the accuracy of our control volume formulation, we have run the Noh problem using an equiangular 100×3 polar grid, knowing that this scheme does not preserve symmetry. The final grid for the first-order control volume scheme is displayed in Figure 3.58 (left). We note the severe distortion of the grid due to the loss of symmetry of the scheme. The grid obtained using the high-order extension of the control volume scheme is displayed in Figure 3.58 (right) and the corresponding density is plotted in Figure 3.59. We note the dramatic improvement induced by the high-order extension of the control volume scheme. Using this high-order extension, symmetry is not perfectly achieved, however the quality of the numerical result has been considerably enhanced.

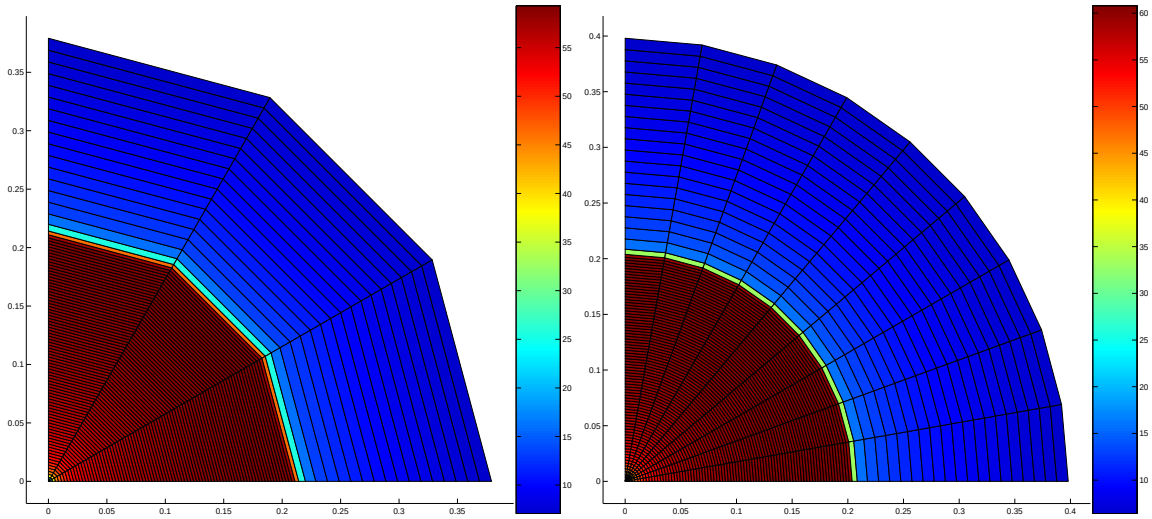

Figure 3.55: Mesh and density map for the Noh problem at time $t = 0.6$. The computations are performed using the high-order area-weighted scheme with 100 equal radial zones. The left side result corresponds to a mesh composed of 3 equal angular zones whereas the right side one corresponds to a mesh composed of 9 equal angular zones.

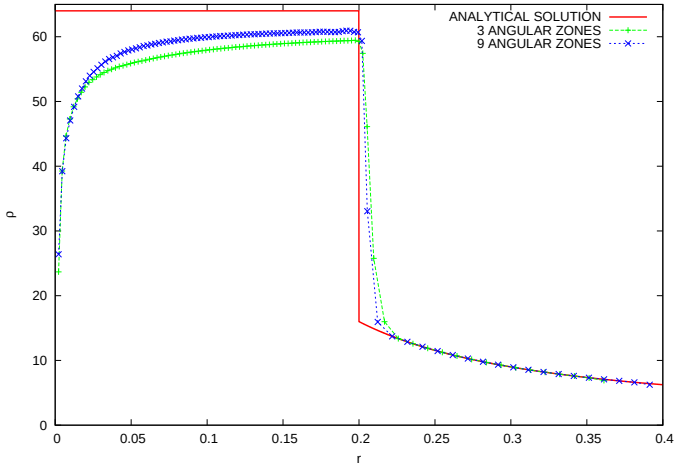

Figure 3.56: Density as a function of radius for the Noh problem at stopping time $t = 0.6$. Comparison between the numerical results obtained using the high-order area-weighted scheme, respectively with a 3 equal angular zones grid and a 9 equal angular zones grid.

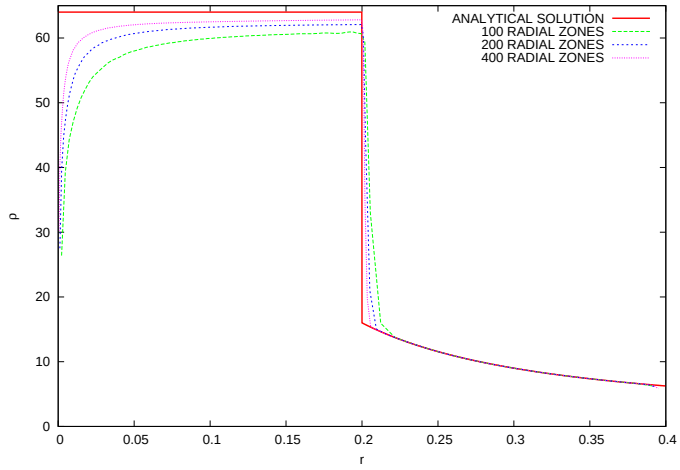

Figure 3.57: Noh problem: convergence analysis for the high-order area-weighted scheme, density as a function of radius at the stopping time $t = 0.6$.

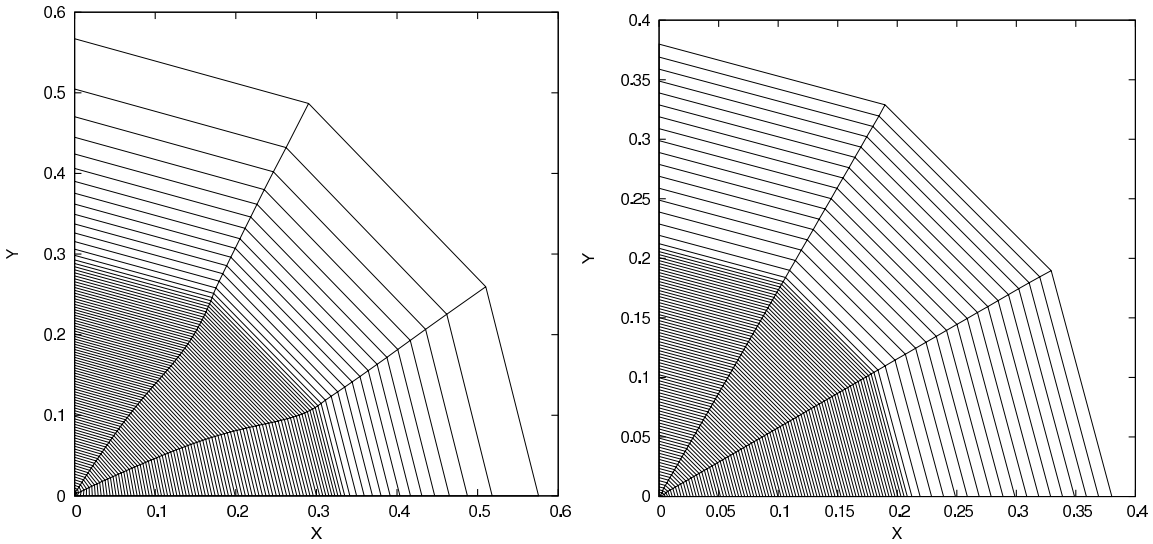

Figure 3.58: Noh problem run using the control volume scheme: grid at the stopping time for the first-order scheme (left) and the high-order scheme (right).

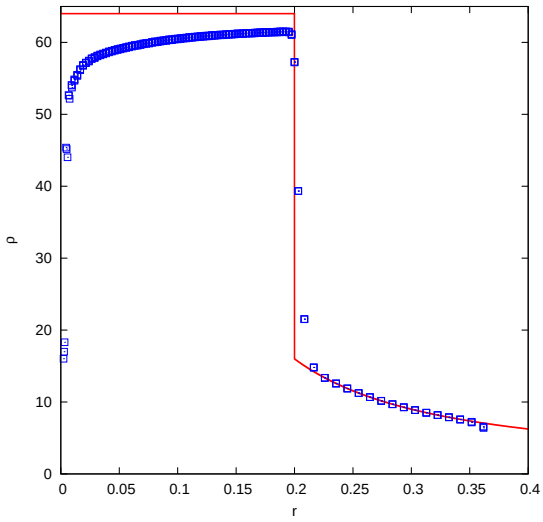

Figure 3.59: Noh problem run using the high-order control volume scheme: density as a function of cell center radii versus analytical solution.

Chapter 4

Cell-centered diffusion schemes for Lagrangian hydrodynamics

In this chapter, we present a finite volume scheme to solve diffusion equations on two-dimensional unstructured grids. This scheme is the extension to anisotropic diffusion of the work initially described in [28]. In deriving this numerical method, we aim at developing numerical modeling of physical phenomena encountered in plasma physics. More precisely, we are concerned by heat transfer within laser-heated plasma flows such as those obtained in the domain of direct drive Inertial Confinement Fusion [11]. Let us emphasize that for such flows, the heat conduction equation is strongly coupled to the gas dynamics equations describing the plasma motion. These latter equations, otherwise called Lagrangian hydrodynamics equations, are solved employing a Lagrangian numerical method wherein the computational grid is moving with the fluid. In addition, the thermodynamic variables, that is, the density, the pressure, the specific internal energy and the temperature are located at the cell center. Bearing in mind this coupling between Lagrangian hydrodynamics and diffusion, leads to the following requirements concerning the diffusion scheme under consideration:

- It should be a finite volume scheme wherein the primary unknown, *i.e.*, the temperature, is located at the cell center.
- It should be sufficiently accurate and robust scheme to handle highly distorted grids which result from the fluid motion.

The present work aims at describing a finite volume scheme which fulfils the previous requirements. On that account, we denominate it using the acronym CCLAD which stands for Cell-Centered LAgrangian Diffusion. Before describing the main features of CCLAD scheme, let us briefly give an overview of the existing cell-centered diffusion schemes.

It is well known, see [58], that the standard finite volume algorithms, such as the five-point scheme, behave poorly on highly skewed quadrilateral grids. In this situation, the five-point scheme produces a numerical solution wherein the diffusion front is aligned with the grid distortions. This undesirable behavior is due to the crude finite difference approximation used for discretization of the face fluxes.

Kershaw, in his pioneering work [75] has proposed a nine-point scheme on structured quadrilateral grids, which partially resolves the above mentioned difficulties. His scheme consists of a cell-centered variational method based on a smooth mapping between the logical mesh coordinates and the spatial coordinates. This algorithm reduces to the classical five-point scheme on an orthogonal grid. In addition, it leads to a diffusion matrix, which is symmetric positive definite. Although this method is restricted to structured quadrilateral grids, it has been

successfully used in many Lagrangian codes devoted to the numerical simulation of Inertial Confinement Fusion, see for instance [120]. Note that Kershaw's scheme has been recently extended to unstructured grids [137] and to anisotropic diffusion [135]. However, the underlying assumption of a smooth mapping used by Kershaw is too restrictive. As it has been shown in [118], a mesh refinement with Kershaw's scheme does not give a convergent solution unless the mesh becomes smooth as it is refined. Moreover, it appears that the normal flux continuity across cell interfaces is not ensured.

These drawbacks have motivated the work of Morel and his co-authors. In [118] they developed a cell-centered diffusion scheme, which treats rigorously material discontinuities and gives a second order accuracy regardless of the smoothness of the mesh. However, this scheme has two disadvantages: there are cell-edge unknowns in addition to the cell-centered unknowns and the diffusion matrix is asymmetric.

A significant improvement was provided by Shashkov and Steinberg. In [151], [150] they derived an algorithm using the *Support Operators Method* (SOM), also named *mimetic finite difference method*. This method, see [149], constructs discrete analogs of the divergence and flux operators that satisfy discrete analogs of important integral identities relating the continuum operators. By this way, the discrete flux operator is the negative adjoint of the discrete divergence in an inner scalar product weighted by the inverse conductivity. This SOM diffusion scheme gives the second order accuracy on both smooth and non smooth meshes either with or without material discontinuities. It has a non local stencil and a dense symmetric positive definite matrix representation for the diffusion operators. The introduction of both cell-centered and face-centered unknowns in [119] leads to a variant of this scheme, which has a local stencil. Many extensions of this algorithm have been recently developed. One can find in [73, 80, 91, 67, 93], developments that take into account non-isotropic materials, polygonal and non-conformal meshes, and also polyhedral meshes. This method has been also recently applied to solve the three-dimensional diffusion equation in multi-material domains containing mixed cells [62].

In [121], the authors present mimetic preconditioners for mixed discretizations of the diffusion equation. In this paper, SOM is used with two fluxes per edge in order to construct the local flux discretization. Recently, Lipnikov, Shashkov and Yotov developed a local flux mimetic finite difference method in [95, 96], which is very similar to our derivation. They also use two degrees of freedom per edge to approximate the flux. They obtained a symmetric, cell-centered finite difference scheme. Moreover, they demonstrated theoretically the second-order convergence for the temperature in the case of simplicial meshes.

In [2],[3] and [1] Aavatsmark and co-authors have proposed an alternative approach named *Multi-Point Flux Approximation* (MPFA). There, the flux is approximated by a multi-point flux expression based on transmissibility coefficients. These coefficients are computed using continuity of the flux and the temperature across the cell interfaces. This method has only cell-centered unknowns and a local stencil. In [77], Klausen and Russel present the relationships between the *Mixed Finite Element Method* (MFEM), the *Control Volume Mixed Finite Element Method* (CVMFEM), the SOM and the MPFA. The latter can be applied in the physical space to quadrilateral and to unstructured grids. For quadrilaterals, which are not parallelograms the MPFA provides a second order scheme [4] but the diffusion matrix is non-symmetric. In [5], the authors develop a MPFA method for quadrilateral grids in the reference space and its relationship to the MFEM. This approach yields a system of equations with a symmetric matrix. It shows a second-order convergence on smooth distorted grids. However for rough grids the reference space method suffers from a reduction or loss of convergence.

The relation between the finite volume and the MFEM is also studied by Thomas and Trujillo in [157]. These authors use a sub-triangulation, identical to the one used in the present

paper. They are also able to eliminate auxiliary unknowns. However, the degrees of freedom for the scalar unknown are located on the vertices of the mesh.

Another class of finite volumes schemes for solving anisotropic diffusion equations on two and three-dimensional unstructured grids has been developed by Hermeline [69, 70]. This type of scheme, termed as Discrete Duality Finite Volume (DDFV) scheme, also arises from the construction of discrete analogs of the divergence and flux operators which fulfil the discrete counterpart of vector calculus identities. However, this method requires to solve the diffusion equation not only over the primal grid but also over a dual grid. Namely, there are both cell-centered and vertex centered unknowns. Compared to a classical cell-centered finite volume scheme, the DDFV method necessitates twice as much degrees of freedom over quadrangular grids. Let us point out that this method might be difficult to use in the context of the coupling between Lagrangian hydrodynamics and diffusion.

We also mention the papers [42] and [56] where local expressions for the diffusion flux has been derived in the context of finite volume scheme for the diffusion equation. In the same framework, Le Potier has derived a local flux approximation in [131] and [129] which is very similar to the MPFA symmetric method and to our method.

We conclude this non-exhaustive review by quoting recent works concerning the development of monotone finite volume methods for diffusion equation which preserve the positivity of the solution. It is well known that high-order linear methods, such as the multi-point flux approximation, mixed finite element and mimetic finite difference methods, are not monotone on strongly anisotropic meshes or for diffusion problems with strongly anisotropic coefficients. On the other hand, the finite volume method with linear two-point flux approximation is monotone but not even first-order accurate in these cases. This flaw has been corrected by constructing monotone finite volume schemes wherein the discretization is based on a non-linear two-point flux approximation [130, 94, 97]. The drawback of these methods lies in the fact that they require the solution of a global non-linear problem by means of an iterative procedure such as a fixed point algorithm, even in the case of a linear diffusion equation.

Finally, it seems that the diffusion scheme derived from the SOM has the best combination of ideal properties of any previous finite-difference scheme. The only drawback lies in the fact that there are both cell-centered and face-centered unknowns. For instance, using a bi-dimensional computational domain $\mathcal{D}$ paved with $C_{\mathcal{D}}$ triangular (quadrangular) cells one has asymptotically $2.5\,C_{\mathcal{D}}$ ($3\,C_{\mathcal{D}}$) unknowns. In addition, the treatment of the supplementary face-centered unknowns leads to a more complicated algorithm than usual when coupling the diffusion scheme to hydrodynamics.

This disadvantage has motivated us to propose the CCLAD scheme, which retains as well as possible the good properties of the SOM diffusion scheme.

The main feature of CCLAD scheme lies in introduction of two half-edge normal fluxes and two half-edge temperatures on each edge. A local variational formulation written for each cell corner provides the discretization of the half-edge normal fluxes. This discretization shows that the half-edge normal fluxes depend on the half-edge temperatures defined on the two edges impinging on a node and also on the corresponding cell-centered temperature. The continuity of both half-edge temperatures and half-edge normal fluxes written for each edge surrounding the node leads to a local, positive definite linear system provided that the conductivity tensor is definite positive. The resolution of the above linear system allows to eliminate locally the half-edge temperatures as functions of the mean cell temperatures. At each node, we can construct a local discrete effective conductivity tensor which is symmetric positive definite provided the conductivity tensor is also symmetric positive definite. Collecting the contribution of each nodal tensors, leads to a global diffusion matrix which is positive semi-definite. Finally, the time discretization results in a linear system satisfied by the cell-centered unknowns, which always

admits a unique solution. Let us emphasize that the node-based construction of CCLAD scheme is particularly well adapted to unstructured grids and to the treatment of boundary conditions.

In summary, CLADD scheme has the following properties.

- It is characterized by cell-centered unknowns and a local stencil; it reduces to a nine-point scheme on quadrangular distorted grids.
- It has a positive definite (resp. symmetric) representation for the diffusion operator if the conductivity tensor is positive definite (resp. symmetric).
- For triangular grids, it preserves linear solutions and gives the second order accuracy with or without material discontinuities.
- For rectangular grids, in the case of isotropic diffusion, it reduces to the standard five-point scheme and the treatment of discontinuous conductivity coefficients is equivalent to the well known harmonic averaging procedure.
- For non-orthogonal grids, it gives an accuracy which is almost second-order with or without material discontinuities.

It is interesting to note that CCLAD scheme, like the MPFA reference space method [5] suffers from a reduction or the loss of convergence on quadrangular random grids i.e., the grids with perturbations of order h, where h is the mesh size parameter. However, such grids are seldom encountered in real life simulations wherein the numerical method solving the diffusion equation is coupled to Lagrangian hydrodynamics. Moreover, let us point out that in the context of Arbitrary Lagrangian Eulerian (ALE) computations, the rezoning procedure inherent to the ALE algorithm produces smooth grid for which our scheme exhibits an almost second-order convergence.

The remainder of this chapter is organized as follows. In Section 4.1 we first give the problem statement introducing the governing equations, the notation and assumptions and our motivation regarding the underlying physical model. This is followed by Section 4.2 which is devoted to the space discretization. In this section we derive the half-edge fluxes approximation by means of a sub-cell-based variational formulation. We also describe the elimination of the half-temperatures in terms of the cell-centered unknowns to achieve the construction of the global discrete diffusion operator. After stating the main properties of the semi-discrete scheme, we conclude this section by giving indications related to boundary conditions implementation and by presenting the extension of CCLAD scheme to cylindrical geometry. We pursue by presenting the time discretization in Section 4.3. Finally, the robustness and the accuracy of CCLAD scheme are assessed using various representative test cases in Section 4.4.

4.1 Problem statement

4.1.1 Governing equations

Let $\mathcal{D}$ be an open set of the d-dimensional space $\mathbb{R}^d$, occupied by a thermally and possibly electrically conductive material. Let $\boldsymbol{x}$ denotes the vector position of an arbitrary point inside the domain $\mathcal{D}$ and $t > 0$ the time. The unsteady thermal state of the domain under consideration is described by means of the specific internal energy field $\varepsilon = \varepsilon(\boldsymbol{x}, t)$. In the absence of fluid motion, heat propagation throughout the domain is governed by a partial differential equation, which is known as the heat conduction equation (refer to Comment 4) and writes as

$$\rho \frac{\partial \varepsilon}{\partial t} + \nabla \cdot \boldsymbol{q} = \rho r. \tag{4.1}$$

Here, ρ is a positive real valued function, which stands for the mass density of the material. The source term, r, corresponds to the specific heat supplied to the material. Specific internal energy is expressed in terms of the mass density and the temperature, T, through the use of an equation of state written under the form $\varepsilon = \varepsilon(\rho, T)$. Introducing the specific heat capacity at constant volume $C_v = (\frac{\partial \varepsilon}{\partial T})_\rho$ leads to rewrite the heat conduction equation as

$$\rho C_v \frac{\partial T}{\partial t} + \nabla \cdot \boldsymbol{q} = \rho r. \tag{4.2}$$

In writing this equation, we have assumed that either ε does not depend on density or ρ does not depend on time. Let us note that C_v is a positive real valued function, it is also an intrinsic material properties which may depend on temperature. In the sequel, we assume that ρ, C_v, and r are known functions. The vector valued function, $\boldsymbol{q}$, stands for the heat flux. It is expressed in terms of the temperature gradient by means of the generalized Fourier law

$$\boldsymbol{q} = -\mathsf{K}\boldsymbol{\nabla} T.$$

The second-order tensor K is the conductivity tensor which is also an intrinsic property of the material under consideration. Let us point out that this representation for the flux based on the linear relation between the flux and the temperature gradient fails if the particle mean free path becomes comparable to the temperature scale length. This occurs very often in laser driven plasma flows. There more complicated models are employed related either to local flux limitation (flux limiters) or to the non-local relation between the flux and the temperature gradient, refer to [11]. In the sequel, we will study uniquely classical heat transfer phenomena wherein the heat flux is described using the above Fourier law.

According to the Second Law of thermodynamics, Fourier law has to obey the constraint

$$\boldsymbol{q} \cdot \boldsymbol{\nabla} T \leq 0. \tag{4.3}$$

This requirement on the constitutive law of the heat flux simply states that heat flux direction is opposite to temperature gradient, that is, heat flows from hot region to cold region. Mathematically speaking, this thermodynamic constraint amounts to state that the conductivity tensor is a positive definite tensor

$$\mathsf{K}\boldsymbol{\phi} \cdot \boldsymbol{\phi} > 0, \quad \forall \boldsymbol{\phi} \in \mathbb{R}^d. \tag{4.4}$$

Depending on the material under consideration, the conductivity tensor may be either symmetric, *i.e.*, $\mathsf{K}^t = \mathsf{K}$ or may satisfy $\mathsf{K}(-\boldsymbol{B}) = \mathsf{K}^t(\boldsymbol{B})$ if the material is in the magnetic field $\boldsymbol{B}$, [45]. For an isotropic material, heat flux does not depend on the space directions and thus conductivity tensor reduces to

$$\mathsf{K} = \kappa\, \mathsf{I}_d, \tag{4.5}$$

where κ denotes the heat conductivity, which is a positive scalar valued function and I_d denotes the unit tensor.

Being given the material properties, ρ, C, K and the heat supply r, we want to solve the heat conduction equation (4.2) on the computational domain $\mathcal{D}$. To do so, we need to define initial and boundary conditions. The initial condition is prescribed as

$$T(\boldsymbol{x}, 0) = T^0(\boldsymbol{x}), \qquad \forall \boldsymbol{x} \in \mathbb{R}^d, \tag{4.6}$$

where T^0 denotes the initial temperature field. Regarding the boundary conditions, three types can be imposed on the boundary of the domain, $\partial\mathcal{D}$. These are: Dirichlet, Neumann and Robin boundary conditions, they consists in specifying respectively the temperature, the flux

and a weighted combination of the temperature and the flux. Introduction of the partition $\partial\mathcal{D} = \partial\mathcal{D}_D \cup \partial\mathcal{D}_N \cup \partial\mathcal{D}_R$ of the boundary domain, allows to write the boundary conditions as

$$T(\boldsymbol{x},t) = T^\star(\boldsymbol{x},t), \qquad \forall \boldsymbol{x} \in \partial\mathcal{D}_D, \tag{4.7a}$$

$$\boldsymbol{q}(\boldsymbol{x},t)\cdot\boldsymbol{n} = q_N^\star(\boldsymbol{x},t), \qquad \forall \boldsymbol{x} \in \partial\mathcal{D}_N, \tag{4.7b}$$

$$\alpha T(\boldsymbol{x},t) + \beta \boldsymbol{q}(\boldsymbol{x},t)\cdot\boldsymbol{n} = q_R^\star(\boldsymbol{x},t), \qquad \forall \boldsymbol{x} \in \partial\mathcal{D}_R. \tag{4.7c}$$

Here, $T^\star$, $q_N^\star$ and $q_R^\star$ denote respectively the prescribed temperature and fluxes. In addition, $\alpha = \alpha(\boldsymbol{x},t)$ and $\beta = \beta(\boldsymbol{x},t)$ are real valued specified functions.

Comment 15 *Let us remark that the normal component of the heat flux at the interface between two media* 1 *and* 2 *with different properties is continuous,*

$$(\mathsf{K}\boldsymbol{\nabla}T)_1 \cdot \boldsymbol{n}_{12} = (\mathsf{K}\boldsymbol{\nabla}T)_2 \cdot \boldsymbol{n}_{12},$$

where $\boldsymbol{n}_{12}$ is the unit normal to the interface. The temperature itself is also continuous.

4.1.2 Underlying physical models

In deriving a numerical method to solve the heat conduction equation (4.2), we aim at developing numerical modeling of physical phenomena encountered in plasma physics. More precisely, we are concerned by heat transfer within laser-heated plasma flows such as those obtained in the domain of direct drive Inertial Confinement Fusion, refer to [11]. In this context, the energy released by the laser is transferred throughout the plasma flows by means of electron heat conduction. Omitting the pressure work term, which results from coupling to hydrodynamics, the electron temperature, T_e, is governed by a heat conduction equation similar to (4.2). In the classical regime, the electron heat flux, $\boldsymbol{q}_e$ is given by the Spitzer-Härm law: $\boldsymbol{q}_e = -\kappa_e \boldsymbol{\nabla} T_e$, where the electron thermal conductivity, κ_e, depends on the electron temperature as a power law, *i.e.*, $\kappa_e(T_e) \sim T_e^{\frac{5}{2}}$, refer to [43, 169]. This corresponds to an isotropic nonlinear heat conduction equation. However, in presence of magnetic fields, this isotropic model for heat conduction is not valid anymore. Such a situation occurs frequently for laser driven plasma wherein the density and pressure gradients are not colinear. In this particular case, a self-generated magnetic field, $\boldsymbol{B}$, is created by the rotational component of the ambipolar electric field, $\boldsymbol{E} = -\frac{1}{eN_e}\boldsymbol{\nabla} P_e$, where e is the electron charge, N_e is the electron density per unit volume and P_e is the electron pressure, refer to [43]. Knowing that the magnetic field is governed by the Faraday law, *i.e.*, $\frac{\partial \boldsymbol{B}}{\partial t} + \boldsymbol{\nabla}\times\boldsymbol{E} = \boldsymbol{0}$, we deduce that the time evolution of the magnetic field is governed by the following equation

$$\frac{\partial \boldsymbol{B}}{\partial t} = \frac{1}{e}\boldsymbol{\nabla}\left(\frac{1}{N_e}\right) \times \boldsymbol{\nabla} P_e. \tag{4.8}$$

The magnetic field dramatically modifies electron heat transport leading to a anisotropic electron conductivity. It implies not only a reduction of the magnitude of the heat flux but also its rotation. Using plasma kinetic theory, Braginskii [26] has obtained the following expression of the electron heat flux with magnetic field

$$\boldsymbol{q}_e = -\kappa_\parallel(\boldsymbol{\nabla}T_e\cdot\boldsymbol{b})\boldsymbol{b} - \kappa_\perp[\boldsymbol{\nabla}T_e - (\boldsymbol{\nabla}T_e\cdot\boldsymbol{b})\boldsymbol{b}] - \kappa_\wedge \boldsymbol{b}\times\boldsymbol{\nabla}T_e, \tag{4.9}$$

where $\boldsymbol{b} = \frac{\boldsymbol{B}}{|\boldsymbol{B}|}$ is unit vector corresponding to the direction of the magnetic field and $\kappa_\parallel$, $\kappa_\perp$ and $\kappa_\wedge$ are scalar conductivities given in [26]. Let us consider a two-dimensional plasma flow in planar geometry. Let $(\boldsymbol{e}_x, \boldsymbol{e}_y, \boldsymbol{e}_z)$ be the orthonormal basis of $\mathbb{R}^3$ and suppose that the two-dimensional flow is contained in the frame (x,y) equipped with the orthonormal basis $(\boldsymbol{e}_x, \boldsymbol{e}_y)$.

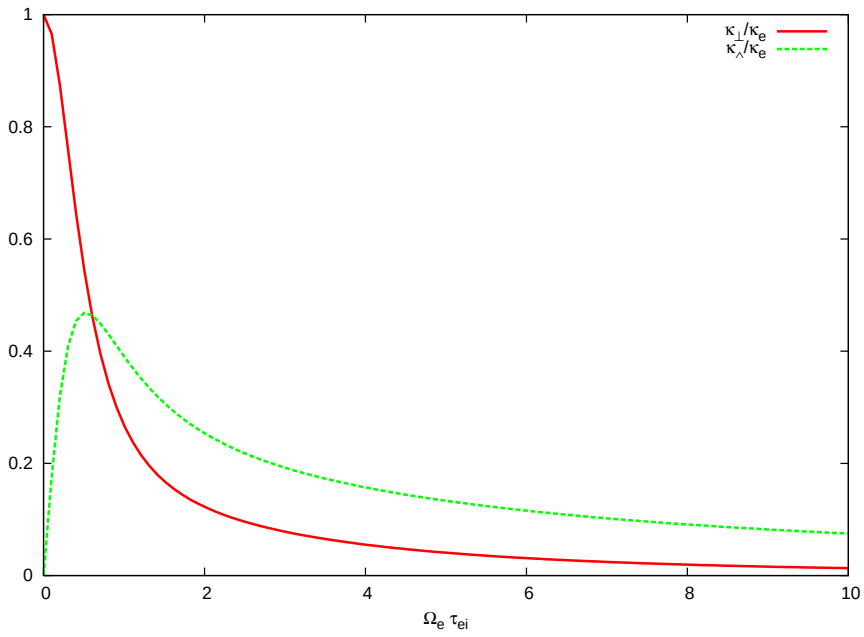

Figure 4.1: Normalized Braginskii transport coefficients $\kappa_\perp$ and $\kappa_\wedge$ versus normalized parameter $\Omega_e\tau_{ei}$.

By virtue of (4.8), it is obvious that the self-generated magnetic field is transverse to the two-dimensional flow, that is, $\boldsymbol{B} = B\boldsymbol{e}_z$. Setting $b = \frac{B}{|B|}$, we have $\boldsymbol{b} = b\boldsymbol{e}_z$, where $b^2 = 1$. Bearing this in mind, the electron heat flux expression (4.9) collapses to

$$\boldsymbol{q}_e = -\kappa_\perp \boldsymbol{\nabla} T_e - \kappa_\wedge \boldsymbol{b} \times \boldsymbol{\nabla} T_e. \tag{4.10}$$

Developing the above equation over the Cartesian frame (x, y) allows to write the electronic heat flux

$$\boldsymbol{q}_e = -\mathsf{K}_e \boldsymbol{\nabla} T_e, \tag{4.11}$$

where the second-order tensor K_e corresponds to the electronic conductivity defined by

$$\mathsf{K}_e = \begin{pmatrix} \kappa_\perp & -b\kappa_\wedge \\ b\kappa_\wedge & \kappa_\perp \end{pmatrix}. \tag{4.12}$$

The Braginskii transport coefficients $\kappa_\parallel$, $\kappa_\perp$ and $\kappa_\wedge$ can be expressed in terms of the Spitzer-Härm conductivity, κ_e, as

$$\kappa_\parallel = \kappa_e, \quad \kappa_\perp = \kappa_e f_\perp(\Omega_e\tau_{ei}), \quad \kappa_\wedge = \kappa_e f_\wedge(\Omega_e\tau_{ei}),$$

where $f_\perp$, $f_\wedge$ are the functions describing the magnetization of the heat flux. In addition, $\Omega_e \sim \mid \boldsymbol{B} \mid$, is the electron cyclotron frequency and τ_{ei} the electron-ion collision frequency. Note that Ω_e has the dimension of the reciprocal of time, thus parameter $\Omega_e\tau_{ei}$ is dimensionless; it describes the effect of the magnetic field on the electron heat conductivity as a ratio between the electron gyration time in the magnetic field and the electron collision time. Bearing this in mind we have displayed in Figure 4.1 the normalized Braginskii transport coefficients with respect to the normalized parameter $\Omega_e\tau_{ei}$ knowing that $f_\perp(x) = \frac{1}{1+x^2}$, $f_\wedge(x) = \frac{x}{1+x^2}$. For a weak magnetic field, that is, $\Omega_e\tau_{ei} \in [0, 1]$, we have $\kappa_\perp > \kappa_\wedge$, whereas for a strong magnetic filed $\kappa_\perp < \kappa_\wedge$. In the limit $\mid \boldsymbol{B} \mid \to 0$, the normalized parameter $\Omega_e\tau_{ei}$ also tends to zero and the

Braginskii coefficients behave as follows: $\kappa_\perp \to \kappa_e$ and $\kappa_\wedge \to 0$. In this regime, the anisotropic conductivity tensor K_e recovers the isotropic Spitzer-Härm conductivity, *i.e.*, $\mathsf{K}_e \to \kappa_e \mathsf{I}_2$.

We conclude this section by remarking that K_e is not symmetric and transforms as $\mathsf{K}_e(-b) = \mathsf{K}_e^t(b)$. This non-symmetry of the conductivity tensor is a consequence of the presence of the magnetic field, this behavior is known as the Righi-Leduc effect, refer to [45] chapter XI. It rotates the heat flux vector without changing its absolute value. This property corresponds to the following result: for all arbitrary vector $\boldsymbol{\phi}$

$$\mathsf{K}_e \boldsymbol{\phi} \cdot \boldsymbol{\phi} = \kappa_\perp \mid \boldsymbol{\phi} \mid^2 .$$

Since $\kappa_\perp$ is positive, the above result shows that K_e is a positive definite tensor which satisfies the thermodynamic requirement (4.4). It is interesting to note that for an arbitrary vector $\boldsymbol{\phi}$, $\mathsf{K}_e \boldsymbol{\phi}$ can be decomposed as follows

$$\mathsf{K}_e \boldsymbol{\phi} = \kappa_\perp \boldsymbol{\phi} + b \kappa_\wedge \mathcal{R}_{\frac{\pi}{2}} \boldsymbol{\phi}, \tag{4.13}$$

where $\mathcal{R}_{\frac{\pi}{2}}$ denotes the counterclockwise rotation through the angle $\frac{\pi}{2}$. The above equation states that the anisotropic conductivity tensor acts as an isotropic conductivity tensor supplemented by a rotation tensor which follows directly from the magnetic field. Finally, computing the divergence of the anisotropic heat flux (4.10) yields

$$\nabla \cdot \boldsymbol{q}_e = -\nabla \cdot (\kappa_\perp \boldsymbol{\nabla} T_e) + \boldsymbol{A} \cdot \boldsymbol{\nabla} T_e, \tag{4.14}$$

where $\boldsymbol{A} = [-\frac{\partial}{\partial y}(b\kappa_\wedge), \frac{\partial}{\partial x}(b\kappa_\wedge)]^t$. Under this form the anisotropic diffusion operator appears as the sum of an isotropic diffusion operator plus an advection operator characterized by the velocity-like vector $\boldsymbol{A}$. This decomposition suggests to solve the anisotropic heat conduction equation discretizing separately the isotropic diffusion operator and the advection operator. However, such a splitting strategy may suffer from a lack of robustness in case of strong magnetic fields, refer to [142]. That is why, we prefer to develop a computational method devoted to the discretization of the whole anisotropic diffusion operator. This computational method, which will be presented in the sequel, is the natural extension to anisotropic heat conduction of the finite volume scheme that has been initially derived in [28].

4.1.3 Notation and assumptions

Our motivation is to describe a finite volume scheme that solves the anisotropic heat conduction equation on two-dimensional unstructured grids. Before we proceed any further, let us introduce the notation and the assumptions required for the present work. Let $\mathcal{D}$ be an open set of the two-dimensional space $\mathbb{R}^2$. We aim at constructing a numerical scheme to solve the following initial-boundary-value problem

$$\rho C_v \frac{\partial T}{\partial t} + \nabla \cdot \boldsymbol{q} = \rho r, \qquad (\boldsymbol{x}, t) \in \mathcal{D} \times [0, \mathfrak{T}], \tag{4.15a}$$

$$T(\boldsymbol{x}, t) = T^0(\boldsymbol{x}), \qquad \boldsymbol{x} \in \mathcal{D}, \tag{4.15b}$$

$$T(\boldsymbol{x}, t) = T^\star(\boldsymbol{x}, t), \qquad \boldsymbol{x} \in \partial\mathcal{D}_D, \tag{4.15c}$$

$$\boldsymbol{q}(\boldsymbol{x}, t) \cdot \boldsymbol{n} = q_N^\star(\boldsymbol{x}, t), \qquad \boldsymbol{x} \in \partial\mathcal{D}_N, \tag{4.15d}$$

where $\mathfrak{T} > 0$ denotes the final time. Equation (4.15a) is a partial differential parabolic equation of second order for the temperature T, wherein the conductive flux, $\boldsymbol{q}$, is defined according to

$$\boldsymbol{q} = -\mathsf{K} \boldsymbol{\nabla} T. \tag{4.16}$$

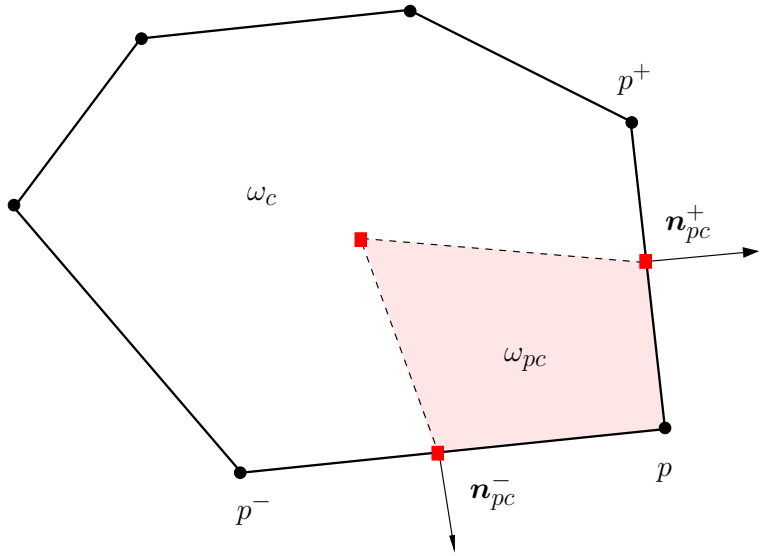

Figure 4.2: Notation related to polygonal cell ω_c and one of its sub-cell ω_{pc}.

We suppose that the second-order tensor K is positive definite to ensure thermodynamic consistency. In addition, we make the assumption that there exists $h > 0$ such that

$$\mathsf{K}\boldsymbol{\phi} \cdot \boldsymbol{\phi} \geq h \mid \boldsymbol{\phi} \mid^2, \quad \forall \boldsymbol{\phi} \in \mathcal{D}. \tag{4.17}$$

This condition states that the diffusion operator in (4.15a) is strongly elliptic [127], this ensures the well-posedness of problem (4.15) by means of the Lax-Milgram theorem [133].

Having defined the problem we want to solve, let us introduce some notation necessary to develop the discretization scheme. Let $\cup_c \omega_c$ denotes a partition of the computational domain $\mathcal{D}$ into polygonal cells ω_c. The counterclockwise ordered list of vertices (points) of cell c is denoted by $\mathcal{P}(c)$. In addition, p being a generic point, we define its position vector denoted as $\boldsymbol{x}_p$ and the set $\mathcal{C}(p)$ which contains all the cells surrounding point p. Being given $p \in \mathcal{P}(c)$, p^- and p^+ are the previous and next points with respect to p in the ordered list of vertices of cell c. Let ω_c be a generic polygonal cell, for each vertex $p \in \mathcal{P}(c)$, we define the sub-cell ω_{pc} by connecting the centroid of ω_c to the midpoints of edges $[p^-, p]$ and $[p, p^+]$ impinging at node p, refer to Figure 4.2. In two dimensions the sub-cell, as just defined, is always a quadrilateral regardless of the type of cells that compose the underlying grid. The boundaries of the cell ω_c and the sub-cell ω_{pc} are denoted respectively $\partial\omega_c$ and $\partial\omega_{pc}$. Finally, considering the intersection between the cell and sub-cell boundaries, we introduce half-edge geometric data. As the name implies, a half-edge is a half of an edge and is constructed by splitting an edge down its length. More precisely, we define the two half-edges related to point p and cell c as $\partial\omega_{pc}^- = \partial\omega_{pc} \cap [p^-, p]$ and $\partial\omega_{pc}^+ = \partial\omega_{pc} \cap [p, p^+]$. The unit outward normal and the length related to half-edge $\partial\omega_{pc}^\pm$ are denoted respectively $\boldsymbol{n}_{pc}^\pm$ and $l_{pc}^\pm$.

To proceed with the construction of numerical scheme, let us integrate (4.15a) over ω_c and make use of the divergence formula. This leads to the weak form of the heat conduction equation

$$\frac{d}{dt} \int_{\omega_c} \rho C_v T(\boldsymbol{x}, t) \, \mathrm{d}v + \int_{\partial\omega_c} \boldsymbol{q} \cdot \boldsymbol{n} \, \mathrm{d}s = \int_{\omega_c} \rho r(\boldsymbol{x}, t) \mathrm{d}v, \tag{4.18}$$

where $\boldsymbol{n}$ denotes the unit outward normal to $\partial\omega_c$. We shall first discretize this equation in the spatial variable $\boldsymbol{x}$. The physical data, ρ, C_v and r are supposed to be known functions with respect to space and time variables. We represent them using a piecewise constant approximation over each cell ω_c. The piecewise constant approximation of any variable will be denoted

using subscript c. The tensor conductivity K space approximation is also constructed using a piecewise constant representation over each cell, which is denoted by K_c. Concerning the unknown temperature field, the discretization method we are going to use is the finite volume method for which the finite dimensional space to which the approximate solution belongs is also the space of piecewise constant functions. Bearing this in mind, (4.18) rewrites

$$m_c C_{vc} \frac{d}{dt} T_c + \int_{\partial\omega_c} \boldsymbol{q} \cdot \boldsymbol{n} \, \mathsf{d}s = m_c r_c, \tag{4.19}$$

Here, m_c denotes the mass of the cell, that is, $m_c = \rho_c \mid \omega_c \mid$ where $\mid \omega_c \mid$ stands for the volume of the cell. Let us point out that $T_c = T_c(t)$ is nothing but the mean value of the temperature over ω_c

$$T_c(t) = \frac{1}{\mid \omega_c \mid} \int_{\omega_c} T(\boldsymbol{x}, t) \, \mathsf{d}v.$$

To define completely the space discretization it remains to discretize the surface integral in the above equation. To do so, let us introduce the following piecewise constant approximation of the normal heat flux over each half-edge

$$q_{pc}^{\pm} = \frac{1}{l_{pc}^{\pm}} \int_{\partial\omega_{pc}^{\pm}} \boldsymbol{q} \cdot \boldsymbol{n} \, \mathsf{d}s. \tag{4.20}$$

The scalar $q_{pc}^{\pm}$ stands for the half-edge normal flux related to the half-edge $\partial\omega_{pc}^{\pm}$. Knowing that $\partial\omega_c = \cup_{p\in\mathcal{P}(c)} \partial\omega_{pc}^{\pm}$, the discretized heat conduction equation writes as

$$m_c C_{vc} \frac{d}{dt} T_c + \sum_{p\in\mathcal{P}(c)} l_{pc}^{-} q_{pc}^{-} + l_{pc}^{+} q_{pc}^{+} = m_c r_c. \tag{4.21}$$

We conclude this paragraph by introducing as auxiliary unknowns the half-edge temperatures $T_{pc}^{\pm}$ defined by

$$T_{pc}^{\pm} = \frac{1}{l_{pc}^{\pm}} \int_{\partial\omega_{pc}^{\pm}} T(\boldsymbol{x}, t) \, \mathsf{d}s. \tag{4.22}$$

In writing this equation, we have also assumed a piecewise constant approximation of the temperature field over each half-edge.

By virtue of Comment 15, the piecewise constant approximations of the normal heat flux and temperature along each edge are defined such that these half-edge-based quantities are continuous across each edge. To exhibit these continuity conditions, let us consider two neighboring cells, denoted by subscripts c and d, which share a given edge, refer to Figure 4.3. This edge corresponds to the segment $[p, p^+]$, where p and p^+ are two consecutive points in the counterclockwise numbering attached to cell c. It also corresponds to the segment $[r^-, r]$, where r^- and r are two consecutive points in the counterclockwise numbering attached to cell d. Obviously, these four labels define the same edge and thus their corresponding points coincide, *i.e.*, $p \equiv r$, $p^+ \equiv r^-$. The sub-cell of cell c attached to point $p \equiv r$ is denoted ω_{pc}, whereas the sub-cell of cell d attached to point $r \equiv p$ is denoted ω_{rd}. This double notation, in spite of its heaviness, allows to define precisely the half-edge fluxes and temperatures at the half-edge corresponding to the intersection of the two previous sub-cells. Namely, viewed from sub-cell ω_{pc} (resp. ω_{rd}), the half-edge flux and temperature are denoted q_{pc}^{+} and T_{pc}^{+} (resp. q_{rd}^{-} and T_{rd}^{-}). Bearing this notation in mind, continuity conditions at the half-edge $(\omega_{pc} \cup \omega_{rd})$ for the half-edge fluxes and temperatures write explicitly as

$$q_{pc}^{+} + q_{rd}^{-} = 0, \tag{4.23a}$$

$$T_{pc}^{+} = T_{rd}^{-}. \tag{4.23b}$$

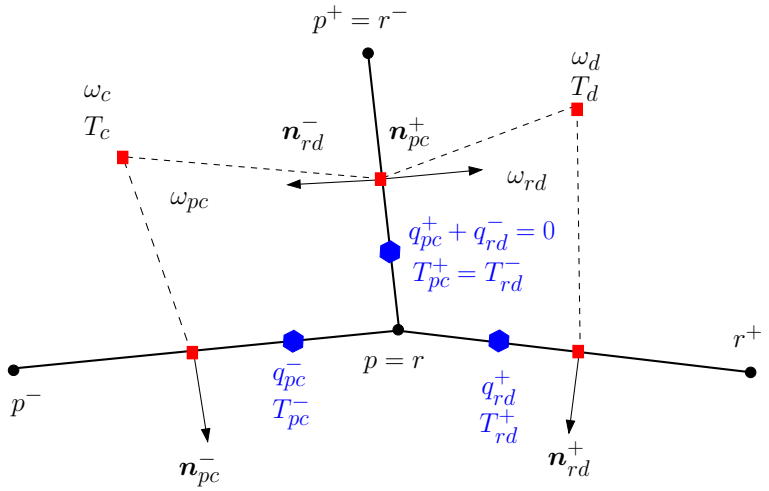

Figure 4.3: Continuity conditions for the half-edges fluxes and temperatures at a half-edge shared by two sub-cells attached to the same point. Labels c and d denote the indices of two neighboring cells. Labels p and r denote the indices of the same point relatively to the local numbering of points in cell c and d. The neighboring sub-cells are denoted by ω_{pc} and ω_{rd}. The half-edge fluxes, $q^{\pm}_{pc}$, $q^{\pm}_{rd}$ and temperatures, $T^{\pm}_{cp}$, $T^{\pm}_{rd}$ are displayed using blue color.

The continuity condition for the heat flux follows from the definition of the unit outward normals related to $(\omega_{pc} \cup \omega_{rd})$, *i.e.*, $\boldsymbol{n}^+_{pc} = -\boldsymbol{n}^-_{rd}$.

To achieve the space discretization of (4.21), it remains to construct a consistent approximation of the half-edge normal flux, that is, to define a numeric half-edge-based flux function $h^{\pm}_{pc}$ such that

$$q^-_{pc} = h^-_{pc}(T^-_{pc} - T_c, T^+_{pc} - T_c), \quad q^+_{pc} = h^+_{pc}(T^-_{pc} - T_c, T^+_{pc} - T_c). \tag{4.24}$$

Here, $h^{\pm}_{pc}$ denotes a real valued function which is continuous with respect to its arguments. Let us note that we have expressed this function in terms of the temperature difference $T_c - T^{\pm}_{pc}$ since the heat flux is proportional to the temperature gradient. The next steps in the design of our finite volume scheme will be the following:

- Construction of the half-edge numerical fluxes by means of a **local variational formulation over the sub-cell**.
- Elimination of the half-edge temperatures through the use of the **continuity condition** (4.23) **across sub-cell interface**.

These tasks will be the main topics of the next section.

4.2 Space discretization

Before proceeding any further, we start by giving a useful and classical result concerning the representation of a vector in terms of its normal components. This result leads to the expression of the standart inner product of two vectors, which will be one the tools utilized to derive the sub-cell variational formulation. Here, we recall briefly the methodology which has been thoroughly exposed by Shashkov in [149, 119].

4.2.1 Expression of a vector in terms of its normal components

Let $\boldsymbol{\phi}$ be an arbitrary vector of the two-dimensional space $\mathbb{R}^2$ and $\boldsymbol{\phi}_{pc}$ its piecewise constant approximation over the sub-cell ω_{pc}. Let $\phi_{pc}^{\pm}$ be the half-edge normal components of $\boldsymbol{\phi}_{pc}$, that is,

$$\begin{aligned}\boldsymbol{\phi}_{pc} \cdot \boldsymbol{n}_{pc}^{-} &= \phi_{pc}^{-},\\ \boldsymbol{\phi}_{pc} \cdot \boldsymbol{n}_{pc}^{+} &= \phi_{pc}^{+}.\end{aligned}$$

Introducing the corner matrix $\mathsf{J}_{pc} = [\boldsymbol{n}_{pc}^{-}, \boldsymbol{n}_{pc}^{+}]$, the above 2×2 linear system rewrites

$$\mathsf{J}_{pc}^{t} \boldsymbol{\phi} = \begin{pmatrix} \phi_{pc}^{-} \\ \phi_{pc}^{+} \end{pmatrix},$$

where superscript t denotes the transpose matrix. Provided that $\boldsymbol{n}_{pc}^{-}$ and $\boldsymbol{n}_{pc}^{+}$ are not colinear, the above system has always a unique solution written under the form

$$\boldsymbol{\phi}_{pc} = \mathsf{J}_{pc}^{-t} \begin{pmatrix} \phi_{pc}^{-} \\ \phi_{pc}^{+} \end{pmatrix}. \tag{4.25}$$

This equation allows to express any vector in terms of its normal components on two non-colinear unit vectors. This representation allows to compute the inner product of two vectors $\boldsymbol{\phi}_{pc}$ and $\boldsymbol{\psi}_{pc}$ as follows

$$\boldsymbol{\phi}_{pc} \cdot \boldsymbol{\psi}_{pc} = (\mathsf{J}_{pc}^{t} \mathsf{J}_{pc})^{-1} \begin{pmatrix} \psi_{pc}^{-} \\ \psi_{pc}^{+} \end{pmatrix} \cdot \begin{pmatrix} \phi_{pc}^{-} \\ \phi_{pc}^{+} \end{pmatrix}. \tag{4.26}$$

The 2×2 matrix $\mathsf{H}_{pc} = \mathsf{J}_{pc}^{t} \mathsf{J}_{pc}$ is defined by

$$\mathsf{H}_{pc} = \begin{pmatrix} \boldsymbol{n}_{pc}^{-} \cdot \boldsymbol{n}_{pc}^{-} & \boldsymbol{n}_{pc}^{-} \cdot \boldsymbol{n}_{pc}^{+} \\ \boldsymbol{n}_{pc}^{+} \cdot \boldsymbol{n}_{pc}^{-} & \boldsymbol{n}_{pc}^{+} \cdot \boldsymbol{n}_{pc}^{+} \end{pmatrix} = \begin{pmatrix} 1 & -\cos\theta_{pc} \\ -\cos\theta_{pc} & 1 \end{pmatrix}, \tag{4.27}$$

where θ_{pc} denotes the measure of the angle between the two half-edges of sub-cell ω_{pc} impinging at point p, refer to Figure 4.4. This matrix admits an inverse provided that $\theta_{pc} \neq k\pi$, where k is an integer. Under this condition, H_{pc}^{-1} is readily obtained

$$\mathsf{H}_{pc}^{-1} = \frac{1}{\sin^2\theta_{pc}} \begin{pmatrix} 1 & \cos\theta_{pc} \\ \cos\theta_{pc} & 1 \end{pmatrix}.$$

This matrix, which is symmetric definite positive, represents the local metric tensor associated to the sub-cell ω_{pc}. Let us remark that we have recovered exactly the expressions initially derived in [119].

4.2.2 Half-edge fluxes approximation based on a local variational formulation

Sub-cell-based variational formulation

We construct an approximation of the half-edge fluxes by means of a local variational formulation written over the sub-cell ω_{pc}. Contrary to the classical cell-based variational formulation used in the context of Mimetic Finite Difference Method [73], the present sub-cell-based variational formulation leads to a local **explicit expression of the half-edges fluxes** in terms of the half-edges temperatures and the mean cell temperature. The local and explicit feature of the half-edge fluxes expression is of great importance, since it allows to construct a numerical scheme with only one unknown per cell.

Our starting point to derive the sub-cell-based variational formulation consists in writing the partial differential equation satisfied by the flux. From the heat flux definition (4.16), it follows that $\boldsymbol{q}$ satisfies

$$\mathsf{K}^{-1}\boldsymbol{q} + \boldsymbol{\nabla} T = \mathbf{0}. \tag{4.28}$$

Let us point out that the present approach is stronlgy linked to the mixed formulation utilized in the context of mixed finite element discretization [157, 5, 95]. Dot-multiplying this equation by an arbitrary vector $\boldsymbol{\phi} \in \mathcal{D}$ and integrating over the cell ω_{pc} yields

$$\int_{\omega_{pc}} \boldsymbol{\phi} \cdot \mathsf{K}^{-1}\boldsymbol{q}\, \mathrm{d}v = -\int_{\omega_{pc}} \boldsymbol{\phi} \cdot \boldsymbol{\nabla} T\, \mathrm{d}v, \quad \forall \boldsymbol{\phi} \in \mathcal{D}. \tag{4.29}$$

Integrating by part the right-hand side and applying the divergence formula leads to the following variational formulation

$$\int_{\omega_{pc}} \boldsymbol{\phi} \cdot \mathsf{K}^{-1}\boldsymbol{q}\, \mathrm{d}v = \int_{\omega_{pc}} T\nabla \cdot \boldsymbol{\phi}\, \mathrm{d}v - \int_{\partial\omega_{pc}} T\boldsymbol{\phi} \cdot \boldsymbol{n}\, \mathrm{d}s, \quad \forall \boldsymbol{\phi} \in \mathcal{D}. \tag{4.30}$$

This sub-cell-based variational formulation is the base to construct a local and explicit numerical approximation of the half-edge fluxes. Replacing T by its piecewise constant approximation T_c in the first integral of the right-hand side and applying the divergence formula to the remaining volume integrals leads to

$$\int_{\omega_{pc}} \boldsymbol{\phi} \cdot \mathsf{K}^{-1}\boldsymbol{q}\, \mathrm{d}v = T_c \int_{\partial\omega_{pc}} \boldsymbol{\phi} \cdot \boldsymbol{n}\, \mathrm{d}s - \int_{\partial\omega_{pc}} T\boldsymbol{\phi} \cdot \boldsymbol{n}\, \mathrm{d}s.$$

Partitioning the sub-cell boundary as $\partial\omega_{pc} = (\partial\omega_{pc} \cap \partial\omega_c) \cup (\partial\omega_{pc} \cap \omega_c)$ in the latter equation yields

$$\int_{\omega_{pc}} \boldsymbol{\phi}\cdot\mathsf{K}^{-1}\boldsymbol{q}\, \mathrm{d}v = T_c \int_{\partial\omega_{pc}\cap\partial\omega_c} \boldsymbol{\phi}\cdot\boldsymbol{n}\, \mathrm{d}s + T_c \int_{\partial\omega_{pc}\cap\omega_c} \boldsymbol{\phi}\cdot\boldsymbol{n}\, \mathrm{d}s - \int_{\partial\omega_{pc}\cap\partial\omega_c} T\boldsymbol{\phi}\cdot\boldsymbol{n}\, \mathrm{d}s - \int_{\partial\omega_{pc}\cap\omega_c} T\boldsymbol{\phi}\cdot\boldsymbol{n}\, \mathrm{d}s.$$

Replacing T by T_c in the fourth surface integral of the right-hand side and noticing that the second integral is equal to the last one allows to write the sub-cell-based variational formulation under the form

$$\int_{\omega_{pc}} \boldsymbol{\phi} \cdot \mathsf{K}^{-1}\boldsymbol{q}\, \mathrm{d}v = T_c \int_{\partial\omega_{pc}\cap\partial\omega_c} \boldsymbol{\phi} \cdot \boldsymbol{n}\, \mathrm{d}s - \int_{\partial\omega_{pc}\cap\partial\omega_c} T\boldsymbol{\phi} \cdot \boldsymbol{n}\, \mathrm{d}s. \tag{4.31}$$

At this point it is interesting to remark that this sub-cell-based formulation is a sufficient condition to recover the classical cell-based variational formulation. Since the set of sub-cells of ω_c is a partition of this cell, we have

$$\omega_c = \bigcup_{p\in\mathcal{P}(c)} \omega_{pc}, \quad \partial\omega_c = \bigcup_{p\in\mathcal{P}(c)} (\partial\omega_{pc} \cap \partial\omega_c).$$

Thus, by summing (4.31) over all the sub-cells of ω_c, we obtain

$$\int_{\omega_c} \boldsymbol{\phi} \cdot \mathsf{K}^{-1}\boldsymbol{q}\, \mathrm{d}v = T_c \int_{\partial\omega_c} \boldsymbol{\phi} \cdot \boldsymbol{n}\, \mathrm{d}s - \int_{\partial\omega_c} T\boldsymbol{\phi} \cdot \boldsymbol{n}\, \mathrm{d}s. \tag{4.32}$$

This last equation corresponds to cell-based variational formulation of the partial differential equation (4.28). This form is used in the context of Mimetic Finite Difference Method [73] to obtain a discretization of the heat flux. More precisely, it leads to a $\mid \mathcal{P}(c) \mid \times \mid \mathcal{P}(c) \mid$ linear

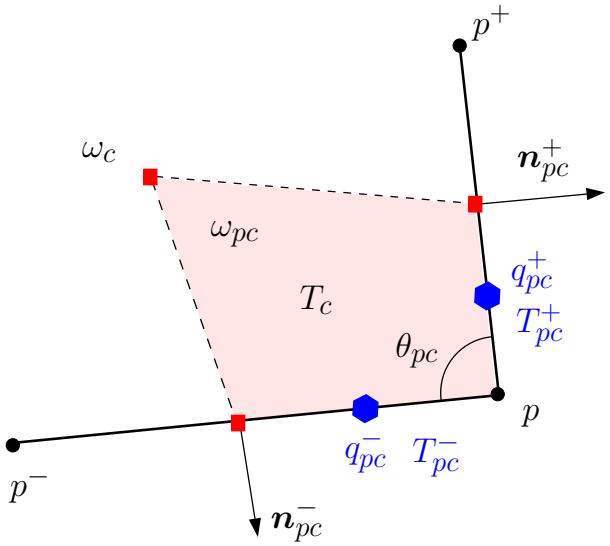

Figure 4.4: Fragment of a polygonal cell ω_c. Notation for the sub-cell ω_{pc}: The half-edge fluxes, $q_{pc}^{\pm}$, and temperatures, $T_{pc}^{\pm}$ are displayed using blue color.

system satisfied by the edge-based normal components of the heat flux. This results in a non explicit expression of the edge-based normal components of the flux with respect to the edge-based temperatures and the mean cell temperature, which leads to a finite volume discretization characterized by edge-based and cell-based unknowns. In contrast to this approach, the sub-cell based variational formulation (4.31) yields a finite-volume discretization with one unknown per cell.

Returning to the sub-cell based variational formulation, we discretize the right-hand side of (4.31) by introducing the half-edge normal components of $\boldsymbol{\phi}$ and the piecewise constant approximation of the half-edge temperatures as follows

$$\int_{\omega_{pc}} \boldsymbol{\phi} \cdot \mathsf{K}^{-1}\boldsymbol{q}\, \mathrm{d}v = -[l_{pc}^-(T_{pc}^- - T_c)\phi_{pc}^- + l_{pc}^+(T_{pc}^+ - T_c)\phi_{pc}^+]. \tag{4.33}$$

Assuming a piecewise constant representation of the test function allows to compute the volume integral in the left-hand side thanks to the quadrature rule

$$\int_{\omega_{pc}} \boldsymbol{\phi} \cdot \mathsf{K}^{-1}\boldsymbol{q}\, \mathrm{d}v = w_{pc}\boldsymbol{\phi}_{pc} \cdot \mathsf{K}_c^{-1}\boldsymbol{q}_{pc}, \tag{4.34}$$

Here, K_c denotes the piecewise constant approximation of the conductivity tensor and $\boldsymbol{\phi}_{pc}$, $\boldsymbol{q}_{pc}$ are the piecewise constant approximations of vectors $\boldsymbol{\phi}$ and $\boldsymbol{q}$, refer to Figure 4.4. In addition, w_{pc} denotes some positive corner volume related to sub-cell ω_{pc}, which will be determined later. Note that the corner volumes associated to the same cell ω_c must satisfy the consistency condition

$$\sum_{p \in \mathcal{P}(c)} w_{pc} = \mid \omega_c \mid . \tag{4.35}$$

Namely, the corner volumes of a cell sums to the volume of the cell. This is the minimal requirement to ensure that constant functions are exactly integrated using the above quadrature rule. Now, combining (4.34) and (4.33) and using the expression of the vectors $\boldsymbol{q}$ and $\boldsymbol{\phi}$ in terms of their half-edge normal components leads to the following variational formulation

$$w_{pc}(\mathsf{J}_{pc}^t \mathsf{K}_c \mathsf{J}_{pc})^{-1} \begin{pmatrix} q_{pc}^- \\ q_{pc}^+ \end{pmatrix} \cdot \begin{pmatrix} \phi_{pc}^- \\ \phi_{pc}^+ \end{pmatrix} = - \begin{bmatrix} l_{pc}^-(T_{pc}^- - T_c) \\ l_{pc}^+(T_{pc}^+ - T_c) \end{bmatrix} \cdot \begin{pmatrix} \phi_{pc}^- \\ \phi_{pc}^+ \end{pmatrix}. \tag{4.36}$$

Knowing that this variational formulation must hold for any vector $\boldsymbol{\phi}_{pc}$, this implies

$$\begin{pmatrix} q_{pc}^- \\ q_{pc}^+ \end{pmatrix} = -\frac{1}{w_{pc}} (\mathsf{J}_{pc}^t \mathsf{K}_c \mathsf{J}_{pc}) \begin{bmatrix} l_{pc}^-(T_{pc}^- - T_c) \\ l_{pc}^+(T_{pc}^+ - T_c) \end{bmatrix}. \tag{4.37}$$

This equation constitutes the approximation of the half-edge normal fluxes over a sub-cell. This local approximation is coherent with expression of the constitutive law (4.16) in the sense that the numerical approximation of the heat flux is equal to a tensor times a numerical approximation of the temperature gradient. This tensor can be viewed as an effective conductivity tensor associated to the sub-cell ω_{pc}. Thus, it is natural to set

$$\mathsf{K}_{pc} = \mathsf{J}_{pc}^t \mathsf{K}_c \mathsf{J}_{pc}. \tag{4.38}$$

Let us emphasize that this corner tensor inherits all the properties of the conductivity tensor K_c. Namely, K_c being positive definite, K_{pc} is also positive definite. This comes from the fact that

$$\mathsf{K}_{pc}\boldsymbol{\phi} \cdot \boldsymbol{\phi} = \mathsf{K}_c(\mathsf{J}_{pc}\boldsymbol{\phi}) \cdot (\mathsf{J}_{pc}\boldsymbol{\phi}), \quad \forall \boldsymbol{\phi} \in \mathbb{R}^2.$$

Using a similar argument, note that if K_c is symmetric, K_{pc} is also symmetric. Recalling that $\mathsf{J}_{pc} = [\boldsymbol{n}_{pc}^-, \boldsymbol{n}_{pc}^+]$, we readily obtain the expression of the corner tensor K_{pc} in terms of the unit normal $\boldsymbol{n}_{pc}^{\pm}$

$$\mathsf{K}_{pc} = \begin{pmatrix} \mathsf{K}_c\boldsymbol{n}_{pc}^- \cdot \boldsymbol{n}_{pc}^- & \mathsf{K}_c\boldsymbol{n}_{pc}^+ \cdot \boldsymbol{n}_{pc}^- \\ \mathsf{K}_c\boldsymbol{n}_{pc}^- \cdot \boldsymbol{n}_{pc}^+ & \mathsf{K}_c\boldsymbol{n}_{pc}^+ \cdot \boldsymbol{n}_{pc}^+ \end{pmatrix}. \tag{4.39}$$

Let us remark that in the isotropic case, *i.e*, $\mathsf{K}_c = \kappa_c \mathsf{I}_d$, the corner tensor collapses to

$$\mathsf{K}_{pc} = \kappa_c \mathsf{H}_{pc}, \tag{4.40}$$

where κ_c denotes the piecewise constant scalar conductivity over cell ω_c and H_{pc} is the second-order tensor defined by (4.27).

We conclude by claiming that a sub-cell-based variational formulation has allowed to construct the following numerical approximation of the half-edge normal fluxes

$$\begin{pmatrix} q_{pc}^- \\ q_{pc}^+ \end{pmatrix} = -\frac{1}{w_{pc}} \mathsf{K}_{pc} \begin{bmatrix} l_{pc}^-(T_{pc}^- - T_c) \\ l_{pc}^+(T_{pc}^+ - T_c) \end{bmatrix}. \tag{4.41}$$

Here, w_{pc} is a positive volume weight, which will be determined later, and the corner conductivity tensor, K_{pc} is expressed by (4.39).

Comment 16 *It is interesting to remark that the corner tensor* K_{pc} *is a linear function with respect to the piecewise constant approximation of the conductivity tensor* K_c*. This follows directly from* (4.38)*. In addition, the corner tensor corresponding to the transpose of* K_c *is the transpose of* K_{pc}*, i.e.,* $\mathsf{K}_{pc}(\mathsf{K}_c^t) = \mathsf{K}_{pc}^t(\mathsf{K}_c)$.

Fundamental inequality satisfied by the discrete approximation of the half-edge fluxes

The goal of this paragraph is to show that the discrete approximation of the half-edges normal fluxes (4.41) derived from the sub-cell-based variational formulation satisfies a discrete version of the fundamental inequality (4.3), which follows from the Second Law of thermodynamics. This discrete analogous of the fundamental inequality states that for half-edge fluxes defined according to (4.41) the following inequality holds

$$\sum_{c \in \mathcal{C}(p)} (l_{pc}^- q_{pc}^- + l_{pc}^+ q_{pc}^+) T_c \geq 0, \tag{4.42}$$

where $\mathcal{C}(p)$ denotes the set of cells surrounding point p. To prove this inequality, let us introduce I_p as being the nodal quantity defined by

$$I_p = \sum_{c \in \mathcal{C}(p)} (l_{pc}^- q_{pc}^- + l_{pc}^+ q_{pc}^+) T_c. \tag{4.43}$$

We shall prove that I_p is always non-negative using the sub-cell variational formulation derived in Section 4.2.2. From (4.36) it follows that for all vector $\boldsymbol{\phi}$ the following identity holds

$$w_{pc} \mathsf{K}_{pc}^{-1} \begin{pmatrix} q_{pc}^- \\ q_{pc}^+ \end{pmatrix} \cdot \begin{pmatrix} \phi_{pc}^- \\ \phi_{pc}^+ \end{pmatrix} = - \begin{bmatrix} l_{pc}^-(T_{pc}^- - T_c) \\ l_{pc}^+(T_{pc}^+ - T_c) \end{bmatrix} \cdot \begin{pmatrix} \phi_{pc}^- \\ \phi_{pc}^+ \end{pmatrix},$$

where w_{pc} is the positive volume weight and K_{pc} the definite positive corner conductivity tensor. Applying this identity for $\boldsymbol{\phi} = \boldsymbol{q}$ and rearranging the right hand-side yields

$$w_{pc} \mathsf{K}_{pc}^{-1} \begin{pmatrix} q_{pc}^- \\ q_{pc}^+ \end{pmatrix} \cdot \begin{pmatrix} q_{pc}^- \\ q_{pc}^+ \end{pmatrix} = (l_{pc}^- q_{pc}^- + l_{pc}^+ q_{pc}^+) T_c - (l_{pc}^- q_{pc}^- T_{pc}^- + l_{pc}^+ q_{pc}^+ T_{pc}^+).$$

We notice that the left-hand side of the above equation is always non-negative since K_{pc} is positive definite. Summing the above equation over all the cells surrounding point p leads to

$$\sum_{c \in \mathcal{P}(c)} w_{pc} \mathsf{K}_{pc}^{-1} \begin{pmatrix} q_{pc}^- \\ q_{pc}^+ \end{pmatrix} \cdot \begin{pmatrix} q_{pc}^- \\ q_{pc}^+ \end{pmatrix} = \sum_{c \in \mathcal{P}(c)} (l_{pc}^- q_{pc}^- + l_{pc}^+ q_{pc}^+) T_c - \sum_{c \in \mathcal{P}(c)} (l_{pc}^- q_{pc}^- T_{pc}^- + l_{pc}^+ q_{pc}^+ T_{pc}^+). \tag{4.44}$$

It is interesting to mention that the above equation is the discrete analogous of the following integral identity

$$- \int_{\omega_p} \boldsymbol{\nabla} T \cdot \boldsymbol{q} \, \mathrm{d}v = \int_{\omega_p} T \nabla \cdot \boldsymbol{q} \, \mathrm{d}v - \int_{\partial \omega_p} T \boldsymbol{q} \cdot \boldsymbol{n} \, \mathrm{d}s, \tag{4.45}$$

where ω_p denotes the dual cell which results from the union of the sub-cells surrounding point p, *i.e.*, $\omega_p = \bigcup_{c \in \mathcal{C}(p)} \omega_{pc}$. Returning to (4.44), we observe that the second term in the right-hand side vanishes due to the continuity condition of the fluxes at the half-edges impinging at point p, refer to (4.23a). Finally, (4.44) turns to

$$I_p = \sum_{c \in \mathcal{C}(p)} w_{pc} \mathsf{K}_{pc}^{-1} \begin{pmatrix} q_{pc}^- \\ q_{pc}^+ \end{pmatrix} \cdot \begin{pmatrix} q_{pc}^- \\ q_{pc}^+ \end{pmatrix} \geq 0. \tag{4.46}$$

Let us emphasize that inequality (4.42) follows directly from the fact that we have used a variational formulation to derive the numerical approximation of the flux. This inequality will be of great importance to prove several crucial results regarding the properties of our finite volume scheme.

Volume weight computation

In this paragraph, we aim at deriving practical formulas to compute the volume weight, w_{pc}, present in the flux approximation (4.41). To begin with, let us consider a triangular cell, ω_c, characterized by its counterclockwise ordered vertices p^-, p and p^+, refer to Figure 4.5. **We state that the flux approximation** (4.41) **preserves linear fields over triangular cells provided that the volume weight is such that**

$$w_{pc}^{\mathrm{tri}} = \frac{1}{3} \mid \omega_c \mid . \tag{4.47}$$

To prove this result, let us consider $T_h = T_h(\boldsymbol{x})$ a piecewise linear approximation of the

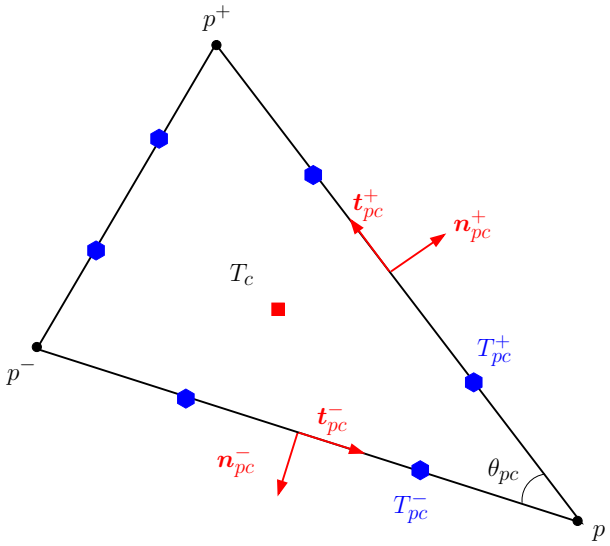

Figure 4.5: Notation for a triangular cell. Half-edge degrees of freedom are displayed in blue color.

temperature field, *i.e.*,

$$T_h(\boldsymbol{x}) = T_c + (\boldsymbol{\nabla} T)_c \cdot (\boldsymbol{x} - \boldsymbol{x}_c), \quad \forall \boldsymbol{x} \in \omega_c. \tag{4.48}$$

Here, $\boldsymbol{x}_c = \frac{1}{3}(\boldsymbol{x}_{p^-} + \boldsymbol{x}_p + \boldsymbol{x}_{p^+})$ is the centroid of ω_c and $T_c = T_h(\boldsymbol{x}_c)$ denotes the mean temperature of the cell. In addition, $(\boldsymbol{\nabla} T)_c$ corresponds to the uniform temperature gradient of the cell. Using the piecewise constant approximation of the conductivity tensor, K_c, this gradient is rewritten $(\boldsymbol{\nabla} T)_c = -\mathsf{K}_c^{-1}\boldsymbol{q}_c$, where $\boldsymbol{q}_c$ is the piecewise constant approximation of the flux. With this notation, (4.48) transforms into

$$T_h(\boldsymbol{x}) = T_c - \mathsf{K}_c^{-1}\boldsymbol{q}_c \cdot (\boldsymbol{x} - \boldsymbol{x}_c), \quad \forall \boldsymbol{x} \in \omega_c. \tag{4.49}$$

Expressing the two vectors $\boldsymbol{q}_c$ and $(\boldsymbol{x} - \boldsymbol{x}_c)$ in terms of their half-edge normal components by means of (4.25) yields

$$T_h(\boldsymbol{x}) = T_c - \mathsf{K}_{pc}^{-1} \begin{pmatrix} q^-_{pc} \\ q^+_{pc} \end{pmatrix} \cdot \begin{bmatrix} (\boldsymbol{x} - \boldsymbol{x}_c)^-_{pc} \\ (\boldsymbol{x} - \boldsymbol{x}_c)^+_{pc} \end{bmatrix}, \quad \forall \boldsymbol{x} \in \omega_c, \tag{4.50}$$

where $\mathsf{K}_{pc} = \mathsf{J}^t_{pc}\mathsf{K}_c\mathsf{J}_{pc}$. Since this equation holds for all points in ω_c, we apply it to $\boldsymbol{x}^-_{pc}$ and $\boldsymbol{x}^+_{pc}$ given by

$$\boldsymbol{x}^-_{pc} = \frac{2\boldsymbol{x}_p + \boldsymbol{x}_{p^-}}{3}, \quad \boldsymbol{x}^+_{pc} = \frac{2\boldsymbol{x}_p + \boldsymbol{x}_{p^+}}{3}. \tag{4.51}$$

This results in

$$T_h(\boldsymbol{x}^\pm_{pc}) - T_c = -\mathsf{K}_{pc}^{-1} \begin{pmatrix} q^-_{pc} \\ q^+_{pc} \end{pmatrix} \cdot \begin{bmatrix} (\boldsymbol{x}^\pm_{pc} - \boldsymbol{x}_c)^-_{pc} \\ (\boldsymbol{x}^\pm_{pc} - \boldsymbol{x}_c)^+_{pc} \end{bmatrix}.$$

Knowing that

$$\begin{aligned} \boldsymbol{x}^-_{pc} - \boldsymbol{x}_c &= \frac{1}{3}(\boldsymbol{x}_p - \boldsymbol{x}_{p^+}) = -\frac{2}{3} l^+_{pc} \boldsymbol{t}^+_{pc}, \\ \boldsymbol{x}^+_{pc} - \boldsymbol{x}_c &= \frac{1}{3}(\boldsymbol{x}_p - \boldsymbol{x}_{p^-}) = \frac{2}{3} l^-_{pc} \boldsymbol{t}^-_{pc}, \end{aligned}$$

where $\boldsymbol{t}_{pc}^{\pm}$ are the half-edge unit tangent vectors such that $\boldsymbol{n}_{pc}^{\pm} \times \boldsymbol{t}_{pc}^{\pm} = \boldsymbol{e}_z$, refer to Figure 4.5, using $\boldsymbol{t}_{pc}^{-} \cdot \boldsymbol{n}_{pc}^{+} = \sin\theta_{pc}$ and $\boldsymbol{t}_{pc}^{+} \cdot \boldsymbol{n}_{pc}^{-} = -\sin\theta_{pc}$ leads to

$$T_h(\boldsymbol{x}_{pc}^{-}) - T_c = -\frac{2}{3} l_{pc}^{+} \sin\theta_{pc} \mathsf{K}_{pc}^{-1} \begin{pmatrix} q_{pc}^{-} \\ q_{pc}^{+} \end{pmatrix} \cdot \begin{pmatrix} 1 \\ 0 \end{pmatrix},$$
$$T_h(\boldsymbol{x}_{pc}^{+}) - T_c = -\frac{2}{3} l_{pc}^{-} \sin\theta_{pc} \mathsf{K}_{pc}^{-1} \begin{pmatrix} q_{pc}^{-} \\ q_{pc}^{+} \end{pmatrix} \cdot \begin{pmatrix} 0 \\ 1 \end{pmatrix}.$$

Rearranging the above equations allows to express the half-edge normal components of the flux as

$$\begin{pmatrix} q_{pc}^{-} \\ q_{pc}^{+} \end{pmatrix} = -\frac{3}{2 l_{pc}^{-} l_{pc}^{+} \sin\theta_{pc}} \mathsf{K}_{pc} \begin{bmatrix} l_{pc}^{-}(T_h(\boldsymbol{x}_{pc}^{-}) - T_c) \\ l_{pc}^{+}(T_h(\boldsymbol{x}_{pc}^{+}) - T_c) \end{bmatrix}. \tag{4.52}$$

In writing this equation we have obtained an expression of the half-edge fluxes which is exact for a linear approximation of the temperature field over a triangular cell. The comparison between this formula and the general formula obtained previously shows that the volume weight is given by $w_{pc} = \frac{2}{3} l_{pc}^{-} l_{pc}^{+} \sin\theta_{pc}$, which is nothing but one third of the cell volume. In addition, this comparison reveals that the piecewise constant half-edge approximations of the temperature have a clear geometrical interpretation since $T_{pc}^{\pm} = T_h(\boldsymbol{x}_{pc}^{\pm})$, refer to Figure 4.5.

Having defined the volume weight for triangular cells, we conclude this paragraph by giving some indications about the volume weight definition for other types of cells. For quadrangular cells, according to [73], a reasonable choice is to set

$$w_{pc}^{\text{quad}} = l_{pc}^{-} l_{pc}^{+} \sin\theta_{pc}. \tag{4.53}$$

This results in a corner volume equal to the half of the area of the triangle formed by points p^{-}, p and p^{+}, refer to Fig 4.5. Unfortunately this choice does not allow to preserve linear solution on quadrangular grids, except on grids made of parallelograms, refer to Comment 18. However, the numerical results obtained on quadrangular grids with this choice appeared to be quite satisfactory as we shall see in the section devoted to the numerical results. For general polygonal cells, two possible choices are obtained setting

$$w_{pc}^{\text{poly1}} = \frac{1}{\mid \mathcal{P}(c) \mid} \mid \omega_c \mid, \quad w_{pc}^{\text{poly2}} = \mid \omega_{pc} \mid, \tag{4.54}$$

where $\mid \mathcal{P}(c) \mid$ is the total number of sub-cells in cell c. Since the behavior of the numerical method will not be assessed on general polygonal grids, we do not pursue investigations about an optimal choice of the volume weight for polygonal cell.

Comment 17 *Let us point out that all these volume weights must be positive and consequently they have been defined assuming that we are dealing with valid cells, that it, is convex cells. The occurence of non-convex cells can be treated using the rough remedy which consists in replacing the original volume weight by its absolute value.*

4.2.3 Finite difference approximation of the half-edge fluxes

In this section, we aim at deriving a finite difference approximation of the half-edge fluxes which preserves linear solutions regardless the shape of the cell. Doing so, we enforce the accuracy of our space discretization. However, since this approximation does not result from a variational formulation, in general, we cannot insure the transfer of the good properties of the conductivity tensor to the discrete approximation. For instance, it will not be possible to ensure that the inequality (4.42) holds for a finite difference approximation of the fluxes.

Let ω_c be an arbitrary cell and ω_{pc} its sub-cell associated to point p. To define a finite difference approximation which is linear preserving, we reuse the piecewise linear approximation of the temperature over ω_c introduced in the latter paragraph as

$$T_h(\boldsymbol{x}) = T_c - \mathsf{K}_c^{-1}\boldsymbol{q}_c \cdot (\boldsymbol{x} - \boldsymbol{x}_c), \quad \forall \boldsymbol{x} \in \omega_c.$$

Let us recall, that $\boldsymbol{x}_c$ is the centroid of the cell, *i.e.*, $\boldsymbol{x}_c = \frac{1}{|\omega_c|}\int_{\omega_c} \boldsymbol{x}\, \mathrm{d}v$, and T_c is the cell averaged temperature. In writing the above equation we have used the piecewise constant definition of the heat flux, *i.e.*, $\boldsymbol{q}_c = -\mathsf{K}_c(\boldsymbol{\nabla} T)_c$. Let $i^{\pm}$ denotes the midpoint of the segment $[p, p^{\pm}]$ and $\boldsymbol{x}_{i^{\pm}}$ its corresponding position vector. Assuming that the half-edge temperature $T_{pc}^{\pm}$ is given by $T_{pc}^{\pm} = T_h(\boldsymbol{x}_{i^{\pm}})$ leads to

$$\begin{aligned} T_{pc}^{-} - T_c &= -\mathsf{K}_c^{-1}\boldsymbol{q}_c \cdot (\boldsymbol{x}_i^{-} - \boldsymbol{x}_c), \\ T_{pc}^{+} - T_c &= -\mathsf{K}_c^{-1}\boldsymbol{q}_c \cdot (\boldsymbol{x}_i^{+} - \boldsymbol{x}_c). \end{aligned} \tag{4.55}$$

Setting $\boldsymbol{\mu}_{pc}^{\pm} = \boldsymbol{x}_i^{\pm} - \boldsymbol{x}_c$ and using (4.25), we transform (4.55) by expressing the vectors $\boldsymbol{q}_c$ and $\boldsymbol{\mu}_{pc}^{\pm}$ in terms of their normal components

$$\begin{aligned} T_{pc}^{-} - T_c &= -\mathsf{K}_c^{-1}\mathsf{J}_{pc}^{-t}\begin{pmatrix} q_{pc}^{-} \\ q_{pc}^{+} \end{pmatrix} \cdot \mathsf{J}_{pc}^{-t}\begin{pmatrix} \boldsymbol{\mu}_{pc}^{-} \cdot \boldsymbol{n}_{pc}^{-} \\ \boldsymbol{\mu}_{pc}^{-} \cdot \boldsymbol{n}_{pc}^{+} \end{pmatrix}, \\ T_{pc}^{+} - T_c &= -\mathsf{K}_c^{-1}\mathsf{J}_{pc}^{-t}\begin{pmatrix} q_{pc}^{-} \\ q_{pc}^{+} \end{pmatrix} \cdot \mathsf{J}_{pc}^{-t}\begin{pmatrix} \boldsymbol{\mu}_{pc}^{+} \cdot \boldsymbol{n}_{pc}^{-} \\ \boldsymbol{\mu}_{pc}^{+} \cdot \boldsymbol{n}_{pc}^{+} \end{pmatrix}. \end{aligned}$$

Introducing the sub-cell conductivity tensor K_{pc} defined by (4.38) and after some manipulations, the above equation rewrites as

$$\begin{pmatrix} T_{pc}^{-} - T_c \\ T_{pc}^{+} - T_c \end{pmatrix} = -\begin{pmatrix} \boldsymbol{\mu}_{pc}^{-} \cdot \boldsymbol{n}_{pc}^{-} & \boldsymbol{\mu}_{pc}^{-} \cdot \boldsymbol{n}_{pc}^{+} \\ \boldsymbol{\mu}_{pc}^{+} \cdot \boldsymbol{n}_{pc}^{-} & \boldsymbol{\mu}_{pc}^{+} \cdot \boldsymbol{n}_{pc}^{+} \end{pmatrix} \mathsf{K}_{pc}^{-1}\begin{pmatrix} q_{pc}^{-} \\ q_{pc}^{+} \end{pmatrix}.$$

The rows of the first matrix in the right-hand side corresponds to the half-edge normal components of vectors $\boldsymbol{\mu}_{pc}^{-}$ and $\boldsymbol{\mu}_{pc}^{+}$. This matrix is non-singular provided these two vectors are not colinear. Assuming this and solving the above linear system leads to the final expression of the half-edge normal fluxes

$$\begin{pmatrix} q_{pc}^{-} \\ q_{pc}^{+} \end{pmatrix} = -\frac{1}{\Delta_{pc}}\mathsf{K}_{pc}\begin{pmatrix} \boldsymbol{\mu}_{pc}^{+} \cdot \boldsymbol{n}_{pc}^{+} & -\boldsymbol{\mu}_{pc}^{-} \cdot \boldsymbol{n}_{pc}^{+} \\ -\boldsymbol{\mu}_{pc}^{+} \cdot \boldsymbol{n}_{pc}^{-} & \boldsymbol{\mu}_{pc}^{-} \cdot \boldsymbol{n}_{pc}^{-} \end{pmatrix}\begin{pmatrix} T_{pc}^{-} - T_c \\ T_{pc}^{+} - T_c \end{pmatrix}, \tag{4.56}$$

where $\Delta_{pc} = (\boldsymbol{\mu}_{pc}^{-} \cdot \boldsymbol{n}_{pc}^{-})(\boldsymbol{\mu}_{pc}^{+} \cdot \boldsymbol{n}_{pc}^{+}) - (\boldsymbol{\mu}_{pc}^{-} \cdot \boldsymbol{n}_{pc}^{+})(\boldsymbol{\mu}_{pc}^{+} \cdot \boldsymbol{n}_{pc}^{-})$ is the determinant of the matrix defined by the normal components of $\boldsymbol{\mu}_{pc}^{\pm}$. Equation (4.56) constitutes a finite difference approximation of the half-edge normal fluxes which is linear preserving since it has been deduced from a piecewise linear approximation of the temperature field. However, the matrix form of this approximation reveals that the property transfer, which characterizes the flux approximation derived through the use of variational formulation, does not hold here. This is due to the fact that the matrix defined by the normal components of $\boldsymbol{\mu}_{pc}^{\pm}$ is not a symmetric positive definite matrix in general. Using such an approximation for the normal flux, leads to a finite volume discretization characterized in general by a non-symmetric discrete diffusion operator, which renders the resolution of the corresponding linear system less easy. The main advantage in using this scheme lies in the fact that it preserves linear solution regardless the shape of the cells. We postpone further investigation about this non-symmetric formulation to a forthcoming paper, knowing that here, we have chosen to develop our finite volume discretization using the approximation of the normal fluxes resulting from the sub-cell-based variational formulation.

Comment 18 *It is interesting to investigate further the finite difference approximation* (4.2.3) *in the case where ω_{pc} is a parallelogram. In this particular case, we have $\boldsymbol{\mu}_{pc}^- = -l_{pc}^+ \boldsymbol{t}_{pc}^+$ and $\boldsymbol{\mu}_{pc}^+ = l_{pc}^- \boldsymbol{t}_{pc}^-$ where $\boldsymbol{t}_{pc}^-$ and $\boldsymbol{t}_{pc}^+$ denote the unit tangent vectors to the two half-edges impinging at point p. Bearing this in mind, we have $\boldsymbol{\mu}_{pc}^- \cdot \boldsymbol{n}_{pc}^- = -l_{pc}^+ \sin\theta_{pc}$ and $\boldsymbol{\mu}_{pc}^+ \cdot \boldsymbol{n}_{pc}^+ = l_{pc}^- \sin\theta_{pc}$. Using these results, the finite difference approximation* (4.2.3) *turns into*

$$\begin{pmatrix} q_{pc}^- \\ q_{pc}^+ \end{pmatrix} = -\frac{1}{l_{pc}^- l_{pc}^+ \sin\theta_{pc}} \mathsf{K}_{pc} \begin{pmatrix} l_{pc}^-(T_{pc}^- - T_c) \\ l_{pc}^+(T_{pc}^+ - T_c) \end{pmatrix}. \tag{4.57}$$

We have recovered a form which coincides with the one resulting from the variational formulation (4.41). *In addition, we can identify the volume weight as being $w_{pc} = l_{pc}^- l_{pc}^+ \sin\theta_{pc}$, which is exactly the weight* (4.53) *introduced in the latter paragraph for quadrangular cells. This shows, that the flux approximation resulting from the sub-cell-based variational formulation, with the latter definition of the volume weight, is able to preserve linear solution on quadrangular grids made of parallelograms.*

4.2.4 Elimination of the half-edge temperatures

From (4.41), it appears that the numerical approximation of the half-edge fluxes at a corner depends on the difference between the mean cell temperature and the half-edges temperatures. The mean cell temperature is the primary unknown whereas the half-edge temperatures are auxiliary unknowns, which can be eliminated by means of continuity argument (4.23a). Namely, we use the fact that the half-edge normal fluxes are continuous across each half-edges impinging at a given point. This local elimination procedure, which will be describe below, yields a linear system satisfied by the half-edge temperatures. We will show that this system admits always a unique solution which allows to express the half-edge temperatures in terms of the mean temperatures of the cells surrounding the point under consideration. Therefore, this local elimination procedure results in a finite volume discrete scheme with one unknown per cell.

Local notation around a point

To derive the local elimination procedure, we shall introduce some convenient notation. Let p denotes a generic point which is not located on the boundary $\partial\mathcal{D}$. The treatment of boundary points is postponed to Section 4.2.7, which is devoted to boundary conditions implementation. Let $\mathcal{C}(p)$ be the set of cells that surround point p. The edges impinging at point p are labelled using the subscript c ranging from 1 to $\mathfrak{C}_p$, where $\mathfrak{C}_p$ denotes the total number of cells surrounding point p. The cell (sub-cell) numbering follows the edge numbering, that is, cell ω_c (sub-cell ω_{pc}) is located between edges c and $c+1$, refer to Figure 4.6. The unit outward normal to cell ω_c at edge c is denoted by $\boldsymbol{n}_c^c$ whereas the unit outward normal to cell ω_c at edge $c+1$ is denoted by $\boldsymbol{n}_c^{c+1}$. Assuming the continuity of the half-edge temperatures leads to denote by $\overline{T}_c$ the unique half-edge temperature of the half-edge c impinging at point p. Note that we have omitted the dependency on point p in the indexing each time this is possible to avoid too heavy notion. With this notation, the expression of the half-edge fluxes (4.41) turns into

$$\begin{pmatrix} q_c^c \\ q_{c+1}^c \end{pmatrix} = -\frac{1}{w_{pc}} \mathsf{K}_{pc} \begin{bmatrix} l_c(\overline{T}_c - T_c) \\ l_{c+1}(\overline{T}_{c+1} - T_c) \end{bmatrix}, \quad \forall c \in \mathcal{C}(p). \tag{4.58}$$

Here, q_c^c (resp. q_{c+1}^c) denotes the half-edge normal flux at edge c (resp. $c+1$) viewed from cell c. In addition l_c denotes the half of the length of edge c. In writing these equations, we assume a periodic numbering around the point p. According to (4.39), the sub-cell conductivity tensor is defined as

$$\mathsf{K}_{pc} = \begin{pmatrix} \mathsf{K}_c \boldsymbol{n}_c^c \cdot \boldsymbol{n}_c^c & \mathsf{K}_c \boldsymbol{n}_{c+1}^c \cdot \boldsymbol{n}_c^c \\ \mathsf{K}_c \boldsymbol{n}_c^c \cdot \boldsymbol{n}_{c+1}^c & \mathsf{K}_c \boldsymbol{n}_{c+1}^c \cdot \boldsymbol{n}_{c+1}^c \end{pmatrix}, \quad \forall c \in \mathcal{C}(p), \tag{4.59}$$

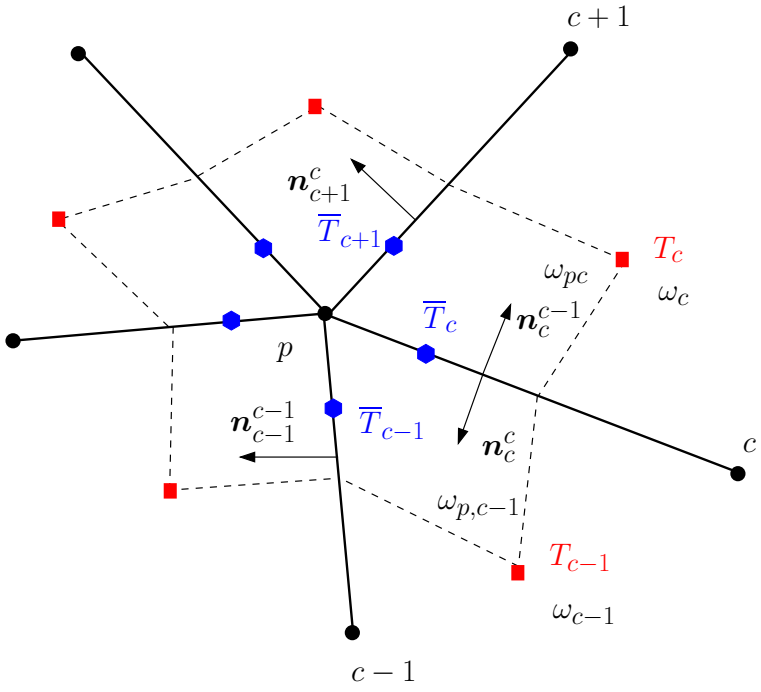

Figure 4.6: Notation for sub-cells surrounding point p.

where K_c is the piecewise constant approximation of the conductivity tensor in cell c. Combining (4.58) and (4.59) yields the explicit expressions

$$q_c^c = -\alpha_c[l_c(\mathsf{K}_c\boldsymbol{n}_c^c\cdot\boldsymbol{n}_c^c)(\overline{T}_c - T_c) + l_{c+1}(\mathsf{K}_c\boldsymbol{n}_{c+1}^c\cdot\boldsymbol{n}_c^c)(\overline{T}_{c+1} - T_c)], \tag{4.60a}$$

$$q_{c+1}^c = -\alpha_c[l_c(\mathsf{K}_c\boldsymbol{n}_c^c\cdot\boldsymbol{n}_{c+1}^c)(\overline{T}_c - T_c) + l_{c+1}(\mathsf{K}_c\boldsymbol{n}_{c+1}^c\cdot\boldsymbol{n}_{c+1}^c)(\overline{T}_{c+1} - T_c)], \tag{4.60b}$$

where we have introduced the inverse of the volume weight setting $\alpha_c = \frac{1}{w_{pc}}$. Shifting index c, *i.e.*, $c \to c-1$, in (4.60b) leads to the following expression for the half-edge normal flux at edge c viewed from cell $c-1$

$$q_c^{c-1} = -\alpha_{c-1}[l_{c-1}(\mathsf{K}_{c-1}\boldsymbol{n}_{c-1}^{c-1}\cdot\boldsymbol{n}_c^{c-1})(\overline{T}_{c-1} - T_{c-1}) + l_c(\mathsf{K}_{c-1}\boldsymbol{n}_c^{c-1}\cdot\boldsymbol{n}_c^{c-1})(\overline{T}_c - T_{c-1})]. \tag{4.61}$$

Linear system satisfied by the half-edge temperatures

Bearing this in mind, we are now in position to proceed with the elimination of the half-edge temperatures by writing the continuity of the half-edge normal fluxes at each edge c. This continuity condition at edge c reads as

$$l_c q_c^{c-1} + l_c q_c^c = 0, \quad \forall c \in \mathcal{C}(p). \tag{4.62}$$

Let us remark that this continuity condition provides $\mathfrak{C}_p$ equations for the $\mathfrak{C}_p$ auxiliary unknowns $\overline{T}_c$. Substituting (4.61) and (4.60a) into the continuity condition yields

$$\begin{aligned}
&\alpha_{c-1}l_{c-1}l_c(\mathsf{K}_{c-1}\boldsymbol{n}_{c-1}^{c-1}\cdot\boldsymbol{n}_c^{c-1})\overline{T}_{c-1} + \\
&[\alpha_{c-1}l_c^2(\mathsf{K}_{c-1}\boldsymbol{n}_c^{c-1}\cdot\boldsymbol{n}_c^{c-1}) + \alpha_c l_c^2(\mathsf{K}_c\boldsymbol{n}_c^c\cdot\boldsymbol{n}_c^c)]\overline{T}_c + \\
&\alpha_c l_c l_{c+1}(\mathsf{K}_c\boldsymbol{n}_{c+1}^c\cdot\boldsymbol{n}_c^c)\overline{T}_{c+1} = \\
&\alpha_{c-1}l_c[l_{c-1}(\mathsf{K}_{c-1}\boldsymbol{n}_{c-1}^{c-1}\cdot\boldsymbol{n}_c^{c-1}) + l_c(\mathsf{K}_{c-1}\boldsymbol{n}_c^{c-1}\cdot\boldsymbol{n}_c^{c-1})]T_{c-1} + \\
&\alpha_c l_c[l_c(\mathsf{K}_c\boldsymbol{n}_c^c\cdot\boldsymbol{n}_c^c) + l_{c+1}(\mathsf{K}_c\boldsymbol{n}_{c+1}^c\cdot\boldsymbol{n}_c^c)]T_c.
\end{aligned}$$

To write this equation under a more concise form, let us introduce $\boldsymbol{T} = (T_1, \ldots, T_{\mathfrak{C}_p})^t$ as the vector of the cell-centered temperatures around point p and $\overline{\boldsymbol{T}} = (\overline{T}_1, \ldots, \overline{T}_{\mathfrak{C}_p})^t$ as the vector of the half-edge temperatures around point p. The continuity condition (4.62) amounts to write that $\overline{\boldsymbol{T}}$ satisfies the following $\mathfrak{C}_p \times \mathfrak{C}_p$ linear system

$$\mathsf{M}\overline{\boldsymbol{T}} = \mathsf{S}\boldsymbol{T}. \tag{4.63}$$

Let us remark that M is a tridiagonal cyclic matrix. This cyclic form is natural consequence of the periodic numbering we have used in solving continuity equations (4.62). The non-zero terms corresponding to the cth row of this matrix write as

$$\begin{cases} \mathsf{M}_{c,c-1} = \alpha_{c-1} l_{c-1} l_c (\mathsf{K}_{c-1} \boldsymbol{n}_{c-1}^{c-1} \cdot \boldsymbol{n}_c^{c-1}), \\ \mathsf{M}_{c,c} = \alpha_{c-1} l_c^2 (\mathsf{K}_{c-1} \boldsymbol{n}_c^{c-1} \cdot \boldsymbol{n}_c^{c-1}) + \alpha_c l_c^2 (\mathsf{K}_c \boldsymbol{n}_c^c \cdot \boldsymbol{n}_c^c), \\ \mathsf{M}_{c,c+1} = \alpha_c l_c l_{c+1} (\mathsf{K}_c \boldsymbol{n}_{c+1}^c \cdot \boldsymbol{n}_c^c). \end{cases} \tag{4.64}$$

From the first equation it follows that

$$\mathsf{M}_{c+1,c} = \alpha_c l_c l_{c+1} (\mathsf{K}_c \boldsymbol{n}_c^c \cdot \boldsymbol{n}_{c+1}^c).$$

The comparison of this term with $\mathsf{M}_{c,c+1}$ shows that M is symmetric if and only if the conductivity tensor, K_c is also symmetric. Regarding S, it is a bidiagonal cyclic matrix, the non-zero terms corresponding to the cth row are:

$$\begin{cases} \mathsf{S}_{c,c-1} = \alpha_{c-1} l_c [l_{c-1} (\mathsf{K}_{c-1} \boldsymbol{n}_{c-1}^{c-1} \cdot \boldsymbol{n}_c^{c-1}) + l_c (\mathsf{K}_{c-1} \boldsymbol{n}_c^{c-1} \cdot \boldsymbol{n}_c^{c-1})], \\ \mathsf{S}_{c,c} = \alpha_c l_c [l_c (\mathsf{K}_c \boldsymbol{n}_c^c \cdot \boldsymbol{n}_c^c) + l_{c+1} (\mathsf{K}_c \boldsymbol{n}_{c+1}^c \cdot \boldsymbol{n}_c^c)]. \end{cases} \tag{4.65}$$

We remark that M can be decomposed as

$$\mathsf{M} = \mathsf{LNL}. \tag{4.66}$$

Here, L is the diagonal matrix defined by $\mathsf{L}_{c,d} = l_c \delta_{c,d}$, where $\delta_{c,d}$ denotes the Kronecker symbol, *i.e.*, $\delta_{c,d} = 1$ if $c = d$ and $\delta_{c,d} = 0$ if $c \neq d$. Matrix N is also a tridiagonal cyclic matrix and its non-zero components read as

$$\begin{aligned} \mathsf{N}_{c,c-1} &= \alpha_{c-1} (\mathsf{K}_{c-1} \boldsymbol{n}_{c-1}^{c-1} \cdot \boldsymbol{n}_c^{c-1}), \\ \mathsf{N}_{c,c} &= \alpha_{c-1} (\mathsf{K}_{c-1} \boldsymbol{n}_c^{c-1} \cdot \boldsymbol{n}_c^{c-1}) + \alpha_c (\mathsf{K}_c \boldsymbol{n}_c^c \cdot \boldsymbol{n}_c^c), \\ \mathsf{N}_{c,c+1} &= \alpha_c (\mathsf{K}_c \boldsymbol{n}_{c+1}^c \cdot \boldsymbol{n}_c^c). \end{aligned}$$

Let us write this matrix explicitly in the particular case $\mathfrak{C}_p = 4$, which corresponds to a point surrounding by 4 cells

$$\mathsf{N} = \begin{pmatrix} \alpha_4 (\mathsf{K}_4 \boldsymbol{n}_1^4 \cdot \boldsymbol{n}_1^4) + \alpha_1 (\mathsf{K}_1 \boldsymbol{n}_1^1 \cdot \boldsymbol{n}_1^1) & \alpha_1 (\mathsf{K}_1 \boldsymbol{n}_2^1 \cdot \boldsymbol{n}_1^1) & 0 & \alpha_4 (\mathsf{K}_4 \boldsymbol{n}_4^4 \cdot \boldsymbol{n}_1^4) \\ \alpha_1 (\mathsf{K}_1 \boldsymbol{n}_1^1 \cdot \boldsymbol{n}_2^1) & \alpha_1 (\mathsf{K}_1 \boldsymbol{n}_2^1 \cdot \boldsymbol{n}_2^1) + \alpha_2 (\mathsf{K}_2 \boldsymbol{n}_2^2 \cdot \boldsymbol{n}_2^2) & \alpha_2 (\mathsf{K}_2 \boldsymbol{n}_3^2 \cdot \boldsymbol{n}_2^2) & 0 \\ 0 & \alpha_2 (\mathsf{K}_2 \boldsymbol{n}_2^2 \cdot \boldsymbol{n}_3^2) & \alpha_2 (\mathsf{K}_2 \boldsymbol{n}_3^2 \cdot \boldsymbol{n}_3^2) + \alpha_3 (\mathsf{K}_3 \boldsymbol{n}_3^3 \cdot \boldsymbol{n}_3^3) & \alpha_3 (\mathsf{K}_3 \boldsymbol{n}_4^3 \cdot \boldsymbol{n}_3^3) \\ \alpha_4 (\mathsf{K}_4 \boldsymbol{n}_1^4 \cdot \boldsymbol{n}_4^4) & 0 & \alpha_3 (\mathsf{K}_3 \boldsymbol{n}_3^3 \cdot \boldsymbol{n}_4^3) & \alpha_3 (\mathsf{K}_3 \boldsymbol{n}_4^3 \cdot \boldsymbol{n}_4^3) + \alpha_4 (\mathsf{K}_4 \boldsymbol{n}_4^4 \cdot \boldsymbol{n}_4^4) \end{pmatrix}.$$

A closer inspection of the above matrix reveals an interesting block-structure. Namely, N can be decomposed as

$$\mathsf{N} = \sum_{c=1}^{4} \alpha_c \mathsf{N}_c,$$

where N_c are 4×4 sparse matrices which read

$$\mathsf{N}_1 = \begin{pmatrix} \mathsf{K}_1 \boldsymbol{n}_1^1 \cdot \boldsymbol{n}_1^1 & \mathsf{K}_1 \boldsymbol{n}_2^1 \cdot \boldsymbol{n}_1^1 & 0 & 0 \\ \mathsf{K}_1 \boldsymbol{n}_1^1 \cdot \boldsymbol{n}_2^1 & \mathsf{K}_1 \boldsymbol{n}_2^1 \cdot \boldsymbol{n}_2^1 & 0 & 0 \\ 0 & 0 & 0 & 0 \\ 0 & 0 & 0 & 0 \end{pmatrix}, \quad \mathsf{N}_2 = \begin{pmatrix} 0 & 0 & 0 & 0 \\ 0 & \mathsf{K}_2 \boldsymbol{n}_2^2 \cdot \boldsymbol{n}_2^2 & \mathsf{K}_2 \boldsymbol{n}_3^2 \cdot \boldsymbol{n}_2^2 & 0 \\ 0 & \mathsf{K}_2 \boldsymbol{n}_2^2 \cdot \boldsymbol{n}_3^2 & \mathsf{K}_2 \boldsymbol{n}_3^2 \cdot \boldsymbol{n}_3^2 & 0 \\ 0 & 0 & 0 & 0 \end{pmatrix},$$

$$\mathsf{N}_3 = \begin{pmatrix} 0 & 0 & 0 & 0 \\ 0 & 0 & 0 & 0 \\ 0 & 0 & \mathsf{K}_3 \boldsymbol{n}_3^3 \cdot \boldsymbol{n}_3^3 & \mathsf{K}_3 \boldsymbol{n}_4^3 \cdot \boldsymbol{n}_3^3 \\ 0 & 0 & \mathsf{K}_3 \boldsymbol{n}_3^3 \cdot \boldsymbol{n}_4^3 & \mathsf{K}_3 \boldsymbol{n}_4^3 \cdot \boldsymbol{n}_4^3 \end{pmatrix}, \quad \mathsf{N}_4 = \begin{pmatrix} \mathsf{K}_4 \boldsymbol{n}_1^4 \cdot \boldsymbol{n}_1^4 & 0 & 0 & \mathsf{K}_4 \boldsymbol{n}_4^4 \cdot \boldsymbol{n}_1^4 \\ 0 & 0 & 0 & 0 \\ 0 & 0 & 0 & 0 \\ \mathsf{K}_4 \boldsymbol{n}_1^4 \cdot \boldsymbol{n}_4^4 & 0 & 0 & \mathsf{K}_4 \boldsymbol{n}_4^4 \cdot \boldsymbol{n}_4^4 \end{pmatrix}.$$

This decomposition extends readily to the general case as

$$\mathsf{N} = \sum_{c=1}^{\mathfrak{C}_p} \alpha_c \mathsf{N}_c, \tag{4.67}$$

where N_c is the $\mathfrak{C}_p \times \mathfrak{C}_p$ defined by

$$\mathsf{N}_c = \begin{pmatrix} 0 & \cdots & 0 & 0 & \cdots & 0 \\ \vdots & \ddots & \vdots & \vdots & & \vdots \\ 0 & \cdots & \mathsf{K}_c \boldsymbol{n}_c^c \cdot \boldsymbol{n}_c^c & \mathsf{K}_c \boldsymbol{n}_{c+1}^c \cdot \boldsymbol{n}_c^c & \cdots & 0 \\ 0 & \cdots & \mathsf{K}_c \boldsymbol{n}_c^c \cdot \boldsymbol{n}_{c+1}^c & \mathsf{K}_c \boldsymbol{n}_{c+1}^c \cdot \boldsymbol{n}_{c+1}^c & \cdots & 0 \\ \vdots & & \vdots & \vdots & \ddots & \vdots \\ 0 & \cdots & 0 & 0 & \cdots & 0 \end{pmatrix}. \tag{4.68}$$

The non-zero terms of this matrix consist of 2×2 block which is located at the intersection of the cth and $c+1$th columns and rows. In addition, this 2×2 block coincides with the sub-cell conductivity matrix K_{pc} defined by (4.59).

Bearing this decomposition in mind, we claim that M is a **positive definite matrix**, that is,

$$\mathsf{M}\overline{\boldsymbol{T}} \cdot \overline{\boldsymbol{T}} > 0, \quad \forall \overline{\boldsymbol{T}} \in \mathbb{R}^{\mathfrak{C}_p}. \tag{4.69}$$

To prove this fundamental result we proceed in two steps. First, we note that M is positive definite if and only if N is positive definite. This first result follows from

$$\begin{aligned} \mathsf{M}\overline{\boldsymbol{T}} \cdot \overline{\boldsymbol{T}} =& (\mathsf{LNL})\overline{\boldsymbol{T}} \cdot \overline{\boldsymbol{T}}, \quad \text{thanks to (4.66)} \\ =& \mathsf{L}[(\mathsf{NL})\overline{\boldsymbol{T}}] \cdot \overline{\boldsymbol{T}} \\ =& \mathsf{N}(\mathsf{L}\overline{\boldsymbol{T}}) \cdot (\mathsf{L}\overline{\boldsymbol{T}}), \end{aligned}$$

since L is symmetric, *i.e.*, $\mathsf{L}^t = \mathsf{L}$. Second, we prove that N is positive definite by computing $\mathsf{N}\overline{\boldsymbol{T}} \cdot \overline{\boldsymbol{T}}$ using the decomposition (4.67)

$$\begin{aligned} \mathsf{N}\overline{\boldsymbol{T}} \cdot \overline{\boldsymbol{T}} &= \sum_{c=1}^{\mathfrak{C}_p} \alpha_c \mathsf{N}_c \overline{\boldsymbol{T}} \cdot \overline{\boldsymbol{T}} \\ &= \sum_{c=1}^{\mathfrak{C}_p} \alpha_c \mathsf{K}_{pc} \begin{pmatrix} \overline{T}_c \\ \overline{T}_{c+1} \end{pmatrix} \cdot \begin{pmatrix} \overline{T}_c \\ \overline{T}_{c+1} \end{pmatrix}. \end{aligned}$$

Since α_c is positive and K_{pc} is positive definite, the right-hand side of the last equation is always positive, which ends the proof. This shows that matrix M inherits the properties of the corner

conductivity matrix K_{pc} which results from the discretization of the half-edge normal fluxes. Particularly, M is symmetric provided that K_{pc} is also symmetric. This properties transfer from K_{pc} to M also emphasizes that the first step in the numerical scheme derivation, *i.e.*, the half-edge normal fluxes discretization, must be performed with great care. **We state that the linear system** (4.63) **has always a unique solution which provides the half-edge temperatures in terms of the mean cell temperatures surrounding a given point** p

$$\overline{\boldsymbol{T}} = (\mathsf{M}^{-1}\mathsf{S})\boldsymbol{T}, \tag{4.70}$$

where the matrices M and S are defined respectively by (4.64) and (4.65). The solution of the corresponding tridiagonal cyclic system is easily obtained by using the numerical algorithm proposed in [132].

Comment 19 *It is important to note that the solution of the linear system* (4.70) *has to preserve uniform temperatures field. Thus, matrix* $\mathsf{M}^{-1}\mathsf{S}$ *satisfies the following property*

$$(\mathsf{M}^{-1}\mathsf{S})\mathbf{1}_{\mathfrak{C}_p} = \mathbf{1}_{\mathfrak{C}_p}, \tag{4.71}$$

where $\mathbf{1}_{\mathfrak{C}_p} \in \mathbb{R}^{\mathfrak{C}_p}$ *is vector whose all entries are equal to* 1*. This means that* $\mathbf{1}_{\mathfrak{C}_p}$ *is the eigenvector of* $\mathsf{M}^{-1}\mathsf{S}$ *associated to the eigenvalue* 1*.*

It is interesting to mention that matrices M et S exhibit a linear dependency on the conductivity tensor K. This result is a direct consequence of the definitions (4.64) and (4.65). In addition, the matrix M associated to the transpose of K corresponds to the transpose of the matrix M associated to K, *i.e.*,

$$\mathsf{M}(\mathsf{K}_1^t, \ldots, \lambda\mathsf{K}_{\mathfrak{C}_p}^t) = \mathsf{M}^t(\mathsf{K}_1, \ldots, \mathsf{K}_{\mathfrak{C}_p}). \tag{4.72}$$

By way of contrast, the matrix S associated to the transpose of K does not correspond the transpose of the matrix S associated to K since S is a bidiagonal matrix. In this case, we need to introduce the new matrix $\tilde{\mathsf{S}}$ defined as

$$\tilde{\mathsf{S}}(\mathsf{K}_1, \ldots, \mathsf{K}_{\mathfrak{C}_p}) = \mathsf{S}(\mathsf{K}_1^t, \ldots, \lambda\mathsf{K}_{\mathfrak{C}_p}^t). \tag{4.73}$$

From this definition and (4.64), the non-zero entries of $\tilde{\mathsf{S}}$ write explicitly

$$\begin{cases} \tilde{\mathsf{S}}_{c,c-1} = \alpha_{c-1} l_c [l_{c-1}(\mathsf{K}_{c-1}\boldsymbol{n}_c^{c-1} \cdot \boldsymbol{n}_{c-1}^{c-1}) + l_c(\mathsf{K}_{c-1}\boldsymbol{n}_c^{c-1} \cdot \boldsymbol{n}_c^{c-1})], \\ \tilde{\mathsf{S}}_{c,c} = \alpha_c l_c [l_c(\mathsf{K}_c\boldsymbol{n}_c^c \cdot \boldsymbol{n}_c^c) + l_{c+1}(\mathsf{K}_c\boldsymbol{n}_c^c \cdot \boldsymbol{n}_{c+1}^c)]. \end{cases} \tag{4.74}$$

Here, we have used the fact that $\mathsf{K}_c^t\boldsymbol{n} \cdot \boldsymbol{m} = \mathsf{K}_c\boldsymbol{m} \cdot \boldsymbol{n}$ for all vectors $(\boldsymbol{n}, \boldsymbol{m}) \in \mathbb{R}^2 \times \mathbb{R}^2$. **Note that** $\tilde{\mathsf{S}} = \mathsf{S}$ **if and only if the conductivity tensor is symmetric**.

Maximum principle for the half-edge temperatures in the case of a symmetric positive definite conductivity tensor

In this paragraph, we aim at deriving sufficient conditions such that the half-edges temperatures satisfy a maximum principle, in the case of a symmetric positive definite conductivity tensor. More precisely, suppose that the mean cell temperatures are such that $0 < T_c \leq \Theta$ for all $c \in \mathcal{C}(p)$, we want to exhibit conditions related to matrices M and S so that the half-edge temperatures satisfy also $0 < \overline{T}_c \leq \Theta$ for all $c \in \mathcal{C}(p)$, where $\Theta > 0$ is a given temperature. To derive these sufficient conditions, we need to introduce the notion of **M-matrix**. Following the definition of [161], a real matrix A with non-positive off-diagonal entries is an M-matrix if A is non-singular and the entries of A^{-1} are non-negative. A useful characterization of M-matrix

is given by the following proposition: *if* A *is a symmetric positive definite matrix with non-positive off-diagonal entries, then it is an M-matrix.* This latter kind of matrix is sometimes called Stieltjes matrix [161]. Bearing this in mind, we are going to find a sufficient condition to ensure that M is an M-matrix. First, let us point out that M is symmetric definite positive since by assumption the conductivity tensor, K_c, is symmetric definite positive. Thus, observing the off-diagonal entries of M given by (4.64), a sufficient condition to ensure that M is an M-matrix consists in prescribing

$$(\mathsf{K}_c \boldsymbol{n}_{c+1}^c \cdot \boldsymbol{n}_c^c) \leq 0, \quad \forall c \in \mathcal{C}(p). \tag{4.75}$$

Since K_c is symmetric positive definite, Schwartz inequality leads to

$$\frac{\mid (\mathsf{K}_c \boldsymbol{n}_{c+1}^c \cdot \boldsymbol{n}_c^c) \mid}{(\mathsf{K}_c \boldsymbol{n}_{c+1}^c \cdot \boldsymbol{n}_{c+1}^c)^{\frac{1}{2}} (\mathsf{K}_c \boldsymbol{n}_c^c \cdot \boldsymbol{n}_c^c)^{\frac{1}{2}}} \leq 1.$$

Hence, there exists a unique $\nu_c \in [0, \pi]$ such that

$$\cos \nu_c = -\frac{(\mathsf{K}_c \boldsymbol{n}_{c+1}^c \cdot \boldsymbol{n}_c^c)}{(\mathsf{K}_c \boldsymbol{n}_{c+1}^c \cdot \boldsymbol{n}_{c+1}^c)^{\frac{1}{2}} (\mathsf{K}_c \boldsymbol{n}_c^c \cdot \boldsymbol{n}_c^c)^{\frac{1}{2}}}, \quad \forall c \in \mathcal{C}(p). \tag{4.76}$$

Defining the symmetric positive definite tensor U_c as being the square root of K_c, *i.e.*, $\mathsf{K}_c = \mathsf{U}_c^2$, the angle ν_c rewrites as

$$\cos \nu_c = -\frac{(\mathsf{U}_c \boldsymbol{n}_{c+1}^c \cdot \mathsf{U}_c \boldsymbol{n}_c^c)}{(\mathsf{U}_c \boldsymbol{n}_{c+1}^c \cdot \mathsf{U}_c \boldsymbol{n}_{c+1}^c)^{\frac{1}{2}} (\mathsf{U}_c \boldsymbol{n}_c^c \cdot \mathsf{U}_c \boldsymbol{n}_c^c)^{\frac{1}{2}}}, \quad \forall c \in \mathcal{C}(p).$$

This shows that $\pi - \nu_c$ is the measure of the angle between the vectors $\mathsf{U}_c \boldsymbol{n}_{c+1}^c$ and $\mathsf{U}_c \boldsymbol{n}_c^c$, which are the images of the unit normal vectors $\boldsymbol{n}_{c+1}^c$ and $\boldsymbol{n}_c^c$ in the transformation associated to the local metric defined by tensor K_c. With this notation, sufficient condition (4.75), turns into the more explicit form

$$\nu_c \in [-\frac{\pi}{2}, \frac{\pi}{2}], \quad \forall c \in \mathcal{C}(p). \tag{4.77}$$

Assuming this condition, we have $\mathsf{M}_{c,d}^{-1} \geq 0$ for all $(c, d) \in \mathcal{C}^2(p)$. Recalling that $\overline{\boldsymbol{T}} = (\mathsf{M}^{-1} S)\boldsymbol{T}$, to ensure the maximum principle for $\overline{\boldsymbol{T}}$ it remains to exhibit a sufficient condition such that the entries of S are non-negative. Introducing the angle ν_c in the expressions of S entries (4.65), this condition readily writes as

$$\cos \nu_c \leq \min\left(\frac{l_c}{l_{c+1}} \frac{(\mathsf{K}_c \boldsymbol{n}_c^c \cdot \boldsymbol{n}_c^c)^{\frac{1}{2}}}{(\mathsf{K}_c \boldsymbol{n}_{c+1}^c \cdot \boldsymbol{n}_{c+1}^c)^{\frac{1}{2}}}, \frac{l_{c+1}}{l_c} \frac{(\mathsf{K}_c \boldsymbol{n}_{c+1}^c \cdot \boldsymbol{n}_{c+1}^c)^{\frac{1}{2}}}{(\mathsf{K}_c \boldsymbol{n}_c^c \cdot \boldsymbol{n}_c^c)^{\frac{1}{2}}}\right), \quad \forall c \in \mathcal{C}(p). \tag{4.78}$$

This condition results in a limitation of the permitted values of ν_c, this limitation expressing in terms of the cell aspect ratio with respect to the local metric defined by K_c.

Finally, we claim that the maximum principle for the half-edge temperatures holds provided the sufficient conditions (4.77) and (4.78) are satisfied. Indeed, assuming (4.77) and (4.78) implies that the entries of $\mathsf{M}^{-1} S$ are non-negative. In addition, by virtue of Comment 4.71 we have

$$\sum_{d \in \mathcal{C}(p)} (\mathsf{M}^{-1} S)_{c,d} = 1, \quad \forall c \in \mathcal{C}(p).$$

Thus, the entries of $\mathsf{M}^{-1} S$ satisfy the following inequality

$$0 \leq (\mathsf{M}^{-1} S)_{c,d} \leq 1, \quad \forall (c, d) \in \mathcal{C}(p)^2.$$

Therefore, each component of $\overline{\boldsymbol{T}} = \mathsf{M}^{-1}S\boldsymbol{T}$ is a convex combination of the components of $\boldsymbol{T}$ since

$$\overline{T}_c = \sum_{c\in\mathcal{C}(p)} (\mathsf{M}^{-1}S)_{c,d} T_d.$$

Using the above arguments it is clear that if $T_d \in [0,\Theta]$ then $\overline{T}_c \in [0,\Theta]$, which ends the proof.

We conclude by stating the following maximum principle for the half-edge temperatures: being given a symmetric positive definite conductivity tensor and assuming that the following geometric conditions hold for all $c \in \mathcal{C}(p)$

$$\begin{aligned}
&\nu_c \in [-\frac{\pi}{2}, \frac{\pi}{2}],\\
&\cos\nu_c \leq \min\Big(\frac{l_c}{l_{c+1}}\frac{(\mathsf{K}_c\boldsymbol{n}_c^c\cdot\boldsymbol{n}_c^c)^{\frac{1}{2}}}{(\mathsf{K}_c\boldsymbol{n}_{c+1}^c\cdot\boldsymbol{n}_{c+1}^c)^{\frac{1}{2}}}, \frac{l_{c+1}}{l_c}\frac{(\mathsf{K}_c\boldsymbol{n}_{c+1}^c\cdot\boldsymbol{n}_{c+1}^c)^{\frac{1}{2}}}{(\mathsf{K}_c\boldsymbol{n}_c^c\cdot\boldsymbol{n}_c^c)^{\frac{1}{2}}}\Big),
\end{aligned}$$

where ν_c is the angle defined by (4.76). If the mean cells temperature are such that $T_c \in [0,\Theta]$ for all $c \in \mathcal{C}(p)$ then the half-edge temperatures satisfy $\overline{T}_c \in [0,\Theta]$ for all $c \in \mathcal{C}(p)$.

Let us notice that these geometric conditions are quite difficult to use since they also depend on the local value of the conductivity tensor. We will see in the next paragraph that they are easier to interpretate in the case of an isotropic conductivity.

The case of isotropic conductivity

It is interesting to investigate the particular case of an isotropic conductivity, *i.e.*, $\mathsf{K}_c = \kappa_c\,\mathsf{I}_d$, where $\kappa_c > 0$ denotes the piecewise constant approximation of the scalar conductivity κ in cell c. If θ_c denotes the measure of the angle between edges c and $c+1$ then $\boldsymbol{n}_c^c\cdot\boldsymbol{n}_{c+1}^c = -\cos\theta_c$. It follows from (4.64) that the cth row of matrix M reduces to

$$\begin{cases}
\mathsf{M}_{c,c-1} = -\alpha_{c-1}\kappa_{c-1}l_{c-1}l_c\cos\theta_{c-1},\\
\mathsf{M}_{c,c} = \alpha_{c-1}\kappa_{c-1}l_c^2 + \alpha_c\kappa_c l_c^2,\\
\mathsf{M}_{c,c+1} = -\alpha_c\kappa_c l_c l_{c+1}\cos\theta_c.
\end{cases} \tag{4.79}$$

It turns out that M is a symmetric matrix. Using the result of the previous paragraphs, we know that M is definite positive. However, it is quite instructive to demonstrate this directly. Recalling that $\theta_c \neq k\pi$, where k is an integer, implies that $\mathsf{M}_{c,c} > \mid \mathsf{M}_{c,c-1} \mid + \mid \mathsf{M}_{c,c+1} \mid$ for all $c \in \mathcal{C}(p)$, thus M is **strictly diagonally dominant**. Noticing that all the diagonal entries of M are positive real numbers allows to claim that this matrix is nonsingular and all its eigenvalues are positive [161]. In addition, the off-diagonal entries are negative provided that $\theta_c \in [-\frac{\pi}{2}, \frac{\pi}{2}]$ for all $c \in \mathcal{C}(p)$. Namely, M is an **M-matrix** provided that the previous angular condition holds. Let us note that we have recovered the angular condition (4.77). Indeed by setting $\mathsf{K}_c = \kappa_c\,\mathsf{I}_d$ into the definition of ν_c (4.76), we find that ν_c coincides with θ_c. Bearing this in mind, we deduce from the previous paragraph the isotropic version of the maximum principle for the half-edge temperatures: under the geometric conditions

$$\forall c \in \mathcal{C}(p), \quad \begin{cases}
\theta_c \in [-\frac{\pi}{2}, \frac{\pi}{2}],\\
\cos\theta_c \leq \min(\frac{l_{c+1}}{l_c}, \frac{l_c}{l_{c+1}}),
\end{cases} \tag{4.80}$$

if the mean cell temperatures are such that $0 < T_c \leq \Theta$ for all $c \in \mathcal{C}(p)$, then the half-edge temperatures satisfy the inequality $0 < \overline{T}_c \leq \Theta$, for all $c \in \mathcal{C}(p)$, where $\Theta > 0$ is a given temperature. Note the second condition ensure that the entries of S are non-negative. This

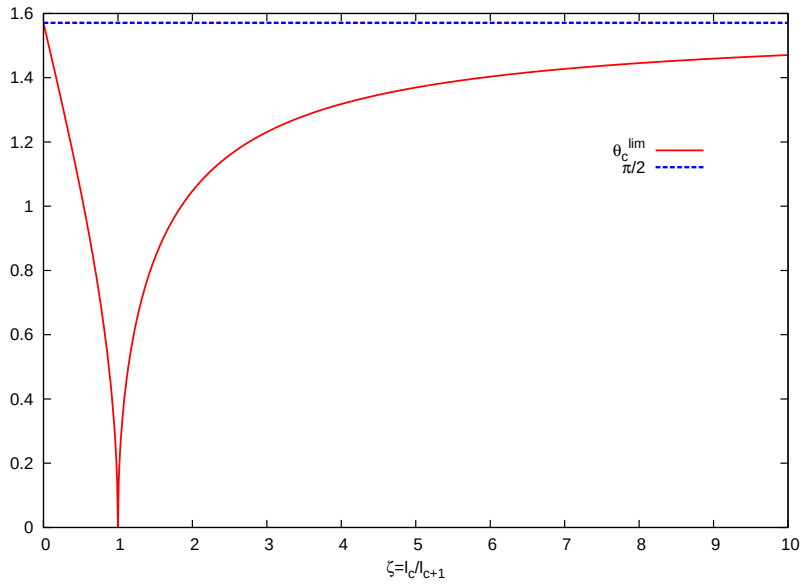

Figure 4.7: Limit angle $\theta_c^{\lim}$ versus sub-cell aspect ratio $\zeta = \frac{l_c}{l_{c+1}}$. The permitted angular domain to satisfy the geometric condition (4.80) is the region located between the red and the blue curves.

condition could have been obtained proceeding directly with S entries knowing that in the isotropic case they simply write

$$\begin{cases} \mathsf{S}_{c,c-1} = \alpha_{c-1}\kappa_{c-1}l_c(l_c - l_{c-1}\cos\theta_{c-1}), \\ \mathsf{S}_{c,c} = \alpha_c\kappa_c l_c(l_c - l_{c+1}\cos\theta_c). \end{cases} \tag{4.81}$$

To investigate further the impact of the geometric conditions, being given the half-edge lengths l_c and l_{c+1}, let us introduce the limit angle $\theta_c^{\lim} = \arccos[\min(\frac{l_{c+1}}{l_c}, \frac{l_c}{l_{c+1}})]$. Condition (4.80) is equivalent to the requirement that $\theta_c \in [-\frac{\pi}{2}, -\theta_c^{\lim}] \cup [\theta_c^{\lim}, \frac{\pi}{2}]$. In Figure 4.7, we have plotted the limit angle variation in terms of the sub-cell aspect ratio $\zeta = \frac{l_c}{l_{c+1}}$. Note that we have only displayed the positive value knowing that the negative value is obtained by symmetry about zero. The permitted values of the sub-cell angle θ_c to ensure that the geometric conditions hold is the domain delimited at the bottom by the curve $\theta_c = \theta_c^{\lim}(\zeta)$ and at the top by the straight line $\theta_c = \frac{\pi}{2}$. This graph shows that for moderate aspect ratios the geometric condition (4.80) is not too much restrictive. However, for high aspect ratios, this conditions becomes very restrictive in the sense that the permitted angles are closed to right angles.

Comment 20 *We note that in the case of a rectangular grid, the present scheme recovers the well known five-point scheme. In this case, each vertex of the grid is surrounded by four rectangular grids, thus* $\theta_c = \frac{\pi}{2}$ *for all* $c = 1 \ldots 4$. *Defining the volume weights* w_{pc} *according to* (4.53) *yields* $\alpha_c = \frac{1}{l_c l_{c+1}}$. *We obtain that* M *reduces to the diagonal matrix defined as*

$$\mathsf{M}_{c,d} = l_c(\frac{\kappa_{c-1}}{l_{c-1}} + \frac{\kappa_c}{l_{c+1}})\delta_{c,d}.$$

Regarding S, *its* c*th row writes as*

$$\mathsf{S}_{c,c-1} = l_c\frac{\kappa_{c-1}}{l_{c-1}}, \quad \mathsf{S}_{c,c} = l_c\frac{\kappa_c}{l_{c+1}}.$$

The half-edge temperatures are readily deduced from the solution of the diagonal 4×4 *linear system* (4.63)

$$\overline{T}_c = \frac{\frac{\kappa_{c-1}}{l_{c-1}} T_{c-1} + \frac{\kappa_c}{l_{c+1}} T_c}{\frac{\kappa_{c-1}}{l_{c-1}} + \frac{\kappa_c}{l_{c+1}}}.$$

Substituting the above result in the half-edge flux expression (4.60a) *leads to*

$$q_c^c = \frac{1}{\frac{l_{c-1}}{\kappa_{c-1}} + \frac{l_{c+1}}{\kappa_c}} (T_c - T_{c-1}).$$

We have recovered the expression of the normal flux which corresponds to the classical five-point scheme characterized by a weighted harmonic averaging of the scalar conductivity at the cell interface.

4.2.5 Construction of the diffusion matrix

After having expressed the half-edge temperatures in terms of the mean cell temperatures, we are now in position to achieve the construction of the scheme by gathering the previous results.

Local diffusion matrix at a generic point

We start by deriving the local diffusion matrix at a generic point p. To this end, we first recall the semi-discrete scheme which has been obtained in Section 4.1.3

$$m_c C_{vc} \frac{d}{dt} T_c + \sum_{p \in \mathcal{P}(c)} l_{pc}^- q_{pc}^- + l_{pc}^+ q_{pc}^+ = m_c r_c.$$

In this equation, the half-edge fluxes (q_{pc}^-, q_{pc}^+) attached to sub-cell ω_{pc}, express in terms of the half-edge temperatures by means of (4.41). In addition, the half-edge temperatures express in terms of the mean cell temperatures surrounding point p through the use of the solution of the linear system (4.70). Therefore, to write the semi-discrete scheme in terms of the primary unknowns, that is, the mean cell temperatures, it remains to substitute the expression of the half-edge temperatures in terms of the mean cell temperatures into the half-edge normal fluxes. To perform this substitution, it is convenient to define the contribution of the sub-cell ω_{pc} to the diffusion flux as

$$Q_{pc} = l_{pc}^- q_{pc}^- + l_{pc}^+ q_{pc}^+. \tag{4.82}$$

Using the local notation at point p introduced in Section 4.2.4, it turns out that Q_{pc} rewrites as

$$Q_{pc} = l_c q_c^c + l_{c+1} q_{c+1}^c.$$

Using the expression of the half-edge fluxes in terms of the half-edge temperatures (4.60) yields

$$\begin{aligned} Q_{pc} = &- \alpha_c l_c [l_c (\mathsf{K}_c \boldsymbol{n}_c^c \cdot \boldsymbol{n}_c^c) + l_{c+1} (\mathsf{K}_c \boldsymbol{n}_c^c \cdot \boldsymbol{n}_{c+1}^c)] (\overline{T}_c - T_c) \\ &- \alpha_c l_{c+1} [l_c (\mathsf{K}_c \boldsymbol{n}_{c+1}^c \cdot \boldsymbol{n}_c^c) + l_{c+1} (\mathsf{K}_c \boldsymbol{n}_{c+1}^c \cdot \boldsymbol{n}_{c+1}^c)] (\overline{T}_{c+1} - T_c). \end{aligned} \tag{4.83}$$

Recalling the definition of the matrix $\tilde{\mathsf{S}}$ from (4.74)

$$\begin{aligned} \tilde{\mathsf{S}}_{c,c-1} &= \alpha_{c-1} l_c [l_{c-1} (\mathsf{K}_{c-1} \boldsymbol{n}_c^{c-1} \cdot \boldsymbol{n}_{c-1}^{c-1}) + l_c (\mathsf{K}_{c-1} \boldsymbol{n}_c^{c-1} \cdot \boldsymbol{n}_c^{c-1})], \\ \tilde{\mathsf{S}}_{c,c} &= \alpha_c l_c [l_c (\mathsf{K}_c \boldsymbol{n}_c^c \cdot \boldsymbol{n}_c^c) + l_{c+1} (\mathsf{K}_c \boldsymbol{n}_c^c \cdot \boldsymbol{n}_{c+1}^c)], \end{aligned}$$

leads to recast (4.83) under the more compact form

$$Q_{pc} = -\tilde{\mathsf{S}}_{c,c} (\overline{T}_c - T_c) - \tilde{\mathsf{S}}_{c+1,c} (\overline{T}_{c+1} - T_c).$$

Due to the sparse structure of $\tilde{\mathsf{S}}$, this last equation turns into

$$Q_{pc} = -\sum_{d\in\mathcal{C}(p)} \tilde{\mathsf{S}}^t_{c,d}(\overline{T}_d - T_c).$$

Finally, recalling that the vector of half-edge temperatures, $\overline{\boldsymbol{T}}$, is expressed in terms of the vector of the mean cell temperatures, $\boldsymbol{T}$, through the use of the solution of the linear system (4.70), *i.e.*, $\overline{\boldsymbol{T}} = (\mathsf{M}^{-1}\mathsf{S})\boldsymbol{T}$, allows to write Q_{pc} as

$$Q_{pc} = -\sum_{d\in\mathcal{C}(p)} \Gamma^p_{c,d}(T_d - T_c). \tag{4.84}$$

Here, Γ^p denotes the $\mathfrak{C}_p \times \mathfrak{C}_p$ matrix defined at point p by

$$\Gamma^p = \tilde{\mathsf{S}}^t\mathsf{M}^{-1}\mathsf{S}. \tag{4.85}$$

In deriving (4.84), we have used that $\sum_{d\in\mathcal{C}(p)} \Gamma^p_{c,d} = \sum_{d\in\mathcal{C}(p)} \tilde{\mathsf{S}}^t_{c,d}$ which follows from the fact that $\mathbf{1}_{\mathcal{C}(p)}$ is the eigenvector of $\mathsf{M}^{-1}\mathsf{S}$ associated to the eigenvalue 1, refer to Comment 19. Let us note that the entries of Γ^p have the physical dimension of a conductivity. Thus, Γ^p can be viewed as the effective conductivity tensor at point p. More precisely, it follows from (4.84) that the entry $\Gamma^p_{c,d}$ stands for the effective conductivity between cells c and d through the point p. **We claim that the effective conductivity tensor at point p, Γ^p, is symmetric positive definite provided that the physical conductivity tensor is symmetric positive definite**. To prove this, observe that

$$\begin{aligned}\Gamma^p\boldsymbol{T}\cdot\boldsymbol{T} =& (\tilde{\mathsf{S}}^t\mathsf{M}^{-1}\mathsf{S})\boldsymbol{T}\cdot\boldsymbol{T}\\ =& \mathsf{M}^{-1}(\mathsf{S}\boldsymbol{T})\cdot(\tilde{\mathsf{S}}\boldsymbol{T}).\end{aligned}$$

Since K_c is symmetric positive definite, by virtue of (4.73) one deduces that $\tilde{\mathsf{S}} = \mathsf{S}$, in addition M is symmetric positive definite, which ends the proof.

In the general case, for which the physical conductivity tensor, K_c, is only positive definite, we make the conjecture that Γ^p is also positive definite since we are not able to prove this result directly.

Comment 21 *We want to mention that in the case of a symmetric positive definite conductivity tensor, under the geometrical conditions* (4.77) *and* (4.78)*, the entries of the matrix* Γ^p *are non-negative.*

The global diffusion matrix

Gathering the previous results, leads to write the finite volume semi-discrete scheme over cell c as follows

$$m_c C_{vc}\frac{d}{dt}T_c - \sum_{p\in\mathcal{P}(c)}\sum_{d\in\mathcal{C}(p)} \Gamma^p_{c,d}(T_d - T_c) = m_c r_c, \tag{4.86}$$

where Γ^p is the effective conductivity tensor defined at point p by (4.85). To put the above equation under a more compact form, let us introduce the following global notation. Let $\boldsymbol{\mathcal{T}}$ be the vector of the cell averaged temperatures, that is, $\boldsymbol{\mathcal{T}} = (T_1, \dots T_{C_\mathcal{D}})^t$, where $C_\mathcal{D}$ denotes the total number of cells covering the domain $\mathcal{D}$. Let us denote by $\mathfrak{M}$ and C_v the $C_\mathcal{D}\times C_\mathcal{D}$ diagonal matrices whose entries are given by $m_c\delta_{c,d}$ and $C_{vc}\delta_{c,d}$. We also introduce $\boldsymbol{R} = (r_1, \dots, r_{C_\mathcal{D}})^t$ as the source term vector. Finally, let A be the $C_\mathcal{D}\times C_\mathcal{D}$ matrix which stands for the global

diffusion matrix associated to the above semi-discrete scheme. Observing (4.86), we readily deduce that its diagonal and off-diagonal entries write as

$$\mathsf{A}_{c,c} = \sum_{p\in\mathcal{P}(c)} \sum_{d\in\mathcal{C}(p)} \mathsf{\Gamma}^p_{c,d}, \tag{4.87a}$$

$$\mathsf{A}_{c,d} = -\sum_{p\in\mathcal{P}(c)} \mathsf{\Gamma}^p_{c,d}. \tag{4.87b}$$

Bearing this notation in mind, our semi-discrete finite volume scheme reads

$$\mathfrak{M}\mathsf{C}_v \frac{d\boldsymbol{\mathcal{T}}}{dt} + \mathsf{A}\boldsymbol{\mathcal{T}} = \mathfrak{M}\boldsymbol{R}. \tag{4.88}$$

This results in a differential system satisfied by the vector of the cell averaged temperatures. Note that the above system has been derived without taking into account the boundary conditions.

In writing the entries of the global diffusion matrix, we have to pay attention to the fact that indices in the left-hand side of (4.87) refer to the global numbering of the cells, whereas in the right-hand side they refer to the local numbering of cells surrounding point p. In addition, index p refers to the local numbering of points belonging to cell c.

Let us point out that the global diffusion matrix results in assembling the small[1] node-based $\mathfrak{C}_p \times \mathfrak{C}_p$ matrices $\mathsf{\Gamma}^p$. This node-based underlying data structure allows to handle easily general unstructured grids. However, the assembling of the global diffusion matrix requires the knowledge of the local matrix $\mathsf{\Gamma}^p$ at each grid point p. This matrix is computed as $\mathsf{\Gamma}^p = \tilde{\mathsf{S}}^t \mathsf{M}^{-1} \mathsf{S}$ where matrices $\tilde{\mathsf{S}}$, M and S are sparse $\mathfrak{C}_p \times \mathfrak{C}_p$ matrices explicitly given by formulas (4.74), (4.65) and (4.64). Within the framework of a time-marching algorithm, these matrices have to be stored at the beginning of each time step for each grid point. In addition, the computation of the inverse matrix M^{-1} is performed using an efficient algorithm well adapted to cyclic tridiagonal matrices [132].

The stencil of the finite volume discretization (4.86) results directly from the structure of the above diffusion matrix. Being given a point p, its surrounding cells c and d are connected through point p by means of the diffusion exchange term $\Gamma^p_{c,d}$. Therefore, the stencil of cell c corresponds to the set of neighboring cell d which shares a point with itself, refer to Figure 4.8. For a quadrangular grid, this results in a **nine-point scheme**.

4.2.6 Properties of the semi-discrete scheme

In this section, we state two fundamental properties which characterize our semi-discrete finite volume scheme. The first one concerns the positive semi-definiteness of matrix A and the second one consists of the L^2-stability of the semi-discrete scheme.

Positive semi-definiteness of the global diffusion matrix

We claim that the global diffusion matrix is positive semi-definite, that is,

$$\mathsf{A}\boldsymbol{\mathcal{T}} \cdot \boldsymbol{\mathcal{T}} \geq 0, \quad \forall \boldsymbol{\mathcal{T}} \in \mathbb{R}^{C_{\mathcal{D}}}. \tag{4.89}$$

Let us emphasize that this statement will be of fundamental importance to ensure the solvability of the linear system associated to the time discretziation of (4.88). This result follows directly

[1] For quadrangular grids, $\mathfrak{C}_p = 4$.

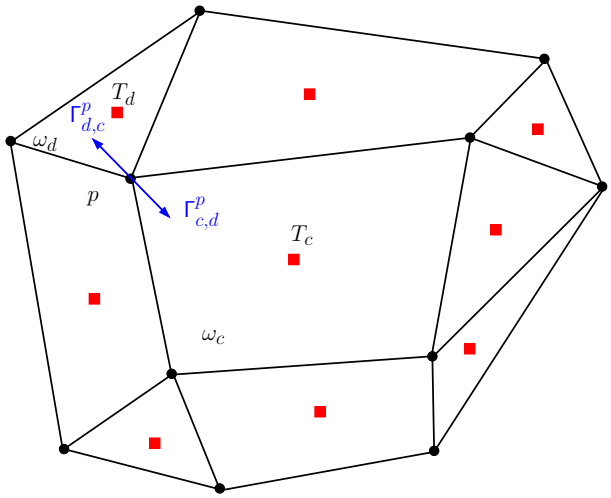

Figure 4.8: Stencil of the finite volume scheme for a given cell ω_c in a fragment of an unstructured grid. The degrees of freedom are displayed using red squares. The blue arrow shows the diffusion flux exchange through point p between cell c and d.

from the discrete inequality (4.42) satisfied by the numerical approximation of the half-edge fluxes (4.41). To prove (4.89), let us remark that the cth entry of vector $\mathsf{A}\boldsymbol{\mathcal{T}}$ writes as

$$(\mathsf{A}\boldsymbol{\mathcal{T}})_c = \sum_{p\in\mathcal{P}(c)} (l^-_{pc}q^-_{pc} + l^+_{pc}q^+_{pc}).$$

Using the above equation allows to rewrite the left-hand side of (4.89) as

$$\mathsf{A}\boldsymbol{\mathcal{T}}\cdot\boldsymbol{\mathcal{T}} = \sum_{c=1}^{C_{\mathcal{D}}} \sum_{p\in\mathcal{P}(c)} (l^-_{pc}q^-_{pc} + l^+_{pc}q^+_{pc})T_c.$$

Now, switching round the order of summation in the right-hand side leads to

$$\begin{aligned}\mathsf{A}\boldsymbol{\mathcal{T}}\cdot\boldsymbol{\mathcal{T}} &= \sum_{p}^{P_{\mathcal{D}}} \sum_{c\in\mathcal{C}(p)} (l^-_{pc}q^-_{pc} + l^+_{pc}q^+_{pc})T_c,\\ &= \sum_{p}^{P_{\mathcal{D}}} I_p,\end{aligned}$$

where $P_{\mathcal{D}}$ denotes the total number of points inside $\mathcal{D}$ and I_p is given by (4.43). By virtue of (4.42), the nodal quantity I_p is non-negative, thus the right-hand side of the above equation is also non-negative, which ends the proof.

We conclude this paragraph by claiming that the global diffusion matrix inherits some properties of the small matrix Γ^p. Namely, if Γ^p is symmetric positive definite[2], A is also symmetric positive but only semi-definite since by construction for a given row, the diagonal entry is equal to the sum of the off-diagonal entries, refer to (4.87). In addition, under the geometrical conditions (4.77) and (4.78), the diagonal entries of A are non-negative whereas the off-diagonal entries are non-positive, refer to Comment 21.

[2]This is precisely the case when the physical conductivity tensor is symmetric positive definite.

L^2-stability of the semi-discrete scheme

In this section, we prove the stability of our semi-discrete finite volume scheme, in absence of source term, *i.e.*, $r = 0$, in the sense of the discrete weighted L^2 norm defined as follows

$$\|\boldsymbol{\mathcal{T}}\|_{w2}^2 = \sum_{c}^{C_{\mathcal{D}}} m_c C_{vc} T_c^2, \tag{4.90}$$

where m_c and C_{vc} denote the piecewise constant approximation over cell c of the mass and the specific heat capacity, which are positive quantities. To study the L^2 stability of the semi-discrete scheme, we first recall that in absence of source term, vector $\boldsymbol{\mathcal{T}}$ satisfies the following semi-discrete system

$$\mathfrak{M}\mathsf{C}_v \frac{d\boldsymbol{\mathcal{T}}}{dt} + \mathsf{A}\boldsymbol{\mathcal{T}} = \mathbf{0},$$

where $\mathfrak{M}$ and C_v are the diagonal mass and heat capacity matrix. Dot-multiplying the above equation by $\boldsymbol{\mathcal{T}}$ yields

$$\mathfrak{M}\mathsf{C}_v \frac{d\boldsymbol{\mathcal{T}}}{dt} \cdot \boldsymbol{\mathcal{T}} + \mathsf{A}\boldsymbol{\mathcal{T}} \cdot \boldsymbol{\mathcal{T}} = 0.$$

Knowing that A is positive semi-definite leads to

$$\frac{d}{dt}(\mathfrak{M}\mathsf{C}_v \boldsymbol{\mathcal{T}} \cdot \boldsymbol{\mathcal{T}}) \leq 0. \tag{4.91}$$

In writing this equation, we have supposed that $\mathfrak{M}$ and C_v does not depend on time. In addition, we are ignoring the contribution of the boundary terms, assuming for instance periodic boundary conditions. Using the definition (4.90) of the weighted L^2 norm, the above equations rewrites as

$$\frac{d}{dt}(\frac{1}{2}\|\boldsymbol{\mathcal{T}}\|_{w2}^2) \leq 0. \tag{4.92}$$

This inequality ensures that the weighted L^2 norm of the semi-discrete solution remains bounded by the weighted L^2 norm of the initial data, which corresponds to the L^2-stability of our semi-discrete finite volume scheme. This L^2-stability is a direct consequence of the half-edge normal fluxes construction through the use of the sub-cell variational formulation. Once more, this shows the great importance of deriving the numerical approximation of the normal fluxes using a variational formulation.

4.2.7 Boundary conditions implementation

This section describes indications related to boundary conditions implementation. Let us point out that boundary conditions treatment relies on a straightforward extension of the half-edge temperatures elimination procedure which has been developed in Section 4.2.4 for internal nodes. The boundary conditions are prescribed at the two boundary half-edges connected to a point located on the boundary, they will be either of Neumann type (prescribed normal flux) or of Dirichlet type (prescribed temperature). Here, we are going to expose the main steps of the Neumann boundary conditions discretization without going into the detail of the computations. Concerning the Dirichlet boundary conditions discretization the interesting reader can refer to [28].

Let us consider a boundary node, p, which is surrounded by internal cells. As before, we denote by $\mathfrak{C}_p$ the number of cells surrounding point p. Note that the number of half-edges impinging on point p is equal to $\mathfrak{C}_p + 1$. The edges impinging at point p are labelled using the subscript c ranging from 1 to $\mathfrak{C}_p + 1$. The cell (sub-cell) numbering follows the edge numbering,

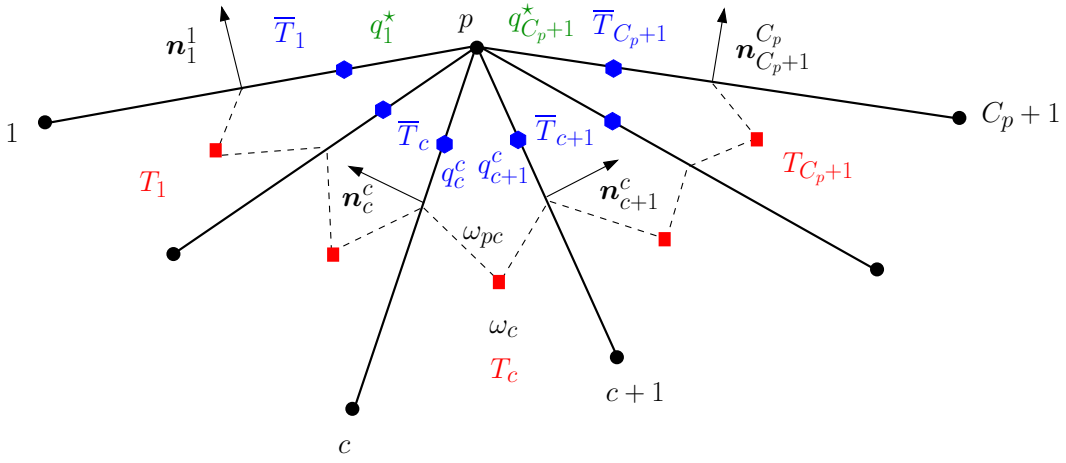

Figure 4.9: Fragment of an unstructured grid in the vicinity of a boundary point where are imposed Neumann boundary conditions. The prescribed fluxes, $q_1^\star$ and $q^\star_{\mathfrak{C}_p+1}$ are displayed using green color.

that is, cell ω_c (sub-cell ω_{pc}) is located between edges c and $c+1$, refer to Figure 4.9. The unit outward normal to cell ω_c at edge c is denoted by $\boldsymbol{n}_c^c$ whereas the unit outward normal to cell ω_c at edge $c+1$ is denoted by $\boldsymbol{n}_c^{c+1}$. The prescribed heat fluxes on the first and the last half-edge are denoted respectively by $q_1^\star$ and $q^\star_{\mathfrak{C}_p+1}$. Let us recall that the half-edge fluxes corresponding to the internal edges are expressed in terms of the half-edge and the mean cells temperatures using for $c=2,\ldots,\mathfrak{C}_p$

$$\begin{cases} q_c^{c-1} = -\alpha_{c-1}[l_{c-1}(\mathsf{K}_{c-1}\boldsymbol{n}_{c-1}^{c-1}\cdot\boldsymbol{n}_c^{c-1})(\overline{T}_{c-1}-T_{c-1}) + l_c(\mathsf{K}_{c-1}\boldsymbol{n}_c^{c-1}\cdot\boldsymbol{n}_c^{c-1})(\overline{T}_c - T_{c-1})], \\ q_c^c = -\alpha_c[l_c(\mathsf{K}_c\boldsymbol{n}_c^c\cdot\boldsymbol{n}_c^c)(\overline{T}_c - T_c) + l_{c+1}(\mathsf{K}_c\boldsymbol{n}_{c+1}^c\cdot\boldsymbol{n}_c^c)(\overline{T}_{c+1}-T_c)]. \end{cases} \tag{4.93}$$

Here, q_c^c (resp. q_c^{c-1}) denotes the half-edge normal flux at edge c viewed from cell c (resp. $c-1$). In addition, $\overline{T}_c$ is the temperature on the cth half-edge whereas T_c corresponds to the mean temperature of cell c.

The elimination of the half-edge temperatures is obtained by writing the flux continuity conditions (4.62) for all internal half-edges. This system of $\mathfrak{C}_p-1$ equations is completed by the two boundary conditions for the first and last half-edges. Finally, this results in the following system

$$l_1 q_1^1 = l_1 q_1^\star, \tag{4.94a}$$
$$l_c q_c^{c-1} + l_c q_c^c = 0, \quad \text{for } c=2,\ldots,\mathfrak{C}_p, \tag{4.94b}$$
$$l_{C+1} q_{C+1}^C = l_{C+1} q_{C+1}^\star. \tag{4.94c}$$

Substituting (4.93) into (4.94b) leads to the following $(\mathfrak{C}_p+1)\times(\mathfrak{C}_p+1)$ linear system satisfied by the $\mathfrak{C}_p+1$ half-edges temperatures

$$\mathsf{M}\overline{\boldsymbol{T}} = \mathsf{S}\boldsymbol{T} - \boldsymbol{B}. \tag{4.95}$$

Here, $\overline{\boldsymbol{T}}\in\mathbb{R}^{\mathfrak{C}_p+1}$ denotes the vector of half-edge temperatures whereas $\boldsymbol{T}\in\mathbb{R}^{\mathfrak{C}_p}$ is the vector of cell centered temperatures. In addition, M and S are respectively a $(\mathfrak{C}_p+1)\times(\mathfrak{C}_p+1)$ tridiagonal matrix and a $(\mathfrak{C}_p+1)\times\mathfrak{C}_p$ bidiagonal matrix. Their entries are computed developing (4.94). Boundary conditions are taken into account by means of $\boldsymbol{B}\in\mathbb{R}^{\mathfrak{C}_p+1}$ with

$\boldsymbol{B} = (l_1 q_1^\star, \ldots, l_{\mathfrak{C}_p+1} q_{\mathfrak{C}_p+1}^\star)^t$. Proceeding with the matrices M and S as before, one can show that (4.95) always admits a unique solution. This allows to compute the contribution of the sub-cell ω_{pc} to the diffusion flux as

$$Q_{pc} = -\sum_{d\in\mathcal{C}(p)} \Gamma^p_{c,d}(T_d - T_c) + (\tilde{\mathsf{S}}\mathsf{M}^{-1}\boldsymbol{B})_c. \tag{4.96}$$

Here, Γ^p denotes the effective conductivity tensor at boundary point p, it is a $\mathfrak{C}_p \times \mathfrak{C}_p$ matrix defined by $\Gamma^p = \tilde{\mathsf{S}}^t\mathsf{M}^{-1}\mathsf{S}$, where the matrix $\tilde{\mathsf{S}}$ is deduced from S by means of (4.73). From the above equation, we collect the contributions to the entries of the global diffusion matrix, A, following

$$\mathsf{A}_{c,c} = \sum_{p\in\mathcal{P}(c)} \sum_{d\in\mathcal{C}(p)} \Gamma^p_{c,d},$$
$$\mathsf{A}_{c,d} = -\sum_{p\in\mathcal{P}(c)} \Gamma^p_{c,d}.$$

Having taken into account the boundary conditions, the semi-discrete finite volume scheme (4.88) turns into

$$\mathfrak{M}\mathsf{C}_v \frac{d\boldsymbol{\mathcal{T}}}{dt} + \mathsf{A}\boldsymbol{\mathcal{T}} = \mathfrak{M}\boldsymbol{R} + \boldsymbol{\mathcal{S}},$$

where $\boldsymbol{\mathcal{S}} \in \mathbb{R}^{C_\mathcal{D}}$ is the source term vector which represents the boundary conditions contribution. According to (4.96), its cth entry reads as $\boldsymbol{\mathcal{S}}_c = -(\tilde{\mathsf{S}}\mathsf{M}^{-1}\boldsymbol{B})_c$.

We conclude by stating that using similar arguments to those employed in Section 4.2.6, it is possible to show that matrix A is still positive semi-definite. Moreover, for homogeneous Neumann boundary conditions, *i.e.*, $q_1^\star = q_{\mathfrak{C}_p+1}^\star = 0$, the L^2-stability of the semi-discrete scheme still holds.

4.2.8 Extension to cylindrical geometry

The purpose of this section is to present the straightforward extension of CCLAD scheme to cylindrical geometry. To this end, let us introduce some notation. First, we note that the case of Cartesian or cylindrical geometry can be combined by introducing the pseudo Cartesian frame (O, x, y), equipped with the orthonormal basis $(\boldsymbol{e}_x, \boldsymbol{e}_y)$, through the use of the pseudo radius

$$\mathcal{R}(y) = 1 - \alpha + \alpha y,$$

where $\alpha = 1$ for cylindrical geometry and $\alpha = 0$ for Cartesian geometry. We remark that y corresponds to the radial coordinate in the cylindrical case. This means that we assume rotational symmetry about x axis, refer to Figure 4.10. We note that if we refer to standard cylindrical coordinates, (r, z), then x corresponds to z and y to r. In this framework, the volume v is obtained by rotating the area a about the x axis. Thus, the volume element, $\mathrm{d}v$, writes $\mathrm{d}v = \mathcal{R}\,\mathrm{d}a$, where $\mathrm{d}a = \mathrm{d}x\mathrm{d}y$ is the area element with respect to Cartesian coordinates (x, y). Note that we have omitted the factor 2π due to the integration in the azimuthal direction, namely we consider all integrated quantities to be defined per unit radian. The surface s, which bounds the volume v, is obtained by rotating, l, the boundary of the area a, about the x axis. Thus, the surface element, $\mathrm{d}s$, writes $\mathrm{d}s = \mathcal{R}\,\mathrm{d}l$, where $\mathrm{d}l$ is the line element along the perimeter of a.

In view of subsequent spatial discretization, we shall express the volume integral associated to the divergence operator using the Green formula. We recall that, in the pseudo Cartesian

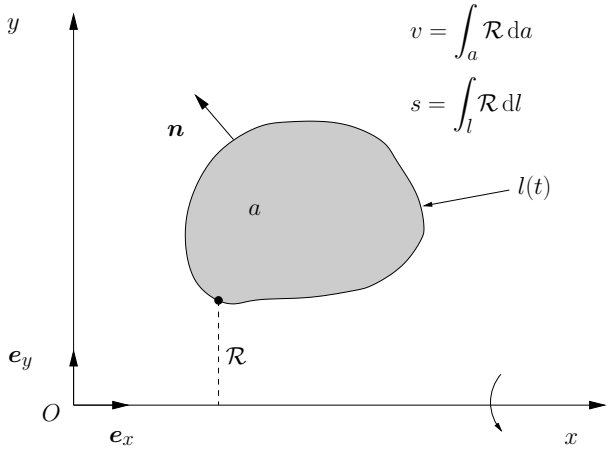

Figure 4.10: Notation related to cylindrical geometry.

frame, for an arbitrary vector $\boldsymbol{\phi} \in \mathbb{R}^2$, the divergence operator writes

$$\begin{aligned}\nabla \cdot \boldsymbol{\phi} =& \frac{\partial \phi}{\partial x} + \frac{1}{\mathcal{R}} \frac{\partial}{\partial y}(\mathcal{R}\psi) \\ =& \frac{\partial \phi}{\partial x} + \frac{\partial \psi}{\partial y} + \alpha \frac{\psi}{\mathcal{R}} \\ =& \frac{1}{\mathcal{R}} \left[\frac{\partial}{\partial x}(\mathcal{R}\phi) + \frac{\partial}{\partial y}(\mathcal{R}\psi) \right],\end{aligned}$$

where (ϕ, ψ) are the components of the vector $\boldsymbol{\phi}$. The gradient operator writes as usual

$$\boldsymbol{\nabla} T = \frac{\partial T}{\partial x} \boldsymbol{e}_x + \frac{\partial T}{\partial y} \boldsymbol{e}_y.$$

Let us replace the volume integral form of the divergence operator by its surface integral form, employing the previous notation

$$\begin{aligned}\int_v \nabla \cdot \boldsymbol{\phi}\,\mathrm{d}v &= \int_a \frac{1}{\mathcal{R}} \left[\frac{\partial}{\partial x}(\mathcal{R}\phi) + \frac{\partial}{\partial y}(\mathcal{R}\psi) \right] \mathcal{R}\,\mathrm{d}a \\ &= \int_a \left[\frac{\partial}{\partial x}(\mathcal{R}\phi) + \frac{\partial}{\partial y}(\mathcal{R}\psi) \right] \mathrm{d}a \\ &= \int_l \boldsymbol{\phi} \cdot \boldsymbol{n} \mathcal{R}\,\mathrm{d}l,\end{aligned}$$

where $\boldsymbol{n}$ is the unit outward normal to the contour l. Thus, the Green formula using pseudo Cartesian coordinates reads

$$\int_v \nabla \cdot \boldsymbol{\phi}\,\mathrm{d}v = \int_l \boldsymbol{\phi} \cdot \boldsymbol{n} \mathcal{R}\,\mathrm{d}l. \tag{4.97}$$

Applying this Green formula, the weak form of the heat conduction equation (4.18) rewrites as

$$\frac{d}{dt} \int_{\omega_c} \rho C_v T(\boldsymbol{x}, t)\,\mathsf{d}v + \int_{\partial\omega_c} \boldsymbol{q} \cdot \boldsymbol{n} \mathcal{R}\,\mathsf{d}l = \int_{\omega_c} \rho r(\boldsymbol{x}, t) \mathsf{d}v, \tag{4.98}$$

where ω_c denotes a generic cell of the computational domain, $\partial\omega$ its boundary and $\boldsymbol{n}$ the corresponding unit outward. Introducing as before a piecewise constant approximation of the physical variables allows to transform (4.98) into

$$m_c C_{vc} \frac{d}{dt} T_c + \int_{\partial\omega_c} \boldsymbol{q} \cdot \boldsymbol{n} \mathcal{R}\,\mathsf{d}l = m_c r_c, \tag{4.99}$$

where the mass of the cell is given as usual by $m_c = \rho_c \mid \omega_c \mid$, whereas the cell volume is obtained rotating the polygonal cell ω_c about x axis, *i.e*, $\mid \omega_c \mid = \int_{\omega_c} \mathsf{d}v = \int_{\omega_c} \mathcal{R}\, \mathsf{d}a$. In addition, $T_c = T_c(t)$ denotes the mean cell temperature defined by

$$T_c(t) = \frac{1}{\mid \omega_c \mid} \int_{\omega_c} T(\boldsymbol{x}, t)\, \mathsf{d}v.$$

To complete the space discretization it remains to discretize the surface integral in the above equation. To this end, we proceed as before introducing the piecewise constant approximation of the normal heat flux over each half-edge impinging on point p

$$q_{pc}^{\pm} = \frac{1}{l_{pc}^{\pm}} \int_{\partial\omega_{pc}^{\pm}} \boldsymbol{q} \cdot \boldsymbol{n}\, \mathsf{d}l. \tag{4.100}$$

The scalar $q_{pc}^{\pm}$ stands for the half-edge normal flux related to the half-edge $\partial\omega_{pc}^{\pm}$, refer to Figure 4.2. Note that the above piecewise constant approximation of the half-edge fluxes, coincides exactly with the one used in Cartesian geometry, refer to (4.20). Using the partition of the cell into sub-cells, *i.e.*, $\partial\omega_c = \cup_{p\in\mathcal{P}(c)} \partial\omega_{pc}^{\pm}$, the discretized heat conduction equation writes as

$$m_c C_{vc} \frac{d}{dt} T_c + \sum_{p\in\mathcal{P}(c)} \mathcal{R}_p (l_{pc}^{-} q_{pc}^{-} + l_{pc}^{+} q_{pc}^{+}) = m_c r_c, \tag{4.101}$$

where $\mathcal{R}_p = 1 - \alpha + \alpha y_p$ and y_p is the y-coordinate of point p. Note that the above equation has been derived by means of the following quadrature rule

$$\int_{\partial\omega_{pc}^{-} \cup \partial\omega_{pc}^{+}} \boldsymbol{q} \cdot \boldsymbol{n} \mathcal{R}\, \mathsf{d}l = \mathcal{R}_p (l_{pc}^{-} q_{pc}^{-} + l_{pc}^{+} q_{pc}^{+}).$$

Now, the space discretization is achieved by using the half-edge flux approximation which has been previously constructed in Section 4.2.2. Then, the construction of the scheme is performed using the same steps than before. Let us point out that the above quadrature rule has been specifically chosen to ensure spherical symmetry preservation when solving heat conduction equation over equal angle polar grids. In addition, one has to use the volume weight defined for quadrangular cells by 4.53, as it has been already noticed in [119].

4.3 Time discretization

In this section, we describe the time discretization related to our finite volume scheme. Let us recall that the semi-discrete scheme resulting from the space discretization writes under the form of the following system of differential equations

$$\mathfrak{M}\mathsf{C}_v \frac{d\boldsymbol{\mathcal{T}}}{dt} + \mathsf{A}\boldsymbol{\mathcal{T}} = \mathfrak{M}\boldsymbol{R} + \boldsymbol{\mathcal{S}}, \tag{4.102}$$

where $\boldsymbol{\mathcal{T}}$ is the cell centered temperatures vector, $\mathfrak{M}$ and C_v denote respectively the diagonal mass and heat capacity matrices, whereas A is the global diffusion matrix. In addition, $\boldsymbol{R}$ is the heat supply vector and $\boldsymbol{\mathcal{S}}$ is the vector taking into account the prescribed boundary conditions. The above system is completed by prescribing the initial condition $\boldsymbol{\mathcal{T}}(0) = \boldsymbol{\mathcal{T}}^0$. We solve the previous system over the time interval $[0, \mathfrak{T}]$ using the subdivision

$$0 = t^1 < t^2 < \ldots < t^n < t^{n+1} < \ldots < t^N = \mathfrak{T}.$$

We denote by Δt^n the generic time step, *i.e.*, $\Delta t^n = t^{n+1} - t^n$. The time approximation of a quantity at time t^n is denoted using the superscript n, for instance $\boldsymbol{\mathcal{T}}^n = \boldsymbol{\mathcal{T}}(t^n)$. Knowing that explicit time discretization of the diffusion operator requires a stability constraint on the time step which is quadratic with respect to the smallest cell size, we prefer to use an implicit time discretization for this term. Depending on whether the heat capacity and the conductivity tensor depend on the temperature or not, the above system might be linear or not with respect to temperature. This leads us to separate the description of the time discretization in two cases.

4.3.1 Linear case

In this case, we assume that the heat capacity and the conductivity tensor does not depend on temperature. Integrating (4.102) over the time interval $[t^n, t^{n+1}]$ yields the first-order time implicit discrete scheme

$$\mathfrak{M}\mathsf{C}_v \frac{\boldsymbol{\mathcal{T}}^{n+1} - \boldsymbol{\mathcal{T}}^n}{\Delta t^n} + \mathsf{A}\boldsymbol{\mathcal{T}}^{n+1} = \mathfrak{M}\boldsymbol{R}^n + \boldsymbol{\mathcal{S}}^n. \tag{4.103}$$

The cell centered temperatures vector is updated by solving the following linear system

$$(\frac{\mathfrak{M}\mathsf{C}_v}{\Delta t^n} + \mathsf{A})\boldsymbol{\mathcal{T}}^{n+1} = \frac{\mathfrak{M}\mathsf{C}_v}{\Delta t^n}\boldsymbol{\mathcal{T}}^n + \mathfrak{M}\boldsymbol{R}^n + \boldsymbol{\mathcal{S}}^n.$$

Let us recall that A^n is positive semi-definite. Knowing that the entries of the diagonal matrix $\mathfrak{M}\mathsf{C}_v$ is always positive, we deduce that matrix $\frac{\mathfrak{M}\mathsf{C}_v}{\Delta t^n} + \mathsf{A}$ is positive definite which implies that the above linear system always admits a unique solution. Note that, if A is symmetric, the matrix of the linear system is also symmetric. In this latter case, it also interesting to mention that in the absence of source term and for homogeneous boundary conditions, if the geometric conditions (4.77) and (4.78) hold, then $\frac{\mathfrak{M}\mathsf{C}_v}{\Delta t^n} + \mathsf{A}$ is an M-matrix, which means that the positivity of the temperature field is preserved by the scheme. The above linear system is solved using classical linear system solvers. For instance, in the case of a symmetric positive matrix, one can use an Incomplete Cholesky Conjugate Gradient (ICCG), whereas in the case of a positive definite matrix one can utilize the Generalized Minimal Residual method (GMRES), refer to [84].

4.3.2 Non-linear case

In this case, which frequently occurs in plasma physics, the material properties depend on temperature. It is more convenient to rewrite the heat conduction equation using the specific internal energy as

$$\rho \frac{\partial \varepsilon}{\partial t} + \nabla \cdot \boldsymbol{q} = \rho r.$$

Let us recall that the specific internal energy, ε, expresses in terms of the density and the temperature by means of an equation of state written under the form $\varepsilon = \varepsilon(\rho, T)$. Here, the specific heat capacity is computed as the partial derivative of the specific internal energy with respect to temperature, the density being fixed, *i.e.*, $C_v = (\frac{\partial \varepsilon}{\partial T})_\rho$. The semi-discrete system corresponding to the above partial differential equation writes

$$\mathfrak{M}\frac{d\boldsymbol{\mathcal{E}}}{dt} + \mathsf{A}\boldsymbol{\mathcal{T}} = \mathfrak{M}\boldsymbol{R} + \boldsymbol{\mathcal{S}}, \tag{4.104}$$

where $\boldsymbol{\mathcal{E}}$ denotes the specific internal energy vector which depends on ρ and T through the use of the equation of state. Assuming the absence of fluid motion, $\boldsymbol{\mathcal{E}}$ exhibits only a non-linear

dependency on T. Integrating (4.104) over the time interval $[t^n, t^{n+1}]$ leads to the first-order time implicit discretization

$$\mathfrak{M}\frac{\boldsymbol{\mathcal{E}}^{n+1}-\boldsymbol{\mathcal{E}}^{n}}{\Delta t^n}+\mathsf{A}^n\boldsymbol{\mathcal{T}}^{n+1}=\mathfrak{M}\boldsymbol{R}^n+\boldsymbol{\mathcal{S}}^n. \tag{4.105}$$

In writing this equation, we have made the choice of an explicit treatment of the non-linear dependency on temperature of the diffusion matrix. Namely, A^n corresponds to an evaluation of the diffusion matrix wherein the conductivity tensor has been computed using the temperature at the beginning of the time step. The above equation results in a non-linear system of differential equations, which requires an iterative method to be solved. This iterative method consists in defining a sequence of approximations of (4.105) by using a Newton-like method. To this end, let us denote by $\boldsymbol{\mathcal{T}}^q$ the sequence of temperatures vector, where q is natural integer. We initialize this sequence by setting for $q=0$, $\boldsymbol{\mathcal{T}}^0=\boldsymbol{\mathcal{T}}^n$. Introducing the increment of the temperatures vector as $\Delta\boldsymbol{\mathcal{T}}=\boldsymbol{\mathcal{T}}^{q+1}-\boldsymbol{\mathcal{T}}^q$ allows to define the specific internal energies vector increment as

$$\boldsymbol{\mathcal{E}}(\boldsymbol{\mathcal{T}}^{q+1})=\boldsymbol{\mathcal{E}}(\boldsymbol{\mathcal{T}}^q)+\mathsf{C}_v(\boldsymbol{\mathcal{T}}^q)\Delta\boldsymbol{\mathcal{T}}. \tag{4.106}$$

This equation has been obtained through the use of the first-order Taylor expansion

$$\varepsilon[T_c^q+(\Delta T)_c]=\varepsilon(T_c^q)+(\frac{\partial\varepsilon}{\partial T})_\rho(T_c^q)(\Delta T)_c,$$

where $(\Delta T)_c$ is the cth entry of vector $\Delta\boldsymbol{\mathcal{T}}$. Substituting, the Taylor expansion (4.106) into (4.105) leads to the following linear system satisfied by $\Delta\boldsymbol{\mathcal{T}}$

$$\left[\frac{\mathfrak{M}}{\Delta t^n}\mathsf{C}_v(\boldsymbol{\mathcal{T}}^q)+\mathsf{A}^n\right]\Delta\boldsymbol{\mathcal{T}}=-\left\{\frac{\mathfrak{M}}{\Delta t^n}\left[\boldsymbol{\mathcal{E}}(\boldsymbol{\mathcal{T}}^q)-\boldsymbol{\mathcal{E}}^n\right]+\mathsf{A}^n\boldsymbol{\mathcal{T}}^q-\mathfrak{M}\boldsymbol{R}^n-\boldsymbol{\mathcal{S}}^n\right\}. \tag{4.107}$$

Let us point out that this linear system admits always a unique solution since the matrix between bracket in the left-hand side is positive definite. The updated value of the sequence, $\boldsymbol{\mathcal{T}}^{q+1}$, is computed as $\boldsymbol{\mathcal{T}}^{q+1}=\boldsymbol{\mathcal{T}}^q+\Delta\boldsymbol{\mathcal{T}}$ by solving the above linear system in $\Delta\boldsymbol{\mathcal{T}}$. This process is repeated until a sufficiently accurate solution is reached. More precisely, we assess the convergence of the iterative method by computing the value of a residual characterizing the accuracy at which the non-linear equation is solved. A relevant choice for the residual consists in defining it as being equal to a certain norm of the left-hand side. Setting

$$\boldsymbol{\mathfrak{R}}^q=\frac{\mathfrak{M}}{\Delta t^n}\left[\boldsymbol{\mathcal{E}}(\boldsymbol{\mathcal{T}}^q)-\boldsymbol{\mathcal{E}}^n\right]+\mathsf{A}^n\boldsymbol{\mathcal{T}}^q-\mathfrak{M}\boldsymbol{R}^n-\boldsymbol{\mathcal{S}}^n,$$

we define the stopping criterion of the iterative procedure as

$$\frac{\|\boldsymbol{\mathfrak{R}}^q\|}{\|\boldsymbol{\mathfrak{R}}^0\|}\leq\eta, \tag{4.108}$$

where η is a fixed in advance positive real number. The usually employed norm is the maximum norm, *i.e.*, $\|\boldsymbol{\mathfrak{R}}^q\|_\infty=\max_c(\mathfrak{R}_c^q)$. The main advantage in using this stopping criterion lies in the fact that it provides an indication on the accuracy at which the energy conservation is ensured.

4.4 Numerical results

The aim of this section is to assess the robustness and the accuracy of CCLAD scheme against analytical test cases using various types of triangular and quadrangular grids. We conclude this section by presenting two tests which are not very far from the problems encountered in the

context of the numerical simulation of Inertial Confinement Fusion. We also want to mention that CCLAD scheme has been successfully used within a set of two-dimensional hydrodynamic simulations, which were performed to reproduce experimental measurements resulting from laser plasma experiments, wherein electron heat transport was strongly modified by self-generated magnetic fields, refer to [143].

4.4.1 Methodology for convergence analysis

Most of the test cases presented in this section are performed using a standard test problem which consists in solving the following diffusion equation over the domain $\mathcal{D} = [0,1]^2$

$$\rho C_v \frac{\partial T}{\partial t} - \nabla \cdot (\mathsf{K} \boldsymbol{\nabla} T) = \rho r, \tag{4.109a}$$

$$T(\boldsymbol{x}, 0) = T^0(\boldsymbol{x}), \tag{4.109b}$$

where $r = r(\boldsymbol{x})$ is a source term. Most of the analytical solutions being stationary, we compute them starting with the initial condition $T^0(\boldsymbol{x}) = 0$, and we run the numerical simulation until the steady state is reached. Density and the specific heat capacity are specified such that $\rho = 1$ and $C_v = 1$. The boundary conditions, the source term and the heat conductivity tensor, K, will be prescribed for each test case.

Bearing this in mind, let us describe the methodology used to perform the convergence analysis. Knowing that the computational domain is paved using $C_{\mathcal{D}}$ cells, we define the mesh resolution as

$$h = \sqrt{\frac{\mid \mathcal{D} \mid}{C_{\mathcal{D}}}},$$

where $\mid \mathcal{D} \mid$ denotes the domain volume. Let $\hat{T} = \hat{T}(\boldsymbol{x})$ be the steady analytical solution of (4.109). Being given a computational grid characterized by h, we denote by $\hat{T}_c^h$ the value of the analytical solution computed at the centroid of the cell ω_c, *i.e.*, $\hat{T}_c^h = \hat{T}(\boldsymbol{x}_c)$. If T_c^h denotes the cell averaged temperature corresponding to the numerical solution obtained by the finite volume scheme, we define the asymptotic numerical errors based on the maximum norm and the l^2 norm as

$$E_{\max}^h = \max_{c=1\ldots C_{\mathcal{D}}} \mid T_c^h - \hat{T}_c^h \mid, \tag{4.110a}$$

$$E_{\mathrm{l}^2}^h = \sqrt{\sum_{c=1}^{C_{\mathcal{D}}} (T_c^h - \hat{T}_c^h)^2 \mid \omega_c \mid}. \tag{4.110b}$$

The asymptotic error for both norms is estimated by

$$E_\alpha^h = C_\alpha h^{q_\alpha} + O(h^{q_\alpha + 1}), \quad \text{for } \alpha = \max, \mathrm{l}^2,$$

where q_α denotes the order of truncation error and C_α the convergence rate-constant which is independent of h. Having computed the asymptotic errors corresponding to two different grids characterized by mesh resolutions h_1 and $h_2 < h_1$, we deduce an estimation of the order of truncation error as

$$q_\alpha = \frac{\log(\frac{E_\alpha^{h_1}}{E_\alpha^{h_2}})}{\log(\frac{h_1}{h_2})}. \tag{4.111}$$

4.4.2 Anisotropic linear problem with discontinuous conductivity tensor

This problem consists in finding the steady solution of (4.109) with $r = 0$ and an anisotropic discontinuous conductivity tensor given by

$$\mathsf{K}(x,y) = \begin{cases} \begin{pmatrix} \mathsf{K}_l^{xx} & \mathsf{K}_l^{xy} \\ \mathsf{K}_l^{yx} & \mathsf{K}_l^{yy} \end{pmatrix} & \text{if } 0 \le x \le \frac{1}{2}, \\ \\ \begin{pmatrix} \mathsf{K}_r^{xx} & \mathsf{K}_r^{xy} \\ \mathsf{K}_r^{yx} & \mathsf{K}_r^{yy} \end{pmatrix} & \text{if } \frac{1}{2} \le x \le 1. \end{cases}$$

The one-dimensional solution, *i.e.*, $\hat{T} = \hat{T}(x)$ which corresponds to Dirichlet boundary conditions: $\hat{T}(0) = 0$ and $\hat{T}(1) = 1$, writes as

$$\hat{T}(x) = \begin{cases} \dfrac{2\mathsf{K}_r^{xx}}{\mathsf{K}_l^{xx} + \mathsf{K}_r^{xx}} x, & \text{if } 0 \le x \le \dfrac{1}{2}, \\ \\ \dfrac{\mathsf{K}_r^{xx} - \mathsf{K}_l^{xx}}{\mathsf{K}_r^{xx} + \mathsf{K}_l^{xx}} + \dfrac{2\mathsf{K}_l^{xx}}{\mathsf{K}_l^{xx} + \mathsf{K}_r^{xx}} x, & \text{if } \dfrac{1}{2} \le x \le 1. \end{cases}$$

This is a linear continuous solution for which the heat flux $\hat{\boldsymbol{q}} = -\mathsf{K}\boldsymbol{\nabla} T$ writes as

$$\hat{\boldsymbol{q}} = -\begin{cases} \begin{pmatrix} 2\dfrac{\mathsf{K}_l^{xx}\mathsf{K}_r^{xx}}{\mathsf{K}_l^{xx} + \mathsf{K}_r^{xx}} \\ 2\dfrac{\mathsf{K}_l^{yx}\mathsf{K}_r^{xx}}{\mathsf{K}_l^{xx} + \mathsf{K}_r^{xx}} \end{pmatrix} & \text{if } 0 \le x \le \frac{1}{2}, \\ \\ \begin{pmatrix} 2\dfrac{\mathsf{K}_l^{xx}\mathsf{K}_r^{xx}}{\mathsf{K}_l^{xx} + \mathsf{K}_r^{xx}} \\ 2\dfrac{\mathsf{K}_l^{xx}\mathsf{K}_r^{yx}}{\mathsf{K}_l^{xx} + \mathsf{K}_r^{xx}} \end{pmatrix} & \text{if } \frac{1}{2} \le x \le 1. \end{cases}$$

The normal component of the heat flux is continuous at the interface $x = \frac{1}{2}$ whereas its tangential component undergone a jump discontinuity since in general $\mathsf{K}_l^{yx}\mathsf{K}_r^{xx} \neq \mathsf{K}_l^{xx}\mathsf{K}_r^{yx}$.

The boundary conditions applied on the top and the bottom boundaries of the computational domain are Dirichlet boundary conditions deduced from the analytical solution. For the numerical applications we have defined the entries of the conductivity tensor as $\mathsf{K}_l^{xx} = 1$, $\mathsf{K}_l^{xy} = \mathsf{K}_l^{yx} = -1$, $\mathsf{K}_l^{yy} = 4$ and $\mathsf{K}_r^{xx} = 10$, $\mathsf{K}_r^{xy} = \mathsf{K}_r^{yx} = -3$, $\mathsf{K}_r^{yy} = 2$. To assess the ability of our finite volume scheme to preserve this linear solution, we run this test problem on a triangular grid and on various quadrangular grids.

Triangular grid

We compute the steady numerical solution using a triangular grid which is made of 246 cells. This grid is displayed in Figure 4.11(left). Note that the unstructured grid has been constructed such that the interface $x = \frac{1}{2}$ coincides with the cell interfaces. The temperature isolines of the numerical solution are plotted in Figure 4.11(right). These are vertical straight lines which match perfectly with the analytical solution. In addition, we observe that the obtained asymptotic errors are equal to zero up to machine precision. As expected, **our finite volume scheme preserves linear solutions on triangular grids**.

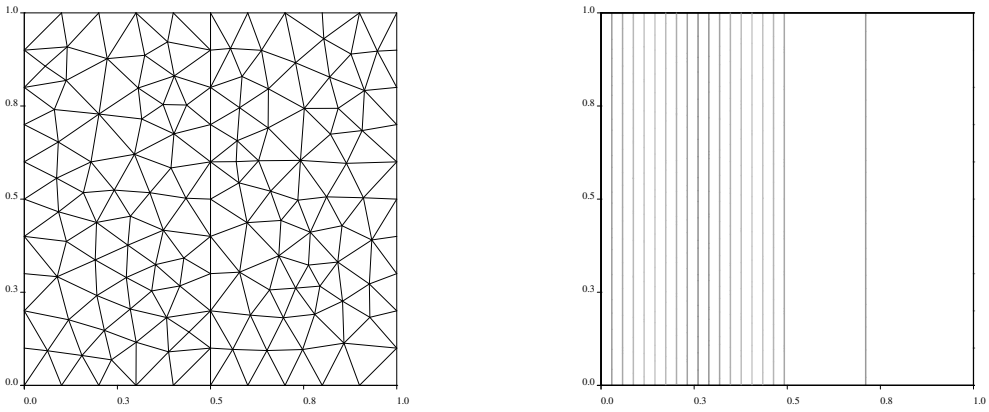

Figure 4.11: Anisotropic linear problem with discontinuous conductivity tensor: Triangular grid (left) and temperature isolines of the numerical steady solution (right).

Quadrangular grids

The numerical solution computed using a 10×10 Cartesian grid also matches perfectly with the analytical solution and the temperature isolines plot is identical to the one obtained previously, refer to Figure 4.11(right). This result is coherent with the fact that the flux approximation used in our finite volume scheme preserves linear solutions on cells which are parallelograms. Next, we study the accuracy of our scheme for a sequence of distorted grids which result from an analytical transformation of Cartesian grids. Following the approach described in [151], we first introduce the smooth distorted grids resulting from the mapping defined on the unit square by

$$\begin{cases} x(\xi,\eta) = \xi + a_0 \sin(2\pi\xi)\sin(2\pi\eta), \\ y(\xi,\eta) = \eta + a_0 \sin(2\pi\xi)\sin(2\pi\eta). \end{cases} \tag{4.112}$$

The three smooth grids resulting from this mapping with $a_0 = 0.1$ are displayed in Figure 4.12. We also define randomly distorted grids by means of the following mapping defined on the unit square by

$$\begin{cases} x(\xi,\eta) = \xi + a_0 h \cos(2\pi\theta), \\ y(\xi,\eta) = \eta + a_0 h \sin(2\pi\theta), \end{cases} \tag{4.113}$$

where h corresponds to the mesh spacing of the initial Cartesian grid and θ is a random number chosen in $[0,1]$. We have plotted the three random grids obtained with this mapping for $a_0 = 0.2$ in Figure 4.13. Note that we do not apply this mapping to the nodes located on the line $\xi = 0.5$ in order to preserve the interface.

The convergence analysis for smooth grids is performed computing the asymptotic errors and the corresponding orders of truncation error using formulas (4.110) and (4.111). The results displayed in Table 4.1(a) show that the convergence rate is almost second-order in the l^2 norm and a little bit less in the maximum norm. Proceeding with the convergence analysis for random grids as before, we have displayed the corresponding results in Table 4.1(b). We observe an erratic behavior regarding the asymptotic errors and the rate of convergence in both norms which clearly shows a lack of convergence for our scheme with this type of random grids. Note that this behavior has been already observed in the case of isotropic diffusion test cases [28].

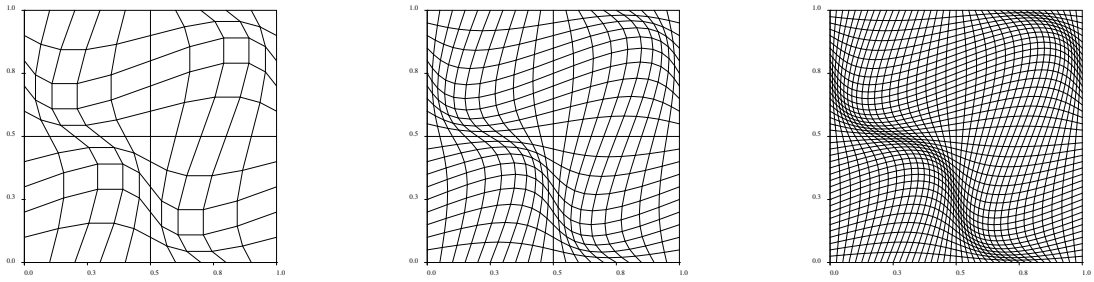

Figure 4.12: Smooth distorted quadrangular grids: $10\times$ cells (left), 20×20 cells (middle) and 40×40 cells (right).

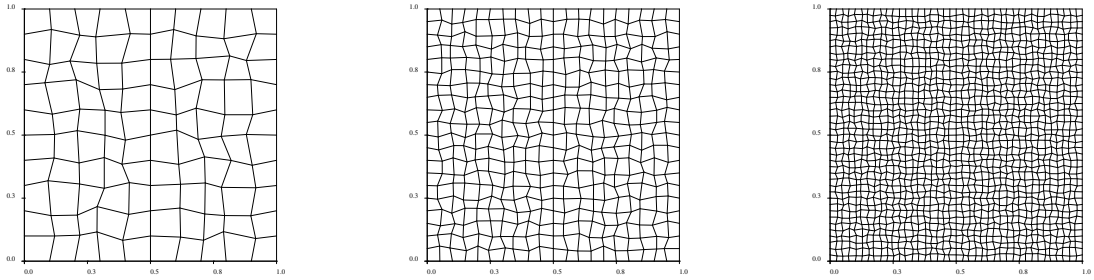

Figure 4.13: Random distorted quadrangular grids with interface $\xi = \frac{1}{2}$ preserved: $10\times$ cells (left), 20×20 cells (middle) and 40×40 cells (right).

Table 4.1: Anisotropic linear problem with discontinuous conductivity tensor: asymptotic errors in both maximum and l^2 norms and corresponding truncation error orders for quadrangular grids.

(a) Smooth grids.

h	$E^h_{\max}$	$q^h_{\max}$	$E^h_{l^2}$	$q^h_{l^2}$
1.00D-1	8.93D-3	**1.51**	3.26D-3	**1.75**
5.00D-2	3.14D-3	**1.53**	9.67D-4	**1.89**
2.50D-2	1.09D-3	-	2.63D-4	-

(b) Random grids.

h	$E^h_{\max}$	$q^h_{\max}$	$E^h_{l^2}$	$q^h_{l^2}$
1.00D-1	5.25D-3	**0.47**	1.77D-3	**0.67**
5.00D-2	3.78D-3	**0.10**	1.11D-3	**0.50**
2.50D-2	3.57D-3	-	7.87D-4	-

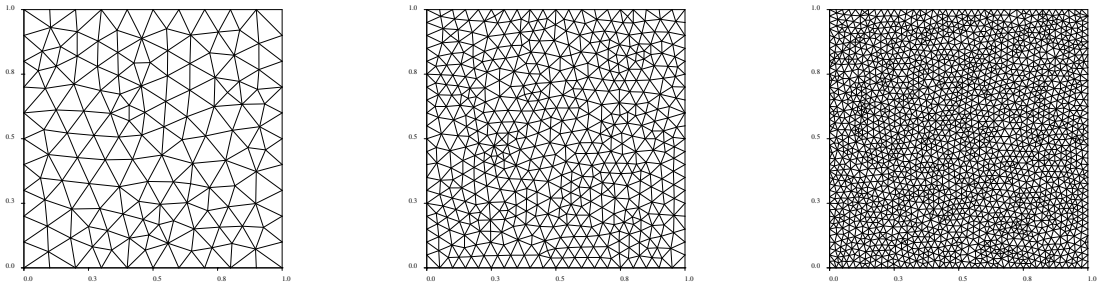

Figure 4.14: Triangular grids: 254 cells (left), 988 cells (middle) and 3984 cells (right).

h	$E^h_{\max}$	$q_{\max}$	$E^h_{\mathrm{l}^2}$	q_{l^2}
6.27D-2	2.87D-2	**2.15**	9.83D-3	**2.09**
3.18D-2	6.66D-3	**1.57**	2.38D-3	**2.05**
1.58D-2	2.22D-3	-	5.66D-4	-

Table 4.2: Anisotropic linear problem with a non-uniform symmetric positive definite conductivity tensor: asymptotic errors in both maximum and l^2 norms and corresponding truncation error orders for triangular grids.

4.4.3 Anisotropic linear problem with a non-uniform symmetric positive definite conductivity tensor

This test problem has been presented in [130]. Once more, it consists in finding the steady solution of (4.109). However, it is characterized by an anisotropic non-uniform conductivity tensor which writes for all $(x, y) \in [0, 1]^2$

$$\mathsf{K}(x, y) = \begin{pmatrix} y^2 + \eta x^2 & -(1-\eta)xy \\ -(1-\eta)xy & x^2 + \eta y^2 \end{pmatrix},$$

where η is a positive parameter characterizing the level of anisotropy. This tensor is symmetric positive definite. Its eigenvalues are $\lambda^+ = x^2 + y^2$ and $\lambda^- = \eta(x^2 + y^2)$. Thus, its condition number is equal to $\frac{1}{\eta}$. The source term, r, is computed such that the analytical solution (4.109) is given by

$$\hat{T}(x, y) = \sin^2(\pi x) \sin^2(\pi y).$$

We apply a homogeneous Dirichlet boundary condition on the boundaries of the computational domain, *i.e.*, $T(\boldsymbol{x}, t) = 0,\ \forall \boldsymbol{x} \in \partial\mathcal{D}$. For numerical applications, we choose $\eta = 10^{-2}$. We assess the accuracy of our finite volume scheme by running this test problem on sequence of triangular and distorted quadrangular grids.

Triangular grids

We run this test problem on a sequence of three triangular grids which are displayed in Figure 4.14. The convergence analysis results corresponding to the numerical simulations using the three triangular grids are displayed in Table 4.2. They show that our finite volume scheme has a second-order convergence rate in l^2 norm on triangular grids.

Quadrangular grids

Concerning the quadrangular grids we perform the convergence analysis on three types of grids: rectangular, smooth and random. We start by giving in Table 4.3(a) the convergence analysis

Table 4.3: Anisotropic linear problem with a non-uniform symmetric positive definite conductivity tensor: asymptotic errors in both maximum and l^2 norms and corresponding truncation error orders for quadrangular grids.

(a) Rectangular grids.

h	$E^h_{\max}$	$q_{\max}$	$E^h_{l_2}$	q_{l^2}
1.00D-1	3.97D-2	**2.08**	1.69D-2	**2.07**
5.00D-2	9.40D-3	**2.02**	4.03D-3	**2.02**
2.50D-2	2.32D-3	-	9.95D-4	-

(b) Smooth grids.

h	$E^h_{\max}$	$q_{\max}$	$E^h_{l^2}$	q_{l^2}
1.00D-1	1.09D-1	**1.84**	2.66D-2	**2.06**
5.00D-2	3.04D-2	**1.88**	6.37D-3	**2.01**
2.50D-2	8.26D-3	-	1.58D-3	-

(c) Random grids.

h	$E^h_{\max}$	$q_{\max}$	$E^h_{l^2}$	q_{l^2}
1.00D-1	8.25D-2	**1.04**	2.96D-2	**1.62**
5.00D-2	4.02D-2	**1.31**	9.60D-3	**1.41**
2.50D-2	1.62D-2	-	3.61D-3	-

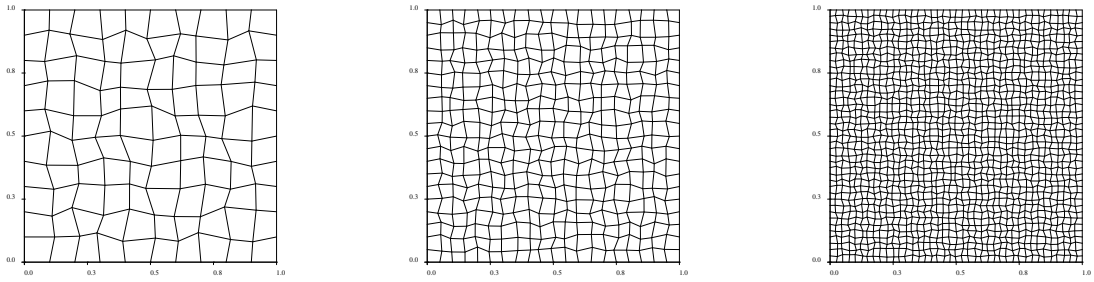

Figure 4.15: Random distorted quadrangular grids: $10\times$ cells (left), 20×20 cells (middle) and 40×40 cells (right).

data for a sequence of three rectangular grids. These data demonstrate that our finite volume scheme exhibits a second-order rate of convergence on rectangular grids. Next, we pursue our investigations using the sequence of the three smooth distorted grids plotted in Figure 4.12. The convergence analysis results obtained with these three grids are presented in Table 4.3(b). Once more, we observe a second-order convergence rate in l^2 norm, whereas the convergence rate in maximum norm is almost second-order. Finally, we achieve the convergence analysis of the present problem by performing computations on a sequence of three random grids which are displayed in Figure 4.15. Note that these grids differ from the previous ones plotted in Figure 4.13 since this time all the nodes have been displaced according to (4.113). The results of the convergence analysis corresponding to this sequence of random grids are given in Table4.3(c). In comparison to the previous results, these ones are representative of an erratic behavior which clearly does not correspond to second-order.

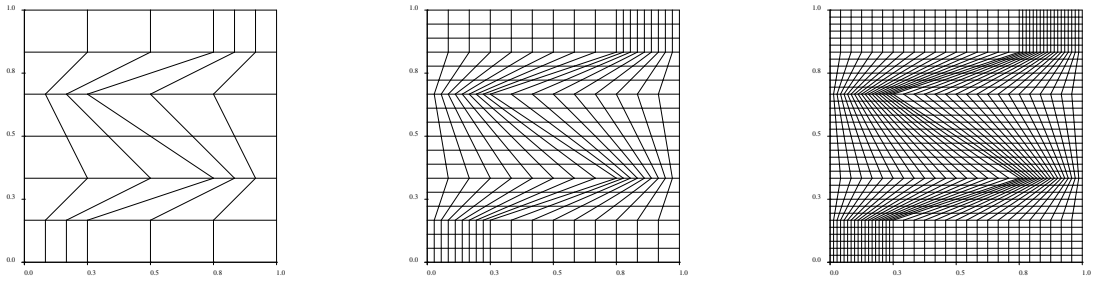

Figure 4.16: Kershaw grids: 36 cells (left), 324 cells (middle) and 1296 cells (right).

4.4.4 Anisotropic linear problem with a non-uniform non-symmetric conductivity tensor

Here, we aim at assessing the accuracy of our finite volume scheme on an analytical problem characterized by a non-symmetric positive definite conductivity tensor which writes for all $(x, y) \in [0, 1]^2$ as

$$\mathsf{K}(x, y) = \begin{pmatrix} a & by \\ -by & a \end{pmatrix},$$

where a and b are positive real numbers. Note that this tensor is always positive definite since for all $\boldsymbol{\phi} \in \mathbb{R}^2$ we have $\mathsf{K}\boldsymbol{\phi} \cdot \boldsymbol{\phi} = a \mid \boldsymbol{\phi} \mid^2$. The interest of this test case lies in the fact that the above non-symmetric positive definite tensor is representative of the structure of the electron heat conductivity tensor used in plasma physics in the presence of a magnetic field, refer to Section 4.1.2. Setting $r = 0$, the one-dimensional analytical steady solution of (4.109) corresponding to the Dirichlet boundary conditions, $\hat{T}(0) = 0$ and $\hat{T}(1) = 1$, writes as

$$\hat{T}(x) = \frac{\exp(\frac{b}{a}x) - 1}{\exp(\frac{b}{a}) - 1}, \quad \forall x \in [0, 1].$$

The boundary conditions prescribed at the top and bottom boundaries of the computational domain are Dirichlet boundary conditions deduced from the above analytical solution. For numerical applications, we choose $a = 1$ and $b = 2$.

We study the convergence analysis for this problem using three different types of quadrangular grids. We reuse the smooth and the random grids which has been introduced previously. We also make use of the Kershaw grids [75]. These highly skewed grids are displayed in Figure 4.16. For each type of grids, we perform a sequence of three computations increasing the mesh refinement. The resulting asymptotic errors and rate of convergence in both maximum and l^2 norms are displayed respectively in Tables 4.4(a) and 4.4(b) for smooth and Kershaw grids. From these results it follows that our finite volume scheme exhibits a rate of convergence which is located between first-order and second-order for these types of grids. The results associated to the sequence of random grids are displayed in Table 4.4(c). Once more, they reveal an erratic behavior of our scheme regarding its convergence on random grids.

Table 4.4: Anisotropic linear problem with a non-uniform non-symmetric conductivity tensor: asymptotic errors in both maximum and l^2 norms and corresponding truncation error orders for quadrangular grids.

(a) Smooth grids.

h	$E^h_{\max}$	$q_{\max}$	$E^h_{\mathrm{l}^2}$	q_{l^2}
1.00D-1	1.56D-2	**1.24**	6.86D-3	**1.48**
5.00D-2	6.59D-3	**1.57**	2.45D-3	**1.81**
2.50D-2	2.22D-3	-	6.99D-4	-

(b) Kershaw grids.

h	$E^h_{\max}$	$q_{\max}$	$E^h_{\mathrm{l}^2}$	q_{l^2}
1.67D-1	7.32D-2	**1.27**	3.54D-2	**1.50**
5.55D-2	1.81D-2	**1.32**	6.81D-3	**1.76**
2.78D-2	7.24D-3	-	2.01D-3	-

(c) Random grids.

h	$E^h_{\max}$	$q_{\max}$	$E^h_{\mathrm{l}^2}$	q_{l^2}
1.00D-1	9.63D-3	**0.92**	3.07D-3	**1.09**
5.00D-2	5.08D-3	**0.16**	1.43D-3	**0.17**
2.50D-2	4.56D-3	-	1.27D-3	-

4.4.5 Isotropic non-linear problem

In this section, we investigate the numerical solution of the following non-linear heat conduction equation

$$\begin{aligned} &\rho C_v \frac{\partial T}{\partial t} - \nabla \cdot (\kappa(T) \boldsymbol{\nabla} T) = 0, \\ &T(\boldsymbol{x}, 0) = T^0(\boldsymbol{x}). \end{aligned}$$

The isotropic heat conductivity, κ, is a non-linear function with respect to temperature. Here, we define $\kappa(T) = T^{\frac{5}{2}}$, this type of non-linearity corresponds to the so-called Spitzer-Härm conductivity which is frequently used in plasma physics to describe electron thermal heat flux in the local regime, refer to [169].

The above diffusion equation is solved over a cylindrical domain $\mathcal{D}$ defined by $r \in [0, 1]$ and $\theta \in [0, \frac{\pi}{2}]$, where (r, θ) denote the classical polar coordinates, which express in terms of the Cartesian coordinates (x, y) as $r = \sqrt{x^2 + y^2}$ and $\theta = \arctan \frac{y}{x}$. The mass density and the heat capacity are given by $\rho = 1$ and $C_v = 1$. The initial condition is defined by $T^0(\boldsymbol{x}) = 1$. We prescribe symmetry boundary conditions along axis $x = 0$ and $y = 0$ and we impose the normal flux $q^\star = 1000$ at the outer radius $r = 1$. The unsteady solution is computed until time $\mathfrak{T} = 3.25\,10^{-3}$. At this time a non-linear heat wave has propagated into the cold medium. This wave is characterized by a sharp transition zone displaying a strong temperature gradient. Due to the boundary conditions and the geometry of the domain, the solution of the diffusion equation exhibits a cylindrical symmetry, namely $T(\boldsymbol{x}) \equiv T(r)$.

Unfortunately, the non-linear equation under consideration does not admit exact analytic solutions. That is why, we compute with our finite volume scheme a reference numerical solution using a 50×20 polar grid which is displayed in Figure 4.17(left). Note that this numerical solution preserves perfectly the cylindrical symmetry. Next, we construct a distorted grid from

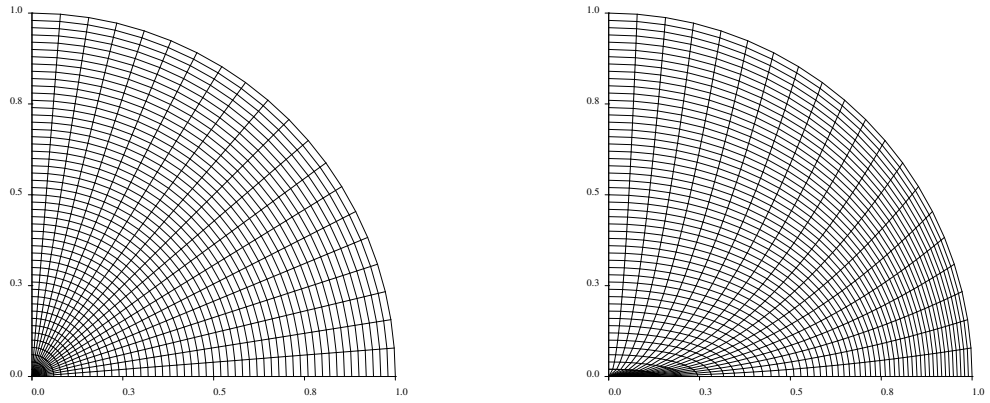

Figure 4.17: Isotropic non-linear problem: 50×20 polar grid (left) and its distorted counterpart (right).

the polar grid applying the following mapping: $(x, y) \in \mathcal{D} \longmapsto (x', y') \in \mathcal{D}$ such that

$$x' = \sqrt{r}\cos\theta,$$
$$y' = r\sin\theta,$$

where (r, θ) are the polar coordinates corresponding to the Cartesian coordinates (x, y). The resulting distorted grid is plotted in Figure 4.17(right). Now, we compute the numerical solution of the non-linear test problem on the above distorted grid, using three different schemes. These are: the classical five-point scheme, the Kershaw scheme [75] and the present finite volume scheme. The numerical solution resulting from the five-point scheme is displayed in Figure 4.18. We have displayed the temperatures in all cells as function of the cell center radius versus the reference solution. In this figure, we observe the main flaw of the five-point scheme: in spite of its robustness, it produces a numerical solution wherein the temperature front is aligned with the grid distortion. The corresponding numerical solution is not able to preserve the cylindrical symmetry. In addition, the comparison to the reference solution, shows that the timing of the thermal wave is completely wrong. Let us emphasize that this test case is not a fake problem. It is representative of situations which frequently occur in the framework of plasma physics simulation wherein the heat conduction equation is coupled with a numerical method solving Lagrangian hydrodynamics equations. In this case, grid distortions are induced by fluid motion and thus the use of the five-point scheme to solve the heat conduction equation is not recommended at all. This weakness of the five-point scheme follows from the fact that its construction is based on a two-point flux approximation[3], which becomes inaccurate in the presence of strong grid distortions. The correction of this flaw requires the use of finite volume schemes based on more accurate flux approximations. For the problem under consideration, we are going to compare the numerical solutions obtained using both Kershaw scheme and our finite volume scheme. As it can be observed in Figure 4.19, these two numerical methods, which are nine-point schemes on quadrangular grids, bring us the expected improvement in reproducing quite well the one-dimensional solution. To compare more precisely these two schemes, we have displayed in Figure4.20 an enlarged view in the vicinity of the thermal front. Contrary to our

[3]The two-point flux approximation corresponds to a finite difference approximation of the normal flux at an edge, wherein the gradient is approximated through the use of the temperatures of the two cells sharing that edge.

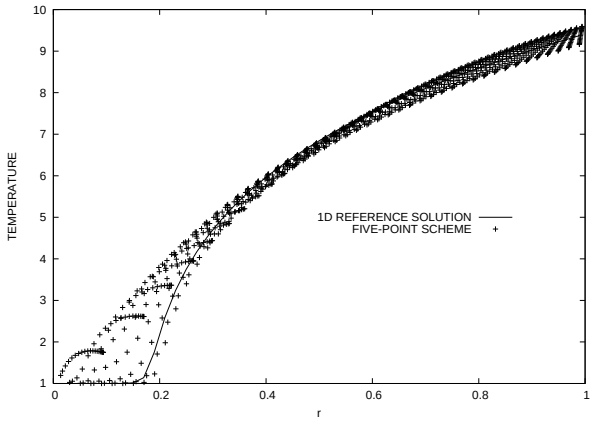

Figure 4.18: Isotropic non-linear problem: temperatures in all the cells versus cell center radius at the stopping time $\mathfrak{T} = 3.25\,10^{-3}$. The computation is performed using the five-point scheme on the 50×20 distorted polar grid.

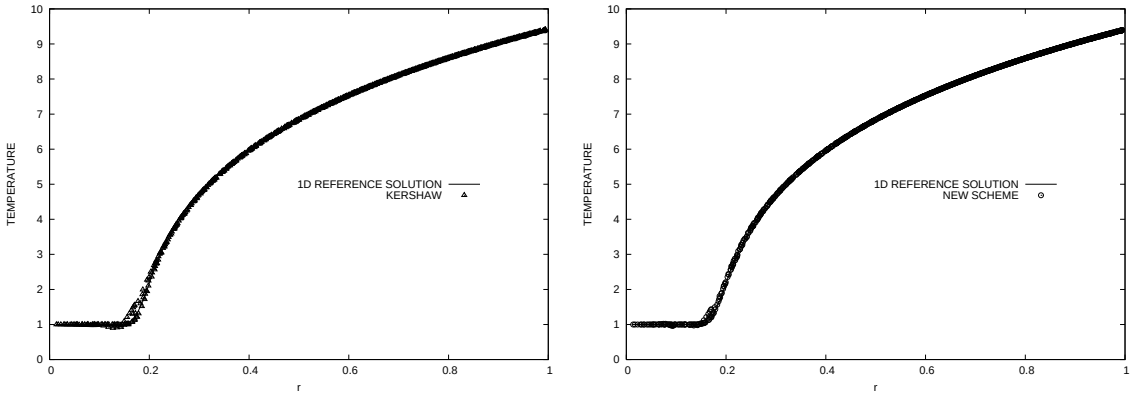

Figure 4.19: Isotropic non-linear problem: temperatures in all the cells versus cell center radius at the stopping time $\mathfrak{T} = 3.25\,10^{-3}$ for the 50×20 distorted polar grid. Comparison between Kershaw scheme (left) and the present finite volume scheme (right).

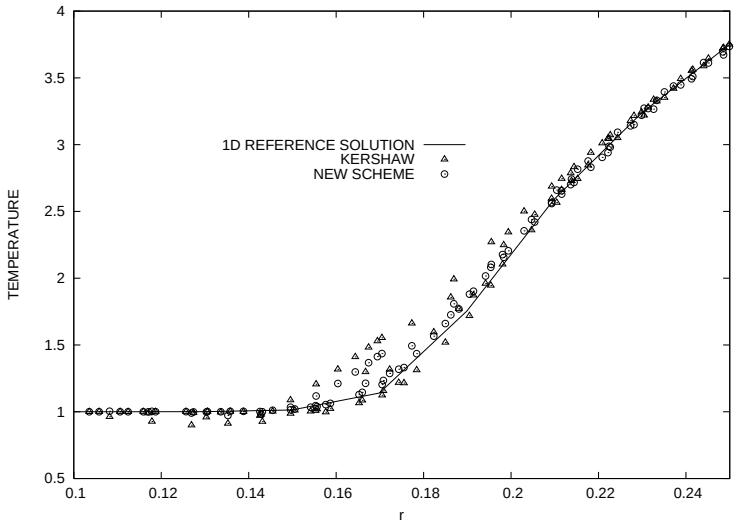

Figure 4.20: Isotropic non-linear problem: temperatures in all the cells versus cell center radius at the stopping time $\mathfrak{T} = 3.25\,10^{-3}$ for the 50×20 distorted polar grid. Comparison between Kershaw scheme and the present finite volume scheme in the vicinity of the thermal front.

finite volume scheme, we notice that Kershaw scheme produces some temperature undershoots located in the cold medium in front of the thermal wave and thus does not respect the maximum principle.

4.4.6 Anisotropic non-linear problem

The goal of this section consists in assessing our finite volume scheme against a test case which is representative of electron heat transport in a magnetized plasma [29]. In this situation, the classical isotropic Spitzer-Härm conductivity has to be replaced by the anisotropic Braginskii tensor conductivity, refer to Section 4.1.2. We aim at solving the electron heat conduction equation in this particular context to assess the ability of our finite volume scheme to handle such a physical phenomenon. To this end, let us consider a two-dimensional plasma at rest and confined in the domain $\mathcal{D} = [0, \delta] \times [0, \delta]$, where $\delta = 20\,\mu$m. The initial electron temperature of the plasma is defined for all $\boldsymbol{x} \in \mathcal{D}$ as

$$T_e^0(\boldsymbol{x}) = \begin{cases} 10^3\,\text{K if } 0 \leq x \leq 18\,\mu\text{m}, \\ 3\,10^7\,\text{K if } 18\,\mu\text{m} \leq x \leq 20\,\mu\text{m}. \end{cases}$$

The density and the specific heat capacity of the plasma are given by $\rho = 0.025\,\text{g/cm}^3$ and $C_v = 5\,10^7\,\text{erg/K/g}$. Let us point out that these values correspond roughly to a layer of a hot underdense Deuterium-Tritium plasma contacting with the cold material of the same density. The magnetization of the plasma results from the prescribed magnetic field $\boldsymbol{B} = B_z(x, y)\boldsymbol{e}_z$, where the z-component is given by $B_z(x, y) = B^0 \exp(-4\frac{r}{\delta})^4$ with $r^2 = (x - \frac{\delta}{2})^2 + (y - \frac{\delta}{2})^2$ and $B^0 = -10^7\,\text{G}$. The $B_z(x, y)$ contours are plotted in Figure 4.21. The electron temperature, $T_e(\boldsymbol{x}, t)$ is governed by the anisotropic heat conduction equation

$$\rho C_v \frac{\partial T_e}{\partial t} - \nabla \cdot (\mathsf{K}_e \boldsymbol{\nabla} T_e) = 0.$$

According to (4.12) the anisotropic Braginskii conductivity tensor, K_e, writes

$$\mathsf{K}_e = \begin{pmatrix} \kappa_\perp & \kappa_\wedge \\ -\kappa_\wedge & \kappa_\perp \end{pmatrix},$$

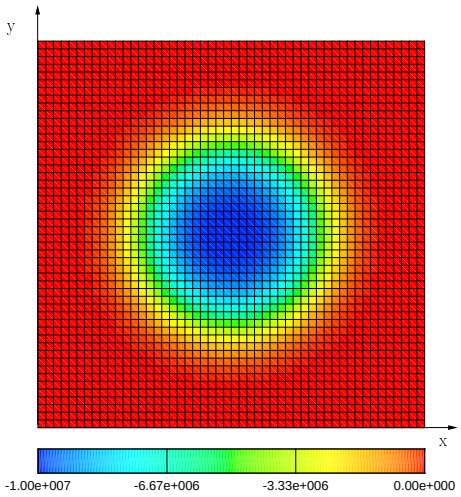

Figure 4.21: Anisotropic non-linear problem: contours of z-component of the prescribed magnetic field.

where the Braginskii transport coefficients are expressed in terms of the Spitzer-Härm conductivity by means of functions describing the magnetization of the heat flux, refer to Figure 4.1 and [26]. To better understand the action of the above anisotropic conductivity tensor, observe that for any arbitrary vector $\boldsymbol{\phi} \in \mathbb{R}^2$

$$\mathsf{K}_e \boldsymbol{\phi} = \kappa_\perp \boldsymbol{\phi} - \kappa_\wedge \mathcal{R}_{\frac{\pi}{2}} \boldsymbol{\phi},$$

where $\mathcal{R}_{\frac{\pi}{2}}$ is the counterclockwise rotation through the angle $\frac{\pi}{2}$. This equation shows that the action of K_e decomposes in an isotropic part, which corresponds to a multiplication by $\kappa_\perp$, completed by a rotation. This last term follows directly from the magnetic field since $\kappa_\wedge$ is directly proportional to the magnitude of the magnetic field. This corresponds to the so-called Righi-Leduc effect.

Bearing this in mind, we proceed to compute numerical solutions of the above problem using our finite volume scheme. The computational domain has been paved using a 50×50 Cartesian grid and stopping time is $\mathfrak{T} = 25\,10^{-12}\,\mathrm{s}$. We prescribe Neumann homogeneous boundary conditions at the boundaries of the computational domain. The first computation has been done suppressing the Righi-Leduc term, that is, setting $\kappa_\wedge = 0$. In this case the conductivity tensor reduces to the isotropic form $\mathsf{K}_e = \kappa_\perp \mathsf{I}_d$. The corresponding temperature contours are displayed in Figure 4.22(left) wherein we can observe a leftward thermal wave propagating from hot to cold region. Note that the propagation of the thermal wave is strongly inhibited by the presence of the magnetic field. This follows from the fact that the Braginskii coefficient $\kappa_\perp$ is a decreasing function with respect to the magnitude of magnetic field, refer to Figure 4.1. The second computation is performed using the complete form of the anisotropic conductivity tensor, that is, including the Righi-Leduc effect. This term, as it can be observed in Figure 4.22(right), rotates the temperature contours.

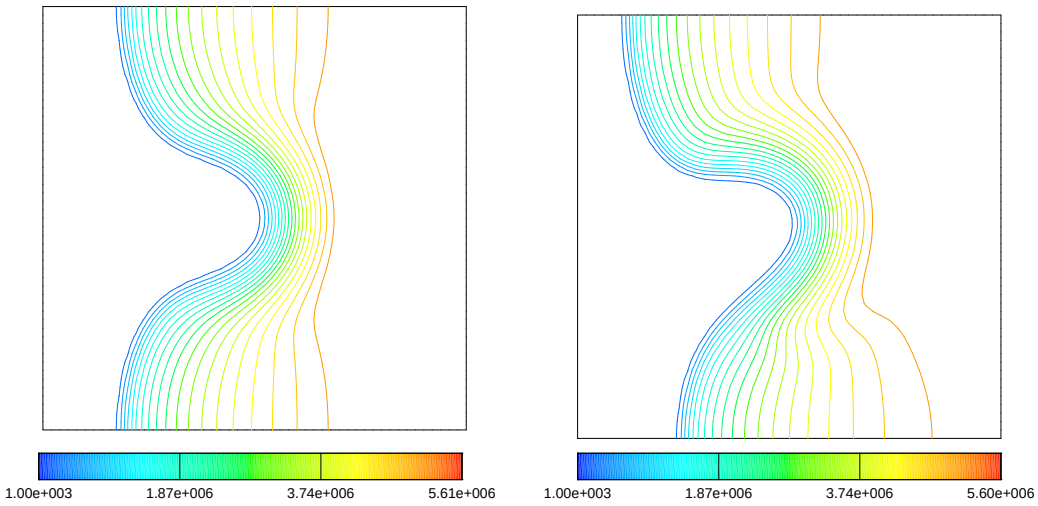

Figure 4.22: Anisotropic non-linear problem: temperature contours at time $\mathfrak{T} = 25\ 10^{-12}$ s, obtained respectively using the anisotropic conductivity tensor without Righi-Leduc term, *i.e.*, $\kappa_\wedge = 0$ (left), and with Righi-Leduc term (right).

Chapter 5

Conclusion and perspectives

This document presents a part of the numerical works that have been performed between 2003 and 2009 at the CELIA laboratory. These research works have as main objective the conception and the development of robust and accurate numerical schemes dedicated to the numerical simulation of experiments concerning high energy density physics such as the ICF, the laboratory astrophysics and the laser processing. Bearing this context in mind, we have constructed the EUCCLHYD and CCLAD schemes that respectively solve the two-dimensional Lagrangian hydrodynamics equations and the two-dimensional anisotropic diffusion equation. These schemes, which have been thoroughly described in this document, are the numerical basis of the CHIC code that has been developed at CELIA.

More precisely, CCLAD is a cell-centered high-order finite volume scheme devoted to the numerical resolution of the non-linear anisotropic heat conduction equation on two-dimensional unstructured distorted grids composed of triangular or quadrangular cells. This scheme, which can be used either in Cartesian or cylindrical geometry, has been derived utilizing a sub-cell variational formulation, it is characterized by cell-centered unknowns and has a local stencil. Its robustness and its accuracy have been demonstrated by means of various test cases. In the future, we intend to extend this scheme to the three-dimensional geometry.

Regarding the EUCCLHYD scheme, its has been derived employing a sub-cell force-based discretization which applies to unstructured polygonal grids. This general formalism, which has been described in both Cartesian and cylindrical geometry, allows to construct a family of cell-centered Lagrangian schemes, wherein numerical fluxes are expressed in terms of sub-cell forces. The general form of the sub-cell force is obtained by requiring the scheme to satisfy a semi-discrete entropy inequality. Sub-cell force and nodal velocity are computed consistently with the cell volume variation by means of a node-centered solver, which results from the total energy conservation. The high-order extension of this family of cell-centered schemes is achieved using a one-step time discretization, wherein the fluxes are computed by means of a Taylor expansion. The time derivatives of the fluxes are obtained through the use of a node-centered solver which can be viewed as a two-dimensional extension of the Generalized Riemann Problem methodology introduced by Ben-Artzi and Falcovitz [21]. The robustness and the accuracy of this scheme are assessed using representative test cases of compressible fluid flows. In the future, we aim at studying alternative very high-order extensions of this cell-centered Lagrangian scheme by using a Discontinuous Galerkin approach [163]. We intend to revisit the three-dimensional extension that has been derived in [111] by means of the sub-cell force concept. Furthermore, we have in mind to pursue the investigations undertaken in [110], which concern the study of the links between the sub-cell force-based staggered and cell-centered discretizations. We also want to enrich the capability of this discretization which is limited to the gas dynamics equations by extending it to include material strength modeling. We have chosen to limit our investigation to

the case of hypo-elastic constitutive laws for material characterized by Elastic Perfectly Plastic behavior [166].

We conclude by noticing that as all Lagrangian methods, the present scheme suffers from a lack of robustness when the vorticity and shear within the flow become too important. The consequence of this is the appearance of non-convex, or even tangled, cells. To remedy this type of problem, we have developed a multi-material Arbitrary Lagrangian Eulerian (ALE) method within the code CHIC, which is described in [59]. The main elements of this ALE algorithm are an explicit Lagrangian phase in which the solution and the grid are updated, a rezoning phase in which a new grid is defined by improving the geometric quality of the cells and a remapping phase in which the Lagrangian solution is conservatively interpolated onto the new grid.

Appendix A

Notation and reminder related to vectors and tensors

In this appendix, we aim at recalling notation and formulas related to vectors and tensors which are required to derive the mathematical modeling of fluid mechanics. We do not intend to present the complete rigorous tensor theory, which is beyond the scope of the present chapter, but rather introduce useful formulas. The present description has been constructed collecting materials from [24, 148, 25, 141, 63, 86].

In all what follows, we consider $\mathbb{R}^d$, where d is nonnegative integer ranging from 1 to 3, as a d-dimensional Euclidean space. Namely, $\mathbb{R}^d$ is a d-dimensional vector space equipped with an inner product and an orthonormal basis $(\boldsymbol{e}_1, \boldsymbol{e}_2, \ldots, \boldsymbol{e}_d)$. An arbitrary vector in $\mathbb{R}^d$, $\boldsymbol{x}$, is defined by its coordinates, $(x_1, x_2, \ldots, x_d)$, as $\boldsymbol{x} = \sum_{i=1}^{d} x_i \boldsymbol{e}_i$. The inner product of two vectors $\boldsymbol{x}$ and $\boldsymbol{x'}$ is defined by $\boldsymbol{x} \cdot \boldsymbol{x'} = \sum_{i=1}^{d} x_i x'_i$. The inner product of $\boldsymbol{x}$ with itself is always nonnegative and allows us to define the Euclidean norm on $\mathbb{R}^d$ as

$$\|\boldsymbol{x}\| = \sqrt{\boldsymbol{x} \cdot \boldsymbol{x}} = \sqrt{\sum_{i=1}^{d} x_i^2}.$$

A.1 Introduction to second-order tensors

A.1.1 Definitions

Let $\boldsymbol{a}$ and $\boldsymbol{b}$ be two vectors of $\mathbb{R}^d$. The tensor product, otherwise named dyadic product, of $\boldsymbol{a}$ and $\boldsymbol{b}$ is denoted by $\boldsymbol{a} \otimes \boldsymbol{b}$ and defined as

$$\forall \boldsymbol{x} \in \mathbb{R}^d \, , (\boldsymbol{a} \otimes \boldsymbol{b})\boldsymbol{x} = (\boldsymbol{b} \cdot \boldsymbol{x})\boldsymbol{a}. \tag{A.1}$$

This relation defines a linear transformation of $\mathbb{R}^d$ which is characterized by a matrix whose components are written

$$(\boldsymbol{a} \otimes \boldsymbol{b})_{ij} = a_i b_j, \ (i, j = 1, 2 \ldots, d). \tag{A.2}$$

Having in mind the notion of tensor product of two vectors, we define a second-order tensor on $\mathbb{R}^d$ as the sum of tensor products of vectors in $\mathbb{R}^d$. This definition involves that the set of second-order tensors defined on $\mathbb{R}^d$ is a d^2-dimensional vector space equipped with the basis $\boldsymbol{e}_i \otimes \boldsymbol{e}_j$ $(i, j = 1, 2 \ldots, d)$. This definition involves that an arbitrary tensor, T, can be written

$$\mathsf{T} = \sum_{i=1}^{d} \sum_{j=1}^{d} T_{ij} \boldsymbol{e}_i \otimes \boldsymbol{e}_j, \tag{A.3}$$

where T_{ij} are components of the tensor T. Let us remark that to any second-order tensor T corresponds the linear transformation of $\mathbb{R}^d$ defined by

$$\boldsymbol{x'} = \mathsf{T}\boldsymbol{x}, \quad x'_i = \sum_{j=1}^{d} T_{ij} x_j.$$

Note that the second-order tensor T corresponds either to the previous linear transformation or to the matrix defined by its components T_{ij} in an orthonormal basis. We conclude this paragraph recalling the following basic definitions which coincide with the classical definition of linear algebra for matrices.

- Zero tensor: this tensor, which is denoted by O, maps every vector $\boldsymbol{x}$ into the zero vector

$$\mathsf{O}\boldsymbol{x} = \mathbf{0}. \tag{A.4}$$

- Identity or unit tensor: this tensor, which is denoted by I_d, maps every vector into itself

$$\mathsf{I}_d\boldsymbol{x} = \boldsymbol{x}. \tag{A.5}$$

  The components of the matrix associated to the unit tensor are given by $I_{ij} = \delta_{ij}$, where δ_{ij} stands for the Kronecker symbol which takes the values $\delta_{ij} = 1$ if $i = j$ and $\delta_{ij} = 0$ if $i \neq j$.

- Transpose of a tensor: the transpose of the tensor T is the unique tensor T^t defined by

$$\mathsf{T}\boldsymbol{x} \cdot \boldsymbol{x'} = \boldsymbol{x} \cdot \mathsf{T}^t\boldsymbol{x'}. \tag{A.6}$$

  Components of transpose of T are given by $T^t_{ij} = T_{ji}$.

- Symmetric and skew tensors: a tensor T is symmetric if $\mathsf{T}^t = \mathsf{T}$, it is skew if $\mathsf{T}^t = -\mathsf{T}$. Every tensor can expressed uniquely as the sum of a symmetric tensor and a skew tensor as

$$\mathsf{T} = \frac{1}{2}(\mathsf{T} + \mathsf{T}^t) + \frac{1}{2}(\mathsf{T} - \mathsf{T}^t). \tag{A.7}$$

- Trace of a tensor: the trace of a tensor T is the scalar denoted by $\mathrm{tr}(\mathsf{T})$ and defined as

$$\mathrm{tr}(\mathsf{T}) = \sum_{i=1}^{d} T_{ii}. \tag{A.8}$$

  If S and T are two second-order tensors, it is straightforward to check that

$$\mathrm{tr}(\mathsf{ST}) = \mathrm{tr}(\mathsf{TS}). \tag{A.9}$$

- Determinant of a tensor: the determinant of a tensor T is the scalar denoted by $\det \mathsf{T}$ and defined as the determinant of its corresponding matrix. It is computed by means of the following formula

$$\det \mathsf{T} = \sum_{i=1}^{d} T_{ij}(-1)^{i+j} M_{ij} = \sum_{j=1}^{d} T_{ij}(-1)^{i+j} M_{ij}, \tag{A.10}$$

  where M_{ij} denote the minors of matrix T, that is the determinant formed by omitting the ith row and jth column of T.

- Inverse of a tensor: the inverse of a tensor T is the tensor denoted by T^{-1}. It is defined provided that $\det \mathsf{T} \neq O$. It satisfies $\mathsf{T}\mathsf{T}^{-1} = \mathsf{I}_d$ and its components are given by

$$T_{ij}^{-1} = \frac{1}{\det \mathsf{T}}(-1)^{i+j} M_{ji}. \tag{A.11}$$

- Positive definite tensor: a tensor T is positive definite if for an arbitrary vector $\boldsymbol{x}$ the following property holds

$$\mathsf{T}\boldsymbol{x} \cdot \boldsymbol{x} > 0. \tag{A.12}$$

A.1.2 Properties of the dyadic product of two vectors

The dyadic product of two vectors satisfies the following important properties

$$\begin{aligned}
\mathrm{tr}(\boldsymbol{a} \otimes \boldsymbol{b}) =& \boldsymbol{a} \cdot \boldsymbol{b}, && \text{(A.13a)}\\
(\boldsymbol{a} \otimes \boldsymbol{b})^t =& \boldsymbol{b} \otimes \boldsymbol{a}, && \text{(A.13b)}\\
\mathsf{T}(\boldsymbol{a} \otimes \boldsymbol{b}) =& (\mathsf{T}\boldsymbol{a}) \otimes \boldsymbol{b}, && \text{(A.13c)}\\
(\boldsymbol{a} \otimes \boldsymbol{b})\mathsf{T} =& \boldsymbol{a} \otimes (\mathsf{T}^t \boldsymbol{b}), && \text{(A.13d)}\\
(\boldsymbol{x} \otimes \boldsymbol{x'})(\boldsymbol{a} \otimes \boldsymbol{b}) =& (\boldsymbol{x'} \cdot \boldsymbol{a})\boldsymbol{x} \otimes \boldsymbol{b}, && \text{(A.13e)}
\end{aligned}$$

The demonstration of these properties are left to the reader.

A.1.3 Inner product of second-order tensors

Let S and T be two second-order tensors. The inner product of S and T is a scalar denoted by $\mathsf{S} : \mathsf{T}$ and defined as

$$\mathsf{S} : \mathsf{T} = \mathrm{tr}(\mathsf{S}^t \mathsf{T}). \tag{A.14}$$

The inner product can also be expressed in terms of the tensor components as

$$\mathsf{S} : \mathsf{T} = \sum_i \sum_j S_{ij} T_{ij}. \tag{A.15}$$

We note that $\mathsf{S} : \mathsf{T} = \mathsf{T} : \mathsf{S}$ and $\mathsf{S} : \mathsf{I}_d = \mathrm{tr}(\mathsf{S})$. This inner product defines a scalar product over the space of second-order tensor. The corresponding norm is the Frobenius norm defined as

$$\|\mathsf{T}\| = \sqrt{\mathrm{tr}(\mathsf{T}^t \mathsf{T})} = \sqrt{\sum_i \sum_j T_{ij}^2}. \tag{A.16}$$

Using the previous definition, one can show easily the following identities

$$\begin{aligned}
\mathsf{L} : (\mathsf{S}\mathsf{T}) = (\mathsf{S}^t \mathsf{L}) : \mathsf{T} = (\mathsf{L}\mathsf{T}^t) : \mathsf{S}, && \text{(A.17a)}\\
(\boldsymbol{x} \otimes \boldsymbol{x'}) : (\boldsymbol{a} \otimes \boldsymbol{b}) = (\boldsymbol{x} \cdot \boldsymbol{a})(\boldsymbol{x'} \cdot \boldsymbol{b}), && \text{(A.17b)}\\
\mathsf{L} : (\boldsymbol{a} \otimes \boldsymbol{b}) = \boldsymbol{a} \cdot (\mathsf{L}\boldsymbol{b}) = (\boldsymbol{a} \otimes \boldsymbol{b}) : \mathsf{L}. && \text{(A.17c)}
\end{aligned}$$

Let T be a symmetric second-order tensor and S be an arbitrary second-order tensor, then their inner product satisfies the following identity

$$\mathsf{T} : \mathsf{S} = \mathsf{T} : \frac{1}{2}(\mathsf{S} + \mathsf{S}^t). \tag{A.18}$$

This results from the symmetry of T and property of the trace operator (A.9).

A.2 Eigenvalues and eigenvectors of a tensor

Let T be a second-order tensor. Let λ be a scalar and $\boldsymbol{U}$ a vector such that $\mathsf{T}\boldsymbol{U} = \lambda\boldsymbol{U}$. Then λ is called an eigenvalue and $\boldsymbol{U}$ and eigenvector. Note that the eigenvalues and the eigenvectors are independent of the choice of the basis, that is they are invariant under change of basis. Eigenvalues are computed by finding the roots of the characteristic polynomial equation $P_{\mathsf{T}}(\lambda) = 0$, where $P_{\mathsf{T}}(\lambda) = \det(\mathsf{T} - \lambda\mathsf{I}_d)$. A second-order tensor can have at most d eigenvectors and eigenvalues since the space is d-dimensional. We note that if a tensor is positive definite, then its eigenvalues are positive, since by definition $\mathsf{T}\boldsymbol{U}\cdot\boldsymbol{U} = \lambda\|\boldsymbol{U}\|^2 > 0$. If a tensor T admits d real eigenvalues, $\lambda_i,\ i = 1\dots d$, then its trace and its determinant can be expressed in terms of these eigenvalues as

$$\operatorname{tr}(\mathsf{T}) = \sum_{i=1}^{d}\lambda_i, \quad \det\mathsf{T} = \Pi_{i=1}^{d}\lambda_i. \tag{A.19}$$

Therefore, the trace and the determinant are scalar invariants of a tensor.

We conclude this section by recalling the fundamental property satisfies by symmetric tensors. If T is symmetric, it admits d real eigenvalues, $\lambda_i,\ i = 1\dots d$, whose corresponding eigenvectors are mutually orthogonal. Therefore, the normalized eigenvectors, $\boldsymbol{U}_i,\ i = 1\dots d$, form the orthonormal basis of the spectral decomposition which writes as

$$\mathsf{T} = \sum_{i=1}^{d}\lambda_i\boldsymbol{U}_i\otimes\boldsymbol{U}_i. \tag{A.20}$$

This expression is the spectral decomposition of the symmetric tensor T.

A.3 Tensor analysis

In this section, we recall the definition of the divergence and the gradient of a vector and a second-order tensor. It is assumed that the functions employed here are sufficiently smooth so that the limits and derivatives taken are always defined.

A.3.1 Derivative of tensor with respect to a scalar

Let $\mathsf{L} = \mathsf{L}(t)$ be a tensor function of scalar t. The derivative of L with respect to t is the second-order tensor defined by

$$\frac{d}{dt}\mathsf{L} = \lim_{h\to 0}\frac{\mathsf{L}(t+h) - \mathsf{L}(t)}{h}. \tag{A.21}$$

Using this definition, the derivative of the dyadic product of the two vectors $\boldsymbol{a} = \boldsymbol{a}(t)$ and $\boldsymbol{b} = \boldsymbol{b}(t)$ is given by

$$\frac{d}{dt}(\boldsymbol{a}\otimes\boldsymbol{b}) = \frac{d\boldsymbol{a}}{dt}\otimes\boldsymbol{b} + \boldsymbol{a}\otimes\frac{d\boldsymbol{b}}{dt}. \tag{A.22}$$

A.3.2 Derivative of scalar valued functions of vectors

Let $f = f(\boldsymbol{x})$ be a real valued function of the vector $\boldsymbol{x}$. Then, the derivative of $f(\boldsymbol{x})$ with respect to $\boldsymbol{x}$ in the direction $\boldsymbol{a}$ is the vector $\boldsymbol{\nabla}f$ defined as

$$\boldsymbol{\nabla}f\cdot\boldsymbol{a} = \lim_{h\to 0}\frac{f(\boldsymbol{x}+h\boldsymbol{a}) - f(\boldsymbol{x})}{h}. \tag{A.23}$$

Vector $\boldsymbol{\nabla} f$ is the gradient of f, which writes with respect to the orthonormal basis

$$\boldsymbol{\nabla} f = \sum_{i=1}^{d} \frac{\partial f}{\partial x_i} \boldsymbol{e}_i.$$

A.3.3 Derivative of vector valued functions of vectors

Let $\boldsymbol{f} = \boldsymbol{f}(\boldsymbol{x})$ be a vector valued function of the vector $\boldsymbol{x}$. Then, the derivative of $\boldsymbol{f}(\boldsymbol{x})$ with respect to $\boldsymbol{x}$ in the direction $\boldsymbol{a}$ is the second-order tensor $\nabla \boldsymbol{f}$ defined as

$$(\nabla \boldsymbol{f})\boldsymbol{a} = \lim_{h \to 0} \frac{\boldsymbol{f}(\boldsymbol{x} + h\boldsymbol{a}) - \boldsymbol{f}(\boldsymbol{x})}{h}. \tag{A.24}$$

On the orthonormal basis, the gradient tensor $\nabla \boldsymbol{f}$ read as

$$\nabla \boldsymbol{f} = \sum_{i=1}^{d} \sum_{j=1}^{d} \frac{\partial f_i}{\partial x_j} (\boldsymbol{e}_i \otimes \boldsymbol{e}_j).$$

A.3.4 Derivative of scalar valued functions of second-order tensors

Let $f = f(\mathsf{S})$ be a scalar valued function of the second-order tensor S. Then, the derivative of $f(\mathsf{S})$ with respect to S in the direction of the second-order tensor T is the second-order tensor $\frac{\partial f}{\partial \mathsf{S}}$ defined as

$$\frac{\partial f}{\partial \mathsf{S}} : \mathsf{T} = \lim_{h \to 0} \frac{f(\mathsf{S} + h\mathsf{T}) - f(\mathsf{S})}{h}. \tag{A.25}$$

On the orthonormal basis, this second-order tensor writes as

$$\frac{\partial f}{\partial \mathsf{S}} = \sum_{i=1}^{d} \sum_{j=1}^{d} \frac{\partial f}{\partial S_{ij}} (\boldsymbol{e}_i \otimes \boldsymbol{e}_j).$$

Let us consider the composed scalar valued function $f = f(\mathsf{S}(t))$, then its derivative with respect to the scalar variable t is given by

$$\frac{df}{dt} = \frac{\partial f}{\partial \mathsf{S}} : \frac{d\mathsf{S}}{dt}. \tag{A.26}$$

A.3.5 Derivative of the determinant of a tensor

The derivative of the determinant of a second-order tensor T with respect to itself is the second-order tensor

$$\frac{\partial}{\partial \mathsf{T}} (\det \mathsf{T}) = \mathsf{T}^{-t} \det \mathsf{T}, \tag{A.27}$$

where T^{-t} denotes the transpose of the inverse of T. The proof of this result consists in computing the partial derivative of the determinant with respect to its component through the use of (A.10)

$$\frac{\partial}{\partial T_{ij}} (\det \mathsf{T}) = \sum_{i=1}^{d} (-1)^{i+j} M_{ij}.$$

Then, comparing this result with the definition of the inverse (A.11) it is clear that

$$\frac{\partial}{\partial T_{ij}} (\det \mathsf{T}) = T_{ji}^{-1} \det \mathsf{T},$$

which ends the proof.

A.3.6 Divergence of a vector and a tensor

Let $\boldsymbol{U} = \boldsymbol{U}(\boldsymbol{x})$ be a vector function of $\boldsymbol{x}$, its divergence is a scalar denoted by $\nabla \cdot \boldsymbol{U}$ and defined as

$$\nabla \cdot \boldsymbol{U} = \sum_{i=1}^{d} \frac{\partial U_i}{\partial x_i}. \tag{A.28}$$

Let us remark that the divergence of a vector can also be defined as

$$\nabla \cdot \boldsymbol{U} = \mathrm{tr}(\nabla \boldsymbol{U}). \tag{A.29}$$

This alternative definition is more intrinsic since it does not require the use of the components of $\boldsymbol{U}$ provided that the tensor gradient of $\boldsymbol{U}$ is well defined.

Let T be a second-order tensor, its divergence is a vector denoted by $\nabla \cdot \mathsf{T}$ whose components are expressed in terms of the tensor components as follows

$$(\nabla \cdot \mathsf{T})_i = \sum_{j} \frac{\partial T_{ij}}{\partial x_j}. \tag{A.30}$$

A.3.7 Tensor identities

Having in mind the previous notation and definitions it is straightforward to demonstrate the following important identities.

$$\nabla \cdot (\mathsf{T}\boldsymbol{U}) = \nabla \cdot (\mathsf{T}^t) \cdot \boldsymbol{U} + \mathsf{T}^t : \nabla \boldsymbol{U}, \tag{A.31a}$$

$$\nabla \cdot (\boldsymbol{U} \otimes \boldsymbol{V}) = (\nabla \boldsymbol{U})\boldsymbol{V} + \boldsymbol{U}\nabla \cdot \boldsymbol{V}, \tag{A.31b}$$

$$\nabla(\rho \boldsymbol{U}) = \rho \nabla \boldsymbol{U} + \boldsymbol{U} \otimes \boldsymbol{\nabla}\rho, \tag{A.31c}$$

$$\nabla \cdot (\rho \mathsf{T}) = \rho \nabla \cdot \mathsf{T} + \mathsf{T}\boldsymbol{\nabla}\rho, \tag{A.31d}$$

where ρ, $\boldsymbol{U}$, $\boldsymbol{V}$ and T are respectively arbitrary scalar, vectors and second-order tensor.

Comment 22 *Let us remark that tensor identity* (A.31a) *allows to propose the following intrinsic definition of the divergence of a tensor. Let* T *be a second-order tensor and* $\boldsymbol{U}$ *a constant arbitrary vector. The divergence of* T *is the vector denoted* $\nabla \cdot \mathsf{T}$ *such as*

$$(\nabla \cdot \mathsf{T}) \cdot \boldsymbol{U} = \nabla \cdot (\mathsf{T}^t \boldsymbol{U}), \quad \forall \boldsymbol{U}. \tag{A.32}$$

A.4 Integral transformation formulas

The Green formula, otherwise named divergence formula, states that the volume integral of the divergence of a function is equal to the total flux of this function through the surface enclosing the volume. We recall its formulations for vectors and second-order tensors. All the real, vector and tensor valued functions are assumed to be continuously differentiable with respect to the spatial variables. Let ω be a domain of the d-dimensional space enclosed by a surface $\partial\omega$, then for arbitrary second-order tensor T and vector $\boldsymbol{U}$

$$\int_{\omega} \nabla \cdot \mathsf{T}\, \mathrm{d}v = \int_{\partial\omega} \mathsf{T}\boldsymbol{n}\, \mathrm{d}s, \tag{A.33a}$$

$$\int_{\omega} \nabla \cdot \boldsymbol{U}\, \mathrm{d}v = \int_{\partial\omega} \boldsymbol{U} \cdot \boldsymbol{n}\, \mathrm{d}s, \tag{A.33b}$$

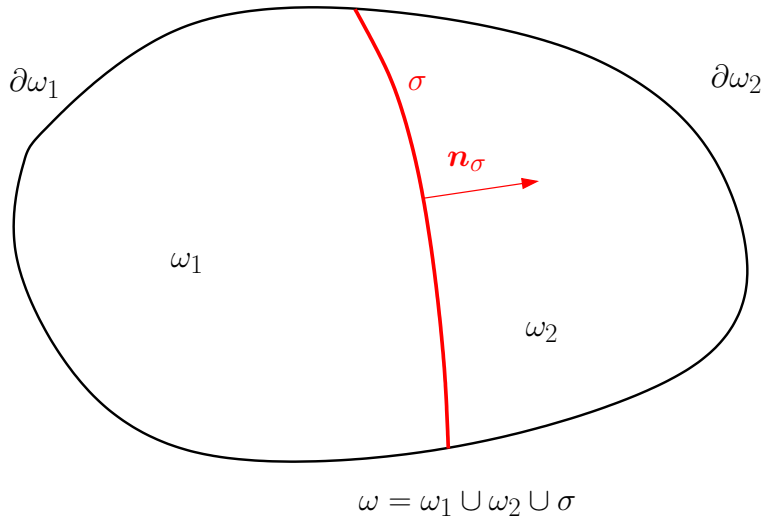

Figure A.1: Volume ω is split into two sub-volumes ω_1 and ω_2 by the discontinuity surface σ.

where $\boldsymbol{n}$ denotes the unit outward normal to the enclose surface $\partial\omega$. Let f denotes a scalar valued function, then using the previous results it is straightforward to demonstrate the following useful formulas

$$\int_\omega \nabla \boldsymbol{U} \,\mathrm{d}v = \int_{\partial\omega} \boldsymbol{U} \otimes \boldsymbol{n} \,\mathrm{d}s, \tag{A.34a}$$

$$\int_\omega \boldsymbol{\nabla} f \,\mathrm{d}v = \int_{\partial\omega} f\boldsymbol{n} \,\mathrm{d}s. \tag{A.34b}$$

We conclude this section by extending the divergence theorem to the case of piecewise continuously differentiable functions. To this end, we assume that ω is divided into two non-overlapping volumes ω_1 and ω_2 over which $\boldsymbol{U}$ and $\boldsymbol{T}$ are continuously differentiable. Let σ be the intersection surface of ω_1 and ω_2, i.e. $\sigma = \omega_1 \cap \omega_2$, refer to Fig. A.1. This is the surface of discontinuity for functions $\boldsymbol{U}$ and T. Let $\boldsymbol{x}_\sigma$ be the position vector of a point located on this surface and $\boldsymbol{n}_\sigma$ the unit normal to σ located at $\boldsymbol{x}_\sigma$ and pointing in the direction of ω_2. The jumps of the functions $\boldsymbol{U}$ and T through the discontinuity surface σ are defined as

$$\begin{aligned}[\![\boldsymbol{U}]\!] &= \boldsymbol{U}_2 - \boldsymbol{U}_1,\\ [\![\mathsf{T}]\!] &= \mathsf{T}_2 - \mathsf{T}_1,\end{aligned}$$

where for an arbitrary $\boldsymbol{x}_\sigma \in \sigma$

$$\begin{aligned}\boldsymbol{U}_1 &= \lim_{h\to 0^+} \boldsymbol{U}(\boldsymbol{x}_\sigma - h\boldsymbol{n}_\sigma), \quad \boldsymbol{U}_2 = \lim_{h\to 0^+} \boldsymbol{U}(\boldsymbol{x}_\sigma + h\boldsymbol{n}_\sigma),\\ \mathsf{T}_1 &= \lim_{h\to 0^+} \mathsf{T}(\boldsymbol{x}_\sigma - h\boldsymbol{n}_\sigma), \quad \mathsf{T}_2 = \lim_{h\to 0^+} \mathsf{T}(\boldsymbol{x}_\sigma + h\boldsymbol{n}_\sigma).\end{aligned}$$

$\boldsymbol{U}$ being continuously differentiable separately over ω_1 and ω_2, application of divergence formula (A.33b) yields

$$\begin{aligned}\int_{\omega_1} \nabla\cdot\boldsymbol{U} \,\mathrm{d}v &= \int_{\partial\omega_1\setminus\sigma} \boldsymbol{U}\cdot\boldsymbol{n} \,\mathrm{d}s + \int_\sigma \boldsymbol{U}_1\cdot\boldsymbol{n}_\sigma \,\mathrm{d}s,\\ \int_{\omega_2} \nabla\cdot\boldsymbol{U} \,\mathrm{d}v &= \int_{\partial\omega_2\setminus\sigma} \boldsymbol{U}\cdot\boldsymbol{n} \,\mathrm{d}s - \int_\sigma \boldsymbol{U}_2\cdot\boldsymbol{n}_\sigma \,\mathrm{d}s.\end{aligned}$$

The sum of the two previous equations leads to

$$\int_{\omega_1 \cup \omega_2} \nabla \cdot \boldsymbol{U} \, \mathsf{d}v + \int_{\sigma} [\![\boldsymbol{U}]\!] \cdot \boldsymbol{n}_{\sigma} \, \mathsf{d}s = \int_{\partial\omega} \boldsymbol{U} \cdot \boldsymbol{n} \, \mathsf{d}s. \tag{A.35}$$

This equation consists of a generalization of divergence formula (A.33b) to piecewise continuously differentiable vector function. The second term in the left-hand side corresponds to the flux through σ resulting from the jump across this surface. We notice that this term cancels when $[\![\boldsymbol{U}]\!] \to 0$. Proceeding with the tensor valued function as before yields

$$\int_{\omega_1 \cup \omega_2} \nabla \cdot \mathsf{T} \, \mathsf{d}v + \int_{\sigma} [\![\mathsf{T}]\!] \boldsymbol{n}_{\sigma} \, \mathsf{d}s = \int_{\partial\omega} \mathsf{T}\boldsymbol{n} \, \mathsf{d}s. \tag{A.36}$$

Applying the same reasoning formulas (A.34a) and (A.34b) transform into

$$\int_{\omega_1 \cup \omega_2} \nabla \boldsymbol{U} \, \mathsf{d}v + \int_{\sigma} [\![\boldsymbol{U}]\!] \otimes \boldsymbol{n}_{\sigma} \, \mathsf{d}s = \int_{\partial\omega} \boldsymbol{U} \otimes \boldsymbol{n} \, \mathsf{d}s, \tag{A.37a}$$

$$\int_{\omega_1 \cup \omega_2} \boldsymbol{\nabla} f \, \mathsf{d}v + \int_{\sigma} [\![f]\!] \boldsymbol{n}_{\sigma} \, \mathsf{d}s = \int_{\partial\omega} f\boldsymbol{n} \, \mathsf{d}s. \tag{A.37b}$$

Appendix B

Properties of the Rankine-Hugoniot equations

The purpose of this appendix is to recall some useful properties of the solution of the one-dimensional Rankine-Hugoniot relations.

B.1 Notation

The Rankine-Hugoniot equations for one-dimensional Lagrangian gas dynamics write as

$$\begin{aligned} &M[\![\frac{1}{\rho}]\!] + [\![u]\!] = 0, \\ &M[\![u]\!] - [\![P]\!] = 0, \\ &M[\![E]\!] - [\![Pu]\!] = 0, \\ &-M[\![\eta]\!] > 0. \end{aligned}$$

These equations, which have been derived in Section 2.3.4, govern the jumps of the fluid variables at a discontinuity surface. Here, the jump of a fluid variable, f, is denoted by $[\![f]\!]$ and corresponds to the difference of the one-sided limits of f on both sides of the discontinuity surface, *i.e.*, $[\![f]\!] = f_2 - f_1$. Let us assume that the mass swept by the discontinuity surface, M, is positive. This particular case corresponds to a rightward shock wave. Now, instead of denoting by subscripts 1 and 2 the one-sided limits on both sides of the shock wave, we only use the subscript 0 to label the one-sided limit located on the right side of the discontinuity. In addition, it will be convenient to denote the specific volume, $\frac{1}{\rho}$, by τ. With this notation Rankine-Hugoniot relations recast as

$$M(\tau - \tau_0) + u - u_0 = 0, \tag{B.1a}$$

$$M(u - u_0) - (P - P_0) = 0, \tag{B.1b}$$

$$M(E - E_0) - (Pu - P_0 u_0) = 0, \tag{B.1c}$$

$$\eta - \eta_0 > 0. \tag{B.1d}$$

Equations (B.1a)-(B.1c) state respectively mass, momentum and total energy conservation across the shock wave. Last equation follows from the Second Law of thermodynamics and states that the specific entropy of a fluid particle crossing the shock wave is always increasing. The thermodynamic closure of the above system is given by the equation of state $P = P(\tau, \varepsilon)$ where $\epsilon = E - \frac{1}{2}u^2$ is the specific internal energy.

B.2 Study of the Hugoniot curve

In this section we aim at studying the thermodynamics properties of a shock wave following the approach developed in [168]. To do so, it is useful to determine the jump relation undergone by specific internal energy. This jump relation is obtained in two steps. First multiplying (B.1b) by $\frac{1}{2}(u+u_0)$ yields the specific kinetic energy jump relation

$$M\frac{1}{2}(u^2-u_0^2)-\frac{1}{2}(u+u_0)(P-P_0)=0.$$

Second, subtracting this last equation from (B.1d) and substituting (B.1a) leads to

$$\varepsilon-\varepsilon_0+\frac{1}{2}(P+P_0)(\tau-\tau_0)=0. \tag{B.2}$$

This determines all the possible thermodynamic states (τ,P) which may be reached across a shock wave from an initial state (τ_0,P_0). Being given an equation of state, (B.2) determines a curve in the thermodynamic plane (τ,P) known as the Hugoniot curve. Eliminating the velocity jump between (B.1a) and (B.1b) provides the useful relation

$$M^2=-\frac{P-P_0}{\tau-\tau_0}. \tag{B.3}$$

This relation determines a straight line in the thermodynamic plane (τ,P) named the Rayleigh line. We also remark that (B.3) implies that along the Hugoniot curve, the pressure, P, is monotonically decreasing in τ. To investigate the behavior of the thermodynamic variables through a shock wave, we shall compute entropy variation along the Hugoniot curve. According to the fundamental Gibbs relation entropy variation writes as

$$T\mathsf{d}\eta=\mathsf{d}\varepsilon+P\mathsf{d}\tau, \tag{B.4}$$

where T denotes the temperature, which is a positive variable. Differentiating Hugoniot equation yields

$$\mathsf{d}\varepsilon+\frac{1}{2}(\tau-\tau_0)\mathsf{d}P+\frac{1}{2}(P+P_0)\mathsf{d}\tau=0.$$

Combining this equation with Gibbs relation leads to

$$T\mathsf{d}\eta=\frac{1}{2}(\tau-\tau_0)\left[\frac{P-P_0}{\tau-\tau_0}-\frac{dP}{d\tau}\right]\mathsf{d}\tau. \tag{B.5}$$

We assume that the thermodynamic variables are sufficiently smooth to allow a Taylor expansion of the term between brackets in the right-hand side in the vicinity of the origin (τ_0,P_0). Performing this Taylor expansion up to third-order terms yields

$$T\mathsf{d}\eta=-\frac{1}{4}(\tau-\tau_0)^2\frac{d^2P}{d\tau^2}(\tau_0)\mathsf{d}\tau+O((\tau-\tau_0)^3). \tag{B.6}$$

At this point, we make the fundamental assumption that the equation of state is such that the Hugoniot curve is convex, *i.e.* $\frac{d^2P}{d\tau^2}>0$. In addition, we recall that a shock wave is an irreversible process across which entropy is always increasing according to the Second Law of thermodynamics, that is, $T\mathsf{d}\eta\geq 0$. Therefore, (B.6) implies that $\mathsf{d}\tau\leq 0$, that is the specific volume decreases across a shock wave. Since along Hugoniot curve, pressure is decreasing in τ, this also implies that the pressure increases across the shock. **We conclude by saying that for a material characterized by a convex Hugoniot curve, shock wave satisfying**

the Second Law of thermodynamics are compressive shock wave. This result has been obtained for an arbitrary equation of state under the assumption of a weak shock wave. Integrating (B.6) along Hugoniot curve yields

$$\int_{\tau_0}^{\tau_f} T\mathrm{d}\,\eta = -\frac{1}{12}(\tau_f-\tau_0)^3\frac{d^2P}{d\tau^2}(\tau_0)+O((\tau_f-\tau_0)^4),$$

where τ_f is a final state such that $\frac{\tau_0-\tau_f}{\tau_0}\ll 1$. Applying the mean value formula to the integral in the left-hand side leads to

$$\tilde{T}(\eta_f-\eta_0) = -\frac{1}{12}(\tau_f-\tau_0)^3\frac{d^2P}{d\tau^2}(\tau_0)+O((\tau_f-\tau_0)^4), \tag{B.7}$$

where $\tilde{T}$ is some intermediate temperature between T_0 and T_f. This equation states that the entropy jump in the vicinity of the origin (τ_0, P_0) of the Hugoniot curve is cubic with respect to the specific volume jump.

We conclude this paragraph by giving the analytical expression of the Hugoniot curve for an ideal gas equation of state, *i.e.*, $P=(\gamma-1)\frac{\varepsilon}{\tau}$. Substituting the equation of state into (B.2) leads to

$$P = P_0\frac{(\gamma+1)\tau_0-(\gamma-1)\tau}{(\gamma+1)\tau-(\gamma-1)\tau_0}. \tag{B.8}$$

Let us point out that this curve admits a vertical asymptote at $\tau=\tau_0\frac{\gamma-1}{\gamma+1}$ at which the pressure becomes infinite and a horizontal one at $P=-P_0\frac{\gamma-1}{\gamma+1}$, refer to Fig. B.1. Alternatively, we can express the specific volume as function of the pressure by inverting the above equation

$$\tau = \tau_0\frac{(\gamma+1)P_0+(\gamma-1)P}{(\gamma+1)P+(\gamma-1)P_0}. \tag{B.9}$$

Passing to the limit $\frac{P}{P_0}\to+\infty$ in the above equation yields $\frac{\tau}{\tau_0}\to\frac{\gamma-1}{\gamma+1}$. This shows that for an infinite strength shock wave, the ratio of density reaches the limit value $\frac{\gamma+1}{\gamma-1}$.

B.3 Pressure jump across a shock wave for an ideal gas

Combining Hugoniot equation (B.9) and (B.3), we express the mass flux swept by the shock in terms of the pressures P and P_0 as

$$M^2 = \frac{\rho_0}{2}[(\gamma+1)P+(\gamma-1)P_0]. \tag{B.10}$$

Introducing the pressure jump $[\![P]\!]=P-P_0$ in the above equation, it rewrites as

$$M^2 = \frac{\gamma+1}{2}\rho_0[\![P]\!]+\rho_0^2c_0^2$$

, where $c_0=\sqrt{\frac{\gamma P_0}{\rho_0}}$ denotes the sound speed. Substituting the latter expression into (B.1b) yields the following quadratic equation in pressure jump

$$[\![P]\!]^2-\frac{\gamma+1}{2}\rho_0[\![u]\!]^2[\![P]\!]-\rho_0^2c_0^2[\![u]\!]^2=0. \tag{B.11}$$

Since its discriminant is positive, it admits two solutions. The relevant physical solution writes

$$[\![P]\!] = \rho_0\left[\frac{\gamma+1}{4}[\![u]\!]+\sqrt{(\frac{\gamma+1}{4})^2[\![u]\!]^2+c_0^2}\right][\![u]\!]. \tag{B.12}$$

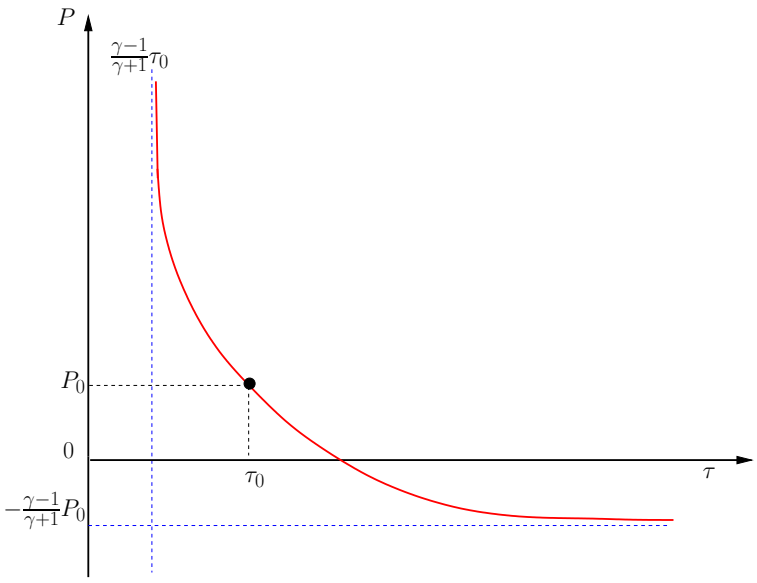

Figure B.1: Hugoniot curve for an ideal gas. Vertical and horizontal asymptotes are plotted in blue.

Let us point out that for infinite strength shock wave, pressure jump tends to $[\![P]\!] \sim \rho_0 \frac{\gamma+1}{2} [\![u]\!]^2$, that is pressure jump is quadratic in velocity jump. In the case of weak shock wave, pressure jump tends to $[\![P]\!] \sim \rho_0 [\![u]\!] c_0$, that is pressure jump is linear in velocity jump. We conclude by writing the expressions of the mass flux swept by the shock wave and its velocity W.

$$M = \rho_0 \left[\frac{\gamma+1}{4} [\![u]\!] + \sqrt{(\frac{\gamma+1}{4})^2 [\![u]\!]^2 + c_0^2} \right], \tag{B.13a}$$

$$W = \frac{\gamma+1}{4} [\![u]\!] + \sqrt{(\frac{\gamma+1}{4})^2 [\![u]\!]^2 + c_0^2}. \tag{B.13b}$$

Bibliography

[1] I. Aavatsmark. An introduction to multipoint flux approximations for quadrilateral grids. *Computational Geosciences*, 6:405–432, 2002.

[2] I. Aavatsmark, T. Barkve, O. Boe, and T. Mannseth. Discretization on unstructured grids for inhomogeneous, anistropic media. Part I: derivation of the methods. *SIAM J. Sci. Comput.*, 19:1700–1716, 1998.

[3] I. Aavatsmark, T. Barkve, O. Boe, and T. Mannseth. Discretization on unstructured grids for inhomogeneous, anistropic media. Part II: discussion and numerical results. *SIAM J. Sci. Comput.*, 19:1717–1736, 1998.

[4] I. Aavatsmark, G. T. Eigestad, and R. A. Klausen. *Numerical convergence of the MPFA O-method for general quadrilateral grids in two and three dimensions.* In Compatible spatial discretizations, D. N. Arnold, P. B. Bochev, R. B. Lehoucq, R. A. Nicolaides and M. Shashkov (Editors)IMA Vol. Ser., Springer, 2006.

[5] I. Aavvatsmark, G.T. Eigestad, R.A. Klausen, M.F. Wheeler, and I. Yotov. Convergence of a symmetric MPFA method on quadrilateral grids. Technical Report TR-MATH 05-14, University of Pittsburgh, 2005.

[6] R. Abgrall, R. Loubère, and J. Ovadia. A Lagrangian Discontinuous Galerkin-type method on unstructured meshes to solve hydrodynamics problems. *Int. J. Numer. Meth. Fluids*, 44:645–663, 2004.

[7] F. L. Adessio, J R Baumgardner, J. K. Dukowicz, N. L. Johnson, B. A. Kashiwa, R. M. Rauenzahn, and C. Zemach. Caveat: a computer code for fluid dynamics problems with large distortion and internal slip. Technical Report LA-10613-MS, Rev. 1, UC-905, Los Alamos National Laboratory, 1992.

[8] F. L. Adessio, D. E. Carroll, J. K. Dukowicz, N. L. Johnson, B. A. Kashiwa, M. E. Maltrud, and H. M. Ruppel. Caveat: a computer code for fluid dynamics problems with large distortion and internal slip. Technical Report LA-10613-MS, Los Alamos National Laboratory, 1986.

[9] S. Atzeni. The physical basis for numerical fluid simulations in laser fusion. *Plasma Phys. Control. Fusion*, 29:1535–1604, 1987.

[10] S. Atzeni, J.-R. Davies, L. Hallo, J.J. Honrubia, P.-H. Maire, M. Olazabal-Loumé, J.-L. Feugeas, X. Ribeyre, A. Schiavi, G. Schurtz, J. Breil, and Ph. Nicolaï. Studies on targets for inertial fusion ignition demonstration at the hiper facility. *Nucl. Fusion*, 49, 2009.

[11] S. Atzeni and J. Meyer-Ter-Vehn. *The physics of inertial fusion.* Oxford Science publications, Oxford University Press, 2004.

[12] A. Barlow. A cell centred lagrangian godunov scheme for shock hydrodynamics. *Computers and Fluids*, 2010. doi:10.1016/j.compfluid.2010.07.017.

[13] A. Barlow, D. Burton, and M. Shashkov. Compatible, Energy and Symmetry Preserving 2D Lagrangian Hydrodynamics in rz-Cylindrical Coordinates. *Procedia Computer Science*, 1:1887–1895, 2010.

[14] A.J. Barlow. A compatible finite element multi-material ALE hydrodynamics algorithm. *Int. J. Numer. Meth. Fluids*, 56(8):953–964, 2008.

[15] T. J. Barth. Numerical methods for conservation laws on structured and unstructured meshes. Technical report, VKI Lecture Series, 2003.

[16] T. J. Barth and D. C. Jespersen. The design and application of upwind schemes on unstructured meshes. In *AIAA paper 89-0366*, 27th Aerospace Sciences Meeting, Reno, Nevada, 1989.

[17] A.L. Bauer, D.E. Burton, E.J. Caramana, R. Loubère, M.J. Shashkov, and P.P Whalen. The internal consistency, stability, and accuracy of the discrete compatible formulation of Lagrangian hydrodynamics. *J. Comp. Phys.*, 218:572–593, 2006.

[18] M. Ben-Artzi and A. Birman. Application of the "Generalized Riemann Problem" method to 1-D compressible flows. *J. Comp. Phys.*, 65:170–178, 1986.

[19] M. Ben-Artzi and J. Falcovitz. A second-order Godunov-type scheme for compressible fluid dynamics. *J. Comp. Phys.*, 55(1):1–32, 1984.

[20] M. Ben-Artzi and J. Falcovitz. An upwind second-order scheme for compressible duct flows. *SIAM J. Sci. Stat. Comput.*, 7(3):744–768, 1986.

[21] M. Ben-Artzi and J. Falcovitz. *Generalized Riemann problems in Computational Fluids Dynamics*. Cambridge University press, 2003.

[22] M. Ben-Artzi, J. Li, and G. Warnecke. A direct Eulerian GRP scheme for compressible fluid flows. *J. Comp. Phys.*, 218:19–43, 2006.

[23] D. J. Benson. Computational methods in Lagrangian and Eulerian hydrocodes. *Comput. Methods Appl. Mech. and Engrg.*, 99:235–394, 1992.

[24] J. Botsis and M. Deville. *Mécanique des milieux continus*. Presses Polytechniques et Universitaires Romandes, 2006.

[25] A. F. Bower. *Applied Mechanics of Solids*. CRC Press, 2010.

[26] S.I. Braginskii. Transport Process in a Plasma. In *Reviews of Plasma Physics*, volume I, pages 205–311. Consultants Bureau, New York, 1965.

[27] J. Breil, L. Hallo, P.-H. Maire, and M. Olazabal-Loumé. Hydrodynamic instabilities in axisymmetric geometry self-similar models and numerical simulations. *Laser and Particle Beams*, 23:155–160, 2005.

[28] J. Breil and P.-H. Maire. A cell-centered diffusion scheme on two-dimensional unstructured meshes. *J. Comp. Phys.*, 224(2):785–823, 2007.

[29] J. Breil, P.-H. Maire, Ph. Nicolaï, and G. Schurtz. Modelling of the magnetic field effects in hydrodynamic codes using a second order tensorial diffusion scheme. In *Journal of Physics: Conference Series*, volume 112. The fifth International Conference on Inertial Fusion Sciences and Applications (IFSA 2007), IOP Publishing, 2008. available at `http://iopscience.iop.org/1742-6596/112/2/022035`.

[30] A. Burbeau-Augoula. A Node-Centered Artificial Viscosity Method for Two-Dimensional Lagrangian Hydrodynamics Calculations on a Staggered Grid. *Commun. Comput. Phys.*, 8:877–900, 2009.

[31] D.E. Burton. Multidimensional Discretization of Conservation Laws for Unstructured Polyhedral Grids. Technical Report UCRL-JC-118306, Lawrence Livermore National Laboratory, 1994.

[32] J.C. Campbell and M.J. Shashkov. A tensor artificial viscosity using a mimetic finite difference algorithm. *J. Comp. Phys.*, 172(4):739–765, 2001.

[33] J.C. Campbell and M.J. Shashkov. A compatible Lagrangian hydrodynamics algorithm for unstructured grids. *Selçuk J. Appl. Math.*, 4(2):53–70, 2003.

[34] E. J. Caramana, M. J. Shashkov, and P. P. Whalen. Formulations of artificial viscosity for multidimensional shock wave computations. *J. Comp. Phys.*, 144:70–97, 1998.

[35] E.J. Caramana, D.E. Burton, M.J. Shashkov, and P.P. Whalen. The construction of compatible hydrodynamics algorithms utilizing conservation of total energy. *J. Comput. Phys.*, 146:227–262, 1998.

[36] E.J. Caramana and M.J. Shashkov. Elimination of artificial grid distorsion and hourglass–type motions by means of Lagrangian subzonal masses and pressures. *J. Comp. Phys.*, 142:521–561, 1998.

[37] E.J. Caramana and P.P Whalen. Numerical preservation of symmetry properties of continuum problems. *J. Comput. Phys.*, 141:174–198, 1998.

[38] G. Carré, S. Delpino, B. Després, and E. Labourasse. A cell-centered Lagrangian hydrodynamics scheme in arbitrary dimension. *J. Comp. Phys.*, 228(14):5160–5183, 2009.

[39] C.E. Castro and E.F. Toro. Solvers for the high-order Riemann problem for hyperbolic balance laws. *J. Comp. Phys.*, 227:2481–2513, 2008.

[40] R. Chéret. *Détonique des Explosifs Condensés*, volume I. Masson, 1988.

[41] B. D. Coleman and W. Noll. The Thermodynamics of Elastic Materials with Heat Conduction and Viscosity. *Arch. Rational Mech. Anal.*, 13(1):167–178, 1963.

[42] P. I. Crumpton, G. J. Shaw, and A. F. Ware. Discretisation and multigrid solution of elliptic equations with mixed derivatives terms and strongly discontinuous coefficients. *J. Comp. Phys.*, 116:343–358, 1995.

[43] R. Dautray and J.-P. Watteau. *La fusion thermonucléaire par laser*, volume II. Eyrolles, 1991.

[44] L. Davison. *Fundamentals of Shock Wave Propagation in Solids*. Springer, 2008.

[45] S.R. de Groot and P. Mazur. *Non-equilibrium thermodynamics*. Dover, 1984.

[46] B. Després. Lagrangian systems of conservation laws. *Numer. Math.*, 89:99–134, 2001.

[47] B. Després. *Lois de Conservation Euleriennes, Lagrangiennes et méthodes numériques.* Springer, 2010.

[48] B. Després. Weak consistency of the cell-centered lagrangian glace scheme on general meshes in any dimension. *Computer Methods in Applied Mechanics and Engineering*, 199:2669–2679, 2010.

[49] B. Després and C. Mazeran. Lagrangian Gas Dynamics in Two Dimensions and Lagrangian systems. *Arch. Rational Mech. Anal.*, 178:327–372, 2005.

[50] V.A. Dobrev, T.E. Ellis, Tz. V. Kolev, and R. N. Rieben. Curvilinear finite elements for Lagrangian hydrodynamics . *Int. J. Numer. Meth. Fluids*, 2010. doi: 10.1002/fld.2366.

[51] J. Donea, A. Huerta, J.-Ph. Ponthot, and A. Rodriguez-Ferran. *Encyclopedia of Computational Mechanics*, chapter 14: Arbitrary Lagrangian-Eulerian methods. John Wiley and Sons, 2004.

[52] R.P. Drake. *High Energy Density Physics.* Springer, 1986.

[53] J. K. Dukowicz. A general, non-iterative Riemann solver for Godunov's method. *J. Comput. Phys.*, 61:119–137, 1984.

[54] J. K. Dukowicz and B. Meltz. Vorticity errors in multidimensional Lagrangian codes. *J. Comp. Phys.*, 99:115–134, 1992.

[55] E.N. Dvorkin and M.B. Goldschmit. *Nonlinear Continua.* Springer, 2005.

[56] M. G. Edwards and C. F. Rogers. Finite volume discretization with imposed flux continuity for the general tensor pressure equation. *Computational Geosciences*, 2:259–290, 1998.

[57] S. Atzeni et al. Studies on targets for inertial fusion ignition demonstration at the HiPER facility. *Nucl. Fusion*, 49(5), 2009.

[58] R. Eymard, T. Gallouët, and R. Herbin. *Finite Volume methods. Handbook of Numerical Analysis.* Elsevier Sciences, 2000.

[59] S. Galera, P.-H. Maire, and J. Breil. A two-dimensional unstructured cell-centered multi-material ale scheme using vof interface reconstruction. *J. Comp. Phys.*, 229:5755–5787, 2010.

[60] G. Gallice. Approximation numérique de systèmes hyperboliques non-linéaires conservatifs ou non-conservatifs. Habilitation à Diriger des Recherches. Université Bordeaux I, 2002.

[61] G. Gallice. Positive and Entropy Stable Godunov-type Schemes for Gas Dynamics and MHD Equations in Lagrangian or Eulerian Coordinates . *Numer. Math.*, 94(4):673–713, 2003.

[62] R.V. Garimella and K. Lipnikov. Solution of the diffusion equation in multi-material domains by sub-division of elements along reconstructed interfaces. *Int. J. Numer. Meth. Fluids*, 2010.

[63] P. Germain. *Mécanique*, volume I. Ellipses, 1986.

[64] W.B. Goad. WAT: A Numerical Method for Two-Dimensional Unsteady Fluid Flow. Technical Report LAMS 2365, Los Alamos National Laboratory, 1960.

[65] E. Godlewski and P.-A. Raviart. *Hyperbolic Systems of Conservation Laws*. Springer Verlag, 2000.

[66] S.K. Godunov, A. Zabrodine, M. Ivanov, A. Kraiko, and G. Prokopov. *Résolution numérique des problèmes multidimensionnels de la dynamique des gaz*. Editions Mir, 1979.

[67] V. Gyrya and K.Lipnikov. High-order mimetic finite difference method for diffusion problems on polygonal meshes. *J. Comp. Phys.*, 227(20):8841–8854, 2008.

[68] L. Hallo, M. Olazabal-Loumé, X. Ribeyre, V. Dréan, G. Schurtz, J.-L. Feugeas, J. Breil, Ph. Nicolaï, and P.-H. Maire. Hydrodynamic and symmetry safety factors of hiper's targets. *Plasma Phys. Control. Fusion*, 51, 2009.

[69] F. Hermeline. A finite volume method for the approximation of diffusion operators on distorded meshes. *J. Comp. Phys.*, 160:481–499, 2000.

[70] F. Hermeline. A finite volume method for approximating 3d diffusion operators on general meshes. *J. Comp. Phys.*, 228(16):5763–5786, 2009.

[71] C.W. Hirt, A. Amsden, and J.L. Cook. An arbitrary Lagrangian–Eulerian computing method for all flow speeds. *J. Comp. Phys.*, 14:227–253, 1974.

[72] W. H. Hui, P. Y. Li, and Z. W. Li. A Unified Coordinate System for Solving the Two-Dimensional Euler Equations. *J. Comp. Phys.*, 153:596–637, 1999.

[73] J. Hyman, J.E. Morel, M. Shashkov, and S. Steinberg. Mimetic finite difference methods for diffusion equations. *Computational Geosciences*, 6:333–352, 2002.

[74] J.R. Kamm and F.X. Timmes. On efficient generation of numerically robust Sedov solutions. Technical Report LA-UR-07-2849, Los Alamos National Laboratory, 2007.

[75] D. S. Kershaw. Differencing of the Diffusion Equation in Lagrangian Hydrodynamic Codes. *J. Comp. Phys.*, 39:375–395, 1981.

[76] R. E. Kidder. Laser-driven compression of hollow shells : power requirements and stability limitations. *Nucl. Fusion*, 1:3–14, 1976.

[77] R. A. Klausen and T. F. Russell. Relationships among some locally conservative discretization methods wich handle discontinuous coefficients. *Computational Geosciences*, 8:341–377, 2004.

[78] Tz.V. Kolev and R.N. Rieben. A tensor artificial viscosity using a finite element approach. *J. Comp. Phys.*, 228(22):8336–8366, 2010.

[79] V. P. Kolgan. Application of the principle of minimizing the derivative to the construction of finite-difference schemes for computing discontinuous solution of gas dynamics. *J. Comp. Phys.*, 2010. doi: 10.1016/j.jcp.2010.12.033.

[80] Y. Kuznetsov, K. Lipnikov, and M. Shashkov. The mimetic finite difference method on polygonal meshes for diffusion-type problems. *Computational Geosciences*, 8:301–324, 2004.

[81] L. Landau and E. Lifchitz. *Mécanique des Fluides*. Mir, 1989.

[82] P. Lascaux. Application de la méthode des éléments finis en hydrodynamique bidimensionnelle utilisant les variables de Lagrange. Technical Report DO 058, CEA-Centre d'Etudes de Limeil, 1972.

[83] P. Lascaux. Application of the Finite Element Method to 2D Lagrangian hydrodynamics. In *Finite element methods in flow problems*, pages 139–152. Proceedings of the International Symposium, Swansea, Wales; 7-11 Jan. 1974., 1974.

[84] P. Lascaux and R. Théodor. *Analyse Numérique matricielle appliquée à l'art de l'ingénieur*, volume II. Dunod, 2000.

[85] P. Lax and B. Wendroff. Systems of conservation laws. *Commun. Pur. Appl. Math.*, 1960.

[86] J. Lemaitre, J.-L. Chaboche, A. Benallal, and R. Desmorat. *Mécanique des matériaux solides*. Dunod, 2009.

[87] E. Lescoute, T. De Rességuier, J.-M. Chevalier, J. Breil, P.-H. Maire, and G. Schurtz. Ejection of spalled layers from laser shock-loaded metals. *J. Appl. Phys.*, 108, 2010.

[88] E. Lescoute, T. De Rességuier, J.-M. Chevalier, J. Breil, P.-H. Maire, and G. Schurtz. Experimental and numerical study of dynamic fragmentation in laser shock-loaded gold and aluminium targets. *Computers Materials and Continua*, 2010.

[89] J. Li and Z. Sun. Remark on the generalized Riemann problem method for compressible fluid flows. *J. Comput. Phys.*, 222:796–808, 2007.

[90] J.D. Lindl. *Inertial Confinement Fusion*. Springer, 1998.

[91] K. Lipnikov, J.E. Morel, and M. Shashkov. Mimetic finite difference methods for diffusion equations on non-othogonal non-conformal meshes. *J. Comp. Phys.*, 199:589–597, 2004.

[92] K. Lipnikov and M. Shashkov. A framework for developing a mimetic tensor artificial viscosity for Lagrangian hydrocodes on arbitrary polygonal meshes. *J. Comp. Phys.*, 229(20):7911–7941, 2010.

[93] K. Lipnikov, M. Shashkov, and D. Svyatskiy. The mimetic finite difference discretization of diffusion problem on unstructured polyhedral meshes. *J. Comp. Phys.*, 211(2):473–491, 2006.

[94] K. Lipnikov, M. Shashkov, D. Svyatskiy, and Yu. Vassilevski. Monotone finite volume schemes for diffusion equations on unstructured triangular and shape-regular polygonal meshes. *J. Comp. Phys.*, 227(1):492–512, 2007.

[95] K. Lipnikov, M. Shashkov, and I. Yotov. Local flux mimetic finite difference methods. Technical Report LA-UR-05-8364, Los Alamos National Laboratory, 2005.

[96] K. Lipnikov, M. Shashkov, and I. Yotov. Local flux mimetic finite difference methods. *Numerische Mathematik*, 112(1):115–152, 2009.

[97] K. Lipnikov, D. Svyatskiy, and Y. Vassilevski. Interpolation-free monotone finite volume method for diffusion equations on polygonal meshes. *J. Comp. Phys.*, 228(3):703–716, 2009.

[98] R. Loubère. *Une Méthode Particulaire Lagrangienne de type Galerkin Discontinu. Application à la Mécanique des Fluides et l'Interaction Laser/Plasma*. PhD thesis, Université Bordeaux I, 2002.

[99] R. Loubère and E.J. Caramana. The force/work differencing of exceptional points in the discrete, compatible formulation of Lagrangian hydrodynamics. *J. Comp. Phys.*, 216:1–18, 2006.

[100] R. Loubère, M. Shashkov, and B. Wendroff. Volume consistency in a staggered Lagrangian hydrodynamics scheme. *J. Comp. Phys.*, 227:3731–3737, 2008.

[101] G. Luttwak and J. Falcovitz. Slope limiting for vectors: a novel vector limiting algorithm. Conference on Numerical methods for multi-material fluid flows; Pavia University on September 21 - 25, 2009. Available at `http://www.eucentre.it/multimat09/media/presentazioni_congresso/luttwak.pdf`.

[102] G. Luttwak and J. Falcovitz. Slope limiting for vectors: A novel vector limiting algorithm. *Int. J. Numer. Meth. Fluids*, 2010. doi: 10.1002/fld.2367.

[103] S. M. Murman M. Berger, M.J. Aftosmis. Analysis of slope limiters on irregular grids. Technical Report NAS-05-007, NAS Technical Report, 2005.

[104] P.-H. Maire. A high-order cell-centered Lagrangian scheme for compressible fluid flows in two-dimensional cylindrical geometry. *J. Comp. Phys.*, 228(18):6882–6915, 2009.

[105] P.-H. Maire. A high-order cell-centered Lagrangian scheme for two-dimensional compressible fluid flows on unstructured meshes. *J. Comp. Phys.*, 228(7):2391–2425, 2009.

[106] P.-H. Maire. A high-order one-step sub-cell force-based discretization for cell-centered lagrangian hydrodynamics on polygonal grids. *Computers and Fluids*, 2010.

[107] P.-H. Maire. A unified sub-cell force-based discretization for cell-centered lagrangian hydrodynamics on polygonal grids. *Int. J. Numer. Meth. Fluids*, 2010.

[108] P.-H. Maire, R. Abgrall, J. Breil, and J. Ovadia. A cell-centered Lagrangian scheme for two-dimensional compressible flow problems. *SIAM J. Sci. Comput.*, 29(4):1781–1824, 2007.

[109] P.-H. Maire and J. Breil. A second-order cell-centered Lagrangian scheme for two-dimensional compressible flow problems. *Int. J. Numer. Meth. Fluids*, 56(8):1417–1423, 2008.

[110] P.-H. Maire, R. Loubère, and P. Vachal. Staggered Lagrangian discretization based on cell-centered Riemann solver and associated hydrodynamics scheme. *Commun. Comput. Phys.*, 2010. accepted.

[111] P.-H. Maire and B. Nkonga. Multi-scale Godunov-type method for cell-centered discrete Lagrangian hydrodynamics. *J. Comp. Phys.*, 228(3):799–821, 2009.

[112] L. Margolin, M. Shashkov, and P. Smolarkiewicz. A discrete operator calculus for finite difference approximations. *Comput. Methods Appl. Mech. Engrg.*, 187:365–383, 2000.

[113] L.G. Margolin and M.J. Shashkov. Using a curvilinear grid to construct symmetry-preserving discretizations for Lagrangian gas dynamics. *J. Comput. Phys.*, 149:389–417, 1999.

[114] L.G. Margolin, M.J. Shashkov, and M.A. Taylor. Symmetry-preserving discretizations for Lagrangian gas dynamics. In P. Neittaanmäaki, T. Tiihonen, and P. Tarvainen, editors, *Proceedings of the 3rd European Conference, Numerical Mathematics and Advanced Applications*, pages 725–732. World Scientific, 2000.

[115] J.E. Marsden and T.J.R. Hughes. *Mathematical Foundations of Elasticity*. Dover, 1994.

[116] C. Mazeran. *Sur la structure mathématique et l'approximation numérique de l'hydrodynamique Lagrangienne bidimensionelle*. PhD thesis, Université Bordeaux I, 2007.

[117] R. Menikoff. Notes on Elastic-Plastic Flow. Technical Report LA-UR-03-0047, Los Alamos National Laboratory, 2003.

[118] J.E. Morel, J.E. Dendy, M.L. Hall, and S.W. White. A Cell-Centered Lagrangian-Mesh Diffusion Differencing Scheme. *J. Comp. Phys.*, 103:286–299, 1992.

[119] J.E. Morel, R. M. Roberts, and M. Shashkov. A local support-operators diffusion discretization scheme for quadrilateral r-z meshes. *J. Comp. Phys.*, 144:17–51, 1998.

[120] G. A. Moses and J. Yuan. Radiation diffusion in DRACO using Kershaw difference scheme. Technical Report UWFDM-1213, Fusion Technology Institute. University of Wisconsin, 2003.

[121] J.D. Moulton, T.M. Austin, M. Shashkov, and J.E. Morel. Mimetic preconditionners for mixed discretizations of the diffusion equation. Available at `http://www.ima.umn.edu/talks/workshops/5-11-15.2004/moulton/moulton.pdf`, LA-UR-01-807, 2004. IMA "Hot Topics" Workshop: Compatible Spatial Discretizations for Partial Differential Equations.

[122] C. D. Munz. On Godunov-type schemes for Lagrangian gas dynamics. *SIAM J. Numer. Anal.*, 31:17–42, 1994.

[123] B. Nkonga. On the conservative and accurate CFD approximations for moving meshes and moving boundaries. *Comput. Methods Appl. Mech. Eng.*, 190(13-14):1801–1825, 2000.

[124] W. F. Noh. Errors for calculations of strong shocks using artificial viscosity and an artificial heat flux. *J. Comp. Phys.*, 72:78–120, 1987.

[125] W. Noll. On the continuity of the solid and fluid states. *J. Rational Mech. Anal.*, 4:3–81, 1955.

[126] S. Del Pino. A curvilinear finite-volume method to solve compressible gas dynamics in semi-Lagrangian coordinates. *Comptes Rendus Mathematique,*, 348(17-18):1027–1032, 2010.

[127] O. Pironneau. *Optimal Shape Design for Elliptic System*. Springer, 1983.

[128] B. J. Plohr and D. H. Sharp. A Conservative Eulerian Formulation of the Equations for Elastic Flows. *Advances in Applied Mathematics*, 9:481–499, 1988.

[129] C. Le Potier. *A finite volume method for the approximation of highly anisotropic diffusion operators on unstructured meshes*. In Finite Volumes for Complex Applications IV, Marrakech, Marocco, 2005.

[130] C. Le Potier. Schéma volumes finis monotone pour des opérateurs de diffusion fortement anisotropes sur des maillages de triangles non structurés. *C.R. Acad. Sci. Paris Ser. I*, 341:787–792, 2005.

[131] C. Le Potier. Schéma volumes finis pour des opérateurs de diffusion fortement anisotropes sur des maillages non structurés. *C.R. Acad. Sci. Paris Ser. I*, 340:921–926, 2005.

[132] W.H. Press, S.A. Teukolsky, W.T. Vetterling, and B.P. Flannery. *Numerical Recipes in Fortran 77*, volume I. Cambridge University Press, 2003. Chapter 2, pp 67–68.

[133] P.A. Raviart and J.M. Thomas. *Introduction à l'analyse numérique des équations aux dérivées partielles*. Masson, 1988.

[134] R.Courant and K. O. Friedrichs. *Supersonic Flow and Shock Waves*, volume I. Interscience Publishers, 1963.

[135] B. Rebourcet. An old scheme adapted to new problems: Kershaw's Finite Differences diffusion scheme adapted to new problems. Workshop on Advanced Methods for the Diffusion Equation on General Meshes; Université Paris 6 on July 5-6, 2010. Available at `http://www.ann.jussieu.fr/~despres/WEB/Talks/Rebourcet.pdf`.

[136] B. Rebourcet. Comments on the filtering of numerical instabilities in Lagrangian hydrocodes. Conference on Numerical methods for multi-material fluid flows; Czech Technical University in Prague on September 10 - 14, 2007. Available at `http://www-troja.fjfi.cvut.cz/~multimat07/presentations/tuesday/Rebourcet_filtering.pdf`.

[137] B. Rebourcet. Some remarks on Kershaw's legacy diffusion scheme. Conference on Numerical methods for multi-material fluid flows; Czech Technical University in Prague on September 10-14, 2007. Available at `http://www-troja.fjfi.cvut.cz/~multimat07/presentations/tuesday/Rebourcet_Kershaw.pdf`.

[138] X. Ribeyre, Ph. Nicolaï, G. Schurtz, M. Olazabal-Loumé, J. Breil, P.-H. Maire, J.-L. Feugeas, L. Hallo, and V.T. Tikhonchuk. Compression phase study of the hiper baseline target. *Plasma Phys. Control. Fusion*, 50, 2008.

[139] R. D. Richtmyer and K. W. Morton. *Difference methods for initial-value problems*. John Wiley, 1967.

[140] R.D. Richtmyer. Taylor instability in shock acceleration of compressible fluids. *Commun. Pure Appl. Math.*, 13:297–319, 1960.

[141] J. Salençon. *Mécanique des milieux continus*, volume I, Concepts généraux. Editions de l'Ecole Polytechnique, 2005.

[142] G. Schurtz. Private communication, 2007.

[143] G. Schurtz, S. Gary, S. Hulin, C. Chenais-Popovics, J-C. Gauthier, F. Thais, J. Breil, F. Durut, J.-L. Feugeas, P.-H. Maire, P. Nicolaï, O. Peyrusse, C. Reverdin, G. Soullié, V. Tikhonchuk, B. Villette, and C. Fourment. Revisiting nonlocal electron-energy transport in inertial-fusion conditions. *Physical Review Letters*, 98(9), 2007.

[144] G. Scovazzi. Stabilized shock hydrodynamics: II. Design and physical interpretation of the SUPG operator for Lagrangian computations. *Comput. Methods Appl. Mech. and Engrg.*, 196:966–978, 2007.

[145] G. Scovazzi, M.A. Christon, T.J.R Hughes, and J.N. Shadid. Stabilized shock hydrodynamics: I. A Lagrangian method. *Comput. Methods Appl. Mech. and Engrg.*, 196:923–966, 2007.

[146] G. Scovazzi and T.J. Hugues. Lecture Notes on Continuum Mechanics on Arbitrary Moving Domains. Technical Report 2007-6312P, Sandia National Laboratories, 2007.

[147] G. Scovazzi, E. Love, and M.J. Shashkov. Multi-scale Lagrangian shock hydrodynamics on Q1/P0 finite elements: Theoretical framework and two-dimensional computations. *Comput. Methods Appl. Mech. and Engrg.*, 197:1056–1079, 2008.

[148] J. Serrin. Mathematical Principles of Classical Fluid Mechanics. In *Handbuch der Physik*, volume VIII, pages 125–263. Springer Verlag, 1959.

[149] M. Shashkov. *Conservative Finite-Difference Methods on General Grids*. CRC Press, 1996.

[150] M. Shashkov and S. Steinberg. Support-Operator Finite-Difference Algorithms for General Elliptic Problems. *J. Comp. Phys.*, 118:131–151, 1995.

[151] M. Shashkov and S. Steinberg. Solving Diffusion Equations with Rough Coefficients in Rough Grids. *J. Comp. Phys.*, 129:383–405, 1996.

[152] Z.J. Shen, G. W. Yuan, J.Y. Yue, and X.Z. Liu. A cell-centered Lagrangian scheme in two-dimensional cylindrical geometry. *Science in China Series A: Mathematics*, 51(8):1479–1494, 2008.

[153] G. A. Sod. A survey of several finite difference methods for systems of non-linear hyperbolic conservation laws. *J. Comp. Phys.*, 27:1–31, 1978.

[154] A.V. Solov'ev and M. Yu. Shashkov. Difference scheme for the Dirichlet particle method in cylindrical coordinates, conserving symmetry of gas-dynamical flow. *Differential Equations*, 24(7):817–823, 1988.

[155] B. Swartz. Good neighborhoods for multidimensional Van Leer limiting. *J. Comp. Phys.*, 154:237–241, 1999.

[156] P. Le Tallec. *Modélisation et calcul des milieux continus*. Editions de l'Ecole Polytechnique, 2009.

[157] J.-M. Thomas and D. Trujillo. Mixed finite volume methods. *International Journal for Numerical Methods in Engineering*, 46:1351–1366, 1999.

[158] V.T. Tikhonchuk and K. Mima. Alternative schemes for the inertial fusion energy. *Fusion Engineering and Design*, 2011. to appear.

[159] B. van Leer. Towards the ultimate conservative difference scheme. v-a second-order sequel to godunov's method. *J. Comput. Phys.*, 32:101–136, 1979.

[160] B. van Leer. A historical oversight: Vladimir P. Kolgan and his high-resolution scheme. *J. Comp. Phys.*, 2010. doi: 10.1016/j.jcp.2010.12.032.

[161] R. S. Varga. *Matrix Iterative Analysis*. Springer Series in Computational Mathematics, 2000. Chapter 3, pp 90–91.

[162] V. Venkatakrishnan. Convergence to steady state solutions of the Euler equations on unstructured grids with limiters. *J. Comp. Phys.*, 118:120–130, 1995.

[163] F. Vilar, P.-H. Maire, and R. Abgrall. Cell-centered discontinuous Galerkin discretizations for two-dimensional scalar conservation laws on unstructured grids and for one-dimensional Lagrangian hydrodynamics. *Computers and Fluids*, 2010.

[164] J. von Neumann and R. D. Richtmyer. A method for the numerical calculations of hydrodynamical shocks. *J. Appl. Phys.*, 21:232–238, 1950.

[165] P. Whalen. Algebraic limitations on two dimensionnal hydrodynamics simulations. *J. Comput. Phys.*, 124:46–54, 1996.

[166] M.L. Wilkins. *Methods in Computational Physics*, volume 3, chapter Calculation of elastic-plastic flows, pages 211–263. Academic Press, 1964.

[167] Y. Yang, Q. Zhang, and D.H. Sharp. Small amplitude theory of Richtmyer-Meshkov instability. *Phys. Fluids*, 6(5):1856–1873, 1994.

[168] Ya. B. Zel'dovich and Yu. P. Raizer. *Physics of Shock Waves and High-Temperature Hydrodynamic Phenomena*, volume I. Academic Press, 1967.

[169] Ya. B. Zel'dovich and Yu. P. Raizer. *Physics of Shock Waves and High-Temperature Hydrodynamic Phenomena*, volume II. Academic Press, 1967.